

# **Catalyst Characterization Science**



ACS SYMPOSIUM SERIES **288**

# **Catalyst Characterization Science**

## **Surface and Solid State Chemistry**

**Marvin L. Deviney, EDITOR**  
*Ashland Chemical Company*

**John L. Gland, EDITOR**  
*Exxon Research & Engineering Company*

Developed from a symposium sponsored by  
the Divisions of Petroleum Chemistry, Inc.  
and Colloid and Surface Chemistry  
at the 188th Meeting  
of the American Chemical Society,  
Philadelphia, Pennsylvania,  
August 26-31, 1984



American Chemical Society, Washington, D.C. 1985



**Library of Congress Cataloging in Publication Data**

Catalyst characterization science.

(ACS symposium series, ISSN 0097-6156; 288)

"Developed from a symposium sponsored by the Divisions of Petroleum Chemistry, Inc. and Colloid and Surface Chemistry at the 188th Meeting of the American Chemical Society, Philadelphia, Pennsylvania, August 26-31, 1984."

Includes bibliographies and indexes.

1. Catalysts—Congresses. 2. Catalysis—Congresses.

I. Deviney, Marvin L., 1929- . II. Gland, John L., 1947- . III. American Chemical Society. Division of Petroleum Chemistry. IV. American Chemical Society. Division of Colloid and Surface Chemistry. V. American Chemical Society. Meeting (188th: 1984: Philadelphia, Pa.) VI. Series.

QD505.C386 1985 541.3'95 85-20081  
ISBN 0-8412-0937-5

Copyright © 1985

American Chemical Society

All Rights Reserved. The appearance of the code at the bottom of the first page of each chapter in this volume indicates the copyright owner's consent that reprographic copies of the chapter may be made for personal or internal use or for the personal or internal use of specific clients. This consent is given on the condition, however, that the copier pay the stated per copy fee through the Copyright Clearance Center, Inc., 27 Congress Street, Salem, MA 01970, for copying beyond that permitted by Sections 107 or 108 of the U.S. Copyright Law. This consent does not extend to copying or transmission by any means—graphic or electronic—for any other purpose, such as for general distribution, for advertising or promotional purposes, for creating a new collective work, for resale, or for information storage and retrieval systems. The copying fee for each chapter is indicated in the code at the bottom of the first page of the chapter.

The citation of trade names and/or names of manufacturers in this publication is not to be construed as an endorsement or as approval by ACS of the commercial products or services referenced herein; nor should the mere reference herein to any drawing, specification, chemical process, or other data be regarded as a license or as a conveyance of any right or permission, to the holder, reader, or any other person or corporation, to manufacture, reproduce, use, or sell any patented invention or copyrighted work that may in any way be related thereto. Registered names, trademarks, etc., used in this publication, even without specific indication thereof, are not to be considered unprotected by law.

PRINTED IN THE UNITED STATES OF AMERICA

American Chemical Society  
Library

1155 16th St., N.W.  
Washington, D.C. 20036

In Catalyst Characterization Science; Deviney, M., et al.;  
ACS Symposium Series; American Chemical Society: Washington, DC, 1985.

# ACS Symposium Series

**M. Joan Comstock, *Series Editor***

## *Advisory Board*

**Robert Baker**  
U.S. Geological Survey

**Martin L. Gorbaty**  
Exxon Research and Engineering Co.

**Roland F. Hirsch**  
U.S. Department of Energy

**Herbert D. Kaesz**  
University of California—Los Angeles

**Rudolph J. Marcus**  
Office of Naval Research

**Vincent D. McGinniss**  
Battelle Columbus Laboratories

**Donald E. Moreland**  
USDA, Agricultural Research Service

**W. H. Norton**  
J. T. Baker Chemical Company

**Robert Ory**  
USDA, Southern Regional  
Research Center

**Geoffrey D. Parfitt**  
Carnegie-Mellon University

**James C. Randall**  
Phillips Petroleum Company

**Charles N. Satterfield**  
Massachusetts Institute of Technology

**W. D. Shults**  
Oak Ridge National Laboratory

**Charles S. Tuesday**  
General Motors Research Laboratory

**Douglas B. Walters**  
National Institute of  
Environmental Health

**C. Grant Willson**  
IBM Research Department

## FOREWORD

The ACS SYMPOSIUM SERIES was founded in 1974 to provide a medium for publishing symposia quickly in book form. The format of the Series parallels that of the continuing ADVANCES IN CHEMISTRY SERIES except that, in order to save time, the papers are not typeset but are reproduced as they are submitted by the authors in camera-ready form. Papers are reviewed under the supervision of the Editors with the assistance of the Series Advisory Board and are selected to maintain the integrity of the symposia; however, verbatim reproductions of previously published papers are not accepted. Both reviews and reports of research are acceptable, because symposia may embrace both types of presentation.

## PREFACE

**A**S THE GROWTH OF INDUSTRIAL heterogeneous catalysis continues to accelerate, the role and contributions of surface scientists and mechanism specialists become increasingly vital. Scientists in these fields are making major efforts to keep pace by developing the fundamental techniques to provide the basic knowledge needed to sustain rapid progress in basic and applied catalysis. Many recent developments in our ability to characterize catalytic materials and reaction mechanisms have resulted in important advances in our understanding of catalytic phenomena. This book highlights a large number of these major new developments in catalyst characterization science, involving both surface and solid state chemistry.

We would like to thank the Colloid and Surface Chemistry Division and the Petroleum Chemistry Division of the American Chemical Society for their support and encouragement. Acknowledgment is also made to the Donors of the Petroleum Research Fund, administered by the American Chemical Society, for partial support of this activity. The encouragement of Ashland Chemical Company, Exxon Research and Engineering Company, and General Motors Research Laboratory is gratefully acknowledged, and special thanks is expressed to James D. Idol, Andrew Kaldor, and John Larson. The excellent cooperation of the many authors and coauthors of the chapters included in this book is sincerely appreciated. Finally, we would like to thank our families, particularly our wives, Marie Deviney and Wanda Gland, for their patience and continuous support.

MARVIN L. DEVINEY  
Ashland Chemical Company  
Columbus, Ohio 43216

JOHN L. GLAND  
Exxon Research & Engineering Company  
Annandale, New Jersey 08801

## Arsenic Poisoning of Hydrodesulfurization Catalysts

Ruth N. Merryfield, Lloyd E. Gardner, and George D. Parks

Phillips Petroleum Company, Bartlesville, OK 74004

X-ray photoelectron spectroscopy (XPS), Mössbauer emission spectroscopy (MES), and activity tests show that arsenic poisons hydrodesulfurization (HDS) catalysts by affecting the chemical nature of the sulfided catalyst. Activity tests show that Co-Mo/ $\text{Al}_2\text{O}_3$  and Mo/ $\text{Al}_2\text{O}_3$  catalysts are deactivated when arsenic is added to the catalyst, either as a contaminant from the reactor feed or as  $\text{As}_2\text{O}_5$  by laboratory impregnation. XPS shows one form of arsenic,  $\text{As}^{+5}$ , on the calcined catalyst and two forms, probably  $\text{As}^{+3}$  and  $\text{As}^0$ , on the sulfided catalyst. XPS also shows sintering of the molybdenum on the sulfided catalyst. We have used MES to study the effect of arsenic on the Co-Mo-S phase (believed to be active for HDS). Arsenic does not destroy this structure, but alters its electronic state. The arsenic appears to be interacting strongly with the cobalt, possibly filling the anion vacancies with atoms or clusters.

Arsenic poisoning of catalysts, particularly reforming and hydrotreating catalysts, is a long standing problem. Interest in shale oil refining emphasized this problem, as shale oils often contain 20-40 ppm arsenic. In this study we have used several methods to clarify the nature of arsenic poisoning on hydrodesulfurization (HDS) catalysts. HDS activity tests were used to determine the extent of poisoning. X-ray photoelectron spectroscopy (XPS), X-ray diffraction (XRD), and Mössbauer emission spectroscopy (MES) have been used to study metals on the catalyst and to identify specific compounds where possible.

Co-Mo/ $\text{Al}_2\text{O}_3$  catalysts have been studied extensively, both for their structure and reaction mechanisms, and many studies have been reported in the literature (1-14). However, the HDS activity is not completely understood and many conflicting views have been reported. No attempt is made here to explain the HDS mechanism,



but only to describe the state of arsenic on these catalysts and its effect on activity.

### Experimental

Catalyst Preparation. Most samples were prepared using a Ketjen alumina (1/16 inch extrudate with 280 m<sup>2</sup>/g surface area and 0.71 ml/g pore volume) and the incipient wetness technique for impregnation. Catalysts were stirred on a hot plate until visibly dry, dried overnight in a 100°C oven, and calcined in air at 500°C for three hours. Ammonium paramolybdate, cobalt nitrate, and arsenic pentoxide solutions were used, with drying and calcining after each addition. Molybdenum was always added first, followed by cobalt where applicable, then the arsenic. On catalysts with high loadings of arsenic, some arsenic was lost during calcination and sulfiding. Catalyst compositions as determined by X-ray fluorescence are given in Table I. Another sample, a Catapal N alumina, was coimpregnated with 9.9% Co and 8.5 % As for use as a reference material.

Table I. Catalyst Composition by X-Ray Fluorescence (Wt. %)

| Catalyst   | Mo  | Co  | As  |
|--|-----|-----|-----|
| Mo/Al <sub>2</sub> O <sub>3</sub>                            | 8.9 |     |     |
| Mo/Al <sub>2</sub> O <sub>3</sub> + As                       | 7.9 |     | 3.6 |
| Co-Mo/Al <sub>2</sub> O <sub>3</sub>                         | 9.6 | 2.4 |     |
| Co-Mo/Al <sub>2</sub> O <sub>3</sub> + As                    | 8.6 | 2.2 | 3.9 |
| Co-Mo/Al <sub>2</sub> O <sub>3</sub> + As<br>(Used Catalyst) | 8.4 | 1.9 | 3.6 |

Arsenic was added to an American Cyanamid HDS-2 catalyst for comparison with a used catalyst containing 3.6% As. This used catalyst was also an American Cyanamid HDS-2 catalyst which had been in service in a refinery distillate HDS unit for about six years. Again, X-ray fluorescence determined compositions are in Table I.

The same Ketjen alumina described earlier was used for the Mössbauer experiments. The samples were prepared identically, with the following exceptions. The extrudate was ground to 20-40 mesh before impregnation, and 0.5 gram samples were prepared using 2 mCi of Co<sup>57</sup>. The samples were prepared to give 8.9% Mo and 1.2% Co (Co/Mo = 0.21). These samples were not analyzed, but the arsenic compositions based on the preparation are given in Table IV.

Catalyst Sulfiding. The calcined samples were sulfided prior to XPS examination by purging the sample at room temperature with nitrogen, heating to 149°C, then switching to 10% H<sub>2</sub>S in hydrogen and raising the temperature gradually over a four hour period to 316°C. After cooling in H<sub>2</sub>S/H<sub>2</sub>, the sample was flushed in nitrogen and placed in a glove box. There it was loaded onto the XPS sample holder and transported to the spectrometer in an air-tight carrier.

Sulfiding for the Mössbauer experiments was similar. All conditions were identical except an 8% H<sub>2</sub>S/H<sub>2</sub> blend was used. Figure

1 shows the reactor used for calcining and sulfiding the radioactive samples. The sample was transferred to the Mössbauer cell without exposure to air and transported to the spectrometer.

Presulfiding for the activity tests was accomplished by first heating the catalyst in nitrogen at 204°C. 10% H<sub>2</sub>S/H<sub>2</sub> was introduced at this temperature and allowed to flow over the catalyst for five hours. The temperature was then raised gradually to 371°C and held for an additional five hours. The catalyst was cooled in nitrogen.

XPS Measurements. XPS measurements were performed using a Physical Electronics Model 548 electron spectrometer with Al K $\alpha$  radiation (1486.6 eV). The spectrometer was interfaced to a Hewlett-Packard 21MX computer for data acquisition and manipulation. The instrument was operated at about  $2 \times 10^{-9}$  torr, with the samples being introduced into the ultrahigh vacuum from a prechamber evacuated to about  $1 \times 10^{-6}$  torr. Binding energies were referenced to Au 4f(7/2) at 84.0 eV. A thin film of gold was evaporated onto the sample after a complete set of spectra had been obtained, and another set of spectra was then taken. On the supported samples, binding energies were referenced to the Al 2s peak at 119.6 eV, as determined by gold referencing. The surface concentrations given in Table III are determined relative to the Al 2s peak as 100 using Scofield's cross sections (15) and the method of calculation described by Carter et al. (16).

Pretreatment of the samples was performed in the prechamber of the spectrometer, except for the sulfiding described previously. Catalysts were calcined in air at 500°C for one hour, or reduced in hydrogen at 310°C or 350°C for up to four hours. The prechamber was then evacuated and the sample introduced into the spectrometer without exposure to the atmosphere.

For the XPS work, reference materials were examined to establish binding energies for the various arsenic oxidation states. Arsenic metal, As<sub>2</sub>O<sub>3</sub>, As<sub>2</sub>S<sub>2</sub>, As<sub>2</sub>S<sub>3</sub>, all from Ventron, and As<sub>2</sub>O<sub>5</sub> from J. T. Baker Chemicals were used. The arsenic metal powder was imbedded in indium foil for examination. An arsenic mirror formed on a reaction flask was also examined.

HDS Activity Measurements. HDS activity measurements were made isothermally in a 3/4 inch i.d. high pressure trickle bed reactor. Catalysts were ground to 20-40 mesh and diluted with alundum (37.5cc alundum to 12.5cc catalyst). After presulfiding, light cycle oil (a cracking product boiling between 177°C and 343°C and containing 1.7 wt % sulfur) was introduced along with hydrogen (7 moles H<sub>2</sub>/mole feed). Most of the sulfur in the oil was present as benzothiophenes and dibenzothiophenes. The reaction was run at 600 psig and 4.0 LHSV. A temperature survey was made from 257°C to 357°C at 14°C intervals over a sixty hour period.

Mössbauer. The Mössbauer emission spectroscopy measurements were made using the Co<sup>57</sup> doped catalyst as a stationary source. The moving absorber was Fe<sup>57</sup> enriched K<sub>4</sub>Fe(CN)<sub>6</sub>·3H<sub>2</sub>O. Both the Co<sup>57</sup> and the absorber were obtained from New England Nuclear. The con-

stant acceleration mode Mössbauer spectrometer was calibrated using a source of  $\text{Co}^{57}$  in palladium and an adsorber of enriched  $\text{Fe}^{57}$  iron foil. The catalyst samples were loaded into a glass cell with a one inch diameter beryllium window. Spectra were accumulated for at least 24 hours and fit by computer for Lorentzian curves using a least squares fit.

### Results and Discussions

**Activity Tests.** Figure 2 shows results of activity tests for a commercial American Cyanamid HDS-2 catalyst which had been in use for about six years. The catalyst was sampled at various depths and results for three samples containing 0.01% As, 0.6% As, and 3.6% As show a decrease in activity with increasing arsenic content. A similar catalyst to which 3.9% arsenic had been added in the laboratory was tested and its activity (Figure 3) compared to the activity of a fresh catalyst and also to that of the used catalyst. The activity loss of the used catalyst containing 3.6% As corresponds closely with that for the prepared sample, indicating that arsenic added by impregnation acts like that deposited under actual operating conditions. When the used catalysts were regenerated in air at  $482^\circ\text{C}$ , the arsenic was not removed.

The molybdenum on alumina catalyst was also tested for activity with and without arsenic. Although this catalyst has a much lower intrinsic activity for HDS, the results in Figure 4 show that 3.6% arsenic almost completely deactivates the catalyst. The small amount of activity remaining is that expected for  $\text{Al}_2\text{O}_3$  alone. Thus arsenic also deactivates catalysts without cobalt promoters.

**XPS.** Several bulk materials and one supported sample were examined by XPS to establish binding energies for the arsenic. These values, given in Table II, correspond closely to those reported in the literature (17-19). The binding energy found for  $\text{As}_2\text{O}_5$  on alumina is comparable to that found on the bulk  $\text{As}_2\text{O}_5$ , indicating that the values for supported arsenic should be similar to those for the bulk materials.

Table II. XPS Binding Energies for Arsenic Reference Materials

|                         | As 3d<br>Be(eV) |  | As 3d<br>Be(eV) |
|-------------------------|-----------------|--|-----------------|
| As metal                | 41.9            | $\text{As}_2\text{S}_2(\text{As}_4\text{S}_4)$ | 42.4            |
| As mirrored on flask    | 41.7            |  |                 |
| $\text{As}_2\text{O}_3$ | 45.2            | $\text{As}_2\text{S}_3$                        | 42.8            |
| $\text{As}_2\text{O}_5$ | 45.6            | $\text{As}_2\text{O}_5/\text{Al}_2\text{O}_3$  | 45.5            |

XPS spectra were obtained for the catalysts in the calcined, sulfided, and sometimes in the reduced state, as described before. Table III gives the binding energies and relative surface concentrations for the  $\text{Mo}/\text{Al}_2\text{O}_3$  and  $\text{Co-Mo}/\text{Al}_2\text{O}_3$  catalysts, with and without arsenic. Data for the used catalysts, which are not listed in the table, are similar to those for the catalysts prepared in the laboratory.

Table III. XPS Results on Prepared Samples

|   | As 3d  |      | Mo3P   |      | Co 2P  |       | S 2P   |      | As Auger |      |
|---|--------|------|--------|------|--------|-------|--------|------|----------|------|
|   | BE(eV) | RSCa | BE(eV) | RSCa | BE(eV) | RSCa  | BE(eV) | RSCa | BE(eV)   | RSCa |
| <u>Mo/Al<sub>2</sub>O<sub>3</sub></u>                     |        |      |        |      |        |       |        |      |          |      |
| Calcined  |        |      | 399.1  | 9.93 |        |       |        |      |          |      |
| Presulfided   |        |      | 399.0  | 1.92 |        |       |        |      |          |      |
|   |        |      | 395.2  | 4.71 |        |       | 162.2  | 11.9 |          |      |
| <u>Mo/Al<sub>2</sub>O<sub>3</sub> + As</u>                |        |      |        |      |        |       |        |      |          |      |
| Calcined  | 45.9   | 4.94 | 399.3  | 6.99 |        |       |        |      | 1217     |      |
| Presulfided   | 44.8   | 1.24 | 398.1  | 1.45 |        |       |        |      | 1218     |      |
|   | 41.9   | 2.16 | 395.3  | 3.22 |        |       | 162.2  | 8.7  | 1224     |      |
| <u>Co-Mo/Al<sub>2</sub>O<sub>3</sub></u>                  |        |      |        |      |        |       |        |      |          |      |
| Calcined  |        |      | 398.9  | 7.15 | 782.5  | 2.29  |        |      |          |      |
| Presulfided   |        |      | 399.3  | 1.72 | 782.2  | {2.21 |        |      |          |      |
|   |        |      | 395.2  | 4.00 | 779.1  |       | 162.2  | 12.5 |          |      |
| <u>Co-Mo/Al<sub>2</sub>O<sub>3</sub> + As</u>             |        |      |        |      |        |       |        |      |          |      |
| Calcined  | 45.1   | 5.44 | 398.8  | 6.04 | 782.3  | 1.96  |        |      | 1218     |      |
| Presulfided   | 44.4   | 1.50 | 398.7  | 1.70 | 782.1  | {1.98 |        |      | 1218     |      |
|   | 42.0   | 2.55 | 394.9  | 3.15 | 779.1  |       | 162.1  | 10.1 | 1225     |      |
| <u>Co-As/Al<sub>2</sub>O<sub>3</sub> (Coprecipitated)</u> |        |      |        |      |        |       |        |      |          |      |
| Dried   | 45.6   | 15.4 |        |      | 782.3  | 17.1  |        |      | 1218     |      |
| Presulfided   | 41.2   | 15.9 |        |      | 777.9  | 16.2  | 161.9  | 12.1 | 1226     |      |
| Reduced   | 44.8   | 4.7  |        |      | 781.7  | {23.2 |        |      | 1218     |      |
|   | 40.9   | 18.9 |        |      | 777.6  |       |        |      | 1226     |      |

a. Relative Surface Concentration, ratioed to Al 2S as 100.

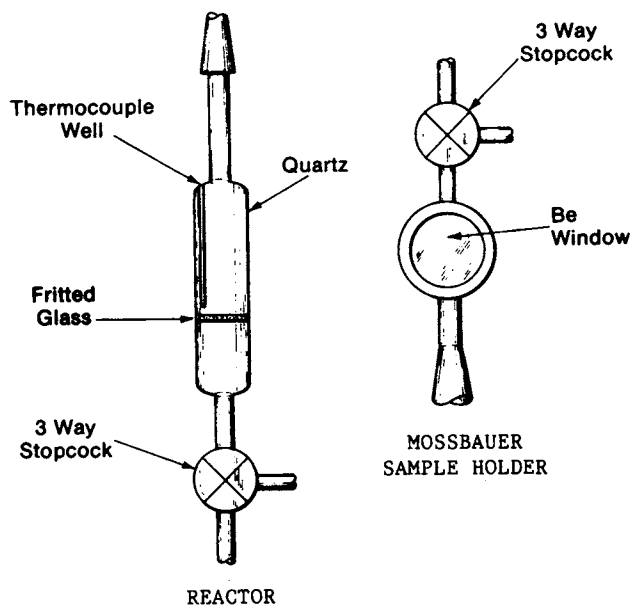


Figure 1. Sample reactor and Mossbauer cell.

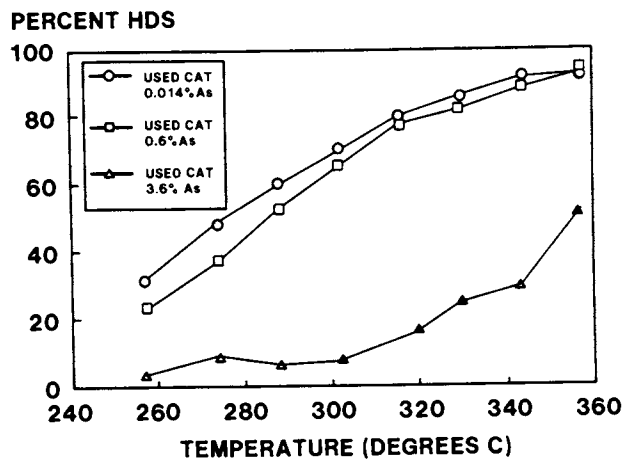


Figure 2. HDS activity of poisoned plant catalysts.

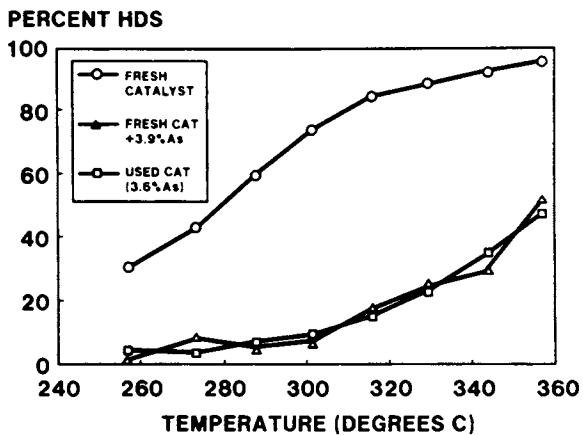


Figure 3. HDS activity of model vs. plant catalysts.

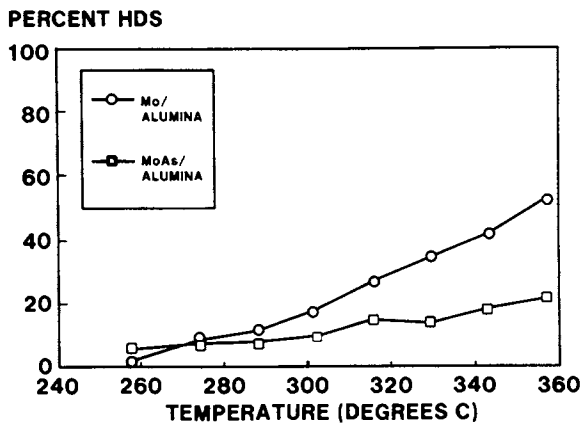


Figure 4. HDS activity of molybdenum catalysts.

Resolution of the Mo 3p peaks showed molybdenum to be present as Mo<sup>+6</sup> for the calcined catalysts, and a mixture of Mo<sup>+6</sup> and Mo<sup>+4</sup> for sulfided catalysts. The Mo 3p peaks were used since both arsenic and sulfur peaks interfere with the Mo 3d doublet. Although some authors have been able to resolve a peak attributed to Mo<sup>+5</sup> on sulfided catalysts (8-9), we were able to resolve our peaks using only two component peaks. Curve resolving consistently showed that about 70% of the molybdenum signal in the sulfided catalysts was due to Mo<sup>+4</sup>.

Table III shows that both cobalt and arsenic affect the Mo/Al ratio as measured by XPS. These elements cause the Mo/Al ratio on both calcined and sulfided catalysts to decrease. Again this is due either to covering of molybdenum by promoters or more likely to some change in molybdenum dispersion induced by the promoters. It is likely that these metals displace molybdenum from surface sites on the alumina, so that they interfere with the strong interaction of the molybdenum and aluminum which keeps the molybdenum well dispersed.

The Mo/Al ratio measured by XPS always decreased upon sulfiding. Bulk analysis showed no change in molybdenum concentration upon sulfiding, indicating that no molybdenum was lost during sulfiding. The drop in intensity can best be explained by assuming that the molybdenum sulfide form is sintering into large clusters. The model of Kerkhof and Moulijn (20) was used to interpret this data. We assumed that all of the Mo<sup>+6</sup> on calcined and sulfided catalysts was present as a well dispersed monolayer. Crystallite sizes were calculated based on the change in Mo/Al ratio upon sulfiding (this method eliminates errors due to inaccuracies in photoionization cross sections). Crystallite sizes ranging from 2nm to 4nm were calculated for the sulfided state. These sizes should be viewed with caution, due to uncertainty in electron mean free paths and dispersion of the oxide species. Incomplete dispersion of Mo<sup>+6</sup> or partial covering of the MoS<sub>2</sub> crystallites by promoter atoms would lead to erroneous results. These crystallite sizes are larger than those proposed by Topsoe et al. (21) based on infrared and EXAFS data. Although the errors mentioned above may affect the absolute size calculated, it does not alter the conclusion that some degree of sintering is occurring on sulfiding.

An interesting effect is noticed if one looks at the relative decrease in the Mo/Al ratio upon sulfiding for each catalyst. When cobalt is present this ratio drops by about 20% after sulfiding (independent of the presence of arsenic). Without cobalt, the ratio is decreased by about 33%. It therefore appears that cobalt helps to lower the amount of sintering which occurs upon sulfiding (although it causes some sintering of the oxidic form of the catalyst). Sulfiding has no effect on XPS Co/Al ratios.

The As 3d peak on calcined catalysts normally appeared as a single peak corresponding to As<sup>+5</sup> (Figure 5). Sulfiding usually gave two peaks, the peak at higher binding energy probably corresponding to As<sup>+3</sup> or an arsenate) which is tied up with the support and difficult to reduce. The peak at lower binding energy corresponds closely to the value for zero valent arsenic. The As/Al ratio decreases when the sample is sulfided. It was found on recalcination of the used catalyst that the As/Al ratio returned to the value

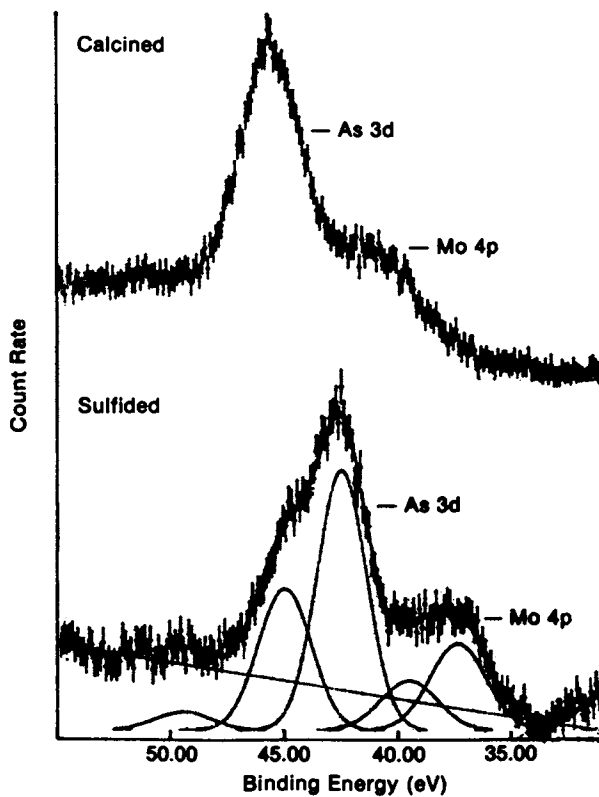


Figure 5. XPS spectra for As on Co-Mo/Al<sub>2</sub>O<sub>3</sub> catalyst.



found on the original calcined sample, implying that sintering was responsible for the lower arsenic signal on the sulfided sample.

The coimpregnated sample with higher levels of cobalt and arsenic on alumina was studied because the concentration of the metals was high enough to give XRD patterns. The only phase identified in other catalysts by XRD was gamma alumina. XRD showed the formation of alloys (CoAs and Co<sub>2</sub>As) when the coprecipitated sample was reduced in hydrogen. However, on sulfiding, XRD gave only a CoAs pattern with broadened and slightly displaced peaks, indicating some distortion of the crystal lattice and a smaller crystallite size. The introduction of sulfur apparently disrupted the alloy formation. XPS results for the coprecipitated catalyst, given in Table III, show a binding energy of 40.9 eV for the As 3d peak on the hydrogen reduced catalyst. A slightly higher value, 41.2 eV, is found for the sulfided sample.

Mössbauer. The radioactive samples, prepared as described above, were examined by MES after calcining and also after presulfiding, both with and without arsenic. Table IV gives the quadrupole splitting,  $\Delta E$ , and the isomer shift,  $\delta$ , measured for the two sets of doublets found in each spectrum. On the sulfided sample, the doublet with the smaller quadrupole splitting corresponds to the Co-Mo-S phase described by Topsoe et al. (11,22,23). The other doublet is assigned to the cobalt in the alumina. As arsenic is added, a decrease is seen in the quadrupole splitting for the Co-Mo-S phase (Figure 6). A decrease in the intensity of the Co:Al<sub>2</sub>O<sub>3</sub> phase is also observed as the arsenic concentration is increased.

Table IV. Mossbauer Parameters for Sulfided Co-Mo/Al<sub>2</sub>O<sub>3</sub> Catalysts.

| g. As Added<br>on 0.5 g Catalyst | Co-Mo-S Doublet |            | Co:Al <sub>2</sub> O <sub>3</sub> Doublet |            |
|----------------------------------|-----------------|------------|---|------------|
|                                  | $\Delta E^a$    | $\delta^b$ | $\Delta E^a$                              | $\delta^b$ |
| 0.000                            | 1.09            | 0.19       | 2.12                                      | 0.89       |
| 0.016                            | 1.02            | 0.21       | 2.22                                      | 0.77       |
| 0.032                            | 0.83            | 0.18       | 2.16                                      | 0.84       |
| 0.048                            | 0.79            | 0.18       | 2.16                                      | 0.82       |

a. Quadrupole splitting, in  $\text{mms}^{-1}$

b. Isomer shift, in  $\text{mms}^{-1}$

Since the structure of the Co-Mo-S phase is not known, it is difficult to propose verifiable explanations for the changes in the Mössbauer spectrum due to arsenic. However, several general observations might be made. The Co-Mo-S phase is not destroyed by arsenic, i.e., the arsenic is not preventing the formation of the phase during sulfiding. The cobalt is not changing oxidation states and the geometry of the cobalt is essentially the same, but a change in electric field at the cobalt nucleus is indicated. This change can be attributed to the presence of the arsenic, apparently interacting strongly with the cobalt, possibly filling the anion vacancies in the Co-Mo-S structure.

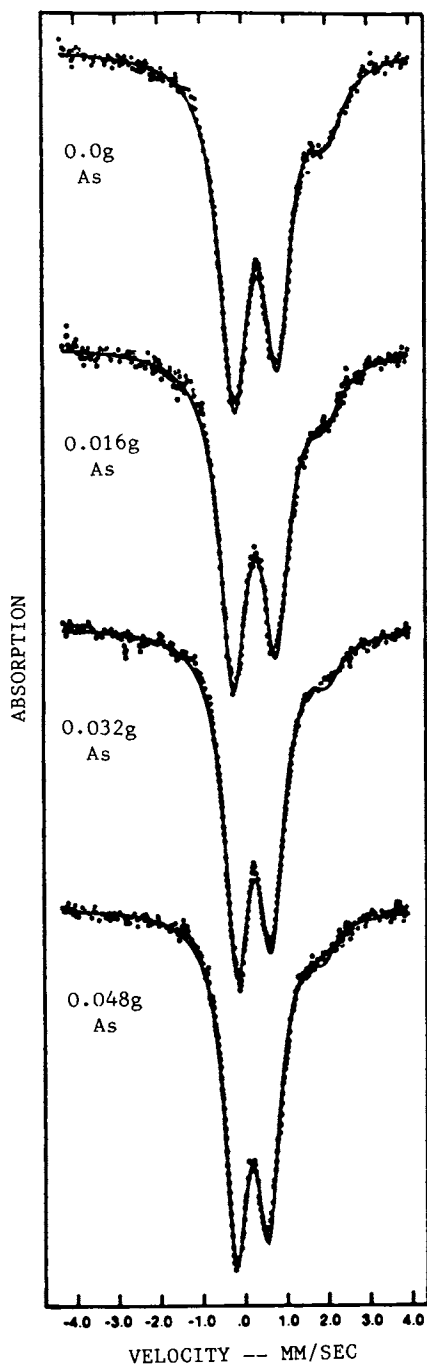


Figure 6. Mössbauer spectra of sulfided catalysts.

### Conclusions

HDS activity tests show conclusively that arsenic poisons the Co-Mo/Al<sub>2</sub>O<sub>3</sub> and the Mo/Al<sub>2</sub>O<sub>3</sub> catalysts. XPS binding energies indicate a zero valent form of arsenic present on the sulfided catalysts (as well as an As<sup>+3</sup> form). When sulfided samples are recalcined, all of the arsenic returns to the oxidized state. Mössbauer spectroscopy indicates that the arsenic is interacting strongly with the cobalt and that while the Co-Mo-S phase still exists, its electronic structure has been altered by the arsenic. These data indicate that the arsenic is altering the electronic structure of the active sites, perhaps by occupying anion vacancies with arsenic atoms or clusters. Similar anion vacancies have been proposed by Valyon and Hall (13) for the unpromoted molybdenum on alumina catalyst. These vacancies could be blocked by arsenic just like those in the promoted catalyst.

### Acknowledgments

The authors wish to acknowledge the following individuals for their assistance in this study: Bill Leroy for carrying out the Mössbauer studies, Ed Farmer for obtaining the XPS spectra, Mike Briggs and Bobby Dodd for conducting the HDS activity tests, and Marvin Johnson, Gary Nowack and Peter Gray for helpful discussions.

### Literature Cited

1. Lipsch, J. M. J. G.; Schuit, G. C. A.; J. Catal., 1969, 15, 163.
2. Friedman, R. M.; Declerck-Grimee, R. I.; Fripiat, J. J.; J. Electron Spectrosc. Relat. Phenom., 1974, 5, 437.
3. Brinen, J. S.; Armstrong, W. D., J. Catal., 1978, 54, 57.
4. Phillips, R. W.; Fote, A. A.; J. Catal., 1976, 41, 168.
5. Walton, R. A., J. Catal., 1976, 44, 335.
6. Delvaux, G.; Grange, P.; Delmon, B.; J. Catal., 1979, 56, 99.
7. Gajardo, P.; Mathieux, A.; Grange, P.; Delmon, B.; Appl. Catal., 1982, 3, 347.
8. Patterson, T. A.; Carver, J. C.; Leyden, D. E.; Hercules, D. M.; J. Phys. Chem., 1976, 80(15), 1700.
9. Okamoto, Y.; Shimokawa, T.; Imanaka, T.; Teranishi, S.; J. Catal., 1979, 57, 153.
10. Gates, B. C.; Katzer, J. R.; Schuit, G. C. A.; "Chem. of Catalytic Processes," McGraw-Hill, Inc., New York, 1979.
11. Topsoe, H.; Clausen, B. S.; Candia, R.; Wivel, C.; Morup, S.; J. Catal., 1981, 68, 433.
12. Chung, K. S.; Massoth, F. E.; J. Catal., 1980, 64, 332.
13. Valyon, J.; Hall, W. K.; J. Catal., 1983, 84, 216.
14. Massoth, F. E.; Muralidhar, G.; Shabtai, J.; J. Catal., 1984, 85, 53.
15. Scofield, J. H., J. Electron Spectrosc. Relat. Phenom., 1976, 8, 129.
16. Carter, W. J.; Schweitzer, G. K.; Carlson, T. A.; J. Electron Spectrosc. Relat. Phenom., 1974, 5, 827.
17. Bahl, M. K.; Woodall, R. O.; Watson, R. L.; Irgolic, K. J.; J. Chem. Phys.; 1976, 64(3), 1210.

18. Taylor, J. A.; J. Vac. Sci. Technol.; 1982, 20(3), 751.
19. Brundle, C. R.; and Seybold, D.; J. Vac. Sci. Technology, 1979, 16(5), 1186.
20. Kerkhof, F. P. J. M.; Moulijn, J. A.; J. Phys. Chem., 1979, 83(12), 1612.
21. Candia, R.; Clausen, B. S.; Bartholdy, J.; Topsoe, N. Y.; Lengeler, B.; Topsoe, H.; Proc. 8th Int. Congr. Catal., 1984, Vol. II, p. 375.
22. Wivel, C.; Candia, R.; Clausen, B.; Morup, S.; Topsoe, H.; J. Catal. 1981, 68, 453.
23. Breyse, M.; Bennett, B. A.; Chadwick, D.; Vrinat, M.; Bull Soc. Chim. Belg., 1981, 90, 1271.

RECEIVED December 6, 1984

## A Pilot Plant Reactor-Surface Analysis System for Catalyst Studies

T. H. Fleisch

Amoco Research Center, Standard Oil Company (Indiana), Naperville, IL 60566

A system has been constructed which allows combined studies of reaction kinetics and catalyst surface properties. Key elements of the system are a computer-controlled pilot plant with a plug flow reactor coupled in series to a minireactor which is connected, via a high vacuum sample transfer system, to a surface analysis instrument equipped with XPS, AES, SAM, and SIMS. When interesting kinetic data are observed, the reaction is stopped and the test sample is transferred from the minireactor to the surface analysis chamber. Unique features and problem areas of this new approach will be discussed. The power of the system will be illustrated with a study of surface chemical changes of a  $\text{CuO}/\text{ZnO}/\text{Al}_2\text{O}_3$  catalyst during activation and methanol synthesis. Metallic Cu was identified by XPS as the only Cu surface site during methanol synthesis.

The development of modern surface characterization techniques has provided means to study the relationship between the chemical activity and the physical or structural properties of a catalyst surface. Experimental work to understand this reactivity/structure relationship has been of two types: fundamental studies on model catalyst systems (1,2) and postmortem analyses of catalysts which have been removed from reactors (3,4). Experimental apparatus for these studies have involved small volume reactors mounted within (1) or appended to (5) vacuum chambers containing analysis instrumentation. Alternately, catalyst samples have been removed from remote reactors via transferable sample mounts (6) or an inert gas glove box (3,4).

Very little research has attempted to relate reaction kinetics to catalyst surface properties as a function of time under actual reactor operating conditions. The goal of the

present design was to couple a pilot plant reactor to a surface analysis instrument in a way which would allow the reaction kinetics of a large catalyst volume to be related to catalyst surface chemical properties as determined by X-ray Photoelectron Spectroscopy (XPS or ESCA) and both Static and Scanning Auger Microscopy (AES/SAM).

### Description of Apparatus

General Description. The major subsystems of the pilot plant/surface analysis system are a computer-controlled pilot plant reactor and a sample introduction transfer system modified to include a minireactor which attaches to a Perkin-Elmer PHI Model 550 ESCA/SAM instrument (Figure 1). For a given experiment, approximately 50 grams of the catalyst of interest are loaded into a plug flow reactor in the pilot plant. A pressed disc of the same catalyst (approximately 0.1 gram) mounted in a special sample holder is inserted into the ESCA/SAM system for surface characterization. The sample holder with catalyst disc is then transferred under high vacuum conditions from the introduction system into the minireactor. A metal/metal seal separates the high pressure reactor side from the high vacuum sample transfer side. After the plug flow reactor, minireactor, and connecting tubing are at operating temperature, reactant gas flow is started. Reaction products are monitored by a gas chromatograph (Figure 1). When an interesting kinetic behavior is observed, the reactant flow is stopped and the catalyst disc is transferred back into the ESCA/SAM system for surface characterization. The cycle of exposure to reaction conditions followed by surface characterization is continued until the experiment is completed.

Pilot Plant. The pilot plant consists of two gas inlet systems, a plug flow reactor, and a gas chromatograph. The plug flow reactor is fabricated from an 86 cm stainless steel tube (3.2 cm O.D. and 2.3 cm I.D.). An Analog Devices MACSYM 2 computer controls pressure, flow rate, and pilot plant reactor and minireactor temperatures. This computer control in conjunction with a number of alarms that trigger reaction shutdown permits unattended operation. Gas chromatographic analysis of reaction products is automated with a gas sampling valve and an HP 5880A level four terminal.

Sample Introduction and Transfer System. The sample introduction and sample transfer system is a lengthened version of the PHI Model 15-720B introduction system which consists of a polymer bellows-covered heating and cooling probe, a transferable sample holder, an eight-port dual-axis cross, and the minireactor interface port and transfer probe (Figure 2). There is also a transfer vessel port with the necessary transfer probe for introduction of air sensitive samples. They are not part of the reactor/surface analysis system. The dual cross and attached hardware are supported by the probe drive mechanism which floats on a block driven vertically and transversely by two micrometers. These micrometers plus the probe drive mechanism allow X-Y-Z

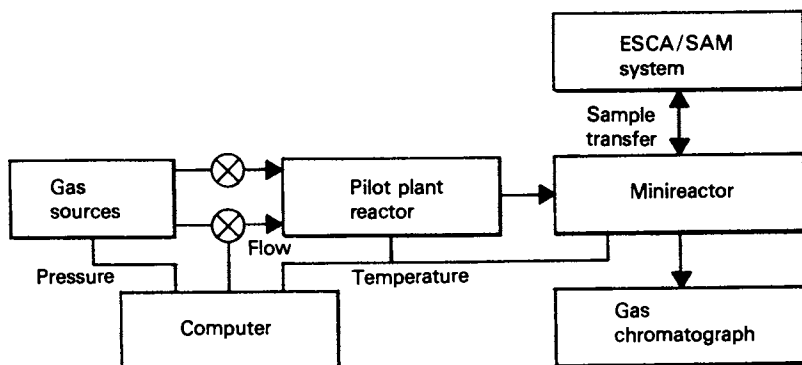


Figure 1. Block diagram showing the subsystems of the combined reactor and surface analysis system.

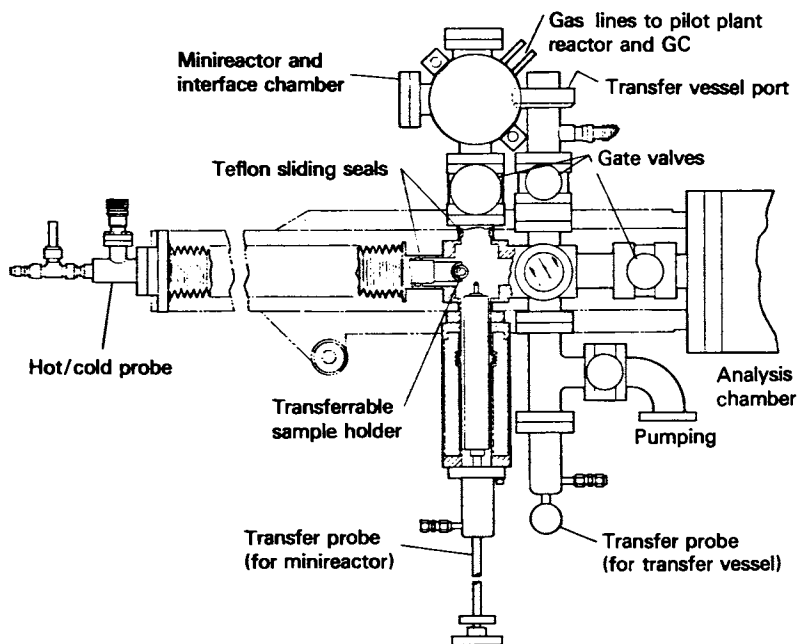


Figure 2. Sample introduction and sample transfer system. (Reproduced with permission from Ref. 7. Copyright 1984, Academic Press.)

sample positioning in the analysis chamber. Pumping for the introduction system is provided by a Balzers Model TSU110 turbomolecular pump backed by a mechanical pump. This latter pump also provides differential pumping for four sets of Teflon sliding seals.

Figure 3 shows an exploded view of the transferable sample holder on which a 1.2 cm diameter pressed catalyst disc is mounted. With the sample holder engaged in the hot/cold probe and the dual cross evacuated, the holder temperature can be varied from  $-170^{\circ}\text{C}$  to  $+650^{\circ}\text{C}$ . When transferring the sample holder from the hot/cold probe, a split pin on the transfer probe is pressed into the hole in the side of the sample holder. The hot/cold probe is then retracted to disengage the holder and provide clearance to move the holder into the interface chamber. By transferring the sample from the hot/cold probe into a reactor rather than reacting the sample while attached to the probe, the sample introduction system can be used very flexibly. Day-to-day analytical work can be performed while long term reaction experiments are in progress.

Reaction Interface and Minireactor. The reaction interface is a five port stainless steel vacuum chamber with the minireactor and sample drive mechanism mounted on the upper and lower 11.4 cm diameter flanges, respectively (Figures 4a,4b). At right angles to the vertical axis are 7 cm diameter ports for sample access, a viewport, and a pumping port plus pressure relief valve. A gate valve separates the reaction interface chamber from the dual cross. In the interface chamber the sample holder is transferred from the transfer probe into a stainless steel cup as shown in Figure 4a.

Vertical motion of the sample holder into the minireactor is provided by a bellows-sealed plate attached to a screw-driven frame. A torque wrench is used to apply a sealing force of 300 pounds to a Sierracin-Harrison type 24105 gold-coated mini-seal which seals the high pressure minireactor from the high vacuum interface chamber (Figure 4b). Helium pressure testing using a UTI 100C quadrupole mass spectrometer showed no detectable helium leakage at 100 psi pressure and a reactor temperature of  $600^{\circ}\text{C}$ .

The minireactor itself is a stainless steel cylinder with a 5.6 cm outside diameter and 2.24 cm inside diameter which is thermally isolated from its 11.4 cm mounting flange by a thin-walled conical section (Figure 4). A gas inlet and outlet port is situated directly above the sample. Six 150 watt cartridge heaters in the minireactor wall provide adequate power to heat the reactor from room temperature to  $600^{\circ}\text{C}$  in 20 minutes. The minireactor temperature is controlled by the MACSYM 2 computer using either of two thermocouples, one embedded in the reactor wall or one in pressure contact with a ledge machined into the sample holder (Figures 3,4). In steady state operation, temperature readings from the two thermocouples agree within  $2^{\circ}\text{C}$ . Operating temperature stability is within  $\pm 1^{\circ}\text{C}$  and the temperature difference between pilot plant reactor and minireactor is always less than  $2^{\circ}\text{C}$ .



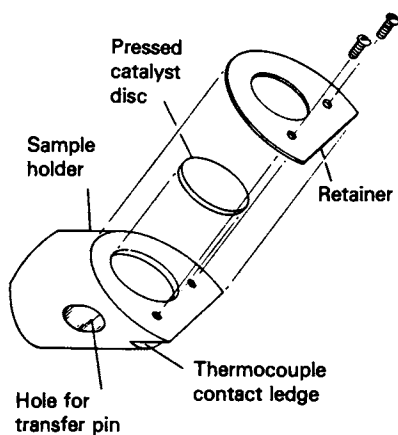


Figure 3. Exploded view of the sample holder and catalyst disc. (Reproduced with permission from Ref. 7. Copyright 1984, Academic Press.)

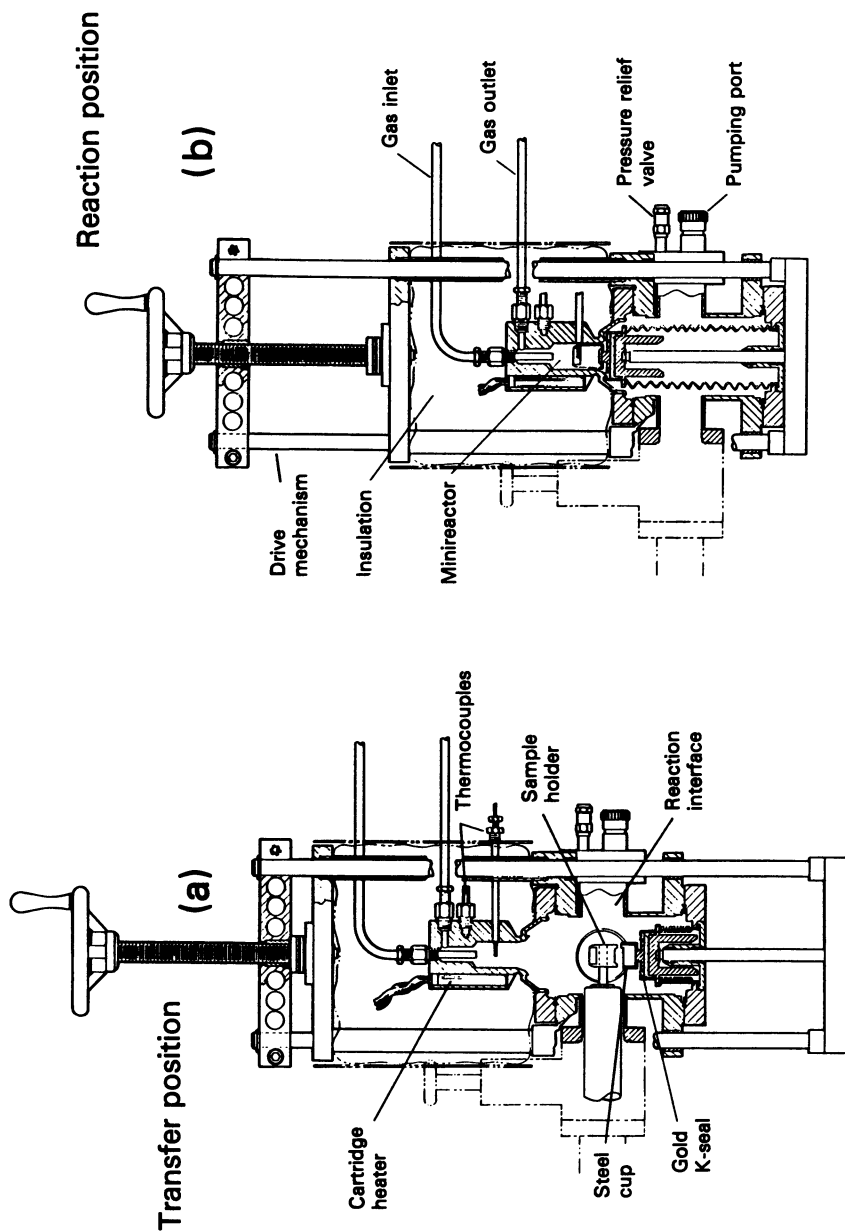


Figure 4. Reaction interface with the sample mechanism retracted for sample transfer (a) and with the sample sealed in the minireactor (b).

### Study of Methanol Synthesis Catalyst

A study of a methanol synthesis catalyst is used to demonstrate the usefulness of the new pilot plant/minireactor/surface analysis system. This work is described in more detail elsewhere (7). Industrial methanol synthesis catalysts are based on  $\text{CuO/ZnO/Al}_2\text{O}_3$  or  $\text{CuO/ZnO/Cr}_2\text{O}_3$  compositions. R. G. Herman et al. (8) studied these catalyst systems in great detail and suggested a Cu+1 solution in ZnO as active phase where Cu+1 non-dissociatively chemisorbs and activates CO and ZnO activates  $\text{H}_2$ . In the range of 15 to 85% CuO in the catalyst, up to 16% Cu+1 became dissolved in the ZnO (9) and Cu+1 has been widely accepted as active site (10). Recently, however, Raney Cu-Zn catalysts have been shown to be very active methanol synthesis catalysts (11). The active component for these Raney catalysts was found to be metallic Cu with an activity maximum at 97 wt% Cu (12).

The catalyst in this study was a commercial catalyst (C18HC, United Catalyst, Inc.) with 42% CuO, 47% ZnO and 10%  $\text{Al}_2\text{O}_3$ . The feed gas consisted of 73%  $\text{H}_2$ , 25% CO and 2%  $\text{CO}_2$ . The chemical state of Cu was studied by XPS (Al K $\alpha$  excitation,  $h\nu=1486.6\text{eV}$ ) using the Cu 2p and Cu ( $\text{L}_3\text{M}_{45}\text{M}_{45}$ ) Auger line. With those two lines Cu+2, Cu+1 and Cu can easily be distinguished employing a so-called chemical state plot (CSP) with the Cu  $2p_{3/2}$  binding energy on the abscissa (decreasing from left to right) and the Cu ( $\text{L}_3\text{M}_{45}\text{M}_{45}$ ) kinetic energy on the ordinate as shown in Figure 5 (13,14). The position of Cu of the untreated catalyst in the CSP (point 1) clearly identifies it as CuO. After synthesis gas conversion at 250°C only metallic Cu is seen on the catalyst surface (point 3). At 100°C, Cu+2 becomes reduced to Cu+1 but no methanol formation is observed. Zinc oxide does not become reduced during methanol synthesis. The small changes in the CSP (Figure 5) are due to drying. Thus, the working catalyst surface is suggested to consist of metallic Cu, ZnO, and  $\text{Al}_2\text{O}_3$ .

Special attention was paid to the detection of residual Cu+1 quantities accompanying the metallic Cu. The relative amounts of Cu+1 and Cu were determined by curve-fitting the Cu (LMM) spectra using the Physical Electronics Version 6 curve-fitting program. The catalyst showed reduction of Cu+2 into a mixture of Cu+1 and Cu after reduction in  $\text{H}_2$  at 250°C for one hour (Figure 6) as evidenced by the two resolved peaks in the Cu (LMM) spectrum at 568.0 and 570.3 eV which are characteristic of Cu and Cu+1, respectively, and by the disappearance of the Cu+2 2p satellite structure. It could be shown that less than 2%, if any, of the total Cu could be present in the +1 oxidation state during methanol formation. However, when the catalyst was briefly exposed to air (1 minute), a few percent of Cu+1 readily formed (7). Thus, any kind of oxidation environment has to be avoided between methanol synthesis and catalyst analysis. Otherwise, appreciable amounts of Cu+1 will be detected.

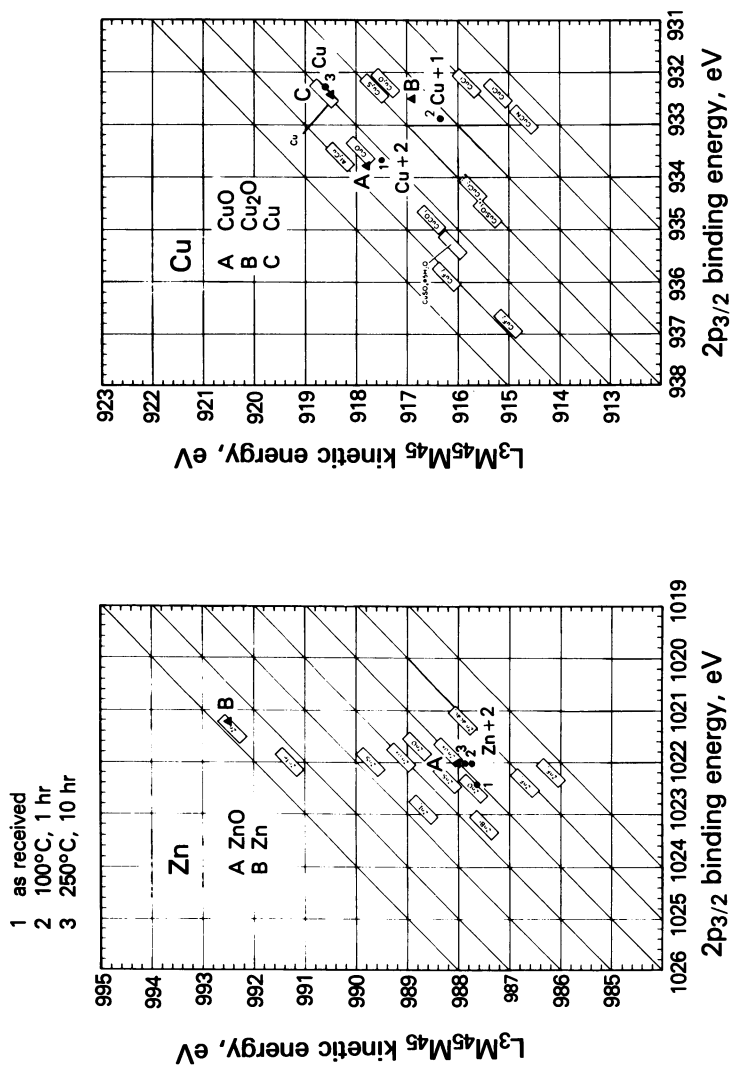


Figure 5. Chemical state changes of Cu and Zn in a commercial CuO/ZnO/Al<sub>2</sub>O<sub>3</sub> catalyst in feed gas (H<sub>2</sub>/CO/CO<sub>2</sub> = 73/25/2, 2 atm).

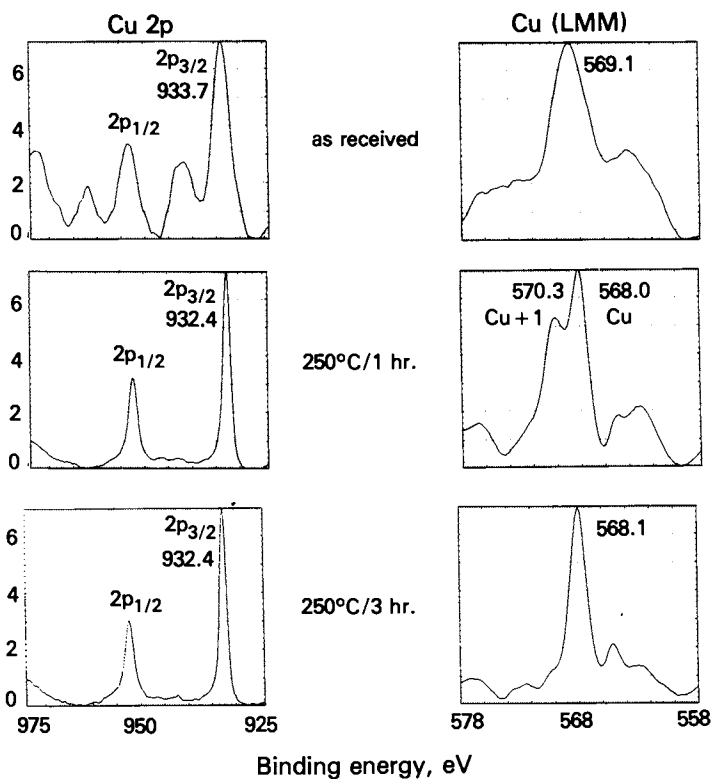


Figure 6. Changes in Cu 2p and Cu(L<sub>3</sub>M<sub>45</sub>M<sub>45</sub>) electron spectra upon in situ reduction in H<sub>2</sub>. (Reproduced with permission from Ref. 7. Copyright 1984, Academic Press.)

### Discussion

Two major questions regarding the applicability of this system remain to be discussed. First, how representative is the catalyst sample in the minireactor of the catalyst in the pilot plant? And second, how does the interruption of the reaction influence kinetic behavior?

The first question can be answered easily. At low conversion and isothermal conditions no significant differences in the catalyst composition as function of catalyst bed position are usually observed. Thus, the surface analysis data from the catalyst in the minireactor should be representative not only of the bottom section but of all the catalyst in the plug flow reactor. In the case of the methanol formation studies reported in this paper, conversion was low (<5%) and isothermal conditions were maintained. However, when reactions are run at high conversion, the analyzed catalyst will closely resemble the catalyst at the bottom of the catalyst bed in the pilot plant since both "see" the same gas composition. If under such conditions catalyst changes at the top of the catalyst bed are to be investigated, the sequence of the pilot plant/minireactor can be reversed with the feed gas first flowing through the minireactor and then through the pilot plant reactor.

Many experiments were performed to answer the question of catalyst property changes due to repeated reaction interruption. Every time the reaction is stopped in the minireactor to analyze the sample, it is necessary to stop the reaction in the pilot plant as well to assure that the catalyst in pilot plant and minireactor maintain identical histories in reaction time. Thus, during some surface analyses of the  $\text{CuO/ZnO/Al}_2\text{O}_3$  catalyst from the minireactor which typically lasted about one hour, the catalyst in the pilot plant reactor was kept at reaction temperature in ultrapure, flowing helium. As soon as the catalyst sample was back in the minireactor and reaction temperature was restored (also in flowing He), feed gas flow was resumed and the reaction continued. It was found that the same activity and methanol selectivity was resumed within a very short period of time alluding to the absence of any irreversible catalyst changes due to the reaction interruption. Cooling the pilot plant reactor to room temperature in flowing He brought about the same behavior as maintaining constant reaction temperature. This latter procedure imitates more closely the temperature changes of the test sample which cools to lower temperatures during transfer and surface analysis. Cooling and reheating in the feed gas itself has to be avoided since this procedure yields ill defined times on-stream at particular reaction temperatures. Therefore, cooling and reheating in He or, more general, in an inert atmosphere is the procedure of choice. It will guarantee the acquisition of reliable kinetic data without influences by the reaction interruptions.

The catalyst surface composition and chemistry remained unchanged for all reaction interruption procedures involved.

Furthermore, identical surfaces were found in postmortem analysis of catalyst samples from the pilot plant reactor and the minireactor. These observations provide assurances that the "working" catalyst surface can be examined with the system described here despite the necessary transfer from high pressure feed gas to ultrahigh vacuum.

### Conclusion

A unique pilot plant/minireactor/surface analysis system has been designed and put into operation. This system represents the closest encounter reported in the literature to date between "real world" catalysis and surface analytical techniques. It allows in depth studies of reaction kinetics and reaction mechanisms and their correlation with catalyst surface properties.

The study of a CuO/ZnO/Al<sub>2</sub>O<sub>3</sub> methanol synthesis catalyst showed the working catalyst surface under our experimental conditions to consist of metallic Cu, ZnO, and Al<sub>2</sub>O<sub>3</sub>. Brief exposure of such catalysts to air results in instant formation of a few percent Cu<sup>+1</sup>. Thus, the use of a combined reaction/analysis system as described here is absolutely essential in surface analytical studies of reactive catalyst surfaces.

### Literature Cited

1. G. A. Somorjai, Catal. Rev., **18**, 173 (1978).
2. H. P. Bonzel, Surf. Sci., **68**, 236 (1977).
3. R. I. Declerk-Grimee, P. Canesson, R. M. Friedman, and J. J. Friplat, J. Phys. Chem., **82**, 885 (1978).
4. J. S. Brinen and W. D. Armstrong, J. Catal., **54**, (1978).
5. T. H. Fleisch, A. Shepard, T. Ridley, W. Vaughn, N. Winograd, W. Baitinger, G. L. Ott, and W. N. Delgass, J. Vac. Sci. Technol., **15**, 1756 (1978).
6. T. A. Patterson, J. C. Carver, D. E. Leyden, and D. M. Hercules, J. Phys. Chem., **80**, 1700 (1976).
7. T. H. Fleisch and R. L. Mieville, J. Catal., **90**, 165 (1984).
8. R. G. Herman, K. Klier, G. W. Simmons, B. P. Finn, J. B. Belko, and T. P. Kobylinski, J. Catal., **56**, 407 (1979).
9. S. Mehta, G. W. Simmons, K. Klier, and R. G. Herman, J. Catal., **57**, 339 (1979).
10. H. H. Kung, Catal. Rev. Sci. Eng. **22**, 235 (1980).
11. W. L. Marsden, M. S. Wainwright and J. B. Friedrich, Ind. Eng. Chem; Prod. Res. Div. **19**, 551 (1980).
12. J. B. Friedrich, M. S. Wainwright, and D. J. Young, J. Catal., **80**, 1 (1983).
13. C. D. Wagner, L. H. Gale, and R. H. Raymond, Anal. Chem., **51**, 466 (1979).
14. T. H. Fleisch and G. J. Mains, Appl. Surf. Sci. **10**, 51 (1982).

RECEIVED December 6, 1984

## Correlation Between Spectroscopic Measurements and Catalytic Behavior of Selective Oxidation Catalysts

J. F. Brazdil, M. Mehicic, L. C. Glaeser, M. A. S. Hazle, and R. K. Grasselli

Sohio Research Center, The Standard Oil Company (Ohio), Cleveland, OH 44128

Direct observations of heterogeneous catalytic processes on a molecular level only became possible with the advent of new spectroscopic techniques and in particular, by utilizing several techniques in concert on a given catalytic process. Combining such spectroscopic investigations with concomitant kinetic investigations provides new insights into the solid state and surface mechanisms of selective olefin oxidation catalysis by mixed metal oxides. The application of multiple techniques including Raman, infrared, XRD, neutron diffraction, and XPS has provided direct evidence of several key aspects of the propylene to acrylonitrile ammoxidation mechanism over bismuth molybdate based catalysts. The mechanistic insights include: 1) direct spectroscopic evidence for solid state disproportionation of the metastable  $\text{Bi}_2\text{Mo}_2\text{O}_9$  phase under redox conditions, 2) identification of key catalytic phases in bismuth-iron molybdate systems, and 3) direct identification of catalytic function of active oxide ions in bismuth molybdate selective olefin oxidation catalysts.

Much of the pioneering work which led to the discovery of efficient catalysts for modern industrial catalytic processes was performed at a time when advanced analytical instrumentation was not available. Insights into catalytic phenomena were achieved through gas adsorption, molecular reaction probes, and macroscopic kinetic measurements. Although Sabatier postulated the existence of unstable reaction intermediates at the turn of this century, it was not until the 1950's that such species were actually observed on solid surfaces by Eischens and co-workers(1) using infrared spectroscopy. Today, scientists have the luxury of using a multitude of sophisticated surface analytical techniques to study catalytic phenomena on a molecular level. Nevertheless, kinetic measurements using chemically specific probe molecules are still the

0097-6156/85/0288-0026\$06.00/0

© 1985 American Chemical Society



mainstay of mechanistic investigations of heterogeneous catalytic processes. It is, however, becoming increasingly apparent that a combination of kinetic and spectroscopic approaches can maximize the useful information about the surface and bulk properties of solid catalysts.

In the case of selective oxidation catalysis, the use of spectroscopy has provided critical information about surface and solid state mechanisms. As is well known(2), some of the most effective catalysts for selective oxidation of olefins are those based on bismuth molybdates. The industrial significance of these catalysts stems from their unique ability to oxidize propylene and ammonia to acrylonitrile at high selectivity. Several key features of the surface mechanism of this catalytic process have recently been described(3-4). However, an understanding of the solid state transformations which occur on the catalyst surface or within the catalyst bulk under reaction conditions can only be deduced indirectly by traditional probe molecule approaches. Direct insights into catalyst dynamics require the use of techniques which can probe the solid directly, preferably under reaction conditions. We have, therefore, examined several catalytically important surface and solid state processes of bismuth molybdate based catalysts using multiple spectroscopic techniques including Raman and infrared spectroscopies, x-ray and neutron diffraction, and photoelectron spectroscopy.

### Experimental

#### Catalyst Preparation

$\text{Bi}_2\text{MoO}_6$  was prepared by the method of Vedrine et al (5).  $\text{Bi}_2(\text{MoO}_4)_3$  and  $\text{Bi}_3\text{FeMo}_2\text{O}_{12}$  were prepared by coprecipitation of bismuth nitrate, ferric nitrate and ammonium molybdate. After drying, the catalysts were heat-treated at 290° and 425°C for 3 hours each. Final calcination at 500°C was 2 hours for  $\text{Bi}_2\text{MoO}_6$  and 3 hours for  $\text{Bi}_2(\text{MoO}_4)_3$  and 610°C for 12 hours for  $\text{Bi}_3\text{FeMo}_2\text{O}_{12}$ . Characterization by both x-ray diffraction and Raman spectroscopy insured that the catalysts were the pure single phases desired.

#### In-Situ Raman Experiments

In-situ Raman experiments were performed on a Spex 1401 double monochromator Raman spectrometer, using a Spectra-Physics Model 165 argon ion laser with an exciting wavelength of 5145 Å. The in-situ Raman cell consists of a quartz tube situated in a temperature controlled heating block. The Raman spectra were collected in the 180° backscattering mode.

Reduction of the catalysts was achieved by passing the reactant gas over the catalyst at elevated temperatures. The time was adjusted to reach the same degree of reduction in each case, and the degree of reduction was checked independently by  $\text{O}_2$  titration. Reoxidation of the catalyst was accomplished by first flushing the system with helium, then introducing oxygen-16 or oxygen-18.

### Kinetic Experiments

A pulse reactor system similar to that described by Brazdil, et al(6) was used to obtain the kinetic data. The reactor was a stainless-steel U-tube, composed of a 1/8" x 6" preheat zone and a 3/8" x 6" reactor zone with a maximum catalyst volume of about 5.0 cm<sup>3</sup>. The reactor was immersed in a temperature controlled molten salt bath.

### Results and Discussion

#### Redox Processes and Solid State Transformations in Bismuth Molybdates

Selective oxidation and ammoxidation of propylene over bismuth molybdate catalysts occur by a redox mechanism whereby lattice oxygen (or isoelectronic NH) is inserted into an allylic intermediate, formed via  $\alpha$ -H abstraction from the olefin. The resulting anion vacancies are eventually filled by lattice oxygen which originates from gaseous oxygen dissociatively chemisorbed at surface sites which are spatially and structurally distinct from the sites of olefin oxidation. Mechanistic details about the reoxidation step are difficult to obtain since it is usually much more rapid than the oxidation of the olefin. Therefore, transient kinetic techniques are required.

Using the pulse microreactor method(6), the general rate expression for reoxidation of bismuth molybdate catalysts was found to be:

$$-d[O_v]/dt_1 = k_{app}[O_v] = k_{reox}[O_2]^{0.5}[O_v]$$

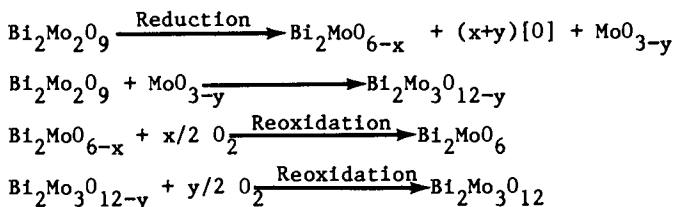
where  $[O_v]$  is the concentration of anion vacancies in the catalyst after reduction with propylene,  $[O_2]$  is the gas phase concentration of oxygen,  $t_1$  is the pulse time, and  $k_{app}$  and  $k_{reox}$  are the apparent and actual reoxidation rate constants, respectively. Examination of the temperature dependence of the reoxidation rate constants indicates the presence of two reoxidation processes (Table I): a low activation energy surface reoxidation process and a higher activation energy process involving reoxidation of anion vacancies in the bulk.

Table I. Activation Energies for Reoxidation (320° to 460°C)

| Catalyst  | Degree of Initial Reduction<br>[[O] x 10 <sup>19</sup> /m] | Activation Energy<br>(kcal/mole) |
|---|--|----------------------------------|
| Bi <sub>2</sub> Mo <sub>3</sub> O <sub>12</sub> | 0.2  | 1.3                              |
|   | 1.4  | 25.9                             |
| Bi <sub>2</sub> Mo <sub>2</sub> O <sub>9</sub>  | 0.1  | 8.1                              |
|   | 0.3  | 9.6                              |
|   | 1.5  | 25.8                             |
| Bi <sub>2</sub> MoO <sub>6</sub>                | 0.2  | 1.2                              |
|   | 1.3  | 7.9                              |

As Table I shows, the  $\text{Bi}_2\text{Mo}_2\text{O}_9$  catalyst exhibits unique redox behavior. Specifically, the similarity in the activation energies for the slightly reduced  $\text{Bi}_2\text{Mo}_2\text{O}_9$  and the more deeply reduced  $\text{Bi}_2\text{MoO}_6$  suggests that similar solid state phases are responsible for reoxidation in both instances. X-ray diffraction of the catalysts after reduction and after reoxidation show only the presence of the pure single phase materials. In order to identify the surface phase composition of the  $\text{Bi}_2\text{Mo}_2\text{O}_9$  under redox conditions, the catalyst was examined using in-situ Raman spectroscopy.

In-situ Raman examination of  $\text{Bi}_2\text{Mo}_2\text{O}_9$  under cyclic redox conditions gives evidence of surface restructuring as shown in Figure 1. It is clear from the spectra that a redox-induced disproportionation occurs. Subjecting the  $\text{Bi}_2\text{Mo}_2\text{O}_9$  phase to reduction and reoxidation results in its disproportionation into  $\text{Bi}_2\text{Mo}_3\text{O}_{12}$  and  $\text{Bi}_2\text{MoO}_6$ . The disproportionation may proceed by the following mechanism.



Based on the kinetic results (Table I), it appears that  $\text{Bi}_2\text{MoO}_6$  is enriched on the surface while  $\text{Bi}_2\text{Mo}_3\text{O}_{12}$  is mainly present in the subsurface layers of the reconstructed material.

Maintaining the sample at elevated temperature results in further decomposition until only  $\text{Bi}_2\text{MoO}_6$  and  $\text{Bi}_2\text{Mo}_3\text{O}_{12}$  phases are observed. Therefore, although  $\text{Bi}_2\text{Mo}_2\text{O}_9$  is meta-stable up to about 500°C(7), it is unstable in the presence of the  $\text{Bi}_2\text{MoO}_6$  and  $\text{Bi}_2\text{Mo}_3\text{O}_{12}$  phases which act as nucleation centers and accelerate the disproportionation. Similar experiments with  $\text{Bi}_2\text{MoO}_6$  and  $\text{Bi}_2\text{Mo}_3\text{O}_{12}$  reveal that they maintain their structural integrity under redox conditions.

Similar disproportionation is likely to occur during catalytic hydrocarbon oxidation since the  $\text{Bi}_2\text{Mo}_2\text{O}_9$  catalyst is subjected to continuous redox cycling under such conditions. Therefore, any kinetic or catalytic information about  $\text{Bi}_2\text{Mo}_2\text{O}_9$  is suspect unless the absence of surface restructuring can be confirmed.

#### Catalytic Behavior and Phase Composition of Bismuth-Iron Molybdates

The structure of the single phase bismuth-iron molybdate compound of composition  $\text{Bi}_3\text{FeMo}_2\text{O}_{12}$  is related to the scheelite structure of  $\text{Bi}_2\text{Mo}_3\text{O}_{12}$ (8). It is reported(6,9) that the catalytic activity and selectivity of bismuth-iron molybdate for propylene oxidation and ammoxidation is not greater than that of bismuth molybdate.

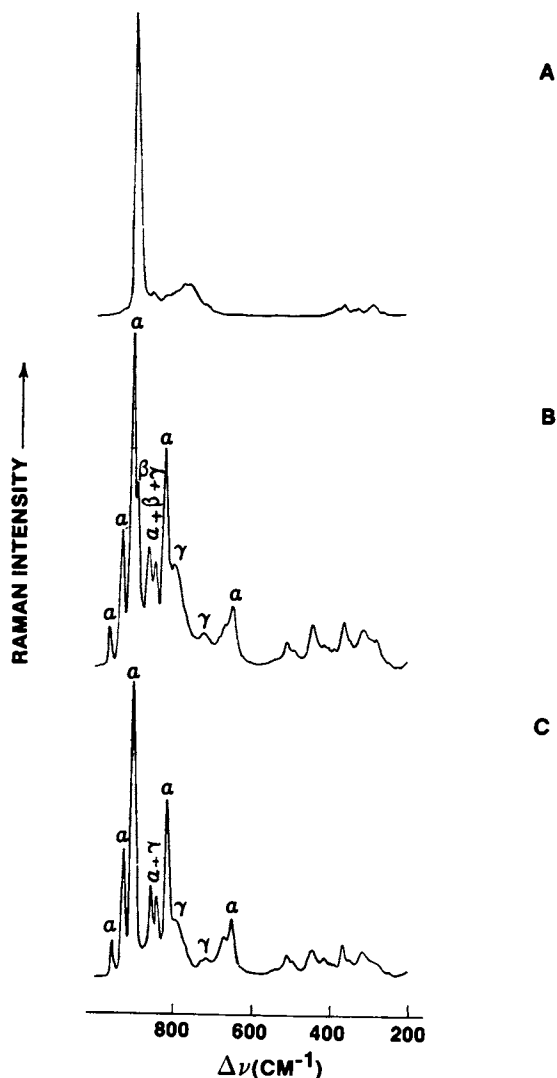


Figure 1. Raman spectra of: (A)  $\text{Bi}_2\text{Mo}_2\text{O}_9$  after  $600^\circ\text{C}$  in air, (B)  $\text{Bi}_2\text{Mo}_2\text{O}_9$  after reduction with propylene and reoxidation with air at  $430^\circ\text{C}$ , and (C) after further reoxidation in air at  $480^\circ\text{C}$ .  $\alpha$  refers to  $\text{Bi}_2\text{Mo}_3\text{O}_{12}$ ,  $\beta$  to  $\text{Bi}_2\text{Mo}_2\text{O}_9$ , and  $\gamma$  to  $\text{Bi}_2\text{MoO}_6$ . Reproduced with permission from Ref. 32. Copyright 1981, The Royal Society of Chemistry.

However, we have found that reaction induced restructuring of  $\text{Bi}_3\text{FeMo}_2\text{O}_{12}$  produces a marked enhancement in catalytic behavior (Table II). X-ray diffraction, *in-situ* Raman spectroscopy, and photoelectron spectroscopy reveal that the restructuring produces a multiphase system consisting of unreacted  $\text{Bi}_3\text{FeMo}_2\text{O}_{12}$ , in combination with  $\text{Bi}_2\text{Mo}_3\text{O}_{12}$ ,  $\beta\text{-FeMoO}_4$  and a small amount of  $\text{Bi}_2\text{Mo}_6\text{O}_{16}$ . The key features of the Raman spectra of the activated catalyst are summarized in Table III.

Table II. Catalytic Activity<sup>a</sup> for Propylene Ammoxidation Over Bismuth-Iron Molybdate

| Catalyst                                | Acrylonitrile Yield (%) | Acrylonitrile Selectivity (%) |
|---|-------------------------|-------------------------------|
| $\text{Bi}_3\text{FeMo}_2\text{O}_{12}$ | 50.9                    | 78.4                          |
| After restructuring <sup>b</sup>        | 73.0                    | 83.3                          |

a) Reaction temperature: 430°C  
Feed Ratios:  $\text{C}_3\text{H}_6/\text{NH}_3/\text{O}_2/\text{N}_2=1/1.2/1.9/12.3$

b) Reaction induced restructuring

Table III. Raman Data For  $\text{Bi}_3\text{FeMo}_2\text{O}_{12}$  From Microreactor

| Band Positions<br>( $\text{cm}^{-1}$ ) | Assignments                             |
|--|---|
| 800 vs                                 | $\gamma\text{-Bi}_2\text{Mo}_6$         |
| 872 s                                  | $\text{Bi}_3\text{FeMo}_2\text{O}_{12}$ |
| 902 m                                  | $\alpha\text{-Bi}_2(\text{MoO}_4)_3$    |
| 932 m                                  | $\beta\text{-FeMoO}_4$                  |

vs = very strong

s = strong

m = medium

Comparison of the kinetic and spectroscopic results indicates that the catalytically active phase for propylene ammoxidation is the predominant bismuth containing phase, namely  $\text{Bi}_2\text{Mo}_3\text{O}_{12}$ , and that its catalytic activity is significantly enhanced by the presence of  $\beta\text{-FeMoO}_4$ . The high temperature  $\beta\text{-FeMoO}_4$  phase is stabilized by the presence of  $\text{Bi}_2\text{Mo}_3\text{O}_{12}$  since bismuth molybdate can serve as a template for the nucleation and growth of this ferrous molybdate phase due to the excellent structural match between the [010] crystal planes of the two phases (Figure 2). Thus, based on the previously identified redox role of iron(6), the  $\beta\text{-FeMoO}_4$  phase

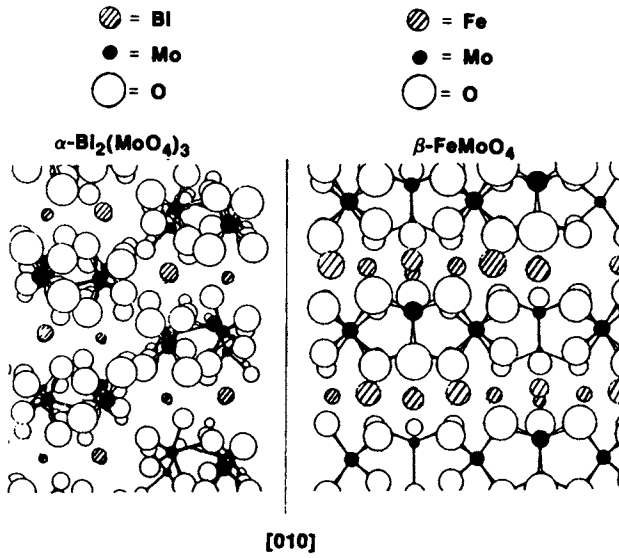


Figure 2. Epitaxial match at the {010} faces of  $\text{Bi}_2\text{Mo}_3\text{O}_{12}$  and  $\beta\text{-FeMoO}_4$ .

is likely to serve as the center for the dissociative chemisorption of gaseous oxygen and the transfer of oxide ions, across a coherent phase boundary, to the catalytically active bismuth molybdate phase.

#### Identification of Functionally Discrete Oxide Ions in $\text{Bi}_2\text{MoO}_6$

It is well recognized that active sites for selective propylene oxidation and ammoxidation must contain two separate functions, namely  $\alpha$ -H abstraction and oxygen insertion(2-4). Investigations of bismuth and molybdenum oxides have suggested that oxygens associated with bismuth are responsible for  $\alpha$ -H abstraction while oxygens bound to molybdenum insert into the allylic intermediate. However, until now, direct evidence for this assignment of function was lacking, as was an understanding of the mechanisms of active site reconstruction and oxide ion transfer in redox catalysts.

Recent oxygen-18 tracer studies by Moro-oka and co-workers(10) have shown that oxide ions responsible for  $\alpha$ -H abstraction and oxygen insertion can be independently probed in  $\text{Bi}_2\text{MoO}_6$  using specific reactant molecules. Identification of these oxygens within the structure of the catalyst, however, was not possible in the reported kinetic investigation. Direct identification of the catalytically distinct oxygens is possible by examining the in-situ Raman spectra of  $\text{Bi}_2\text{MoO}_6$  which had been reduced with butene, propylene, or methanol, and reoxidized with oxygen-18. As Moro-oka correctly conjectured(10), oxidation of butene to butadiene only requires the hydrogen abstracting function of the catalyst while propylene oxidation to acrolein also makes use of the O-insertion function. It is also known that chemisorption of methanol and its subsequent oxidation to formaldehyde occurs on Mo-O centers in molybdates(11).

Table IV. Assignments for Raman and IR High Frequency Bands

| <u>(<math>\text{cm}^{-1}</math>)</u>                                |  |                    |
|---|--|--------------------|
| <u>Raman Band</u><br><u>Positions (<math>\text{cm}^{-1}</math>)</u> | <u>IR Band</u><br><u>Positions (<math>\text{cm}^{-1}</math>)</u> | <u>Assignments</u> |
| 848   | 842  | Mo-O-Mo            |
| 799   | 798  | Mo-O-Mo            |
| 715   | 735  | Mo-O-Mo            |
|   | 600  | Mo-O-Bi            |

Source: Reference (12)

Assignments for the Raman and IR bands (Table IV) have been made by Matsuura and coworkers(12). The molybdenum-oxygen polyhedra, which are assumed to be derived from tetrahedral  $\text{MoO}_4$ , have four vibrational modes,  $\nu_1$ (A),  $\nu_2$ (E),  $\nu_3$ ( $F_2$ ),  $\nu_4$ ( $F_2$ ). All of these vibrations are Raman active, while only the triply degenerate modes are IR active. By comparison with other molybdates, it has

been determined that all of the high frequency bands (around  $800\text{ cm}^{-1}$ ) are associated with the stretching modes of molybdenum-oxygen polyhedra ( $\nu_1(A)$  and  $\nu_3(F_2)$ ). The bending modes ( $\nu_2(E)$  and  $\nu_4(F_2)$ ) are observed between  $300$  and  $400\text{ cm}^{-1}$ . In addition,  $\text{Bi}_2\text{MoO}_6$  displays a weak IR band near  $600\text{ cm}^{-1}$  which is assigned to a Mo-O-Bi mode.

As shown in Table V, reduction of  $\text{Bi}_2\text{MoO}_6$  with butene followed by reoxidation with oxygen-18 produces no immediate shifts in the three high frequency Raman bands at  $853$ ,  $798$  and  $720\text{ cm}^{-1}$  which are assigned to Mo-O stretching modes in the solid. In contrast to this, shifts are observed in the high frequency bands when the catalyst is reduced with propylene or methanol and reoxidized with oxygen-18. Therefore, exchange of lattice oxygen about the molybdenum-oxygen polyhedra occurs only after oxidation of propylene and methanol to acrolein and formaldehyde, respectively, but not after butene oxidation to butadiene. This clearly substantiates our earlier indirect findings(3) that oxygens associated with bismuth are responsible for the hydrogen abstracting function in bismuth molybdate while oxygens associated with molybdenum insert into the allylic intermediate during selective propylene oxidation to acrolein.

Table V. Raman Spectra of Partially Reduced<sup>a</sup>  $\text{Bi}_2\text{MoO}_6$   
Reoxidized with  $^{18}\text{O}$ -Oxygen

| Reductant              | Major Band Positions ( $\text{cm}^{-1}$ ) after: |             |              |             |              |             |             |
|------------------------|--|-------------|--------------|-------------|--------------|-------------|-------------|
|                        | Initial  | First Cycle | Second Cycle | Third Cycle | Fourth Cycle | Fifth Cycle | Sixth Cycle |
| Propylene <sup>b</sup> | 844  | 835         | 832          | 830         | 830          | 830         | 830         |
|                        | 803  | 792         | 792          | 790         | 790          | 786         | 785         |
|                        | 725  | 715         | 715          | 713         | 712          | 710         | 708         |
| Butene <sup>b</sup>    | 844  | 841         | 841          | 841         | 840          | 840         | 840         |
|                        | 803  | 801         | 802          | 802         | 798          | 798         | 797         |
|                        | 725  | 724         | 724          | 725         | 722          | 722         | 723         |
| Methanol <sup>c</sup>  | 844  | 839         | 839          | 838         | 836          | 832         | 831         |
|                        | 803  | 803         | 801          | 802         | 799          | 787         | 787         |
|                        | 725  | 721         | 720          | 719         | 717          | 709         | 709         |

- a) Degree of reduction =  $50\text{ }\mu\text{moles [O] vacancies per m}^2$  per cycle; Raman spectra taken at  $430^\circ\text{C}$ .
- b) Reduced and reoxidized at  $430^\circ\text{C}$ .
- c) Reduced at  $400^\circ\text{C}$ , reoxidized at  $430^\circ\text{C}$ .



Closer examination of the  $\text{Bi}_2\text{MoO}_6$  structure allows a more specific identification of these catalytically active oxygens. Neutron diffraction(13) shows that oxide ions of this structure can be placed into three general categories based on their bonding to bismuth and molybdenum. One type of oxygen is bound only to bismuth and bridges bismuth ions in the  $\text{Bi}_2\text{O}_3$  layer. A second type of oxygen is situated at the apices of the  $\text{MoO}_6$  octahedra and bridges bismuth and molybdenum ions. The third type of oxygen bridges molybdenum ions at the corners of the octahedra. Based on this detailed understanding of the structure and recognizing the need for close spatial proximity of the two catalytic functions, it is reasonable to assign the  $\alpha$ -H abstracting function to oxygens which bridge bismuth and molybdenum. Oxygens which insert into the allylic intermediate are likely to be those at the corners of the octahedra. It can further be reasoned, based on the unique ability of  $\text{Bi}_2\text{O}_3$  oxygen electrolytes to dissociatively chemisorb  $\text{O}_2$ (14), that the two lone pairs of electrons associated with Bi-O-Bi moieties are responsible for reduction of dioxygen and reoxidation of the catalyst under reaction conditions. The structure of these active sites is schematically illustrated in Figure 3.

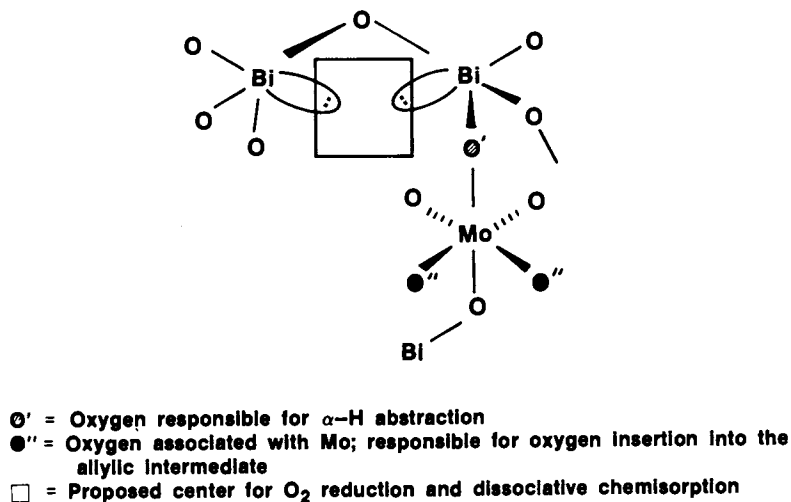


Figure 3. Schematic depiction of the active site structure on the surface of  $\text{Bi}_2\text{MoO}_6$ .

### Concluding Remarks

As illustrated here, the tools of surface science have only recently provided the catalysis researcher the opportunity to rigorously test and challenge possible catalytic mechanisms on a molecular level. Previously, mechanistic evidence has been indirect and conjectured. Surface and solid state aspects of catalytic processes could not readily be evaluated and challenged. Surface science has now provided the opportunity to examine increasingly complex catalyst systems and processes. No longer must the catalyst scientist be bound to the study of simple model systems which only remotely resemble actual, real life catalysts. The promise of surface science, combined with traditional catalytic investigating, is that in depth molecular level understanding of real catalysts will produce the knowledge necessary to achieve major advances in catalytic science and technology.

### Acknowledgments

We wish to thank Dr. Raymond G. Teller for the x-ray and neutron diffraction results and Prof. Edward Kostiner for fruitful discussions.

### Literature Cited

1. Eischens, R. P.; Pliskin, W. A.; Francis, S. A.; J. Chem. Phys. 1954, 22, 1786.
2. Grasselli, R. K.; Burrington, J. D.; Adv. Catal. 1981, 30, 133.
3. Grasselli, R. K.; Burrington, J. D.; Brazdil, J. F.; Discuss. Chem. Soc. 1981, 72, 203.
4. Grasselli, R. K.; Brazdil, J. F.; Burrington, J. D.; Proc. 8th Int. Cong. Catal., Berlin (West), Vol. V, p. 369, (1984).
5. Carson, D.; Coudurier, G.; Forissier, M.; Vedrine, J. C.; J. Chem. Soc., Faraday Trans. 1, 1983, 79, 1921.
6. Brazdil, J. F.; Suresh, D. D.; Grasselli, R. K.; J. Catal., 1980, 66, 347.
7. Egashira, M.; Matsuo, K.; Kagawa, S; Seiyama, T.; J. Catal., 1979, 58, 409.
8. Jeitschko, W.; Sleight, A. W.; McClellan, W. R.; Weiher, J. F.; Acta Cryst., 1976, B32, 1163.
9. Krenzke, L. D.; Keulks, G. W.; J. Catal., 1980, 64, 295.
10. Ueda, W.; Moro-oka, Y.; Ikawa, T.; J. Chem. Soc., Faraday Trans. 1, 1982, 78, 495.
11. Machiels, C. J.; Sleight, A. W.; Proc. 4th Int. Conf. on the Chemistry and Uses of Molybdenum; 1982; 411.
12. Matsuura, I.; Schut, R.; Hirakawa, K.; J. Catal., 1980, 63, 152.
13. Teller, R. G.; Brazdil, J. F.; Grasselli, R. K.; Acta Cryst., in press.
14. Verkerk, M. J.; Hammink, M. W. J.; Burggraaf, A. J.; J. Electrochem. Soc., 1983, 130, 70.

RECEIVED March 20, 1985

## Application of Surface Analysis Techniques in the Study of Catalyst Systems

D. D. Hawn, R. C. Cieslinski, and H. E. Klassen

Analytical Laboratories, The Dow Chemical Company, Midland, MI 48667

The application of x-ray Photoelectron Spectroscopy (XPS) and Auger Electron Spectroscopy (AES) to the solution of complex real world catalyst problems is often difficult and frustrating. Three recent developments in this laboratory have greatly aided in the solution of such problems. These are 1) a dual anode x-ray source using a silicon target, 2) an off-axis, low cost reaction facility for carrying out simple preparative treatments, and 3) installation of a dedicated high-performance Scanning Auger Microprobe (SAM) system.

Advantages of silicon x-radiation include the access of aluminum and magnesium core level (1s) lines and the corresponding (KLL) Auger transitions for chemical state identification and improved quantitation, because these lines are at least 10 times more intense than the corresponding (2p) or (2s) lines. The construction of an off-axis reactor has produced a simple, versatile and inexpensive system easily adapted to any vacuum system. The role of AES and SAM in catalyst research will also be highlighted by examples.

The application of surface analytical techniques, most notably X-ray Photoelectron Spectroscopy (XPS) and Auger Electron Spectroscopy (AES), or its spatially resolved counterpart, Scanning Auger Microanalysis (SAM), is of great value in understanding the performance of a catalyst. However, the results obtained from any of these techniques are often difficult to interpret, especially when only one technique is used by itself.

In this article we describe novel approaches aimed at making surface analytical data easier to obtain and interpret. These include: 1) a small, low cost reaction facility designed to work off-axis to a commercial XPS system, 2) a silicon anode x-ray source for access to higher binding energy photoelectron lines, and 3) the use of dedicated SAM in conjunction with XPS in catalyst problems. Examples showing the utility of each will be discussed.

0097-6156/85/0288-0037\$06.00/0  
© 1985 American Chemical Society

## Experimental

XPS spectra were obtained using a Perkin-Elmer Physical Electronics (PHI) 555 electron spectrometer equipped with a double pass cylindrical mirror analyzer (CMA) and 04-500 dual anode x-ray source. The x-ray source used a combination magnesium-silicon anode, with collimation by a shotgun-type collimator (1). AES/SAM spectra and photomicrographs were obtained with a Perkin-Elmer PHI 610 Scanning Auger Microprobe, which uses a single pass CMA with coaxial lanthanum hexaboride ( $\text{LaB}_6$ ) electron gun.

Reactions were carried out using a facility mounted off-axis to the load lock of the PHI 555 electron spectrometer. This device utilizes a radiant heater to heat a sample and mount inside a glass reactor. This device is shown in Figure 1. It consists of a center section constructed from two Pyrex glass-to-metal adapters on 2.75 inch Conflat flanges joined together. The center glass section is one inch in diameter by 2.5 inches in length. A double-sided 2.75 inch Conflat flange allows feedthrough for gas inlet, outlet and evacuation, and chromel/alumel thermocouple. The reactor is separated from the sample load lock by a high vacuum gate valve. A 0.125 inch thick sample holder is moved from the standard transport/analysis rod of the PHI system to the heater zone of the reactor via a 0.25 inch diameter stainless steel rod. A dovetail mount is used to receive the sample holder on the PHI probe. The 0.25 inch rod is sealed by a pair of graphite-impregnated Teflon seals, riding in a housing constructed on a 2.75 inch Conflat blank flange. The space between the seals is pumped, as is the reactor via the gas outlet, by a mechanical rotary pump equipped with liquid nitrogen trap. The entire assembly operates from  $10^{-6}$  torr to 1 atmosphere of pressure when employing the turbomolecular pump which pumps the PHI load lock.

Heating of the mount is accomplished by a modified halogen projection bulb, with the sample mount temperature regulating the applied lamp power via a digital temperature controller. A stainless steel insulated clam-shell enclosure houses the lamp, and has provisions for lamp cooling and an integral reflector. Temperatures to  $600^\circ\text{C}$  in 1 atmosphere of hydrogen can be achieved at the sample mount. Reactive gases are preheated before passage over the sample by travelling the length of the reactor directly in front of the halogen lamp before making contact with the sample. Alternately, gas can be preheated in a tube furnace before entry into the reactor. However, in this case care should be exercised to not exceed  $450^\circ\text{C}$  during a reaction.

The glass-to-metal adapters used here for the cell body are intended only to be used to  $400^\circ\text{C}$ , while the glass itself can safely withstand  $500^\circ\text{C}$ . Due to the focussing power of the lamp onto the mount, a sample temperature of  $600^\circ\text{C}$  can be achieved at the sample while the glass or glass-to-metal adapters remain significantly below this temperature.

For the copper/aluminum catalyst analyses later described, the sample mount was transferred from the XPS system following treatment and analysis to an inert atmosphere dry box without air exposure. From there individual pellets were transferred to the SAM for subsequent analysis without air exposure. The reverse process was employed for the next reaction cycle.

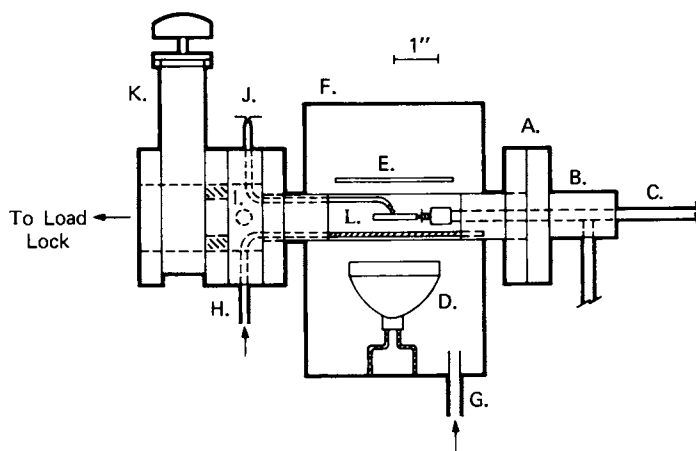


Figure 1. Schematic Diagram of the off-axis radiant heated reactor. A. cell body; B. linear/rotary motion feedthrough; C. transport rod; D. projector bulb; E. reflector; F. insulated stainless steel enclosure; G. air cooling port; H. gas inlet; I. gas outlet/pumping port; J. chromel/alumel thermocouple; K. high vacuum gate valve; L. sample mount.

## Discussion

### 1) Off-Axis Reaction Cell

The ability to treat catalyst materials under controlled conditions followed by transfer to the analysis environment without air exposure, has been an important factor in the solution of many catalyst problems. Early designs of such components have involved the direct heating of the material in a preparation facility directly adjacent to the spectrometer, with subsequent transfer of the material between these two chambers. A more sophisticated modification of this approach, as described by Ganschow and co-workers (2), utilizes a sample module which can be shuttled among several interconnected analytical chambers and a reaction facility. Alternate designs have involved transfer of the sample to a remote facility for reaction (3,4), or sealing of the sample in a reactor housed in the UHV analysis chamber (5,6). A review of the features of each design has been assembled by Ganschow and co-workers (2). The design discussed herein has the advantage of being inexpensive and easily replaced or repaired. With its off-axis design, the spectrometer can still be used while a reaction is being carried out. The design also presents a buffer between the reactor and analysis chamber, thus limiting contamination of the analysis chamber by the reactor. Adverse wall reactions are limited, since the area in the heated zone is glass, and only the sample and its holder are maintained at the reaction temperature.

A carbon supported molybdenum catalyst used for the production of Liquefied Petroleum Gas (LPGs) demonstrates the usefulness and high temperature capabilities of this facility. Figure 2 compares the molybdenum (3d) spectra following extended treatments in helium and hydrogen at 500°C. For the starting catalyst, the Mo(3d 5/2) photoline is centered at 232.4 eV binding energy when referenced to the graphitic support carbon (1s) photoline at 284.3 eV. This binding energy is consistent with that reported for Mo(VI), or MoO<sub>3</sub> (4,7).

Following high temperature exposure to helium (Figure 2B), a series of lower binding energy peaks were observed, with Mo(3d 5/2) components centered at 231.1 and 228.9 eV binding energy. These are attributed to Mo(V) and Mo(IV), respectively, based on previously reported literature values (4) and work performed in this laboratory. In addition, a higher binding energy component at 234.2 eV is observed in this spectrum, and is attributed to molybdate (MoO<sub>4</sub>). We also observed a marked increase in potassium at the surface following this treatment. In this case, the Mo(IV)/Mo(VI) and Mo(V)/Mo(VI) ratios are 0.2 and 0.13 respectively after 6 hours of treatment. Extended reaction times (to 12 hours) do not significantly affect this ratio. Reduction in hydrogen at 500°C produces substantial levels of Mo, as evidenced by the appearance of a peak at 227.8 eV binding energy. Again Mo(IV) is observed, but no molybdates were observed. This reduction was observed to proceed rapidly at first, so that, after 6 hours, the Mo(IV)/Mo(VI) and Mo/Mo(VI) ratios were 0.80 and 2.20, respectively. Extended times (to 9 hours) did not greatly affect these ratios. Patterson and co-workers (4) observed similar behavior for a supported molybdenum catalyst, in which case little further reduction of Mo(VI) to Mo was observed after 7 hours in hydrogen. In this case, the presence of

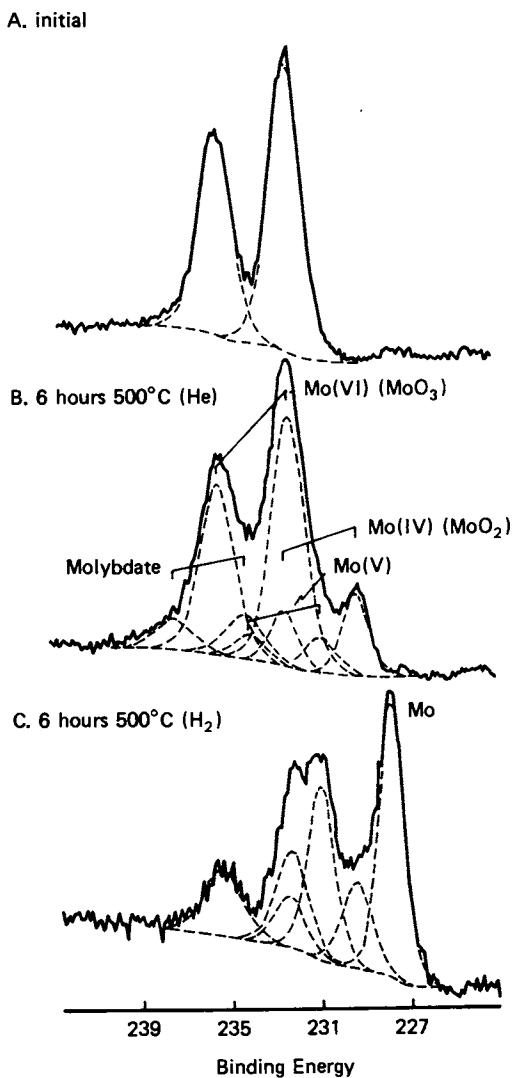


Figure 2. Molybdenum (3d) XPS spectra of a molybdenum on carbon catalyst following various treatment schemes; A. catalyst as prepared; B. following 500°C for 6 hours in helium; C. following 500°C for 6 hours in hydrogen.

Mo(IV), and its optimization on the catalyst surface, is an important consideration in the development of this catalyst, as Mo(IV) is believed to be the active component for several catalytic processes (8).

## 2) Silicon Anode X-Ray Source

Although XPS has been applied with success in a wide variety of catalyst problems, certain situations arise where interferences of photoelectron lines from different elements make the technique difficult to use. An interesting example is the copper/aluminum system, in which case the copper (3s) and (3p) lines interfere with the aluminum(2s) and (2p) lines (Figure 3). These lines cannot be isolated from each other by using a different x-ray line, as is commonly done with Auger lines overlapping XPS photolines. In these special cases, the best solution is to employ a higher energy x-ray source to access deeper, core-level transitions, for example the Al(1s) photoline in the copper/aluminum system.

Several considerations must be made when selecting an anode material. For routine analytical work, one anode of a dual anode source should be magnesium because of the narrow x-ray line width and extensive literature base. Another consideration is the energy range of the analyzer, as photoelectron lines with kinetic energies exceeding the kinetic energy range of the analyzer would be inaccessible. Therefore, in the PHI 555 system with an energy range of 2400 electron volts, gold ( $M\alpha=2122.9$  eV), zirconium ( $L\alpha=2042.4$  eV), and silicon ( $K\alpha=1739.4$  eV) would be possible choices. Castle and co-workers have discussed the use of  $SiK\alpha$  (9) and  $ZrL\alpha$  (10), while the use of  $AuM\alpha$  has been demonstrated by Wagner (11).

Another consideration is the natural line width and satellite structure of the x-ray line used. Titanium ( $TiK\alpha=4510.9$  eV) has seen limited use (12) for non-destructive depth profiling, but the observed spectra are complicated by the  $TiK\alpha$  satellite structure and the large natural line width of 2.0 eV (13).

$SiK\alpha$  is a good choice because of its energy and narrow line width of 1.0 eV (9). Figure 4 shows some of the element core levels which can be excited with magnesium ( $K\alpha=1253.6$  eV), aluminum ( $K\alpha=1486.6$  eV) and silicon ( $K\alpha=1739.4$  eV) sources. The high cross section of 6.01 for the Al(1s) photoline, as measured relative to the fluorine (1s) photoline using  $SiK\alpha$  x-radiation, is substantially greater than that of the Al(2p) photoline, at 0.170. In addition, the resulting Auger transitions, such as the Al(KLL) series, allow the development of Auger parameters for this series.

Figure 5 shows such an Auger parameter plot for a series of aluminum compounds. Due to crowding, several values given in Table I are omitted from this plot. Most of the compounds are grouped to the lower left, whereas aluminum metal is at the upper right. Intermediate between these are sodium zeolite and zinc aluminate ( $ZnAl_2O_4$ ).

Although the range covered by the Al(1s) line for the compounds is nearly the same as that for the Al(2p) line (5.4 eV as compared to 4.3 eV), the added dimension of the Auger ( $KL_{23}L_{23}$ ) line allows differentiation of compounds not distinguishable using their Al(2p) lines alone (for example,  $Al(OH)_3$  and  $AlCl_3$ ).

Beryllium (7 micron), silicon dioxide (10 micron), and aluminum (2 micron) were tried as x-ray windows. Beryllium was the best



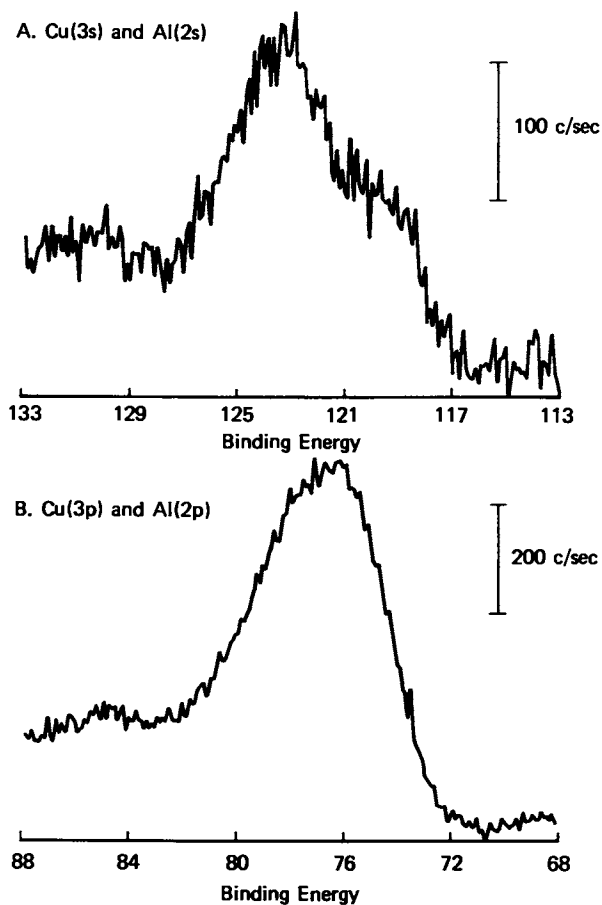


Figure 3. XPS spectra of alumina-supported copper catalyst, showing interference of XPS photolines: A. copper (3s) and aluminum (2s) regions; B. copper (3p) and aluminum (2p) regions.

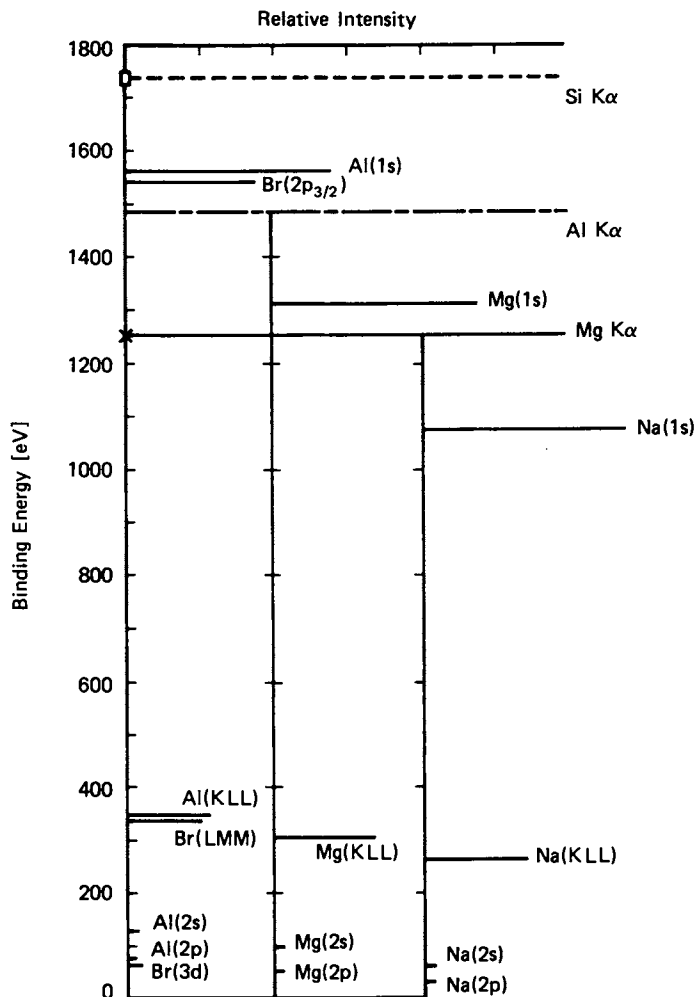


Figure 4. Positions and relative intensities of XPS and Auger transitions using silicon, aluminum, and magnesium x-ray sources.

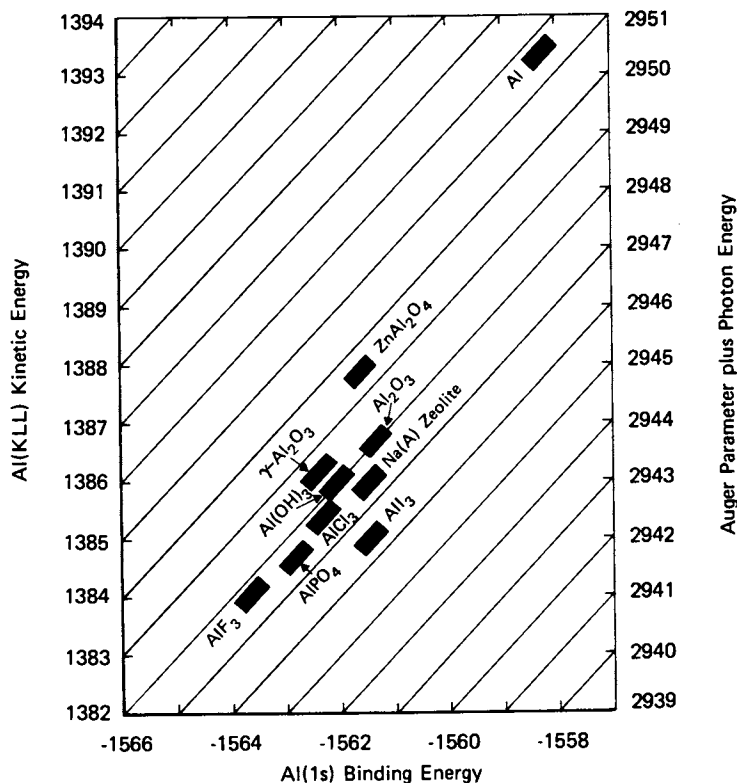


Figure 5. Auger chemical state plot for aluminum compounds as obtained using silicon  $K\alpha$  x-radiation.

Table I. Chemical State Data For Various Aluminum Compounds Obtained Using Silicon  $K\alpha$  X-Radiation (1739.4)

| Compound                                 | Al(1s) | Al(KL <sub>23</sub> L <sub>23</sub> ) <sub>BE</sub> | Al(KL <sub>23</sub> L <sub>23</sub> ) <sub>KE</sub> | $\alpha+h\nu$ | Al(2p) <sup>*</sup> |
|--|--------|---|---|---------------|---------------------|
| Al                                       | 1558.3 | 364.1   | 1393.3  | 2951.6        | 72.2                |
| $\gamma$ -Al <sub>2</sub> O <sub>3</sub> | 1562.4 | 353.2   | 1386.2  | 2948.6        | 75.3                |
| Al <sub>2</sub> O <sub>3</sub>           | 1561.3 | 353.8   | 1386.7  | 2948.0        | 74.7                |
| Al(OH) <sub>3</sub>                      | 1562.1 | 353.4   | 1386.0  | 2948.1        | 74.9                |
| Al(PO <sub>4</sub> ) <sub>3</sub>        | 1562.8 | 354.7   | 1384.7  | 2947.5        | 75.8                |
| Al(NO <sub>3</sub> ) <sub>3</sub>        | 1562.0 | 353.8   | 1385.7  | 2947.7        | 75.2                |
| Al Cl <sub>3</sub>                       | 1562.3 | 354.1   | 1385.4  | 2947.7        | 75.8                |
| Al I <sub>3</sub>                        | 1561.4 | 354.5   | 1385.0  | 2946.4        | 76.0                |
| Al F <sub>3</sub>                        | 1563.7 | 355.3   | 1384.1  | 2947.8        | 77.0                |
| Na(A)Zeolite                             | 1561.5 | 353.6   | 1385.9  | 2947.4        | 74.4                |
| ZnAl <sub>2</sub> O <sub>4</sub>         | 1561.6 | 351.6   | 1387.8  | 2949.4        | 74.7                |
| 1:1 Cu/Al                                | 1562.1 | 353.5   | 1386.0  | 2948.1        | --                  |

\*Using Mg  $K\alpha$  radiation

Binding energy referenced to Au(4f 7/2) level at 83.8 eV for thin layer of gold evaporated onto sample.

choice since the highest count rates were observed, producing Ag(3d 5/2) count rates 26 percent that of the magnesium anode with a 2 $\mu$ m aluminum window at the same analyzer pass energy. Silicon dioxide and aluminum windows lowered the observed count rates on silver to 4 percent of that of magnesium. When using aluminum as the window material, ghost lines due to copper were 25 percent of the intensity of the Ag(3d 5/2) photoline. Some cracking of the SiO<sub>2</sub> window was observed with use, presumably due to heat distortion. The narrowest full-width-at-half-maximum peak height (FWHM) for Ag(3d 5/2) was 1.36 eV, in which case some assymetry of the line was observed due to separation of the SiK $\alpha$ <sub>1,2</sub> components. This was not a problem in routine use. The Ag (3d 5/2) FWHM observed using the same analyzer pass energy and magnesium K $\alpha$  x-radiation was 0.96 eV.

### 3) Application of XPS Using Silicon Anode X-Ray Source, Scanning Auger Microprobe, and Reaction Facility in a Copper/Aluminum Catalyst System

The use of this anode in catalyst analysis was demonstrated on a commercially available pelletized catalyst with a bulk composition of 84 weight percent CuO, 14% Al<sub>2</sub>O<sub>3</sub>, 1% Na<sub>2</sub>O, and 1% graphite binder. This catalyst has the form of hard glossy pellets approximately 3 mm in diameter by 3 mm in length. The catalyst is widely used in the reduced form for hydrolysis of primary amines. Periodic regeneration of this catalyst involves mild reoxidation to burn off residual hydrocarbons, followed by re-reduction. The goal of this work was to understand the surface compositional changes which occurred during repeated regenerations. Referring again to Figure 3, it was impossible to discern the role of aluminum in this catalyst due to the interference of copper photolines with the Al(2s) and Al(2p) photolines.

Figure 6 compares the XPS survey scans obtained from the as-received material, and after reduction in a hydrogen/helium gas mixture at 200°C for 12 hours. Both spectra were obtained using SiK $\alpha$  x-radiation. The most notable differences between these two spectra are the increased intensity of the Al(1s) and Na(1s) photolines, and the loss of satellite structure in the copper (2p) region due to reduction of Cu(II) species to Cu(I) or Cu metal. The large carbon (1s) intensity was surprising considering the low level of graphite added as binder. That carbon is segregated to the pellet surface is clearly indicated by comparison of the carbon (1s)/aluminum (1s) atomic ratios in rows A or C-F to rows B or G in Table II. In this case, the powdered material is intended to be representative of the bulk catalyst. These powders were dusted onto conductive tape for analysis, and therefore the carbon-to-aluminum ratios may be slightly in error due to the sample preparation.

The exceptionally high C(1s)/Al(1s) ratio for the pelletized starting material results from the presence of surface hydrocarbons deposited during processing or subsequent handling. The carbon (1s) peak was very broad due to this contribution at 284.6 eV binding energy, as well as graphitic type carbon at 284.3 eV. The carbon (1s) peak for the powdered starting material was narrower due to the reduced contribution of this 284.6 eV component to the spectrum. Following reduction and oxidation, the carbon was predominantly graphitic in nature, in which case the hydrocarbon contaminants were quickly burned off during treatment. Also note the substantial

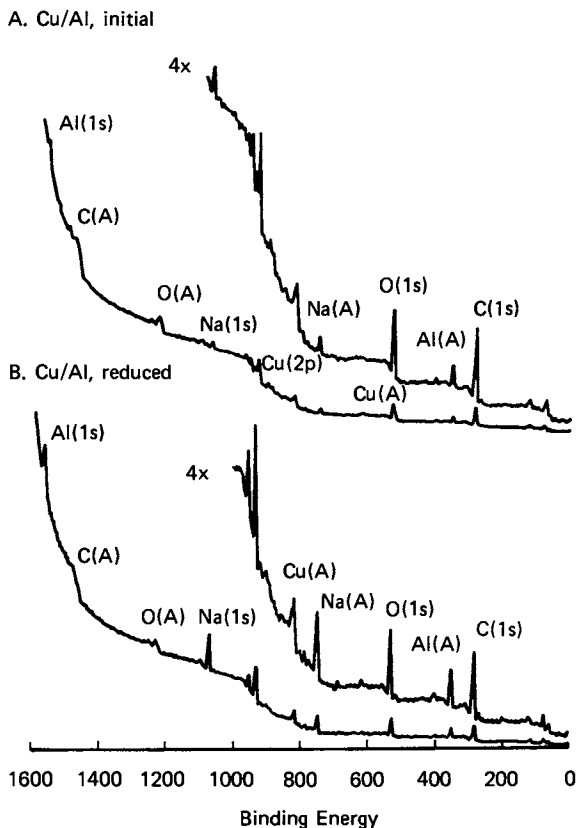


Figure 6. XPS wide scans of a commercial copper/aluminum extruded catalyst obtained using silicon  $K\alpha$  x-radiation: A. untreated catalyst; B. following 200°C for 12 hours in 10% hydrogen/90% helium gas mixture.

American Chemical Society  
Library

1155 16th St., N.W.

In Catalyst Characterization Science; Deviney, M., et al.;  
ACS Symposium Series; American Chemical Society: Washington, DC, 1985.

Table II. Elemental Atomic Ratios for Copper/Aluminum Catalyst Following Various Treatments as Obtained Using Silicon K $\alpha$  X-Radiation

|                          | Condition | $\frac{\text{Cu}(2p\ 3/2)}{\text{Al}(1s)}$ | $\frac{\text{Na}(1s)}{\text{Al}(1s)}$ | $\frac{\text{O}(1s)}{\text{Al}(1s)}$ | $\frac{\text{C}(1s)}{\text{Al}(1s)}$ |
|--------------------------|-----------|--|---------------------------------------|--------------------------------------|--------------------------------------|
| A Starting Material      | Pellet    | 2.0  | 0.9                                   | 9.6                                  | 28.2                                 |
| B Starting Material      | Powdered  | 1.0  | 0.3                                   | 3.7                                  | 4.8                                  |
| C (R)                    | Pellet    | 0.6  | 1.8                                   | 3.2                                  | 10.7                                 |
| D (R),(O)                | Pellet    | 1.6  | 3.1                                   | 6.7                                  | 10.3                                 |
| E (R),(O),<br>(R),(O)    | Pellet    | 1.5  | 2.3                                   | 5.0                                  | 9.5                                  |
| F (R),(O),(R)<br>(O),(R) | Pellet    | 0.4  | 2.2                                   | 2.1                                  | 5.1                                  |
| G Same as F              | Powdered  | 0.5  | 0.3                                   | 2.4                                  | 2.3                                  |

Preparation Code:

(R) 12 hours at 200°C in 10% H<sub>2</sub>/He

(O) 12 hours at 200°C in 10% O<sub>2</sub>/He

increase in sodium at the pellet surface following reduction and oxidation, demonstrating the mobility of sodium, especially under reducing conditions. The lower atomic ratios for the other components in the catalyst result in part from surface coverage by sodium as discussed later.

High resolution scanning Auger microprobe (SAM) analysis indicated that the high surface carbon was related to the presence of exposed graphite islands on the surface of the catalyst pellets. Figure 7A shows a secondary electron (SEM) photomicrograph of the surface of the untreated catalyst. Point mode Auger spectra obtained from the darker areas in this photomicrograph showed only carbon to be present. In comparison, spectra obtained from the grey areas evident in this photomicrograph showed the presence of carbon, oxygen, copper, sodium, and aluminum. Figure 7B shows the carbon (KLL) Auger map corresponding to the area shown in 7A. Note the correspondence of dark areas in the SEM image to the high carbon content areas evident in the Auger map.

Following initial reduction at 200°C, photomicrographs showed the development of distinct light-colored islands on the catalyst surface, in addition to the dark (carbon) islands and grey areas previously observed (Figure 8A).

Point mode spectra (8 kV, 10 nanoamp primary beam) obtained in these light areas indicated primarily copper and oxygen to be present, similar to point mode spectra obtained from grey areas in the photomicrograph. Auger spectra acquired from the entire area imaged in Figure 8A indicated that sodium and oxygen were the main surface components. The sodium (KLL) Auger map obtained in the (peak-background)/background mode corresponding to Figure 8A is shown in Figure 8B. Note the correspondence of the light colored areas in the SEM image to high sodium areas observed in Figure 8B. The oxygen (KLL) Auger map (Figure 8) shows significant correlation with the sodium Auger map, suggesting that these light colored areas observed in Figure 8A are sodium oxide ( $\text{Na}_2\text{O}$ ).

The conflict between nil sodium observed in the point mode in light areas of the SEM photomicrograph, and substantial sodium in the sodium maps in these areas, points to the migration of sodium caused by the primary electron beam. Even though the primary beam currents used here were low (10 nA), the beam current density in the point mode was high (approximately 0.5 amps per square centimeter). Delocalization of the primary beam by rastering, or by deflection as is done during mapping, produced sufficiently lower beam current density, thus alleviating sodium migration.

The islanding of sodium oxide as observed in this case is most likely caused by the inability of sodium oxide to wet the reduced copper surface. These islands were observed only during the initial reduction step; a uniform surface distribution of sodium was observed following subsequent oxidation, in which case the oxide nature of surface would be more wettable. Referring again to Table II and the XPS results, the high  $\text{Na}(1s)/\text{Al}(1s)$  atomic ratio observed following reduction and oxidation (row D) is a result of more uniform coverage of the surface by sodium.

When running hydrolysis reactions in the liquid phase, it was observed that the sodium could be washed from the bed by flushing with water and monitoring the change in pH of the bed effluent. If this precaution was not observed, initial low yields of product were observed until sodium was entirely removed from the bed.

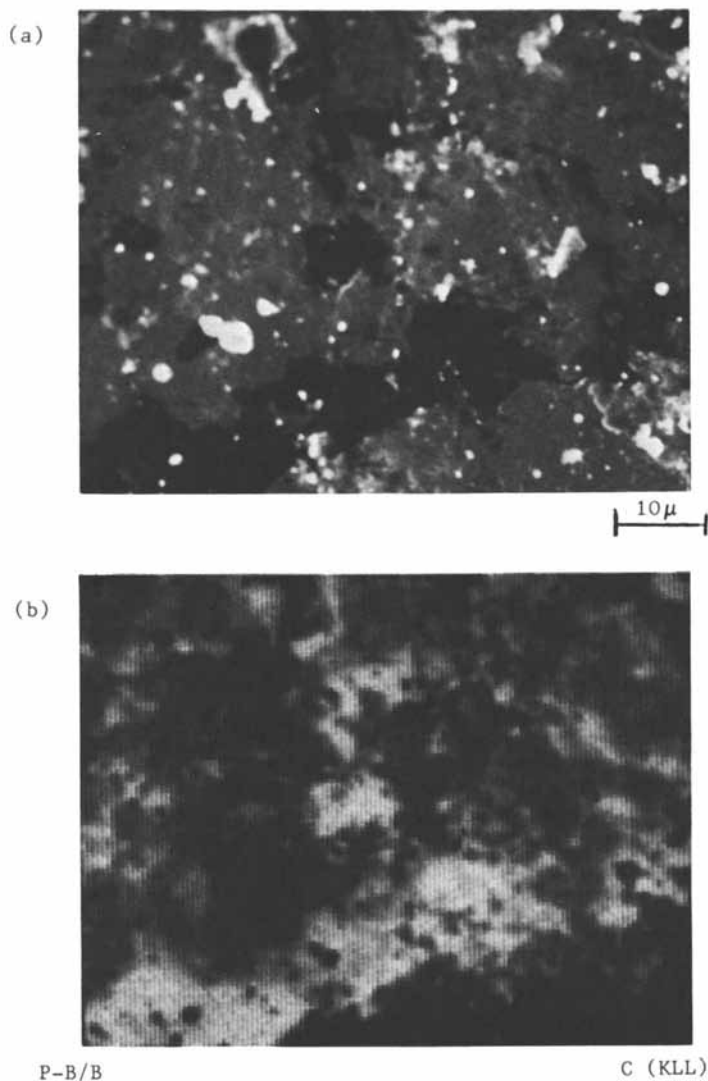


Figure 7. Secondary electron micrograph and carbon (KLL) map of untreated catalyst: A. photomicrograph obtained at 8kV, 0.1nA primary beam; B. corresponding carbon (KLL) Auger map obtained in (peak-background)/ background mode, at 8kV, 10nA primary beam.



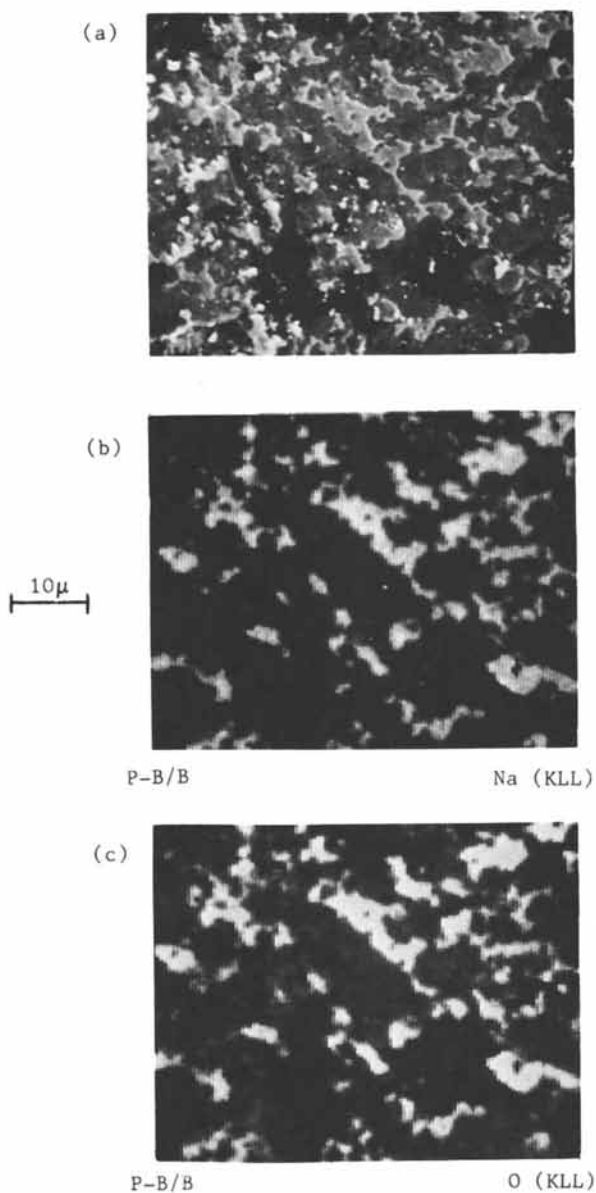


Figure 8. Secondary electron photomicrograph, sodium (KLL), and oxygen (KLL) Auger maps of catalyst following single reduction: A. SEM photomicrograph obtained with 8kv, 0.1 nA primary beam; B. corresponding sodium (KLL) auger map obtained in (peak-background) /background mode; C. corresponding oxygen (KLL) Auger map obtained in (peak-background) /background mode with 8kv, 10nA primary beam.

Photomicrographs obtained following the second oxidation showed the appearance of small cracks throughout the pellets. In actual use, these cracks would be detrimental since they are the precursor to pellet fracture and subsequent compaction, which would result in increased pressure drop across the reactor.

Examination of aluminum (1s) and copper (2p) spectra suggest that a strong metal-support interaction occurs in this catalyst. Aluminum (1s) spectra obtained after various treatments are shown in Figures 9 and 10. The initial catalyst Al(1s) spectrum is composed of two peaks, with the higher binding energy component at 1562.4 eV consistent with aluminum oxide. The lower binding energy component is centered at 1560.4 eV, while the Al(KLL) transition is located at 352.2 eV binding energy. Following repeated reduction and oxidation, two additional components appear in the aluminum (1s) spectrum, at binding energies of 1558.0 eV and 1555.6 eV. Although the 1558.0 eV component is indicative of aluminum metal, aluminum metal is not expected under oxidative conditions, as in Figure 9C. In addition, the plasmon lines associated with the Al(1s) line, similar to those observed for the Al(2s) line, are not observed in this case.

This should be compared to the Al(1s) spectrum for the powdered catalyst, shown in Figure 10C, which shows a single component at 1562.4 eV. The Al(KLL) Auger transition was observed at 353.3 eV binding energy, suggesting that the bulk aluminum is present as an aluminum oxide ( $\gamma$ -Al<sub>2</sub>O<sub>3</sub>). As in the powdered catalyst, no changes in either the Al(1s) or Al(KLL) Auger spectra were observed for pellets which were cleaved and subjected to the same treatment cycles, so that Al<sub>2</sub>O<sub>3</sub> was the only aluminum compound observed.

The copper (2p) spectra for this catalyst obtained with magnesium K $\alpha$  x-radiation showed similar unusual behavior, as illustrated in Figure 11. Whereas the powdered material showed only Cu(II) oxide to be present following oxidation and copper metal following reduction, the surface exhibited predominately copper metal following reduction, and two copper components at 932.4 eV and 934.8 eV either initially or following oxidation. The 934.8 eV component is attributed to copper (II) carbonate, and is supported by the presence of an additional peak in the carbon (1s) spectrum at 289.6 eV binding energy, indicative of carbonate. The 932.4 eV copper peak, along with the copper (LMM) auger transition at 335.9 eV binding energy, suggests a copper (I) species. This is also supported by the low intensity of the shake-up lines relative to the Cu(2p) lines. Note particularly that this behavior was not observed in powder material or in cleaved pellets subjected to the same treatments.

Similar experiments with copper dispersed on Al<sub>2</sub>O<sub>3</sub> did not show any unusual behavior of the Al(1s) or Cu(2p) photolines. In this case, the copper could be easily cycled between CuO under oxidative conditions, to Cu metal during reducing conditions. We observed only a slight shift (<0.4 eV) of the aluminum (1s) line upon initial heating, which was attributed to the loss of water in the alumina matrix.

The lower binding energy aluminum (1s) photolines observed may be an indication of the strong interaction of aluminum and copper, which is evident only on the pellet surface. The lower binding

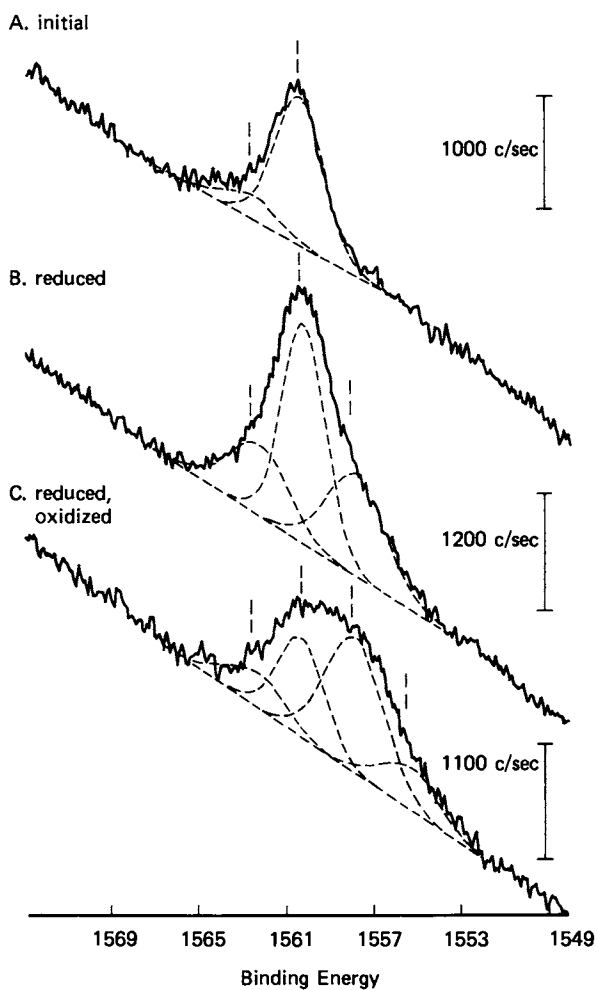


Figure 9. Aluminum (1s) XPS spectra following various stages of treatment: A. untreated catalyst; B. 200°C for 12 hours in 10% hydrogen/90% helium; C. as B., but following additional 12 hours at 200°C in 10% oxygen/ 90% helium.

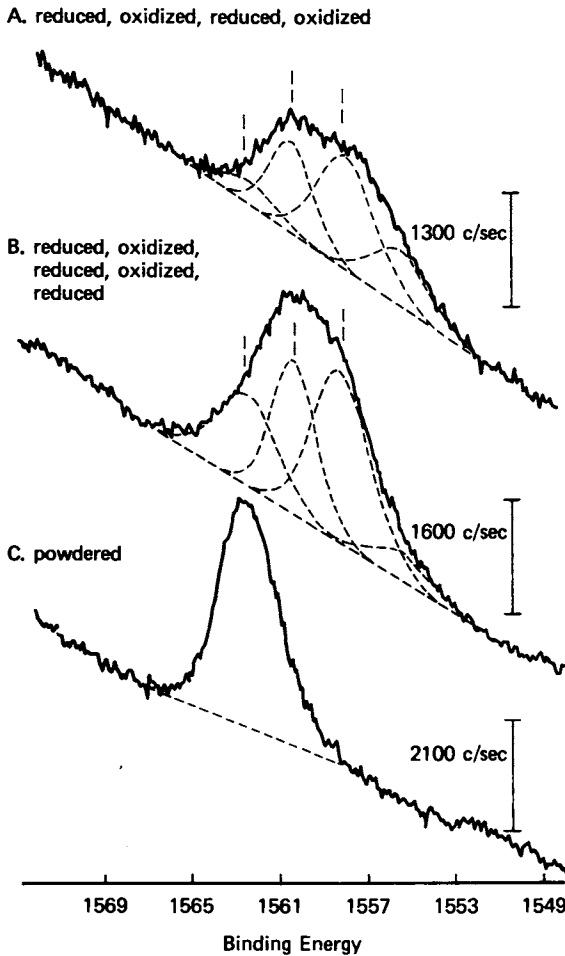


Figure 10. Aluminum (1s) XPS spectra following extended treatment: A. as 9C, but following additional 12 hours at 200°C in 10% hydrogen/90% helium and 12 hours at 200°C in 10% oxygen/90% helium, B. as 10A, with additional 12 hours at 200°C in 10% hydrogen/90% helium; C. powdered catalyst as treated in 10B.

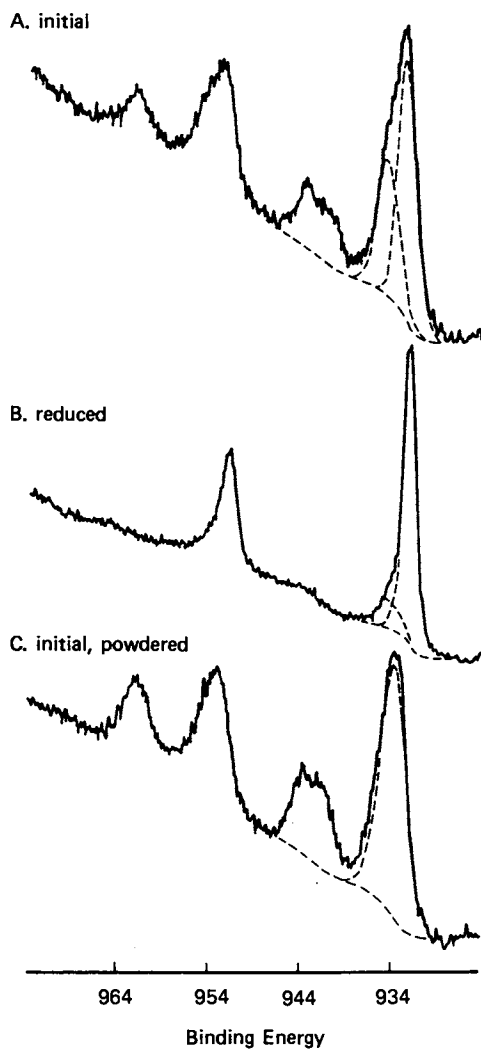


Figure 11. Copper (2p) XPS spectra following various stages of treatment: A. untreated catalyst; B. 200°C for 12 hours in 10% hydrogen/90% helium; C. powdered, untreated catalyst.

energy component evident in the copper (2p) spectra following oxidation supports this conclusion. This interaction is further supported by the trends observed for aluminum in sodium zeolites. In this case, the aluminum (1s) binding energies are intermediate between aluminum and aluminum oxide. Shyu and co-workers (14) have observed a decrease in the aluminum (2p) binding energy for zeolites following modification of the structure by dealumination. The same trends (decrease in binding energy) would be expected in the aluminum (1s) spectra of dealuminated zeolites. It is proposed that the observed Al(1s) peaks arise from different copper-aluminum structures or from different coordination between copper and aluminum, in which case the copper plays a substantial role in donating electron density to the aluminum atoms.

### Conclusion

The utility of a SiK $\alpha$  x-ray source in the study of catalyst systems, and especially its utility in the observation of previously undetected metal-support interactions has been demonstrated. Scanning Auger microprobe data were also useful in understanding the quantitative changes observed by XPS. Finally, the ability to treat materials in a controlled manner, and perform the subsequent analyses without exposure to the ambient atmosphere, made the experiment possible.

### Literature Cited

1. Hawn, D. D. Rev. Sci. Instrum. 1983, 54, 767.
2. Ganschow, O; Jede, R.; An, L. D.; Manske, E.; Neelson, J.; Wiedmann, L; Benninghoven, A. Vac. Sci. Technol. A 1983, 1, 1491.
3. Ng, K. T.; Hercules, D. M. J. Phys. Chem. 1976, 80, 2094.
4. Patterson, T. A.; Carver, J. C; Leyden, D. E., Hercules, D. M., J. Phys. Chem. 1976, 80, 1700.
5. Blakely, D. W.; Kozah, E.I.; Sexton, B. A.; Somorjai, G. A. J. Vac. Sci Technol. 1976, 13, 1091.
6. Keck, K. E.; Kasemo, B; Höglund, A. Rev. Sci Instrum. 1983, 54, 574.
7. Kim, K. S; Battinger, W. E.; Amy, J. W.; Winograd, N. J. Electron Spectrosc. 1974, 5, 351.
8. Somorjai, G. A., personal communication.
9. Castle, J. E.; West, R. H. J. Electron Spectrosc. and Relat. Phenom. 1980, 19, 409.
10. Castle, J. E.; Hazell, L. B.; West, R. H. J. Electron Spectrosc. 1979, 16, 97.
11. Wagner, C. D. J. Vac. Sci. Technol. 1978, 15, 518.
12. Clark, D. T. In "Photon, Electron, and Ion Probes of Polymer Structure and Properties"; Dwight, D. W.; Fabish, T. J.; Thomas, H. R., Eds.; ACS Symposium Series No. 162, American Chemical Society: Washington, D.C. 1981; pp. 247-291.
13. Barrie, A. In "Handbook of x-Ray and Ultraviolet Photoelectron Spectroscopy"; Briggs, D., Ed.; Heyden: Philadelphia, 1977; pp. 79-119.
14. Shyu, J. Z.; Skopinski, E. T.; Sayari, A.; Goodwin, J. G. 6th Symposium on Applied Surface Analysis, 1984, p. E-8.

RECEIVED April 17, 1985

## Valence State of Rhenium in Reduced Bimetallic Catalysts With and Without Alkali Metals

Sayra R. Adkins and Burtron H. Davis

Institute for Mining and Minerals Research, University of Kentucky, Lexington, KY 40512

Platinum-rhenium catalysts have been reduced in one atmosphere of flowing hydrogen and then examined, without exposure to the atmosphere, by ESCA. The spectra indicate that the Group VIII metal is present in a metallic state in the reduced catalyst and that the majority of the rhenium is present in a valence state higher than Re(0).

The introduction of a Pt-Re bimetallic reforming catalyst in the late 1960's had an immediate impact (1,2) and revolutionized the reforming technology much like the introduction of the Pt-Al<sub>2</sub>O<sub>3</sub> catalyst had done about twenty-five years earlier (3). Initially it was viewed that the superior performance of the bimetallic catalyst was due to alloy formation (2). Evidence for alloy formation has been obtained from temperature programmed reduction studies (4,5,6). However, Peri did not obtain evidence for alloy formation with Pt-Re catalysts in his i.r. study. In addition, it appears that pretreatment and reduction conditions may play an important role in determining the chemical state of Re in these catalysts (7). The role of water vapor in determining the extent of reduction dates to at least 1974 (8,9). Two recent papers describe the chemical state of the metals in Pt-Re catalysts and emphasize the uncertainty associated with defining the valence of Re. Burch (10) concludes that alloy formation is uncertain while Charcosset (11) reports that hydrogen-oxygen titrations provide evidence of the presence of small particles of pure rhenium in platinum bimetallic alumina supported catalysts. Recent x-ray absorption spectroscopic data (12) indicate that Re is neither zero valent nor significantly associated with Pt. Davis (13,14) found that the aromatics formed from alkane dehydrocyclization were altered from that of Pt by the presence of either Re or Sn and that these metals produced effects that resembled those of gaseous promoters on Pt. This suggests that both Re and Sn interact directly with Pt. Mieville (15) recently reported that the ease of reduction of Re depended on the calcination temperature

0097-6156/85/0288-0057\$06.00/0  
© 1985 American Chemical Society

and that those catalysts pretreated at lower temperatures were easier to reduce.

Sodium or potassium severely poisons Pt-Re catalysts but the manner in which the alkali metal operates is not apparent. The present study was designed to use ESCA to determine the valence state of Re in Pt-Re bimetallic catalysts. The valence state would be determined in samples that had been reduced and transferred to the instrument without exposure to an oxidizing atmosphere. Catalysts with and without potassium would be examined.

### Experimental

Catalysts. Two alumina support types were used in this study; an alumina from Degussa Corp. with 110 m<sup>2</sup>/g BET surface area and non-acidic Al<sub>2</sub>O<sub>3</sub> prepared by precipitation from a potassium aluminate solution with carbon dioxide (Al<sub>2</sub>O<sub>3</sub>-III, with 1%K and 210 m<sup>2</sup>/g BET surface area and Al<sub>2</sub>O<sub>3</sub>-19 containing 1.3%K and a BET surface area of 200 m<sup>2</sup>/g). The supports were calcined at 600°C prior to surface area measurements. An incipient wetness technique was used to prepare the catalysts. For preparations A and B (Table I) an amount of aqueous Re<sub>2</sub>O<sub>7</sub> needed to produce a final catalyst containing ca. 2 wt.% Re was used. These catalysts were dried in air at 110°C overnight and then calcined in air for 3 to 4 hours at 500°C. Catalysts C and D were prepared to contain 0.8% Rh by making a second impregnation of catalysts

Table I. Composition of Catalysts Used in This Study

| Catalyst | Support                             | Metal, wt. % |     |     |     |
|----------|-------------------------------------|--------------|-----|-----|-----|
|          |                                     | %Re          | %Rh | %Pt | %K  |
| A        | Al <sub>2</sub> O <sub>3</sub> -III | 2.8          | --- | --- | 1.0 |
| B        | Degussa                             | 2.2          | --- | --- | --- |
| C        | Al <sub>2</sub> O <sub>3</sub> -III | 2.5          | 0.8 | --- | 1.0 |
| D        | Degussa                             | 2.3          | 0.8 | --- | --- |
| E        | Al <sub>2</sub> O <sub>3</sub> -III | 2.7          | --- | 0.8 | 1.0 |
| F        | Degussa                             | 2.1          | --- | 0.8 | --- |
| G        | Al <sub>2</sub> O <sub>3</sub> -19  | 2.4          | --- | 0.7 | 1.3 |
| H        | Degussa                             | 2.5          | --- | 0.7 | --- |



A and B using an aqueous solution of  $(\text{NH}_4)_3\text{RhCl}_6 \cdot \text{H}_2\text{O}$ . These catalysts were dried and calcined following the procedure used for A and B. Catalysts E and F were also prepared by a double impregnation technique using aqueous chloroplatinic acid to procedure a catalyst with 0.8 wt.% Pt. Drying at  $120^\circ\text{C}$  overnight and then calcining at  $500^\circ\text{C}$  for 3 to 4 hours were done after each impregnation for the above six catalysts. Catalysts G and H were prepared the same as E and F, respectively, except that they were not calcined after the air drying.

ESCA Sample Pretreatment. Samples were pelleted and cut to fit into a rectangular depression in an ESCA sample probe similar in design to one used by Hercules (16). The portion of the probe holding the catalyst sample could be withdrawn into an outer cylinder and sealed under an atmosphere of the pretreatment gas. For pretreatment the calcined samples were exposed to a hydrogen flow at one atmosphere and heated to  $400^\circ\text{C}$ . After this pretreatment the sample was withdrawn into the insertion tube, sealed in the pretreatment gas, inserted into the ESCA, evacuated, and then the ESCA spectra were recorded. A similar procedure was followed for the uncalcined catalysts except that the temperature was first increased in hydrogen flow to  $300^\circ\text{C}$  and held at this temperature for 3 to 4 hours; the sample was then heated to  $400^\circ\text{C}$  and held at this temperature for 18 hours.

### Results and Discussion

Platinum-tin is a bimetallic reforming catalyst that was introduced about the same time as the Pt-Re catalyst. This catalyst has been examined by ESCA using the probe that permits reduction at one atmosphere hydrogen pressure and then insertion into the ESCA chamber before evacuating the hydrogen pressure. The intense aluminum 2p ESCA peak masks the small Pt 4f<sub>7/2</sub> peak so that the chemical state of Pt in a Pt-Sn-alumina catalyst could not be directly determined. However, a similar bimetallic Rh-Sn-alumina catalyst was prepared and reduced in the ESCA probe; in this catalyst it was verified that Rh was reduced to the metallic state (17). A Pt-Sn catalyst on carbon, rather than alumina, was also prepared and reduced; the Pt in this catalyst was reduced by hydrogen to what appears to be the Pt(O) state. Thus, by direct measurement, and by inference, it has been observed that the Group VIII metal was reduced to the zero valent state. In all of these catalysts there was no evidence to support the view that a major fraction of the tin was reduced to the zero valent state. The results of this study (17) were consistent with the model for Pt-Sn-alumina shown in figure 1, or with other non-alloy models. Figure 1 is a schematic to emphasize a model with direct Pt and Sn interaction; certainly the total alumina surface cannot be covered with tin aluminate until the tin loading is much greater than is present in these reforming catalysts.

Similar studies were undertaken with Pt-Re catalysts. These catalysts presented difficult experimental problems for the ESCA examination. Even so, the results do provide additional data in the search to define the structure of this important commercial reforming catalyst.

First, the Pt  $4f_{7/2}$  peak is obscured in this catalyst by an intense alumina  $2p$  ESCA peak just as was the case for Pt-Sn-alumina. Therefore, two Rh-Re catalysts were prepared, one using Degussa alumina and the other with the potassium containing alumina. In unreduced catalysts, the Rh peaks correspond to rhodium in a positive valence state. After reduction the binding energy of Rh corresponds to that of the Rh metal binding energy (solid vertical line in figure 2) and indicates that it is present as Rh(0). By inference, it seems reasonable to assign the valence of platinum in the reduced Pt-Re-alumina catalysts as Pt(0).

Interpretation was complicated by the presence of other peaks in the binding energy region of the Re  $4f_{7/2}$  and  $4f_{5/2}$  peaks. The stainless steel probe contains chromium and in these studies a portion of the probe is exposed to the x-ray beam. Thus, depending upon the particular orientation and the exposure of the probe, a chromium peak of variable intensity interfered with the analysis of the Re ESCA spectrum. To eliminate the chromium peak problem the probe was wrapped with an aluminum metal foil. Examination of the alumina supports alone, as well as a Pt-alumina catalyst show a weak, broad ESCA peak in the Re  $4f$  binding energy region. This peak could result from a number of possibilities including, among others, a ghost carbon peak due to aluminum X-ray contamination. It is an appreciable problem, especially for highly dispersed, low Re loaded catalysts.

Initially, the Pt-Re-alumina catalysts were examined in the oxidized state by placing them on copper backed adhesive. The Re  $4f$  peaks for a number of catalysts are shown in figure 3. Distinct peaks for Re  $4f_{7/2}$  and  $4f_{5/2}$  are not observed in figure 3, rather one broad peak is noted. Tisley and Walton (18) report that full width half maximum (FWHM) are typically 1.2 to 1.5 eV for Re while those in figure 3 are nearly 5.7 eV. The peak maximum is located at a position that is near the mid-point of the two peaks reported for  $Re_2O_7$ . A solution of  $Re_2O_7$  was evaporated on the Cu backed tape; this material gave the two peaks expected for Re. Thus, it appears that: (1) Re is partially reduced by the X-ray beam when supported, but not in the unsupported case, so that the Re(7) and peaks due to lower valence Re species merge to give one very broad peak or (2) Re oxides on the support charge sufficiently to cause line broadening with loss of resolution of the two peaks. Even so, it is apparent that Re is in a high valence state in the fresh catalyst. Portions of each of the catalysts whose spectra are shown in figure 3 were reduced with hydrogen in the ESCA probe. There is clear evidence in figure 4 for the formation of Re in a lower valence state but no peak corresponding to Re(0) in the reduced catalysts is evident.

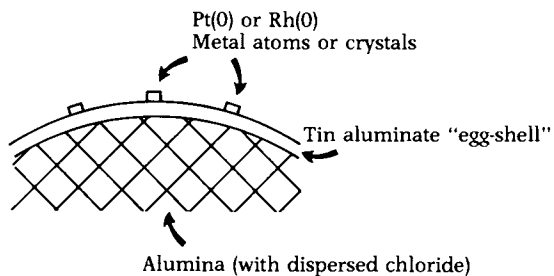


**FIGURE 1.** Schematic of a proposed structure for a Pt-Sn-alumina catalyst.

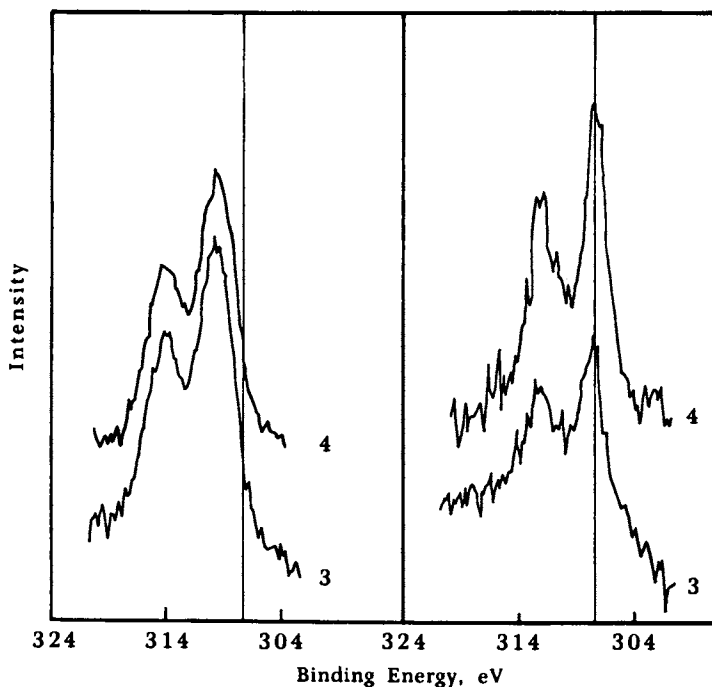


**FIGURE 2.** The Rh  $3d_{5/2}$  and  $3d_{3/2}$  peaks for the oxidized (left) and reduced (right) catalysts: Curve 3 - catalyst D (Re-Rh on Degussa); Curve 4 - catalyst C (Re-Rh on  $Al_2O_3$ -III).

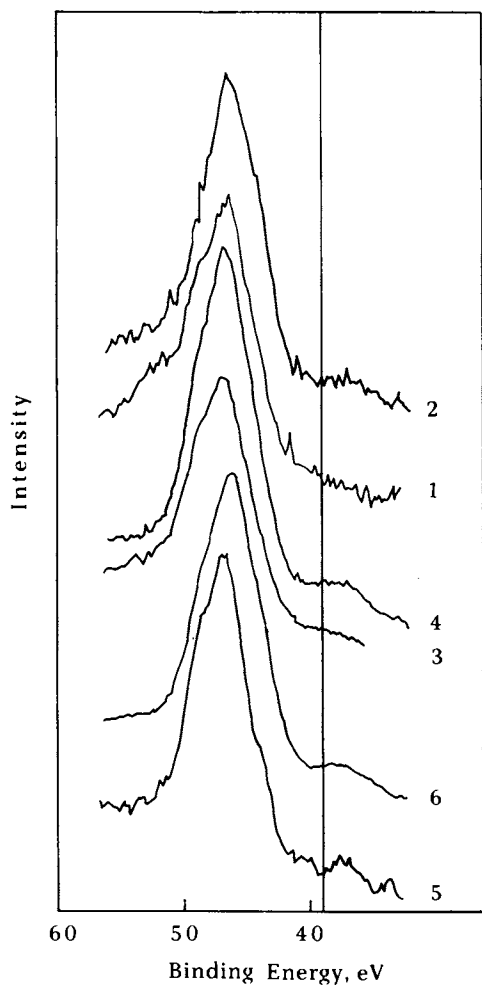


Figure 3. The Re 4f peak for oxidized Pt-Re-alumina catalysts (1) catalyst A (Re on  $\text{Al}_2\text{O}_3$ -III); (2) catalyst B (Re on Degussa); (3) catalyst C (Re-Rh on  $\text{Al}_2\text{O}_3$ -III); (4) catalyst D (Re-Rh on Degussa); (5) catalyst E (Re-Pt on  $\text{Al}_2\text{O}_3$ -III); (6) catalyst F (Re-Pt on Degussa).

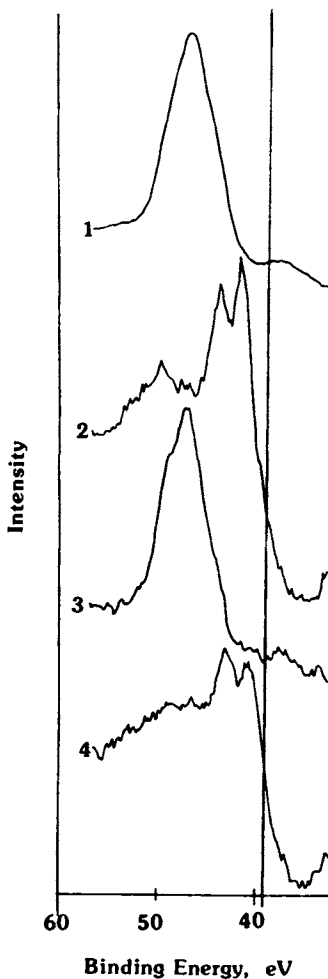


Figure 4. Re 4f peak for Pt-Re catalysts: (1) catalyst F prior to reduction; (2) catalyst F after reduction; (3) catalyst E prior to reduction; (4) catalyst E after reduction.

The catalysts described above had been calcined at 500°C prior to the ESCA studies. Since Mieville (15) reported that it was much easier to reduce catalysts that had been calcined at lower temperatures another series of experiments was performed.

In figure 5 spectra are presented for a Pt-Re catalyst that has just been dried at 120°C (curve 1) and the same catalyst after reducing at 400°C for 18 hours (curve 2). The potassium containing alumina also shows the weak, interfering peak (curve 3, noisy because of a limited number of scans). The Re peak, present as a doublet in this catalyst, resembles the one obtained for  $\text{Re}_2\text{O}_7$  on tape. This suggests, if rhenium hydroxides may be eliminated from consideration, that the calcined rhenium catalysts may have some rhenium in a valence state lower than +7. However, even reduction at 400°C of the uncalcined Pt-Re sample does not produce an observable amount of  $\text{Re(O)}$ .

Samples of Pt-Re on  $\text{Al}_2\text{O}_3\text{-K}$  and on Degussa alumina that had been dried at 120°C in air, but not calcined, were reduced in flowing hydrogen in the probe. The ESCA spectra for these two reduced catalysts are shown in figure 6 along with a spectrum of a Pt- $\text{Al}_2\text{O}_3$  catalyst; fewer scans were made for the Pt- $\text{Al}_2\text{O}_3$  catalyst so that this spectrum shows much noise. The solid vertical line is the binding energy for metallic Re. It is apparent that Re in both of these catalysts has been reduced from the state shown in figure 5 for the uncalcined catalyst but not to the zero valence state. Thus, even for the uncalcined catalyst, ESCA spectra of the reduced catalysts do not provide evidence for  $\text{Re(O)}$ , and hence, for metal alloy formation.

Pt-Re-alumina catalysts were prepared, using alumina containing potassium to eliminate the support acidity, in order to carry out alkane dehydrocyclization studies that paralleled earlier work with nonacidic Pt-alumina catalysts. The potassium containing Pt-Re catalyst was much less active than a similar Pt catalyst. It was speculated that the alkali metal formed salts of rhenic acid to produce a catalyst that was more difficult to reduce. However, the present ESCA results indicate that the poisoning effect of alkali in Pt-Re catalysts is not primarily due to an alteration in the rhenium reduction characteristics.

The data collected to date for Pt-Re or Rh-Re are similar to those obtained with Pt-Sn. Thus, these preliminary Pt-Re data are consistent with a model for Pt-Re that resembles that shown in figure 1 for Pt-Sn in which Re would replace tin. However, instrument sensitivity to  $\text{Re(O)}$ , proof of complete reduction, and other problems do not permit us to eliminate the presence of any  $\text{Re(O)}$  in these catalysts, and certainly not for catalysts under commercial reforming conditions. Even if we could confirm the absence of  $\text{Re(O)}$  in these catalysts, the ESCA data alone could not be used to define the location of Re

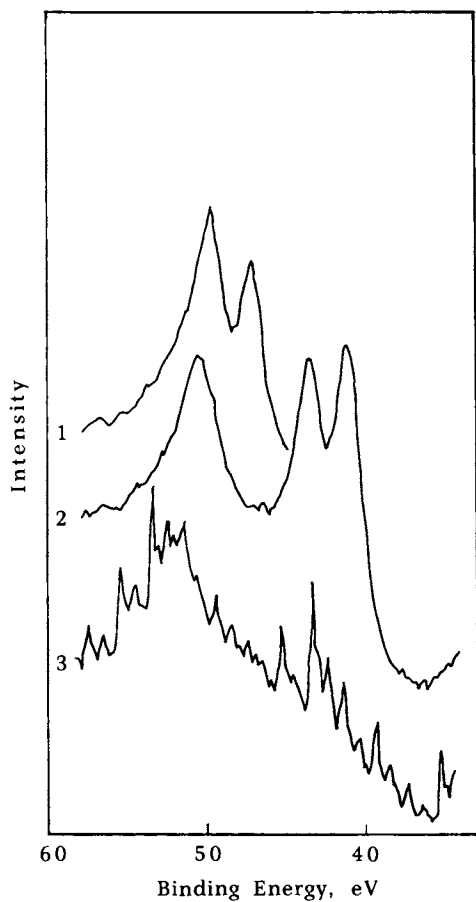


Figure 5. The Re 4f peak for: (1) catalyst G (Re-Pt on  $\text{Al}_2\text{O}_3$ -19) after drying at  $120^\circ\text{C}$ ; (2) catalyst G after reduction at  $400^\circ\text{C}$  for 18 hours and (3) the alumina support.

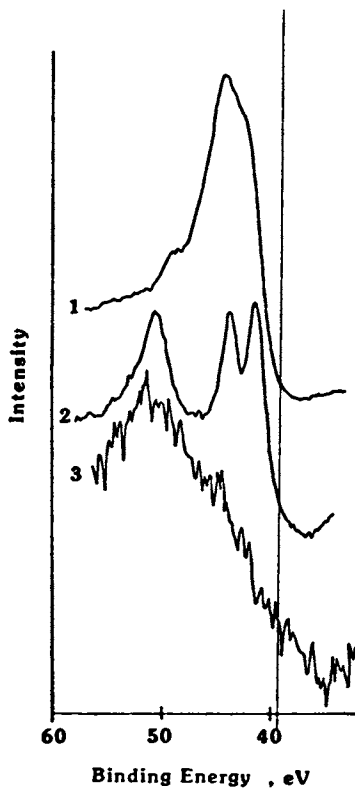


Figure 6. Re ESCA spectra for reduced catalysts: (1) catalyst H (Re-Pt on Degussa); (2) catalyst G (Re-Pt on  $\text{Al}_2\text{O}_3$ -19); (3) a Pt-alumina catalyst. Catalyst G and H had not been calcined prior to reduction.

relative to Pt. The figure 1 model is an attempt to reconcile our catalytic selectivity data obtained for alkane dehydrocyclization (13,14) with the valence state data obtained from ESCA. Sn and Re alter the selectivity for aromatics formation from that of Pt alone, presumably by a mechanism that involves physical contact of the two components. The figure 1 model provides the maximum surface coverage of alumina by either Sn or Re. As shown, the eggshell cannot provide complete surface coverage for 2 wt.% Sn or Re metal loading; thus, it may be more appropriate to refer to the structure as either "rhenium- or tin-aluminate two-dimensional rafts". Even for a 10 wt.% loading of tin on alumina, x-ray diffraction provides no evidence for tin oxide particles; this also supports a raft, or raft-like, structure for the rhenium- or tin-aluminate. The study is continuing and the data in this manuscript will be compared to those obtained with catalysts that have been calcined, sulfided and then reduced. The role of the alkali metal is not clear from the results of the current investigation.

#### Acknowledgment

Funding was provided by the Kentucky Department of Energy Research and Development, Kentucky Energy Cabinet.

#### Literature Cited

1. R. L. Jacobson, M. E. Kluksdahl and C. S. McCoy, *API, Proc. Div. of Refining*, **49**, 504 (1969).
2. M. E. Kluksdahl, U.S. Patent 3,415,737 (1968).
3. V. Haensel in "Heterogeneous Catalysis: Selected American Histories", (B.H. Davis and W. P. Hettinger, Jr., Eds.) *ACS Symposium Series*, **222**, 141 (1983).
4. C. Bolivar, M. Charcosset, R. Ferty, M. Primet, and L. Tournayan, *J. Catal.*, **37**, 424 (1975).
5. N. Wagstaff and R. Prims, *J. Catal.*, **59**, 434 (1979).
6. B. D. McNicol, *J. Catal.*, **46**, 438, (1977).
7. J. H. Onuferko, D. R. Short and M. J. Kelley, 7th North American Catalysis Society Meeting, Philadelphia, PA, May 1-4, 1982, paper B-20.
8. M. F. L. Johnson and V. M. LeRoy, *J. Catal.*, **35**, 434 (1974).
9. A. Webb, *J. Catal.*, **39**, 485-487 (1975).
10. R. Burch, *Platinum Metals Rev.*, **22**, 57 (1978).

11. H. Charcosset, Platinum Metals Rev., **23**, 18 (1979).
12. D. R. Short, S. M. Khalid, J. R. Katzer and M. J. Kelley, J. Catal., **72**, 288 (1981).
13. B. H. Davis, J. Catal., **46**, 348 (1977).
14. B. H. Davis, G. A. Westfall, J. Watkins and J. Pezzanite, Jr., J. Catal., **42**, 247 (1976).
15. R. L. Mieville, ACS Div. Petroleum Chem. Preprints, **28** (#2) 464 (1983).
16. T. Patterson, J. Carver, D. Leyden and D. Hercules, J. Phys. Chem., **80**, 1700 (1976).
17. S. R. Adkins and B. H. Davis, J. Catal., **89**, 371 (1984).
18. D. G. Tisley and R. A. Walton, J. Molecular Structure, **17**, 401 (1973).

RECEIVED June 21, 1985



## Frequency Response Chemisorption Studies of Carbon Monoxide Hydrogenation Catalysts

J. G. Goodwin, Jr.<sup>1</sup>, J. E. Lester<sup>2</sup>, G. Marcelin<sup>2</sup>, and S. F. Mitchell<sup>1</sup>

<sup>1</sup>Department of Chemical and Petroleum Engineering, University of Pittsburgh, Pittsburgh, PA 15261

<sup>2</sup>Gulf Research & Development Company, Pittsburgh, PA 15230

The role of the support on hydrogen chemisorption on supported rhodium catalysts was studied using static and frequency response techniques. In all instances, several kinetically distinct H<sub>2</sub> chemisorptive sites were observed. On the basis of the kinetics, at least one site appears to sorb H<sub>2</sub> molecularly at temperatures below 150°C, regardless of the support. At higher temperatures, a dissociative mechanism may become dominant. Inducement of the SMSI state in Rh/TiO<sub>2</sub> does not significantly alter its equilibrium H<sub>2</sub> chemisorption.

One of the pervasive problems in heterogeneous catalysis is the assessment of the number and nature of active sites participating in a reaction pathway. One would like to have a technique of general applicability. Partial solutions to the problem are afforded by static chemisorption techniques which measure the total number of sites to which an adsorbate bonds, but give little information about site energetics; and temperature programmed desorption which measures the site density as a function of binding energy, but is difficult to apply to weakly bonding sites (1). The technique of Frequency Response Chemisorption (FRC), first proposed by Naphtali and Polinski (2) and further developed by Yasuda (3), offers a very useful alternative approach to the measurement of catalytic sites. Because the technique is applied to a catalyst-adsorbate system essentially at equilibrium, it allows one to elucidate the number and kinetic parameters of sites having a wide range of adsorption energies and rate constants.

To illustrate the utility of the technique, we have addressed the question of the anomalous chemisorptive behavior of titania-supported group VIII metals reduced at high temperatures. The suppression of strong H<sub>2</sub> chemisorption on these catalysts has been ascribed to a strong-metal-support interaction (SMSI) (4). It has also been found that the reaction activity and selectivity patterns of the catalysts are different in normal and SMSI states

(5). Current evidence indicates that the effect may be ascribed to the formation of a  $\text{TiO}_x$  film on the surface of the group VIII metal particles (6,7). Whatever the cause of the SMSI state, it is certainly the case that it has altered site energetics and possibly their density on the catalysts. The extraction of site densities and adsorption-desorption kinetics for these systems with considerable site heterogeneity, should provide a good measure of the applicability of FRC.

### Background

The FRC technique consists of measuring the pressure variation induced by a sinusoidally varying volume. By measuring the dependence of phase difference and adsorption amplitude on the frequency of variation, it is possible to study adsorption-desorption phenomena occurring on different surface sites, even though they are occurring simultaneously.

In the limit of small pressure perturbations, any kinetic equation modeling the response of a catalyst surface can be reduced to first order. Following Yasuda's derivation (3), the system can be described by a set of functions which describe the dependence of pressure, coverage amplitude, and phase on  $T$ ,  $P$ , and frequency. After a mass balance, the equations can be separated into real and imaginary terms to yield a real response function, RRF, and an imaginary response function, IRF:

$$\text{RRF}(T, P, \omega) = \frac{v}{p} \cos \phi - 1 = \sum_j \frac{\alpha_j \beta_j}{\beta_j^2 + \omega^2} \quad (1)$$

$$\text{IRF}(T, P, \omega) = \frac{v}{p} \sin \phi = \sum_j \frac{\alpha_j \omega}{\beta_j^2 + \omega^2} \quad (2)$$

where  $v$  and  $p$  are the volume and pressure amplitudes, respectively;  $\phi$  is the volume-pressure phase shift; and  $\omega$  is the modulation frequency. Equation 2 is also called the adsorption rate spectrum because it exhibits peaks when  $\beta_j = \omega$ . The asymptotic value of the RRF as  $\omega \rightarrow 0$ , is related to the gradient of the adsorption isotherm by:

$$\sum_j \frac{\alpha_j}{\beta_j} = \frac{RT}{V} \left( \frac{dN}{dP} \right)_e \quad (3)$$

These functions serve as phenomenological fingerprints of the system, but more importantly can be related to theoretical models of the adsorption process.

For a non-dissociative Langmuir model, the parameters  $\alpha$  and  $\beta$  are given by:

$$\frac{1}{\alpha_j} = \frac{V}{N_j RT} \left( \frac{P}{k_{dj}} + \frac{1}{k_{aj}} \right) \quad \text{and} \quad \beta_j = k_{aj} P + k_{dj} \quad (4)$$

where  $k_{aj}$  and  $k_{dj}$  are the adsorption and desorption rate constants for site  $j$  and  $N_j$  is the number of sites  $j$ . A plot of  $\beta_j$  vs  $P$  should yield a straight line with slope  $k_{aj}$  and intercept  $k_{dj}$ ; and a plot of  $1/\alpha_j$  vs  $P$  gives a slope of  $\frac{V}{N_j RT k_{dj}}$  and intercept of  $\frac{V}{N_j RT k_{aj}}$ .

For a Langmuir model where a diatomic gas dissociatively adsorbs, the relationships between  $\alpha_j$ ,  $\beta_j$  and the kinetic parameters are given by:

$$\beta_j = 2N_j \sqrt{k_{aj} k_{dj} P} \quad \text{and} \quad \frac{1}{\sqrt{\alpha_j}} = \frac{1}{N_j} \sqrt{\frac{V}{RT k_{aj}}} + \frac{1}{N_j} \sqrt{\frac{VP}{RT k_{dj}}} \quad (5)$$

Thus, a plot of  $\beta_j$  vs  $\sqrt{P}$  should yield a line with slope  $2N_j \sqrt{k_{aj} k_{dj}}$  and a zero intercept; while a plot of  $1/\sqrt{\alpha_j}$  vs  $\sqrt{P}$  will yield a line with:

$$\text{slope} = \frac{1}{N_j} \sqrt{\frac{V}{RT k_{dj}}} \quad \text{and} \quad \text{intercept} = \frac{1}{N_j} \sqrt{\frac{V}{RT k_{aj}}} \quad (6)$$

Other models may be easily derived using Yasuda's formalism.

### Experimental

Catalysts. Rhodium catalysts were prepared from  $\text{RhCl}_3$  using standard aqueous impregnation techniques. The  $\text{SiO}_2$  was Davison Grade 59; the  $\text{TiO}_2$  was Degussa P25. All catalysts were reduced at 400°C under flowing hydrogen for 16 hrs, then passivated at 25°C before introduction into the static chemisorption or FRC apparatus. The catalysts were then reduced at low or high temperature to obtain the final state catalyst. A summary of the catalysts is presented in Table I.

Table I. Properties of the Rhodium Catalysts

| Catalyst            | State | Rh | Reduction |      | Surf. Area            | Dispersion |
|---------------------|-------|----|-----------|------|-----------------------|------------|
|                     |       |    | Temp      | Time |                       |            |
| Rh/SiO <sub>2</sub> | Norm  | 1% | 250       | 16 h | 250 m <sup>2</sup> /g | 60%        |
| Rh/TiO <sub>2</sub> | Norm  | 3% | 250       | 16 h | 50 m <sup>2</sup> /g  | 65%        |
| Rh/TiO <sub>2</sub> | SMSI  | 3% | 450       | 16 h | 50 m <sup>2</sup> /g  | 65%        |

Static Chemisorption. Measurements were made by two procedures. In the first, the catalyst was evacuated at ca. 250°C for at least 8 hrs and cooled to the measurement temperature under vacuum. Hydrogen was then admitted at progressively higher pressures and the amount of gas adsorbed after 15-30 min at each pressure recorded. The sample was then evacuated for 30 min and the dosing procedure repeated so as to obtain a measure of the reversibly adsorbed gas. In the second (saturation) procedure, after reduction and evacuation, the catalyst was cooled to the

measurement temperature and exposed to the highest pressure of  $H_2$  for 36-48 hr so as to saturate the kinetically inaccessible sites (8). The isotherm was then measured by reducing the pressure and determining the residually adsorbed  $H_2$  at two hr intervals. Metal dispersions were obtained from the total  $H_2$  chemisorption isotherms at 25°C, assuming  $Rh/H = 1$ .

**Frequency Response Chemisorption.** A partial diagram of the experimental system is shown in Figure 1. The FRC apparatus was constructed of 3/4-in stainless steel tubing with a glass sample region. Standard high vacuum techniques were followed in its construction leading to an ultimate vacuum below  $1 \times 10^{-7}$  Torr. Volume modulation was provided by a motor-driven cam which in turn compressed a bellows in the sample region. The pressure amplitude was measured using a Datametrics 1 Torr differential capacitance manometer referenced to the initial fill pressure, and volume displacement was monitored with a linear reluctance transducer connected to the bellows drive rod. Angular frequencies from  $10^{-2}$  rad/sec to 10 rad/sec were achieved using a series of four motor-drive combinations. Control of the frequency, data acquisition, and data handling were performed using a Data Translation A/D board in an IBM personal microcomputer. The  $p, v$  data were converted into real and imaginary response functions using Equations 1 and 2.

A catalyst sample, between 1 to 10 grams, was loaded into the apparatus, evacuated, reduced in 1 atm of  $H_2$  at 250 or 450°C overnight and then evacuated at the reduction temperature before cooling and admitting  $H_2$  at the chemisorption temperature. Initial equilibration was very slow for all catalysts indicating the presence of states which are, kinetically, relatively inaccessible (8). In some cases, 10-20 hrs were required for pressure equilibration.

In order to eliminate the possibility that the observed FRC signal was due to diffusion effects or other experimental artifacts, two types of blank runs were performed with each catalyst. In one set of experiments,  $He$  was used as the "adsorbing" gas with a reduced catalyst; while in a second set,  $H_2$  was used with a non-reduced catalyst. Neither type of experimental led to any observable FRC signal.

## Results and Discussion

**Static Chemisorption.** Figure 2 presents the isotherms at 25°C for the  $Rh/SiO_2$  catalyst and the  $Rh/TiO_2$  catalyst in both the normal and SMSI states, obtained using both the adsorption and desorption methods. It is obvious that high pressure saturation for an extended period of time results in significantly higher uptake of  $H_2$  for some catalysts. Since all catalysts had been prereduced and evacuated to desorb weakly bound  $H_2$  prior to any chemisorption measurements, the increased  $H_2$  uptake must be interpreted as being due to slow chemisorption on the metal surface and not to further reduction of either the metal or, in the case of  $TiO_2$ -supported catalysts, the support. This is consistent with the observed extended time required for equilibration in the FRC measurement at low temperatures and with the observations of Dumesic and

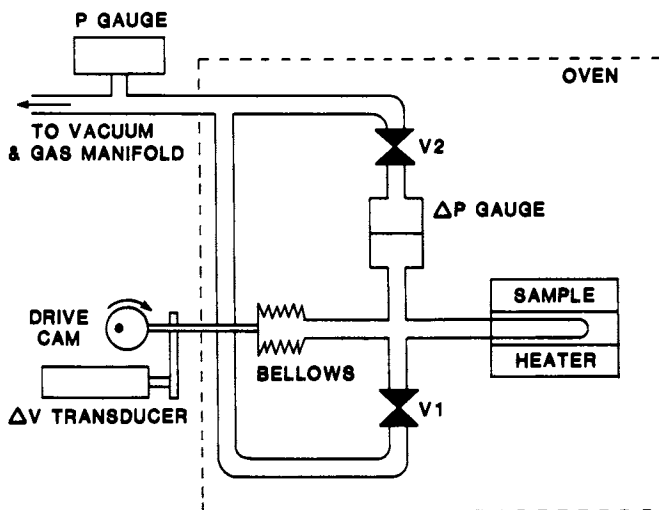


Figure 1. Schematic diagram of frequency response chemisorption apparatus.

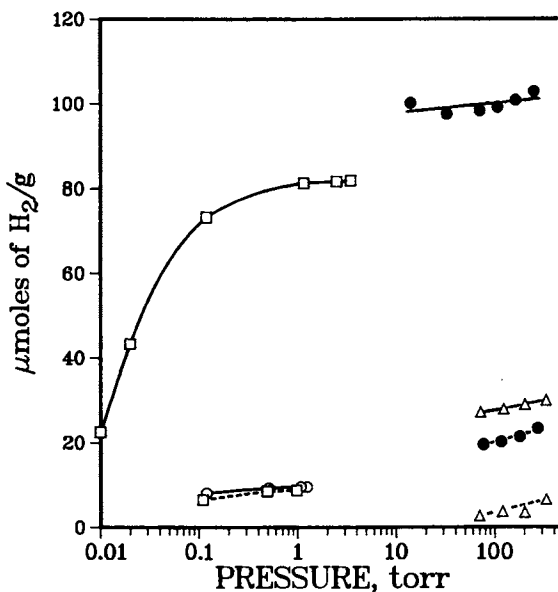


Figure 2. Hydrogen adsorption and desorption isotherms for rhodium catalysts. Solid lines denote total adsorption and dashed lines denote reversible adsorption. The meaning of symbols is as follows:

- - Rh/TiO<sub>2</sub> (SMSI), desorption; ○ - Rh/TiO<sub>2</sub> (SMSI), adsorption; □ - Rh/TiO<sub>2</sub> (non-SMSI), adsorption; Δ - Rh/SiO<sub>2</sub>, desorption.

coworkers (8). The remarkable coincidence of the data for "normal" and SMSI Rh/TiO<sub>2</sub> taken in the saturation mode, indicates that the H<sub>2</sub> chemisorption sites are still present in the SMSI state, but are kinetically much less accessible. These results are consistent with a model of the SMSI catalyst in which a TiO<sub>2</sub> film covers the rhodium and in which H atoms can diffuse through or under the film to Rh sites. One should also note the agreement between the reversible adsorption on normal and SMSI Rh/TiO<sub>2</sub>.

It is apparent from even the static chemisorption results that not all chemisorbing sites have the same energetics, since in all catalysts a sizeable portion of the sorbed gas could be removed by pumping for a few minutes. The exact fraction of the reversible portion depends on support and temperature. For the catalysts used in this study, the reversible portion ranged between 10-30% of the total chemisorption.

Frequency Response Chemisorption. The results of the H<sub>2</sub> FRC experiments are characterized by response function curves having one or more components. In addition, for all catalysts tested, slow initial H<sub>2</sub> equilibration indicated the presence of at least one other chemisorption state. Figure 3a gives the RRF and 3b the IRF for H<sub>2</sub> on non-SMSI Rh at 158°C and 0.40 Torr. Although there is appreciable scatter in the low frequency data, it is apparent that more than one component is necessary to fit the data. The  $\alpha$  and  $\beta$  parameters derived from the IRF and RRF are essentially identical, as they should be for a consistent data set, since the response functions are derived from the same raw data. Figure 4 displays the IRF for H<sub>2</sub> on SMSI-Rh at similar pressures at 50 and 158°C. It is apparent from a comparison of the FRC spectra shown in Figures 3 and 4 that the low frequency peak positions and amplitudes are insensitive to whether the Rh is or is not in the SMSI state. For the high frequency peak at 50°C this is also the case. However, at 158°C there is some decrease in the second peak height and a small shift to lower frequency, indicating that there is a minor observable difference in the FRC behavior of normal- and SMSI-Rh evident in the reversible chemisorption states.

Figure 5 presents data for the non-interacting Rh/SiO<sub>2</sub> catalyst at similar pressures and at 48, 158, and 333°C. Even with the scatter in the 333°C data, there is an obvious transition in the spectra as the temperature is increased. The predominant peak around 10 rad/sec diminishes and the one around .5 rad/sec increases to dominate the spectrum, a trend similar to that observed in the Rh/TiO<sub>2</sub> spectra. Presumably, these trends are the result of differences in apparent activation energies for H<sub>2</sub> adsorption and desorption on the various types of sites.

A comparison of the qualitative features of the FRC spectra for the catalyst studied show a clear distinction between Rh/SiO<sub>2</sub> and Rh/TiO<sub>2</sub>, in terms of their reversible H<sub>2</sub>-chemisorption. Surprisingly, little difference was observed between normal and SMSI-Rh/TiO<sub>2</sub>. "Normal" Rh/TiO<sub>2</sub> behaved quite differently from Rh/SiO<sub>2</sub>, in spite of their similarities in total, i.e., static, chemisorption behavior.

In order to extract adsorption and desorption rate constants from these data, it is necessary to adopt a model. The normal

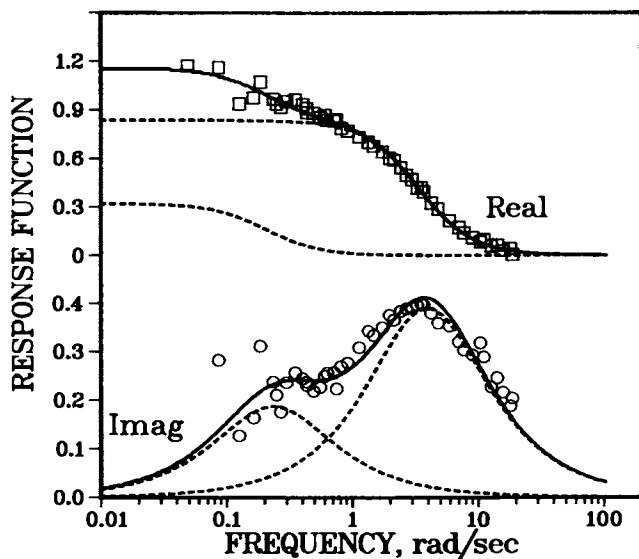


Figure 3. Real and imaginary response functions for  $H_2$  on non-SMSI Rh/TiO<sub>2</sub> at 0.4 Torr and 158°C.

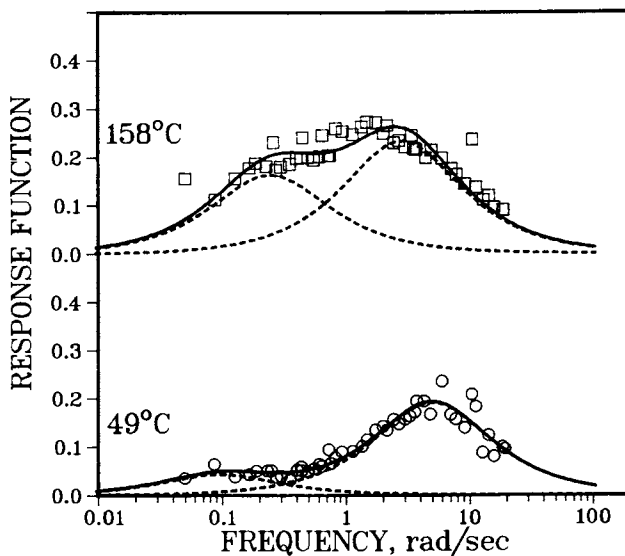
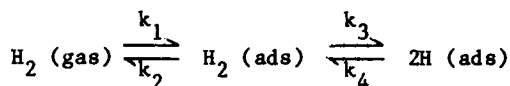


Figure 4. Imaginary response functions for  $H_2$  on SMSI Rh/TiO<sub>2</sub> at 0.34 Torr and 158°C, and at 0.4 Torr and 49°C.

presumption for  $H_2$  on metals is that it dissociates. Thus, a plot of peak positions  $\beta_j$  vs  $P$  should pass through the origin for each temperature. Figure 6 has plots of peak positions vs  $P$ . It is obvious that an intercept of zero is very improbable for any of the low temperature curves. At  $158^\circ C$ , a zero intercept also is not probable for the  $Rh/SiO_2$ . Although the least square lines for the  $Rh/TiO_2$  do not intercept the origin, there is a much higher probability that the dissociative model is consistent with the data. If the  $H_2$  does not dissociate on adsorption, then a plot of  $\beta$  vs  $P$  should be linear. These plots are given in Figure 7. Over the pressure range investigated the molecular adsorption model yields a reasonable fit for both temperatures, indicating that at  $50^\circ C$  the predominant adsorption is molecular, while at  $158^\circ C$  the case is uncertain until a wider pressure range is studied. The parameters extracted from these data are collected in Table II.

The concept of  $H_2$  chemisorbing on Rh as a molecular species may appear at first to be contradictory to other studies; e.g., isotope exchange and TPD; but it is not, given the existence of kinetically distinct sites. An adsorption/desorption process can occur on a specific site via:



with  $k_1 \cdot k_2$  being significantly larger than  $k_3 \cdot k_4$  at  $T < 150^\circ C$ . The existence of molecular adsorption as an observable step does not preclude atomic adsorption, since FRC measures only weak chemisorption on distinct sites. In fact, we are in agreement with previous investigators that the strong chemisorption, accounting for over 70% of the sites, is dissociative in nature. However, the existence of a molecular state of hydrogen on rhodium catalysts has been reported previously (9). On the basis of microcalorimetric measurements, the last 20-30% of a monolayer coverage was found to have a  $\Delta H_{\text{ads}}$  of 3.6 to 7.5 kcal/mole, whereas the initial 0-70% sorbed exhibited a  $\Delta H_{\text{ads}}$  of 46 to 15 kcal/mole with a distinct break in the  $\Delta H$  versus  $\theta$  curve at 70-80% coverage. This weakly-bound hydrogen was assigned to a molecularly adsorbed state. The calculated site density for the high frequency peak on  $Rh/TiO_2$ ,  $\sim 3 \times 10^{-6}/g$ , is consistent with the static chemisorption (Figure 2) in that it corresponds to about 1/3 of the available sites on the SMSI material and 1/3 of the reversible sites on the non-SMSI material. The other observed site and the kinetically slow site(s) could easily account for the remainder of the surface sites.

If such a process is operative and there is an activation energy barrier between the molecular and dissociated states, then one can rationalize the observations. At low temperatures the  $H_2$  readily exchanges between the gas phase and the molecular state, but the second activation energy is too high for a significant flux of  $H_2$  to cross that barrier. At higher temperatures, however, the flux of  $H_2$  crossing the molecular-atomic barrier makes an appreciable contribution to the exchange flux and thus to the observed pressure amplitude and phase-shift. As this latter state has different kinetic parameters, one would expect to see an



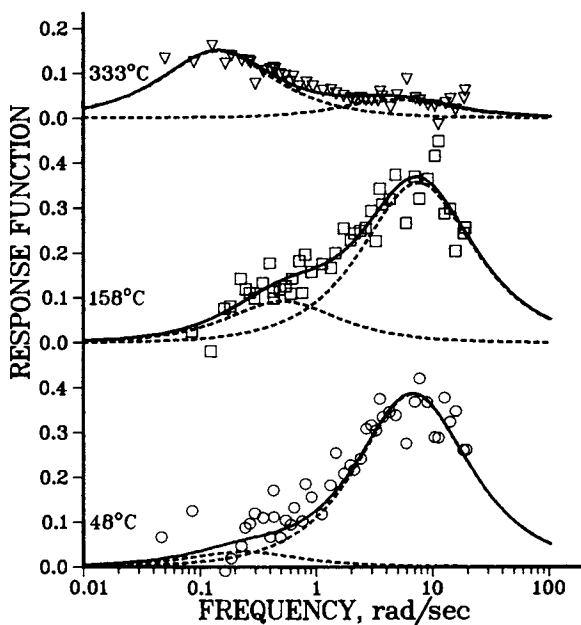


Figure 5. Imaginary response functions for  $H_2$  on  $Rh/SiO_2$  at 0.26 Torr and  $48^\circ C$ , 0.2 Torr and  $158^\circ C$ , and 0.2 Torr and  $333^\circ C$ .

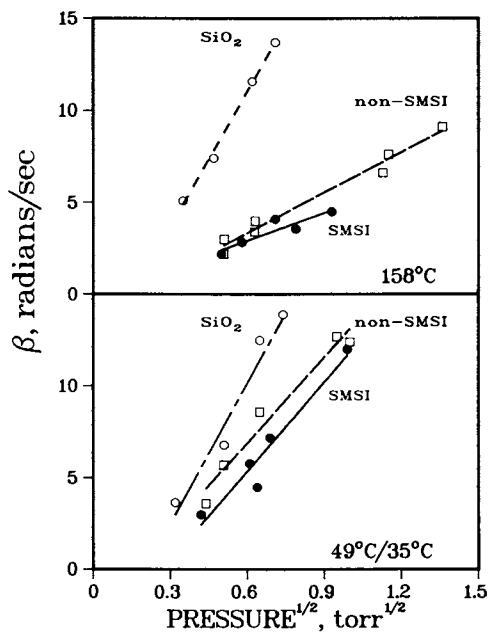


Figure 6. Peak positions in IRF for  $Rh/SiO_2$  at 49 and  $158^\circ C$  and for  $Rh/TiO_2$  at 35 and  $158^\circ C$  as a function of the square root of the  $H_2$  pressure.

apparent shift from one mechanism to another (the classic analogy is unimolecular gas phase decomposition at low pressures). Of course, in our case, parallel rather than sequential adsorption to molecular and atomic hydrogen could yield similar results if there were a fortuitous equality in kinetic parameters at the temperatures and pressures studied. Further experiments over wider T, P and  $\omega$  ranges should allow us to sort out the mechanistic possibilities for these adsorption reactions.

TPD studies tend to depopulate the molecular state sites during the initial evacuation or carrier gas sweep. Thus, they are only sampling the slow sites which may well be dissociative as we have not examined this frequency region. The presence of an intermediate molecular adsorbate would allow us to easily rationalize the possible change in observed molecularity of the FRC results as the temperature was raised in that the dissociative sites would become accessible at the higher temperatures.

A comparison of the Rh/SiO<sub>2</sub> and Rh/TiO<sub>2</sub> plots of  $\beta$  vs p and the derived rate constants serves to further show the similarity between normal- and SMSI-Rh/TiO<sub>2</sub> and their dissimilarity with Rh/SiO<sub>2</sub>. The Rh/SiO<sub>2</sub>  $\beta$  vs p plots at 48 and 158°C are superimposable within our experimental error, while they are significantly different from those for Rh/TiO<sub>2</sub>, normal or SMSI.

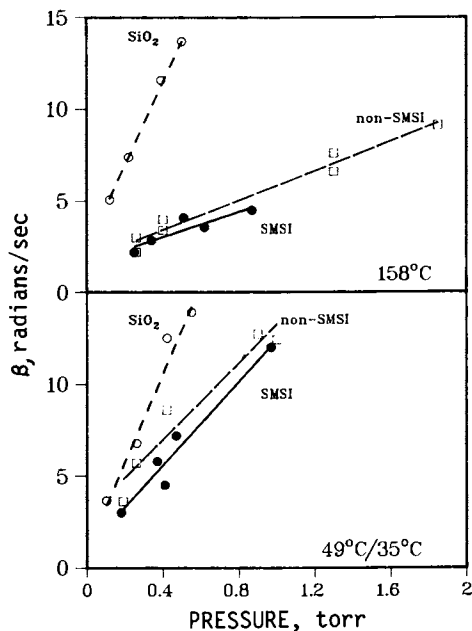


Figure 7. Peak positions in IRF for Rh/SiO<sub>2</sub> at 49 and 158°C and for Rh/TiO<sub>2</sub> at 35 and 158°C as a function of  $H_2$  pressure.

Table II. FRC Kinetic Parameters for the High Frequency Peak

| Catalyst               | State | T°C | $k_a$<br>( $\text{torr}^{-1} \text{sec}^{-1}$ ) | $k_d$<br>( $\text{sec}^{-1}$ ) | $K_{eq}$<br>( $\text{torr}^{-1}$ ) | Sites<br>( $\mu$ moles/g) |       |
|------------------------|-------|-----|---|--------------------------------|------------------------------------|---------------------------|-------|
|                        |       |     |   |                                |                                    | FRC                       | Total |
| Molecular Model        |       |     |   |                                |                                    |                           |       |
| 1% Rh/SiO <sub>2</sub> | Norm  | 48  | 24  | .96                            | 25                                 | 8                         | 3     |
| 3% Rh/TiO <sub>2</sub> | Norm  | 35  | 13  | 1.0                            | 13                                 | 3                         | --    |
|                        | SMSI  | 35  | 13  | 1.4                            | 9                                  | 3                         | 5     |
| 1% Rh/SiO <sub>2</sub> | Norm  | 158 | 23  | 2.4                            | 9.6                                | 1.3                       | 8     |
| 3% Rh/TiO <sub>2</sub> | Norm  | 158 | 3.8   | 2.2                            | 1.7                                | 6.7                       | --    |
|                        | SMSI  | 158 | 4.0   | 1.0                            | 4.0                                | 3.3                       | 12    |
| Dissociative Model     |       |     |   |                                |                                    |                           |       |
| 3% Rh/TiO <sub>2</sub> | Norm  | 158 | $1 \times 10^5$                                 | $5 \times 10^5$                | .2                                 | 11                        | --    |
|                        | SMSI  | 158 | $2 \times 10^5$                                 | $1 \times 10^6$                | .2                                 | 7                         | 12    |
|                        |       |     |   |                                |                                    |                           | 20    |

However, the normal and SMSI Rh/TiO<sub>2</sub> are quite similar. At T < 50°C, the non-SMSI data lie between the Rh/SiO<sub>2</sub> and SMSI Rh/TiO<sub>2</sub>, but by 160°C the Rh/TiO<sub>2</sub> plots are within experimental error of one another.

These results are consistent with recently reported results by Haller, et al. (10) on the reactions of CO/H<sub>2</sub> and NH<sub>3</sub> over Rh catalysts in which no significant differences were observed between catalysts reduced at low and high temperatures (presumably "normal" and SMSI) but in which Rh/SiO<sub>2</sub> was found to behave differently. Thus, there appears to be some correlation between the FRC chemisorption results and the reactivity patterns of supported rhodium catalysts which we would like to believe supports the assertion that the sites at which hydrogen sorbs reversibly are those at which catalytically important reactions occur, and that FRC can monitor the density and relative kinetics of these sites.

### Conclusions

Studies of the static and frequency response chemisorption of hydrogen on Rh catalysts supported on SiO<sub>2</sub> and TiO<sub>2</sub> have shown that:

1. The reversible H<sub>2</sub> chemisorption behavior of Rh/SiO<sub>2</sub> is different from that of Rh/TiO<sub>2</sub>.
2. In its H<sub>2</sub> chemisorption behavior, Rh/TiO<sub>2</sub> in the "normal" state is more like Rh/TiO<sub>2</sub> in the SMSI state than Rh/SiO<sub>2</sub>.
3. There are at least three kinetically distinct modes of H<sub>2</sub> chemisorption on all of the catalysts.
4. Hydrogen chemisorbs reversibly on Rh/SiO<sub>2</sub> and Rh/TiO<sub>2</sub> as a species which can be treated as molecular hydrogen in terms of its adsorption kinetics.

### Literature Cited

1. Cvetanovic, R. J.; Amenomiya, Y. Adv. Catal. related subj., 1967, 17, 103.
2. Naphtali, L. M.; Polinski, L. M. J. Phys. Chem. 1963, 67, 368.
3. Yasuda, Y. J. Phys. Chem. 1976, 80, 1867; *ibid*, 1870.
4. Tauster, S. J.; Fung, S. C.; Baker, R.T.K.; Horsley, J. A. Science 1981, 211, 1121.
5. Vannice, M. A.; Garten, R. L. J. Catal. 1978, 50, 236; Ko, E.I.; Garten R.L. J. Catal. 1981, 68, 233.
6. Santos, J.; Phillips, J.; Dumesic, J. A. J. Catal. 1983, 81, 147.
7. Reasco, D. E.; Haller, G. L. J. Catal. 1983, 82, 279.
8. Jiang, X. Z.; Hayden, T. F.; Dumesic, J. A. J. Catal. 1983, 83, 168.
9. Zakumbaeva, G. D.; Omashev, Kh. G. Kinetik. & Katal. 1977, 18, 450.
10. Haller, G. L.; Henrich, V. E.; McMillan, M.; Reasco, D. E.; Sadeghi, H. R.; Sakellson, S. Proc. 8th International Congress on Catalysis, Berlin, 1984.

RECEIVED March 20, 1985

## Spectroscopy of Metal-Titanium Dioxide Systems

Y.-M. Sun, D. N. Belton, and J. M. White

Department of Chemistry, The University of Texas—Austin, Austin, TX 78712

We have investigated thin film models of catalysts which are known to show strong metal-support interactions. These models consist of vapor-deposited platinum or rhodium on titanium dioxide films prepared in ultrahigh vacuum by oxidation of Ti(0001). Thermal desorption spectroscopy, Auger electron spectroscopy and static secondary ion mass spectrometry have been used to characterize the surfaces of these films before and after thermal treatment in vacuum and with or without chemisorbed carbon monoxide. The results indicate that heating in vacuum to temperatures near 750 K leads to the migration of a reduced form of titania to the surface of the metal films. This migration is accompanied by significant suppression of carbon monoxide and hydrogen chemisorption just as is found in powdered oxide-supported transition metal catalysts. Sputtering removes the segregated titanium-oxygen species, and the chemisorption of carbon monoxide is nearly completely recovered. In thin films of metal that are one to two monolayers thick with no surface titania species, there is no significant suppression of hydrogen chemisorption, indicating that surface segregation is, by itself, not fully responsible for the observed changes in the extent and energetics of hydrogen chemisorption on these surfaces. Clearly, both site-blocking and electronic (bonding) effects play a role in the observed strong metal-support interaction effects.

Recently there has been a great deal of interest in the systems which exhibit strong metal-support interactions (SMSI) (1-12). This activity was stimulated by the work of Tauster et al. (1,2) reported in 1978 which showed that Group VIII transition metals supported on reducible metal oxides were subject to large-scale suppression of chemisorption of hydrogen when the oxides were reduced at high temperatures. Since then there have been a number of papers and conferences on this subject. Proposed explanations include the migration or segregation of oxide species over the transition metal

particles and electronic effects including Pt-titania bonding and/or charge transfer from the support to the metal.

We have undertaken a series of experiments involving thin film models of such powdered transition metal catalysts (13,14). In this paper we present a brief review of the results we have obtained to date involving platinum and rhodium deposited on thin films of titania, the latter prepared by oxidation of a titanium single crystal. These systems are prepared and characterized under well-controlled conditions. We have used thermal desorption spectroscopy (TDS), Auger electron spectroscopy (AES) and static secondary ion mass spectrometry (SSIMS). Our results illustrate the power of SSIMS in understanding the processes that take place during thermal treatment of these thin films. Thermal desorption spectroscopy is used to characterize the adsorption and desorption of small molecules, in particular, carbon monoxide. AES confirms the SSIMS results and was used to verify the surface cleanliness of the films as they were prepared.

### Experimental

The experiments were conducted in an ultrahigh vacuum chamber equipped with a cylindrical mirror electron energy analyzer, a quadrupole mass spectrometer with a Bessel box energy filter for analysis of secondary ions, and an  $\text{Ar}^+$  gun. A Ti(0001) single crystal was mounted on a liquid nitrogen cooled and resistively heated manipulator assembly. The surfaces were cleaned by argon ion bombardment and annealing cycles. The transition metals were deposited using thermal evaporation sources. During the experiments, pressures were routinely  $3 \times 10^{-10}$  torr.

The titania-based thin film catalyst models were constructed by first oxidizing the titanium surface in  $5 \times 10^{-7}$  torr of  $\text{O}_2$  for approximately 30 minutes at 775 K. This produced an AES lineshape consistent with fully oxidized  $\text{TiO}_2$ . The metal was then vapor deposited onto the oxide support with the latter held at 130 K. The thickness of the metal overlayer and its cleanliness were verified by AES. After various annealing and adsorption procedures, these thin films were further characterized using SSIMS, AES and TDS. For comparison, some work was done with Pt on  $\text{Al}_2\text{O}_3$ . In this case a Mo foil covered with  $\text{Al}_2\text{O}_3$  replaced the Ti(0001) substrate.

### Results

Figure 1 shows AES data for the oxidized titanium surface before and after deposition of 30 Å of platinum with the substrate held at 130 K. The platinum thickness was calculated from the attenuation of the oxygen AES signal assuming layered growth of the metal. From the spectra it is clear that the platinum was sufficient to completely attenuate the underlying features of the titanium oxide. The spectra of the oxide surface prior to metal deposition is characteristic of fully oxidized titanium. In the region just below 435 eV the lineshape is significantly different for different oxides of titanium (15).

Figure 2 shows the results of heating a model system consisting of a 30 Å platinum film on oxidized titanium. A linear temperature ramp was applied until the foil reached 760 K, after which the temp-

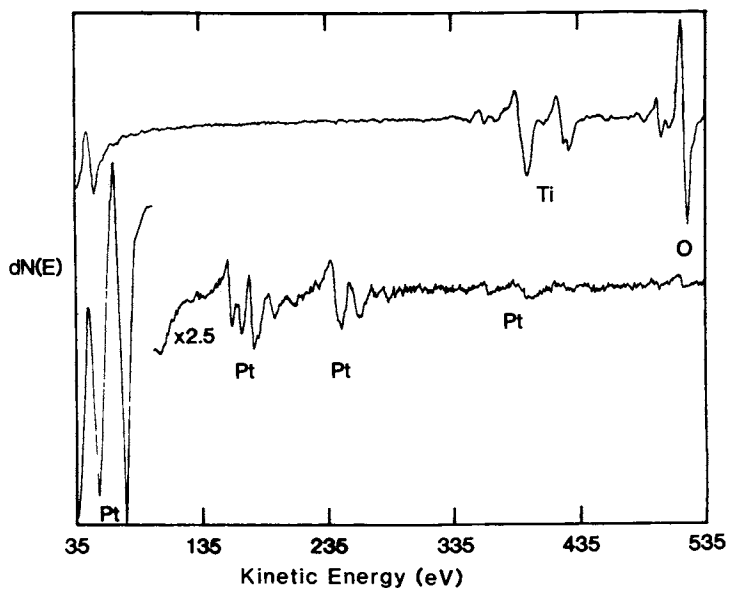


Figure 1. AES spectra of oxidized Ti(0001) (top) and oxidized Ti with 30 Å Pt (bottom).

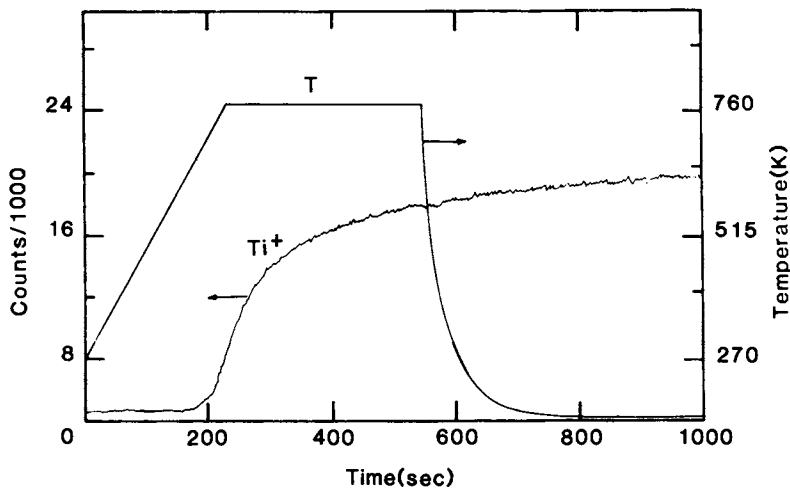


Figure 2. TPSSIMS for 30 Å Pt on oxidized Ti(0001).

erature was held constant for approximately 5 minutes and then the sample was cooled. During these temperature changes the  $Ti^+$  SSIMS signal was followed. Near 615 K the  $Ti^+$  signal begins to rise sharply. This signal continues to rise during the period when the temperature is held constant at 760 K. Upon cooling there was no tendency for the signal to decrease.

A similar sample was heated as above and then subjected to argon ion sputtering, as indicated in Fig. 3. An argon ion current of 0.3  $\mu A$  was utilized and the  $Ti^+$  signal was followed as a function of sputtering time. This figure indicates a sharp decay of the  $Ti^+$  signal followed by a relatively wide region where very little signal is noted. Deeper into the sample the  $Ti^+$  signal rises steadily, maximizes at about 600 seconds and then decays.

On a third sample, thermal desorption of carbon monoxide was carried out before and after annealing to 760 K and after sputtering into the region where the  $Ti^+$  was a minimum (i.e., about 180 seconds in Fig. 3). The TDS results are summarized in Table I. The last column gives the integrated peak desorption area for carbon monoxide.

Table I. CO Thermal Desorption Spectra.

| Substrate                      | Anneal Temp (K) | Desorption Peak (T) | Total Peak Area |
|--------------------------------|-----------------|---------------------|-----------------|
| TiO <sub>2</sub>               | 525             | 400                 | 1.00            |
| TiO <sub>2</sub>               | 775             | 355                 | 0.33            |
| TiO <sub>2</sub> (S)           | 525             | 400                 | 0.95            |
| Al <sub>2</sub> O <sub>3</sub> | 525             | 400                 | 1.00            |
| Al <sub>2</sub> O <sub>3</sub> | 775             | 400                 | 0.98            |

(S)=sputtered (see text)

Two CO desorption peaks (400 and 510 K) were observed on the as-deposited Pt layer. However, for a sample annealed to 525 K the intensity of the high temperature CO peak was  $\approx$ one third its original value. Thus, after annealing to 525 K, the desorption profile consisted of a large peak at 400 K with a shoulder at 510 K. For this reason we report the peak temperature for the low temperature peak only; however, the 510 K shoulder is included in the reported peak area. Comparison of our data to results from other surfaces shows reasonable agreement. Polycrystalline Pt(415 K, 507 K) (16), Pt(110) (430 K, 530 K) (17) and Pt(111) (420 K, 530 K) (18) all have two desorption peaks in the 400-550 K range. For both titania- and alumina-supported Pt, the areas are normalized to the desorption area after annealing the 30 Å overlayer to 525 K and adsorbing CO to saturation at 130 K. For titania annealed to 775 K the peak desorption temperature is decreased by about 45 K, and the total area is decreased by a factor of 3. After sputtering to the minimum and reannealing to 525 K, the peak temperature returns to 400 K and the total peak area increases to approximately its value before the



annealing experiment was carried out. Similar experiments were done with Pt on alumina. As indicated in Table I, annealing to 760 K does not change either the desorption temperature or the area under the carbon monoxide desorption peak.

Similar SSIMS and TDS results were obtained for rhodium on titania and for hydrogen chemisorption on both substrates. In a blank experiment involving no metal overlayer, temperature programming while following the  $Ti^+$  and  $TiO^+$  SIMS signals (Fig. 4) shows that the titania thin film does not begin to change until the temperature reaches about 760 K, well beyond the 615 K where  $Ti^+$  was first noted to increase on the systems with thin metal overlayers.

To explore the possibility of electronic interaction between the reduced titanium oxide and Pt, 1 ML of Pt was deposited on both fully oxidized and partially reduced  $TiO_2$ . The reduced sample was prepared by  $Ar^+$  sputtering of the  $TiO_2$  substrate prior to metal deposition, introducing reduced Ti centers at the Pt-Ti interface.  $H_2$  TDS was used as the highest  $H_2$  desorption temperature (370 K) occurs below the temperature regime of encapsulation. For the reduced sample there was a 70% decrease in  $H_2$  chemisorption and a 33 K shift to lower temperatures when the unannealed sample (first  $H_2$  TDS) was compared to the sample annealed at 370 K (second  $H_2$  TDS). No change in the AES was observed after either the first or second TDS, showing that the Pt overlayer does not island or encapsulate. We take these low Pt coverage experiments to indicate an electronic interaction (preferably bond formation, which does not require significant charge transfer) between Pt and reduced Ti species that is activated at about 370 K.

For the fully oxidized sample the results were somewhat different. After annealing at 370 K there was 25% less  $H_2$  adsorption, and the peak split into two peaks, one shifted higher and one lower, each by about 30 K. There were also small changes in the AES Pt/Ti ratio after the first TDS. Since  $TiO_2$  migrates at lower temperatures for reduced titania, as compared to fully oxidized, we do not favor  $TiO_x$  migration as the explanation. Rather, we suggest that the changes observed after the 370 K anneal of the oxidized sample are due to small changes in the morphology of the Pt overlayer. These alter the number and kind of exposed Pt sites.

### Discussion

From the SIMS, AES and TDS data the following picture emerges. Oxidation of titanium in situ leads to the formation of a film of fully oxidized titania that is thick enough to completely attenuate metal and suboxide contribution to the AES spectra. Heating these overlayers, which are judged to be more than 60 Å thick, results in no detectable changes by SIMS or by AES (not shown) until the temperature exceeds 760 K. Since thermal effects are observed at significantly lower temperature when metal overlayers are present, we conclude that those observations are not due to degradation of the oxide layer via diffusion of oxygen into the bulk metal.

The AES signals observed after deposition of platinum (Fig. 1) indicate that platinum goes down reasonably uniformly under our conditions. This result is confirmed by a more detailed analysis of the attenuation of the oxygen and titanium signals as a function

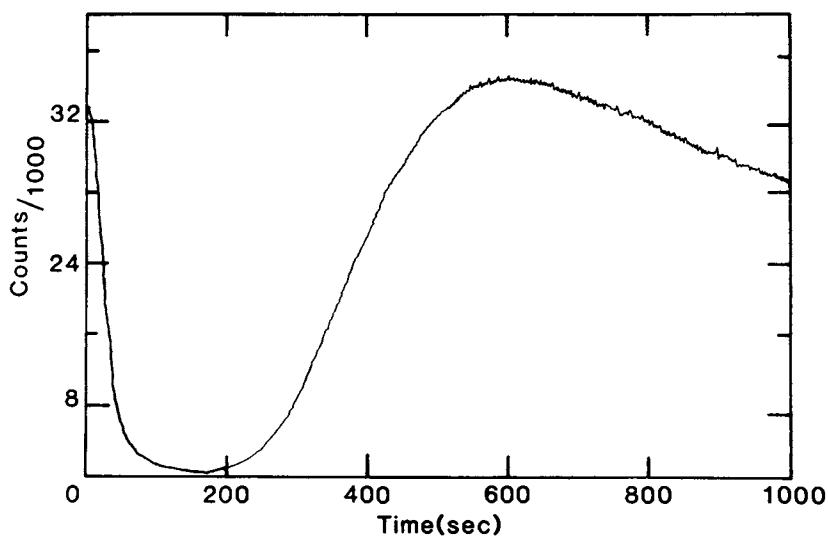


Figure 3.  $\text{Ti}^+$  SIMS depth profile of 30 Å Pt on oxidized Ti(0001) annealed to 760 K.

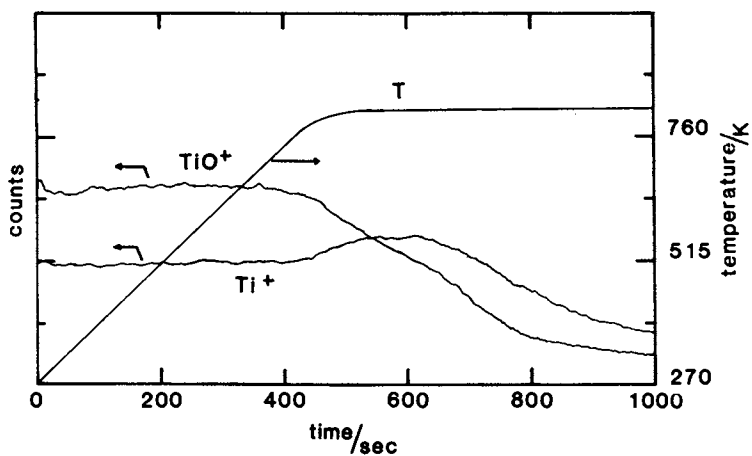


Figure 4. TPSSIMS of the oxidized Ti(0001) substrate without a metal overlayer.

of platinum dosing time. From these results (not shown) we conclude that platinum deposition occurs in a very nearly layer-by-layer fashion at 130 K. Annealing these films to 525 K does nothing to the  $Ti^+$  SIMS signal, but at around 600 K  $Ti^+$  signals begin to appear in the SIMS spectra. These rise sharply to a fairly steady value which increases slowly with time. This is a thermally irreversible change since, upon cooling, (Fig. 2) the  $Ti^+$  signal does not return to a low value. The species formed is largely segregated to the surface as indicated by this sputtering profile of Fig. 3. Sputtering removes this overlayer and leads to metallic platinum. After sputtering through the platinum the oxide region is again reached. After 600 seconds the metal layer is removed, and the  $Ti^+$  signal begins to drop. This final drop is the result of a decreasing cross-section for ion desorption which accompanies the preferential removal of oxygen.

The observed thermal desorption results are entirely consistent with the picture that emerges from Figs. 2 and 3. Annealing to 525 K (Table I) gives a thermal desorption peak for carbon monoxide like that observed from bulk platinum films. Annealing to 775 K lowers the desorption peak temperature and, more importantly, attenuates sharply the amount of carbon monoxide that will adsorb. Sputtering to the minimum of the  $Ti^+$  signal followed by an anneal to 525 K and adsorption gives a result that is very much like that observed prior to the high-temperature anneal. From these and other more detailed results involving Auger lineshape studies, we conclude that the species that migrates to the surface of the platinum is probably  $TiO$ .

For similar samples on alumina, these effects are not observed, as indicated in Table I. No migration of aluminum or oxygen species is observed in AES, and the capacity of the film to adsorb carbon monoxide is not altered by changing the annealing temperature from 525 to 760 K.

All of these results are consistent with the notion that surface migration of titanium oxide species is an important factor that contributes to the suppression of carbon monoxide chemisorption. The  $H_2$  chemisorption experiments on 1-2 ML of Pt, where no migration is observed, strongly indicate that electronic (bonding) interactions are also occurring. Thus, for the titania system, both electronic interactions and surface site blocking due to titanium oxide species must be considered in interpreting SMSI effects.

#### Acknowledgments

This work was supported in part by the Office of Naval Research.

#### Literature Cited

1. Tauster, S. J.; Fung, S. C.; Garten, R. L. J. Am. Chem. Soc. 1978, 100, 170.
2. Tauster, S. J.; Fung, S. C. J. Catal. 1978, 55, 29.
3. Imelik, B. et al., eds. "Metal-Support and Metal Additive Effects in Catalysis"; Elsevier: Amsterdam, 1982, and references cited therein.

4. Huizinga, T., "Metal Support Interactions in Pt and Rh Al<sub>2</sub>O<sub>3</sub> and TiO<sub>2</sub> Catalysts," Ph.D. Thesis, Eindhoven University of Technology, 1983.
5. Jiang, X.-J.; Hayden, T. F.; Dumesic, J. A. J. Catal. 1983, 83, 68.
6. Resasco, D. E.; Haller, G. L. J. Catal. 1983, 82, 279.
7. Vannice, M. A.; Twu, C. C. J. Catal. 198, 82, 213.
8. Short, D. R.; Mansour, A. N.; Cook, J. W. Jr.; Sayers, D. E.; Katzen, J. R. J. Catal. 1982, 82, 299.
9. Fang, S.-M.; White, J. M. J. Catal. 1983, 83, 1.
10. Tanaka, K.; White, J. M. J. Catal. 1983, 79, 81.
11. Baker, R. T. K. J. Catal. 1980, 63, 523.
12. Fung, S. C. J. Catal. 1982, 76, 225.
13. Belton, D. N.; Sun, Y.-M.; White, J. M. J. Am. Chem. Soc. (in press).
14. Belton, D. N.; Sun, Y.-M.; White, J. M. J. Phys. Chem. (in press).
15. Davis, G. D.; Natan, M.; Anderson, K. A. Applic. Surface Sci. 1983, 15, 321.
16. Thrush, K. A.; White, J. M., unpublished results.
17. McCabe, R. W.; Schmidt, L. D. Surface Sci. 1976, 60, 85.
18. Collins, D. M.; Spicer, W. E. Surface Sci. 1977, 69, 55.

RECEIVED January 8, 1985

## Isotopic Tracers in Catalysis: Aromatics from *n*-Paraffins over Te-NaX Zeolite

Joe W. Hightower and Geoffrey L. Price<sup>1</sup>

Department of Chemical Engineering, Rice University, Houston, TX 77251

Both radioactive and stable isotopic tracers are used in catalysis to validate reaction networks, test for intermediates, confirm reaction orders, determine intra- or inter-molecular mechanisms, establish rate limiting steps, document direct participation of surface atoms in fluid-solid reactions, etc. Several of these uses are illustrated in studies of the formation of aromatics from *n*-paraffins over the highly selective Te-NaX zeolite. Tests with <sup>14</sup>C-labeled molecules have shown that olefins are exclusive intermediates in the aromatization reactions. Alkylcyclohexanes are not intermediates even though they can be readily dehydrogenated under reaction conditions (about 450 C, 10% HC in hydrogen, 1 atm). The catalyst acts primarily as a dehydrogenation agent with cyclization probably occurring thermally from 1,3,5-hexatriene. When D<sub>2</sub> replaces H<sub>2</sub>, there is little scrambling with the H atoms in the hydrocarbons. A primary kinetic isotope effect indicates that C-H cleavage is involved in the rate limiting step of the reaction.

Stable and radioactive tracers have been used extensively in catalysis to validate reaction networks, test for intermediates, confirm reaction orders, distinguish between intra- and inter-molecular mechanisms, establish rate limiting steps, document direct participation of surface atoms in fluid-solid reactions, etc. A unique feature of tracer studies is that individual reaction steps can be followed in a complicated set of reactions without perturbing the chemical composition of the

<sup>1</sup>Current address: Department of Chemical Engineering, Louisiana State University, Baton Rouge, LA 70803

reacting mixture. Several books (1-3) have highlighted many tracer studies, and the techniques have become so common that a reaction mechanism can scarcely be considered as established without use of tracers.

The purpose of this article is to focus on a single series of reactions and to illustrate some of these uses of isotopic tracers. The set of reactions involves the dehydrocyclization of n-paraffins into aromatics over non-acidic Te NaX zeolite (4-7).

### Experimental

The catalyst was prepared according to a recipe formulated by researchers at the Mobil Research Labs in Princeton (8-9). 11% (wt) Te metal was ball-milled with NaX zeolite (13X), and the resulting powder was activated by heating in a stream of dry hydrogen at 500 C. Reactions were carried out in either a batch recirculation reactor at about half an atm pressure or in a plug flow reactor at one atm. Reaction mixtures were usually in the ratio of about 1/10 to 1/4 hydrocarbon/hydrogen. Excess hydrogen was required to stabilize the Te and prevent it from eluting from the bed. Aliquots of the product stream were separated by GLC, and the components were individually collected and transferred to a mass spectrometer (for deuterium) or a scintillation counter (for  $^{14}\text{C}$ ) for isotopic measurements. The radioactivity is expressed as specific activity (counts/min mmole).

### Results

Reaction Intermediates:  $^{14}\text{C}$  Tracers. Yields of benzene well in excess of 95% can be obtained over this catalyst in a flow reactor from a mixture of n-hexane and hydrogen. The only significant other products are the n-hexenes (in thermodynamic equilibrium with each other), and their mole fractions pass through a maximum when plotted against n-hexane conversion (see Figure 1). This suggests that the n-hexenes may be intermediates in the formation of benzene.

To test this theory, a mixture of n-hexane and  $^{14}\text{C}$ -labeled 1-hexene was reacted in hydrogen over the catalyst at various space velocities. The specific activity of each of the products (the n-hexenes were lumped together) are shown in Figure 2. The important observation is made at zero conversion. When extrapolated to infinite space velocity, the benzene has approximately the same specific activity as the hexene, thus clearly indicating that essentially all the benzene is formed in a reaction sequence that involves equilibrium with gaseous n-hexenes. It may then be concluded that olefins are intermediates in the aromatization process.

We (4) have also shown that cyclohexane can be readily converted into benzene under these reaction

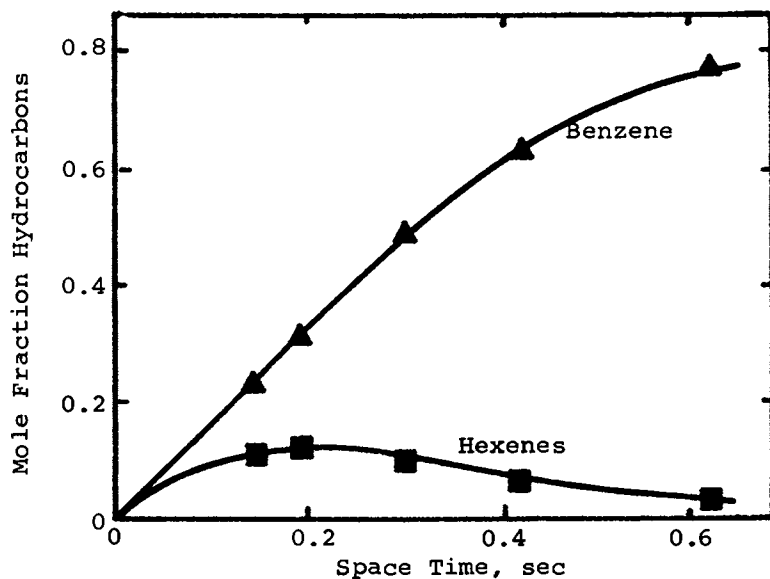


Figure 1. Products from n-hexane/ $H_2$  reaction at  $540^\circ C$  over Te-NaX zeolite in a flow reactor.

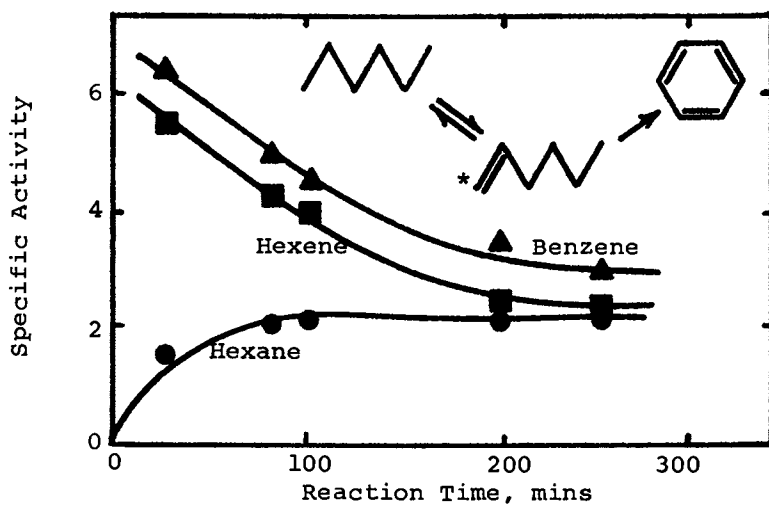


Figure 2. Radioactivity in products from n-hexane/ $^{14}C$ -1-hexene/ $H_2$  over Te-NaX at  $460^\circ C$ .

conditions. Another possibility to consider is that the dehydrocyclization process may involve cyclization at an early stage to cyclohexane, followed by dehydrogenation to benzene. This was tested by reacting a mixture of cyclohexane and  $^{14}\text{C}$ -n-hexane or  $^{14}\text{C}$ -1-hexene. As shown in Figure 3, there was no measureable radio-activity in the unreacted cyclohexane. This means that cyclization must necessarily occur further along the reaction sequence than cyclohexane, i.e. cyclohexane is not an intermediate.

It is quite possible that more highly dehydrogenated products (e.g. hexadiene or hexatriene) may also be involved in the reaction sequence. However, none of these species was observed in the GLC. This is not surprising since both these species are highly reactive and may not have accumulated to any measurable extent. One could have used labeled diolefins or triolefins in mixture with n-hexane to test this possibility. Although this experiment was not attempted, we would speculate that most of the radioactivity would have been quickly incorporated into the benzene with a small amount perhaps flowing temporarily upstream into the olefins and the paraffin.

Additional experiments were carried out to examine the formation of toluene from n-heptane (10). When the heptane was labeled with  $^{14}\text{C}$  in the 1-position, half the radioactivity was in the methyl group and the other half was in the aromatic ring of the toluene. This clearly indicates that ring formation involves 1,6 or 2,7 closure and excludes the possibility of any interconversion between five membered and six membered rings. Perhaps this is not surprising since the catalyst's acid sites are neutralized by the sodium.

Bond Cleavage with Deuterium. Even though cyclohexane can be ruled out as a direct intermediate in n-hexane dehydrocyclization, it will dehydrogenate to benzene at temperatures well below those required for the n-hexane reaction. We decided to study the reaction of cyclohexane at the molecular level with D tracers. The first experiment was to react a mixture of cyclohexane and  $\text{D}_2$  (50 torr/200 torr) and look for the incorporation of D atoms into the hydrocarbons at 500 C. Surprisingly, there was very little scrambling of the D and H atoms. The unreacted cyclohexane contained almost no D, and the benzene product (at conversions up to 80%) contained approximately a constant level of 1 D/molecule. Clearly, a D atom (and only one D atom) from the gaseous  $\text{D}_2$  somehow participates in the dehydrogenation reaction. Even though 6 H atoms are lost from the hydrocarbon, one D atom is added. When mixtures of  $\text{C}_6\text{H}_6/\text{C}_6\text{D}_6$  or  $\text{C}_6\text{H}_6/\text{D}_2$  are circulated over the catalyst under the same reaction conditions, there is essentially no H/D exchange or intermolecular scrambling.

Since scrambling of H and D atoms does not occur



either among hydrocarbon molecules or between hydrocarbons and gaseous D<sub>2</sub>, the C-H bonds must be relatively stable in presence of this catalyst. It is then possible that cleavage of C-H bonds may be involved in the rate limiting step of the reaction. This was tested by comparing the reaction rates of cyclohexane-H<sub>12</sub> and cyclohexane-D<sub>12</sub> in either H<sub>2</sub> or D<sub>2</sub> under identical conditions. As shown in Figure 4, the lightweight cyclohexane-H<sub>12</sub> reacts about 2.5 times more rapidly than does the perdeuterated cyclohexane-D<sub>12</sub>. Whether the gas phase contains H<sub>2</sub> or D<sub>2</sub> has no effect on the reaction rate. The conclusion from the large primary isotope effect is that indeed C-H bond cleavage is involved in the rate limiting step of the reaction. Armed with this information, one can then be assured that increasing the ability to break C-H bonds will improve the overall catalytic activity.

Solid State NMR. Two solid state Na NMR spectra are shown in Figure 5. The top figure is for the initial NaX zeolite and the bottom curve shows the Te-NaX zeolite after activation in hydrogen. It is apparent that the presence of the Te alters the position and shape of the Na spectrum. The conditions for these spectra were the following: scan range - 500 gauss, time constant - 3 seconds, receiver gain - 200, field set - 17,845 gauss, scan time - 4 minutes, and microwave frequency - 20,000 Hertz.

XPS Spectra. The following table compares the XPS results for the NaX and the Te-NaX materials.

XPS Spectra of NaX and Te-NaX

|                | <u>NaX Alone</u>          |                              | <u>Te-NaX</u>             |                              |
|----------------|---------------------------|------------------------------|---------------------------|------------------------------|
|                | <u>Binding Energy(ev)</u> | <u>Relative No. of Atoms</u> | <u>Binding Energy(ev)</u> | <u>Relative No. of Atoms</u> |
| Te(3d)         | ---                       | ---                          | 573.6                     | 0.42 (Te <sup>0</sup> )      |
|                |                           |                              | 576.6                     | 0.35 (Te <sup>4+</sup> )     |
| Na(1s)         | 1072.55                   | 29.4                         | 1072.40                   | 17.5                         |
| Al(2s)         | 119.15                    | 17.3                         | 119.20                    | 13.6                         |
| Si(2p)         | 102.3                     | 23.4                         | 102.3                     | 18.9                         |
| O(1s)          | 531.4                     | 94                           | 531.5                     | 87                           |
| Na( $\alpha$ ) | 574.0                     |                              | 574.2                     |                              |
| O( $\alpha$ )  | 552.8                     |                              | 552.8                     |                              |

All these spectra were corrected to C(1s) = 284.6 ev. It should also be pointed out that the peak corresponding to Te(+4) disappeared after 30 mins of radiation. However, the other peaks remained unchanged and no new peaks appeared.

Discussion

Careful kinetic measurements have been combined with

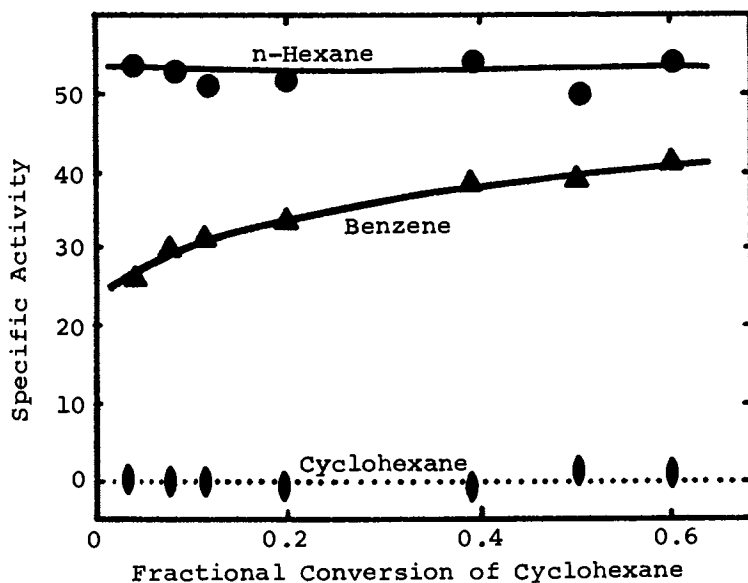


Figure 3. Radioactivity in products. n-Hexane- $^{14}\text{C}$ /Cyclohexane/ $\text{H}_2$  over Te-NaX at  $450^\circ\text{C}$ .

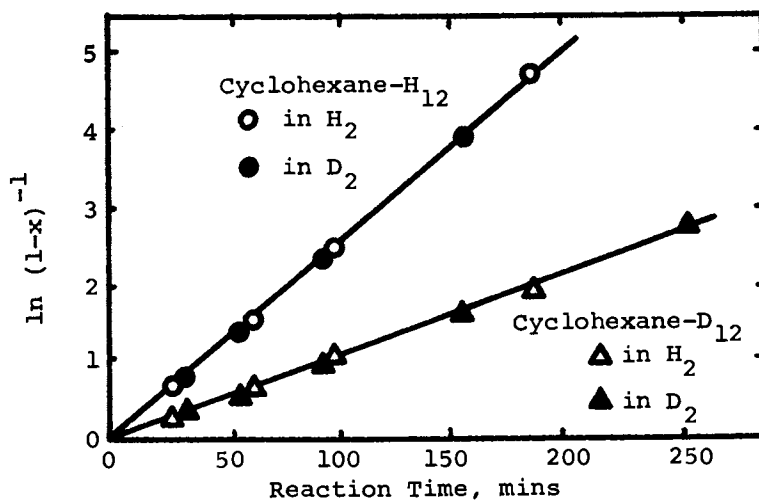


Figure 4. Reactivity of cyclohexane- $\text{H}_{12}$  and - $\text{D}_{12}$  in recirculation reactor at  $400^\circ\text{C}$ .

isotopic tracers to shed considerable light on the quantitative aspects of n-paraffin dehydrocyclization over a Te NaX zeolite catalyst. There can be little doubt that olefins are involved as intermediates in the overall reaction scheme. Their rise and decline with conversion (Figure 1) is typical of the behavior of intermediates, and the correspondence between the benzene and hexene specific activities in Figure 2 confirms this conclusion. Furthermore, the reversible nature of the paraffin-olefin reaction is seen in the accumulation of radioactivity in the unreacted n-hexane. This reaction is not at complete equilibrium, however, since deuterium is not scrambled extensively into the product molecules when the carrier gas is D<sub>2</sub> instead of H<sub>2</sub>.

Even though cyclohexane is rapidly converted into benzene under these conditions, the results in Figure 3 clearly prove that it cannot be a gas phase intermediate in the n-hexane reaction. If it were, there would have been radioactivity in the unreacted cyclohexane when it was mixed with labeled n-hexane; none was observed. This proves that the cyclization step must be further along the reaction stream and must not involve an olefin forming cyclohexane which then dehydrogenates to the aromatics.

It also points out another advantage of isotopic tracers. The fact that a suspected intermediate reacts quantitatively to form the final product does not necessarily mean that it is an intermediate. Just because a compound is formed, or because it may give the desired final product, does not prove that the compound in question is a gas phase intermediate in the overall reaction. It must be shown that the compound behaves properly under dynamic reaction conditions, and isotopic tracers can test this behavior most effectively.

In the n-paraffin reactions, let us suggest that the reaction scheme shown in Figure 6 satisfies most of the observations. The solid lines represent reactions that have been observed, while the dashed lines are proposed reactions involving products whose steady state concentrations are too small to be measured with our analytical equipment.

According to this scheme, the catalyst serves primarily to promote dehydrogenation. Cyclization of the hexatriene was shown years ago (11) to occur thermally in the gas phase at temperatures well below these dehydrocyclization conditions. Thus, the overall reaction is projected to be the combination of several catalytic dehydrogenation steps and a non-catalytic cyclization step. This projection implies that the design of the catalytic reactor may be important in order to optimize the ratio of void space for cyclization and catalyst space for dehydrogenation.

The dehydrogenation studies with labeled cyclohexane suggest that C-H cleavage is involved in the rate

limiting reaction step. We (5) have shown that each Te atom is capable of holding two H atoms. Extraction of the H atoms from the hydrocarbons may well involve a series of steps like the ones shown in Figure 7. The exact nature of the active site is not known. However, solid state Na NMR spectra in Figure 5 indicate that the Na environment in the catalyst is altered considerably by the presence of the Te (5). This probably means that the Te atoms are somehow located in close proximity to the Na ions and possibly involve a chemical interaction between the two. The XPS spectra summarized in the table indicate that the Te in the reduced catalyst is about equally distributed between the zero and +4 oxidation states.

### Conclusions

This Te NaX zeolite is a highly selective catalyst for converting n-paraffins (C<sub>6</sub> or larger) into aromatics. The presence of the Na probably reduces the inherent acidity to the point where skeletal isomerization and cracking of the hydrocarbon do not occur to any appreciable extent. Olefins are intermediates in the reaction. However, cyclohexane is not a gas phase intermediate, even though it can be quantitatively converted into the correct benzene product under reaction conditions. The rate limiting step is cleavage of C-H bonds. Most likely, the reaction is a combination of catalytic dehydrogenation reactions and a rapid noncatalytic cyclization step. The Te species probably act to remove the H atoms from the hydrocarbons by forming a surface di-hydride which can subsequently release H<sub>2</sub>. While the exact location of the Te atoms in the zeolite structure remains elusive, they are probably located in positions sufficiently close to the Na ions to influence the nuclear magnetic properties of the sodium.

### Acknowledgments

The authors are grateful to the Robert A. Welch Foundation, the National Science Foundation, the Phillips Petroleum Foundation, and Haldor Topsoe A/S (Denmark) for financial support. We express our thanks to the Exxon Research and Engineering Co. for measuring the solid state NMR spectra and the Shell Development Company for the ESCA measurements. Finally, we acknowledge the participation of Dr. Zinifer R. Ismagilov in part of the cyclohexane studies.

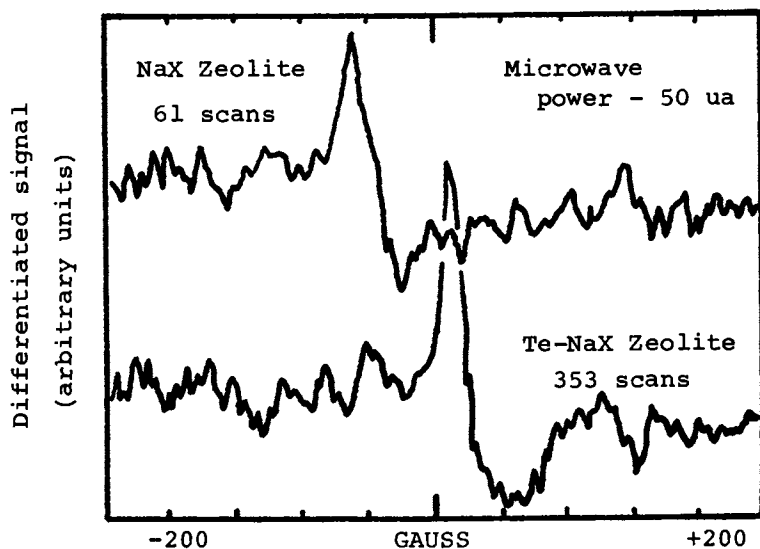


Figure 5. Na NMR spectra for starting NaX zeolite and hydrogen activated Te-NaX zeolite.

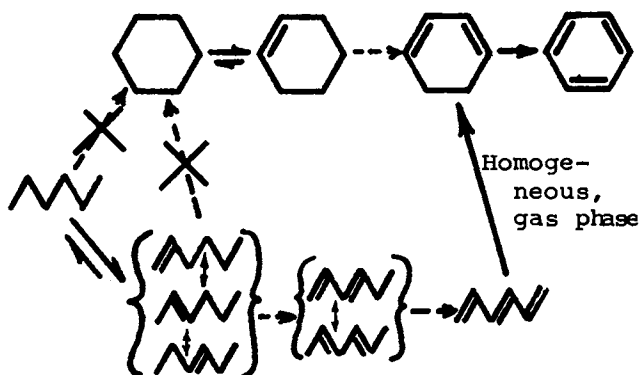


Figure 6. Proposed reaction scheme during dehydrocyclization of n-paraffins over Te-NaX.

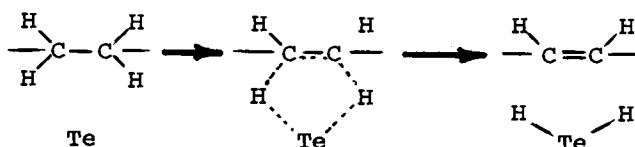


Figure 7. Possible formation of Te dihydride during dehydrogenation of paraffins over Te-NaX zeolite.

Literature Cited

1. Ozaki, A. "Isotopic Studies of Heterogeneous Catalysis"; Kodansha Ltd./Academic Press; 1977.
2. Happel, J.; Hnatow, M. A. "The Use of Tracers to Study Heterogeneous Catalysis"; New York Academy of Sciences, No. AA9213; 1973.
3. Tamaru, K. "Dynamic Heterogeneous Catalysis"; Academic Press; New York; 1978.
4. Price, G. L.; Ismagilov, Z. R.; Hightower, J. W. J. Catalysis 1982, 361, 73.
5. Price, G. L.; Ismagilov, Z. R.; Hightower, J. W. J. Catalysis 1983, 369, 81.
6. Price, G. L.; Ismagilov, Z. R.; Hightower, J. W. Proc. 7th International Congress on Catalysis, 1980, p. 708.
7. Price, G. L.; Egedy, C. J. Catalysis 1983, 467, 84.
8. Maile, J. N.; Weisz, P. B. J. Catalysis 1971, 288, 20.
9. Lang, W. H.; Mikovsky, R. J.; Silvestri, A. J. Catalysis 1971, 293, 20.
10. Price, G. L. Ph.D. Thesis, Rice University, Houston, Texas, 1979.
11. Lewis, K. E.; Steiner, H. J. Chem. Soc. 1964, 8080.

RECEIVED March 11, 1985

# Titanium Dioxide Single-Crystal and Powder Surfaces in the Presence and Absence of Platinum

## An Auger Electron Spectroscopic and Electron-Stimulated Desorption Study

M. A. Vannice<sup>1</sup>, P. Odier<sup>2</sup>, M. Bujor<sup>3</sup>, and J. J. Fripiat<sup>3</sup>

<sup>1</sup>Department of Chemical Engineering, The Pennsylvania State University, University Park,  
PA 16802

<sup>2</sup>C.N.R.S.-C.R.P.H.T., Orleans La Source 45045, France

<sup>3</sup>C.N.R.S.-C.R.S.O.C.I., Orleans La Source 45045, France

This study examined the changes in surface composition, as indicated by O/Ti and C/Ti ratios measured by AES, as temperatures were varied from 300 to 1075K and surfaces were exposed to H<sub>2</sub>, O<sub>2</sub>, and CO. ESD studies were also conducted by continuous exposure of one region to the Auger electron beam and comparison to another region outside the beam. On the single crystals without Pt, initial O/Ti ratios between 1.5 and 2.0 increased rapidly between 650K and 850K to values near or above 2.5. The addition of Pt eliminated the high O/Ti ratios at 900K. The high O/Ti ratios attained above 900K infer that the slow step in the reduction of TiO<sub>2</sub> is the removal of oxygen from the surface, and either ESD or Pt enhances this step.

Recently, metal/TiO<sub>2</sub> systems have attracted attention because of observed changes in adsorption behavior, catalytic activity, and the possibility of electron transfer between the metal and titania (1-15). This study was undertaken to examine the changes in surface composition, as indicated by O/Ti and C/Ti ratios measured by Auger Electron Spectroscopy (AES), as temperatures were varied from 300 to 1075K and exposures to H<sub>2</sub>, O<sub>2</sub> and CO were employed. The effect of temperature was of principal importance because reduction of metal/TiO<sub>2</sub> catalysts, such as Pt/TiO<sub>2</sub>, at temperatures near 775K is typically required to induce the SMSI state; reduction at lower temperatures produces catalysts with normal adsorption properties (2). We wished to compare the behavior of a single crystal of TiO<sub>2</sub> to that of a TiO<sub>2</sub> powder frequently used for catalyst preparation, so the rutile TiO<sub>2</sub> (100) plane was studied and compared to pressed powder wafers containing small crystallites of TiO<sub>2</sub>. The influence of Pt was examined by placing H<sub>2</sub>PtCl<sub>6</sub> on the surfaces of both the single crystal and the powder wafer. Electron Stimulated Desorption (ESD) studies were conducted by continuously exposing one region of the surface to the Auger electron beam and comparing the surface composition to that in another region outside the beam.

0097-6156/85/0288-0098\$06.00/0

© 1985 American Chemical Society

### Experimental

This study was conducted in an ultrahigh vacuum (UHV) stainless steel chamber pumped by a 200 l/s ion pump which contained an Auger Cylindrical Mirror Analyser (CMA) and Low Energy Electron Diffraction (LEED). The residual vacuum obtained after a 12 h baking was generally near  $10^{-9}$  Torr and could be lowered to about  $5 \times 10^{-10}$  Torr by circulating liquid nitrogen against the chamber wall. The gas composition was continuously monitored by a quadrupole mass spectrometer. A sample manipulator allowed the rotation and positioning of the sample.

The  $\text{TiO}_2$  single crystals were cut from a single crystal rod in the shape of disks, 10 mm wide and 1 mm thick, which displayed the (100) face. The sintered powders were pellets cut from a rod of pure Degussa P25  $\text{TiO}_2$  powder compacted in an isostatic press at high pressure (400 MPa) after heating at 873K in air for 3 hours before compacting. The 2% wt Pt/ $\text{TiO}_2$  powder sample was not heated before compacting to avoid the loss of Pt by formation of volatile Pt oxides. Two Pt/ $\text{TiO}_2$  (100) samples were prepared using a solution of  $\text{H}_2\text{PtCl}_6$  to give nominal Pt monolayer coverages of 0.5 and 1.

Auger spectra were recorded in the derivative mode from 20 to 600 eV to detect all the surface elements, including contaminants, at the various  $\text{TiO}_2$  surfaces. Continuous variations of the O and Ti surface concentrations during heat treatments or gas adsorption were followed by scanning alternatively only the energy regions of the O and Ti auger peaks. A peak selector was used to produce this selective scanning every few seconds. The peak-to-peak heights of the Auger peaks were used as a close approximation to the surface concentration. The 387 eV Auger peak of Ti was chosen to follow Ti concentrations because it is much less sensitive to the chemical environment than the 418 eV peak and therefore its variation is more closely related to changes in the surface concentration of Ti. This choice is consistent with other authors (21,31).

### Results

Initial studies were made on two single crystals to determine cleaning procedures and variations in O/Ti intensity ratios. The carbon peak at 273 eV was removed by heating above 823K in vacuum for periods of 5 minutes or longer. Heating in  $\text{O}_2$  ( $1.3 \times 10^{-2}$  Pa) facilitated carbon removal and the C peak began to decrease at lower temperatures. Also, cooling in  $\text{O}_2$  retarded the growth of the carbon peak. When present, the small S(151 eV), K(251 eV) and Ca(293 eV) peaks could be removed by a 20 minute Ar ion bombardment at 300K; however, this enhanced the C peak and, in agreement with previous work (16), it reduced the O/Ti ratio to values between 1.3 and 1.4. Figure 1 shows Auger spectra for a (100) surface from crystal A. The initial high O/Ti ratios near 2.4 were reduced by ion bombardment to 1.5 and increased to only 2.1 after another heat cycle to 953K. Considering that the sensitivity to the Ti(387 eV) peak is 10% lower than that to the O(510 eV) peak (17), the intensity ratio of 2.1 corresponds to an O/Ti atomic ratio near 1.9, which is close to stoichiometric for  $\text{TiO}_2$ .



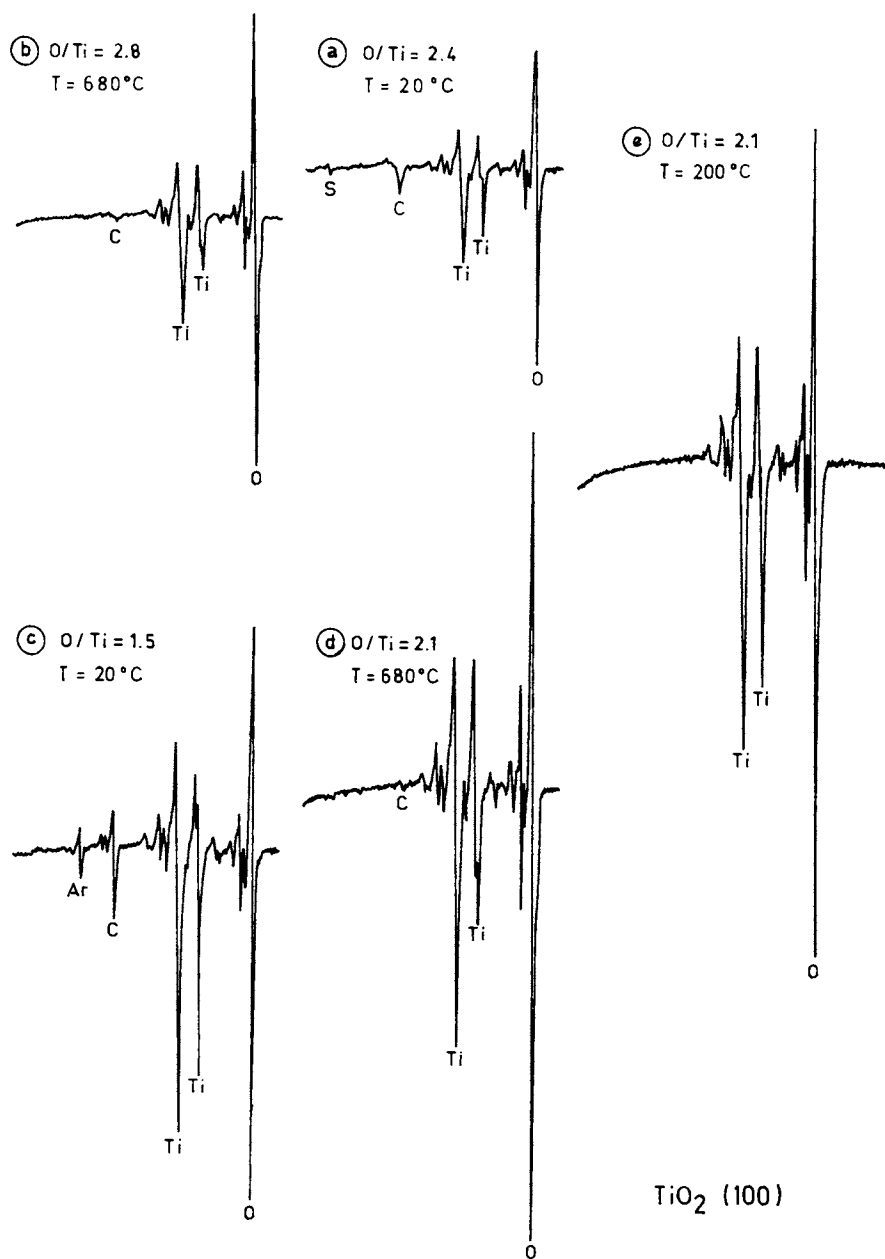


Figure 1. Auger spectra on  $\text{TiO}_2(100)$  during cleaning procedures.  
 1a. Before ion etching - Room temperature  
 1b. Before ion etching - Heating at  $680^\circ\text{C}$   
 1c. After ion etching - Room temperature  
 1d. After ion etching - Heating at  $680^\circ\text{C}$   
 1e. After ion etching, heating and cooling at  $200^\circ\text{C}$  under  $5 \times 10^{-7}$  torr  $\text{O}_2$ .

On all the  $\text{TiO}_2(100)$  crystals further investigated, maximum C/Ti ratios between 0.2 and 0.3 were sometimes observed after standing for long periods at 300K in the UHV system and before high temperature treatments, as shown in Figure 1a, for example.

A second crystal (B) gave higher intensity ratios between 2.8 and 2.9 at 923K when heated in vacuo. Exposure at this temperature to  $\text{H}_2(1.3 \times 10^{-2} \text{ Pa})$ ,  $\text{O}_2(1.3 \times 10^{-3} \text{ Pa})$  or  $\text{CO}(1.3 \times 10^{-2} \text{ Pa})$  had essentially no effect on these O/Ti intensities during exposure time periods of 5-20 min (300-1200 L).

To study the effects of ESD and temperature on surface composition in more detail, a third crystal (C) was used which had a Pt coating on its back to improve contact with the holder. The first study of the effects of ESD and temperature on  $\text{TiO}_2$  involved the continuous monitoring of the O(510 eV) and Ti(387 eV) peak intensities as the temperature was slowly increased to 1073K. The behavior is shown in Figure 2 for a portion of the surface with an initial O/Ti ratio of 2.3. Later, a complete heating-cooling cycle was run on a portion of the surface with an initial O/Ti ratio of 1.70, and the results are also shown in Figure 2. The final O/Ti ratio at high temperature was very near that of the initial run.

To clarify the role of EDS in these heating/cooling cycles, two regions on the crystal surface 1mm apart were examined simultaneously. One region was continuously exposed to the electron beam whereas the other region was exposed to the beam for only a short period of time (1-2 min) during which the O(510 eV) and Ti(387 eV) peaks were measured using the peak selector described previously. The differences in behavior regarding surface composition are clearly shown in Figure 3. The intensities of the two peaks versus temperature are shown in Figure 4. The Ti peak decreases continuously during the cycle whereas the O signal increases between 373 and 823K during heating and decreases continually during the cooling cycle. The indicated final values are those measured the following day after 16 hr at 300K in the UHV system.

The single crystal covered with  $1.2 \times 10^{15}$  Pt atoms ( $\approx 1$  monolayer) was characterized by AES prior to any heat treatment or reduction procedure, and peaks at 40 and 67 eV indicated the Pt was detectable. Additional spectra at 513K showed weak additional Pt peaks at 151 and 168 eV and a Cl peak at 181 eV. A stepwise heating/cooling cycle was conducted under the electron beam and with no beam on. The O/Ti ratios for the two regions are represented in Figure 5. Quite similar O/Ti ratios were found in both regions and essentially no hysteresis occurred during cooling. After this series of experiments, the sample was heated to 1073K, cooled to 503K, and exposed to  $\text{O}_2(3.3 \times 10^{-2} \text{ Pa})$ . Little change in the O/Ti ratio occurred in either region. Following this, a number of regions were examined by AES to detect Pt, but all Pt peaks found were barely distinguishable from the background noise level.

The stepwise heating/cooling cycle was conducted on the  $\text{TiO}_2$  wafer (84% rutile after being heat treated in  $\text{O}_2$ ) and a typical correlation of O/Ti ratio versus temperature is shown in Figure 6 for one particular run. Surface reduction is facilitated by ESD, and additional cycles continually reduced both maximum O/Ti ratio obtained at high temperature and the minimum O/Ti ratio observed at room temperature, and a final value of 0.7 was measured at the com-

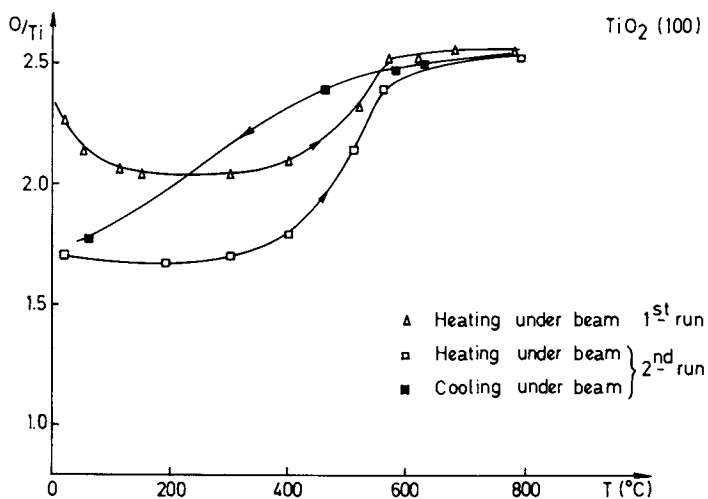


Figure 2. Variations of the O/Ti Auger signal ratio on the TiO<sub>2</sub>(100) surface: heating and cooling under the electron beam.

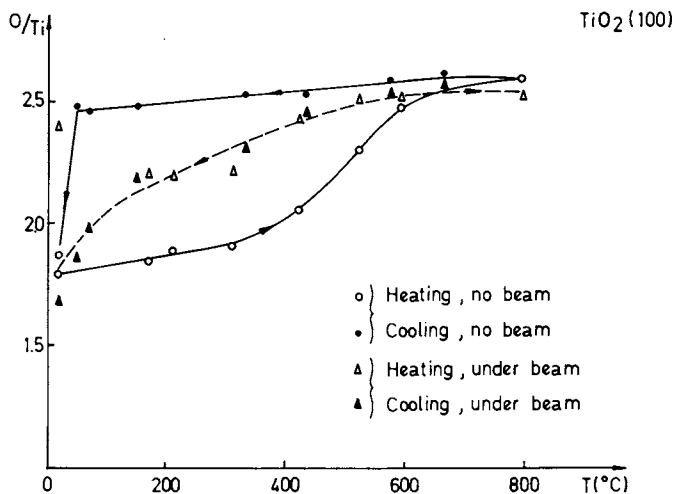


Figure 3. Variations of the O/Ti Auger signal ratio on the TiO<sub>2</sub>(100) surface: heating and cooling under the beam and with no beam.

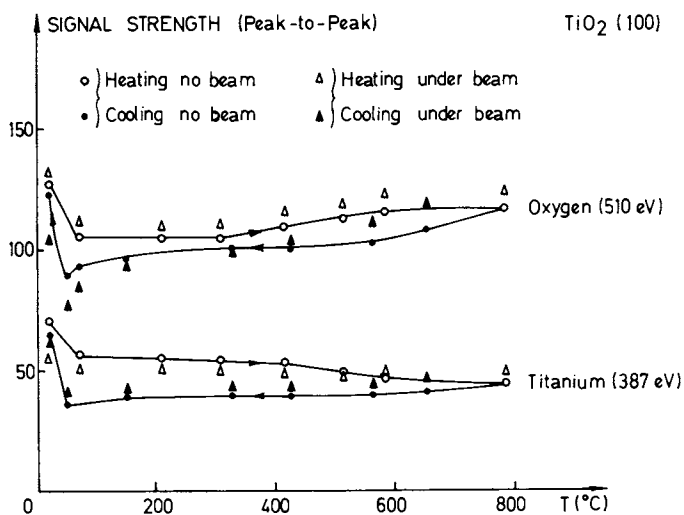


Figure 4. Variations of the O and Ti Auger signal strength during heating and cooling of the  $\text{TiO}_2(100)$  surface.

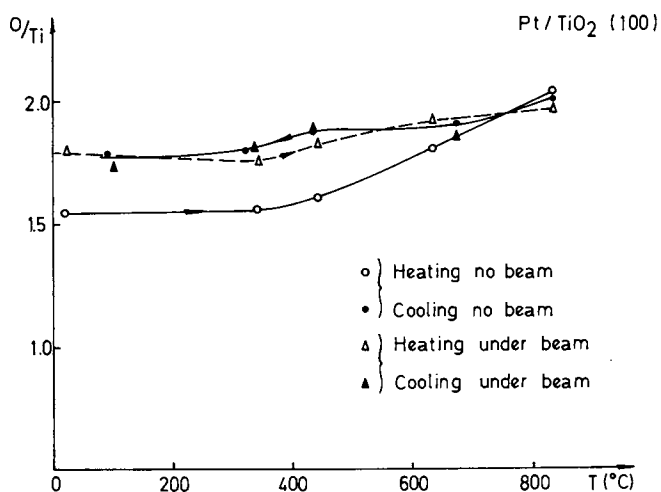


Figure 5. Variations of the O/Ti Auger signal ratio on the 2% wt Pt/ $\text{TiO}_2(100)$  surface: heating and cooling under the beam and with no beam.

pletion of these experiments. The region out of the beam reproducibly followed the pattern in Figure 6, cycling between O/Ti ratios of 1.8 and 2.1. Exposure at 493K to H<sub>2</sub> had little effect on peak intensities, and exposure to O<sub>2</sub> produced only a small reversible increase. Finally, C(273 eV) peaks were quite small on all areas of this wafer, typically giving C/Ti ratios below 0.1, but they were always smaller in the regions not continuously exposed to the electron beam.

The results from the stepwise heating/cooling cycle for the 2% Pt/TiO<sub>2</sub> wafer prepared from this impregnated titania (anatase) powder are also shown in Figure 6. Similar to the Pt/TiO<sub>2</sub> (100) sample, some charging was observed in the beginning at temperatures below 373K. Several high temperature treatments removed this problem. High O/Ti ratios between 2.8 and 3.0 were obtained at 903K even after H<sub>2</sub> exposures up to  $3 \times 10^5$  L. Exposure to O<sub>2</sub> ( $5.3 \times 10^{-2}$  Pa) at 493K produced a small reversible increase in the O/Ti ratio. Finally, extremely high initial values of O/Ti and C/Ti ratios, 7-8 and 1-4 respectively, were observed on various regions of the wafer indicating a high level of contamination. Heating in  $10^{-5}$  Pa O<sub>2</sub> at 773K for 35 min reduced these ratios to near 1.9 and 0.5, respectively, and a subsequent heat treatment at 1033K in vacuo gave more typical O/Ti ratios near 2.8 and C/Ti ratios below 0.1. After this treatment, the maximum C peak intensities obtained on this TiO<sub>2</sub> powder catalysts were much smaller than those on the single crystals, and the C/Ti ratios ranged between 0.04 and 0.19. This surface carbon concentration was much lower than that reported in a previous study of Pt/TiO<sub>2</sub> powder (9). A representative Auger spectrum after all runs were made is shown in Figure 7.

### Discussion

Numerous studies have been devoted to the characterization of TiO<sub>2</sub> (16,18-40), and many of them involved surface analytical techniques such as AES, XPS, UPS, LEED, and EELS (18-32). More recent studies have been devoted to metal/TiO<sub>2</sub> systems (7,9,12-15,41-47). However, these surface characterization studies were typically conducted on surfaces at 300K after various annealing treatments while our particular interest was the actual state of the surface at various temperatures, particularly in the region between 473-773K, which is required to induce SMSI behavior. Previous studies (16, 23) had found clear evidence for electron beam damage when AES is utilized, and its effect on the surface composition of titania was examined in terms of ESD over a wide temperature range. Finally, because of the significant changes in H<sub>2</sub> and CO chemisorption on TiO<sub>2</sub>-supported metals, the knowledge that bulk TiO<sub>2</sub> becomes oxygen deficient when heated to high temperature in vacuo or in H<sub>2</sub> (33, 34), and the possibility that titanium oxide species may form on the dispersed metal surface, the effects of H<sub>2</sub>, CO and O<sub>2</sub> exposure were considered. The composition of the TiO<sub>2</sub> surface and the effect of ESD was determined on single crystals and titania powders before and after Pt was dispersed on their surfaces.

Some results from this study of TiO<sub>2</sub> surfaces were in good agreement with previous reports. For example, the C(372) peak could be removed by heating above 875K (20,21,23); Ar ion bombard-

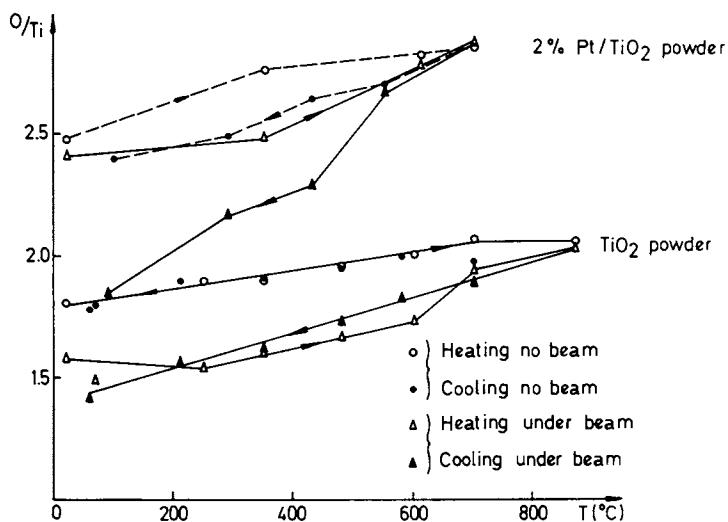


Figure 6. Variations of the O/Ti Auger signal ratio of the TiO<sub>2</sub> powder and the 2% wt Pt/TiO<sub>2</sub> powder.

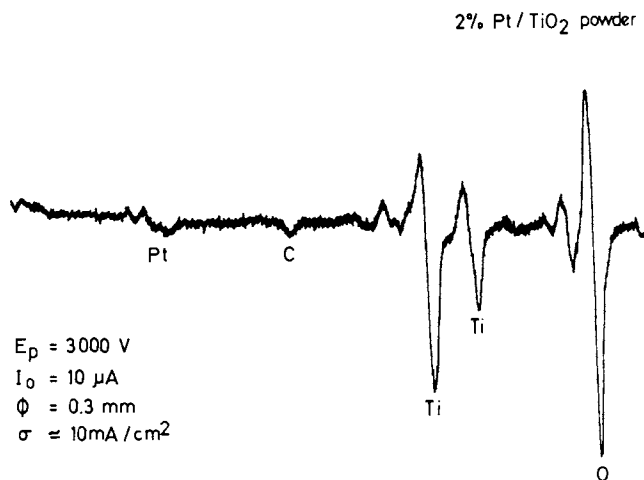


Figure 7. Typical Auger spectrum of the surface of the 2% wt Pt/TiO<sub>2</sub> powder.

ment at 300K produced low O/Ti ratios below 1.5 (16); and after several heat cycles above 875K, typical O/Ti ratios were between 1.5 and 2.0 after cooling to 300K, which frequently required over one hour (20,21,23).

The  $\text{TiO}_2$  (100) surface repeatedly showed a marked increase in the O/Ti ratio between 575 and 875K, as shown in Figures 2 and 3, behavior which is in excellent agreement with that reported by Tait and Kasowski (23) although their Auger results were obtained at 300K after annealing at each given temperature. Recently, Nishigaki (31) has found the same qualitative behavior showing that the oxygen contribution to the interatomic transition [L(Ti)M(Ti) V(O)] rises with the annealing temperature at the expense of the titanium contribution. This increase is attributed to the diffusion of bulk lattice oxygen towards the surface and results in raising the local oxygen coordination to Ti atoms. The present study does not give any information on the nature of the bonding of oxygen at the surface at these conditions: similar XPS studies would be very helpful to get such information. It should be mentioned that the O/Ti increase becomes appreciable only above 600K where bulk diffusion enables the reduction of  $\text{TiO}_2$  to start significantly (33,34). This marked change in surface composition between 575 and 875K is particularly intriguing because this is the temperature range during which SMSI behavior is induced in  $\text{TiO}_2$ -supported metal catalyst systems (2,6).

The effect of the Auger electron beam on the composition of the (100) surface in the absence of Pt is clearly demonstrated in Figure 2 and 3: it greatly facilitates removal of surface oxygen, gives little hysteresis in the heating/cooling loop, and it repeatedly gives low O/Ti ratios between 1.5 and 2.0. The electron beam damage observed here is related to electron stimulated desorption, ESD, (28). In their paper, Knotek and Feibelman have proposed that ESD of positive ions ( $\text{O}^+$ ) occurs as a consequence of an interatomic Auger transition, a view supported by the recent findings of Nishigaki (31). Intensive beam damage can occur, as reported previously for other  $\text{TiO}_2$  surfaces (16,23), and surfaces with O/Ti ratios as low as those expected for stoichiometric  $\text{Ti}_2\text{O}_3$  are easily obtained at low temperature ( $< 500\text{K}$ ) by continuous electron beam exposure.

During heating, the region under the beam behaves globally as the region outside the beam; however, it is noticeably different during cooling. The former follows the heating line while the latter decreases only slightly, giving significant hysteresis as in Figure 3. However, after standing out of the beam an O/Ti ratio below 2.0 was again obtained as shown in that Figure.

One of the surprising results in this study was the high O/Ti ratio routinely achieved at and above 875K, and values between 2.5 and 3.0 frequently were measured. Higher ratios of O/Ti than predicted for stoichiometric  $\text{TiO}_2$  [2.2, taking into account the relative sensitivities of the O(510) and Ti(387) peaks at 3 keV] are sometimes found in the literature (19,22,32), and they should not be taken as the clean oxide values because the AES signal does not discriminate between adsorbed oxygen and true metal oxide oxygen. We are aware that changes in line width can alter peak-to-peak ratios; however, we have assumed that the O/Ti ratios indicate aver-

age surface composition even if individual phases are difficult to identify unambiguously (32). On this basis the surface appears to be  $\text{TiO}_2$  and may even contain excess oxygen; therefore, an interesting paradox exists under these high-temperature conditions. Bulk reduction of  $\text{TiO}_2$  is known to occur (33) and, indeed, the initially yellowish crystals were blue when removed from the chamber; however, the surface is composed of  $\text{TiO}_2$  which may even be oxygen-rich during this reduction process. The data in Figure 4 show that a net increase in the O signal strength occurs above 575K whereas a continual decline occurs in the Ti signal intensity. These results infer that the slow step in the bulk reduction of  $\text{TiO}_2$  is the removal of surface oxygen, which presumably requires the recombination of two O atoms in the absence of any ESD process. As stated in the Results section, the presence of  $\text{H}_2$ ,  $\text{O}_2$  or CO did not significantly affect the results; therefore, if these gases enhanced the rate of oxygen removal, the rate of diffusion of oxygen to the surface still remained equal to or greater than the desorption rate.

It is not easy to propose a surface structure that can allow oxygen concentrations greater than that of stoichiometric  $\text{TiO}_2$ ; however, O vacancies created when bulk reduction occurs can trap up to two electrons and these sites may allow the formation of  $\text{O}_2^-$  on the surface (23,48). If  $\text{Ti}^{3+}$  cations had migrated away from the surface, O/Ti ratios greater than 2.2 could be achieved in the surface region. It is also known that reduction of  $\text{TiO}_2$  occurs by interstitial titanium formation (34,40) ( $\text{TiO}_2 \rightarrow \text{Ti}_i^{4+} + 4e^- + \text{O}_2$ ) releasing oxygen without the need of any vacant sites in the surface. Such behavior may also provide a favorable situation for oxygen accumulation at the surface. Although it may be possible that hydroxyl groups form, thereby increasing the O/Ti ratio at the surface, this formation would not be expected at these high temperatures.

The surface of the  $\text{TiO}_2$  powder showed differences from the rutile (100) surface, which may well be attributable to the fact that it was initially 84% anatase. This behavior may also be a consequence of the presence of the small (10-50 nm) crystallites which exist in this particular  $\text{TiO}_2$  powder as received (2). Although the O/Ti ratio increased with increasing temperatures, the transition between 575 and 875K was not so sharp and the O/Ti ratios at high temperature never exceeded 2.1. Little hysteresis was found for this powder wafer both in the beam or out of the beam, as shown in Figure 6. Again, though, ESD led to lower O/Ti ratios after cooling to below 350K. In fact, oxygen appeared to be more easily removed by ESD from this powder surface than from the (100) surface because repeated heat cycles in the beam produced a continuous, irreversible decrease in the O/Ti ratios at both high and low temperatures. After numerous heating/cooling cycles, the final observed O/Ti ratio of 0.7 at 300K produced by beam damage was so low that the presence of metallic Ti( $\text{Ti}^0$ ) or perhaps a  $\text{TiO}_2$  phase (49) is required to explain this value. Again, surface reconstruction and reduction may be more easily achieved on small crystallites than on large single crystals because of differences in surface free energy. In the absence of ESD, the O/Ti ratio repeatedly cycled between 1.8 at 300K and 2.1 at 975K or higher.



The addition of 0.5 monolayer of Pt to the (100) surface had a major effect. It removed the hysteresis observed without the Pt, and regions both in and out of the electron beam showed similar, reversible O/Ti ratios during the heating/cooling cycle. Although a small difference existed in initial O/Ti ratios in the two regions, values were identical during the cooling period. Both O and Ti peak intensities declined continuously during the cycle. Similar behavior was observed on the second sample which contained twice as much Pt distributed over a small fraction of the surface, as shown in Figure 5. On this sample, lower O/Ti ratios were attained at 1100K, but both regions again exhibited almost identical surface compositions during the cooling cycle. Pt seems to facilitate oxygen removal, resulting in lower O/Ti ratios on the (100) surface, compared to the Pt-free surface, and a similarity in behavior between Pt-covered surfaces and ESD. Platinum is known to readily dissociate oxygen and could easily work in the reverse direction to act as a porthole for recombination and desorption of O atoms (50). The effect of Pt on the TiO<sub>2</sub> powder was more pronounced, as indicated in Figure 6. Increases in the O/Ti ratio were again observed in both regions as temperature increased, with values over 2.8 being attained. However, during the cooling cycle a significant decrease in the O/Ti ratio occurred in the region continuously exposed to the electron beam producing a value near 1.8, whereas a much smaller hysteresis loop existed for the region not affected by ESD, and O/Ti ratios remained near 2.4.

### Conclusions

In the presence of H<sub>2</sub>, platinum can activate hydrogen and allow hydrogen spillover onto metal oxides (50), and this route has been proposed for Pt-catalyzed reduction of TiO<sub>2</sub> under hydrogen (44,51). Moreover, this study indicates that Pt may also catalyze the reduction of TiO<sub>2</sub> by facilitating the desorption of molecular oxygen from the surface. Above 600K, bulk oxygen diffusion rates become significant and oxygen migrates readily to the surface. The O/Ti ratios much higher than 2.2 (the approximate value for stoichiometric TiO<sub>2</sub>), observed in this study at higher temperatures, are interpreted to mean that the slow step in the reduction of TiO<sub>2</sub> is the desorption of molecular oxygen from the surface. ESD results in lower O/Ti ratios because it can remove oxygen in the form of positive ions, such as O<sup>+</sup>, whereas Pt acts as a porthole for desorbing molecular oxygen.

### Literature Cited

1. For example, a) A. J. Bard, *Science* 207, 139 (1980).  
b) M. Gratzel, *Acc. Chem. Res.* 14, 376 (1981).
2. a) S. J. Tauster, S. C. Fung and R. L. Garten, *J. Am. Chem. Soc.* 100, 170 (1978).  
b) S. J. Tauster and S. C. Fung, *J. Catal.* 55, 29 (1978).
3. M. A. Vannice & R. L. Garten, *J. Catal.* 56, 236 (1979).
4. M. A. Vannice, *J. Catal.* 74, 199 (1982).
5. M. A. Vannice and C. C. Twu, *J. Catal.* 82, 213 (1983).

6. S. J. Tauster, S. C. Fung, R. T. K. Baker and J. A. Horsley, *Science* 211, 1121 (1981).
7. a) J.-M. Herrmann and P. Pichat, *J. Catal.* 78, 425 (1982).  
b) J. Disdier, J.-M. Herrmann and P. Pichat, *J.C.S. Faraday Tr. I* 79, 651 (1983).  
c) C. Naccache et al., *J. Catal.* 75, 243 (1982).
8. R. Burch and R. Flambard, *J. Catal.* 78, 389 (1982).
9. B. H. Chen and J. M. White, *J. Phys. Chem.* 86, 3534 (1982).
10. X. Z. Jiang, T. F. Hayden and J. A. Dumesic, *J. Catal.* 83, 168 (1983).
11. D. E. Resasco and G. L. Haller, *J. Catal.* 82, 279 (1983).
12. C.-C. Kao, S.-C. Tsai, and Y-W Chung, *J. Catal.* 73, 136 (1982).
13. B. A. Sexton, A. E. Hughes and K. Foger, *J. Catal.* 77, 85 (1982).
14. S-H. Chien, B. N. Shelimov, D. E. Resasco, E. H. Lee and G. L. Haller, *J. Catal.* 77, 301 (1982).
15. S. C. Fung, *J. Catal.* 76, 225 (1982).
16. S. Thomas, *Surf. Sci.* 55, 754 (1976).
17. *Handbook of Auger Electron Spectroscopy*, Physcial Electronics (Perkin Elmer) (1978).
18. J. S. Solomon and W. L. Baun, *Surf. Sci.* 51, 228 (1975).
19. N. R. Armstrong and R. K. Quinn, *Surf. Sci.* 67, 451 (1977).
20. Y. W. Chung, W. J. Lo and G. A. Somorjai, *Surf. Sci.* 64, 588 (1977).
21. W. J. Lo, Y. W. Chung and G. A. Somorjai, *Surf. Sci.* 71, 199 (1978).
22. C. N. Sayers and N. R. Armstrong, *Surf. Sci.* 77, 301 (1978).
23. R. H. Tait and R. V. Kasowski, *Phys. Rev. B* 20, 5178 (1979).
24. R. V. Kasowski and R. H. Tait, *Phys. Rev. B* 20, 5168 (1979).
25. C. N. R. Rao and D. H. Sarma, *Phys. Rev. B* 25, 2927 (1982).
26. L. A. Grunes, R. D. Leapman, C. N. Wilker, R. Hoffmann and A. B. Kunz, *Phys. Rev. B* 25, 7157 (1982).
27. M. L. Knotek and J. E. Houston, *Phys. Rev. B* 15, 1580 (1977).
28. M. L. Knotek and P. J. Feibelman, *Phys. Rev. Lett.* 40, 964 (1978).
29. M. L. Knotek, *Surf. Sci.* 91, L17 (1980).
30. L. E. Firment, *Surf. Sci.* 116, 205 (1982).
31. S. Nishigaki, *Surf. Sci.* 125, 762 (1983).
32. G. D. Davis, M. Natan, and K. A. Anderson, *Appl. Surf. Sci.*, 15, 321 (1983).
33. J. B. Goodenough, "Prog. in Solid State Chem.", H. Reiss, Ed., Pergamon Press, NY, Chap. 4 (1971).
34. L. A. Bursill, B. G. Hyde, "Prog. in Solid State Chem.", H. H. Reiss, Ed., Pergamon Press, N.Y., Chap. 6 (1972).
35. a) J.-M. Herrmann, *J. Chim. Phys.* 73, 474 (1976).  
b) J.-M. Herrmann, P. Montgolfier and P. Vergnon, *J. Chim. Phys.* 73, 479 (1976).
36. T. Awaki, *Bull. Chem. Soc. Japan* 46, 1631 (1973).
37. T. Awaki, M. Komuro, K. Hirose and M. Miura, *J. Catal.* 39, 324 (1975).
38. T. Awaki, K. Katsuta and M. Miura, *J. Catal.* 68, 492 (1981).
39. T. Awaki, *J. C. S. Faraday Tr I* 79, 137 (1983).

40. H. Sawatari, E. Iguchi and R. J. D. Tilley, *J. Phys. Chem. Solids* 43, 1147 (1982).
41. N. Yamamoto, S. Tonomura, T. Matsuoka and H. Tsubomura, *Surf. Sci.* 92, 400 (1980).
42. C. C. Kao, S. C. Tsai, M. K. Bahl and Y-W. Chung, *Surf. Sci.* 95, 1 (1980).
43. T. Huizinga and R. Prins, *J. Phys. Chem.* 87, 173 (1983).
44. J. C. Conesa and J. Soria, *J. Phys. Chem.* 86, 1392 (1982).
45. S. J. DeCanio, T. M. Apple and C. R. Dybowski, *J. Phys. Chem.* 87, 194 (1983).
46. T. M. Apple and C. Dybowski, *Surf. Sci.* 121, 243 (1982).
47. T. M. Apple, P. Gajardo and C. Dybowski, *J. Catal.* 68, 103 (1981).
48. R. D. Iyengar and M. Codell, *Adv. Coll. Interface Sci.* 3, 365 (1972).
49. "Nonstoichiometric Oxides," O. T. Sorensen, Ed., Academic Press, 1983, p. 46.
50. M. Boudart, M. A. Vannice and J. E. Benson, *Z. Physik. Chem. N.F.* 64, 171 (1969).
51. R. T. K. Baker, E. B. Prestridge and R. L. Garten, *J. Catal.* 56, 390 (1979); *Ibid.* 59, 293 (1979).

RECEIVED March 20, 1985

## Clusters: Molecular Surfaces

A. Kaldor, D. M. Cox, D. J. Trevor, and R. L. Whetten

Corporate Research Science Laboratories, Exxon Research & Engineering Company,  
Annandale, NJ 08801

There is considerable scientific and technological interest in obtaining an understanding of the chemical and physical properties of clusters of atoms, both metallic and non-metallic, in the range of 2 to 200 atoms, for it is widely believed that in this regime the transition from molecular to bulk properties occurs. Much work has already been done to explore the scientific issues in this regime, mostly with clusters supported on "inert" materials, such as carbon films or inorganic oxides. (1) Other efforts included producing and isolating few atom clusters in low temperature matrices. (2) In the past years, as a result of a significant triumph in synthetic efforts, metal cluster compounds as large as  $[\text{Pt}_{38}(\text{CO})_{44}\text{H}_x]^{2-}$  have been prepared and structurally characterized. (3) But despite all the elegant work in the past, a general technique to prepare and study the properties of coordinatively unsaturated, unsupported clusters had yet to emerge. The purpose of this paper is to briefly review the recent development of a general technique to prepare and study many properties of such clusters.

Since the demonstration by Schumacher et al (4) of the use of alkali metal vapor inclusion into a supersonic beam to produce clusters, there have been a number of attempts to generalize the approach. It has recently been recognized that instead of high temperature ovens, with their concomitant set of complex experimental problems, an intense pulsed laser beam focused on a target could be effectively used to produce metal atoms in the throat of a supersonic expansion valve. (5) If these atoms are injected into a high pressure inert gas, such as helium, nucleation to produce clusters occurs. This development has as its most important result that clusters of virtually any material now can be produced and studied with relative ease.

0097-6156/85/0288-0111\$06.00/0  
© 1985 American Chemical Society

The pulsed cluster source (Figure 1) is characterized only in a limited sense and substantial opportunities remain to develop it into a fully predictable and controllable source. As an example of some of the important unresolved issues, consider the question of the internal energy content of the emerging clusters: We still need to know how it varies as a function of cluster size, and whether it can be controlled and measured. An equally important issue is whether the cluster size distribution can be controlled; ideally one would like to produce a monosized cluster beam chosen by simple changes in operation of the source. Effort in this direction is only beginning. Another issue concerns the mechanism of the cluster nucleation. What we know about the source derives primarily from optical spectroscopy of dimers and trimers, (6) and from work on large molecules we had done in our laboratory. (7) Early experiments indicate that small metal clusters (dimers, trimers) can be produced rotationally cold (<10K), but with significant vibrational energy content (100K to 600K), depending on expansion conditions. Little is known regarding the internal energy content of larger clusters. From experiments on alloy clusters (Figure 2) we have inferred that metal clusters grow by atom addition, (8) but clusters of non-conductors such as carbon form by more complex mechanisms. (9)

The pulsed molecular beam cluster source has produced clusters of virtually every material--we have made clusters of even the most refractory transition metals, of group IIIB and IVB elements, and numerous oxides, carbides, and intermetallic alloys of these elements.

The most unusual cluster distribution produced was that of carbon (Figure 3). This work is discussed in some detail in a recent paper. (9) For the purpose of this discussion it suffices to emphasize that a bimodal distribution was produced, one consisting of clusters of  $C_x$  composition,  $x = 1-30$ , with an internal distribution similar to that produced by a variety of other earlier experiments, ranging from high temperature evaporation techniques to secondary ion mass spectrometry experiments. The second distribution, made up of large clusters ( $x > 40$ ), contained only even clusters; to see odd-numbered clusters required large photoionization laser intensities, enough to cause cracking to occur. The unit of growth for this form of carbon cluster is evidently  $C_2$ , and the material may be the unusual phase of carbon called carbyne, which consists of linear carbon chains of alternating short and long bonds with weaker interchain interactions. (10) Some indication of packing effects, sometimes called "magic numbers", (11) may be evident in the distribution, but only to a minor extent.

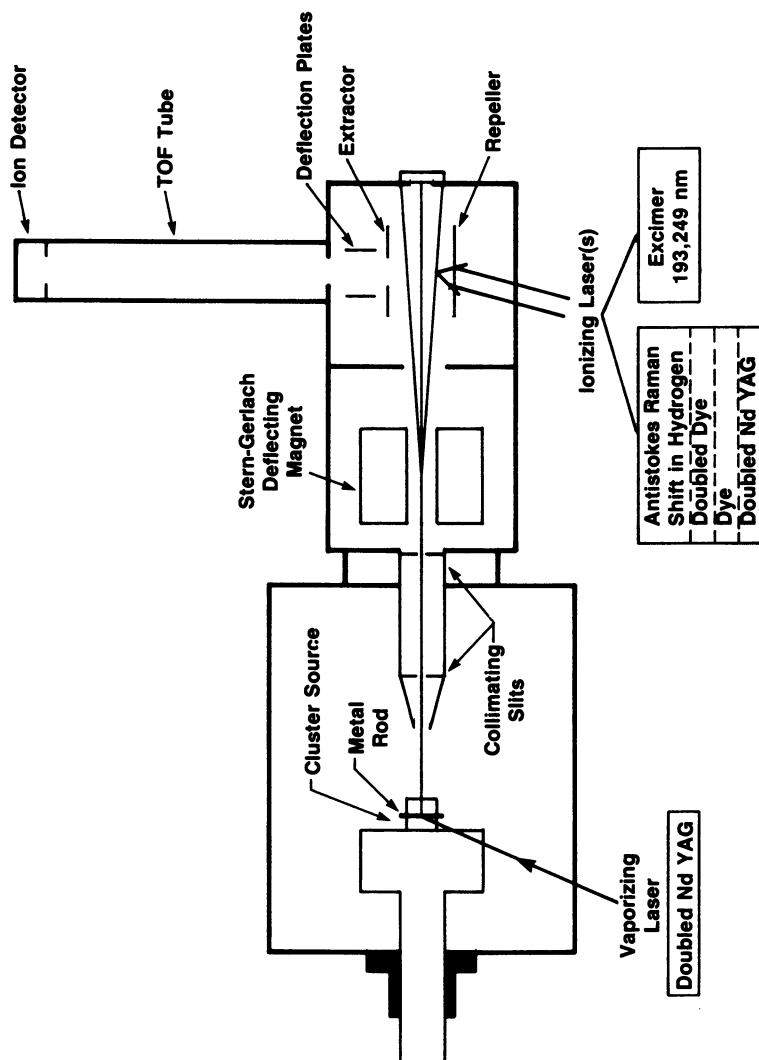


Figure 1. Schematic illustration of the laser-vaporization supersonic cluster source. Just before the peak of an intense He pulse from the nozzle (at left), a weakly focused laser pulse strikes from the rotating metal rod. The hot metal vapor sputtered from the surface is swept down the condensation channel in dense He, where cluster formation occurs through nucleation. The gas pulse expands into vacuum, with a skimmed portion to serve as a collimated cluster beam. The deflection magnet is used to measure magnetic properties, while the final chamber at right is for measurement of the cluster distribution by laser photo-ionization time-of-flight mass spectroscopy.

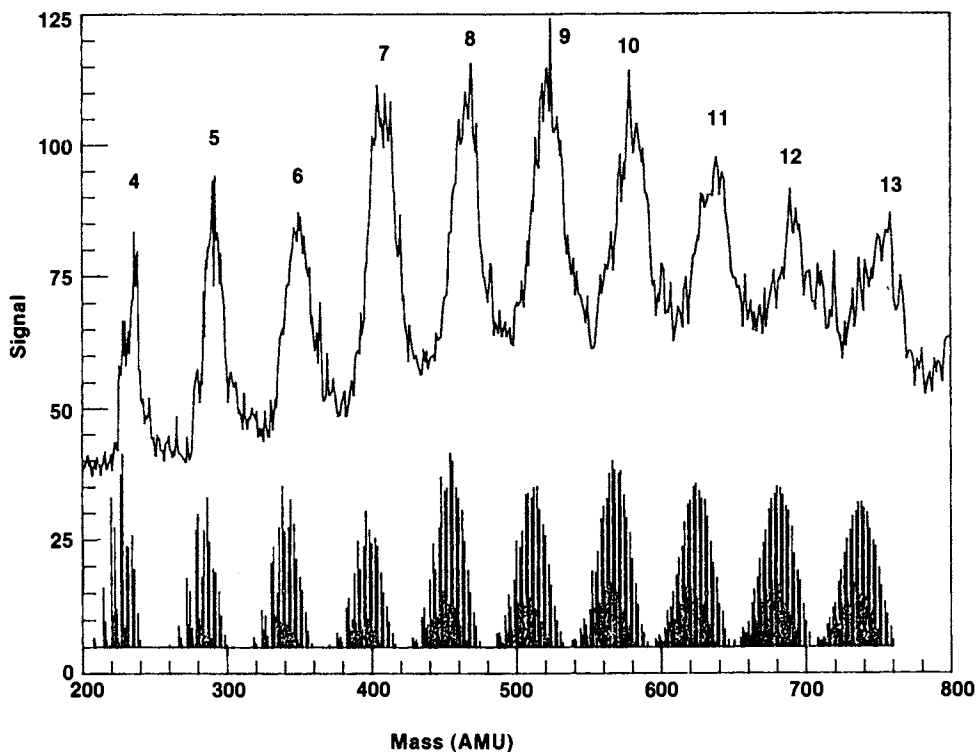


Figure 2. Evidence for an atom addition mechanism of cluster growth is provided by analysis of the  $Ni_xCr_y$  cluster distribution produced by vaporization of a nichrome surface. The simulated distribution below assumes that the probability of Ni or Cr occurring in a cluster is related only to its composition in the source material. Reproduced from Ref. 8. Copyright 1985, American Chemical Society.





Measurement of the ionization potential of the clusters using a combination of laser intensity dependence at a number of fixed-frequency laser transitions and by tunable vacuum ultraviolet lasers is one of the tools available to probe the electronic structure of these novel materials. One simple question which can now be probed is how the ionization potential varies as a function of cluster size, and more specifically when and how it approaches the bulk work function. Carbon exhibits some sharp transitions in ionization potential (IP) as the cluster size changes from 12 to 13 atoms, and again near 40 atoms. Aluminum behaves nearly like a free electron metal beyond six Al atoms, following the spherical droplet correction for the work function of a flat surface. Small clusters of Ni or Al exhibit some oscillations in IP as a function of size. (12) The most interesting system from this perspective is iron. (13) The IP of iron clusters was determined by direct photoionization measurements. These measurements revealed structure in the IP as a function of cluster size, with inflections at 2-4 atoms, and in the 9-13 atom cluster regime. These may well be due to structural differences in the clusters, but further experiments must be done to establish this conclusion. This observation has already stimulated a significant theoretical effort to examine the electronic structure of iron clusters. (14) More powerful experimental probes (e.g. photoelectron spectroscopy) are needed, however, for the ionization threshold is not a particularly sensitive probe of the development of the cluster d-band; it only probes the highest occupied electronic orbital of the system. (Fig. 4.)

Other probes of the electronic structure of clusters include the determination of the magnetic moment of the clusters as a function of cluster size. Early measurements on aluminum and iron clusters have already revealed an interesting contrast, (15) an example of which is shown in Figure 5. Specifically, we find that larger clusters of aluminum are essentially undeflected in a Stern-Gerlach experiment, but Al<sub>2</sub>, Al<sub>3</sub>, Al<sub>6</sub>, and Al<sub>7</sub> exhibit significant deflection. Similar experiments on Fe<sub>x</sub>, Fe<sub>x</sub>O, and Fe<sub>x</sub>O<sub>2</sub> indicate that Fe<sub>x</sub>O and Fe<sub>x</sub>O<sub>2</sub> have much larger moments than Fe<sub>x</sub>, and to a first approximation the moment of Fe<sub>x</sub> is a linear function of x.

The final probe of molecular clusters is that of selected chemical reactions. The use of probe reactions to study supported cluster catalysts is well established, and we are attempting the development of similar probes of unsupported clusters. The first steps in this direction are the design of a pulsed chemical reactor to go with the pulsed cluster source and the development of criteria for reactions. It is important to recall that at present

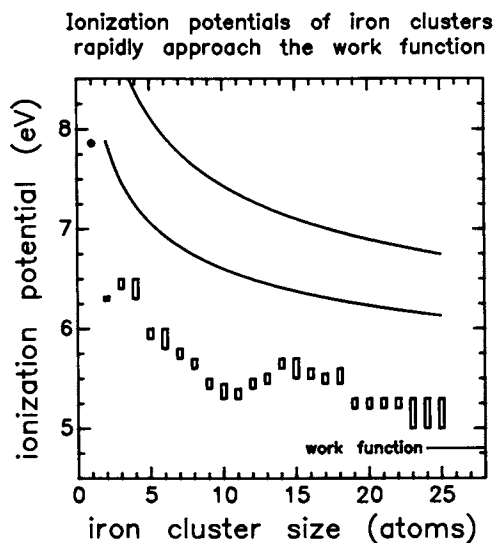


Figure 4. Fe cluster ionization thresholds as a function of cluster size, as determined by photoionization yield measurements using tunable UV/VUV laser radiation.

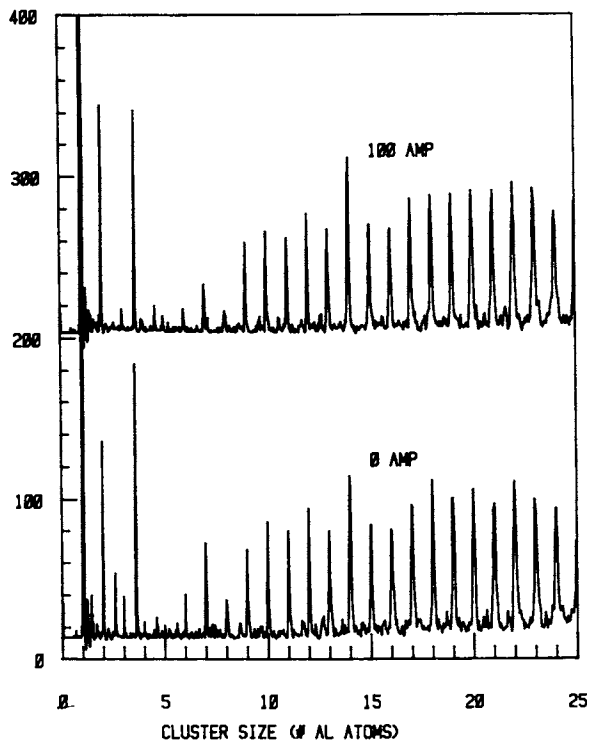


Figure 5a. Variation in the magnetic properties of metal clusters are investigated by measuring the depletion of a highly collimated cluster beam by an inhomogeneous magnetic field. Al clusters at zero and high field, showing that only small clusters are appreciably deflected.

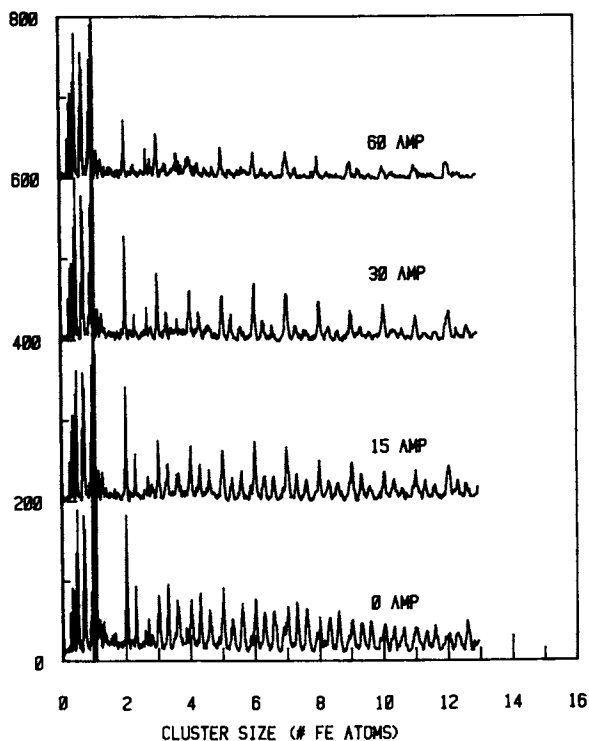


Figure 5b. Variation in the magnetic properties of metal clusters are investigated by measuring the depletion of a highly collimated cluster beam by an inhomogeneous magnetic field. Fe clusters and their oxides ( $\text{Fe}_x\text{O}$  and  $\text{Fe}_x\text{O}_2$ ) at several applied fields. The uniform depletion of  $\text{Fe}_x$  clusters indicates that their magnetic moments increase approximately linearly with number of atoms, as would be anticipated for incipient ferromagnetic iron. Unexpected, however, is the much larger depletion of iron oxide clusters. (The currents in the figure refer to that supplied to the magnet.)

the only probe of the cluster beam is that of photoionization mass spectrometry and that fragmentation may play a destructive role in the detection process.

The cluster reactor is attached to the pulsed cluster source's condensation channel, as shown in Figure 6. (16) To it is attached a high-pressure nozzle from which a helium/hydrocarbon mixture is pulsed into the reactor at a time selected with respect to the production and arrival of the clusters. The effect of turbulent mixing with the reactant pulse perturbs the beam, but clusters and reaction products which survive the travel from the source to the photoionization regime ( 600  $\mu$  sec) and the photoionization process are easily detected.

Figure 7 shows some of the early results for the formation of adducts between Pt clusters and benzene. (17) Among the most striking results is that  $\text{Pt}_2(\text{C}_6\text{H}_6)_2^+$  is always the dominant species,  $\text{Pt}_2(\text{C}_6\text{H}_6)^+$  being much weaker. Benzene adducts with the Pt atom,  $\text{Pt}(\text{C}_6\text{H}_6)^+$  or  $\text{Pt}(\text{C}_6\text{H}_6)_2^+$ , as well as other Pt atom containing fragments are virtually undetected. Larger  $\text{Pt}_x$  clusters form higher number of adducts, with  $\text{Pt}_x(\text{C}_6\text{H}_6)$  disappearing for cluster complexes larger than  $\text{Pt}_4$ . For clusters larger than  $\text{Pt}_3$  dehydrogenation of the higher order adducts is observed, with a loss of up to eight H atoms. This is more discernible with  $\text{C}_6\text{D}_6$ , where the mass discrimination is better. Significantly, the degree of dehydrogenation depends more on the number of Pt atoms in the cluster than on the number of adducts attached to it. It is additionally rather interesting that hydrogen loss occurs from the cluster - this may be either the direct result of the chemisorption process or fragmentation during ionization. Experiments with n-hexane, cyclohexane and 2,3 dimethylbutane indicate that chemical reaction is more likely than photofragmentation. The results for  $\text{C}_6$  isomers, for example, clearly demonstrate that the alkanes form complexes with the Pt atom, and that larger Pt clusters dehydrogenate to produce species with H/C ratio slightly in excess of corresponding aromatic species. This suggests that, for multiple adducts, aromatization, some hydrogen chemisorption, and perhaps in some cases even C-C bond cracking are likely to occur, with significant (up to 20 amu) devolatilization.

These early results demonstrating the richness of unsupported cluster chemistry are very promising, and much more extensive studies are currently in progress.

Preliminary indications are quite clear that coordinatively unsaturated transition metal clusters are reactive, and, importantly, reactive in a controlled way. This chemistry is likely to include RC-H insertion, aromatization etc., with the chemistry tending to produce

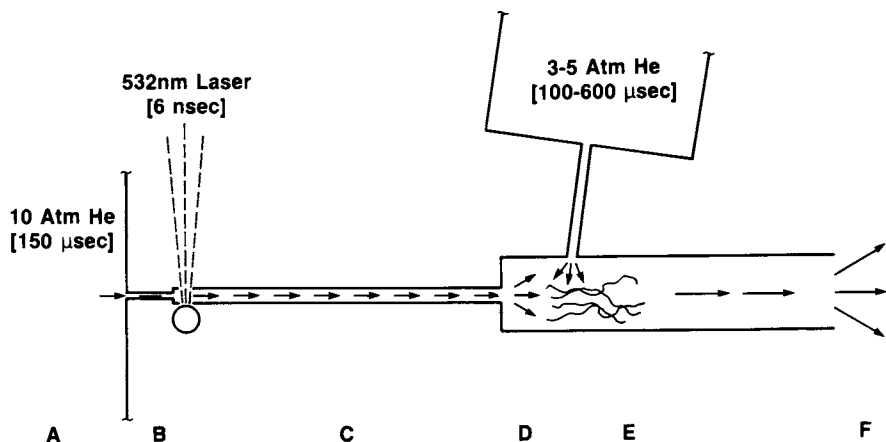


Figure 6. Scale-drawn schematic of the cluster reactor in relation to the pulsed cluster source. The letters A-F indicate the various stages of cluster preparation or synthesis, cooling, mixing and reacting, and finally flowing into vacuum toward detection.

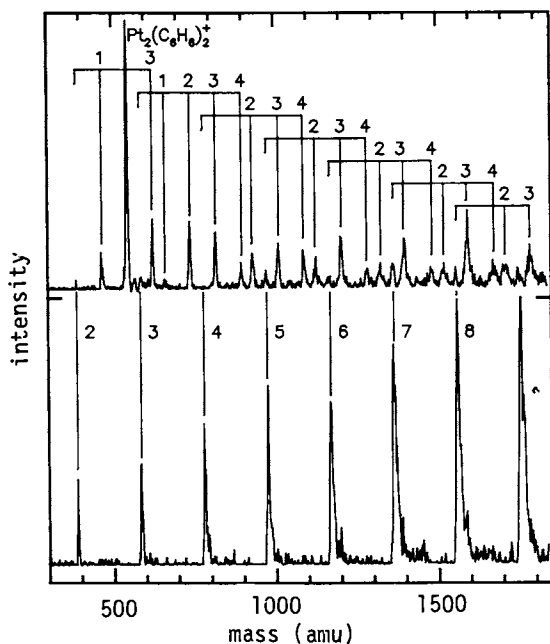


Figure 7. Time-of-flight mass spectra showing results of platinum cluster reactions with benzene. The lower trace is clean metal without reactant. The upper trace is with the pulsed addition of .21 % benzene in helium. The notation indicates the number of adducts on each metal cluster. The metal cluster are all two photon ionized, while the observed products are single photon ionized, hence the enhancement of the product over metal signals. Reproduced from Ref. 17. Copyright 1985, American Chemical Society.

species which satisfy the coordination requirements of the system. It should also be clear that more detailed electronic structural probes are required before we can speak with assurance about the chemical behavior of these systems. It is evident, however, that the study of clusters, particularly of the transition metals, as models for molecular surfaces has emerged as an exciting scientific regime.

#### Literature Cited

1. K. J. Klabunde and Y. Tanaka, *J. Mol. Catalysis* 21, 57 (1983).
2. G. A. Ozin, *Far. Symp. Chem. Soc.* 14, 7 (1980); W. Schulze, F. Frank, K.-P. Charle, and B. Tesche, *Ber. Bunsenges. Phys. Chem.* 88, 263 (1984).
3. For a summary of synthetic work on large saturated clusters see E. L. Muetterties, *Chemical and Engineering News*, 30 Aug. 1982, pp. 28-42. Also P. Chini, *J. Organometal. Chem.* 200, 37 (1980).
4. S. Leutwyler, A. Herrmann, L. Woste and E. Schumacher, *Chem. Phys.* 48, 253 (1980); M. M. Kappes, R. W. Kunz and E. Schumacher, *Chem. Phys. Lett.* 91, 413 (1982). See also: W. D. Knight, *R. Monat*, E. R. Dietz and A. R. George, *Phys. Rev. Lett.* 40, 1324 (1978).
5. T. G. Dietz, M. A. Duncan, D. E. Powers and R. E. Smalley, *J. Chem. Phys.* 74, 6511 (1981); D. E. Powers, S. G. Hansen, M. E. Geusic, A. C. Puiu, J. B. Hopkins, T. G. Dietz, M. A. Duncan and R. E. Smalley, *J. Phys. Chem.* 86, 2556 (1982); V. E. Bondebey and J. H. English, *J. Chem. Phys.* 76, 2165 (1982).
6. For reviews of this work, see: M. D. Morse and R. E. Smalley, *Ber. Bunsenges. Phys. Chem.* 88, 228 (1984); R. E. Smalley, *Laser Chem.* 2, 167 (1983).
7. T. G. Dietz, M. A. Duncan, R. E. Smalley, D. M. Cox, J. A. Horsley and A. Kaldor, *J. Chem. Phys.* 77, 4417 (1982).
8. E. A. Rohlfing, D. M. Cox, R. Petkovic-Luton and A. Kaldor, *J. Phys. Chem.*, in press.
9. E. A. Rohlfing, D. M. Cox and A. Kaldor, *J. Chem. Phys.* 81, 3322, 1984.
10. A. El Goresy and G. Donnay, *Science* 161, 363 (1968).
11. J. Muhlbach, K. Sattler, P. Pfau and E. Recknagel, *Phys. Lett.* 87A, 415 (1982); W. D. Knight, K. Clemenger, W. A. de Heer, W. A. Saunders, M. Y. Chou and M. L. Cohen, *Phys. Rev. Lett.* 52, 2141 (1984).
12. E. A. Rohlfing, D. M. Cox and A. Kaldor, *J. Phys. Chem.* 87, 4497 (1984).
13. E. A. Rohlfing, D. M. Cox and A. Kaldor, *Chem. Phys. Lett.* 99, 161 (1983); E. A. Rohlfing, D. M. Cox, A. Kaldor and K. H. Johnson, *J. Chem. Phys.*, in press.

14. K. Lee and J. Calloway, "Electronic Structure of Small Iron Clusters," Submitted for publication; C. Y. Yang, K. H. Johnson, D. R. Salahub, J. Kaspar and R. P. Messmer, *Phys. Rev. B* 24, 5673 (1981).
15. D. M. Cox, D. J. Trevor, R. L. Whetten and A. Kaldor, to be published. For a review of this and other work on transition metal clusters, see: R. L. Whetten, D. M. Cox, D. J. Trevor and A. Kaldor, *Surf. Sci.*, in press.
16. An alternative approach is to mix reactant and clusters prior to expansion. See: S. J. Riley, E. K. Parks, G. C. Nieman, L. G. Pobo and S. Wexler, *J. Chem. Phys.* 80, 1360 (1984); S. J. Riley, E. K. Parks, L. G. Pobo and S. Wexler, *Ber. Bunsenges. Phys. Chem.* 88, 287 (1984).
17. D. J. Trevor, R. L. Whetten, D. M. Cox and A. Kaldor, *J. Am. Chem. Soc.*, submitted.

RECEIVED March 20, 1985



## Iron Fischer-Tropsch Catalysts: Surface Synthesis at High Pressure

D. J. Dwyer

Corporate Research Science Laboratories, Exxon Research & Engineering Company,  
Annandale, NJ 08801

An XPS investigation of iron Fischer-Tropsch catalysts before and after exposure to realistic reaction conditions is reported. The iron catalyst used in the study was a moderate surface area ( $15\text{M}^2/\text{g}$ ) iron powder with and without 0.6 wt.%  $\text{K}_2\text{CO}_3$ . Upon reduction, surface oxide on the fresh catalyst is converted to metallic iron and the  $\text{K}_2\text{CO}_3$  promoter decomposes into a potassium-oxygen surface complex. Under reaction conditions, the iron catalyst is converted to iron carbide and surface carbon deposition occurs. The nature of this carbon deposit is highly dependent on reaction conditions and the presence of surface alkali.

In recent years the coupling of atmospheric pretreatment or reactor systems directly to UHV surface analysis systems has become common place. This combination of techniques has established a clear relevancy for UHV surface science in the area of catalysis. It permits both detailed mechanistic studies over well defined model surfaces, as well as characterization of industrial catalysts in their true activated form. One catalyst system which has received this type of attention is the iron Fischer-Tropsch catalyst.<sup>(1-5)</sup> The iron catalyst is a complex material whose composition is somewhat dynamic. The catalyst is generally prepared as a high surface area oxide ( $\text{Fe}_2\text{O}_3$ ) with the addition of both textural ( $\text{SiO}_2$ , Cu) and chemical (K) promoters. Prior to use the catalyst is subjected to various pretreatments which involve either reduction in  $\text{H}_2$  or direct contact with  $\text{CO}/\text{H}_2$  mixtures. The purpose of these pretreatments is to synthesize a working surface which exhibits a desirable catalytic response. Control of the surface synthesis step is a key technological challenge in industrial catalysis. In this paper we report how a high pressure reactor/UHV electron spectrometer system can be used to monitor changes in surface composition that accompany these pretreatments. The two catalysts studied were moderate surface area powders ( $15\text{M}^2/\text{g}$ ) with and without 0.6 wt.%

$K_2CO_3$ . The results indicate that the working catalytic surface is a carbided form of iron which is synthesized under  $CO/H_2$ . It is also found, that the type of carbon deposit that forms on the surface is sensitive to the presence of surface alkali.

### Experimental

The experimental apparatus shown schematically in Figure 1 has been described elsewhere.(6) It consists of a medium pressure micro-reactor coupled to an ultra-high vacuum system equipped to perform x-ray photoelectron spectroscopy. The XPS system consisted of a LHS-10 electron energy analyzer and a dual anode x-ray source (Mg and Al). The micro-reactor was a small UHV compatible tube furnace. The reactor's internal volume was approximately 10 cc and the walls were gold plated for inertness. The reactor was designed such that the sample and reactants were isothermal and that good gas mixing takes place in the reactor. The powder samples were pressed into a gold mesh backing material which in turn was mounted on a gold sample boat. The sample and boat could be moved directly from the reactor into the UHV system via a magnetically coupled motion feed through.

The iron powder was prepared by reducing ultra-high purity  $Fe_2O_3$  in a separate tube furnace. The reduction was carried out to completion at 675K, 1 atm  $H_2$  for approximately 24 hours. The surface of this pyrophoric material was then passivated by exposure to 1% oxygen in a helium carrier for 2 hours. The passivated powder was characterized by x-ray diffraction (XRD) and only  $\alpha$ -iron was detected. XPS analysis of the surface of this material revealed only  $Fe_2O_3$  present. These results suggest that the iron bulk is covered with a relatively thin oxide skin.

2.5 grams of this passivated material was coated with .015 grams of  $K_2CO_3$  through a standard aqueous impregnation technique. The amount of alkali was chosen to match the 0.6% by weight called for in many iron catalyst preparations.(7) This loading of  $K_2CO_3$  is thought to produce the maximum promotional effect. The impregnated catalyst was air dried at 335 K for 12 hours to remove excess water. The physical surface areas of the two samples (with and without  $K_2CO_3$ ) were measured by a standard BET method after a second hydrogen reduction. The alkali treated catalyst had a surface area of  $16M^2$ /gram and the untreated catalyst a surface area of  $18 M^2$ /gram. Assuming complete dispersion of the alkali and an iron surface site density of  $10^{15}$  sites/ $cm^2$ , the alkali surface coverage on the promoted catalyst is approximately 1/3 of a monolayer.

The gases used were purchased premixed in aluminum cylinders to avoid carbonyl formation. The high purity gas mixture was further purified by a zeolite water trap and a copper carbonyl trap. The gas pressure in the reactor was measured with a capacitance manometer and the flow monitored with a mass flow controller. The typical gas flow rates were 15 cc/min (STP) and the maximum conversion was  $\approx$  1% based on integration of hydrocarbon products. The hydrocarbon products were analyzed by gas chromatography (temperature programmed chromosorb 102, FID).

## MEDIUM PRESSURE REACTOR/X-RAY PHOTOELECTRON SPECTROMETER

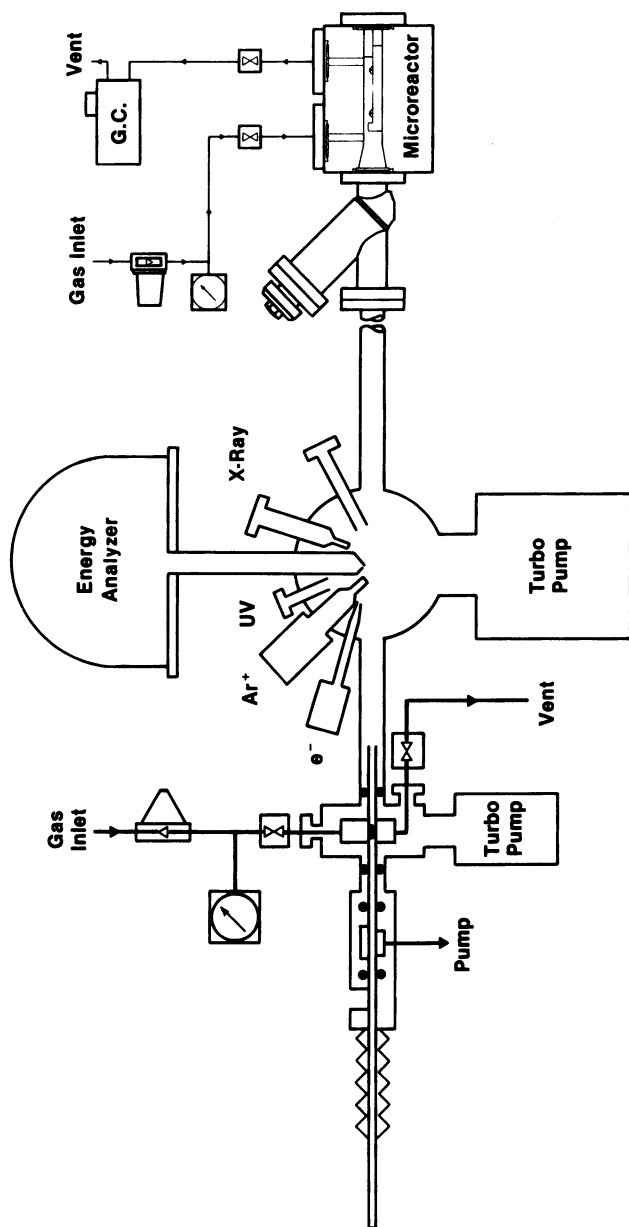


Figure 1. Schematic of Experimental Apparatus.

## Results

In this section the results of two studies are summarized. The first study was carried out with an unpromoted iron powder. The second study used the potassium promoted iron powder. A detailed report of the first study has been previously published.(6) The key features of this study are summarized here to facilitate a comparison between the catalytic response of the promoted and unpromoted powder.

Unpromoted Iron Powder. The XPS spectrum of the freshly prepared iron powder is shown in Figure 2a. The iron  $2p^{3/2}$  photoline is centered at 710.7 eV and the oxygen line is centered at 529.7 eV. The position and intensities of these lines are consistent with a surface layer of  $Fe_2O_3$  on the iron powder.(8) In addition to the iron oxide, a small amount of carbon impurity is also present on the surface of the catalyst. After surface characterization, the sample was moved to the reactor and reduced in  $H_2$  at 625 K for approximately 2 hours. This pretreatment, as shown in Figure 2b, was sufficient to reduce the surface oxide to metal (B.E.  $Fe2p^{3/2} = 706.6$  eV). The only detectible impurities on the surface of the catalyst after reduction were trace amounts of sulfur, carbon and oxygen. Using standard XPS cross sections it was estimated that these impurities were less than 1 atom % of the XPS sampling volume.

After reduction and surface characterization, the iron sample was moved to the reactor and brought to the reaction conditions (7 atm, 3:1  $H_2:CO$ , 540 K). Once the reactor temperature, gas flow and pressure were stabilized (~ 10 min.) the catalytic activity and selectivity were monitored by on-line gas chromatography. As previously reported, the iron powder exhibited an induction period in which the catalytic activity increased with time. The catalyst reached steady state activity after approximately 4 hours on line. This induction period is believed to be the result of a competition for surface carbon between bulk carbide formation and hydrocarbon synthesis.(6,9) Steady state synthesis is reached only after the surface region of the catalyst is fully carbided.

To verify that steady state catalytic activity had been achieved, the catalyst was allowed to operate uninterrupted for approximately 8 hours. The catalyst was then removed from the reactor and the surface investigated by XPS. The results are shown in Figure 2c. The two major changes in the XPS spectrum were a shift in the iron  $2p^{3/2}$  line to 706.9 eV and a new carbon 1s line centered at 283.3 eV. This combination of iron and carbon lines indicates the formation of an iron carbide phase within the XPS sampling volume.(6) In fact after extended operation, XRD of the iron sample indicated that the bulk had been converted to  $Fe_5C_2$  commonly referred to as the Hagg carbide.(7) It appears that the bulk and surface are fully carbided under differential reaction conditions.

The steady state rates of hydrocarbon synthesis over the carbided iron surface are given in Table I. The reaction rates have been normalized to the physical surface area of the starting iron powder [ $18 M^2/g$ ] and are reported in molecules/cm<sup>2</sup> sec. A turnover

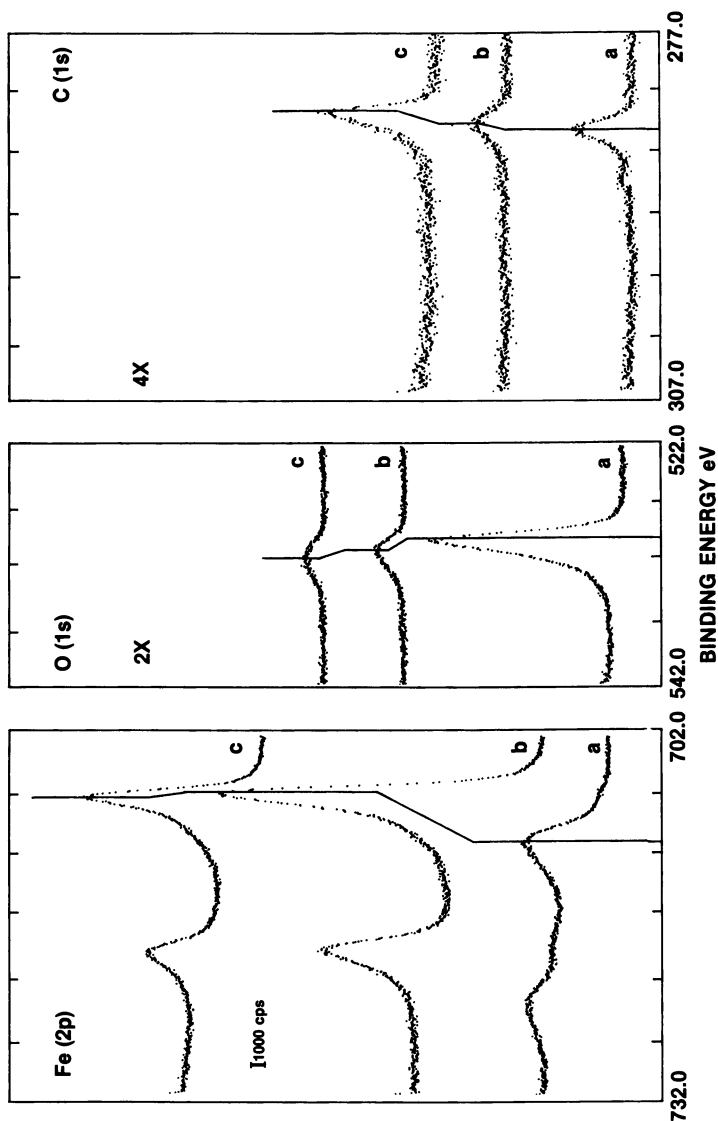


Figure 2. XPS spectra of iron powder after exposure to various environment. a) Freshly prepared air exposed powder. b) After hydrogen reduction 2 atm  $H_2$  at 625 K. c) After steady state operation for 8 hr, 3:1  $H_2$ :CO 7 atm, 540 K.

**Table I. Steady State Rates of Hydrocarbon Synthesis Over Iron Carbide**

| Carbon Number  | 540 K, 3:1 H <sub>2</sub> :CO, 7 atm                    |   |
|----------------|---|---|
|                | Iron Carbide<br>Rate<br>(Molecules/cm <sup>2</sup> sec) | Potassium Promoted<br>Rate<br>(Molecules/cm <sup>2</sup> sec) |
| C <sub>1</sub> | 4.5 X 10 <sup>12</sup>                                  | 4.1 X 10 <sup>11</sup>  |
| C <sub>2</sub> | 2.4 X 10 <sup>12</sup>                                  | 3.2 X 10 <sup>11</sup>  |
| C <sub>3</sub> | 1.6 X 10 <sup>12</sup>                                  | 3.2 X 10 <sup>11</sup>  |
| C <sub>4</sub> | 7.4 X 10 <sup>11</sup>                                  | 1.9 X 10 <sup>11</sup>  |
| C <sub>5</sub> | 3.9 X 10 <sup>11</sup>                                  | 1.4 X 10 <sup>11</sup>  |
| C <sub>6</sub> | 1.8 X 10 <sup>11</sup>                                  | 9.6 X 10 <sup>10</sup>  |

number has not been reported since the iron surface site density of the carbided material is unknown. If a site density of 10<sup>19</sup>/cm<sup>2</sup> is chosen the steady state methanation rate is on the order of 10<sup>-3</sup> molecules/site sec. This turnover frequency is considerably lower than that reported in earlier studies (range .05 to 2).<sup>(2,4,9)</sup> This result suggest that only a small fraction of the iron carbide surface is active.

Potassium Modified Iron Powder. Surface analysis (XPS) of the freshly prepared potassium modified surface is given in Figure 3a. The iron 2p<sup>3/2</sup> binding energy is located at 710.6 eV and the dominant oxygen 1s line is at 529.7 eV. These values are again consistent with a surface layer of Fe<sub>2</sub>O<sub>3</sub>. In addition to the surface oxide, K<sub>2</sub>CO<sub>3</sub> is also present on the surface of the catalyst. The presence of the carbonate is indicated by a potassium 2p<sup>3/2</sup> peak at ≈ 293 eV and a carbonate carbon line at ≈ 289 eV. A high binding energy shoulder is also present on the oxygen 1s line but an exact binding energy is difficult to measure due to the overlap with the strong iron oxide signal. These results are in general agreement with those reported by Bonzel and co-workers<sup>(5)</sup> for K<sub>2</sub>CO<sub>3</sub> treated iron foils.

The potassium treated material was then moved to the micro-reactor and reduced under conditions identical to those used for the unpromoted iron. Figure 3b contains the XPS spectrum of the modified surface after hydrogen reduction. Once again the iron 2p<sup>3/2</sup> peak is centered at 706.6 eV indicating the reduction of the iron oxide to metallic iron. The main oxide oxygen 1s signal at 529.7 eV is almost totally removed from the spectrum suggesting complete reduction of the oxide. In the potassium 2p and the carbon 1s region of the spectrum important changes take place. The key features are that the potassium 2p signal increases relative to the carbonate carbon signal (BE≈289), and the appearance of a

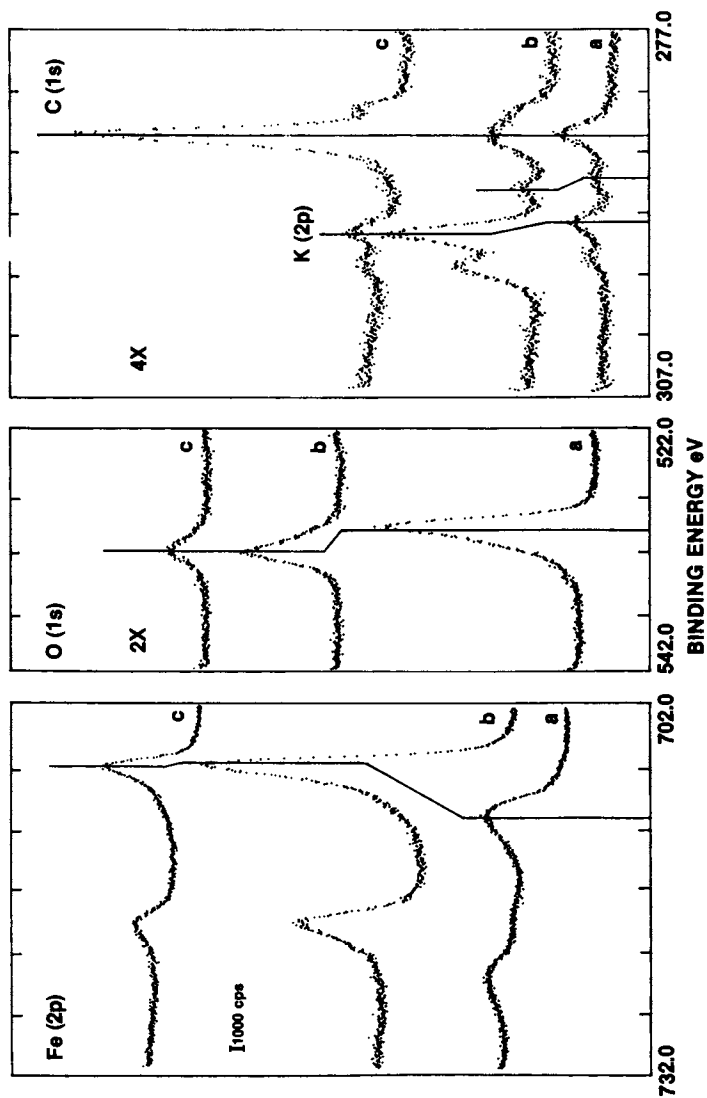


Figure 3. XPS spectra of potassium modified iron powder after various treatments. a) freshly prepared, b) after hydrogen reduction (2 atm, H<sub>2</sub>, 625 K), c) after steady state operation for 8 hr.

strong oxygen 1s line at 531.9 eV. These results are consistent with the partial decomposition of  $K_2CO_3$  into a surface KOH layer as described by Bonzel and co-workers.<sup>(2,5)</sup> The change in the ratio of carbonate carbon to potassium signal intensity suggests that some of the carbonate carbon is lost during the reduction. The oxygen 1s feature at 531.9 eV is indicative of the formation chemisorbed KOH.<sup>(5)</sup>

The freshly reduced potassium modified surface was tested for catalytic activity under conditions identical to those used for unpromoted material (540K, 3:1  $H_2:CO$ , 7 atm). The promoted iron powder exhibited an induction period wherein the catalyst activity increased with time. However, the induction period was considerably shorter ( $\sim 1$  hr) than that observed over the unpromoted surface. This result may indicate a more rapid carbiding of the iron surface region. The steady state hydrocarbon synthesis rates are given in Table I. In terms of the rate of hydrocarbon production, the most significant difference between the promoted and unpromoted materials is the much lower methanation rate over the promoted surface. On a physical surface area basis (reduced promoted iron  $15m^2/g$ ) the methanation activity over the promoted catalyst is suppressed by almost an order of magnitude. The rates of formation of other molecules in the  $C_1$  to  $C_6$  range were also suppressed but to a decreasing degree with increasing chain length. For example, the production of methane was approximately 13% of the unpromoted rate. The rate of  $C_6$  production was 53% of the unpromoted rate.

Once the steady state activity had been verified by continuous operation for eight hours without loss of activity, the sample was removed from the reactor for surface analysis. The XPS results are given in Figure 3c. The major change in the XPS spectrum is the large increase in the carbon 1s signal intensity. Close inspection of the carbon region reveals that two distinct carbon signals are present. The major peak is centered at 285.7, the other at 283.3 eV. In addition, the iron  $2p^{3/2}$  is centered at 706.9 eV. Once again, we believe that the 283.3 eV carbon feature and the 706.9 eV iron signal are clear indicators of iron carbide formation. The key question, however, is the nature of the intense carbon feature centered at 285.7. Previous work has suggested that potassium increases the rate of graphite deposition on iron surfaces under reaction conditions.<sup>(1,3)</sup> We believe that the carbon species is not graphitic but is an adsorbed hydrocarbon phase (growing chains or high molecular weight products) on the surface. The argument for this assignment is two-fold. First, the 285.7 eV binding energy is identical to that measured for octacosane ( $C_{28}H_{60}$ ) adsorbed on a iron foil<sup>(6)</sup>. Second, is the mass spectrum of material desorbed from this sample upon heating to 425 K in the vacuum system. It consists of a cracking pattern starting at mass 15 and continuing at multiples of mass 14 as high as the mass spectrometer permitted (200 amu). This cracking pattern is clearly that of linear saturated hydrocarbons similar to polymethylene ( $n-CH_2-$ ).

Based on the attenuation of the iron  $2p^{3/2}$  signal and assuming a mean free path for the iron electrons of 1.5 to 2 nanometers, it is estimated that the carbon overlayer is at least 1.8 to 2.5 nano-



meters thick. It is interesting to note, that in spite of this heavy build up of material on the catalyst, the catalytic activity remains at steady state.

### Conclusions

This XPS investigation of small iron Fischer-Tropsch catalysts before and after the pretreatment and exposure to synthesis gas has yielded the following information. Relatively mild reduction conditions (350°C, 2 atm, H<sub>2</sub>) are sufficient to totally reduce surface oxide on iron to metallic iron. Upon exposure to synthesis gas, the metallic iron surface is converted to iron carbide. During this transformation, the catalytic response of the material increases and finally reaches steady state after the surface is fully carbided. The addition of a potassium promoter appears to accelerate the carbidation of the material and steady state reactivity is achieved somewhat earlier. In addition, the potassium promoter causes a build up on carbonaceous material on the surface of the catalysts which is best characterized as polymethylene.

### Literature Cited

1. Bonzel, H. P.; Krebs, H. J. Surface Science, 1981, 109, L527.
2. Krebs, H. J.; Bonzel, H. P. Surface Science, 1982, 88, 269.
3. Bonzel, H. P.; Chem. Ing. Tech, 1982, 54, 908.
4. Dwyer, D. J.; Somorjai, G. A. J. Catalysis, 1970, 52, 291.
5. Bonzel, H. P.; Broden, G.; Krebs, H. J. Applications of Surface Science, 1983, 16, 373.
6. Dwyer, D. J.; Hardenbergh, J. H. J. Catalysis, 1984, 87, 66.
7. Storch, H. H.; Golumbic, N.; Anderson, R. B. "The Fischer-Tropsch and Related Synthesis," John Wiley: New York, 1951.
8. Hirohawa, H.; Okee, H. Talanta, 1979, 26, 855.
9. Vannice, M. A. J. Catalysis, 1975, 37, 449.

RECEIVED May 2, 1985

## Low-Energy Ion-Scattering Spectroscopy: Applications to Catalysts

James C. Carver, S. Mark Davis, and Duane A. Goetsch

Exxon Research & Development Laboratories, Baton Rouge, LA 70821

Over the last several years surface science techniques such as XPS, AES, and SIMS have been used to study the surfaces of catalysts with varying degrees of success. Low Energy Ion Scattering Spectroscopy (LEISS), also known as Ion Scattering Spectroscopy (ISS), has in general not received as much attention as the other techniques, although LEISS offers unique surface sensitivity to the topmost atomic layer of a catalyst or, under different conditions, to the second or third layer. We have used LEISS to study supported metal, metal oxide, and metal sulfide catalysts. With single crystal layered sulfides such as  $\text{MoS}_2$ , conditions were adjusted so that first layer analysis was possible. The top layer was sulfur and the second layer was Mo. Support of  $\text{MoS}_2$  on alumina causes distinctly different spectra from the unsupported material which suggests that the crystal orientations differ. In addition, contaminants such as Na or K, which sometimes can unexpectedly dominate a surface, are also clearly seen by LEISS, while other substances such as carbon, which may be abundant on a surface, are difficult to see because their scattering cross-section is so small. In such cases combination of LEISS with XPS or SIMS can provide unique and invaluable information about catalysts.

During the past several years, Surface Science has begun to have a major impact on the field of catalysis.<sup>(1,2)</sup> Numerous tools have been developed for application to studying catalysts. One of these tools, Low Energy Ion Scattering Spectroscopy (also known as ISS or LEISS), provides unique data arising from the top one or two layers of a surface. However, this technique has been used only sparingly for these kinds of studies.<sup>(3)</sup> Its lack of popularity may be due to experimental difficulties associated with examining insulators, or perhaps because of ambiguous data interpretation for practical samples. The basic

theories have been discussed at length, but for the most part these theories have concentrated on metals and semiconductors.(4,5) In addition, much of the early experimental data were obtained at rather high ion fluxes and with rather poor vacuum.(6) We recognize now that misleading data can arise from such a procedure, and instead, LEISS should be done in a UHV system using nA ion currents and with a low energy beam.(7) Also, sample charging can complicate the situation greatly. As with any charged particle technique, surface charging can be a limiting problem when attempting to do LEISS on insulating surfaces such as catalysts.(7) With proper charge compensation and careful control of the ion beam current, these limitations can be overcome and LEISS can be a very powerful tool for catalyst studies.

LEISS data are presented on a variety of catalysts to demonstrate the unique features and problem areas of the technique. LEISS can provide complementary data to other techniques but also yield new data requiring reinterpretation of other data. LEISS can seldom stand alone, especially with insulators. However, we find LEISS to be extremely useful in research on catalysts.

### Experimental

Low Energy Ion Scattering experiments were done on a Leybold Heraeus spectrometer which uses a hemispherical analyzer with a lens. The ion gun was continuously controllable from about 200 eV to 5000 eV with ion currents at the sample ranging from about  $\text{nA}/(\text{cm})^2$  to several  $\mu\text{A}/(\text{cm})^2$ . As complementary data, Secondary Ion Mass Spectrometry and X-ray Photoelectron Spectroscopy were performed using the LH instrument.  $^4\text{He}^+$  ions were used as the primary source, although  $^3\text{He}^+$ ,  $^{20}\text{Ne}^+$ , and  $^{40}\text{Ar}^+$  ions were also available. The laboratory scattering angle for ion scattering is  $120^\circ$ .

### Qualitative Aspect of LEISS

Low Energy Ion Scattering Spectroscopy is quite simple in principle. The process depends on the domination of a single binary elastic collision. Figure 1 illustrates the fundamental principles upon which LEISS is based. An incoming ion with a mass of  $M_o$  at an energy of  $E_o$  and at a velocity of  $V_o$  collides with a solid surface. The primary ion is then scattered from that surface at some angle ( $\theta$ ) with an energy ( $E'$ ) and a velocity ( $V'$ ) which are determined by the target atom it strikes. This target atom, which has a mass of  $M_t$  and is initially at rest, recoils into the solid at an angle ( $\phi$ ) and a velocity  $V_t$ , carrying with it an energy  $E_t$ . Using classical relationships, the following equation can be generated:

$$E'/E_o = [M_o/(M_o+M_t)]^2 [\cos \theta + [(M_t/M_o)^2 - \sin^2 \theta]^{1/2}]^2 \quad (1)$$

Therefore, it is clear that if there are only single collisions and there are no energy losses except kinematic, then the spectra are quite simple and straightforward. However, we are

dealing with ions as the primary beam, and thus we have to deal with ion neutralization of the exiting beam. The details of this phenomenon are discussed elsewhere and will only be briefly reviewed here.<sup>(5)</sup> Only a few percent of the ions which impinge onto the surface remain ions upon scattering. Much of the neutralization occurs by an Auger type process in which the incoming ion gains an electron from the target. The longer the interaction time, the greater the chance for neutralization. Thus, as the energy of the primary ion is lowered, it is more likely to be neutralized. In addition, scattering from the second or third layers increases the residence time of the primary ion and enhances its chances of neutralization. When scattering from these deeper layers occurs or when non-kinematic energy losses occur, a shoulder on the lower energy side of the primary peak can be seen. If double scattering occurs, then a shoulder on the higher side of the primary peaks results.<sup>(7)</sup> As the primary ion's energy is increased, the ions tend to scatter more from deeper layers and more sputtering occurs. In Figure 2 we can observe the increased background between peaks and a slight skewing of the stronger peaks toward lower energy. Though not shown here, at higher ion currents even more pronounced skewing occurs and some double scatter peaks begin to arise.<sup>(7)</sup>

Finally, when dealing with insulators, the angles  $\theta$  and  $\phi$  are altered as shown in Figure 3. If the surface has a positive charge, the incoming positive ion is repelled causing the ion to curve either away from the surface or to be focused through the first layer to deeper layers. The scattered ions and sputtered ions also are repelled from the surface causing them to gain energy. Therefore, since the scattering angle  $\theta$  is no longer well defined, the exact peak position can deviate from its theoretical position. Further, the velocity of the exiting ion will be altered from simple theory causing an additional deviation from the expected peak position. Also, the deviation from theory will not necessarily be linear for a given sample.

Charge compensation with a low energy electron flood gun allows one to obtain meaningful spectra even though the measured peak positions do not always coincide with the expected positions. The sputter peak is diminished and the scatter peaks emerge from the background when a flood gun is used on an insulating sample.<sup>(7)</sup> Although peak identification is not absolute, in general, when coupled with XPS or SIMS, surface species can be determined.

#### Quantitative Aspects of LEISS

The intensity for LEISS using a noble gas as the primary ion source is quite low since, as previously discussed, most incoming ions are neutralized upon scattering and thus go undetected. Further, the relative intensity of the various components is a strong function of the incident ion energy as shown in Figure 2. These changes in intensity can be attributed to several factors as described below:

$$I_1 = I_0 \theta_1 N_0(\text{ISP}) \frac{d\sigma}{d\theta} G_1 T D d\theta \quad (2)$$

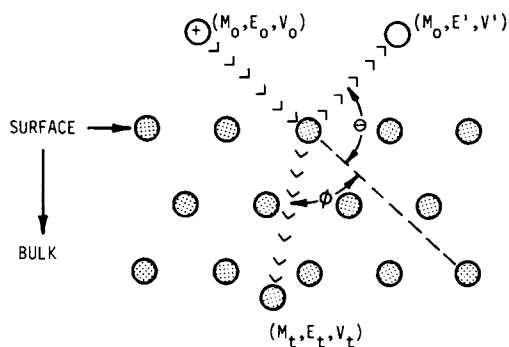


Figure 1. Fundamental Process for Low Energy Ion Scattering.  $M_o, E_o, V_o$  represent mass, energy and velocity of incident ion;  $M_t, E_t, V_t$  represent mass, energy and velocity of target ion,  $M_o, E', V'$  represent mass, energy and velocity of scatter ion,  $\theta$  is the scattering angle, and  $\phi$  is the recoil angle.

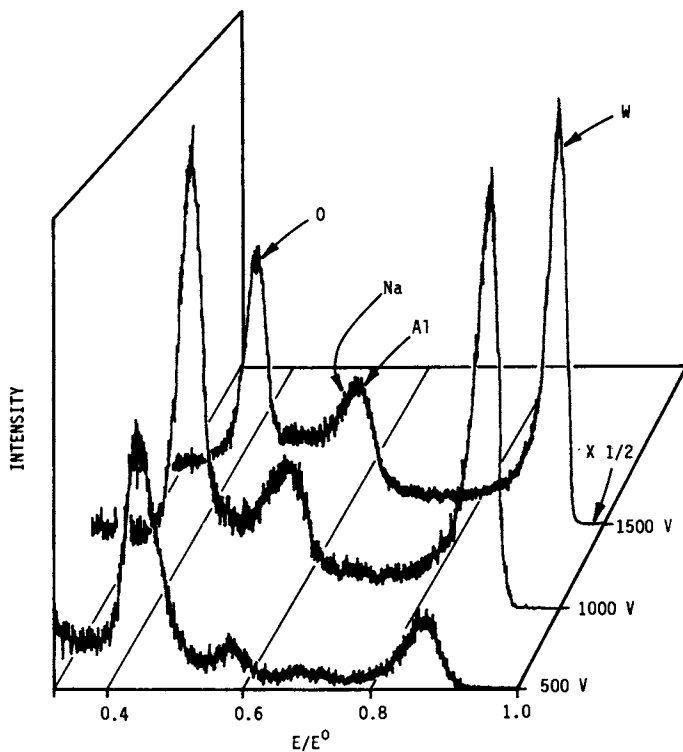


Figure 2. Relative Intensities of Peaks in LEIS as a Function of Ion Energy for  $WO_3/Al_2O_3$ .

where  $I_i$  = scattered ion intensity from the  $i$ th species,  $I_0$  = incident beam intensity,  $\theta_i$  = atomic fraction of  $i$ th species at the surface,  $d\sigma/d\theta$  = differential scattering cross-section of the  $i$ th species, ISP = ion survival probability,  $G_i$  = geometric or shadowing factor,  $T$  = analyzer transmission factor,  $D$  = detector efficiency,  $d\theta$  = solid angle of acceptance for the analyzer.

The incident ion beam intensity can be measured, and there are several tabulations of cross-section calculations. (8) Also, the analyzer parameters,  $T$ ,  $D$ , and  $d\theta$  can be determined. The three aspects of this equation, which are not well understood nor easily determined, include the number of atoms of a particular kind, the ion survival probability, and the shadowing or geometric term. The first quantity is quite often that which you would like to determine. The second two are often difficult to separate. Shadowing can be particularly important when trying to observe second layer effect or when trying to determine the location of adsorbates. (9) However, shadowing for polycrystalline samples, though important, is very difficult to deal with quantitatively.

Ion neutralization (or ion survival) can dominate this technique. A number of theories have arisen to account for this phenomenon, but all seem to include both Auger transitions and resonance tunneling processes as the dominant means of ion neutralization. (4,5) For very slow ions, as in LEISS, Auger transitions seem to be more important. The ion survival probability at constant scattering angle can be defined as follows (assuming only Auger transitions):

$$\text{ISP} = A[\exp(-b/v^f)] \quad (3)$$

where  $b$  can be considered a characteristic neutralization constant, (10) largely independent of energy. The term  $b$  does include a small contribution from the incident energy of the ion beam, but under the range of energies normally encouraged in LEISS (i.e., ~500-2000 eV), this contribution is insignificant. (3,4,10)

### Applications to Catalysts

Surface Sensitivity. Using these ideas, one can gather information on a catalyst which can indicate exactly which elements are on the surface and which are in second or deeper layers. To illustrate this idea, consider  $\text{MoS}_2$ . This material has a layered structure which has Mo sandwiched between sulfur layers. LEISS data reported elsewhere show that at low energies (<600 eV) almost no Mo is observed. (11) At higher energies, such as often reported in the literature, we see a pronounced signal from Mo. Sputtering does occur for these samples, but this increased Mo signal is not due to that effect. The implication is that LEISS data must be taken at very low voltages to reflect only first layer contributions.

One of the concerns in doing LEISS on catalysts is that the information will be of little use because either the first layer may be primarily carbon or the surface may be too rough.

Therefore, in order to be sure that our data were meaningful, we also examined polycrystalline  $\text{MoS}_2$  as well as  $\text{MoS}_2$  supported on alumina. In addition, the supported  $\text{MoS}_2$ , in some cases was promoted with other metals such as Co or Ni, which are commonly used in commercial hydrotreating catalysts. Again, as seen in the single crystal case, the spectra for polycrystalline  $\text{MoS}_2$  is dominated by sulfur at 500 v. At higher energies, we see the Mo signal begin to show through. However, the supported  $\text{MoS}_2$  shows significant Mo even at 500 v, suggesting that the  $\text{MoS}_2$  is not oriented basal plane up but possibly edge up.<sup>(11)</sup> When Co or Ni is added to the Mo on the alumina, we find that the Mo is unchanged.

More qualitatively, we can plot the reciprocal of the perpendicular velocity versus the log of the ion survival probability. Ions arising from different depths should have different slopes or intercepts (see Equation 3). The slope of the resulting line corresponds to the Auger neutralization constant that is sensitive to the electronic structure and the depth distribution of the scattering centers. Clearly, geometric considerations (or shadowing) play an important role in these experiments. The radius of the shadow cone of the incident ion can be represented by an equation which includes energy. However, directionally the effect will be the same as neutralization and thus will only exaggerate the results.<sup>(12)</sup> With the single crystal  $\text{MoS}_2$  system, we found that scattering from the S atoms changed very slowly with respect to the ion energy, while the molybdenum intensity changed sharply with energy. Such an analysis is consistent with the idea that the sulfur is at the surface. Ions scattered from the molybdenum (which is in the second layer) are preferentially neutralized, particularly at low energy. At 500 eV, greater than 90% of the scattering intensity originates from first layer collisions, while at 2000 eV about 70% of the intensity arises from first layer scattering. When this same analysis is applied to the supported  $\text{MoS}_2$  systems, the molybdenum and the sulfur have similar intensities. The Al sites seem to be almost completely covered. These data are consistent with  $\text{MoS}_2$  assuming a different surface structure when supported than it does in a bulk form.

Metals Dispersion from LEISS. Since  $\text{He}^+$  scattering is very selective to the outermost surface layer, one should anticipate that LEISS would be a valuable tool for studies of metals dispersion for supported catalysts. For low metal concentrations on high area supports, the (metal/support) LEISS intensity ratio should be directly proportional to metals dispersion. Recent studies in our laboratory have confirmed that expectation.

In Figure 4, the Pt/Al ratio from LEISS is shown for a series of  $\text{Pt/Al}_2\text{O}_3$  catalysts with variable Pt content (0.2-2.0 wt.%) following treatments with  $\text{O}_2$  at 500°C and 600°C. For catalysts treated at 500°C, the Pt/Al intensity ratio varies linearly with metal loading. However, after the 600°C treatment, the Pt/Al intensity ratio is lowered substantially, especially at higher Pt loadings. This change in the Pt/Al intensity ratio reflects a restructuring of the metal component during high

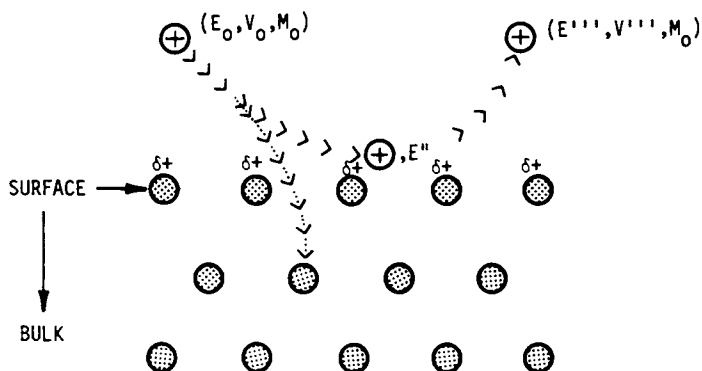


Figure 3. Basic Relationships for Insulating Surfaces;  $\theta$  and  $\phi$  no longer well defined. Ion interactions with charged surface alters trajectories.

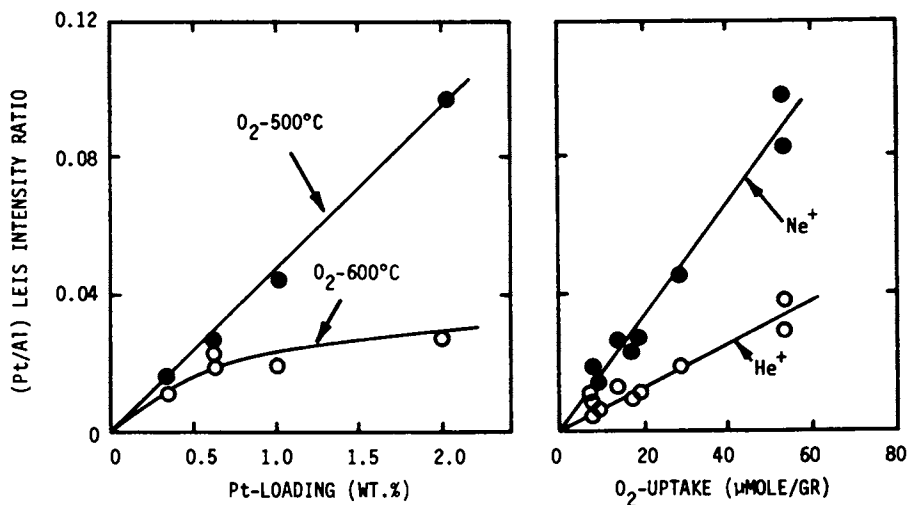


Figure 4. Platinum Agglomeration and Dispersion Measured by Ion Scattering.



temperature oxygen treatments. In particular, the growth of larger platinum and/or platinum oxide crystallites appears to take place.

These catalysts were also examined by  $O_2$  chemisorption to test the validity of our interpretation of the LEISS data. A plot of these results is also shown in Figure 4. Catalysts treated with oxygen at  $500^\circ\text{C}$ , and subsequently reduced at  $200\text{--}500^\circ\text{C}$ , showed high oxygen uptakes ( $O/\text{Pt} \sim 1.1$ ), which indicate essentially complete Pt dispersion. However, for catalysts treated with oxygen at  $600^\circ\text{C}$ , the oxygen chemisorption capacity was significantly reduced ( $O/\text{Pt} \sim 0.26\text{--}1.0$ ). In Figure 4 all catalysts, regardless of treatment, fall on the same plot. Within the uncertainty of the LEISS intensity ratios an excellent 1:1 correlation exists, confirming that LEISS is sensitive only to the fraction of exposed platinum and thus is a good probe of dispersion.

Morphology Studies. Another system which we have examined is  $\text{WO}_3/\text{Al}_2\text{O}_3$ . Several materials which varied in percent monolayer coverage of tungsten oxide all showed a discernable Al peak (see Figure 5). In addition, there was a significant Na contamination on these samples. Whereas XPS and Laser Raman spectroscopy had shown a linear increase in W/Al up to monolayer coverage, (18) LEISS shows that the W/Al ratio is almost constant up to monolayer coverage where the Na apparently begins to dominate the surface (Figure 6). Beyond monolayer coverage, Raman has shown that bulk-like  $\text{WO}_3$  forms on the surface. We also see a significant change in the LEISS data. The lack of consistency between XPS and LEISS is important since both techniques should measure surface concentrations. However, the theory for estimating crystallite size from XPS breaks down for very small particles. (14,15) The small  $\text{WO}_3$  crystallite may also be growing into raft-like morphologies. For thin rafts, XPS would still show almost a linear increase of W/Al intensity ratios, although the actual number of surface tungstens would change much less. The fact that a change in structure to  $\text{WO}_3$  or  $\text{Al}_2(\text{WO}_4)_3$  is reflected in the LEISS data shows that the technique is sensitive to structural changes. Therefore, these data suggest that no significant change in the surface structure seems to occur between samples that have less than one monolayer equivalent and catalysts which have approximately one monolayer equivalent of tungsten. This fact is shown even more clearly upon plotting the ISPs versus the reciprocal of the velocity. As shown in Figure 7, a sample calcined at  $500^\circ\text{C}$  (which should be well under a monolayer) and a sample calcined at  $950^\circ\text{C}$  (which should be right at a monolayer) seem to be quite similar. In contrast, the sample calcined at  $1050^\circ\text{C}$  which should be  $\text{Al}_2(\text{WO}_4)_3$ , shows quite different slopes and intercepts (see Figure 7). Though only the neutralization aspect of the change in scattering intensity is treated here, it would be wrong to imply that other factors, such as shadowing and the target atom's electron configuration, do not play a role. Clearly, they do, but their effects do not alter our conclusions. Thus, it appears that LEISS may also be quite valuable as a qualitative probe for changes in surface morphology. (16)

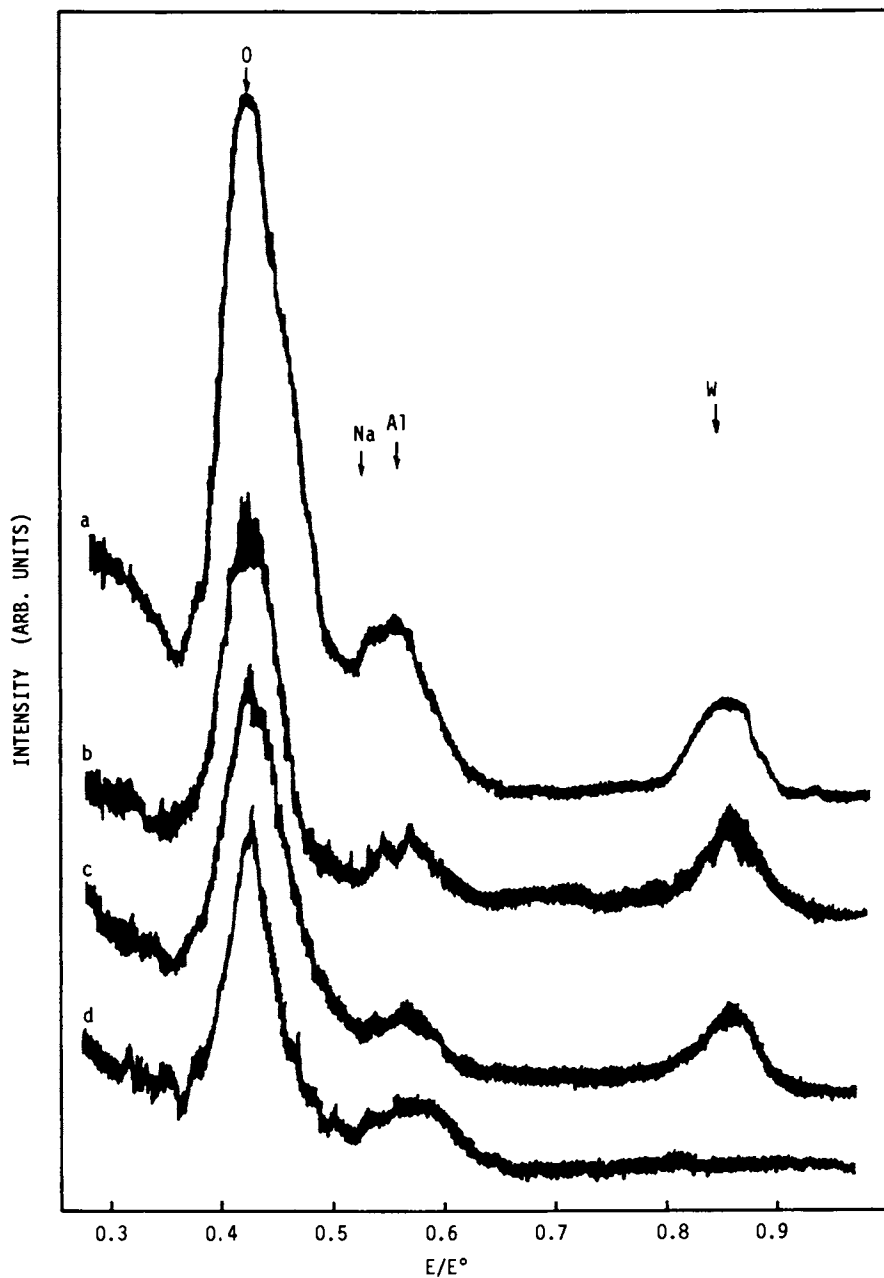


Figure 5. LEISS Data for Series of  $\text{WO}_3/\text{Al}_2\text{O}_3$  Catalysts (a) 10%  $\text{WO}_3/\text{Al}_2\text{O}_3$ ; Calcined at  $500^\circ\text{C}$ ; (b) 10%  $\text{WO}_3/\text{Al}_2\text{O}_3$ ; Calcined at  $950^\circ\text{C}$ ; (c) 25%  $\text{WO}_3/\text{Al}_2\text{O}_3$ ; Calcined at  $500^\circ\text{C}$ ; (d) Alumina, Calcined at  $500^\circ\text{C}$ .

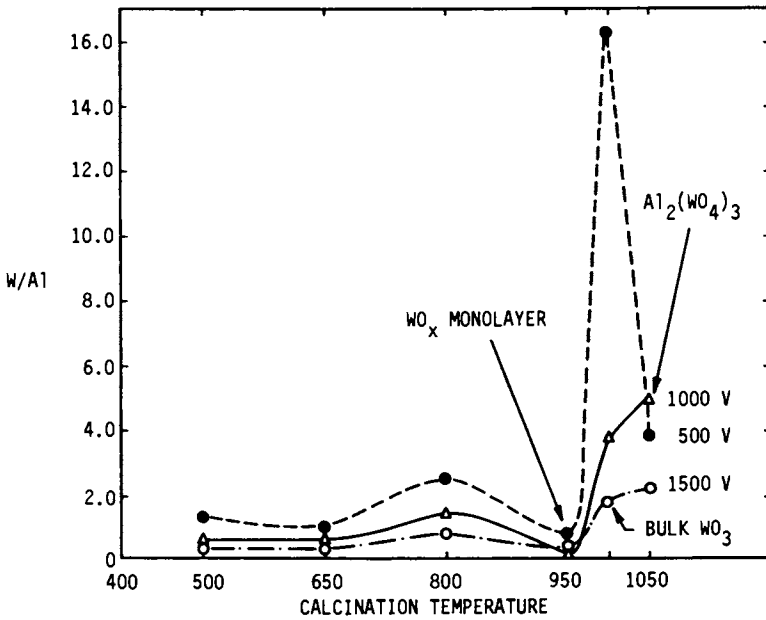


Figure 6. Ion Intensity Ratios for 10%  $WO_3/Al_2O_3$  as a Function of Calcination Temperature.

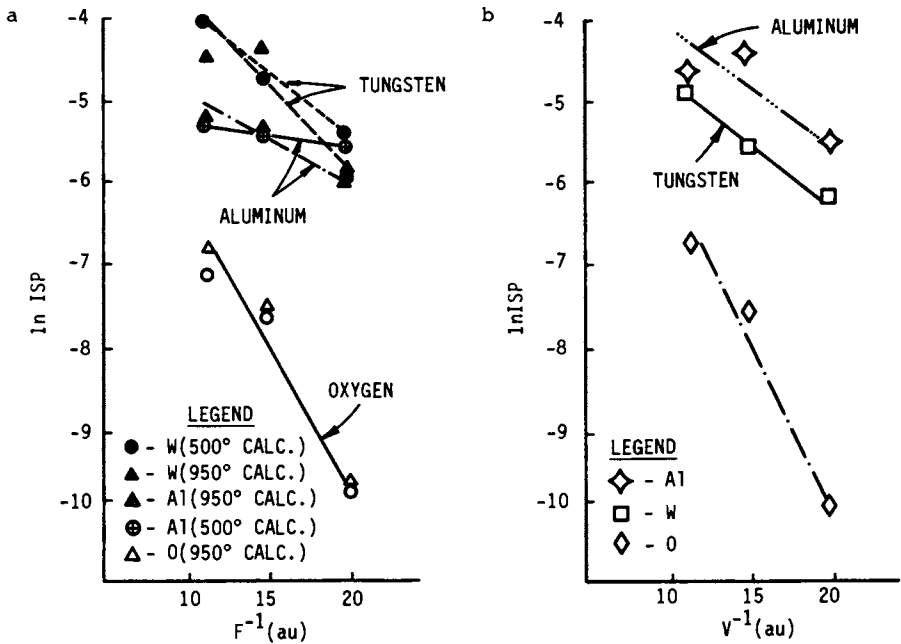


Figure 7. Ion Survival Probability for 10%  $WO_3/Al_2O_3$  (a) Calcined at 500°C and 900°C; (b) Calcined at 1050°C.

### Conclusions

LEISS has proven to be an important tool for studying catalysts. The technique can be deceptively simple, but for meaningful surface analysis great care must be taken. Very low energy ion beams at low currents are required for exclusively first layer data. Catalysts which in general are insulators require proper charge compensation. Quantitation is possible on a relative scale and peak identification should be confirmed by another tool such as XPS or SIMS. With these precautions, LEISS is capable of determining the composition of the outermost portion of a catalyst. It can provide complementary data, yet more often it provides unique information due to its extreme surface sensitivity.

### Acknowledgments

The authors wish to thank R. G. Misita, H. D. Wicker, J. J. Cassidey, J. L. Blakes, and S. R. Coleman for their experimental assistance, I. E. Wachs for his assistance on the tungsten work, and K. L. Riley for his useful comments.

### Literature Cited

1. P. Grange, *Catal. Rev.-Sci. Eng.*, 21, 135(1980).
2. For example, (a) H. Jeziorowski, H. Knozinger, E. Taglauer, and C. Vogdt, *J. Catal.*, 80, 286(1983).
3. R. L. Chin, D. M. Hercules, *J. Phys. Chem.*, 86, 3079(1982).
4. H. D. Hagstrum, *Phys. Rev.*, 96, 336(1954).
5. B. R. Haight, L. C. Feldman, T. M. Buck, and W. M. Gibson, *Phys. Rev. B*, 30, 734(1984).
6. R. F. Goff and D. P. Smith, *J. Vac. Sci. Technol.*, 7, 72(1970).
7. H. F. Helbig, P. J. Adelman, A. C. Miller, and A. W. Czanderna, *Nucl. Inst. and Methods*, 149, 581(1978).
8. G. C. Nelson, Sandia Laboratory Report, 79-0712 (1979).
9. S. H. Overbury and P. C. Stair, *J. Vac. Sci. Technol. A*, 1, 1055(1983)
10. D. P. Woodruff, *Surface Science*, 111, L219(1982).
11. S. M. Davis, J. C. Carver, and A. Wold, *Surface Science*, L12, 124(1983).
12. L. Marchut, T. M. Buck, G. H. Wheatley, and C. J. McMahon, Jr., *Surface Science*, 141, 549(1984).
13. S. S. Chan, I. E. Wachs, and L. L. Murrell, *J. Catal.*, in press.
14. S. M. Davis, *J. Catal.*, to be submitted.
15. S. C. Fung, *J. Catal.* 58, 454(1979).
16. R. C. McCune, *J. Vac. Sci. Technol.*, 18, 700(1981), and other references therein discuss similar use of LEISS.

RECEIVED March 11, 1985

# X-ray Photoelectron and X-ray Absorption Spectroscopic Characterization of Cobalt Catalysts Reduction and Sulfidation Behavior

D. G. Castner and P. R. Watson<sup>1</sup>

Chevron Research Company, Richmond, CA 94802-0627

We have observed spectroscopically, on a real-time basis, the changes in catalyst structure and composition which occur during reduction and sulfidation reactions. This capability was demonstrated by examining the reduction and sulfidation properties of bulk  $\text{Co}_3\text{O}_4$  (~3000 nm particles), 10%  $\text{Co}/\text{SiO}_2$ -62 (~20 nm  $\text{Co}_3\text{O}_4$  particles in ~500 nm aggregates) and 10%  $\text{Co}/\text{SiO}_2$ -923 (<5 nm  $\text{Co}_3\text{O}_4$  particles) with X-ray photoelectron spectroscopy (XPS) and X-ray absorption spectroscopy (XAS). In situ experiments were done in a catalyst-treatment system and a controlled atmosphere cell.  $\text{CoO}$  was observed as an intermediate in the  $\text{H}_2$  reduction of the  $\text{Co}_3\text{O}_4$  particles to  $\text{Co}$ . The smallest  $\text{Co}_3\text{O}_4$  particles were the hardest to reduce to metallic cobalt. Sulfidation of the  $\text{Co}_3\text{O}_4$  particles with  $\text{H}_2\text{S}/\text{H}_2$  proceeded through  $\text{CoO}$  and  $\text{Co}$  intermediates, forming  $\text{Co}_9\text{S}_8$ . On the supported catalysts the direct reaction of  $\text{CoO}$  to  $\text{Co}_9\text{S}_8$  was observed. In contrast to the reduction results, the smaller  $\text{Co}_3\text{O}_4$  particles were the easiest to sulfide.

The performance of a supported metal or metal sulfide catalyst depends on the details of its preparation and pretreatment. For petroleum refining applications, these catalysts are activated by reduction and/or sulfidation of an oxide precursor. The amount of the catalytic component converted to the active phase and the dispersion of the active component are important factors in determining the catalytic performance of these materials. This investigation examines the process of reduction and sulfidation on unsupported  $\text{Co}_3\text{O}_4$  and silica-supported  $\text{Co}_3\text{O}_4$  catalysts with different  $\text{Co}_3\text{O}_4$  dispersions. The  $\text{Co}_3\text{O}_4$  particle sizes were determined with electron microscopy, X-ray diffraction (XRD), and

<sup>1</sup>Current address: Department of Chemistry, Oregon State University, Corvallis, OR 97331

0097-6156/85/0288-0144\$06.00/0  
© 1985 American Chemical Society

XPS. The changes in catalyst composition during reduction and sulfidation were determined by XAS and XPS.

#### Experimental

Catalyst Preparation. The unsupported  $\text{Co}_3\text{O}_4$  was obtained from Johnson Matthey Chemicals (Puratronic grade) and was used as received. The supported catalysts with nominal Co loadings of 10 wt % were prepared by pore-fill impregnation with an aqueous solution of  $\text{Co}(\text{NO}_3)_2$  on Davison Grade 62 and 923 silica supports. The two supported catalysts will be referred to as  $\text{Co}/\text{SiO}_2$ -62 and  $\text{Co}/\text{SiO}_2$ -923. The silica supports were first calcined at  $500^\circ\text{C}$  for two hours, then impregnated, equilibrated in a capped bottle for five days, dried under vacuum ( $\sim 300$  torr) at  $100^\circ\text{C}$  for four hours, and finally recalcined at  $250^\circ\text{C}$  for one hour and  $450^\circ\text{C}$  for two hours.

XPS Analysis. The ultrahigh vacuum (UHV) catalyst treatment-surface analysis system employed to characterize and treat the cobalt catalysts has been described previously (1, 2). The catalyst treatment and data analysis procedures have also been described (1). Briefly, the samples were treated in quartz reactors and then transferred under UHV into a modified Hewlett-Packard 5950A ESCA spectrometer for analysis. Peak areas were normalized with theoretical cross-sections (3) to obtain relative atomic compositions.

XAS Analysis. All of the XAS experiments were done on line VII-3 at the Stanford Synchrotron Radiation Laboratory (SSRL) with the electron storage ring operating at 3 GeV and  $\sim 40$  mAmps. The spectra were collected in the transmission mode using a wiggler insertion device, a double Si (220) crystal monochromator, and  $\text{N}_2$  filled ion chambers. Both X-ray absorption near edge structure (XANES) and extended X-ray absorption fine structure (EXAFS) measurements at the cobalt K edge (7709.5 eV) were made. Before and after each reduction or sulfidation experiment detailed high resolution XANES and EXAFS spectra were taken. During the treatments low resolution XANES spectra were taken approximately every two minutes. Both temperature-programmed ( $\sim 5^\circ\text{C}/\text{min.}$ ) and isothermal experiments were done in a controlled atmosphere cell. The XAS cell was a modified version of a cell used in infrared spectroscopy experiments (4) and will be described in detail elsewhere (5). Briefly, the cell was modified by replacement of the Pt wire heater with two 500-watt quartz halogen lamps, replacement of the salt windows with mylar windows, addition of water cooling to the outer stainless steel jacket, enlargement of the diameter of sample wafers from 1.27 cm to 1.91 cm, and reduction in size of the entire cell so it would fit into the experimental hutches at SSRL. The cell was capable of operation at temperatures from  $-196$  to over  $650^\circ\text{C}$  at pressures from  $10^{-8}$  to  $10^3$  torr. A gas manifold was used to flow the selected gas ( $\text{He}$ ,  $\text{H}_2$ , or  $2\% \text{H}_2\text{S}/\text{H}_2$ ) through the cell and a turbomolecular pump was used to evacuate the cell.

This paper presents the results from the XANES spectra taken during temperature-programmed reduction and sulfidation experiments. All spectra were normalized to a step height of unity after removing a linear pre-edge background. The zero point of the energy scale was set to the first inflection point of Co foil. Each normalized XANES spectra was then decomposed into the contributions from various cobalt species by least squares fitting. The reference spectra for  $\text{Co}_3\text{O}_4$ , CoO, Co, and  $\text{Co}_9\text{S}_8$  used for this decomposition are in Figure 1. The reference spectra were taken at the same resolution conditions as the spectra taken during reduction and sulfidation. An example of the decomposition is shown in Figure 2.

Electron Microscopy Analysis. Transmission and scanning electron microscopy (TEM and SEM) studies were performed on a JEOL 100CX TEMSCAN. The unsupported  $\text{Co}_3\text{O}_4$  powder was dispersed on double-sided sticky tape and coated lightly with a Pd-Au alloy. Images were obtained in the SEM mode at 40 and 60 KeV. Ground powder from the  $\text{SiO}_2$ -supported samples was embedded in epoxy, then microtomed with a diamond knife to obtain sections  $\sim 600$  Å thick. These thin sections were put on 3-mm TEM grids and coated with a carbon layer ( $<100$  Å). Images and diffraction patterns were obtained in the TEM mode at 100 KeV.

### Results and Discussion

Cobalt Oxide Catalysts. All three catalysts were characterized in their oxide form prior to the reduction and sulfidation experiments. For the two supported catalysts the XAS, XPS, XRD, and TEM results all showed that  $\text{Co}_3\text{O}_4$  was the major cobalt species present. The main difference between the three samples was in the size of the  $\text{Co}_3\text{O}_4$  particles. For bulk  $\text{Co}_3\text{O}_4$ , SEM images showed the particles were octahedral and ranged in size from 1000 to 5000 nm. The  $\text{Co}_3\text{O}_4$  particle size on the  $\text{SiO}_2$ -supported catalysts was determined from TEM images, XPS measured Co/Si ratios (6), and the XRD peak widths (7). XPS and XRD results show the  $\text{Co}_3\text{O}_4$  particle size was between 10 and 30 nm for the Co/ $\text{SiO}_2$ -62 catalyst. TEM observations showed that these 10- to 30-nm particles were tightly clustered into aggregates ranging in size from 100 to 1000 nm. The  $\text{Co}_3\text{O}_4$  particles in each aggregate had essentially the same crystallographic orientation. TEM and XPS both showed the Co/ $\text{SiO}_2$ -923 sample to have a high dispersion, with the  $\text{Co}_3\text{O}_4$  particles 5 nm and smaller in size. Thus  $\text{Co}_3\text{O}_4$  was the major cobalt species present in all three samples with average particle sizes of 3000 nm for bulk  $\text{Co}_3\text{O}_4$ ,  $\sim 20$  nm in  $\sim 500$  nm aggregates for Co/ $\text{SiO}_2$ -62, and  $<5$  nm for Co/ $\text{SiO}_2$ -923.

Reduction of the  $\text{Co}_3\text{O}_4$  Catalysts. For all three samples the reduction of the surface of the  $\text{Co}_3\text{O}_4$  particles to metallic cobalt was observed by XPS following reaction in one atmosphere of flowing  $\text{H}_2$ . After one hour at 350°C bulk  $\text{Co}_3\text{O}_4$  was completely reduced, while for  $\text{Co}_3\text{O}_4/\text{SiO}_2$ -62 the reduction was only about 80% complete. The  $\text{Co}_3\text{O}_4/\text{SiO}_2$ -923 sample was about 60% reduced at

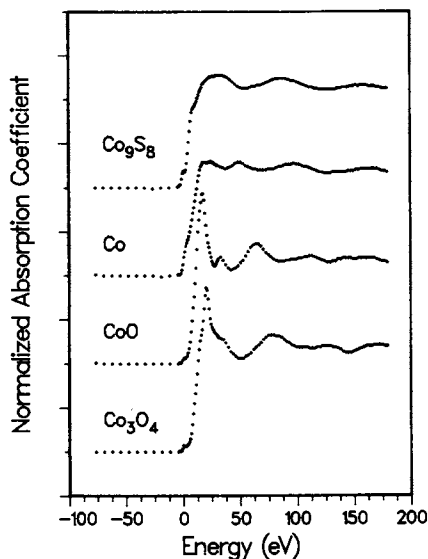


Figure 1. The fast scan Co XANES reference spectra for  $\text{Co}_9\text{S}_8$ , Co, CoO, and  $\text{Co}_3\text{O}_4$ .

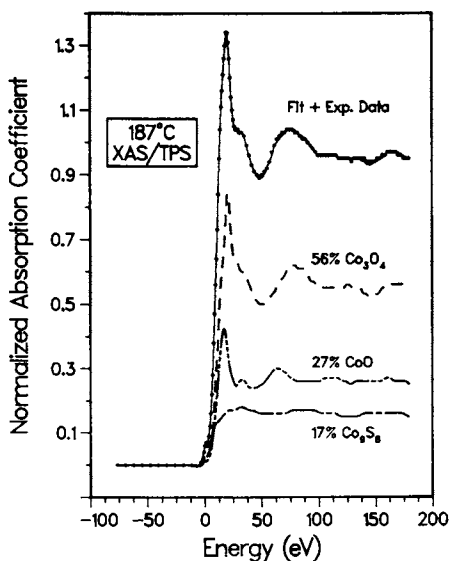


Figure 2. A decomposition example for a spectrum taken during an XAS/TPS experiment on  $\text{Co}_3\text{O}_4/\text{SiO}_2$ -923 in 1 atmosphere of flowing 2%  $\text{H}_2\text{S}/\text{H}_2$ . The temperature ramp was  $5^\circ\text{C}/\text{minute}$ .

American Chemical Society  
Library



350°C and both SiO<sub>2</sub> supported catalysts were completely reduced after an hour at 500°C. These results indicate that the smaller Co<sub>3</sub>O<sub>4</sub> particles were harder to reduce to metallic cobalt.

XAS was used to follow the reduction process in detail. Figure 3 and Table I summarize the XANES results from spectra taken approximately every two minutes during temperature programmed reduction (TPR) experiments on the three catalysts. These results show that CoO was an intermediate in the reduction of Co<sub>3</sub>O<sub>4</sub> to Co. The identification of CoO was from direct XAS measurements during the reduction, not inferred from the changes observed in the gas phase composition (viz., decrease of the H<sub>2</sub> concentration or increase of the H<sub>2</sub>O concentration) as is generally done in conventional TPR experiments (8). The combination XAS/TPR measurements have even a greater advantage in multicomponent systems (e.g., Co-Mo catalysts) since the behavior of each element can be isolated separately.

Table I. XAS Results From TPR Experiments in One Atmosphere of Flowing H<sub>2</sub> for Co<sub>3</sub>O<sub>4</sub>, Co<sub>3</sub>O<sub>4</sub>/SiO<sub>2</sub>-62 and Co<sub>3</sub>O<sub>4</sub>/SiO<sub>2</sub>-923

| Sample  | Particle Size (nm) | Reduction Temp. (°C) | Delta Reduction Temp. (°C) |
|---|--------------------|----------------------|----------------------------|
| Co <sub>3</sub> O <sub>4</sub>                        | 1000-5000          | 315                  | 5                          |
| Co <sub>3</sub> O <sub>4</sub> /SiO <sub>2</sub> -62  | 10-30              | 310                  | 60                         |
| Co <sub>3</sub> O <sub>4</sub> /SiO <sub>2</sub> -923 | <5                 | 290                  | 250                        |

We characterize the reduction process by defining the reduction temperature as the point where the Co<sub>3</sub>O<sub>4</sub> concentration has dropped to 50% and the delta reduction temperature as the temperature difference between the points at which 50% Co<sub>3</sub>O<sub>4</sub> and 50% Co were reached. These definitions are arbitrary and their values will change with experimental conditions, but they are useful for comparing samples examined at the same conditions. Both of these temperature parameters must be considered when assessing the reduction properties of the samples.

As the starting Co<sub>3</sub>O<sub>4</sub> particle size decreased from microns to nanometers, the reduction temperatures were similar (315°C to 290°C), but the delta reduction temperatures increased noticeably (5°C to 250°C). These results indicate for the reduction of Co<sub>3</sub>O<sub>4</sub> to Co the Co<sub>3</sub>O<sub>4</sub> to CoO step was nearly independent of the particle size, while the CoO to Co step was strongly dependent on the particle size. Thus the smaller Co<sub>3</sub>O<sub>4</sub> particles were more difficult to reduce to Co because of the differences observed in the CoO + Co step. Previously it had been observed for the Co/Al<sub>2</sub>O<sub>3</sub> (9), Ni/SiO<sub>2</sub> (10), and Fe/SiO<sub>2</sub> (11, 12) systems that highly dispersed oxide species (small particles) were more difficult to reduce than their corresponding bulk or bulk-like oxides. Nucleation, interaction with the support, and reaction with the support were given as possible explanations for these differences. Further experiments are needed to determine the reasons for the observed particle size effect on the Co/SiO<sub>2</sub> system.

Sulfidation of the  $\text{Co}_3\text{O}_4$  Catalysts. XPS and XAS results show that the cobalt in all three samples was converted to  $\text{Co}_9\text{S}_8$  after reaction at  $400^\circ\text{C}$  for one hour in  $\text{H}_2\text{S}/\text{H}_2$ . Again XANES spectra taken during sulfidation were used to follow the reaction in detail. The results from temperature programmed sulfidation (TPS) experiments are summarized in Figure 4 and Table II.

Table II. XAS Results From TPS Experiments in One Atmosphere of Flowing 2%  $\text{H}_2\text{S}/\text{H}_2$  for  $\text{Co}_3\text{O}_4$ ,  $\text{Co}_3\text{O}_4/\text{SiO}_2$ -62 and  $\text{Co}_3\text{O}_4/\text{SiO}_2$ -923

| Sample                                    | Particle Size (nm) | Sulfidation Temp. ( $^\circ\text{C}$ ) | Delta Sulfidation Temp. ( $^\circ\text{C}$ ) |
|---|--------------------|--|--|
| $\text{Co}_3\text{O}_4$                   | 1000-5000          | 370                                    | 25   |
| $\text{Co}_3\text{O}_4/\text{SiO}_2$ -62  | 10-30              | 250                                    | 65   |
| $\text{Co}_3\text{O}_4/\text{SiO}_2$ -923 | $\leq 5$           | 190                                    | 55   |

The XAS results show that both  $\text{CoO}$  and  $\text{Co}$  were present as intermediates during the sulfidation of  $\text{Co}_3\text{O}_4$  to  $\text{Co}_9\text{S}_8$ . On the silica supported catalysts 20 to 30 percent  $\text{Co}_9\text{S}_8$  was formed before any cobalt metal was detected. This implies either  $\text{Co}_9\text{S}_8$  can be formed directly from a cobalt oxide phase without passing through  $\text{Co}$ , or the rate of the  $\text{Co} + \text{Co}_9\text{S}_8$  step was sufficiently faster than the rate limiting step of the  $\text{Co}_3\text{O}_4 + \text{Co}$  process so that any  $\text{Co}$  formed was immediately sulfided. Results from isothermal experiments on the  $\text{Co}_3\text{O}_4 + \text{Co}$  and  $\text{Co} + \text{Co}_9\text{S}_8$  reactions should help determine the correct explanation.

The sulfidation temperature decreased noticeably with the starting  $\text{Co}_3\text{O}_4$  particle size (370 to  $190^\circ\text{C}$ ). The delta sulfidation temperatures (50%  $\text{Co}_9\text{S}_8$  - 50%  $\text{Co}_3\text{O}_4$ ) were similar on the two supported catalysts (65 and  $55^\circ\text{C}$ ), both larger than for bulk  $\text{Co}_3\text{O}_4$  ( $25^\circ\text{C}$ ). Thus because of their lower sulfidation temperatures, the smaller  $\text{Co}_3\text{O}_4$  particles were easier to sulfide.

The increased difficulty of sulfidation with increased  $\text{Co}_3\text{O}_4$  particle size could be due to constraints of the diffusing species ( $\text{Co}$  atoms,  $\text{H}_2\text{S}$ ,  $\text{S}$ , etc.) in the larger particles. This is because the distance the diffusing species must travel to sulfide a particle increases with the increasing size of that particle. Sulfidation of the larger particles would then require higher temperatures and/or longer times to overcome any diffusion constraints. This difficulty is not as important in the reduction process since hydrogen diffusion is more facile. Direct sulfidation of  $\text{Co}_3\text{O}_4$  or  $\text{CoO}$  can explain the fact the delta sulfidation temperatures for the  $\text{Co}/\text{SiO}_2$  catalysts were similar while their delta reduction temperatures were noticeably different. Direct sulfidation would eliminate the  $\text{CoO} + \text{Co}$  step of the reaction, which was the step that caused the smaller particles to be more difficult to reduce. This implies the property that increased the difficulty of reduction with decreasing particle size (nucleation, support

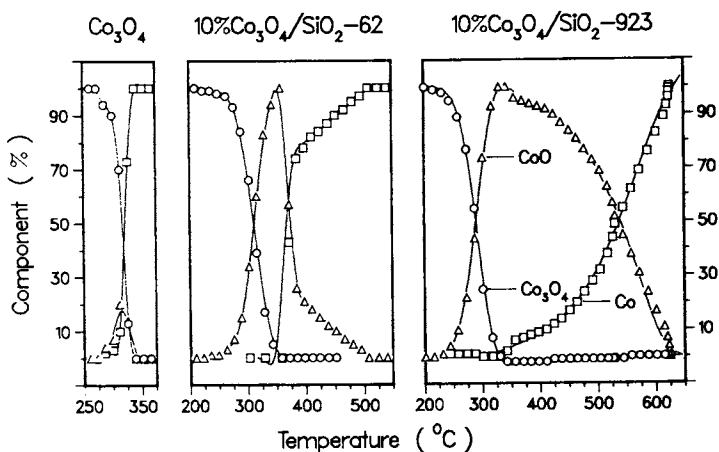


Figure 3. XAS/TPR results for  $\text{Co}_3\text{O}_4$ ,  $\text{Co}_3\text{O}_4/\text{SiO}_2$ -62 and  $\text{Co}_3\text{O}_4/\text{SiO}_2$ -923 in 1 atmosphere of flowing  $\text{H}_2$ . The temperature ramp was  $5^\circ\text{C}/\text{minute}$ .

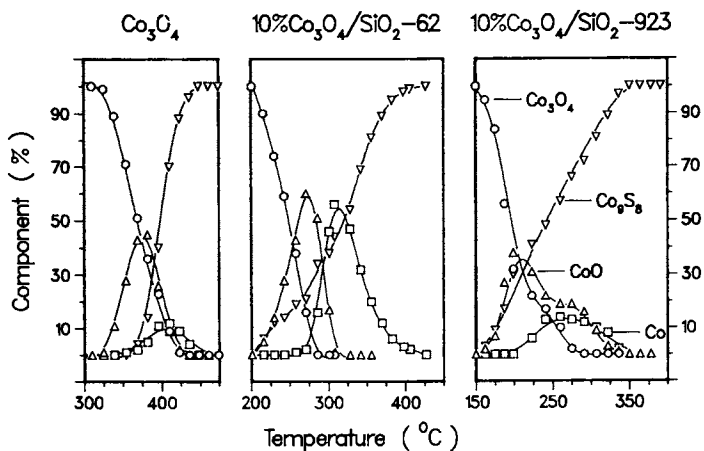


Figure 4. XAS/TPS results for  $\text{Co}_3\text{O}_4$ ,  $\text{Co}_3\text{O}_4/\text{SiO}_2$ -62 and  $\text{Co}_3\text{O}_4/\text{SiO}_2$ -923 in 1 atmosphere of flowing  $2\% \text{H}_2\text{S}/\text{H}_2$ . The temperature ramp was  $5^\circ\text{C}/\text{minute}$ .

effects, etc.) would not be an important part of the sulfidation process. Thus direct sulfidation of Co oxide and diffusional differences can account for the observation that the smaller  $\text{Co}_3\text{O}_4$  particles are both harder to reduce and easier to sulfide than the larger  $\text{Co}_3\text{O}_4$  particles.

### Conclusions

We have shown that XANES spectra for catalysts can be obtained in two minutes. This enables us to spectroscopically monitor changes in catalyst composition in real time. Our controlled atmosphere cell allowed us to do these experiments on catalysts under reaction conditions.

The reaction sequence of unsupported  $\text{Co}_3\text{O}_4$  and silica supported  $\text{Co}_3\text{O}_4$  catalysts for  $\text{H}_2$  reduction was  $\text{Co}_3\text{O}_4 \rightarrow \text{CoO} \rightarrow \text{Co}$ . Sulfidation of the  $\text{Co}_3\text{O}_4$  catalysts proceeded as  $\text{Co}_3\text{O}_4 \rightarrow \text{CoO} \rightarrow \text{Co} \rightarrow \text{Co}_9\text{S}_8$  with some direct sulfidation of  $\text{CoO} \rightarrow \text{Co}_9\text{S}_8$  occurring on the supported catalysts. The reduction temperatures were fairly constant while the sulfidation temperatures decreased markedly with decreasing  $\text{Co}_3\text{O}_4$  particle size. The delta reduction temperatures increased with decreasing  $\text{Co}_3\text{O}_4$  particle size.

### Acknowledgments

We wish to thank R. O. Billman for his assistance in designing and assembling the XAS controlled atmosphere cell and the XPS catalyst treatment system. I. Y. Chan did the TEM and SEM experiments. Part of the work reported herein was performed at SSRL, which is supported by the Department of Energy, Office of Basic Energy Sciences; the National Science Foundation, Division of Materials Research; and the National Institutes of Health, Biotechnology Resource Program, Division of Research Resources.

### Literature Cited

1. Castner, D. G.; Santilli, D. S. in "Catalytic Materials: Relationship Between Structure and Reactivity"; Whyte, T. E., Jr.; Dalla Betta, R. A.; Derouane, E. G.; Baker, R. T. K., Eds.; ACS SYMPOSIUM SERIES No. 248, American Chemical Society: Washington, D.C., 1984; pp 39-56.
2. Castner, D. G. Proc. Adv. Catal. Chem. II, 1982, submitted.
3. Scofield, J. H. J. Electron Spectrosc. Relat. Phenom. 1976, 8, 129-137.
4. Ryason, P. R. Rev. Sci. Instrum. 1973, 44, 772-3.
5. Castner, D. G.; Billman, R. O. to be published.
6. Kerkhof, F. P. J. M.; Moulijn, J. A. J. Phys. Chem. 1979, 83, 1612-9.
7. Klug, H. P.; Alexander, L. E. "X-Ray Diffraction Procedures for Polycrystalline and Amorphous Materials;" Wiley-Interscience, 1974; pp 634-642.
8. Hurst, N. W.; Gentry, S. J.; Jones, A.; McNicol, B. D. Catal. Rev.-Sci. Eng. 24, 1982, 233-309.
9. Chin, R. L.; Hercules, D. M. J. Phys. Chem. 1982, 86, 360-7.

10. Houalla, M.; Delannay, F.; Matsuura, I.; Delmon, B. J. Chem. Soc. Faraday I 1980, 76, 2128-41.
11. Topsøe, H.; Dumesic, J. A.; Mørup, S. in "Applications of Mossbauer Spectroscopy"; Vol 2, Cohen, R. L., Ed.; Academic Press, New York, 1980; p 55.
12. Lund, C. R. F.; Dumesic, J. A. J. Phys. Chem. 1981, 85, 3175-80.

RECEIVED June 21, 1985

## Studies of the Kinetics and Mechanisms of Ammonia Synthesis and Hydrodesulfurization on Metal Single-Crystal Surfaces

A. J. Gellman, M. Asscher, and G. A. Somorjai

Materials and Molecular Research Division, Lawrence Berkeley Laboratory,  
Department of Chemistry, University of California—Berkeley, Berkeley, CA 94720

We have studied the ammonia synthesis reaction over Fe and Re single crystal surfaces and the hydrodesulfurization of thiophene over the Mo(100) single crystal surface. The studies have been performed using UHV surface science tools with the capability of exposing the surfaces to high pressure, high temperature reaction conditions. The ammonia synthesis reaction was shown to be extremely sensitive to surface structure on both Fe and Re, favoring surfaces with a rough or open topography. The HDS reaction on the Mo(100) surface has been shown to be similar to that on MoS<sub>2</sub> and appears to proceed via a reaction path that does not produce a strong Mo-S bond as an intermediate species.

The use of surface science techniques as probes for the study of catalytic processes was for many years hampered by the lack of direct connection between the great volume of information obtained under UHV conditions and studies performed under the high pressure, high temperature conditions of industrial catalysis. There are very few techniques for studying surfaces while exposing them to high pressures of gases, while on the other hand there are a large number of probes of the surface/vacuum interface. Our approach to bridging the gap between these two extremes of conditions has been to develop a system allowing direct transfer of samples between a high pressure catalytic environment and the UHV conditions under which it is possible to prepare, study and characterize their surfaces and adsorbates on these surfaces (1). Using this approach we have been able to investigate a number of catalytic problems on both single crystal and polycrystalline samples.

In this paper we will discuss the results that we have obtained studying two important processes, the synthesis of ammonia over Fe and Re catalysts and the hydrodesulfurization of thiophene on Mo. These examples illustrate two problems in catalysis to which our methods are particularly sensitive. The first is the effect of the structure of the catalyst on reaction rates. The sensitivity of the

0097-6156/85/0288-0154\$06.00/0  
© 1985 American Chemical Society

reaction rate to the nature of the catalytic surface is exhibited to an extreme extent by the ammonia synthesis reaction on both Fe and Re. The second is the effect on thiophene hydrodesulfurization of the addition of sulfur to the surface of a Mo single crystal.

Ammonia synthesis is one of the oldest industrial catalytic processes and has been studied by a large number of investigators. Most work has been performed using Fe based catalysts and it has been shown that the rate limiting step in this reaction is the dissociative chemisorption of nitrogen (2). Other work has shown that nitrogen adsorbs preferentially on the Fe(111) surface (3) and the suggestion has been made that it is the seven-coordinate atoms in the second layer below the surface that are indeed most active in the synthesis (4). By comparison very little work has been done using Re as a catalyst. Here we report the results of some of the work that has been completed in our laboratory studying ammonia synthesis over both Fe and Re single crystal surfaces.

The extreme sensitivity of the reforming catalysts to poisoning by sulfur has stimulated much work studying the hydrodesulfurization reaction and hydrotreating reactions in general. The catalysts for this reaction are based on supported molybdenum sulfides. We have chosen to study this reaction by using single crystal molybdenum surfaces and to combine UHV surface science with studies of the hydrodesulfurization of thiophene at high pressures.

### Experimental

The apparatuses used for the studies of both ammonia synthesis and hydrodesulfurization were almost identical, consisting of a UHV chamber pumped by both ion and oil diffusion pumps to base pressures of  $1 \times 10^{-9}$  Torr. Each chamber was equipped with Low Energy Electron Diffraction optics used to determine the orientation of the surfaces and to ascertain that the surfaces were indeed well-ordered. The LEED optics doubled as retarding field analyzers used for Auger Electron Spectroscopy. In addition, each chamber was equipped with a UTI 100C quadrupole mass spectrometer used for analysis of background gases and for Thermal Desorption Spectroscopy studies.

Each UHV chamber was equipped with a cell that could be sealed over the crystal allowing it to be exposed to high gas pressures, simulating reaction conditions. The crystals were spot welded between two metal posts allowing them to be heated resistively both for the purpose of cleaning in vacuum and for heating while exposed to reactant gas mixtures. Crystal temperatures were monitored using thermocouples spot welded to their edges. The high pressure cells were connected to gas handling lines made of 0.25" stainless steel tubing, forming a closed loop, batch reactor through which reactant gases were circulated. Samples of the gas mixture were taken periodically for analysis via a gas sampling valve. The ammonia synthesis mixture was analyzed for ammonia content using a photo-ionization detector (energy = 10.2 eV). The products of the HDS of thiophene were separated on a gas chromatograph and analyzed with a flame ionization detector.

Fe, Re and Mo samples were typically of about  $1 \text{ cm}^2$  area by 0.5 mm thick and were spark cut from single crystal rods. These were subsequently polished using standard metallurgical techniques and

finally cleaned in UHV using various treatments including Ar<sup>+</sup> ion sputtering, and both oxidation and reduction at elevated temperatures. The details of sample preparation and of the procedures used to perform reactions have been described thoroughly elsewhere (6-9).

### Ammonia Synthesis

Kinetics over Fe Crystal Surfaces. A typical ammonia synthesis reaction was performed at 5 atm. of N<sub>2</sub> and 15 atm. of H<sub>2</sub> at a temperature of 736K over an Fe(111) surface. After a period during which the ammonia formed was adsorbed on the walls of the high pressure loop its accumulation rate in the reactor was constant. The corresponding rate of reaction was  $9.9 \times 10^{15}$  molecules/cm<sup>2</sup>/sec. This rate was measured over a 150 K temperature range and showed an Arrhenius type dependence yielding an activation energy of 19.4 kcal/mole. Table I shows the effects on the rate of gross variations in the reactant pressures and in the total pressure. The extensive data necessary for the derivation of a true kinetic rate law was not collected. It can be seen clearly that the reaction rate is positive order in both hydrogen and nitrogen.

Table I. Effect of Reactant Pressure on NH<sub>3</sub> Synthesis (T=748K)

| P(N <sub>2</sub> )<br>(atm) | P(H <sub>2</sub> )<br>(atm) | P(Ar)<br>(atm) | Rate<br>(molec./cm <sup>2</sup> /sec) |
|-----------------------------|-----------------------------|----------------|---------------------------------------|
| 15                          | 5                           | 0              | 15 x 10 <sup>15</sup>                 |
| 5                           | 15                          | 0              | 18 x 10 <sup>15</sup>                 |
| 5                           | 5                           | 10             | 4.5 x 10 <sup>15</sup>                |
| 5                           | 5                           | 0              | 7.0 x 10 <sup>15</sup>                |

The surface after the reaction was found, using AES, to be clean with the exception of the presence of strongly adsorbed nitrogen and some small amounts of sulfur that segregated from the crystal bulk during the course of the reaction. Exposure of this surface to reaction conditions resulted in a reaction rate similar to that over the clean surface. A layer of FeN<sub>4</sub> was prepared by exposing the surface to  $5 \times 10^{-4}$  Torr of ammonia at 673 K for 10 hrs. (5). This surface had an Auger spectrum similar to that of the surface produced during the reaction and exhibited a catalytic activity similar to that of the clean surface. This suggests that during the reaction the amount of nitrogen deposited on the surface is close to that present in the compound FeN<sub>4</sub> and possibly that this is actually present at the surface during the reaction (6).

Structure Sensitivity over Fe. Table II presents the rates of ammonia synthesis over each of the low Miller index planes of Fe. The relative rates are 418 : 25 : 1 for the ordered Fe(111), Fe(100)



and Fe(110) surfaces respectively. These rates are consistent with the chemisorption studies of Ertl (3) which showed that the rate of dissociative nitrogen chemisorption under UHV conditions follows the same pattern of structure sensitivity. This agreement between reaction rates and the chemisorption studies also indicates that it is the dissociative chemisorption step that is rate limiting in the overall reaction pathway.

Table II.  $\text{NH}_3$  Synthesis Structure Sensitivity on Fe

| Surface                          | Rate <sup>a</sup> (molec./cm <sup>2</sup> /sec) |
|----------------------------------|---|
| Fe(111)                          | $27 \times 10^{15}$                             |
| Fe(100), Ordered                 | $1.7 \times 10^{15}$                            |
| Fe(110), Ordered                 | $0.1 \times 10^{15}$                            |
| Fe(100), Disordered <sup>b</sup> | $2.7 \times 10^{15}$                            |
| Fe(110), Disordered <sup>b</sup> | $0.6 \times 10^{15}$                            |

a.  $P(\text{H}_2) = 15 \text{ atm.}$ ,  $P(\text{N}_2) = 5 \text{ atm.}$ ,  $T = 798 \text{ K}$

b. Argon ion bombardment ( $1.5 \times 10^{15} \text{ A/cm}^2$ , 600 sec., 500 V)

The Fe(111) surface is composed of four-fold coordinated atoms and exposed second layer atoms that are seven-fold coordinated while the Fe(110) and Fe(100) planes have only six-fold and four-fold coordinated atoms respectively. Here we have defined the coordination number as the number of nearest neighbor atoms. Dumesic's proposal that the seven-fold coordinated atom is an important component of the catalytically active site is not contradicted by our results (4). It is also worth noting that the relative roughness or openness of the each plane follows the same progression as their catalytic activities. Table II also shows that the activity of each of the two less active surfaces was markedly enhanced by sputtering with Ar. It is possible that sputtering has exposed seven-fold coordinate atoms at the surface or that it is the roughness of the surface that is responsible for the structure sensitivity of the reaction rate.

Kinetics of Ammonia Synthesis on Re Crystal Surfaces. The kinetics of the ammonia synthesis reaction on Re were studied on the Re(11 $\bar{2}$ 0) surface which is composed of atoms having seven-fold coordination. The rate of production at 870 K and 20 atm.  $\text{H}_2/\text{N}_2$  in a 3:1 ratio is  $1.8 \times 10^{17}$  molec/cm<sup>2</sup>/sec. Over long periods of time the rate of production decreased due to product poisoning of the surface as the concentration of ammonia in the reactor loop increased, an effect that was not observed on Fe (7). An Arrhenius plot of the reaction rate yields an activation energy of 20.0 kcal/mole, very close to that observed on Fe suggesting that the rate determining step is identical on the two surfaces. The dependence of the rate on the reactant pressures has been studied in greater detail on Re than on Fe and has been fitted to a rate law of the form (8)

$$r = k P_{N_2}^{1.0} P_{H_2}^{0.67}$$

Structure Sensitivity over Re. As in the case of the Fe catalysts the rate of ammonia synthesis varies greatly over Re single crystal surfaces of different orientations. This phenomenon has been studied over the (0001), (10 $\bar{1}$ 0), (11 $\bar{2}$ 0) and (11 $\bar{2}$ 1) planes in a 3:1 H<sub>2</sub>/N<sub>2</sub> mixture at a total pressure of 20 atm. and a temperature of 870 K. Under these conditions these surfaces catalyze the reaction with relative rates of 1:94:920:2820 respectively, showing a range of activities even greater than that observed on Fe.

Re has a hcp crystal structure and so the (0001), the least active, is a close packed surface while the (10 $\bar{1}$ 0) is somewhat more open and is composed of troughs. The most active planes studied, the Re(11 $\bar{2}$ 0), Re(11 $\bar{2}$ 1) and the Fe(111) surfaces are shown in Figure 1 which shows that the most common feature among them is their open or rough topography. The Fe(111) and Re(11 $\bar{2}$ 0) surfaces both have large numbers of exposed seven-fold coordinate atoms, however, the Re(11 $\bar{2}$ 1), the most active of all surfaces, has none. This tends to contradict the suggestion made previously that it is these seven-fold coordinate atoms at the surface that are particularly active catalytic sites. What seems to be a more general trend is that it is the high coordination of the hollow or vacant sites at the surface that determines the catalytic activity. It is presumably these hollows into which N<sub>2</sub> adsorbs and dissociates.

#### The Hydrodesulfurization of Thiophene

Kinetics over the Mo(100) Crystal Surface. We have studied the hydrodesulfurization of thiophene over the initially clean Mo(100) single crystal surface in the temperature range 520K - 690K and at reactant pressures of 100 Torr  $\leq$  P(H<sub>2</sub>)  $\leq$  800 Torr and 0.1 Torr  $\leq$  P(Th)  $\leq$  10 Torr. Under these conditions the reaction is catalyzed at a constant rate for a period of approximately one hour after which the rate begins to decrease with time. The rates reported here are all initial rates of reaction calculated from data collected in the period over which they remain constant.

The product distribution of the HDS of thiophene over the Mo(100) surface is shown in Table III compared with that reported by Kolboe over a MoS<sub>2</sub> catalyst (14). It is clear that the two are very similar and that our catalyst mimics the MoS<sub>2</sub> catalyst very closely in this respect. An Arrhenius plot (Figure 2) made in the temperature region mentioned above shows that butadiene is the only product whose rate of formation shows true Arrhenius type dependence and yields an activation energy of 14.4 kcal/mole. At high temperatures the rate of butane formation deviates even more sharply than that of the butenes and does so at lower temperatures (9).

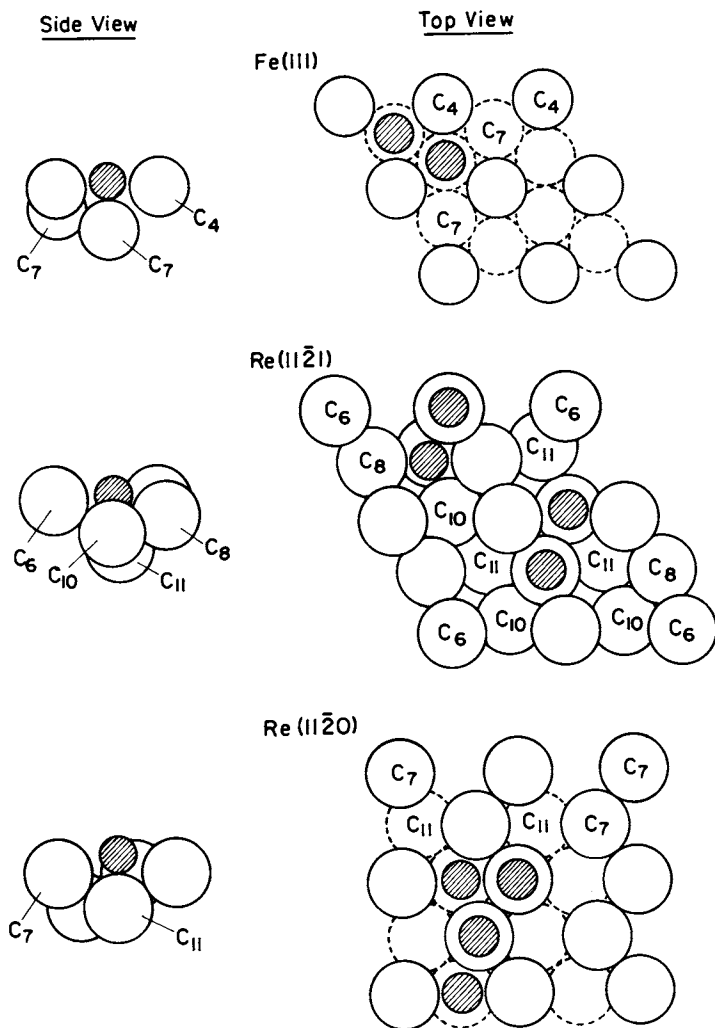


Figure 1. The most active Fe and Re surfaces for ammonia synthesis.

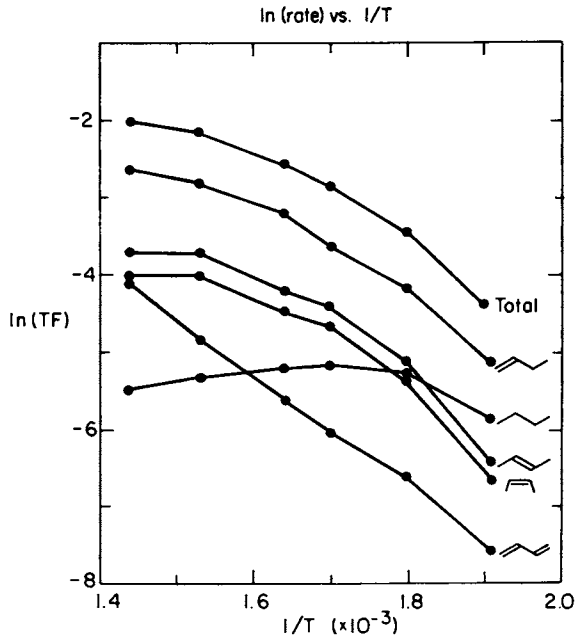


Figure 2. Arrhenius plot for the HDS of thiophene on the Mo(100) surface.  $P(H_2) = 780$  Torr,  $P(Th) = 2.5$  Torr.

Table III. Product Distribution of Thiophene HDS

| Product        | Mo(100) <sup>a</sup> | MoS <sub>2</sub> <sup>b</sup> |
|----------------|----------------------|-------------------------------|
| Butane         | 15.6%                | 11.5%                         |
| 1-Butene       | 47.5%                | 41.7%                         |
| cis-2-Butene   | 14.7%                | 17.8%                         |
| Trans-2-Butene | 18.7%                | 22.8%                         |
| Butadiene      | 4.1%                 | 6.3%                          |

a.  $P(H_2)=780$  Torr,  $P(Th)=2.5$  Torr,  $T=285^\circ C$

b.  $P(H_2)=760$  Torr,  $P(Th)=20$  Torr,  $T=288^\circ C$

The results of variations in reactant pressures are shown in Table IV. Again there are clear variations among each of the products pointing to orders in hydrogen pressure dependence of zero, one-half, and one for butadiene, the butenes and butane respectively. The half-order dependence of the butene rate of formation shows that the hydrogenation must be a reaction with atomic hydrogen on the surface and that the hydrogen concentration on the surface must be in the low coverage regime of the adsorption isotherm. These results also point to the temperature dependence being a result of a decrease in the hydrogen coverage at high temperatures. The rate of butadiene formation, being independent of  $H_2$  pressure, will not be affected by changes in hydrogen coverage and thus, will show Arrhenius type temperature dependence. The rates of butene and butane formation will be affected by decreases in hydrogen coverage at high temperatures. The butane formation rate should be more severely affected than that of the butenes, as is observed.

Table IV. HDS Dependence on Reactant Pressures ( $T=340^\circ C$ )

| Product        | Order of Pressure Dependence ( $H_2$ ) | Order of Pressure Dependence (Th) |
|----------------|--|-----------------------------------|
| Butane         | 1.10                                   | 0.13                              |
| 1-Butene       | 0.54                                   | 0.33                              |
| cis-2-Butene   | 0.58                                   | 0.16                              |
| trans-2-Butene | 0.68                                   | 0.18                              |
| Butadiene      | - 0.18                                 | 0.95                              |

Effects of Sulfur Coverage. The kinetic results reported in the previous section are from reactions performed on surfaces that are initially clean. The surfaces after reaction were examined by AES and shown to be covered with carbon and sulfur at coverages close to a monolayer. It is interesting to note that although this is the case even after reaction times on the order of minutes the reaction rate is constant for a period of approximately one hour. Either the reaction is occurring on top of this carbon/sulfur layer or these species are present as sulfur containing hydrocarbon fragments that are intermediates in the desulfurization process.

Figure 3 shows the effect on the overall reaction rate of sulfur adsorbed onto the surface under UHV conditions. The nature of these sulfur overlayers has been studied in some detail and described elsewhere (10,11). At coverages of less than one half of one monolayer the sulfur has been shown to occupy the four-fold hollow adsorption site on the surface. It is clear that the rate of reaction decreases as the sulfur coverage increases from 0.0 to 0.5 monolayers and at this point the further addition of sulfur has no apparent effect. There are two interesting points about this result. First, it is surprising that the addition of sulfur to the surface has an effect on the reaction rate. If sulfur deposited on the surface during the HDS of thiophene were identical in nature to that deposited before the reaction, then initial sulfiding of the surface should have no effect on the reaction rate whatsoever. The observed effect suggests that the reaction occurs via a mechanism that either does not deposit sulfur onto the surface, as has been suggested by other investigators (12), or one that deposits sulfur in a form that is weakly bound and easily reduced to  $H_2S$ .

The second point of interest is that at coverages greater than ~0.5 monolayers the further addition of sulfur to the surface does not affect the reaction rate. This result lends itself to possible explanation in terms of two of the sulfur binding sites on the surface. At high sulfur coverages it has been suggested that sulfur occupies both the four-fold hollow, occupied at low coverages, and some other, possibly a bridged site (10). Ultra-violet photoelectron spectroscopy studies also support the dual binding site model (13). If the sulfur bound to the surface in this high coverage site is easily removed from the surface by hydrogen, then its presence would have no effect on the reaction rate. Furthermore, it is possible that it is this site into which sulfur from the reaction is actually deposited.

### Conclusions

The studies of ammonia synthesis over Fe and Re and the hydrodesulfurization of thiophene over Mo, described above, illustrate the importance and success of our approach of studying catalysis over single crystal samples at high pressures. The use of surfaces having a variety of orientations allows the study of reactions that are surface structure sensitive and provides insight into the nature of the catalytic site. Here we have shown that the ammonia synthesis

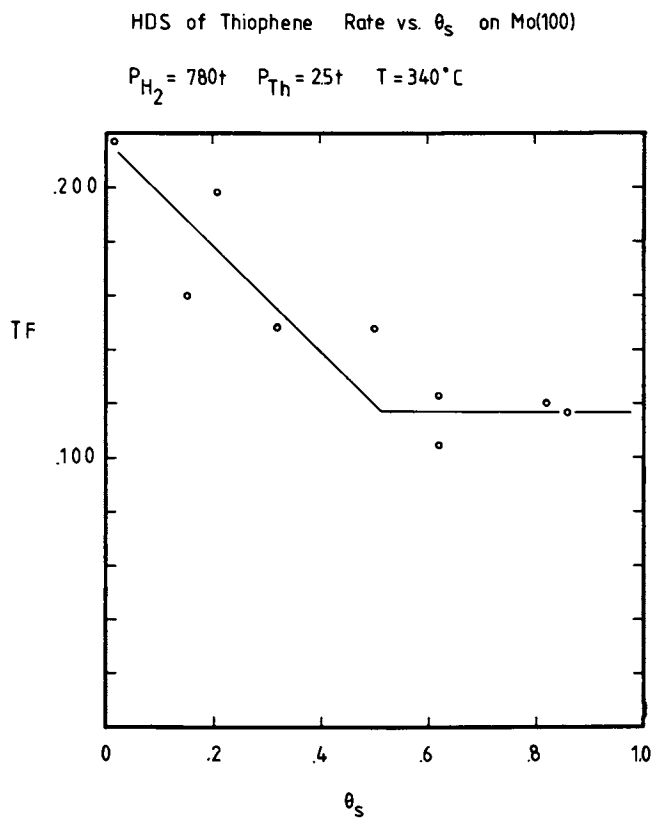


Figure 3. The rate of thiophene HDS on Mo(100) vs.  $\theta_s$ .  
 $P(H_2) = 780$  Torr,  $P(Th) = 2.5$  Torr,  $T = 340$  C.

reaction is highly sensitive to the surface structure and is best catalyzed by surfaces of a rough nature having vacant or hollow sites of high coordination. The ability to prepare surfaces that are well characterized in terms of both composition and structure allows the effects of surface contaminants or dopants to be studied in detail. The presence of ~0.5 monolayers of sulfur on the Mo(100) surface decreases the rate of thiophene hydrodesulfurization to about one half that of the clean surface. Further addition of sulfur does not effect the desulfurization rate. We propose that this may be due to the adsorption of the additional sulfur onto weakly bound sites from which it is easily reduced.

#### Acknowledgments

We would like to thank the Division of Materials Sciences and Office of Basic Energy Sciences of the U.S. Department of Energy for support under Contract No. DE-AC03-76SF00098, and both the Exxon Research and Engineering Co. and the Dow Chemical Co.

#### Literature Cited

1. Blakely, D. W.; Kozak, E.; Sexton, B. A.; Somorjai, G. A. J. Vac. Sci. & Tech. 1976, 13(5), 1091.
2. Emmett, P. H. "The Physical Basis for Heterogeneous Catalysis"; Plenum: New York, 1975; p. 3.
3. Ertl, G. Catal. Rev. Sci. Eng. 1980, 21, 201.
4. Dumesic, J. A.; Topsoe, H.; Boudart, M. J. Catal. 1975, 37, 513.
5. Brill, R.; Richter, E. L.; Ruch R. Angew. Chem. Int. Ed. Engl. 1967, 6, 882.
6. Spencer, N. D.; Schoonmaker, R. C.; Somorjai, G. A. J. Catal. 1982, 74, 129.
7. Spencer, N. D.; Somorjai, G. A. J. Catal. 1982, 78, 142.
8. Asscher, M.; Carrazza, J.; Khan, M. M.; Lewis, K. B.; Somorjai, G. A. in press.
9. Gellman, A. J.; Farias, M. H.; Somorjai, G. A. submitted to J. Catal.
10. Clarke, L. J. Surf. Sci. 1981, 102, 331.
11. Farias, M. H.; Gellman, A. J.; Somorjai, G. A. Surf. Sci. 1984, 140, 181.
12. Micovsky, R. J.; Silvestri, A. J.; Heinemann, H. J. Catal. 1974, 34, 324.
13. Gellman, A. J.; Tysoe, W. T.; Somorjai, G. A. in press.
14. Kolboe, S. Can. J. of Chem. 1969, 47, 352.

RECEIVED December 6, 1984



## Oxygen Interactions and Reactions on Palladium(100): Coadsorption Studies with C<sub>2</sub>H<sub>4</sub>, H<sub>2</sub>O, and CH<sub>3</sub>OH

E. M. Stuve<sup>1</sup>, S. W. Jorgensen, and R. J. Madix

Department of Chemical Engineering, Stanford University, Stanford, CA 94305

The reactions of ethylene, water, and methanol with coadsorbed oxygen on Pd(100) were studied with temperature programmed reaction spectroscopy (TPRS) and high resolution electron energy loss spectroscopy (EELS). Ethylene dehydrogenation was poisoned by oxygen, and direct hydrogen transfer reactions between water and oxygen and between methanol and oxygen were observed. These reactions demonstrate the Brønsted base role of adsorbed oxygen previously found on Ag(110) and show further that more active transition metals which themselves activate C-H bonds catalytically oxidize via a two-step mechanism in which the surface intermediates are scavenged by adsorbed oxygen.

Recent studies /1,2/ have shown that the surface reactivity of Ag(110) can be greatly enhanced by preadsorbed oxygen. The behavior of oxygen with other coadsorbates on Ag(110) can be classified into three categories: (1) Lewis acid or through-surface interaction in which an oxygen atom withdraws charge from the surface and creates one or more electronegative sites elsewhere on the surface that favor the adsorption of charge donating species, (2) Brønsted base interaction in which an electronegative oxygen atom can abstract an acidic proton from another coadsorbed species, and (3) nucleophilic attack in which the electrons of the oxygen atom attack an electron deficient site on another coadsorbed species. It is therefore of interest to know whether these forms of oxygen interactions occur on other metals, in particular, on those more reactive than silver, such as the group VIII transition metals. The higher reactivity of these metals presents an added complication in the study of oxygen interactions in that the coadsorbed species is usually capable of some sort of reaction without oxygen. For reactions on Ag(110), oxygen acts as a promoter, but in the instances where reaction can occur without oxygen, oxygen may alter or even poison a reaction, or perhaps promote an entirely different reaction path (in which oxygen may directly participate). The latter case is analogous to oxidation

<sup>1</sup>Current address: Fritz-Haber-Institut der Max-Planck-Gesellschaft, Faradayweg 4-6, D-1000 Berlin 33, Federal Republic of Germany

reactions on Ag(110). Reaction modification or poisoning may involve the aforementioned oxygen interactions, but an additional effect, known as scavenging, is possible. A general description of oxygen scavenging is as follows. Surface intermediates formed by interaction with the metal may react instead with a scavenger (oxygen) and thereby prohibit or alter subsequent surface reactions which would occur in the absence of the scavenger. In this summary note, we discuss the reactions of  $C_2H_4$ ,  $H_2O$ , and  $CH_3OH$  with oxygen on Pd(100). Lewis acid oxygen interactions are observed with  $C_2H_4$  that contribute to the poisoning of the dehydrogenation reaction; Brønsted base interactions between oxygen and  $H_2O$  and  $CH_3OH$ , in which hydrogen is directly transferred to an oxygen atom, predominate; scavenging of hydrogen produced from  $C_2H_4$  dissociation by adsorbed oxygen accounts for oxidation of  $C_2H_4$ .

### Experimental

The experiments were performed in an ultra-high vacuum chamber (base pressure =  $5 \times 10^{-11}$  Torr) with facilities for high resolution electron energy loss spectroscopy (EELS), temperature programmed reaction spectroscopy (TPRS), Auger spectroscopy, and low energy electron diffraction (LEED), which has been previously described /3/. The reactants were dosed through glass, multi-capillary array, molecular beam dosers which gave an effective beam pressure of between 200 (for  $O_2$ ) and 2000 (for  $C_2H_4$ ) times that of the background pressure which was held to about  $2 \times 10^{-10}$  Torr during the dose. The Pd(100) sample was cleaned by prolonged Ar ion sputtering and annealing treatments /3,4/ and surface cleanliness was verified by TPRS, EELS, and LEED /3,5/. The EELS measurements were performed only in the specular direction with an incident beam energy of about 1 eV. The heating rate for the thermal desorption measurements was about  $15 \text{ K s}^{-1}$ . Additional experimental details can be found elsewhere /3,6,7/.

### Results

#### ETHYLENE ADSORPTION AND REACTION

The adsorption and reaction of  $C_2H_4$  on Pd(100) illustrates the ability of oxygen to modify a surface reaction without being directly involved in the reaction itself. We focus our attention on the adsorption of  $C_2H_4$ ; the reaction mechanism of  $C_2H_4$  on Pd(100) is presented in detail elsewhere /6,8/. Figure 1 shows the  $C_2H_4$  and  $H_2$  TPRS curves for saturation coverage of  $C_2H_4$  on clean and oxygen precovered Pd(100). There are minor differences in the fine structure of  $C_2H_4$  desorption between the clean and oxygen precovered surfaces, but the amount of  $C_2H_4$  adsorbed by each surface, about 0.25 ML of  $C_2H_4$  molecules, is independent of oxygen coverage. The same cannot be said for hydrogen -- a direct measure of C-H bond activation. The  $H_2$  yield following  $C_2H_4$  adsorption decreases from 0.24 ML of  $H_2$  molecules for zero oxygen coverage to essentially 0.0 ML  $H_2$  desorption for 0.25 ML of oxygen atoms. Additional TPRS experiments for oxygen coverages of less than 0.25 ML

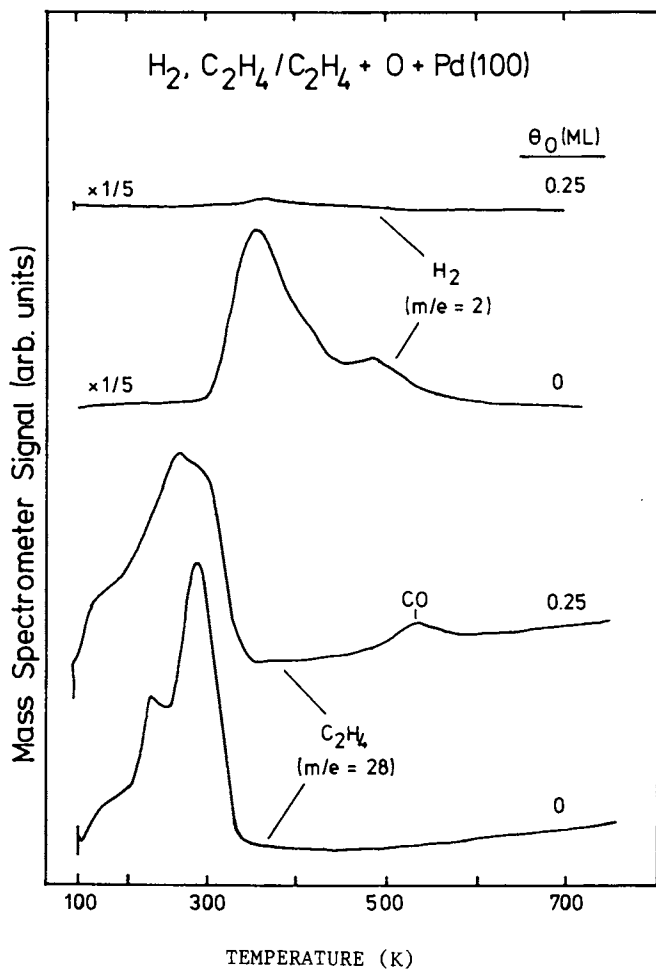
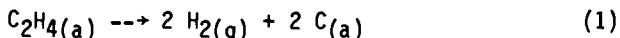


Figure 1. Temperature programmed reaction spectra of  $\text{C}_2\text{H}_4$  and  $\text{H}_2$  following saturation coverage of  $\text{C}_2\text{H}_4$  on the clean and oxygen covered  $\text{Pd}(100)$  surface at 100 K. Atomic oxygen was generated on the surface by exposure to  $\text{O}_2$  at 300 K.

showed that the hydrogen yield (which includes hydrogen that desorbs in the form of  $H_2O$ , see below) decreases linearly with increasing oxygen coverage.

The  $H_2$  desorption in fig. 1 is the result of  $C_2H_4$  dehydrogenation



This was the only reaction detected for  $C_2H_4$  on clean Pd(100); no  $CH_4$ ,  $C_2H_2$ ,  $C_2H_6$ , or  $C_6H_6$  was detected. The effect of increasing oxygen coverage is, therefore, to progressively poison the dehydrogenation reaction. The magnitude of the decrease in hydrogen yield with increasing oxygen coverage indicates that two adsorbed oxygen atoms block the reaction of one  $C_2H_4$  molecule according to the stoichiometry of equation (1). This can be interpreted as a site blocking effect of oxygen. Oxygen is adsorbed into the  $p(2 \times 2)$  structure for coverages between 0.05 and 0.25 ML /3/, and each oxygen atom may block four Pd atoms, assuming that O resides in the four-fold hollow /9/. As two O atoms block the reaction of one  $C_2H_4$  molecule, it follows that an ensemble of eight isolated Pd atoms are required for each  $C_2H_4$  reaction event. Oxygen has an additional, minor effect on  $C_2H_4$  dehydrogenation, that being a limited ability to scavenge some of the reaction products. Small amounts (less than 0.04 ML each) of  $H_2O$  and  $CO_2$  were detected at 330 K and 565 K, respectively, from  $C_2H_4$  and approximately 0.2 ML of coadsorbed oxygen /10/. These side reactions have little effect on  $C_2H_4$  dehydrogenation; the occurrence of this reaction depends on the initial, adsorbed state of  $C_2H_4$  as discussed below.

Electron energy loss spectra for  $C_2H_4$  on clean and oxygen covered Pd(100) are shown in fig. 2. The vibrational spectrum for  $C_2H_4$  on clean Pd(100) (fig. 2a) is as follows /6,8/:  $\nu(CH) = 2980 \text{ cm}^{-1}$ ,  $\delta(CH_2) = 1455 \text{ cm}^{-1}$ ,  $\nu(CC) = 1135 \text{ cm}^{-1}$ ,  $CH_2$  deformations =  $920 \text{ cm}^{-1}$ , and  $C_2H_4$  restricted translation =  $390 \text{ cm}^{-1}$ . Similarly, the assignments for the vibrational spectrum of  $C_2H_4$  on the oxygen covered surface (fig. 2b) are /10/:  $\nu(CH) = 3020 \text{ cm}^{-1}$ ,  $\delta(CH_2) = 1510 \text{ cm}^{-1}$ , and  $CH_2$  deformations =  $940 \text{ cm}^{-1}$ . The  $\nu(CC)$  mode was found at  $1340 \text{ cm}^{-1}$  for  $C_2D_4$  on oxygen covered Pd(100) /10/. The frequencies of the vibrationally coupled  $\delta(CH_2)$  and  $\nu(CC)$  modes enable us to assign the spectrum on clean Pd(100) to di- $\sigma$ -bonded or approximately  $sp^3$  hybridized  $C_2H_4$  and the spectrum on the  $p(2 \times 2)O$  structure to  $\pi$ -bonded or approximately  $sp^2$  hybridized  $C_2H_4$ . The proper assignment of the  $\delta(CH_2)$  and  $\nu(CC)$  modes is not trivial, as we have discussed elsewhere /6,8,10,11/.

The TPRS and EELS results are interpreted as follows. The  $H_2$  desorption yield, a measure of the extent of  $C_2H_4$  dehydrogenation, decreases linearly with increasing oxygen coverage, and the EELS results show that  $C_2H_4$  is di- $\sigma$ -bonded on the clean surface and  $\pi$ -bonded on the oxygen covered surface. Thus, it is the di- $\sigma$ -bonded form of  $C_2H_4$  that undergoes dehydrogenation. The saturation coverage of  $\pi$ -bonded  $C_2H_4$  is approximately 0.25 ML and is independent of oxygen coverage, whereas the saturation of di- $\sigma$ -bonded  $C_2H_4$  decreases

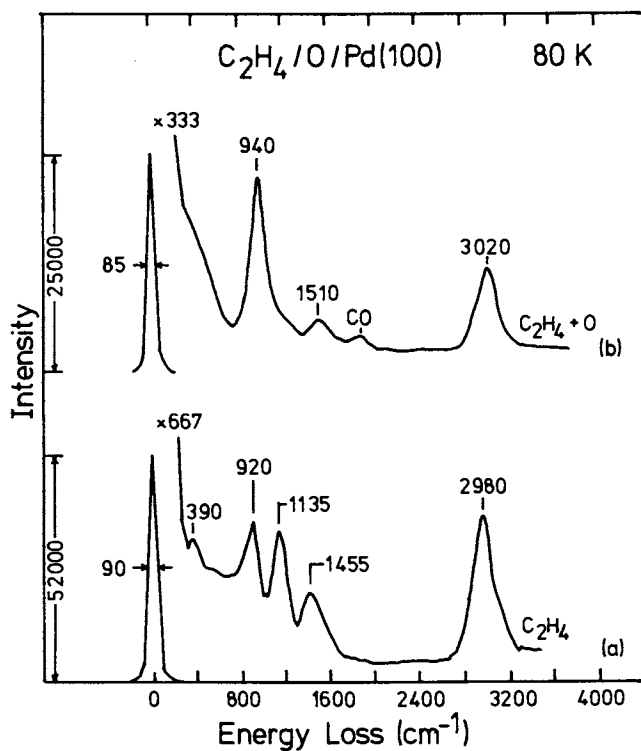


Figure 2. Electron energy loss spectra for saturation coverage of  $C_2H_4$  on clean (a) and oxygen covered (b) Pd(100) at 80 K. Oxygen was dosed as in fig. 1 to a coverage of 0.18 ML.

linearly from 0.12 ML to 0.0 ML as the oxygen coverage is increased to 0.25 ML. (Di- $\sigma$ -bonded  $C_2H_4$  is not detected in fig. 2b as its coverage is estimated to be only 0.035 ML.)

### REACTIONS OF $H_2O$ AND OH

Temperature programmed reaction spectra depicting the reaction of  $H_2O$  and OH groups with oxygen on Pd(100) are shown in fig. 3. Curve (a) was obtained for  $H_2O$  adsorption on the clean surface and contains two peaks, the  $\alpha_1$  state at 167 K of multilayer  $H_2O$ , and the  $\alpha_2$  state at 182 K due to  $H_2O$  bound directly to the surface /7/. An additional state at 255 K, labelled  $\gamma$ , is observed following coadsorption of  $H_2O$  and O (fig. 3b). This state represents the reaction of OH groups /7/



EELS results /7/ show that these OH groups form at about 175 K according to



Equation (2) describes the disproportionation of OH groups, although the  $\gamma$  reaction peak in fig. 3b could also be due to OH dissociation via



Whether the OH groups react via equation (2) or (4) can be tested with TPRS measurements following the formation of OH groups, formed from  $H_2O$  and O coadsorption, with heating to 200 K, by coadsorption of D atoms as shown in curves (c) and (d) of fig. 3. The  $\gamma$  state for  $H_2O$  is seen at 230 K in curve (c), while the  $D_2$  peak at 360 K (the normal temperature for recombinative desorption of  $D_2$ ) verifies that D atoms were indeed coadsorbed. Curve (d) shows that no HDO desorbed at the temperature of the  $\gamma$  state in (c), but that a higher temperature state, labelled  $\beta$ , occurred at 330 K. The  $\beta$   $H_2O$  state is due to the reaction of atomic oxygen and hydrogen to form  $H_2O$  as verified in separate thermal desorption measurements of coadsorbed O and H atoms /7,9/. The H in the  $\beta$  HDO state came from the adsorption of hydrogen from the residual gas in the vacuum chamber as the reactant surface was being prepared (note the high multiplier of curve (d)). Thus, the absence of HDO in the  $\lambda$  state rules out eqn. (4) so the OH reaction must proceed through the direct hydrogen transfer mechanism given in eqn. (2). That the  $\beta$   $H_2O$  state is not seen in fig. 3b shows that  $H_2O$  does not dissociate to OH and H on oxygen covered Pd(100). At no time, then, during the temperature ramp following  $H_2O$  and O coadsorption are H atoms adsorbed on the surface, so the formation of OH groups must also be a direct transfer of hydrogen as depicted in eqn. (3).

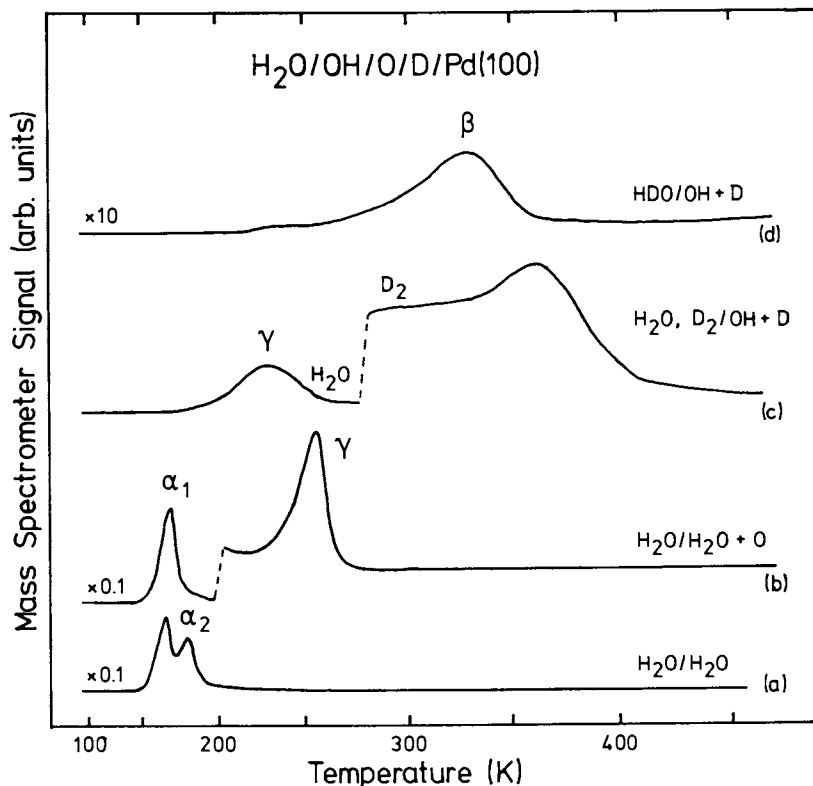
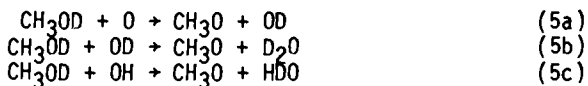


Figure 3. Temperature programmed reaction spectra for the water and oxygen coadsorption system on Pd(100). (a): H<sub>2</sub>O desorption following an exposure of 2 L H<sub>2</sub>O at 100 K. (b): H<sub>2</sub>O desorption following exposure of the surface with 0.16 ML atomic oxygen to 2 L H<sub>2</sub>O at 100 K. (c): H<sub>2</sub>O and D<sub>2</sub> desorption from a surface with coadsorbed OH and D species. The OH groups were generated by adsorbing 0.10 ML atomic oxygen at 300 K, 2 L H<sub>2</sub>O at 100 K, and heating to 200 K. The surface with 0.20 ML of OH groups was exposed to 2 L D<sub>2</sub> at 100 K. (d): HD0 desorption from a surface prepared as in (c), except that the D<sub>2</sub> exposure was 4 L.

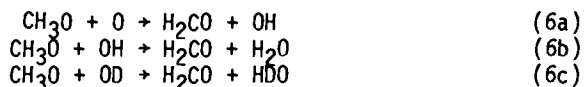
## METHANOL REACTIONS

In this section we present preliminary results of  $\text{CH}_3\text{OH}$  reactions with preadsorbed oxygen. Of primary interest is the mechanism for the removal of the hydroxyl hydrogen during formation of the methoxy ( $\text{CH}_3\text{O}$ ) intermediate. Fig. 4 shows TPRS curves for  $\text{CH}_3\text{OH}$ ,  $\text{H}_2\text{O}$ , and  $\text{H}_2\text{CO}$  following coadsorption of  $\text{CH}_3\text{OH}$  and  $\text{O}$  on  $\text{Pd}(100)$ . Desorption of  $\text{CO}$  and  $\text{CO}_2$  also occurs, but we limit the discussion here to water formation by  $\text{CH}_3\text{OH}$  and  $\text{O}$ . Methanol desorption occurs in three peaks at 155 K, 180 K, and 205 K. The 150 K peak is assigned to multilayers of  $\text{CH}_3\text{OH}$ , and the two higher temperature states are due to  $\text{CH}_3\text{OH}$  in direct contact with the surface. There are two peaks observed for  $m/e = 30$  at 155 K and 215 K. We assign the 155 K peak to the cracking fraction of  $\text{CH}_3\text{OH}$ , but the 215 K peak must be due to formaldehyde ( $\text{H}_2\text{CO}$ ) desorption, since it is slightly higher in temperature and of greater amplitude than the 205 K peak for  $\text{CH}_3\text{OH}$ . Water desorption occurs in three peaks at 155 K, 215 K, and 330 K. As of this writing we are not certain of the source of  $\text{H}_2\text{O}$  that desorbs at 155 K, but believe it to be either from water in the residual gas, or a small impurity in the  $\text{CH}_3\text{OH}$  sample.

We focus more closely on the 215 K and 330 K  $\text{H}_2\text{O}$  desorption states with the results shown in fig. 5. Curves (a)-(c) were obtained following the coadsorption of  $\text{CH}_3\text{OD}$  and  $\text{O}$  and show that none of the deuterium label forms water in the 330 K state. We conclude that the  $\text{H}_2\text{O}$  desorption at 330 K in curve (c) is due to the methyl hydrogens reacting with preadsorbed oxygen. The 330 K peak is the  $\beta$   $\text{H}_2\text{O}$  state for  $\text{O}$  and  $\text{H}$  recombination (section 3.2), so it is clear that the methyl hydrogens were transferred to the surface at a temperature lower than 330 K. The primary route by which the deuterium label is removed is the desorption of  $\text{HDO}$  or  $\text{D}_2\text{O}$  at 215 K, and we assign this peak to the direct transfer of deuterium from  $\text{CH}_3\text{OD}$  to either oxygen or an hydroxyl group with the ensuing formation of  $\text{CH}_3\text{O}$  species



Formation of  $\text{CH}_3\text{O}$ , following  $\text{CH}_3\text{OH}$  and  $\text{O}$  coadsorption and annealing the sample to 175 K, was verified with EELS measurements; the spectra were in good agreement with EEL spectra of  $\text{CH}_3\text{OH}$  on clean  $\text{Pd}(100)/12/$ . The concurrent desorption of  $\text{H}_2\text{CO}$  at 215 K indicates that one of the methyl hydrogens was lost at or below this temperature and is apparently the source of  $\text{H}$  incorporated into the water products at 215 K in curves 5b and 5c according to



Note that reaction (6a) is the source of  $\text{OH}$  for reaction (5c). In curves (d)-(f) of fig. 5, we see that there is no effect upon either



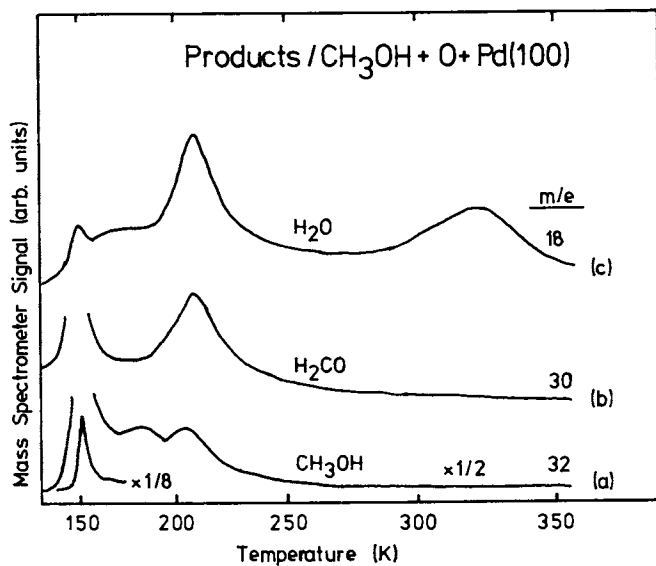


Figure 4. Temperature programmed reaction spectra of CH<sub>3</sub>OH, H<sub>2</sub>CO and H<sub>2</sub>O following adsorption of multilayers of CH<sub>3</sub>OH on Pd(100) at 130 K precovered with 0.25 ML atomic oxygen. The oxygen was adsorbed at 300 K. All traces are on the same scale.

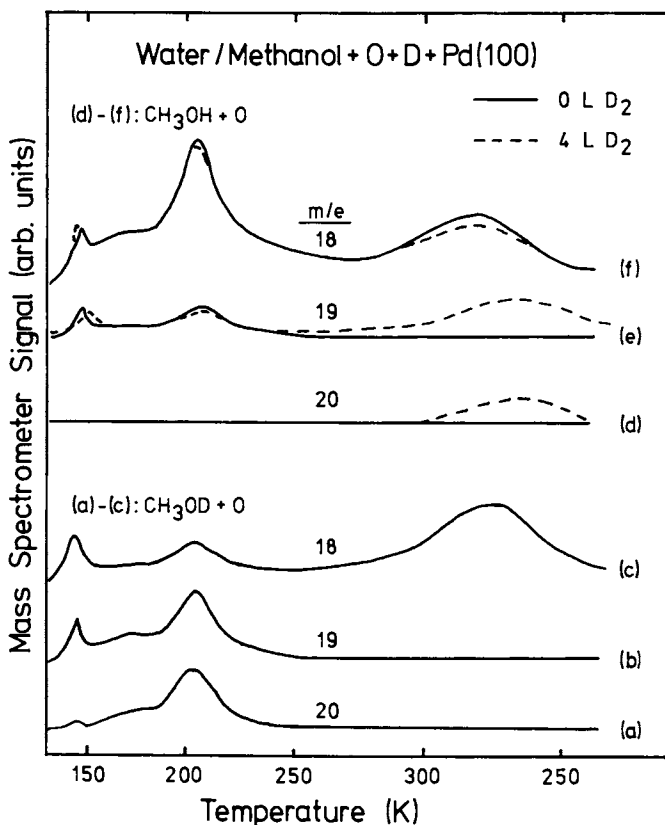


Figure 5. Temperature programmed reaction spectra of water desorption following methanol and oxygen coadsorption on Pd(100). (a)-(c):  $\text{D}_2\text{O}$ ,  $\text{HDO}$ , and  $\text{H}_2\text{O}$  desorption following adsorption of multilayers of  $\text{CH}_3\text{OD}$  at 130 K on the surface precovered with 0.25 ML atomic oxygen. (d)-(f): Solid lines are the same as (a)-(c) except that  $\text{CH}_3\text{OH}$  was used in place of  $\text{CH}_3\text{OD}$ . The dashed lines in curves (d)-(f) demonstrate the effect of coadsorbed D atoms. For these experiments the oxygen precovered surface was exposed to 4 L  $\text{D}_2$  at 130 K prior to  $\text{CH}_3\text{OH}$  exposure.

the 155 K or 215 K  $H_2O$  desorption states when deuterium atoms are co-adsorbed with  $CH_3OH$  and  $O$ . The only differences are the appearance of the  $HDO$  and  $D_2O$   $\beta$  states at 330 K due to the  $D$  atoms. Thus, the water that desorbs at 215 K was formed by a direct transfer of hydrogen from methanol to the preadsorbed oxygen. At the present time we do not know the identity of the surface species responsible for the 215 K  $H_2O$  peak. It is due to either a stabilized form of molecular  $H_2O$ , or to an  $OH$  group more reactive than that found from  $H_2O + O_{(a)} \rightarrow 2OH_{(a)}$ . Both TPRS and EELS measurements (not shown) rule out  $OH$  groups identical to those formed from  $H_2O$  and  $O$  in this case. We are currently working to resolve this question.

### Discussion

The results presented above demonstrate that the Brønsted base behavior of adsorbed oxygen, discussed previously by Barteau and Madix for  $Ag(110)$  /1/, also manifests itself on more active transition metal surfaces. We observe, in addition, the ability of oxygen to scavenge reaction products. The Lewis acid interaction involves charge withdrawal from the surface by adsorbed oxygen which stabilizes charge donating species as in the case of coadsorbed  $C_2H_4$ . Ethylene, however, may adsorb into either of two forms on  $Pd(100)$ . The di- $\sigma$ -bonded form of  $C_2H_4$  can be classified as charge withdrawing with charge going from the surface into the empty, anti-bonding  $\pi$ -orbital of  $C_2H_4$  resulting in rehybridization. The  $\pi$ -bonded form of  $C_2H_4$  can be classified as charge donating with charge going from the filled, bonding  $\pi$ -orbital of  $C_2H_4$  to the surface. The EELS spectrum of fig. 2b shows that the charge donating  $\pi$ -bonded  $C_2H_4$  is indeed stable with the charge withdrawing atomic oxygen, though, according to the  $C_2H_4$  TPD from the clean and  $p(2 \times 2) O$  surfaces, the binding energy does not change appreciably. On the other hand, if Lewis acid oxygen interactions stabilize charge donating species, then they should destabilize charge withdrawing species. This is manifested by the oxygen-induced poisoning of  $C_2H_4$  dehydrogenation which proceeds from di- $\sigma$ -bonded  $C_2H_4$ . The inhibition of  $C_2H_4$  dehydrogenation is due to the poisoning of sites required for di- $\sigma$ -bonded  $C_2H_4$  adsorption, and the requirement of eight  $Pd$  atoms for each di- $\sigma$ -bonded  $C_2H_4$  molecule indicates that a large ensemble is needed for C-H bond activation. We propose that both site blockage and through-surface, Lewis acid interactions between oxygen and di- $\sigma$ -bonded  $C_2H_4$  are responsible for the oxygen-induced poisoning of  $C_2H_4$  dehydrogenation on  $Pd(100)$ .

The direct hydrogen transfer reactions, eqns. (3) and (5a), for  $H_2O$  and  $CH_3OH$  with  $O$  are examples of the Brønsted base behavior of oxygen. In these reactions, the Brønsted acid species,  $H_2O$  or  $CH_3OH$ , gives up its acidic hydrogen to the Brønsted base species, oxygen. The Brønsted base behavior of oxygen is not observed with  $C_2H_4$  because  $C_2H_4$  is a much weaker acid than either  $H_2O$  or  $CH_3OH$  /2/.

The scavenging effect of atomic oxygen, observed with  $C_2H_4$  and  $CH_3OH$ , does not depend in a direct way on the nature of the coadsorbate, but only on the various species evolved during the reaction of the coadsorbate. Oxygen is capable of scavenging hydrogen and carbon produced by  $C_2H_4$  decomposition to form  $H_2O$  in the  $\beta$  state at 330 K

and CO and CO<sub>2</sub> at higher temperatures /10/. These side reactions are believed to have no direct effect on the initial decomposition itself. Oxygen scavenging may play an important role in the stability of adsorbed CH<sub>3</sub>O, however. We have observed that oxygen abstracts the hydroxyl hydrogen of CH<sub>3</sub>OH to form H<sub>2</sub>O, which desorbs at 215 K, and the methyl hydrogens to form H<sub>2</sub>O at 330 K. Oxygen scavenging of the hydroxyl H can act to stabilize CH<sub>3</sub>O species by preventing the CH<sub>3</sub>O rehydrogenation reaction. This effect was previously seen by Gates and Kesmodel for CH<sub>3</sub>OH and O on Pd(111) /13/. Unlike Pd(111), however, CH<sub>3</sub>O species are stable on clean Pd(100) /12/, and we are currently studying whether there is any additional stability of CH<sub>3</sub>O on Pd(100) due to the presence of oxygen.

### Conclusions

The Lewis acid and Brønsted base oxygen interactions previously found on Ag(110) also occur on Pd(100). Through-surface, Lewis acid interactions were inferred between C<sub>2</sub>H<sub>4</sub> and O as the result of the poisoning of the C<sub>2</sub>H<sub>4</sub> dehydrogenation reaction by destabilization of di-σ-bonded C<sub>2</sub>H<sub>4</sub>. Brønsted base interactions were observed between H<sub>2</sub>O and O and between CH<sub>3</sub>OH and O as evidenced by the direct transfer of hydrogen to oxygen to form OH species from H<sub>2</sub>O and an as yet unidentified species from CH<sub>3</sub>OH. Oxygen adsorbed on Pd(100) also scavenges atomic hydrogen produced by C<sub>2</sub>H<sub>4</sub> or CH<sub>3</sub>O decomposition.

### Acknowledgments

We wish to thank Dr. C. R. Brundle of IBM Research-San Jose for the loan of the vacuum chamber used in this work. One of us (SWJ) gratefully acknowledges a fellowship from the National Science Foundation. This work was supported by the National Science Foundation (NSF-CPE 8320072).

### Literature Cited

1. M. A. Barteau and R. J. Madix, in "The Chemical Physics of Solid Surfaces and Heterogeneous Catalysis," Vol. 4, Eds. D. A. King and D. P. Woodruff (Elsevier, Amsterdam, 1982).
2. M. A. Barteau and R. J. Madix, *Surface Science* **120** (1982) 262.
3. E. M. Stuve, R. J. Madix, and C. R. Brundle, *Surface Science*, in press (CO Oxidation on Pd(100)).
4. A. Ortega, F. M. Hoffman, and A. M. Bradshaw, *Surface Science* **119** (1983) 79.
5. R. J. Behm, K. Christmann, G. Ertl, and M. A. Van Hove, *J. Chem. Phys.* **73** (1980) 2984.
6. E. M. Stuve and R. J. Madix, *Surface Science*, in press.
7. E. M. Stuve, S. W. Jorgensen, and R. J. Madix, submitted to *Surface Science* (Water and Oxygen Coadsorption on Pd(100)).
8. E. M. Stuve, R. J. Madix, and C. R. Brundle, *Surface Science*, Proc. ECOS-6, in press.
9. C. Nyberg and C. G. Tenstal, *Surface Science* **126** (1983) 163.
10. E. M. Stuve and R. J. Madix, submitted to *Surface Science*.
11. E. M. Stuve and R. J. Madix, to be submitted.
12. K. Christmann and J. E. Demuth, *J. Chem. Phys.* **76** (1982) 6318.
13. J. A. Gates and L. L. Kesmodel, *J. Catalysis* **83** (1983) 437.

RECEIVED June 21, 1985

## Surface Reactions on Clean Platinum and Rhodium at Low and High Pressures

L. D. Schmidt, D. Hasenberg, S. Schwartz, and G. A. Papapolymerou

Department of Chemical Engineering and Materials Science, University of Minnesota, Minneapolis, MN 55455

High pressure reaction chambers coupled to ultrahigh vacuum systems have been used to study several reactions on polycrystalline and single Pt and Rh crystal surfaces cleaned before reaction and analyzed after reaction by AES and TPD. Reactions described here are NO, NH<sub>3</sub>, N<sub>2</sub>O, and NO<sub>2</sub> decomposition and bimolecular reactions of NO + CO and NH<sub>3</sub> + CH<sub>4</sub>. In all reactions involving NO on Pt the surface residues are always nearly stoichiometric N/O, and all adsorbate coverages are less than one monolayer. On Pt the rate limiting step of NO reacting with CO or H<sub>2</sub> appears to be a true bimolecular process, rather than unimolecular NO decomposition with oxygen scavenging.

Reaction between NH<sub>3</sub> and CH<sub>4</sub> produces a high selectivity to HCN at high temperatures at nearly stoichiometric feed ratios, but only N<sub>2</sub> is produced in excess NH<sub>3</sub> and no reactions occur in excess CH<sub>4</sub>. Analysis by AES and TPD shows that the active surface contains approximately one monolayer of carbon and that a surface containing carbon multilayers is inert.

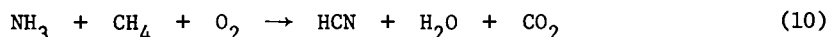
A central problem in relating catalytic processes on well-defined surfaces in the laboratory with those encountered under technological conditions is the large pressure difference: a factor of 10<sup>8</sup>. It is therefore highly questionable to extrapolate surface coverages or surface reaction rates measured between 10<sup>-8</sup> and 10<sup>-6</sup> Torr in order to predict behavior expected in process environments (one Torr to several atmospheres) (1).

We have been concerned for several years with the measurement of rates of simple surface reactions on clean, well-defined surfaces of Pt, Rh and other noble metals at pressures up to 10 Torr

(2-9): We have been particularly interested in reactions of NO



and of  $\text{NH}_3$



These should be simple unimolecular or bimolecular reactions yielding a single or at most two reaction paths. Rates may therefore be fit using Langmuir-Hinshelwood (LH) rate expressions. For  $\text{A} \rightarrow \text{products}$  this should be

$$r_R = \frac{k_R K_A P_A}{1 + K_A P_A} \quad (11)$$

while for a bimolecular reaction,  $\text{A} + \text{B} \rightarrow \text{products}$ , the simplest rate expression should be

$$r_R = \frac{k_R K_A K_B P_A P_B}{(1 + K_A P_A + K_B P_B)^2} \quad (12)$$

In these expressions  $k_R$  is the reaction rate coefficient and  $K$ 's are adsorption equilibrium constants

$$k_R = k_{RO} \exp(-E_R/RT) \quad (13)$$

and

$$K_A = K_{AO} \exp(+E_A/RT) \quad (14)$$

where  $E_R$  and  $E_A$  are reaction activation energy and heat of adsorption of A respectively.

The objectives of this research are therefore 1) to see whether rate expressions such as Equations 11 and 12 provide adequate descriptions of reaction rates and, if not, what rate expressions are appropriate, 2) to determine reaction activation energies, heats of adsorption, and pre-exponential factors, and 3) to compare these quantities with those measured under UHV conditions to determine whether the same processes and surface species might be involved.

In this paper we shall summarize some recent research on reaction kinetics for simple NO and  $NH_3$  reactions. More detailed descriptions of these results and their interpretation can be found in References 1-8.

### Experimental

Experiments of this type are meaningless unless surface coverages can be measured simultaneously with reaction rates. This requires ultra-clean conditions because the surface will contaminate in a time

$$t_{\text{monolayer}} (\text{sec}) = \frac{10^{-6}}{s_j P_j (\text{Torr})} \quad (15)$$

where  $s_j$  is the sticking coefficient of species  $j$  at partial pressure  $P_j$ . A partial pressure of  $10^{-8}$  Torr of a species with a sticking coefficient of unity will contaminate the surface in 100 sec. At 1 Torr contaminant pressures must therefore be less than  $10^{-8}$  Torr which requires a reactant purity of 10 parts per billion! This is far beyond any conventional purification techniques, and it requires in situ ultrapurification to remove carbon and sulfur containing contaminants.

Figure 1 shows two reactor configurations we have used to measure reaction rates on clean surfaces. In Figure 1(a) is shown a high pressure cell inside the UHV system (4) with the sample mounted on a bellows so it can be moved between the reaction cell and the position used for AES analysis. In Figure 1(b) is shown a reaction cell outside the analysis system with the sample translated between heating leads in the reactor and in the UHV analysis system (8).

### NO and $NH_3$ Decomposition

Figure 2(a) shows typical rates of NO decomposition on clean polycrystalline Pt (5) while Figure 2(b) shows corresponding AES spectra. The solid curves show rates predicted using the LH unimolecular rate expression, Equation 11, with

$$r_R (\text{molecules/cm sec}) = \frac{5.53 \times 10^{16} \exp(-5250/RT) P_{NO}}{1 + 6.95 \times 10^{-4} \exp(8250/RT) P_{NO}} \quad (16)$$

These rates would be meaningless without proof that surfaces are clean. Figure 2(b) indicates that surfaces contain ~1 monolayer of N and O after a 20 Langmuir (L) exposure to NO and after a  $10^9$  L

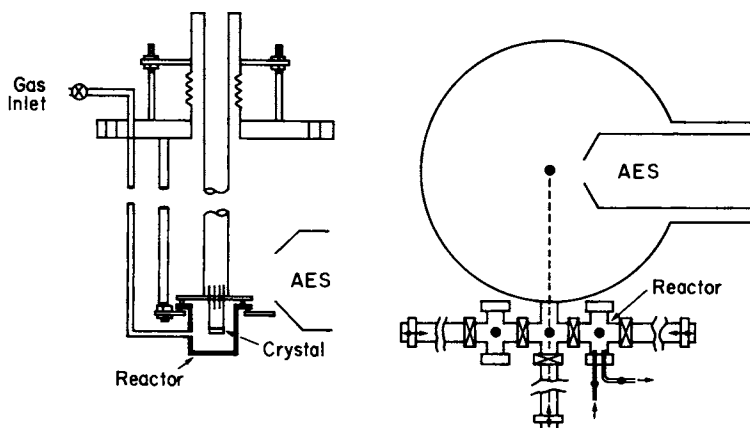


Figure 1. Schematic diagrams of systems used to obtain surface reaction rates at high pressures on surfaces cleaned before reaction and analyzed after reaction by AES and TPD.

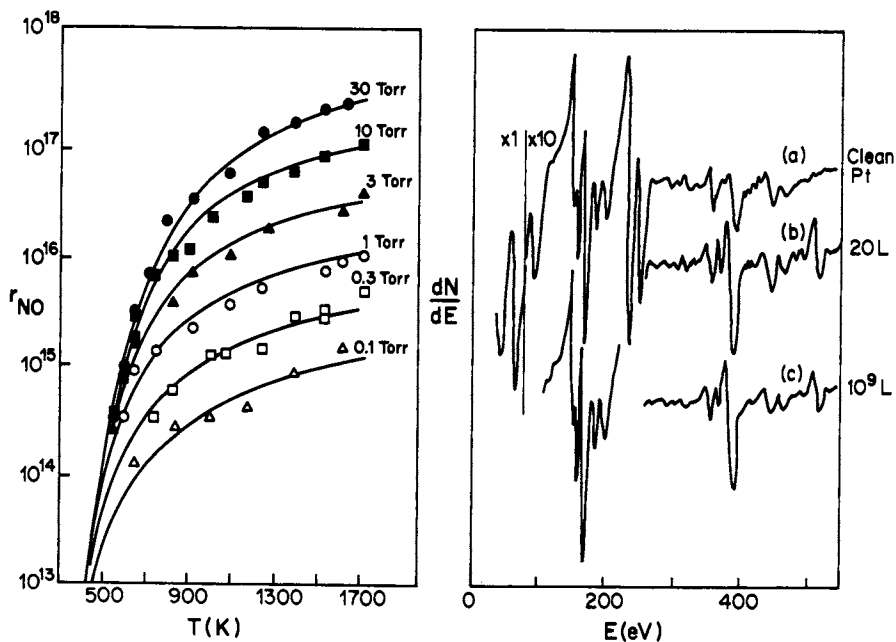


Figure 2. (a) Plot of  $r_{\text{NO}}$  versus surface temperature for NO decomposition on polycrystalline Pt. (b) AES spectra of clean Pt, following a 20L exposure to NO and following a  $10^9$  L exposure to NO.



exposure. This demonstrates that surfaces on which rates are obtained are in fact clean.

Figure 3(a) shows rates of  $\text{NH}_3$  decomposition on clean polycrystalline Rh. As with NO decomposition the rate obeys zeroth order kinetics at low temperature and first order kinetics at higher temperature.

This rate can also be fit quantitatively by the LH unimolecular rate expression (solid curves) with

$$r_R = \frac{7.5 \times 10^{18} \exp(-2130/T) P_{\text{NH}_3}}{1 + 2.5 \times 10^{-5} \exp(7000/T) P_{\text{NH}_3}} \quad (17)$$

AES spectra on these surfaces after reaction also show only N at a density of approximately one monolayer with contaminants (typically, C, S, B, and P) much less than 0.1 monolayer.

#### Other Unimolecular Reactions

Figure 4 summarizes rates for NO,  $\text{N}_2\text{O}$ ,  $\text{NO}_2$ , and  $\text{NH}_3$  decomposition on Pt and Rh. Curves shown are calculated LH unimolecular rate expressions, Equation 11. Although data points are omitted for clarity, all measured rates agree with these curves to at least  $\pm 20\%$ .

Comparisons between reactants and metals reveal several interesting trends.  $\text{NO}_2$  decomposition is very fast and becomes flux limited above 800K with a constant reaction probability of 0.06 on both metals.  $\text{NH}_3$  decomposition is also identical on both metals to within a factor of 2.

NO and  $\text{N}_2\text{O}$  decomposition show large differences between metals with both rates being higher on Pt at low temperatures and higher on Rh at high temperatures. NO decomposition is also found to be more strongly inhibited by  $\text{O}_2$  than  $\text{N}_2\text{O}$  decomposition, and this inhibition is stronger on Rh.

While all rates of these unimolecular reactions can be fit quantitatively by LH expressions, Equation 11, the heats of adsorption determined from the temperature dependence of the adsorption equilibrium constant, Equation 14, do not agree with the measured reaction activation energy except for  $\text{NH}_3$  where  $E_{\text{NH}_3} \approx 16 \pm 2$  kcal/mole. NO has a lower heat of adsorption in the decomposition reaction, and this has been suggested to arise from a reactive precursor intermediate.  $\text{N}_2\text{O}$  does not appear to chemisorb in UHV experiments, although it reacts readily with a high apparent heat of adsorption.

#### The NO + CO Reaction on Pt

Figure 3(b) shows the rate of  $\text{CO}_2$  formation from a 1:1 mixture of CO and NO at pressures between  $10^{-8}$  and 0.8 Torr (7). The solid curves are the fit obtained using the LH expression of Equation 12.

$$r_R = \frac{3.5 \times 10^{17} \exp(5800/RT) P_{\text{NO}}}{1 + 4 \times 10^{-9} \exp(30000/RT) P_{\text{CO}}} \quad (18)$$

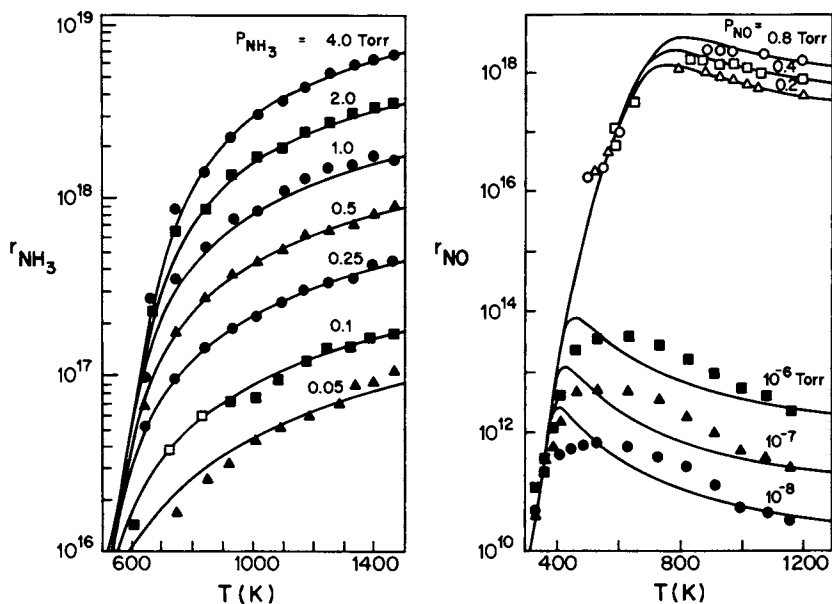


Figure 3. (a) Plots of  $r_{\text{NH}_3}$  versus  $T$  for  $\text{NH}_3$  decomposition on clean Rh. (b)  $r_{\text{NO}}$  versus  $T$  for the  $\text{NO}+\text{CO}$  reaction on clean Pt. Solid curves are fit to data using LH rate models indicated in the text.

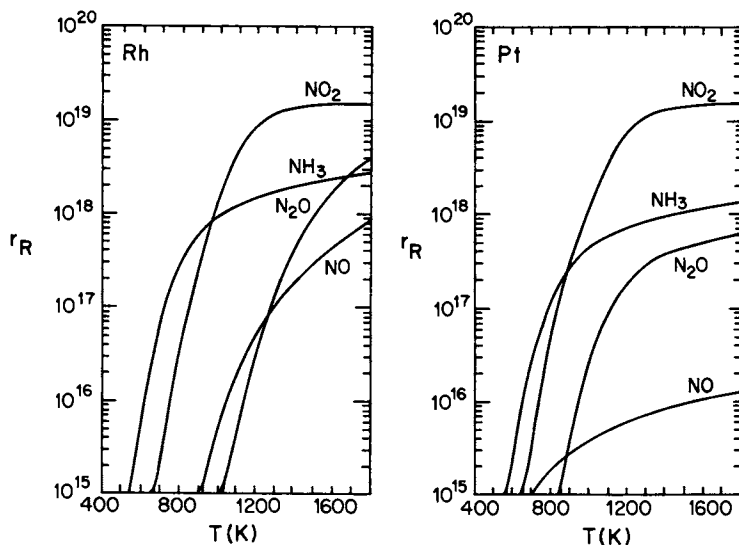


Figure 4. Rates of  $\text{NO}$ ,  $\text{N}_2\text{O}$ ,  $\text{NO}_2$ , and  $\text{NH}_3$  decomposition on Rh and Pt at a reactant pressure of 1.0 Torr.

It is seen that a single expression fits all rate data to within a factor of  $\sim 2$  for pressure variations over a factor of  $10^8$ .

However, all rate data for this reaction are not explained simply by this rate expression. At pressures above  $10^{-2}$  Torr the rate exhibits multiple steady states, long transients, and rate oscillations (7). Clearly other processes are involved than those implied by the simple one state, constant parameter LH model.

#### HCN Synthesis on Rh

Figure 5 shows rates of HCN and  $N_2$  synthesis from  $CH_4$ - $NH_3$  mixtures for fixed  $NH_3$  with  $CH_4$  pressures indicated (8). The rates of HCN production are seen to exhibit a maximum near stoichiometric ratios and fall off for excess  $CH_4$ . These rates can be fit accurately by the expressions

$$r_{\text{HCN}} = \frac{4.5 \times 10^{18} \exp(-1000/T) P_{\text{CH}_4} P_{\text{NH}_3}^{.5}}{(1 + 0.0367 \exp(2500/T) P_{\text{CH}_4} / P_{\text{NH}_3}^{.5})^4} \quad (19)$$

and

$$r_{\text{N}_2} = \frac{7.5 \times 10^{18} \exp(-2130/T) P_{\text{NH}_3}}{(1 + 0.367 \exp(2500/T) P_{\text{CH}_4} / P_{\text{NH}_3}^{.5})^4} \quad (20)$$

The mechanism implied by these expressions is that of a submonolayer of surface carbon which blocks  $n$  sites for  $NH_3$  adsorption. This suppresses  $NH_3$  decomposition which would occur on the clean surface (Figure 3(a)) and allows  $NH_3$  fragments to react with carbon to form HCN. Selectivities of HCN production exceed 90% at 1 Torr, and reaction probabilities (fraction of  $CH_4$  flux yielding HCN) approach 0.01.

AES and TPD on these surfaces confirm that the reactive surface contains less than a monolayer of carbon while the unreactive surface has multilayers of carbon.

#### Summary

Rates of all of the reactions indicated in Equations 1-10 have been examined extensively between 0.1 and 10 Torr, and many have been examined between  $10^{-8}$  and 10 Torr. All rates can be fit under some conditions with good accuracy with LH expressions, although all bimolecular reactions also exhibit reaction "pathologies" at particular compositions and temperatures.

All of these rates are measured on surfaces shown to be clean by AES, and this indicates that these processes occur on surfaces containing only submonolayer coverages of reactant species, exactly the situation required for the Langmuir-Hinshelwood model of surface reactions.

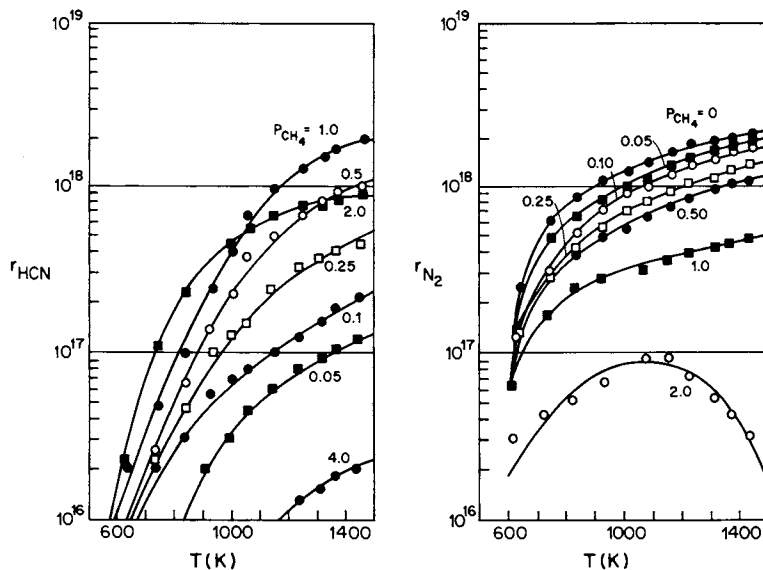


Figure 5. Plots of  $r_{\text{HCN}}$  and  $r_{\text{N}_2}$  for the  $\text{NH}_3+\text{CH}_4$  reaction on clean polycrystalline Rh. Data can be fit accurately using a model in which surface carbon blocks  $\text{NH}_3$  decomposition to  $\text{N}_2$ , Equations 19 and 20.

Acknowledgments. This work was partially supported by NSF under Grant No. 8216729.

#### Literature Cited

- Schmidt, L. D. *J. Vac. Sci. Technol.* 1975, 12, 341.
- Pignet, T.; Schmidt, L. D. *Chem. Eng. Sci.* 1974, 29, 1123.
- Löffler, D. G.; Schmidt, L. D. *J. Catalysis* 1976, 41, 440; Löffler, D. G.; Schmidt, L. D. *Surface Science* 1976, 59, 195.
- Mummey, M. J.; Schmidt, L. D. *Surface Science* 1980, 91, 301.
- Mummey, M. J.; Schmidt, L. D. *Surface Science* 1981, 109, 29; Mummey, M. J.; Schmidt, L. D. *Surface Science* 1981, 109, 43.
- Takoudis, C. G.; Schmidt, L. D. *J. Phys. Chem.* 1983, 87, 958; Takoudis, C. G.; Schmidt, L. D. *J. Phys. Chem.* 1983, 87, 965.
- Klein, R. L.; Schwartz, S.; Schmidt, L. D., to be published.
- Hasenberg, D.; Schmidt, L. D. *J. Catalysis*, to be published.
- Papapolymerou, G. A.; Schmidt, L. D., submitted in *Surface Science*.

RECEIVED March 5, 1985

## Hydrocarbon Synthesis and Rearrangement over Clean and Chemically Modified Surfaces

C. H. F. Peden and D. W. Goodman

Surface Science Division, Sandia National Laboratories, Albuquerque, NM 87185

An important new application of surface analytical methods is the study of catalytic reactions using well defined materials under conditions approaching those typically found in process environments. Recent kinetic and surface analytical studies have provided new information regarding the mechanism of several important catalytic reactions including methanation of CO and CO<sub>2</sub>, alkane hydrogenolysis, and ethylene hydrogenation. These newly developed techniques have been used to study the relationship between surface structure, composition, and reactivity. For the above reactions, studies have been carried out addressing poisoning and promotion of nickel, rhodium, and ruthenium catalysts by surface impurities such as sulfur, phosphorus, silver, and copper. The highlights of recent work are reviewed.

Catalytic processing by metals is of considerable importance in the chemical and petroleum industries, yet few surface reactions are well understood at the molecular level. The last twenty years have produced an array of surface techniques which routinely can be brought to bear on this most intriguing and technologically important area. The surface science of catalysis is relatively new yet promises to be an extremely valuable complement to the more traditional approaches to fundamental catalytic research. During the two decades which produced the available surface techniques, a large inventory of information has been accumulated regarding surface atomic and electronic structure as well as molecular adsorption and reaction. A logical extension of these kinds of studies has been into the area of kinetics at elevated pressures (~1 atm.) combined intimately with surface analytical techniques. Although the integration of kinetics at these conditions with vacuum surface techniques has been limited to a few groups (1-6), the results thus far have been

extremely useful in detailing certain mechanistic information about the reactions investigated. These studies have established this hybrid approach as an important interface between the traditional surface physics and catalytic communities (7).

One promising extension of this approach is surface modification by additives and their influence on reaction kinetics. Catalyst activity and stability under process conditions can be dramatically affected by impurities in the feed streams (8). Impurities (promoters) are often added to the feed intentionally in order to selectively enhance a particular reaction channel (9) as well as to increase the catalyst's resistance to poisons. The selectivity and/or poison tolerance of a catalyst can often times be improved by alloying with other metals (8,10). Although the effects of impurities or of alloying are well recognized in catalyst formulation and utilization, little is known about the fundamental mechanisms by which these surface modifications alter catalytic chemistry.

Possible mechanisms by which an additive alters a catalytic reaction include site blocking of ensembles and electronic or ligand effects. An ensemble refers to a certain number or conformation of surface atoms necessary for a reaction to occur. A ligand or electronic effect assumes the additive modifies the electronic character of the metal in such a way as to alter one or more steps of the reaction. By varying the nature and surface concentration of additives under carefully controlled conditions, the relative importance of ensemble versus ligand effects in surface catalyzed reactions can be addressed. This discussion summarizes the highlights of some of these studies with particular emphasis on what has been learned in comparative experiments with chemical modifiers or alloying with other metals. The results presented primarily focus on recent studies on ruthenium single crystals conducted in our laboratory.

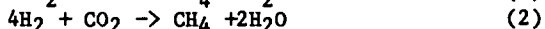
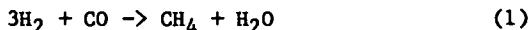
### Experimental

The studies to be described were carried out utilizing the specialized apparatus shown in Figure 1 and discussed in detail in Reference 4. This device consists of two distinct regions, a surface analysis chamber and a microcatalytic reactor. The custom built reactor, contiguous to the surface analysis chamber, employs a retraction bellows that supports the metal crystal and allows translation of the catalyst in vacuo from the reactor to the surface analysis region. Both regions are of ultrahigh vacuum construction, bakeable, and capable of ultimate pressures of less than  $10^{-10}$  Torr. Details of the procedures for depositing and measuring surface concentrations of sulfur and copper are described elsewhere (11,12).

### Discussion

The above apparatus has been used to study reactions over single crystals of nickel, ruthenium, and rhodium (1-7,12-15).

#### Methanation



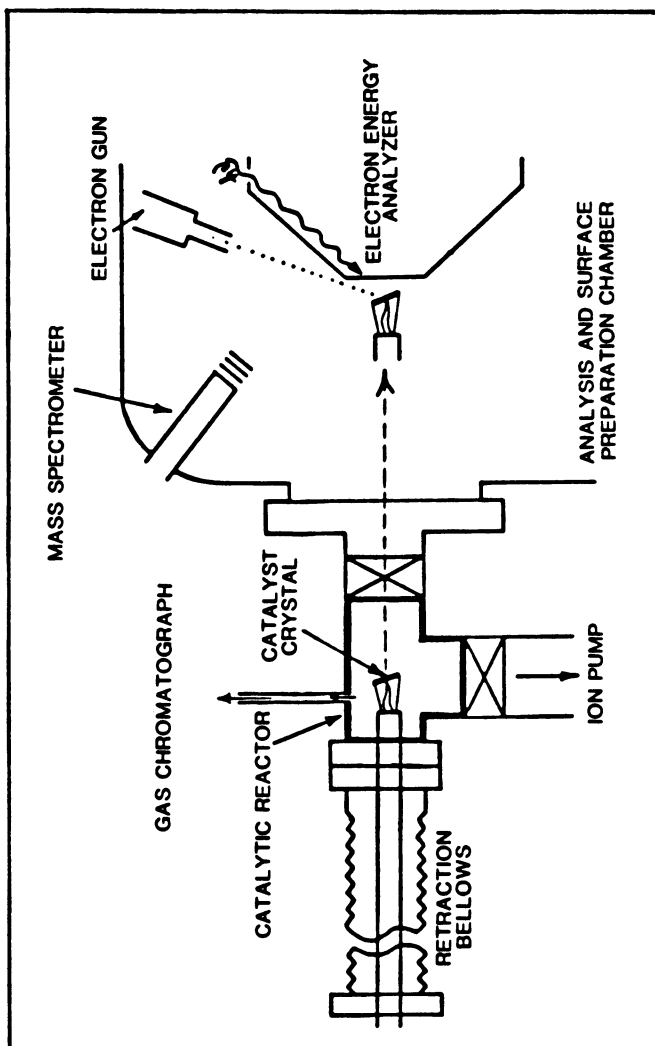
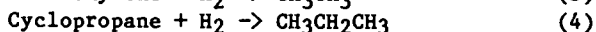
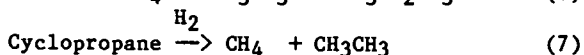
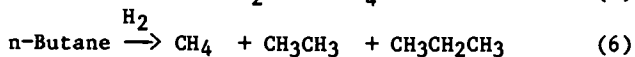
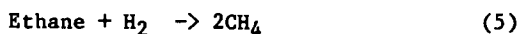


Figure 1. An ultrahigh vacuum apparatus used for the study of single crystal catalysis before and after operation at atmospheric pressure in a catalytic reactor.

## Hydrogenation



## Hydrogenolysis



These are examples of structure insensitive (facile) (Reactions 1-4) and structure sensitive (demanding) reactions (Reactions 5-7).

### Kinetics of Structure Insensitive Reactions Over Clean Single Crystal Surfaces

A critical question in model studies concerns the appropriateness of the model to reflect the parameters of the more realistic system. In this case, the point of interest is the ability of metal single crystals to reproduce the catalytic chemistry generally found for supported catalysts. Sufficient data have been collected (4,7,12-15) for a number of reactions to show that single crystals reproduce in many cases the chemistry of the corresponding supported catalysts. For those reactions listed above which are considered structure insensitive (methanation and hydrogenation) the rates and activation parameters measured for the single crystal catalysts are in excellent agreement with the corresponding values for supported systems. For example, Figure 2 shows an Arrhenius plot of the rate of the methanation reaction (expressed as molecules of methane formed per surface metal atom per second) over two single crystal planes of ruthenium (12,13) as well as data taken on silica- and alumina-supported catalysts (16). Similar results have been obtained on nickel single crystal catalysts (4,7).

These results support the use of these idealized catalysts as relevant models and further suggest that surface characterization of these materials following reaction will, in many respects, reflect the surface condition of the analogous supported-metal particles. For example, surface analysis of active single crystal catalysts has been particularly useful in detailing the important surface species in the methanation reaction. Auger spectroscopy has been used to characterize two distinct forms of surface carbon on nickel (17) and ruthenium (18), a carbidic or active form and a graphitic or inactive type. The kinetics associated with the reactivity of these carbon types with hydrogen have been studied in detail (17,18) and the relationship of the surface concentration of these carbon types with catalytic activity has been documented (13,17,18). Figure 3 shows the changes in the methanation reaction rate over a ruthenium catalyst as the pressure is increased from 1-120 Torr at a fixed H<sub>2</sub>:CO ratio. The departure from linear Arrhenius behavior occurs at lower temperatures as the total pressure is lowered. The onset of non-linearity has been correlated with an increase in the carbon level on the surface of the catalyst following reaction (4). It has been proposed (4) that both of these effects are due to a reduction in the surface coverage of hydrogen below a critical value necessary for an optimum reaction rate.



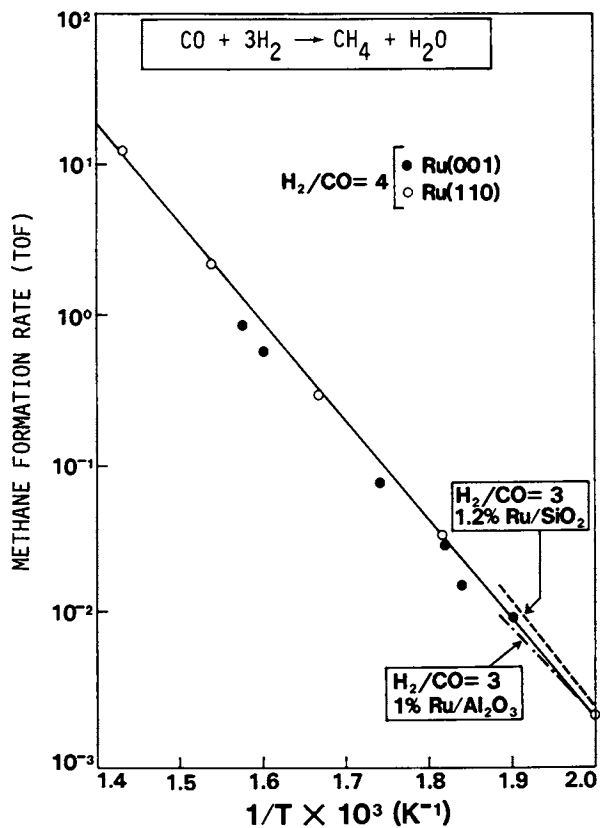


Figure 2. A comparison of the rate (turn-over frequency) of methane synthesis over single crystal and supported ruthenium catalysts. Total reactant pressure for the single crystal studies was 120 Torr.

### Kinetics of Structure Sensitive Reactions Over Clean Single Crystal Surfaces

Reactions known to be responsive to changes in catalyst morphology are also amenable to study using model single crystals. Ethane hydrogenolysis, a well known example of this category of reactions, has been studied over nickel (14,19) and ruthenium (12) single crystals. The activation energies for this reaction on Ni(100) and Ni(111) obtained under identical conditions differ markedly from each other (19). A comparison of specific rates also shows that ethane as well as butane and cyclopropane hydrogenolysis proceed at significantly faster rates over the Ni(100) surface than over the Ni(111) surface (14,19,20). These results suggest that the origin of the structure sensitivity in alkane hydrogenolysis arises mainly from an intrinsic activity difference between facets. Particle size effects result then from facet redistribution during sintering and not from intrinsic electronic differences among metal particles.

Figure 4 shows the rate of ethane hydrogenolysis over a ruthenium catalyst as a function of H<sub>2</sub> partial pressure (12). In agreement with studies on supported catalysts (1), the reaction is negative order with respect to hydrogen for partial pressures of H<sub>2</sub> above 40 Torr. The order of reaction with respect to ethane is observed to be ~+0.85 (12) in excellent agreement with supported systems (1). The order of the reaction with respect to the two reactants reflects the ability of hydrogen to compete more favorably for adsorption sites on the catalyst. The change to positive order at low H<sub>2</sub> pressures indicates the conditions at which the surface concentration of hydrogen falls below the critical optimum value. This surface depletion of hydrogen should manifest itself in a departure of the reaction rate from linear Arrhenius behavior at higher reaction temperatures as observed for the methanation reaction (4). This nonlinearity in Arrhenius behavior is evident in Figure 5.

### Kinetics Over Chemically Modified Single Crystal Surfaces

The above described experiments over atomically clean single crystal catalysts have been extended to studies of the kinetics of various catalytic reactions over chemically modified catalysts. Examples are recent studies into the nature of poisoning by sulfur of the catalytic activity of nickel, ruthenium, and rhodium toward methanation of CO (11,12) and CO<sub>2</sub> (15), ethane (12) and cyclopropane (20) hydrogenolysis, and ethylene hydrogenation (21).

Figure 6 is an Arrhenius plot of the methanation reaction over a Ru(0001) catalyst precovered with various quantities of sulfur (12). Three things are noteworthy in this graph. First, small amounts of sulfur (<0.05ML) produce a precipitous drop in the activity of the catalyst towards methanation. This is shown more clearly in Figure 7 where the relative rate of reaction is plotted versus sulfur surface coverage. A similar behavior has been observed for sulfur poisoned Ni(100) (11) and Rh(111) (22) catalysts. The two possible causes for this effect, a long-range electronic (ligand) effect or an ensemble effect, can be distinguished experimentally. Substituting the similarly sized but less electronegative adatom, phosphorus, in analogous experiments on Ni(100) results in a marked change in the magnitude

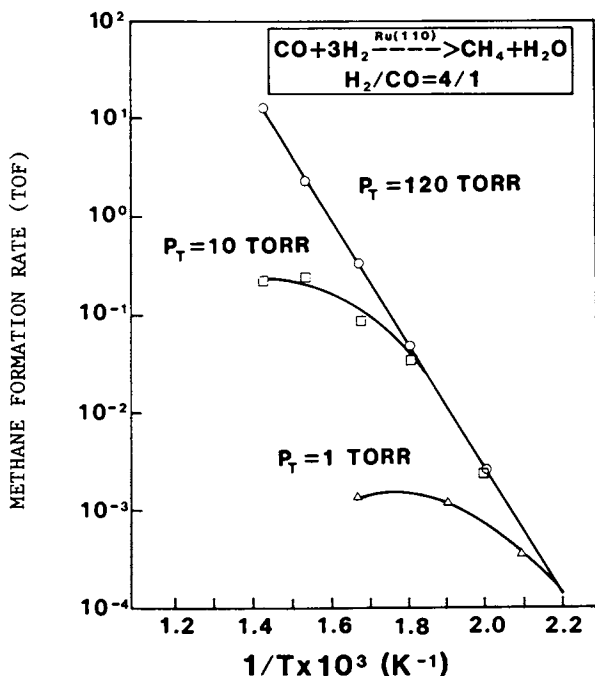


Figure 3. An Arrhenius plot of methane synthesis on a Ru(110) catalyst at total reactant pressures of 1, 10 and 120 Torr.  $\text{H}_2/\text{CO} = 4/1$ .

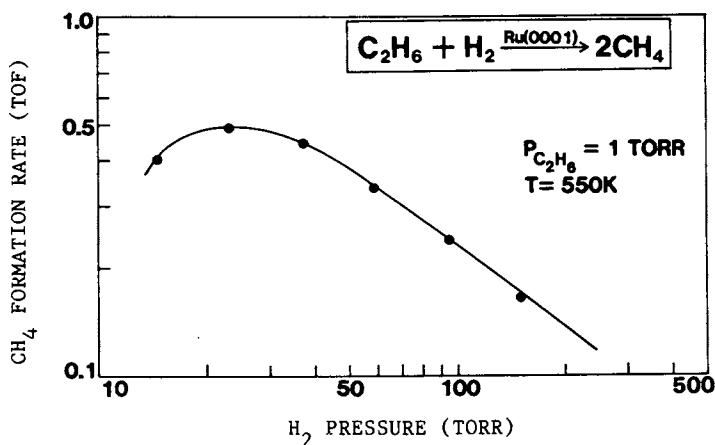


Figure 4. The effect of  $\text{H}_2$  pressure on the rate of ethane hydrogenolysis on a Ru(0001) catalyst.

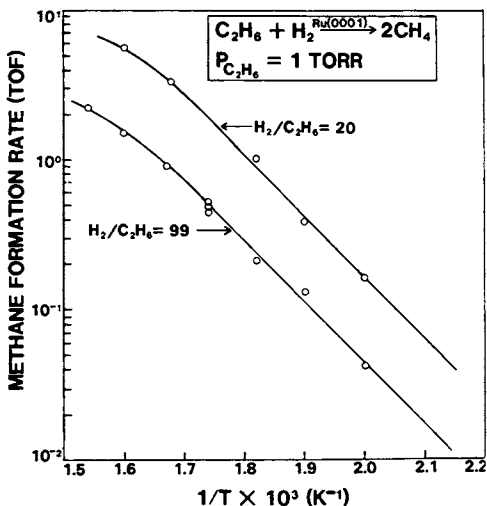


Figure 5. An Arrhenius plot of the rate of ethane hydrogenolysis on a Ru(0001) catalyst at total pressures of 21 and 100 Torr. Partial pressure of  $\text{C}_2\text{H}_6$  was 1 Torr in both cases.

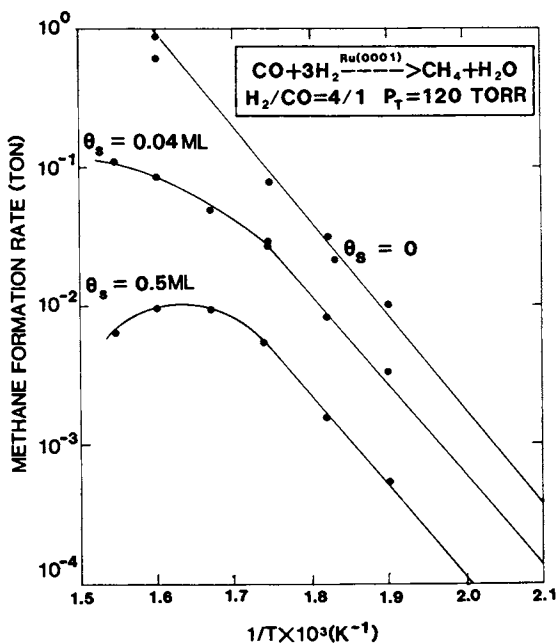


Figure 6. An Arrhenius plot of the rate of methanation over a clean and sulfided Ru(0001) catalyst. Sulfur coverages ( $\theta_s$ 's) are expressed as fractional monolayers.

of poisoning at low coverages (7,23). That the deactivation of the nickel catalyst with impurity coverage is less severe with phosphorus is consistent with the conclusion that electronic rather than ensemble effects are playing a major role in the poisoning mechanism. Chemisorption studies of H<sub>2</sub> and CO on a C, N (24), S, P, and Cl (23,25) precovered Ni(100) surface support this conclusion.

Secondly, the activation energy for the reaction is unchanged by the addition of sulfur in agreement with studies on supported systems (26,27). This suggests that although the rate is slowed, the mechanism of the reaction is fundamentally unchanged. A similar conclusion was reached in studies of the role of potassium promoters on a Ni(100) catalyst (28), although the effect of sulfur and potassium on the individual steps of the reaction are likely quite different (11,12,28).

Finally, the onset of departure from linear Arrhenius behavior is seen to occur at lower temperatures when sulfur is present on the surface (11,12). At low sulfur coverages, this onset coincides with an increase in the surface carbon level during reaction and, as discussed previously, has been interpreted as reflecting a departure of the surface concentration of atomic hydrogen from a saturation or critical coverage. Chemisorption studies of H<sub>2</sub> on partially covered Ni(100) (11) are consistent with these ideas. At higher sulfur coverages, the departure of the rate from linearity is not accompanied by the appearance of surface carbon. At these reaction conditions the carbon formation step has become rate-limiting (11,12).

The effect of sulfur on the rate of ethane hydrogenolysis is shown in Figure 8 (12). This reaction is seen to be much less affected by sulfur than is the methanation reaction. As discussed earlier, at these pressures the reaction is negative order in hydrogen pressure indicating preferential adsorption of hydrogen over ethane. Low sulfur coverages, by significantly reducing the surface hydrogen coverage (11), should lead to an enhanced reaction probability of ethane. The combined effect of the reduction in hydrogenative activity with an increase in ethane dissociative adsorption could result in less severe poisoning by sulfur of ethane hydrogenolysis compared with CO methanation.

Mixed metal catalysts frequently exhibit an improvement in selectivity (10) and stability (8) over single component metal catalysts. A noteworthy example of such a catalyst system and one which has been extensively studied is copper on ruthenium (29-31). Model studies of this mixed metal catalyst have been carried out (12) for the methanation reaction and are shown in Figure 9. For comparison the data for sulfur poisoning is also plotted. The initial slope indicates that copper merely serves as an inactive diluent, blocking sites on a one to one basis. A similar result has been found (22) in an analogous study introducing silver onto a Rh(111) catalyst. The contrast in reaction rate attenuation by copper compared with sulfur could be attributed to differences in relative electronegativities, 2.4 and 1.9, respectively (32), where the more electronegative sulfur alters the surface activity more profoundly than by a simple site blocking mechanism. However, for a proper comparison to be made between the poisoning effects of copper and sulfur additives, the overlayers in question should be uniformly dispersed over the catalyst.

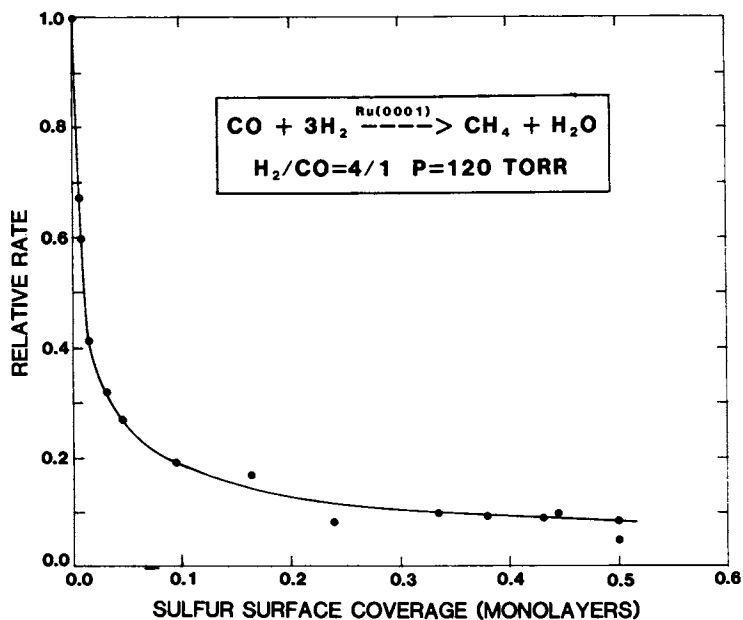


Figure 7. Relative methanation rate as a function of sulfur coverage on a Ru(0001) catalyst. Reaction temperature = 550K.

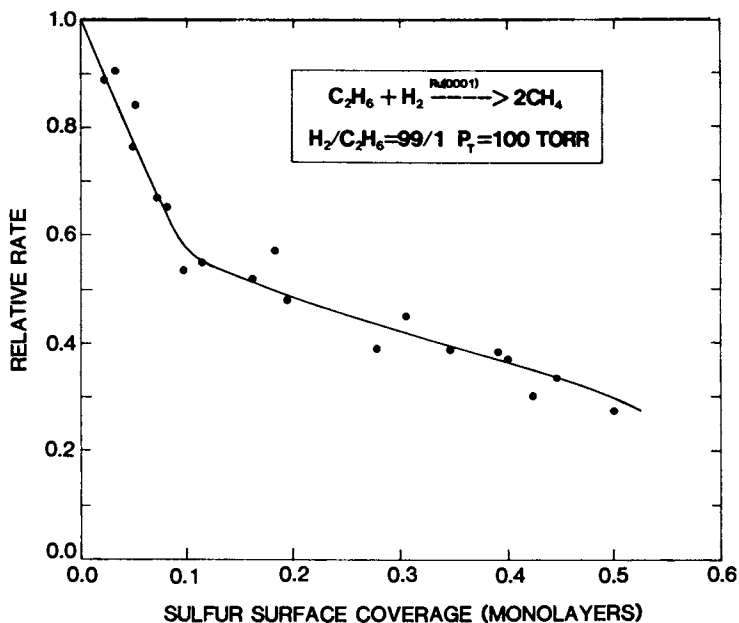


Figure 8. Relative rate of ethane hydrogenolysis on a Ru(0001) catalyst as a function of sulfur coverage. Reaction temperature = 575K. An identical result was obtained at 550K.

For sulfur and phosphorus, LEED studies indicate that uniform spreading takes place over the coverage range from 0.1-0.5 monolayers (11,23). This does not seem to be the case at high copper coverages on Ru(0001) noting that the methanation rate does not fall to zero at one monolayer of copper. It is possible that ruthenium modifies the copper layer in such a way as to activate the copper towards methanation. This, however, is unlikely since the activation energy for the reaction remains unchanged by the addition of copper (12). UPS and SIMS measurements by Vickerman, et al. (29) have shown that under the preparation conditions used in this work, the growth of three dimensional copper islands occurs at roughly a third of a monolayer, coincident with the change in slope of our rate versus copper coverage data (Figure 9). Vickerman (29) has also shown that two dimensional clustering of copper occurs at coverages less than 0.3 monolayers (12). LEED and UPS measurements of silver on Rh(111) (33) have also indicated two dimensional island growth in the submonolayer region. This tendency for two dimensional clustering is related to the electronegativity difference between the overlayer atom and the substrate surface (34). These differences in the overlayer structures of sulfur and copper on ruthenium must be taken into consideration when making comparisons between the relative poisoning effects of these additives.

Similar structural changes of the copper layer on ruthenium are observed for the ethane hydrogenolysis reaction shown in Figure 10 (12). The effect of copper at low coverages is to simply block active ruthenium sites on a one to one basis with three dimensional cluster growth occurring at roughly a third of a monolayer.

Sinfelt (35) has shown that copper in a Cu/Ru catalyst is confined to the surface of ruthenium. Results from the model catalysts discussed here then should be relevant to those on the corresponding supported, bimetallic catalysts. Several such studies have been carried out investigating the addition of copper or other Group 1B metals on the rates of CO hydrogenation (36-38) and ethane hydrogenolysis (38-41) catalyzed by ruthenium. In general, these studies show a marked falloff in activity with addition of the Group 1B metal suggesting a more profound effect of the Group 1B metal on ruthenium than implied from the model studies here. A critical parameter in the supported studies is the measurement of the active ruthenium surface using hydrogen chemisorption techniques. Haller (39,40) has recently suggested that hydrogen spillover during chemisorption may occur from ruthenium to copper. Recent studies in our laboratory (31) have added further evidence that spillover from Ru to Cu can take place and must be considered in the hydrogen chemisorption measurements. H<sub>2</sub> spillover would lead to a significant overestimation of the number of active ruthenium metal sites and thus to serious error in calculating ruthenium specific activity. If this is indeed the case, the results obtained on the supported catalysts, corrected for the overestimation of surface ruthenium, could become more comparable with the model data reported here.

Finally, the activation energies observed on supported catalysts in various laboratories are generally unchanged by the addition of Group 1B metal (36-41) which is in agreement with the present study. A crucial test of the relevance of modeling bimetallic catalysts using single crystals will be the ability of the models to alter the selectivity of the catalyst towards dehydrogenation reactions as is

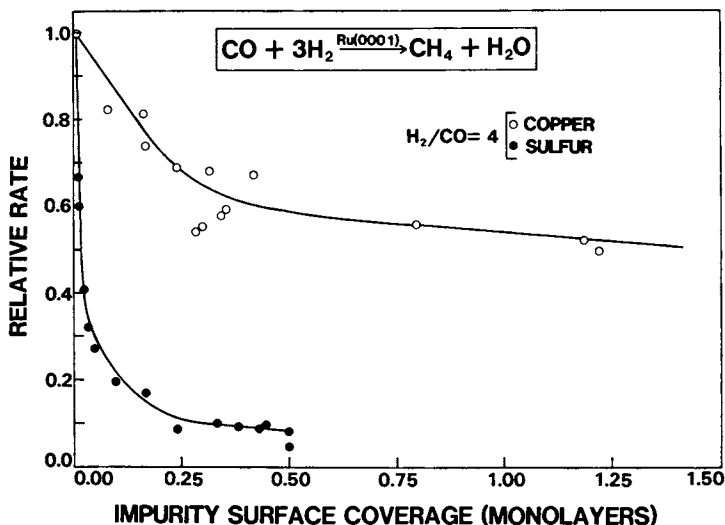


Figure 9. Relative rate of CO hydrogenation as a function of copper coverage on a Ru(0001) catalyst. Reaction temperature = 575K. Results for sulfur poisoning from Figure 7 have been replotted for comparison.

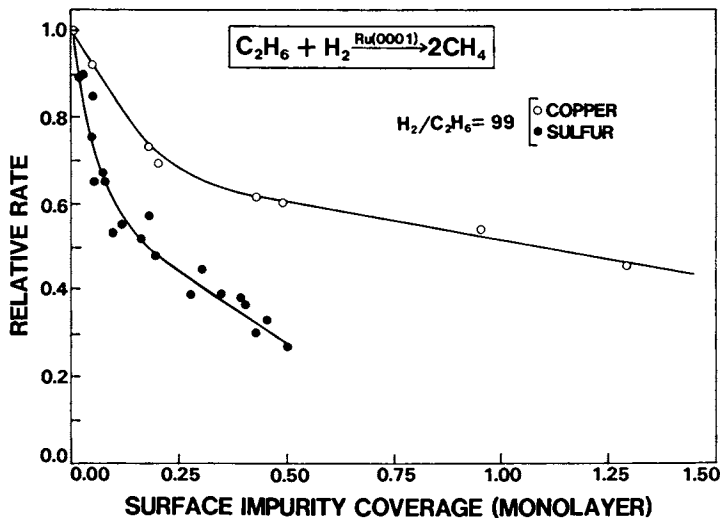


Figure 10. Relative rate of ethane hydrogenolysis on a Ru(0001) catalyst as a function of copper coverage. Reaction temperature = 550K. Sulfur poisoning data from Figure 8 have been replotted for comparison.



generally observed on supported systems (10). These experiments are currently underway in our laboratory. In addition, a recent study of cyclohexane dehydrogenation over a model Au-Pt(111) catalyst has demonstrated just such a selectivity (42).

### Concluding Remark

The examples of the model studies presented show how the meshing of modern surface techniques with reaction kinetics can provide valuable insights into the mechanisms of surface reactions and serve as a useful complement to the more traditional techniques. Close correlations between these two areas holds great promise for a better understanding of the many subtleties of heterogeneous catalysis.

### Acknowledgments

We acknowledge with pleasure the partial support of this work by the Department of Energy, Office of Basic Energy Sciences, Division of Chemical Sciences. We also acknowledge the skilled technical assistance of Kent Hoffman throughout the course of this work.

### Literature Cited

1. Somorjai, G.A. "Chemistry in Two Dimensions"; Cornell University Press: Ithaca, NY, 1981.
2. Bonzel, H.P.; Krebs, H.J. Surf. Sci. 1982, 117, 639-658.
3. Campbell, C.T.; Paffett, M.T. Surf. Sci. 1984, 139, 396-416.
4. Goodman, D.W.; Kelley, R.D.; Madey, T.E.; Yates, J.T., Jr. J. Catal. 1980, 63, 226-234.
5. Dwyer, D.J.; Hardenbergh, J.H. J. Catal. 1984, 87, 66-76.
6. Erley, W.; McBreen, P.H.; Ibach, H. J. Catal. 1983, 84, 229-234.
7. Goodman, D.W. Accts. Chem. Res. 1984, 17, 194-200.
8. Hegedus, L.L.; McCabe, R.W. Catal. Rev.-Sci. Eng. 1981, 23, 377-476.
9. Sittig, M. "Handbook of Catalyst Manufacture"; Noyes Data: Park Ridge, NJ, 1978.
10. Sinfelt, J.H. Science 1977, 195, 641-646.
11. Goodman, D.W.; Kiskinova, M. Surf. Sci. 1981, 105, L265-L270.
12. Peden, C.H.F.; Goodman, D.W. in preparation.
13. Kelley, R.D.; Goodman, D.W. Surf. Sci. 1982, 123, L743-L749.
14. Goodman, D.W. in Proceedings of the Eighth International Conference on Catalysis; Berlin, 1984.
15. Peebles, D.E.; Goodman, D.W.; White, J.M. J. Phys. Chem. 1983, 87, 4378-4387.
16. Kellner, C.S.; Bell, A.T. J. Catal. 1981, 71, 288-295.
17. Goodman, D.W.; Kelley, R.D.; Madey, T.E.; White, J.M. J. Catal. 1980, 64, 479-481.
18. Goodman, D.W.; White, J.M. Surf. Sci. 1979, 90, 201-203.
19. Goodman, D.W. Surf. Sci. 1982, 123, L679-L685.
20. Goodman, D.W. J. Vac. Sci. Technol. A 1984, 2, 873-876.
21. Goodman, D.W. in preparation.
22. Goodman, D.W. in Proceedings of IUCCP Conference; Texas A&M University, 1984.

23. Goodman, D.W.; Kiskinova, M. submitted for publication.
24. Kiskinova, M.; Goodman, D.W. Surf. Sci. 1981, 109, L555-L559.
25. Kiskinova, M.; Goodman, D.W. Surf. Sci. 1981, 108, 64-76.
26. Rostrup-Nielsen, J.R.; Pedersen, K. J. Catal. 1979, 59, 395-404.
27. Fitzharris, W.D.; Katzer, J.R.; Manogue, W.H. J. Catal. 1982, 76, 369-384.
28. Campbell, C.T.; Goodman, D.W. Surf. Sci. 1982, 123, 413-
29. Brown, A.; Vickerman, J.C. Surf. Sci. 1984, 140, 261-274, and references therein.
30. Shi, S.-K.; Lee, H.-I.; White, J.M. Surf. Sci. 1981, 102, 5674.
31. Yates, J.T., Jr.; Peden, C.H.F., Goodman, D.W. in preparation.
32. Allred, A.L. J. Inorg. Nucl. Chem. 1961, 17, 215.
33. Peebles, H.C. Ph.D. thesis, University of Texas, Austin, 1983.
34. Bauer, E.; Kolaczkiwicz, J. in Proc. 9th Int. Vac. Cong. and 5th Int. Conf. Surf. Sci., Madrid, 1983, p. 363.
35. Sinfelt, J.H.; Via, G.H.; Lytle, F.W. Catal. Rev.-Sci. Eng. 1984, 26, 81-140.
36. Bond, G.C.; Turnham, B.D. J. Catal. 1976, 45, 128-136.
37. Luyten, L.J.M.; v. Eck, M.; v. Grondelle, J.; v. Hooff, J.H.C. J. Phys. Chem. 1978, 82, 2000-2002.
38. Datye, A.K.; Schwank, J. J. Catal. in press.
39. Rouco, A.J.; Haller, G.L.; Oliver, J.A.; Kemball, C. J. Catal. 1983, 84, 297-307.
40. Haller, G.L.; Resasco, D.E.; Wang, J. J. Catal. 1983, 84, 477-479.
41. Sinfelt, J.H. J. Catal. 1973, 29, 308-315.
42. Sachtler, J.W.A.; Somorjai, G.A. J. Catal. 1984, 89, 35-43.

RECEIVED March 14, 1985

## Molecular Adsorption and Decomposition on Clean and Sulfur-Modified Metal Surfaces

R. J. Koestner<sup>1</sup>, E. B. Kollin<sup>2</sup>, J. Stöhr<sup>2</sup> and J. L. Gland<sup>2</sup>

<sup>1</sup>Department of Chemistry, University of California—Berkeley, Berkeley, CA 94720

<sup>2</sup>Exxon Research & Engineering Company, Annandale, NJ 08801

A combination of surface spectroscopies is generally required to obtain the critical structural and chemical information for adsorbed molecules and intermediates on surfaces. In order to highlight the type of information which can be obtained using temperature programmed desorption (TPD), high resolution electron energy loss spectroscopy (HREELS) and near edge X-ray absorption fine structure spectroscopy (NEXAFS), we will review chemisorption and decomposition of a number of molecules on clean and sulfur modified metal surfaces. To illustrate the key role that vibrational spectroscopy HREELS (1) and TPD often play in characterizing molecular adsorption and decomposition on metal surfaces, we will first review CO adsorption on the clean and sulfur modified Ni(100) surface. Hydrogen sulfide adsorption and decomposition on the clean and S-covered Pt(111) surface will then be discussed. We will then illustrate that the combination of NEXAFS with TPD and HREELS allows us to determine the orientation of the S-C bonds for thiomethoxy (SCH<sub>3</sub>) and thioformaldehyde (SCH<sub>2</sub>) formed by methanethiol decomposition on the Pt(111) surface. Finally we will discuss ethylene adsorption and decomposition on the Pt(111) surface. A number of different structures were initially proposed for the room temperature phase of ethylene on the Pt(111) surface based primarily on results from a single technique. Only after combining the information obtained from low energy electron diffraction (LEED), TPD and HREELS did ethylidyne ( $\equiv\text{CCH}_3$ ) emerge as the correct structure. NEXAFS spectra acquired recently allow us to directly compare the C-C bond lengths for adsorbed molecular ethylene at low temperature with the C-C bond length in the adsorbed ethylidyne intermediate.

### Carbon Monoxide Adsorption on the Sulfur Modified Ni(100) Surface

To emphasize the important role played by vibrational spectroscopy in developing our understanding of molecular processes on surfaces, recent results for CO adsorption on clean and the sulfided Ni(100) surface (2) will be described. These vibrational results for CO adsorption on sulfided Ni(100) indicate that CO-S

0097-6156/85/0288-0199\$06.00/0  
© 1985 American Chemical Society

interactions are local and that the CO-metal bond is severely weakened at higher sulfur coverages.

Carbon monoxide chemisorbs in atop sites on the clean Ni(100) surface for coverages up to  $\Theta=0.50$  where a well-ordered  $c(2 \times 2)$  lattice is observed. A further increase in CO coverage to the saturation value ( $\Theta=0.67$ ) results in a compression structure with bridged and terminally bound CO. The CO stretching frequency can be used to discriminate between adsorption in bridge ( $1960 \text{ cm}^{-1}$ ) and atop sites ( $2050 \text{ cm}^{-1}$ ).

A  $p(2 \times 2)$ -S covered surface (0.25 monolayer of sulfur) blocks the atop sites and causes CO to adsorb in bridge and hollow sites as indicated by the characteristic stretching frequencies observed at  $1910$  and  $1740 \text{ cm}^{-1}$ , respectively. Thermal programmed desorption has also been used to characterize CO adsorption on the S modified Ni(100) surface. TPD measurements for CO adsorbed on a clean Ni(100) surface indicate that the CO adsorbed in atop sites desorbs near  $425\text{K}$ , while the bridged CO from the compression structure desorbs near  $300\text{K}$ . On the  $(2 \times 2)$ -S covered surface the bridge bonded CO ( $1910 \text{ cm}^{-1}$ ) was removed at  $290\text{K}$  while the CO adsorbed in hollow sites ( $1740 \text{ cm}^{-1}$ ) remained until  $370\text{K}$ . The interaction between CO and coadsorbed sulfur must be predominantly local for two reasons: 1) no continuous shifts in CO stretching frequencies are observed with increasing sulfur coverage, and 2) the  $425\text{K}$  desorption peak characteristic of CO desorption from clean Pt simply decreases in intensity with increasing sulfur coverage but does not shift in temperature. On the other hand, coadsorbed potassium on Pt(111) (3) and Ru(0001) (4) have a long range effect and both the CO adsorption energies and stretching frequencies shift in a continuous manner with increasing potassium coverage.

#### Hydrogen Sulfide Adsorption and Decomposition on the Clean and S-Covered Pt(111) Surface

HREELS and TPD have played a unique role in characterizing the surface chemistry of systems which contain hydrogen since many surface techniques are not sensitive to hydrogen. We have used these techniques to characterize  $\text{H}_2\text{S}$  adsorption and decomposition on the clean and  $(2 \times 2)$ -S covered Pt(111) surface (5). Complete dissociation of  $\text{H}_2\text{S}$  was observed on the clean Pt(111) surface even at  $110\text{K}$  to yield a mixed overlayer of H, S, SH and  $\text{H}_2\text{S}$ . Decomposition is primarily limited by the availability of hydrogen adsorption sites on the surface. However on the  $(2 \times 2)$ -S modified Pt(111) surface no complete dissociation occurs at  $110\text{K}$ , instead a monolayer of adsorbed SH intermediate is formed (5).

Figure 1 shows a set of HREELS spectra taken for increasing  $\text{H}_2\text{S}$  coverages at  $110\text{K}$  on the clean Pt(111) surface. Spectrum (a) was taken following adsorption of a small amount of  $\text{H}_2\text{S}$  ( $\sim 0.2$  monolayers). The only mode present in the vibrational spectrum is an atomic sulfur-Pt stretch at  $375 \text{ cm}^{-1}$  indicating complete dissociation of the adsorbed  $\text{H}_2\text{S}$ . In spectrum (b) taken following adsorption of  $0.5$  monolayers of  $\text{H}_2\text{S}$  two additional modes appear at  $585$  and  $685 \text{ cm}^{-1}$ . These modes are the bending vibrations for two types of adsorbed sulfhydryl (SH) intermediate. Increasing the

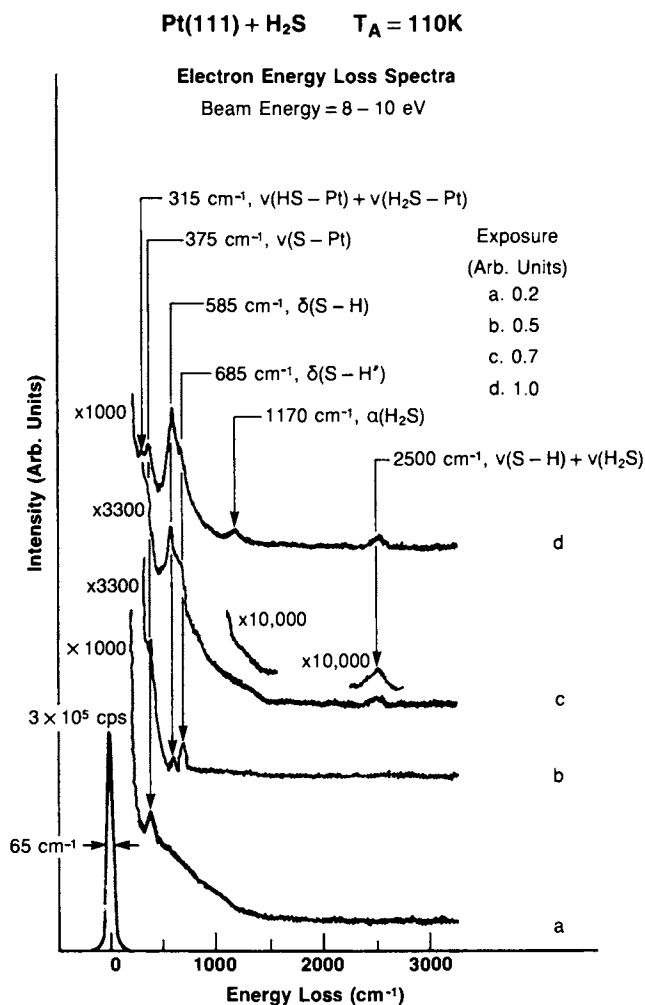


Figure 1. HREELS spectra for increasing H<sub>2</sub>S exposures on the Pt(111) surface at 110K. A value of one in the exposure units corresponds to saturation of the first layer.

$H_2S$  coverage to 0.7 of a monolayer increases the population of SH species on the surface with a  $585\text{ cm}^{-1}$  bending mode, as shown in spectrum (c). Near saturation coverage,  $H_2S$  adsorbs molecularly as illustrated by the  $H_2S$  scissor vibration at  $1170\text{ cm}^{-1}$  in spectrum (d). The stability of adsorbed SH and molecular  $H_2S$  is the result of surface passivation caused by coadsorption with the initial dissociation products of  $H_2S$ . Thermal desorption experiments indicate that only one hydrogen atom can adsorb in a  $(2 \times 2)\text{-S}$  cell at 110K, yet  $H_2S$  would donate two hydrogens to each  $(2 \times 2)$  cell formed if it dissociates completely. At low coverages, the  $H_2S$  dissociates completely to form atomic sulfur and coadsorbed hydrogen. The excess hydrogen which cannot be accommodated in the  $S(2 \times 2)$  cell spills over onto clean Pt areas. At intermediate coverages, adsorbed SH is formed because total dissociation is blocked by previously adsorbed S and H. The last fraction of  $H_2S$  which adsorbs is forced to adsorb molecularly because coadsorbed SH, S and H block all available hydrogen adsorption sites.

$H_2S$  adsorption on the  $(2 \times 2)\text{-S}$  covered Pt(111) surface at 110K contrasts with adsorption on the clean surface. On the  $(2 \times 2)\text{-S}$  surface no complete dissociation is observed at low temperature; instead,  $H_2S$  partially dissociates to form an adsorbed SH intermediate with a characteristic bend vibration at  $585\text{ cm}^{-1}$ . Heating adsorbed SH on the  $(2 \times 2)\text{-S}$  covered surface leads to a  $SH+H$  recombination reaction not observed on clean Pt. The recombination process removes the excess SH so that the stable, high coverage  $(\sqrt{3} \times \sqrt{3})R30^\circ\text{-S}$  lattice can be formed.

### Sequential Dehydrogenation of Methanethiol on the Pt(111) Surface

NEXAFS, HREELS and TPD were used to characterize the sequential decomposition of adsorbed methanethiol ( $CH_3SH$ ) on the Pt(111) surface (6). With increasing temperature, we observe nearly complete conversion of the adsorbed methanethiol first to form thiomethoxy ( $SCH_3$ ) and then to form thioformaldehyde ( $SCH_2$ ). The equivalent production of an adsorbed formaldehyde ( $OCH_2$ ) species from methoxy ( $OCH_3$ ) has not been observed to our knowledge. NEXAFS spectra were used to obtain detailed structural information for these adsorbed intermediates by determining the orientation of the S-C bonds. The  $SCH_3$  species was found to be tilted from the surface normal by  $45^\circ (\pm 10^\circ)$  in marked contrast to  $OCH_3$  which is adsorbed normal to the surface. The adsorbed  $SCH_2$  absorbs in a tilted configuration  $20^\circ$  up from surface plane implying a tradeoff between a fairly strong  $\pi$  bond and S lone pair donation.

Figure 2 shows HREELS and TPD spectra obtained from  $CH_3SH$  adsorbed at 110K. The multilayer HREELS spectrum of  $CH_3SH$  taken at 110K is nearly identical to the gas phase IR spectrum of  $CH_3SH$ . Multilayers of  $CH_3SH$  desorb at 135K. TPD spectra with deuterium labeled methanethiol ( $CH_3SD$ ) indicate that the 210K hydrogen peak is caused only by the loss of the sulfhydryl hydrogen. The vibrational spectrum measured after heating to 255K correspond closely to the vibrational spectrum of the  $SCH_3$  ligand in  $(CH_3)_3Sn(SCH_3)$  and indicate that  $SCH_3$  is formed on the surface (7). S-H bond cleavage is also indicated by the

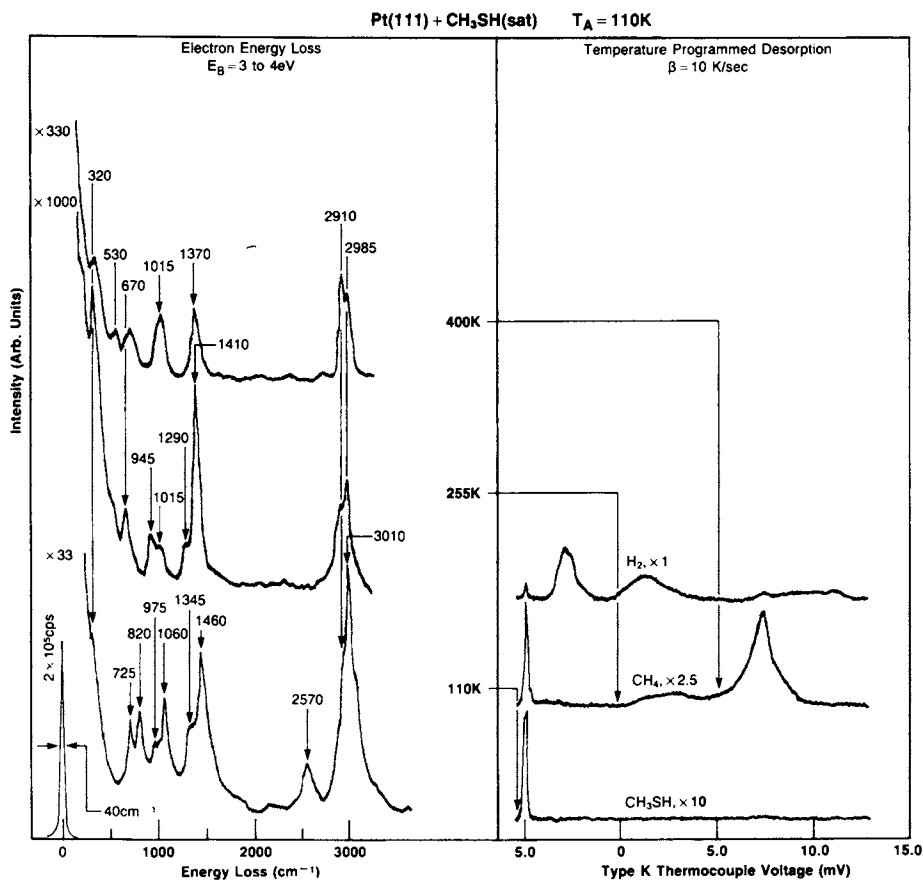


Figure 2. HREELS spectra illustrating sequential CH<sub>3</sub>SH decomposition on the Pt(111) surface. The HREELS spectra were taken following treatment at the temperatures indicated on the reference TPD spectra shown in the right panel.

disappearance of the S-H stretching ( $2750\text{ cm}^{-1}$ ) and bending ( $820\text{ cm}^{-1}$ ) modes.

The  $\text{H}_2$  TPD spectrum in Figure 2 indicates that adsorbed  $\text{SCH}_3$  loses additional hydrogen with heating to 400K. The  $\text{H}_2$  desorption peaks at 210 and 305K have nearly equal areas indicating that the second adsorbed intermediate has an average thioformaldehyde ( $\text{SCH}_2$ ) stoichiometry. The HREELS spectrum in Figure 2 taken after heating to 400K generally corresponds to a matrix isolated (8)  $\text{SCH}_2$ . However the S-C stretch in adsorbed  $\text{SCH}_2$  is dramatically red shifted from  $1050\text{ cm}^{-1}$  for the matrix isolated species to  $670\text{ cm}^{-1}$  indicating a highly perturbed adsorbed  $\text{SCH}_2$  species. The assignment of the  $670\text{ cm}^{-1}$  mode to the  $\nu(\text{C-S})$  vibration for the adsorbed species follows from the low CH character of this mode (a deuterium shift of .03). Analogous shifts to  $560\text{ cm}^{-1}$  have been observed in  $\nu(\text{C-S})$  for an inorganic cluster  $\text{Os}(\eta^2\text{-CH}_2\text{S})([\text{O}]_2(\text{PPh}_3)_2)$  (9) with a  $\eta^2$ -bonded  $\text{CH}_2\text{S}$  ligand. The  $400\text{ cm}^{-1}$  red shift in  $\nu(\text{C-S})$  that we measure implies a strong interaction between the  $\text{CH}_2\text{S}$   $\pi$  orbital and the metal surface. A small fraction of the  $\text{SCH}_3$  layer (10%) decomposes near 350K to give  $\text{CH}_4$  which desorbs and atomic sulfur which remains on the surface.

The NEXAFS spectra in Figure 3 taken at the C K-edge allows us to estimate the tilt angles for the adsorbed  $\text{SCH}_3$  and  $\text{SCH}_2$  species. Spectra were recorded at grazing ( $20^\circ$ ) and normal ( $90^\circ$ ) incidence after heating a multilayer of  $\text{CH}_3\text{SH}$  on Pt(111) to either 230K ( $\text{SCH}_3$ ) or 380K ( $\text{SCH}_2$ ). Only one molecular resonance appears near 288.0eV for the  $\text{SCH}_3$  layer and is assigned to a  $\text{C}(1s) \rightarrow \sigma^*_{\text{C-S}}$  transition. A similar C-S bond  $\sigma^*$ -resonance was observed for multilayer and monolayer thiophene ( $\text{C}_4\text{H}_4\text{S}$ ) on Pt(111) (10). The  $\sigma^*_{\text{C-S}}$  transition intensity follows a  $\cos^2\alpha$  relation where  $\alpha$  is the angle between the E vector and the  $\sigma^*$ -orbital. By normalizing the  $\sigma^*_{\text{C-S}}$  transition intensity to the smooth continuum background which is shown dashed in Figure 3, we obtain a 2:1 ratio in the  $\sigma^*_{\text{C-S}}$  resonance measured at grazing and normal x-ray incidence. This gives a C-S tilt angle from the surface normal of  $45^\circ \pm 10^\circ$ .

The NEXAFS spectra for the  $\text{SCH}_2$  layer again show the structureless background and the  $\text{C}(1s) \rightarrow \sigma^*_{\text{C-S}}$  transition at 288.0eV. A new feature, however, is found at a lower photon energy of 284.5 eV and is assigned to a  $\text{C}(1s) \rightarrow \pi^*_{\text{C-S}}$  transition. Similar  $\pi^*$  excitations have been seen near 284 eV with a number of unsaturated hydrocarbons chemisorbed on Pt(111) (10,11). The presence of this new resonance at 284.5 eV supports the HREELS and the TPD evidence that an unsaturated  $\text{SCH}_2$  species forms above 300K.

The  $\pi^*_{\text{C-S}}$  and  $\sigma^*_{\text{C-S}}$  transition intensities for adsorbed  $\text{SCH}_2$  do not vanish at either incidence angle demonstrating that the S-C bond is again tilted from the surface. Since the  $\pi^*_{\text{C-S}}$  ( $\sigma^*_{\text{C-S}}$ ) intensity at grazing (normal) incidence is about three times larger than that at normal (grazing) incidence, we estimate the C-S bond of adsorbed  $\text{SCH}_2$  to be oriented  $20^\circ \pm 10^\circ$  from the surface plane. Since the  $\nu(\text{Pt-SCH}_2)$  and  $\nu(\text{Pt-SCH}_3)$  stretching frequencies are identical, we believe the sulfur atom of adsorbed  $\text{SCH}_2$  is closer to the surface; the inclined S-C bond of  $20^\circ \pm 10^\circ$  then



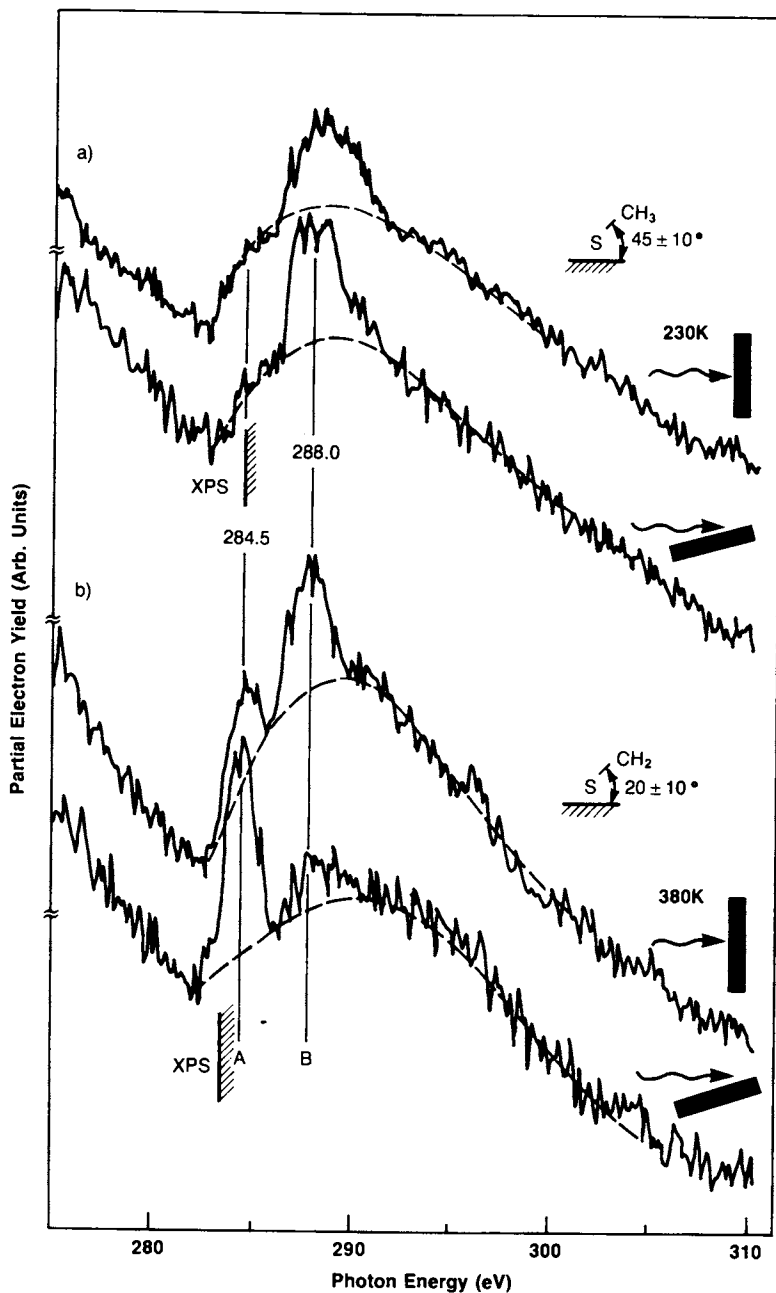


Figure 3. Carbon K-edge NEXAFS of thiomethoxy (SCH<sub>3</sub>) (a) and thioformaldehyde SCH<sub>2</sub> (b). Spectra for two incidence angles (20° and 90°) of the X-ray beam are shown.

allows the sulfur lone pair orbitals to point towards the metal at the expense of carbon p-orbital overlap with metal d-orbitals. The unexpected inclination of adsorbed  $\text{SCH}_2$  can then be explained as a tradeoff between sulfur lone pair and  $\pi$ -bonding to the metal.

### Ethylene Adsorption and Decomposition on Pt(111) Surface

The ethylidyne intermediate which forms during ethylene decomposition on the Pt(111) surface (1,12) has received a large amount of attention in the past few years, owing in part to its relevance in hydrocarbon catalysis and also in part to its stability on a number of other surfaces, namely Pt(100) (13), Rh(111) (14), Pd(111) (15) and Ru(0001) (16). An early LEED experiment (17) suggested that ethylene dehydrogenated to an acetylene species on Pt(111) since the LEED diffraction beam intensity vs. voltage (I-V) profiles for the acetylene and ethylene derived phases were identical at 300K. Ultraviolet Photoemission (UPS) spectra (18) for these two layers were also found to be identical. The postulated acetylene intermediate was challenged by an HREELS study (19) which proposed that ethylene decomposed to form adsorbed ethylidene. In fact, acetylene did not give the same HREELS spectrum as ethylene in the absence of coadsorbed hydrogen on the surface. TPD spectra (20) taken following ethylene adsorption at 300K indicated that one of the four ethylene hydrogens desorbed at 350K without any detectable change in the UPS spectrum. Thus the stoichiometry of the surface intermediate formed was  $\text{C}_2\text{H}_3$  which ruled out both acetylene and ethylidene as possible models. A detailed analysis of LEED data (21) suggested for the first time that adsorbed ethylidyne was being formed, even though the vibrational spectrum reported at that time had too many vibrational modes for symmetric intermediate like ethylidyne. Subsequent vibrational experiments (12) revealed that the "extra" modes could be selectively removed by hydrogen treatment. The assignments in the HREELS spectrum of adsorbed ethylidyne are confirmed by comparison with a recent IR spectrum of an organometallic analog,  $\text{CH}_3\text{C}(\text{Co})_3(\text{CO})_9$  (22). Ethylidyne-like intermediate species are also formed during decomposition of larger hydrocarbons as indicated by a simple comparison (23) of experimental I-V curves from the ethylidyne layer with those from propene- and butene-derived propylidyne ( $\equiv\text{C}(\text{CH}_2)\text{CH}_3$ ) and butylidyne ( $\equiv\text{C}(\text{CH}_2)_2\text{CH}_3$ ) on the Pt(111) surface. The stoichiometry and structure of the adsorbed ethylidyne intermediate was established by combining a group of techniques, each with different sensitivities and perspectives, to study ethylene decomposition on the surface.

Recent NEXAFS (11,24) have confirmed the ethylidyne structure proposed by LEED analyses (14,21) and further determined the structure of adsorbed molecular ethylene. Figure 4 shows the NEXAFS spectra for ethylidyne (a) and ethylene (b) on the Pt(111) surface taken for two incidence angles of the X-ray beam. The transitions observed in these NEXAFS spectra have been assigned using SCF-X $\alpha$  calculations (24). For the ethylidyne spectrum taken at 20° incidence angle peak A is caused by a  $\text{C}(1s) \rightarrow \sigma^*_{\text{C-Pt}}$  transition; peak B is caused by a  $\text{C}(1s) \rightarrow \sigma^*_{\text{C-C}}$  transition. Peak A in the

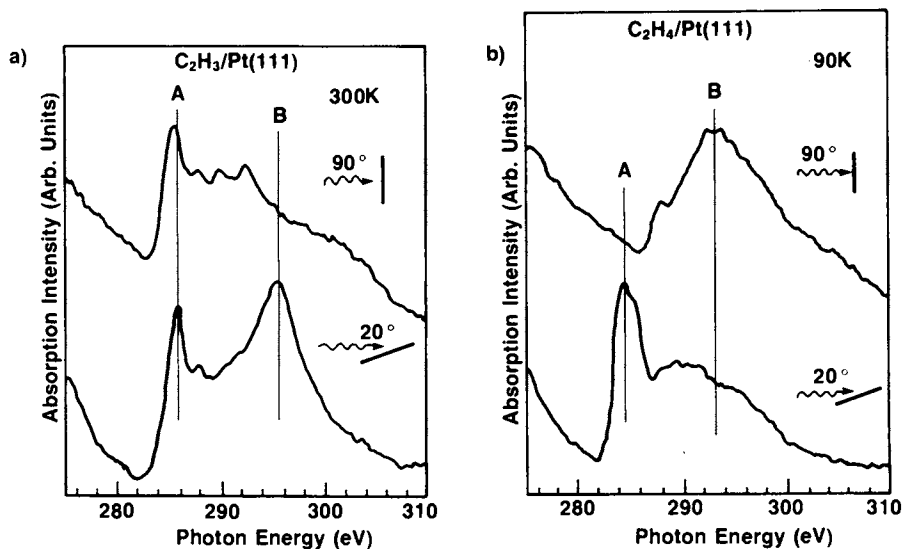


Figure 4. Carbon K-edge NEXAFS spectra of ethylidyne (a) and ethylene (b) adsorbed on the Pt(111) surface. Spectra for two incidence angles (20° and 90°) of the X-ray beam are shown.

ethylidyne spectrum taken at 90° incidence angle is assigned to a  $C(1s) \rightarrow \pi^*_{C-Pt}$  bound state transition. Peak B is missing in the ethylidyne spectrum taken at 90° incidence angle confirming that ethylidyne is adsorbed normal to the surface. For the adsorbed molecular ethylene spectrum taken at 20° incidence angle peak A is caused by a  $C(1s) \rightarrow \pi^*_{C-C}$  bound state transition. While peak B in the molecular ethylene spectrum taken at 90° incidence angle is caused by a  $C(1s) \rightarrow \sigma^*_{C-C}$  transition. The polarization dependence of both peaks A and B for adsorbed molecular ethylene clearly indicates that molecular ethylene adsorbs parallel to the surface.

Gas phase NEXAFS spectra of  $C_2H_2$ ,  $C_2H_4$  and  $C_2H_6$  (11), indicate that the  $\sigma^*_{C-C}$  resonance energy is a sensitive function of interatomic distance and appears to vary linearly with the C-C bond distance. A 1 eV increase in energy corresponds to a 0.02 Å decrease in bond length. Since the  $\sigma^*_{C-C}$  resonance of ethylidyne lies ~1 eV higher than the  $\sigma^*_{C-C}$  resonance of adsorbed molecular ethylene, we directly observe that adsorbed ethylene has a C-C bond 0.03 Å longer than adsorbed ethylidyne even though adsorbed ethylene has a formal C-C double bond while ethylidyne has a formal C-C single bond. Using the gas phase calibration, the C-C bond length for ethylidyne is estimated to be 1.47 Å while the C-C bond length for molecular ethylene is 1.49 Å. The stretched C-C bond in adsorbed molecular ethylene is the result of extensive interaction with the surface.

#### SUMMARY

We have shown the importance of using a combination of complementary techniques to probe molecular processes on surfaces and the key role that HREELS and TPD spectroscopes have played. The important role played by HREELS and TDS in following surface reactions was demonstrated by three examples. Local interaction dominates when CO is coadsorbed with S on the Ni(100) surface.  $H_2S$  decomposition is reduced by coadsorbed sulfur on the Pt(111) surface and the SH surface intermediate is stabilized.  $CH_3SH$  decomposes sequentially on the Pt(111) surface to yield adsorbed thiomethoxy and thioformaldehyde. NEXAFS spectra provided detailed molecular information by characterizing the C-S bond tilt angle for the adsorbed thiomethoxy ( $SCH_3$ ) and thioformaldehyde ( $SCH_2$ ) intermediates. The study of ethylene and ethylidyne phases on Pt(111) was an example which emphasized the need for a multi-technique approach. In fact, recent NEXAFS spectra have shed even more light on the overlayers by directly measuring the C-C bond lengths.

#### Literature Cited

1. Ibach H. and Mills D. L., "Electron Spectroscopy for Surface Analysis," Academic Press, New York, 1982.
2. Gland J. L., Madix R. J., McCabe R. W. and DeMaggio C., Surf. Sci. 143 (1984) 46.
3. Crowell J. E., Garfunkel E. L. and Somorjai G. A., J. Phys. Chem. 86 (1982) 310.

4. DePaola R. A., Hrbek, J. and Hoffmann, F. M., *J. Chem. Phys.* in press.
5. Koestner R. J., Salmeron M., Kollin E. B. and Gland, J. L., to be published.
6. Koestner R. J., Stohr J., Gland J. L., Kollin E. B. and Sette F., submitted to *Chem. Phys. Lett.*
7. Van de Vondel D. F., Van den Berghe E. V. and van den Kelen G. P., *J. Organomet. Chem.* 23 (1970) 105.
8. Torres M., Safarik I., Clement A., and Straus D. P., *Can. J. Chem.* 60 (1982) 1187.
9. Collins T. J. and Roper W. R., *J. Organometl. Chem.* 150 (1978) 73.
10. Stohr J., Gland J. L., Kollin E. B., Koestner R. J., Johnson A. L., Muetterties E. L. and Sette F., *Phys. Rev. Lett.* 53 (1984) 2161.
11. Stohr J., Sette F. and Johnson A. L., *Phys. Rev. Lett.* in press.
12. Steininger H., Ibach H. and Lehwald S., *Surface Science* 117 (1982) 685.
13. Ibach H., "Proc. Int. Conf. on Vibrations in Adsorbed Layers", Jülich, Germany (1978), p. 64.
14. Koestner R. J., Van Hove M. A. and Somorjai G. A., *Surface Science* 117 (1982) 491.
15. Kesmodel L. L. and Gates J. A., *Surface Science* 111 (1981) L747.
16. Barteau W. A, Broughton J. Q. and Menzel D., accepted *Appl. Surface Science*.
17. Stair P. C. and Somorjai G. A., *J. Chem. Phys.* 66 (1977) 2036.
18. Lo W. J., Chung Y. W., Kesmodel L. L., Stair P. C. and Somorjai G. A., *Solid State Comm.* 22 (1977) 335.
19. Ibach H. and Lehwald S., *J. Vac. Sci. Tech.* 15 (1978) 407.
20. Demuth J. E., *Surface Science* 80 (1979) 367.
21. Kesmodel L. L., Dubois L. H. and Somorjai G. A., *J. Chem. Phys.* 70 (1979) 2180.
22. Skinner P., Howard M. W., Oxton I. A., Kettle S. F. A., Powell D. B. and Sheppard N., *J. Chem. Soc. Faraday Trans.* 77 (1981) 1203.
23. Koestner R. J., Frost J. C. , Stair P. C., Van Hove M. A., and Somorjai G. A., *Surface Science* 117 (1982) 491.
24. Koestner R. J., Stohr J., Gland J. L. and Horsley J. A., *Chem. Phys. Lett.* 105 (1982) 332.

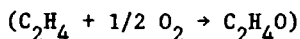
RECEIVED June 24, 1985

## Selective Epoxidation of Ethylene Catalyzed by Silver Mechanistic Details Revealed by Single-Crystal Studies

Charles T. Campbell

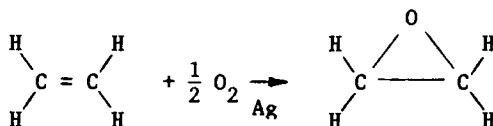
Chemistry Division, Los Alamos National Laboratory, Los Alamos, NM 87545

The selective oxidation of ethylene to ethylene epoxide



over Ag is a simple prototype for the entire class of kinetically-controlled, selective oxidation reactions. We have studied the steady-state kinetics and selectivity of this reaction on clean, well-characterized single-crystal surfaces of silver by using a special apparatus which allows rapid (~20 s) transfer between a high-pressure catalytic microreactor and an ultra-high vacuum surface analysis (AES, XPS, LEED, TDS) chamber. The results of some of our recent studies of this reaction will be reviewed. These single-crystal studies have provided considerable new insight into: the reaction pathway through molecularly adsorbed O<sub>2</sub> and C<sub>2</sub>H<sub>4</sub>, the structural sensitivity of real silver catalysts, and the role of chlorine adatoms in promoting catalyst selectivity via an ensemble effect.

The catalytic oxidation of ethylene to ethylene epoxide (also known as ethylene oxide)



is a several-billion-dollar per year industry, providing the necessary intermediate in the synthesis of ethylene glycol, which is used in polyester and antifreeze production. The most common catalyst is silver supported on  $\alpha$ -Al<sub>2</sub>O<sub>3</sub>, of ~1 m<sup>2</sup> · g<sup>-1</sup> specific surface area, promoted for selectivity by adding trace amounts of chlorinated hydrocarbons to the feed. This reaction is the simplest example of

a kinetically-controlled, selective heterogeneous catalytic reaction. (Metals other than silver generally produce  $\text{CO}_2 + \text{H}_2\text{O}$ , the thermodynamically preferred product.) As such, this reaction is of fundamental importance from the surface science point-of-view and has therefore been the subject of numerous reaction studies (1-21), as well as ultra-high vacuum (UHV) adsorption studies [(22-23) and references therein]. However, most of the basic questions concerning the reaction mechanism and the nature of the active catalyst surface remain unanswered. This is largely due to the fact that the reaction proceeds too slowly to be observable under the vacuum conditions typically employed in surface analysis. This paper reports some of our recent results in which we have studied the reaction on Ag(110) and (111) by directly combining high-pressure kinetic measurements with UHV surface analysis in a single apparatus (24-28). These studies have provided new insights into the reaction mechanism, its structural sensitivity, and the role of chlorine in promoting selectivity.

### Experimental

Details of the apparatus and techniques are presented in related papers (23,25,28). In short, the Ag(110) and (111) samples were cleaned by sputtering and annealing (800 K) in ultra-high vacuum (UHV). Cleanliness and order were proven by Auger electron spectroscopy (AES) and low-energy electron diffraction (LEED). The clean sample was transferred into an evacuated microreactor attached directly to the UHV chamber, pressurized with the reaction mixture (~200 torr) and heated (440-610 K) until a steady-state epoxidation rate (2-4 min) was established. [Steady-state rates could be maintained over times during which >5000 molecules of ethylene per surface Ag atom were converted into product (25,28).] Then the sample was rapidly (17 s) transferred at reaction temperature back into UHV for surface analysis (AES, LEED, TDS, XPS). The coverage of O was quantitatively measured by flash heating the sample immediately after transfer and measuring the area under the 600 K  $\text{O}_2$  thermal desorption peak mass-spectrometrically (25). After transfer, the reaction mixture (still in the batch microreactor) was analyzed by gas chromatography for the amount (rates) of ethylene oxide and  $\text{CO}_2$  produced. As discussed in related papers (25,28), above 480 K the surface contained only atomically adsorbed oxygen and maintained a good LEED pattern after reaction. Below 480 K other adsorbed reactants and products were observed. The sides and back of the crystal were passivated to reaction by a mixed Si, Cu, Ti oxide/carbide film that built up during the early stages of high-pressure reaction attempts.

Coverages ( $\theta$ ) are defined relative to the number of Ag surface atoms [ $\theta = 1$  is  $8.5 \times 10^{14} \text{ cm}^{-2}$  for Ag(110) and  $1.38 \times 10^{15} \text{ cm}^{-2}$  for Ag(111)]. Sample sizes were: Ag(110) = 10 mm  $\times$  6 mm  $\times$  2 mm and Ag(111) = 10 mm  $\times$  7 mm  $\times$  2 mm.

The methods for depositing chlorine adatoms on the (110) surface have been described previously (26), and resulted in surface structures and LEED patterns identical to those achieved by dissociative  $\text{Cl}_2$  adsorption. A  $c(4 \times 2)$ -Cl pattern at  $\theta_{\text{Cl}} = 0.75$  (26) was used to calibrate chlorine coverages, which were taken proportional to the ratio of Cl:Ag AES intensities (26).

## Results and Discussion

**Structural Sensitivity.** Figure 1 shows the steady-state rates of ethylene oxide (EtO) and CO<sub>2</sub> production as a function of temperature, in Arrhenius form, at an ethylene pressure ( $P_{Et}$ ) of 20 torr and  $P_{O_2}$  = 150 torr on clean Ag(110) (24,25). These specific rates in Fig. 1 are expressed in terms of turn-over-number (TON), i.e., the number of molecules of each produced per Ag surface atom (site) per second, assuming  $10^{15}$  Ag surface atoms on our sample. Shown for comparison is the specific rate of EtO production over a high-surface-area, silica-supported Ag catalyst under the same conditions. The activation energy for EtO production decreases from about 22.4 to 5.3 kcal mole<sup>-1</sup> as the temperature increases from 440 to 610 K on Ag(110), almost identical to the behavior on the supported Ag catalyst.

The selectivity for ethylene conversion into EtO ( $S_{EtO} = \text{TON}_{EtO} / [\text{TON}_{EtO} + 1/2 \text{TON}_{CO_2}]$ ) from the data of Fig. 1 for Ag(110) shows a gradual decrease with temperature (24), in agreement with most high-surface-area catalysts (15,17,29). The absolute value of the selectivity (~40%) on Ag(110) falls within the range seen for unpromoted, high-surface-area Ag catalysts (28).

We have found (24,25) that the effects of temperature and reactant pressures upon the rates of EtO and CO<sub>2</sub> production and upon selectivity are virtually identical on Ag(110) and high-surface-area Ag catalysts. However, the absolute specific rates (per surface Ag atom) for the (110) surface were found to be some 100-fold higher than those reported for a variety of high-surface-area catalysts (24). We had postulated that a small percentage of (110) planes or (110)-like sites are responsible for most of the catalytic activity of high-surface-area catalysts (24,25). However, our very recent results for the clean, close-packed Ag(111) face (28) show that its specific activity is only a factor of about two below the (110) face. Since the lowest-energy (111) face is expected to predominate on high-area catalysts, the huge difference in specific activities for single-crystal Ag and high-area catalysts seems no longer to be due to some inactive Ag surface predominating the high-area catalysts. We note that the kinetics (activation energies and reaction orders) on Ag(111) and (110) are very similar (28).

This reaction has long been known to be classically structurally sensitive; i.e., the rates and selectivity depend sensitively upon the size and shape of Ag particles in high-surface-area catalysts (10,14,24,30,31). The rate variations apparently cannot be related to variations in the concentration of active surface facets with particle size. It may be that some impurity from the preparation process or support material poisons the catalyst surface, and the concentration of this poison is dependant upon the same factors in the preparation scheme which allow for particle size adjustment. Three further facts might support this explanation: (1) A strange minimum in specific activity with particle size is observed at the surprisingly large size of 500-700 Å (10,14,30); (2) the variations in specific activity with particle size observed by any given author (10,14,30) are smaller than the variations among authors for catalysts of nominally the same particle size [see Table I in (24)];



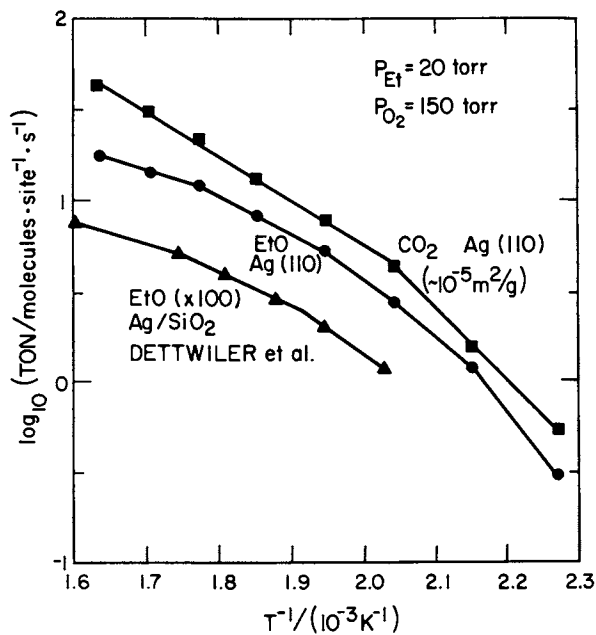


Figure 1. The steady state rates of EtO and CO<sub>2</sub> production as a function of temperature, in Arrhenius form, at  $P_{Et} = 20$  torr and  $P_{O_2} = 150$  torr on clean Ag(110).

and, (3) the specific activities of unsupported, high-area Ag catalysts are at the upper limit of activities seen for high-area catalysts, and only a factor of about 10 below those for Ag(110) or (111) [see Table I in (24)].

For small particles, selectivity increases with particle size (14,30). In our results, Ag(111) has an average selectivity which is about 6% higher (in absolute units) than Ag(110) (28). Since the particle surface should evolve from open, or (110)-like, to close-packed, or (111)-like, with increasing size, these results may be favorably correlated.

### Reaction Kinetics and Mechanism

Figure 2 shows the effect of ethylene pressure upon the steady-state reaction rates for clean Ag(110) at 490 K and 150 torr  $O_2$  (25). Also shown is the steady-state coverage of atomically adsorbed oxygen ( $\theta_o$ ) under reaction conditions (measured as described above). The coverage of atomic oxygen decreases with increasing  $P_{Et}$ , but maintains a significant value ( $\theta_o \cong 0.1$ ) when the rates saturate in ethylene.

We have measured data similar to Fig. 2 where, instead, the effects of  $O_2$  pressure upon the steady-state rates and  $\theta_o$  were observed (25). These data are plotted in Fig. 3 to directly reflect the effects of oxygen adatom coverage upon the rates at a fixed temperature and ethylene pressure. While the order in  $P_{O_2}$  varies strongly with  $P_{O_2}$ , EtO production remains almost first order in  $\theta_o$  throughout the entire range of  $O_2$  pressures. This clearly indicates that adsorbed oxygen adatoms play an important role in the reaction mechanism, such that their coverage enters the rate equation in a linear fashion.

Similar data on Ag(111) indicate that under identical reaction conditions, the atomic oxygen coverage on Ag(111) is a factor of about 15 below  $\theta_o$  on Ag(110), on the average (28). This can be directly ascribed to the much higher dissociative sticking probability for  $O_2$  displayed by the (110) face (22-23,28). Since the epoxidation rates are only a factor of about two smaller on Ag(111), this result suggests that atomically adsorbed oxygen may not be directly involved in the epoxidation step. We will show below further data which support molecularly adsorbed (peroxo-)  $O_2$  as the true oxidizing agent. Since  $O_{2,a}$  is a precursor to  $O$  formation (23), its coverage will be proportional to  $\theta_o$  at constant temperature and ethylene pressure (Fig. 3), provided  $\theta_o$  is low and  $O$  is removed from the surface only via a reaction which is first order in  $\theta_o$  (28).

Interestingly, we have shown by postreaction LEED that those oxygen adatoms reside on the surface under reaction conditions in  $p(2 \times 1)-0$  islands of local coverage  $\theta_o = 0.5$  on Ag(110) or  $p(4 \times 4)-0$  islands of local coverage  $\theta_o \cong 0.4$  on Ag(111). This suggests that reaction occurs at the edges of these islands (25-28).

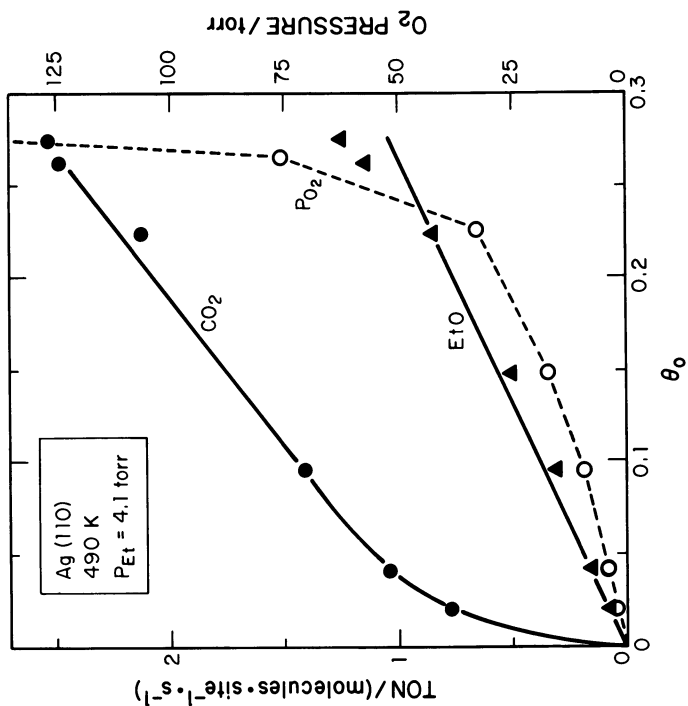


Figure 3. The effect of  $O_2$  pressure upon the steady state reaction rates for clean Ag(110) at 490 K and  $P_{Et} = 4.1$  torr.

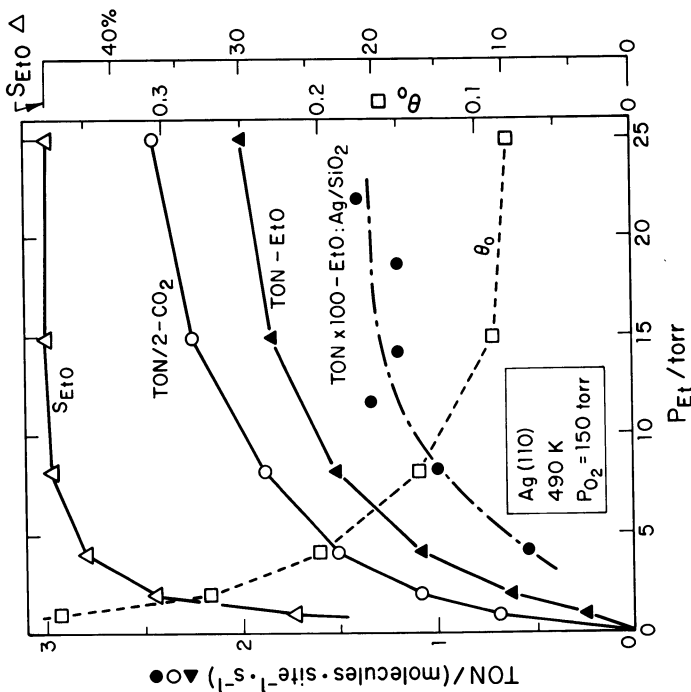


Figure 2. The effect of ethylene pressure upon the steady state reaction rates for clean Ag(100) at 490 K and  $P_{O_2} = 150$  torr.

Note in Fig. 3 a distinct break in CO<sub>2</sub> production rate versus  $\theta_o$ . We relate this break to the existence of two pathways to CO<sub>2</sub> production (25). Under most conditions (in this case for  $\theta > 0.03$ ), CO<sub>2</sub> production is predominated by a mechanism which proceeds through the same rate-determining step as the epoxidation path. Thus exist the very strong kinetic similarities for EtO and CO<sub>2</sub> production (2,3,6,25). The other path to CO<sub>2</sub> is less understood (25) and only predominates under extreme conditions, but is more sensitive to  $\theta_o$ .

The data in Figs. 2 and 3 suggest a reaction which requires a delicate balance between adsorbate coverages, consistent with a Langmuir-Hinshelwood mechanism. More extensive data of this type (24-27) indicate that molecularly adsorbed ethylene and O<sub>2</sub> are the critical species, consistent with the mechanism proposed below.

### The Role of Chlorine Promoters

Figure 4 shows the effects of chlorine adatom coverage ( $\theta_{Cl}$ ) upon the rates, selectivity and  $\theta$  at a set of fixed pressure and temperature conditions on Ag(110) (26). The effects are qualitatively identical to those seen by adding trace quantities of chlorinated hydrocarbons to the feed in real-world Ag catalysts: the selectivity to EtO is promoted at, however, some loss in overall activity (1-2,8,26,32-36). This confirms that the promoter effect is due to direct Cl atom - Ag interactions, and is unrelated to the support material (e.g. Al<sub>2</sub>O<sub>3</sub>). Note that the major effect occurs for chlorine coverages between the p(2x1) structure ( $\theta_{Cl} = 0.5$ ) and the c(4x2) structure ( $\theta_{Cl} = 0.75$ ). The high coverage for those changes and its correlation with distinct overlayer structures indicates that an ensemble rather than electronic factor plays the dominant role in promotion (26).

Note in Fig. 4 that the oxygen adatom coverage is already completely suppressed by  $\theta_{Cl} = 0.25$ , at which point the reaction rates have hardly changed. This further suggests that O<sub>2,a</sub> rather than O<sub>a</sub> plays the dominant role in the reaction mechanism. The decay in  $\theta_o^a$  with  $\theta_{Cl}$  almost perfectly reflects the dramatic decrease in the dissociative sticking probability for O<sub>2</sub> with chlorine coverage (26,27). We further found that, in this coverage range, the adsorption of molecular (peroxo-) O<sub>2</sub> is hardly affected by  $\theta_{Cl}$  (27), consistent with the minor effects of chlorine on the epoxidation rate for  $\theta_{Cl} < 0.25$  (Fig. 4).

The sophistication with which one can monitor the effects of a surface modifier in a catalytic reaction is demonstrated in Fig. 5. Using a whole series of measurements such as Fig. 4, with a broad range of temperatures and reactant pressures near 563 K, P<sub>O<sub>2</sub></sub> = 150 torr, and P<sub>Et</sub> = 20 torr, we were able to determine directly the variations with  $\theta_{Cl}$  in the apparent activation energies (E<sub>a</sub>) and reaction orders (m,n) for both EtO and CO<sub>2</sub> production (27).<sup>a</sup> At a given chlorine coverage, the reaction rates are written as:

$$TON = v \exp[-E_a/RT] P_{O_2}^m P_{Et}^n \quad (1)$$

The results are shown in Fig. 5.

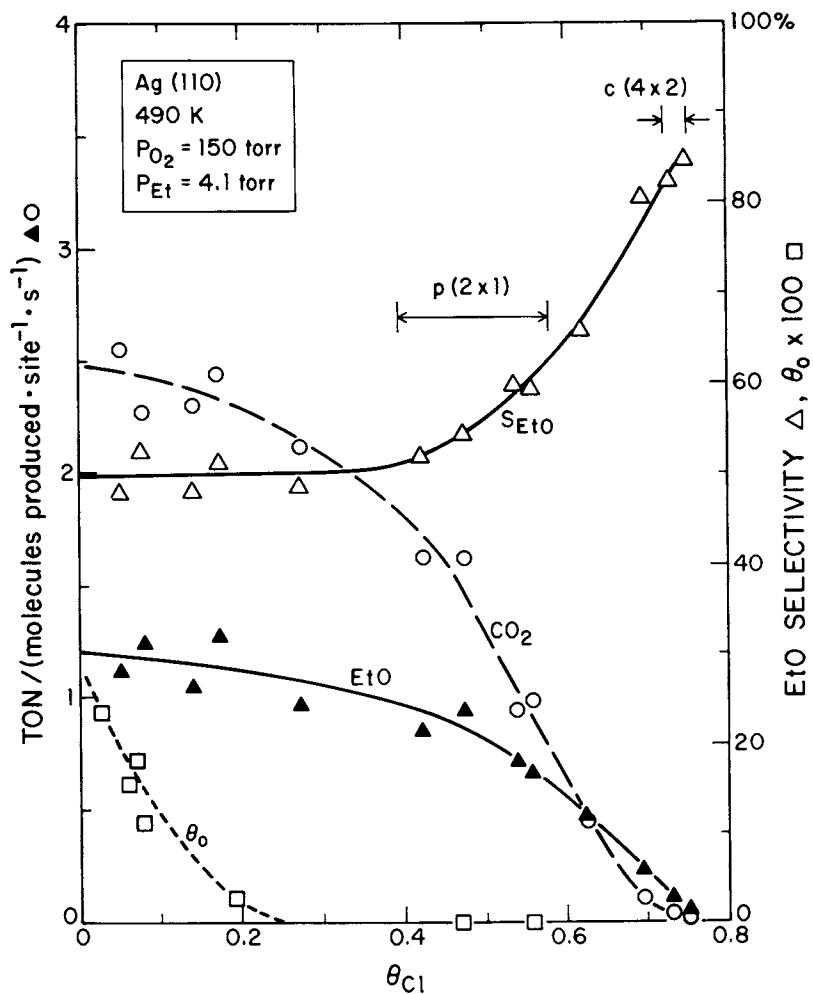


Figure 4. The effects of chlorine adatom coverage ( $\theta_{Cl}$ ) upon the rates, selectivity, and  $\theta_0$  on Ag(110) at 490 K and  $P_{O_2} = 150$  torr and  $P_{Et} = 4.1$  torr.

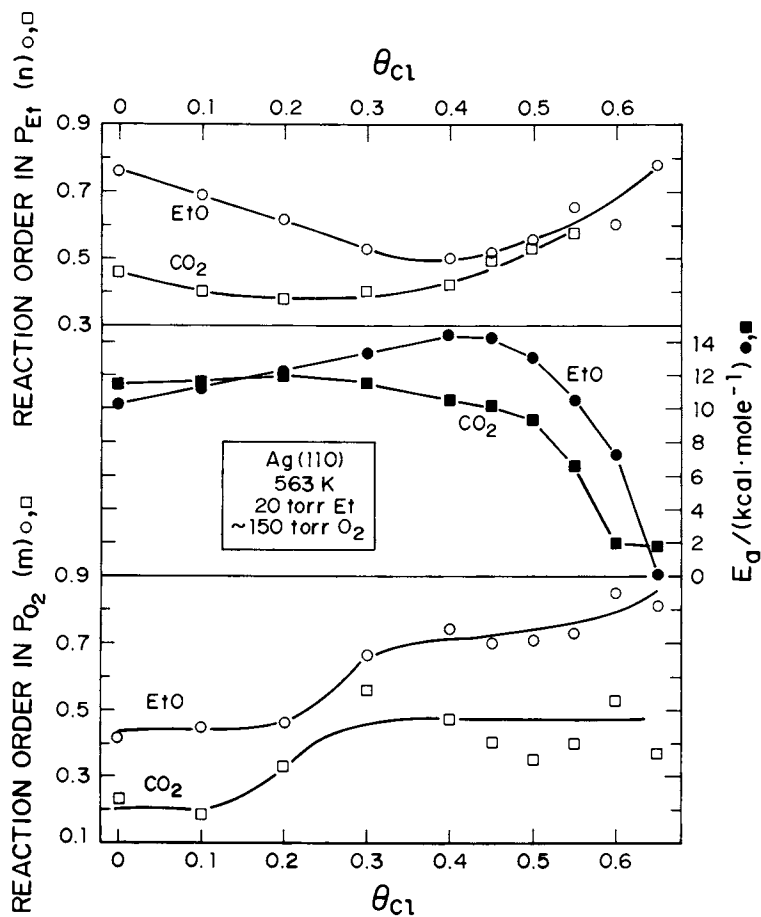


Figure 5. The variations in the apparent activation energies ( $E_a$ ) and reaction orders ( $m$ ,  $n$ ) with  $\theta_{C1}$  for EtO and  $CO_2$  production on Ag(110) at 563 K,  $P_{Et} = 20$  torr, and  $P_{O_2} = 150$  torr.

Mechanism

These results are all consistent with a mechanism which involves the combination of  $O_{2,a}$  and  $Et_a$  in the formation of an adsorbed intermediate,  $I_a$ , which can then branch out to evolve  $EtO$  (leaving an oxygen adatom behind on the surface) or to produce  $CO_2 + H_2O$ . The oxygen adatom thus inherent to  $EtO$  production must itself go on to make either  $CO_2$  or  $H_2O$ , which sets a theoretical upper-limit on the selectivity of 6/7. This agrees within experimental error with the maximum selectivity observed on both high surface area catalysts (2,35,37) and single-crystals (26,27).

Under most conditions the intermediate formation step,  $Et_a + O_{2,a} \rightarrow I_a$ , is rate-limiting. The branching of the intermediate is much faster. The reaction rates can be written

$$TON = v' \theta_{Et} \theta_{O_2} \exp[-E_a^{true}/RT] \quad (2)$$

where  $E_a^{true}$  is the activation energy for that true elementary step. The branching ratio will determine the value of  $v'$  for either  $EtO$  or  $CO_2$  production. The reaction orders in  $P_{O_2}$  and  $P_{Et}$  will depend upon the extent to which  $\theta_{O_2}$  and  $\theta_{Et}$  are saturated on the surface. The apparent activation energy [ $E_a$  in Equation (1)] will be determined by  $E_a^{true}$  and the variations in  $\theta_{Et}$  and  $\theta_{O_2}$  with temperature.

The variations in the kinetic parameters ( $E, m, n$ ) with chlorine coverage shown in Fig. 5 are entirely consistent<sup>a</sup> with our studies by thermal desorption spectroscopy, which show the effects of chlorine upon the heats of adsorption ( $\Delta H_a$ ) of molecularly adsorbed  $O_2$  and ethylene (27). For example, chlorine decreases  $\Delta H_a^{O_2}$ , and therefore  $\theta_{O_2}$ , which leads to the observed increase in  $m$ . Similarly, chlorine increase  $\Delta H_a^{Et}$  for  $\theta_{Cl} < 0.4$  and decreases  $\Delta H_a^{Et}$  for  $\theta_{Cl} > 0.4$  (26), which gives<sup>a</sup> rise to the minimum in  $n$  at  $\theta_{Cl} \cong 0.4$  in Fig. 5. We have also shown that the dependence in  $E_a$  upon  $\theta_{Cl}$  (Fig. 5) is completely consistent with this model and the dependences of  $\Delta H_a$  for  $O_2$  and ethylene upon  $\theta_{Cl}$  (27).

One feature of Fig. 5 is overwhelmingly obvious. Any changes in the kinetic parameters ( $E, m, n$ ) for  $EtO$  production are mimicked almost exactly by those for  $CO_2$  production. Thus there is nothing in Fig. 5 which helps to explain the very large selectivity increase seen under these conditions as  $\theta_{Cl}$  increases from 0.3 to 0.6 (27). This is because the selectivity is, to a large extent, determined by the relative rates of the branching steps after formation of the intermediate,  $I_a$ . Remember that these steps are fast. It is only the slow, intermediate-formation step which is reflected in variations of  $E, m$  or  $n$ . The branching ratio is, however, affected by chlorine.<sup>a</sup> Due to the large coverages for which the major selectivity increases occur ( $\theta_{Cl} > 0.4$ , Fig. 4), we propose that changes in the branching ratio are largely due to an ensemble effect. The process  $I_a \rightarrow EtO + O_a$  requires only a small ensemble of one or two

chlorine-free Ag sites. On the other hand, the decomposition of I into species which yield  $\text{CO}_2 + \text{H}_2\text{O}$  requires the cleavage of many<sup>a</sup> bonds and therefore most likely a larger ensemble of free Ag sites. It is this difference in ensemble size requirement which gives rise to the marked increase in selectivity as chlorine titrates the Ag sites.

### Conclusions

While in this short space we have barely touched upon the salient features of this reaction, we hope it has been sufficient to wet the readers' appetite to pursue the subject in more detail. This new approach to studying catalytic reactions is opening up major new avenues for their understanding.

### Acknowledgments

The author would like to thank M. T. Paffett and B. E. Koel for useful contributions to this work, and D. W. Goodman for valuable discussions.

### Literature Cited

1. H. H. Voge and C. R. Adams, *Adv. Catal.* 17 (1967) 151.
2. P. A. Kilty and W. M. H. Sachtler, *Catal. Rev.-Sci. Eng.* 10 (1974) 1.
3. W. M. H. Sachtler, C. Backx, and R. A. Van Santen, *Catal. Rev.-Sci. Eng.* 23 (1981) 127.
4. R. A. Van Santen, J. Moolhuysen, and W. M. H. Sachtler, *J. Catal.* 65 (1980) 478.
5. C. Backx, J. Moolhuysen, P. Geenen, and R. A. Van Santen, *J. Catal.* 72 (1981) 364.
6. E. L. Force and A. T. Bell, *J. Catal.* 40 (1975) 356.
7. E. L. Force and A. T. Bell, *J. Catal.* 38 (1975) 440.
8. X. E. Verykios, F. P. Stein, and R. W. Coughlin, *Catal. Rev.-Sci. Eng.* 22 (1980) 197.
9. X. E. Verykios, F. P. Stein, and R. W. Coughlin, *J. Catal.* 66 (1980) 147.
10. X. E. Verykios, F. P. Stein, and R. W. Coughlin, *J. Catal.* 66 (1980) 368.
11. M. Egashira, R. L. Kuczkowski, and N. W. Cant, *J. Catal.* 65 (1980) 297.
12. P. D. Klugherz and P. Harriott, *AIChE Journal* 17 (1971) 856.
13. P. L. Metcalf and P. Harriott, *Ind. Eng. Chem. Process Des. Devel.* 11 (1972) 478.
14. J. C. Wu and P. Harriott, *J. Catal.* 39 (1975) 395.
15. M. Stoukides and C. G. Vayenas, *J. Catal.* 69 (1981) 18.
16. M. Stoukides and C. G. Vayenas, *J. Catal.* 70 (1981) 137.
17. H. R. Dettwiler, A. Baiker, and W. Richarz, *Helvetica Chim. Acta* 62 (1979) 1689. (Specific rates taken from this paper were obtained by assuming the Ag surface area equal to the BET surface area of the catalyst. Justification for this is presented in Ref. (24).
18. A. Crzechowski and K. F. MacCormack, *Can. J. Chem.* 32 (1954) 415.
19. M. Akimoto, K. Ichikawa, and E. Echigoya, *J. Catal.* 76 (1982) 333.



20. S. Guseinov, I. Frolkina, L. Vasilevich, A. Avetisov, and A. Gel'bshtein, *Kinet. i Katal.* 18 (1977) 1188.
21. R. Haul, D. Hoge, G. Neubauer, and U. Zeech, *Surface Sci.* 122 (1982) L622.
22. M. A. Barteau and R. J. Madix, "The Chemical Physics of Solid Surfaces and Heterogeneous Catalysis," Ch. IV, Vol. IV, Ed. D. A. King (Elsevier Pub. Co., Amsterdam, 1982).
23. C. T. Campbell and M. T. Paffett, *Surface Sci.* 143 (1984) (in press).
24. C. T. Campbell, *J. Vac. Sci. Technol.* A2 (1984) 1024.
25. C. T. Campbell and M. T. Paffett, *Surface Sci.* 139 (1984) 396.
26. C. T. Campbell and M. T. Paffett, *Appl. Surf. Sci.* 19 (1984), Proc. 1983 Boston MRS Symp. (in press).
27. C. T. Campbell and B. E. Koel, *J. Catal.* (submitted).
28. C. T. Campbell (in preparation).
29. M. Riassian, D. L. Trimm, and P. M. Williams, *J. Catal.* 46 (1977) 82.
30. M. Jarjoui, P. C. Gravelle, and S. J. Teichner, *J. Chemie Physique* 75 (1978) 1069.
31. A. Presland, G. Price, and D. Trimm, *J. Catal.* 26 (1972) 313.
32. J. T. Kummer, *J. Phys. Chem.* 60 (1956) 666.
33. V. E. Ostrovskii, N. V. Kul'kova, V. L. Lopatin, and M. I. Temkin, *Kinet. i Katal.* 3 (1962) 160.
34. L. Y. Margolis, E. K. Enikeev, O. V. Isaev, A. V. Krylova, and M. Y. Kuchnerov, *Kinet. i Katal.* 3 (1962) 153.
35. N. Giordano, J. C. J. Bart, and R. Maggiore, *Z. Phys. Chemie NF* 127 (1981) 109.
36. R. G. Meisenheimer and J. N. Wilson, *J. Catal.* 1 (1962) 151.
37. J. C. Zomerdiijk and M. W. Hall, *Catal. Rev.-Sci. Eng.* 23 (1981) 163.

RECEIVED April 9, 1985

## Surface Structure and Reaction Dynamics in Catalysis

K. Christmann<sup>1</sup> and G. Ertl

Institut für Physikalische Chemie der Universität München, D-8000 München 2, Federal Republic of Germany

The interaction of H<sub>2</sub> and D<sub>2</sub> with Ni(110) and Ni(111) was investigated using molecular beam, LEED, and thermal desorption (TD) techniques to elucidate the interaction dynamics and the surface structure. Elastic H<sub>2</sub> scattering leads to marked diffraction only with Ni(110), whereas Ni(111) shows almost no corrugation. The difference in the elastically scattered H<sub>2</sub> and D<sub>2</sub> intensity reveals that the energy exchange is dominated by phonon and not by electronic excitations. The differences in the sticking probabilities  $s_0$  between the two faces suggest the absence of an activation barrier for Ni(110), but the existence of such a barrier (height ~0.1 eV) for Ni(111). Increasing H (D) coverages  $\theta_{H(D)}$  induce various surface structures on Ni(110) including two reconstructed phases. A one-dimensionally ordered 'streak' phase is the only stable phase above 250 K. With Ni(111) no reconstruction occurs and the H (D) atoms are disordered at 300 K. It is shown that the functions  $s(\theta)$  are influenced by the formation of the reconstructed phases; the implications for surface reactivity are discussed.

In the recent past much experimental and theoretical effort has been undertaken to understand the microscopic steps of heterogeneous surface reactions. The main problem consists of evaluating the total energy of the reacting components (including the surface atoms!) as a function of all nuclear coordinates at any reaction time. The solution of this problem is extremely difficult. Detailed studies with model systems, however, can shed some light upon the various steps of the interaction pattern.

Even the first step, the calculation of the multidimensional ground state energy of a single particle interacting with a surface implies a lot of difficulties. It is, for example, possible that the spacings

<sup>1</sup>Current address: Institut für Physikalische Chemie der FU Berlin D-1000 Berlin 33, Takustr. 3, Federal Republic of Germany

of various adjacent surface atoms change upon interaction with an adsorbate atom (surface relaxation or reconstruction). It is, e.g., well-known that chemisorbed hydrogen tends to reconstruct a number of metal surfaces, e.g., Ni, Pd, Mo, or W (1).

The second step has to include the multi-particle effects, and the total energy as a function of all geometrical configurations of the particles has to be evaluated.

The treatment of the reaction dynamics represents a further difficult barrier in the understanding of the heterogeneous reaction. It requires the knowledge of the cross sections determining the transitions between different states which in turn are correlated with the energy transfer into the various degrees of freedom.

In this article, we shall concentrate only on very simple surface reactions, namely, the adsorption of  $H_2$  and  $D_2$  and the  $H_2/D_2$  exchange reaction on the differently structured Ni(110) and (111) surfaces. Our experimental techniques comprise static techniques such as LEED, thermal desorption spectroscopy (TDS) and work function measurements ( $\Delta\phi$ ) and dynamic techniques like scattering of  $H_2$  and  $D_2$  molecular beams. Details of the experimental methods are given elsewhere (2,3).

The goal of this paper is to demonstrate the internal correlation between the surface structure and the reaction dynamics which, in extreme cases (Pt(100)!) can give rise even to kinetic surface oscillations (4). The Ni(110)/H system is another example where not only several lattice gas phases are formed by hydrogen but also reconstruction can occur depending on the temperature and the chemical potential of the adsorbed hydrogen. Phenomena like 'surface explosions' have been reported previously with this surface in the course of surface reactions, e.g., the decomposition of formic acid (5). We argue that structural changes of the surface during a heterogeneous chemical reaction may be responsible for effects of this kind.

### Experimental

The experiments were carried out in two different UHV chambers equipped with the standard facilities to clean and to characterize a metal single crystal surface. One apparatus was used for the 'static' investigations and contained a Video-LEED system including data processor, a mass spectrometer for TDS, and a Kelvin probe for measuring contact potential differences. The other apparatus consisted of a molecular beam source connected to a UHV scattering chamber with a rotatable mass spectrometer as well as LEED and Auger facilities. In the molecular beam (MB) source, the hydrogen was expanded through a 0.07 mm hole at pressures between 200 and 500 torr. The beam diameter and angular divergence were determined by an aperture in the final pumping stage of the source. At the surface, beam diameters of 1.5 - 2 mm and angular divergence of  $0.06^\circ$  were obtained. Owing to the comparatively mild expansion conditions of the nozzle the rotational distribution of the molecules remains essentially unaltered. Therefore the nozzle temperature determines directly the translational kinetic energy of the pure  $H_2$  or  $D_2$  beams. Kinetic energies of 26 meV and 64 meV beams corresponded to nozzle temperatures of 120 K and 300 K, respectively. Separation of molecules scattered directly from those being trapped

in the chemisorption potential was possible by modulating the incident beam at 63 Hz and using a lock-in technique.

The Ni(110) and (111) samples were prepared and cleaned in the usual manner (6). In the MB experiments, the azimuthal orientation was chosen such that the most corrugated direction was directed to the incident beam: The [001] direction for Ni(110) and the [11 $\bar{2}$ ] direction for Ni(111). Since both surfaces chemisorb hydrogen readily the experimental conditions in the MB experiments were adjusted to assure scattering from surfaces covered with less than 0.01 monolayers of H at all times. The sample orientations as well as the perfection of the surfaces were checked by LEED and by monitoring the relative intensities of the specularly reflected He beams.

## Results

The interaction of hydrogen (deuterium) molecules with a transition metal surface can be conveniently described in terms of a Lennard-Jones potential energy diagram (Fig. 1). It consists of a shallow molecular precursor well followed by a deep atomic chemisorption potential. Depending on their relative depths and positions the wells may or may not be separated by an activation energy barrier  $E^*$  as schematically indicated by the dotted curve in Fig. 1.

Here we shall be concerned with the interaction of incoming diatomic molecules ( $H_2$ ,  $D_2$ ) with either types of potential energy wells: The molecular interaction (responsible for elastic and direct-inelastic scattering with extremely short residence times of the impinging molecules in the potential) and the chemisorptive interaction (leading to dissociative adsorption and associative desorption, respectively, and associated with H (D) atoms trapped in the chemisorption potential for an appreciable time).

The elastic scattering. The elastic scattering of a diatomic molecule obeys the rules for conservation of energy and momentum; there is no energy exchange between the surface and the incident particle. However, the possibility for internal transformation of translational into rotational energy states has to be taken into account particularly with non-symmetric molecules like HD as was, e.g., shown by Cowin et al. (7) for a Pt(111) surface. Translation - vibration energy transformation requires too much energy to occur under our experimental conditions. The modulated beam technique conveniently allows a separation of the elastically scattered molecules from those which have been formed by recombination from chemisorbed atoms. The angular distribution of the scattered molecules is a direct probe to distinguish elastically scattered from inelastically scattered particles (8). In Fig. 2a,b we display the angular distributions obtained for  $H_2$  molecules scattered from Ni(110) and Ni(111) in the zero-coverage limit. The azimuthal orientation of the surfaces is indicated in the figure.

For Ni(110) the angular distribution exhibits pronounced diffraction peaks, in addition to an intense specularly reflected beam. The position of the diffraction maxima agrees with the prediction from the known lattice constant and the initial velocity of the particle.

With Ni(111) there is practically no diffraction visible which clear-

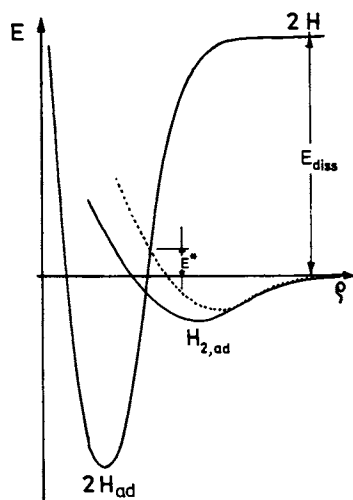


Figure 1. One-dimensional Lennard-Jones potential energy diagram for adsorption of a diatomic molecule (hydrogen).  $\rho$  denotes the reaction coordinate.

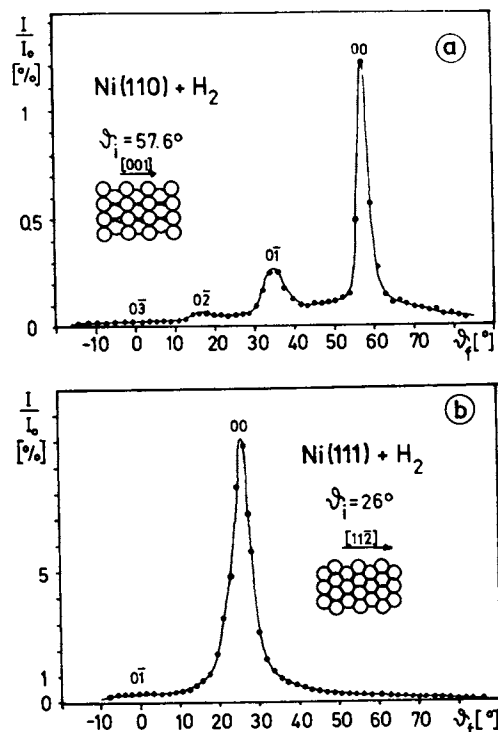


Figure 2. Angular distribution of the relative scattered intensity of hydrogen molecules scattered from a) Ni(110); b) Ni(111). The angle of incidence of the molecular beam and the azimuthal orientation of the surface are indicated in the figure.

ly demonstrates the much smoother nature of this densely packed surface. With both surfaces  $H_2$  scattering leads only to a very small background with a flat maximum in the specular direction. Apparently, most of the incident molecules suffer true elastic scattering.

Angular distributions for  $D_2$  scattering from the same crystal planes are presented in Fig. 3a, b. Again, pronounced diffraction features are apparent only with Ni(110). Interestingly, however, there is now a much larger fraction of diffuse background intensity observed which peaks strongly in the specular direction. This background intensity clearly arises from the so-called direct-inelastic scattering which will be described next.

The direct-inelastic scattering. This type of scattering originates from energy exchange processes between the incident molecule and the surface during a single collision event. Multiple collisions are, to a first approximation, negligible owing to the small mass ratio  $m/M$  where  $m$  denotes the mass of the incident particle and  $M$  stands for the mass of the surface atom. The energy exchange can occur through either electron-hole pair excitation (whereby electrons are excited from just below to just above the Fermi level, a process also referred to as 'electronic friction'), or through excitation of metal phonons which couple to resonance states of the incoming particle. Accordingly, the first process should depend on the electronic configuration of the particle and the density of states at the Fermi level of the substrate, but not on the mass of the incident particle, whereas the second energy dissipation mechanism, the phonon interaction, should be a function of the mass ratio  $m/M$ , that is, of the mass  $m$  of the incident particle. A comparison of the intensities of the elastically scattered beams of hydrogen and deuterium from the same surface reveals that the elastically scattered intensity (for particles with equal velocity, i.e., equal residence time near the surface) is appreciably larger for hydrogen than for the heavier deuterium molecule. It is thus indicated that the accommodation or dissipation of the kinetic energy of the incident particle is dominated by excitation and annihilation of phonons and not by electron-hole pair excitation. This conclusion is in agreement with recent theoretical calculations (9) which showed that the latter process occurs only with very small probability.

The dissociative adsorption. From the MB studies it appears that a great fraction of incident  $H_2$  molecules dissociates. The H atoms are held so tightly on the surface that, even around 300 K, their rate of recombination and thermal desorption is quite small, at least at low surface concentrations  $\theta_H$ .

The sticking probability  $s_0$ . We refer to the sticking probability as to the relative probability for the chemisorption process to occur with respect to the total number of molecules incident on the surface.  $s_0$  is determined from the area under a TDS curve as described elsewhere (10). For Ni(110), we obtain  $s_0 = 0.96$  for equal surface and gas phase temperatures  $T_s = T_g = 300$  K. Our value agrees well with data reported in the literature (11); we also point out that, within our limits of accuracy, no difference was found between  $s(H)$  and  $s(D)$ . It is also important to note that for Ni(110)  $s_0$  does not depend on  $T$  between 100 K and 800 K. In contrast to this face,  $s_0$  is much lower for Ni(111), namely  $s_0 = 0.1$ , which is in agreement with numbers re-

ported previously (12). Unlike Ni(110)/H, we find with Ni(111)/H a pronounced dependence of  $s_0$  on the angle of incidence,  $\vartheta_i$ :

$$s_0(\vartheta_i) = s_0(\vartheta_i = 0^\circ) \cdot \cos^4 \vartheta_i \quad (1)$$

This result indicates that  $s_0$  depends on the kinetic energy of the momentum perpendicular to the surface,  $\langle E_{\perp} \rangle$ . By changing either the angle of incidence  $\vartheta_i$  or the nozzle temperature we could vary  $\langle E_{\perp} \rangle$  between 26 meV and 120 meV. We observe a significant increase of  $s_0$  from very small values ( $< 0.1$ ) at the lowest  $\langle E_{\perp} \rangle$  up to about 0.4 at  $\langle E_{\perp} \rangle = 120$  meV. The shape of the relation  $s_0(\langle E_{\perp} \rangle)$  suggests that higher  $\langle E_{\perp} \rangle$  values would lead to even higher sticking coefficients so that eventually values similar to Ni(110)/H could be expected. We have also investigated the dependence of  $s_0$  on the temperature, for  $\langle E_{\perp} \rangle = 64$  meV. As with Ni(110),  $s_0$  does apparently not depend on the temperature. This finding is in agreement with a report by Rendulic and Winkler (13). Our results can be rationalized in terms of the potential energy diagram of Fig. 1. They suggest the existence of an activation barrier  $E^* > 0$  for the Ni(111)/H system, whereas no such barrier is present with H/Ni(110). Obviously this barrier can be overcome by hydrogen molecules with sufficiently high translational energy (as suggested by the  $\langle E_{\perp} \rangle$  dependence). An increase of the thermal energy of the solid, on the other hand, does not make the sticking process more efficient. Such an influence of the surface temperature would only be expected if dissociation would occur through a molecularly held precursor state. Not only would the activation barrier  $E^*$  be overcome by the thermal energy of the surface but also the phonon assisted trapping in the molecular state should then increase with  $T_s$ . In contrast, our results demonstrate that direct collision from the gas phase is the most efficient channel for dissociation and trapping in the chemisorption potential.

By extending the TDS technique mentioned before to finite coverages,  $\theta_H$ , the function  $s(\theta_H)$  may be evaluated. As will be shown in the next section, there are various different surface phases formed with Ni(110) as the hydrogen coverage increases from 0 to one monolayer. At sufficiently high temperatures ( $T > 250$  K) chemisorbed hydrogen causes a reconstruction of the  $1 \times 1$  surface to a phase ordered in only one direction, the so-called 'streak' phase (2,14). Fig. 4 shows the variation of the relative sticking coefficient,  $s/s_0$ , as a function of the relative coverage,  $\theta/\theta_{\max}$ . Apparently,  $s$  remains constant up to about 40% of the saturation coverage and thereafter decreases to zero. The way in which this data was obtained, namely by TDS, however, brings it about that any fine structure in  $s(\theta)$  maybe largely obscured. The situation changes somewhat if the hydrogen is adsorbed at low temperatures (120 K) and the TD program is run at very high heating rates so that thermally activated phase transformations cannot gain importance. Adsorption at 120 K then leads to a  $s(\theta)$  function which is shown in Fig. 4 as a dotted line. Again, there is a constant sticking probability up to about 0.5 monolayers, thereafter  $s$  drops as expected. However, around 1 monolayer coverage there occurs a spontaneous reconstruction to a  $1 \times 2$  phase which is connected with the generation of 0.5 monolayers of additional H adsorption sites. In the  $s(\theta)$  curve this leads to a second plateau at  $\theta_H = 1$  when

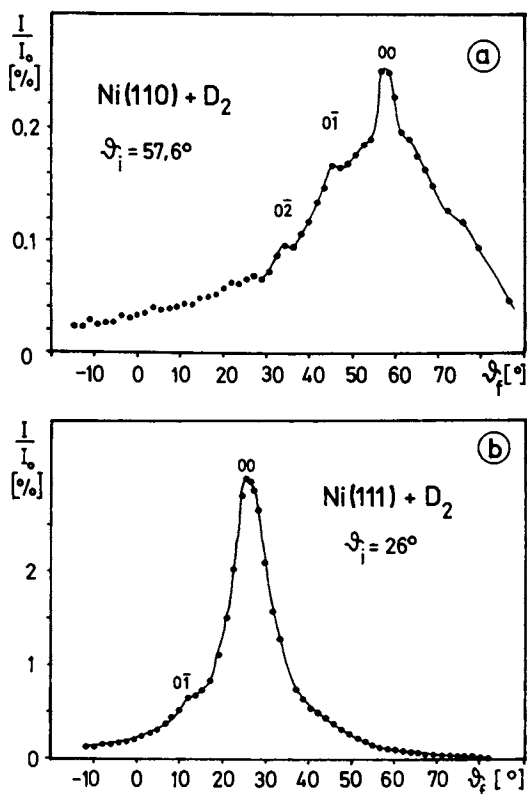


Figure 3. Angular distribution of the relative scattered intensity of deuterium molecules scattered from a) Ni(110); b) Ni(111). The experimental conditions were the same as in Figure 2.

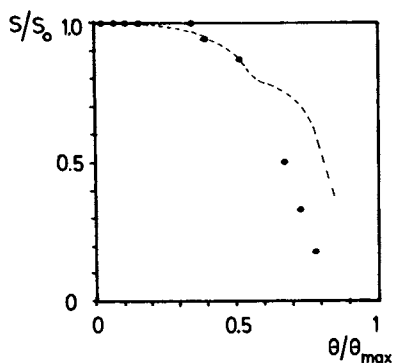


Figure 4. Variation of the relative sticking probability,  $s/s_0$ , with  $\theta(H)_{\text{rel}}$  for H<sub>2</sub> on Ni(110). The dashed line refers to experiments in which the hydrogen was adsorbed at 120 K and rapidly desorbed (see text for details).



the additional adsorption sites become occupied. With Ni(111), the coverage dependence of  $s$  differs markedly from that of Ni(110) as is evident from Fig. 5. Not only is  $s$  much lower for reasons explained before, but  $s/s_0$  decreases quite steeply even at fairly low coverages. Again,  $s_0$  this behavior has been reported previously (11,12). From LEED work (15) it is known that, below 270 K, an ordered  $\sqrt{2} \times \sqrt{2}$  H phase is formed at  $\theta_H = 0.5$  in which the H atoms are arranged in a honeycomb-like structure. The Ni(111) surface thereby does not reconstruct. Unlike the Ni(110)/H system, the formation of the  $\sqrt{2} \times \sqrt{2}$  phase does not have any effect on the sticking probability coverage function. It appears from our data that such an effect is only to be expected if the metal surface undergoes reconstruction and provides a different number of adsorption sites as compared to the unreconstructed surface. On the other hand, the simple fact that a surface is covered with an ordered or disordered overlayer is apparently not sufficient to alter the  $s(\theta)$  relation noticeably.

The hydrogen surface phases. 1. Ni(110). As described in more detail elsewhere (2,6,14,16) hydrogen adsorption at 120 K leads to a variety of surface phases, depending on the temperature and the local coverage. In the submonolayer regime ( $0 < \theta_H < 1$ ) and at temperatures below 180 K at least four lattice gas structures can be observed on the unreconstructed Ni(1x1) surface; the final phase being a  $2 \times 1$ -2H structure at 1.0 monolayer H coverage. In this phase, all H atoms are located in threefold sites and form a zig-zag array as was first proposed from He diffraction work by Rieder and Engel (17). At a critical H coverage of 1.1 monolayers, however, a spontaneous reconstruction occurs to a well-ordered  $1 \times 2$  phase. The topmost Ni atoms are very likely displaced in [001] direction so as to form double rows. This reconstruction leads to the creation of 50% new H adsorption sites to yield a saturation coverage of 1.5 monolayers! The situation is illustrated by means of the structure model of Fig. 6. Interestingly, the  $1 \times 2$  reconstruction represents only one possible reaction channel. Always superimposed is a second reconstruction path (18) which is thermally activated and produces the 'streak' phase. Below 150...180 K the rate of formation of the streak phase is negligibly small. Above 200 K, however, it gains more and more importance until, around 250 K, exposure of hydrogen leads directly and exclusively to the formation of the streak phase. There is still another interesting phenomenon: The low-temperature  $1 \times 2$  phase is thermally unstable and 'explodes' exactly at  $T = 220$  K accompanied by a sudden release of hydrogen in a very narrow TD state (14). This 'surface explosion' is apparently associated with the thermal decomposition of a H-containing surface compound, possibly nickel hydride.

Since the streak phase is the only stable surface structure in the presence of hydrogen at elevated temperatures where most of the heterogeneous surface reactions are run it is worthwhile to communicate some more details about its structure. Although no dynamical analysis has been successful so far it is clear from LEED and He scattering data (14,17) that the long-range periodicity has been lost in the [001] direction whereas the long-range order is retained in the perpendicular  $[1\bar{1}0]$  direction. In Fig. 7 we propose a structure model: It is therein assumed that only locally and randomly adjacent Ni atoms are displaced in [001] direction thereby giving rise to the observed disorder in that direction. There are other possibilities to

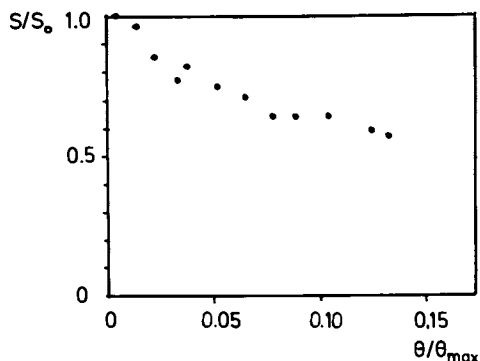


Figure 5. Variation of the relative sticking probability,  $s/s_0$ , with  $\theta(H)_{rel}$ , for  $H_2$  adsorbed on Ni(111). Note the expanded coverage scale!

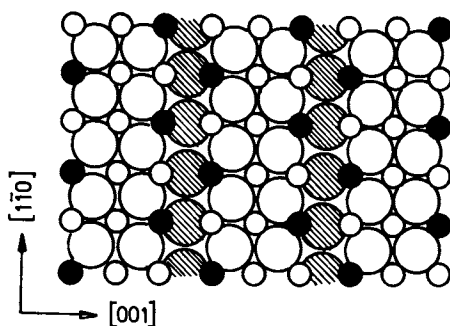


Figure 6. Structure model of the reconstructed  $1 \times 2$  phase formed with Ni(110) at coverages  $> 1$  monolayer. Small circles: H atoms; dark circles: Additionally provided adsorption sites for H. Shaded atoms belong to the second Ni layer.

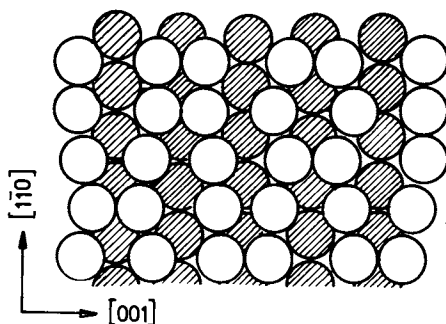


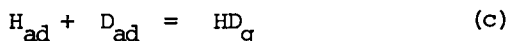
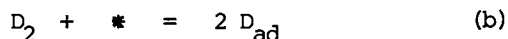
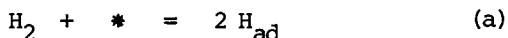
Figure 7. Proposed structure model of the one-dimensionally ordered 'streak' phase, the second reconstructed phase observed with the H/Ni(110) system. Again, shaded circles represent Ni atoms of the second layer.

explain the streak structure. One could argue that something like domain walls separate the Ni atom rows from each other in [001] direction (19): In the 1x2 structure all these domain walls are strictly parallel whereas in the streak phase the distances in [001] direction between two row atoms vary statistically between a minimum and a maximum value. Accordingly, the 'correlation length' in [110] direction may vary between, say, two and 10 to 20 atomic distances. We admit here that more work has to be done in order to elucidate the nature of this interesting surface phase which has been known since the early days of LEED (20).

2. Ni(111). An extensive structure determination based on LEED investigations was given in previous work (12). As mentioned before a c2x2-2H phase is formed by 0.5 monolayers of H below 270 K whereby the (111) face does not reconstruct. Our structure model for the H lattice gas phase is shown in Fig.8 and was confirmed several times in the recent past (21-23).

It is worthwhile to point to an interesting difference between the H/Ni(110) and H/Ni(111) systems. For coverages below about 0.1 monolayer there is a marked difference in the isosteric heat of adsorption. With Ni(110)  $E_{ad}$  values around 17 kcal/mole have been measured whilst with Ni(111) the H atoms are more tightly bound, namely with 25 kcal/mole (24). At medium and higher coverages the two faces then behave more similarly with  $E_{ad}$  values around 22...23 kcal/mole. Again, an important factor here is the H-induced reconstruction which occurs with Ni(110) only and already at very low coverages. One could argue that the energy required to displace the Ni surface atoms is withdrawn from the heat of adsorption.

The  $H_2/D_2$  exchange reaction. This reaction was studied with both surfaces in the wide temperature range from 100 K to 600 K; details are communicated in a separate article (25). The  $H_2/D_2$  exchange is known to be of the Langmuir-Hinshelwood type and proceeds via the following mechanism:



(\* denotes an empty adsorption site)

Since the recombination step (c) does not principally differ from a recombination of two H or D atoms to the respective homonuclear molecule there is no reason to assume a special activation barrier for a H and a D atom to recombine to the HD molecule. Therefore the rate of the HD production is solely determined by the rates of adsorption of H and D, respectively (as long as the reaction is adsorption-controlled, i.e., at high enough temperatures), or by the rate of desorption of HD (provided the reaction is desorption-controlled, i.e., at low temperatures). If we deal with the first case only we may write:

$$r_{ad}(H) = s_o(H) \cdot f(\theta) \cdot P_{H_2}^{1/2} (2\tau mkT) \quad (2)$$

$$\text{and } r_{ad}(D) = s_o(D) \cdot f(\theta) \cdot P_{D_2}^{1/2} (4\tau mkT) \quad (3)$$

For equal sticking probability and coverage function  $s(\theta)$  the reaction rate is obviously controlled by the gas pressures of hydrogen and deuterium:

$$\text{rate } r = \frac{d[\text{HD}]}{dt} \propto s(\theta_{\text{H}}) \cdot s(\theta_{\text{D}}) \cdot P_{\text{H}_2, \text{D}_2} \quad (4)$$

Exactly this behavior was confirmed in the experiment. As can be seen from Eq. (4) the sticking probabilities represent very sensitive parameters which govern the rate of HD formation, or, more generally, the rates of product formation of all surface reactions in which the adsorption of the reactants is rate-limiting. It is immediately realized that irregularities in the  $s(\theta)$  functions, caused by surface reconstruction phenomena, or by segregation of foreign atoms in certain coverage ranges, or by the formation of surface defects may influence the rate of a catalytic reaction substantially.

### Discussion

Concerning the interaction dynamics of  $\text{H}_2$  ( $\text{D}_2$ ) with Ni surfaces in the first place we have elaborated some important differences with regard to the surface orientation and also with regard to the mass of the incident molecule. The Lennard-Jones potential of Fig. 1 has frequently been used to model the dissociative adsorption process although it provides a description only in one dimension. Experimental (26) and theoretical (27) studies on  $\text{H}_2$  interaction with metal surfaces suggest that the depth of the molecular potential well ( $\epsilon_{\text{H}_2}(\text{ad})$ ) ranges from 20 to 50 meV (= 0.5...1.2 kcal/mole). The minimum is located between 2.5 and 3 Å in front of the surface (formed by the plane interconnecting the nuclei of the topmost metal atoms). This distance also represents sort of a van-der-Waals bond length of the physisorbed  $\text{H}_2$  molecule.- As far as the location of the chemisorption potential is concerned there exists a collection of hydrogen-metal binding energy data (28), mainly based on measurements of the isosteric heat of adsorption. For transition metals, these values range from 60 to 65 kcal/mole (= 2.6 to 2.8 eV) for a single H-Me bond. For Ni(110) and Ni(111) these numbers are fairly accurately known, namely, 60 and 64 kcal/mole, respectively. Unfortunately, not very many determinations of the bond lengths of chemisorbed H atoms (=the distance of the chemisorption potential to the surface) have been performed so far, but just for Ni(111)/H our LEED structure determination (12) revealed a Ni-H bond length of 1.84 Å which corresponds to a location of the minimum of the chemisorption potential 1.15 Å in front of the (111) surface plane.

A principal new result of our MB study is the confirmation of a small activation energy barrier for H adsorption on the Ni(111) surface which is responsible for the unusually small sticking probability. Its height can be estimated to be around 0.1 eV. On the other hand, the MB data clearly showed the absence of such a barrier for the Ni(110) surface.

From the one dimensional representation of the potential energy diagram one cannot decide whether the dissociative adsorption takes place through intermediate trapping in the molecular state or through

high kinetic energy to pass the barrier (29). It has been shown that the first of these two mechanisms holds for the system  $H_2/Pt(111)$  (30), and also for  $N_2/Fe(111)$  (31). In the latter case the molecularly adsorbed species could be identified by vibrational spectroscopy at low temperature and thermally activated dissociation (in the absence of gaseous  $N_2$ ) occurred upon raising the temperature. However, for  $H_2/Ni$  our data suggest that the direct collision mechanism holds. They also reveal that, even for high enough initial kinetic energy, not all of the impinging molecules stick but rather are scattered at the molecular potential to yield, in the case of the corrugated  $Ni(110)$  surface, pronounced diffraction features. The energy exchange with the solid is provided by phonons as shown by the difference in elasticity between  $H_2$  and  $D_2$ .

With  $Ni(111)$  the scattering will essentially occur before the crossing point of the molecular and atomic potential curves whereas for  $Ni(110)$  this scattering occurs beyond this crossing point. In order to gain more insight into the detailed scattering mechanism realistic multi-dimensional adiabatic hyperface calculations are required. The only existing calculation of this kind was performed by Nørskov (32) with the system  $Mg(0001)/H_2$ . He calculated the total energy as a function of the distance  $x$  of the  $H_2$  molecule from the surface (oriented parallel to the surface) and of the internuclear distance  $y$  between the two H atoms. Indeed this potential exhibits two activation barriers: Barrier A for adsorption into the molecular state, and barrier B for dissociative adsorption. We neglect barrier A for which we have no hint from our experiments, and display the modified Nørskov potential in Fig. 9 a. Here, an incident  $H_2$  molecule would not automatically transfer its kinetic energy into a H-H vibration parallel to the surface (which would cause dissociation). A much easier channel for this process to occur would be thermal activation of the H-H vibration by phonon coupling to the solid while the molecule is trapped in the molecular state. The fact that the sticking probability is T-independent rules out this mechanism for the present case. Rather, a potential energy diagram of a type shown in Fig. 9 b is adequate to describe the situation. The activation barrier for dissociation is overcome simply by translational energy without the requirement for intermediate trapping in the molecular state. The potential diagrams shown in Fig. 9 resemble those for atom - molecule reactions of the type:  $A + BC \rightarrow AB + C$  (33). Again, the reaction can proceed via translational or via vibrational excitation, depending on whether the barrier of activation is located in the entrance (reactant side) or exit (product) channel.

An important aspect of the present work is the dependence of the sticking probability on the surface coverage of an adsorbate. This will be the topic of the second part of the discussion.

The rate of many surface reactions is governed by the velocity of adsorption of the reactants which in turn depends upon the sticking probability (see, e.g., Eq. (4)). A very illustrative example here is the promotive effect of potassium in the  $NH_3$  synthesis reaction over Fe catalysts (34). As we have shown not only foreign atoms can lead to variations of the sticking probability of several orders of magnitude but also structural changes of a surface of a catalyst during the reaction which may take place whenever certain critical adsorbate coverages are reached. An example is  $Ni(110)/H$  where a  $1 \times 2$  reconstruction

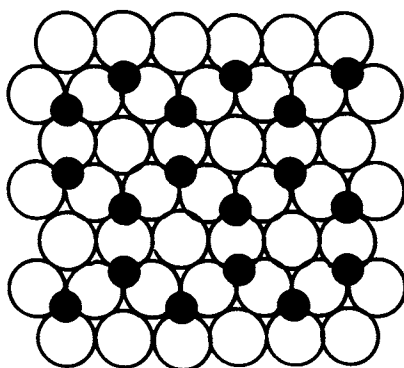


Figure 8. Structure model of the  $c2 \times 2-2H$  phase formed by hydrogen at  $\theta_H = 0.5$  monolayers on Ni(111).

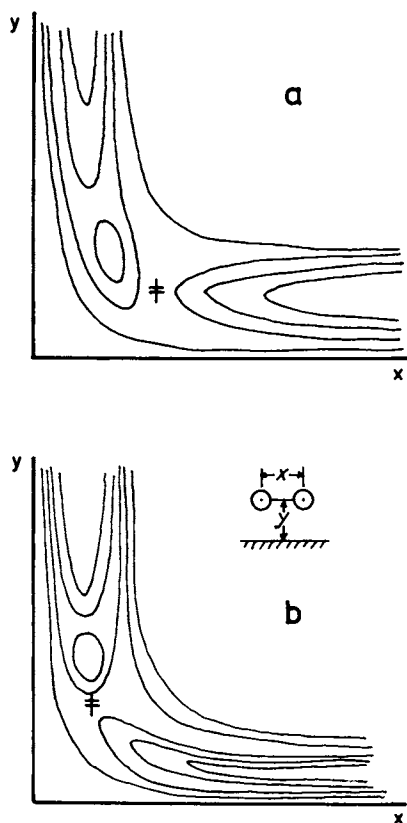


Figure 9. Two-dimensional representation of the potential energy diagram for a  $H_2$  molecule interacting with a solid surface.  
 a) Activation barrier for dissociation in the 'entrance' channel  
 b) Activation barrier for dissociation in the 'exit' channel

at  $\theta_H = 1.0$  creates many new adsorption sites to which the H atoms can stick. Even more spectacular is the situation with the CO oxidation reaction over a Pt(100) surface. It was found (35, 36) that there are periodic variations in the CO<sub>2</sub> production rate provided that certain crucial conditions of temperature and composition of the reaction mixture are fulfilled. A detailed LEED, TDS and  $\Delta\phi$  analysis (37) showed that a cooperative effect between surface structure (which can change by reconstruction from 1x1 to 5x20) and the sticking probabilities for oxygen and carbon monoxide is responsible for this interesting instability of the reaction rate.

Apart from coverage dependences the influence of temperature variations must also be considered. Again, the H/Ni(110) system is a good example to demonstrate this. In the section where the surface phases were described it was mentioned that the 1x2 reconstructed surface phase is thermally unstable and decomposes in a very narrow temperature range. Whenever such decomposition reactions can occur during a heterogeneous reaction dramatic changes in the rates of product formation are to be expected. In such a case the rate of the product is no longer diffusion controlled but depends on the rate of decomposition of the corresponding surface species. An effect of this kind has been reported some years ago by Falconer & Madix (5) with the decomposition of formic acid over a Ni(110) surface. In order to explain the dramatically high ('explosion-like') evolution of CO<sub>2</sub> at a certain temperature the authors assumed an autocatalytic reaction mechanism. From our investigations of the H<sub>2</sub> desorption from Ni(110) we know that the break-down of a certain surface phase can, in a very short period of time, destroy a large number of (formerly occupied) adsorption sites. The respective particles can no longer be held on the surface and are simply released or 'exploded' into the gas phase, whereby momentarily extremely high surface pressures are built up. A similar phenomenon has quite recently been observed with the NO<sub>2</sub> desorption and decomposition on a Pt(100) surface by Niehus (39), where the fore-mentioned 1x1  $\rightarrow$  5x20 phase transformation induced a narrow TD peak to occur. Other examples are provided by co-adsorption studies of CO and H<sub>2</sub> on Ni(110) (38), Ni(100) (40), and Rh(100) (41): It appears that the temperature position and the number of narrow H TD states depends on the surface concentration of the co-adsorbed CO. It is feasible that the more strongly bound CO molecule in some way 'clamps' the unstable 1x2 (for Ni(110)) configuration together so that this phase can exist at temperatures higher than 220 K (the break-down temperature of the Ni(110)-1x2 H phase without CO).

In general, all structural changes which occur during a surface reaction (reconstruction, or removal of reconstruction) can have a marked effect on both the rate of adsorption and desorption. Possible candidates for these phenomena to occur are all metal surfaces which can undergo reconstruction upon interaction with a chemically active adsorbate. Interesting systems here are (besides the already known Pt(100) or Ni(110) faces) Ir(100)/O,CO or W(100)/H and Mo(100)/H.

### Conclusions

It was shown that, for the interaction of H<sub>2</sub> with Ni(110) and (111), dissociative adsorption occurs via a 'direct' collision mechanism. A small activation barrier exists only for Ni(111)/H. The sticking is do-

minated by phonon coupling and not by electron-hole pair excitation. The coverage dependence of the sticking probability generally reflects structural phase transformations of the surfaces as long as significant changes of the number of adsorption sites are accompanied with the reconstruction. Critical coverages or thermal instabilities of surface structures can lead to unusually high reaction rates (so-called 'surface explosions'). This was confirmed with the H/Ni(110) system.

#### Acknowledgments

Financial support of this work through the Deutsche Forschungsgemeinschaft (SFB 6 and 128) is gratefully acknowledged.

#### Literature Cited

1. Christmann, K. In "Atomistics of Fracture"; Latanision, R.M., Pickens, J.R., Ed.; Plenum Press: New York, 1983, p.363.
2. Christmann, K.; Penka, V.; Ertl, G.; Behm, R.J.; Chehab, F.; in preparation
3. Campbell, C.T.; Ertl, G.; Kuipers, H.; Segner, J.; Surface Sci. 1981, 107, 220
4. Ertl, G.; Proc. 6th Eur. Conf. Surf. Sci.; York 1984, in press
5. Falconer, J.L.; Madix, R.J.; Surface Sci. 1974, 46, 473
6. Behm, R.J. Ph.D. Thesis, University of Munich, 1980
7. Cowin, J.; Yu, C.-F.; Sibener, S.J.; Wharton, L.; J. Chem. Phys. 1983, 79, 3537
8. Engel, T.; J. Chem. Phys. 1978, 69, 379
9. Schöenhammer, K.; Gunnarsson, O.; Surface Sci. 1982, 117, 53
10. Christmann, K.; Ertl, G.; Pignet, T.; Surface Sci. 1976, 54, 365
11. Winkler, K.; Rendulic, K.D.; Surface Sci. 1982, 118, 19
12. Christmann, K.; Behm, R.J.; Ertl, G.; van Hove, M.A.; Weinberg, W.H.; J. Chem. Phys. 1979, 70, 4168
13. Rendulic, K.D.; Winkler, K.; J. Chem. Phys. 1983, 79, 515
14. Christmann, K.; Chehab, F.; Penka, V.; Ertl, G.; Surface Sci., in press
15. Van Hove, M.A.; Ertl, G.; Christmann, K.; Behm, R.J.; Weinberg, W.H.; Solid State Commun., 1978, 28, 373
16. Penka, V.; Christmann, K.; Ertl, G.; Surface Sci., 1984, 136, 307
17. Rieder, K.H.; Engel, T.; Phys.Rev.Lett., 1979, 43, 373; 1980, 45, 824
18. Christmann, K.; Penka, V.; Chehab, F.; Ertl, G.; Behm, R.J.; Solid State Commun., 1984, 51, 487
19. Christmann, K.; Rys, F.S., in preparation
20. May, J.W.; Advanc. Catal. Rel. Subj., 1970, 21, 219
21. Domany, E.; Schick, M.; Walker, J.S.; Solid State Commun., 1979, 30, 331
22. Ibach, H.; Bruchmann, H.D.; Phys. Rev. Lett., 1980, 44, 36
23. Varelas, C.; Sailer, E.; Verhandl. Dtsch. Phys. Ges. 1983, 4, 829
24. Christmann, K.; Schober, O.; Ertl, G.; Neumann, M.; J.Chem.Phys., 1974, 60, 4528
25. Robota, H.; Vielhaber, W.; Ertl, G.; Segner, J.; to be published
26. Lapujoulade, J.; Perreau, J.; Physica Scripta, 1983, T4, 138



27. Liebsch, A.; Harris, J.; Surface Sci., 1983, 130, L349
28. Ertl, G.; In "The Nature of the Surface Chemical Bond"; Rhodin, T.N.; Ertl, G., Ed.; North Holland Amsterdam, 1979, p. 315 ff.
29. King, D.A.; CRC Crit. Rev. Solid State and Mater. Sci., 1978, 7, 167
30. Poelsema, B.; Verheij, L.K.; Comsa, G.; Surface Sci., in press
31. Grunze, M.; Golze, M.; Freund, H.-J.; Seip, U.; Tsai, M.C.; Ertl, G.; Küppers, J.; to be published
32. Nørskov, J.K.; Hounvøller, A.; Johansson, P.K.; Lundqvist, B.I.; Phys. Rev. Lett., 1981, 46, 257
33. Polanyi, J.C.; Schreiber, J.L.; In "Physical Chemistry - An Advanced Treatise", Jost, W. Ed.; Academic Press, London, Vol. VIa 1974, ch. 6
34. Ertl, G.; Weiss, M.; Lee, S.B.; Chem. Phys. Lett., 1979, 60, 391
35. Rüstig, J.; Ph.D. Thesis, University of Munich, 1982
36. Ertl, G.; Norton, P.R.; Rüstig, J.; Phys. Rev. Lett. (1982), 49, 177
37. Cox, M.P.; Ertl, G.; Imbihl, R.; Rüstig, J.; Surface Sci., 1983, 134, L517
38. Penka, V.; Behm, R.J.; Ertl, G.; in preparation
39. Schwalke, U.; Niehus, H.; Comsa, G.; Surface Sci., in press
40. A. Goodman, D.W.; Yates, J.T.; Madey, T.E.; Surface Sci.; 1980, 93, L135
40. B. Koel, B.E.; Peebles, D.E.; White, J.M.; Surface Sci.; 1983, 125, 709 and References therein.
41. Peebles, D.E.; Peebles, H.C.; White, J.M.; Surface Sci.; 1984, 136, 463

RECEIVED March 11, 1985

## Laser-Induced Thermal Desorption with Fourier Transform Mass Spectrometric Detection

M. G. Sherman, J. R. Kingsley, R. T. McIver, Jr., and J. C. Hemminger

Department of Chemistry, University of California—Irvine, Irvine, CA 92717

Fourier transform mass spectrometry (FTMS) is utilized to detect molecules thermally desorbed by a pulsed laser from a single crystal surface. Desorbed species are ionized by electron impact and detected in the analyzer cell of the FTMS spectrometer. FTMS has many advantageous features, such as high sensitivity, ultra-high mass resolution, simultaneous detection over a large mass range, and close proximity of the detector with respect to the crystal. The characteristics of the surface temperature jumps and resulting molecular desorption which can be obtained with an excimer laser are described. Laser desorption of CO, C<sub>2</sub>H<sub>4</sub>, C<sub>2</sub>N<sub>2</sub>, CH<sub>3</sub>OH, and C<sub>6</sub>H<sub>6</sub> has been observed from a Pt(s)[7(111) x (100)] surface. In all cases only neutral molecular species are seen to desorb. In the case of benzene, the molecular ion C<sub>6</sub>H<sub>6</sub><sup>+</sup> is observed even in the absence of electron bombardment ionization. It is likely that the benzene is ionized by resonant multiphoton ionization after the desorption process.

Thermal desorption spectroscopy and temperature programmed reaction experiments have provided significant insight into the chemistry of a wide variety of reactions on well characterized surfaces. In such experiments, characterized, adsorbate covered, surfaces are heated at rates of 10-100 K/sec and molecular species which desorb are monitored by mass spectrometry. Typically, several masses are monitored in each experiment by computer multiplexing techniques. Often, in such experiments, the species desorbed are the result of a surface reaction during the temperature ramp.

The laser desorption experiments which we describe here utilize pulsed laser radiation, which is partially absorbed by the metal substrate, to generate a temperature jump in the surface region of the sample. The neutral species desorbed are ionized and detected by Fourier transform mass spectrometry (FTMS). This technique has

0097-6156/85/0288-0238\$06.00/0  
© 1985 American Chemical Society

many varied applications. Adsorbate surface diffusion can be monitored if one laser pulse is used to generate a concentration gradient and subsequent laser pulses are used to interrogate the time evolution of the concentration gradient(1). Since the pulsed laser experiments are inherently time resolved, it is possible to conceive of monitoring the details of desorption dynamics. Most importantly, for surface chemistry studies, laser desorption methods provide a way to observe actual species on the surface and measure reaction kinetics(2). To carry out such experiments, several inherent problems must be addressed successfully. The experiments are inherently pulsed (laser pulses of 10-20 nsec are commonly utilized). This means that desorbed molecules will strike the walls of the chamber within a few hundred microseconds after the laser pulse. Thus if a scanning mass spectrometer, such as a quadrupole, is used as a detector as in references (1-3), only a single mass can be monitored with each laser shot if wall collisions are to be avoided. In addition, typical experiments will only result in small numbers of molecules desorbed. The FTMS technique provides an extremely sensitive detection method which is especially well suited to pulsed experiments.

In this manuscript we will first describe the characteristics of the temperature jumps and the resulting molecular desorption which can be produced by a laser pulse. We then describe how we have implemented FTMS as a detection method in these experiments and present our results on several adsorbate systems.

#### Laser-Induced Temperature Jumps and Molecular Desorption

The laser we use in these experiments is an excimer laser with a pulse width of approximately 20 nsec. In this time regime the laser heating can be treated using the differential equation for heat flow with a well defined value for the thermal diffusivity ( $\kappa$ ) and the thermal conductivity (K) (4).

$$\nabla^2 T(x,y,z,t) - (1/\kappa) \partial T(x,y,z,t)/\partial t = -A(x,y,z,t)/K \quad (1)$$

where  $A(x,y,z,t)$  represents the heat source. The details of the laser time and spatial profiles in conjunction with the thermal parameters of the metal will determine the characteristics of the surface temperature jump.

It is useful for illustrative purposes to consider a laser beam with a Gaussian spatial profile and a square pulse time profile. If the laser has a Gaussian spatial beam profile the temperature at the surface of the irradiated solid ( $z=0$ ) at a time  $t$  after the laser pulse is started is given by(4):

$$\Delta T(r,t) = (d^2/K)(\kappa/\pi)^{1/2} \int \frac{F(t-t') \exp\{-r^2/(4\kappa t'+d^2)\}}{t'^{1/2}(4\kappa t'+d^2)} dt' \quad (2)$$

where  $r$  = the lateral distance from the center of the laser spot.  
 $d$  = the Gaussian beam radius.

$F(t)$  = the adsorbed power per unit area at the center of the Gaussian spot.

For the case of a laser pulse having a square time profile with width  $\tau$  and constant power  $F_0$  at the center of the Gaussian beam, the above integral can be evaluated in closed form. For  $r = 0$  (the center of the laser beam) the temperature increase is given by:

$$\begin{aligned} \Delta T(r=0,t) &= (F_0 d / K\pi^{1/2}) \tan^{-1}\{2(\kappa t)^{1/2}/d\} \quad \text{for } t \leq \tau \quad (3) \\ &= (F_0 d / K\pi^{1/2}) [\tan^{-1}\{2(\kappa t)^{1/2}/d\} - \tan^{-1}\{2[\kappa(t-\tau)]^{1/2}\}] \quad \text{for } t > \tau \end{aligned}$$

For the solids of interest to us at present (metals)  $\kappa$  is typically  $0.1 \text{ cm}^2/\text{sec}$ . If we restrict  $t$  to be less than 10 microseconds then  $4\kappa t < 10^{-6} \text{ cm}^2$  and we will always have  $4\kappa t \ll d^2$ . In this limit the temperature jump for nonzero values of  $r$  is simply:

$$\Delta T(r,t) = T(r=0,t) \exp(-r^2/d^2) \quad (4)$$

Figure 1 shows the expected surface temperature rise under the laser for a nickel sample and  $10 \text{ MW/cm}^2$  of adsorbed power. The peak surface temperature under the center of the laser beam is  $990^\circ\text{C}$  above the starting surface temperature. The detailed temporal shape of the surface temperature will depend on the detailed time profile of the laser pulse. However, two important characteristics of the temperature jump which is generated will be retained: (1) it is localized in time, and (2) there is very little lateral spreading of the temperature gradient (only the material under the laser beam changes temperature significantly). The spatial localization of the heating allows us to probe the surface without modifying the areas a few millimeters from the laser. This allows for experiments in which the time evolution of chemistry on the surface is followed by sequentially probing different areas on the surface.

Desorption Rates. Using the above model for the temperature jump associated with pulsed laser heating, the rate of desorption versus time and the total number of molecules desorbed from a finite surface area heated by the laser can be calculated. For the particular case of first-order desorption kinetics, the desorption rate is:

$$\text{Rate}(t) = -d\theta/dt = v\theta \exp\{-E/RT(t)\} \quad (5)$$

This leads to:  $\ln\{\theta/\theta_0\} = -v\int dt' \exp\{-E/RT(t')\}$ .  
Substituting into equation 5 for  $\theta$  gives the following for the rate.

$$\text{Rate}(t) = v\theta_0 \exp\{-v\int dt' \exp\{-E/RT(t')\}\} \exp\{-E/RT(t)\} \quad (6)$$

where  $\theta_0$  = the initial surface coverage and  $E$  is the activation energy for desorption. Figure 2 shows a plot of the desorption rate and the integrated number of molecules versus time for an activation energy of  $20 \text{ kcal/mole}$  and the temperature jump shown in Figure 1. For the case of initial coverage of  $10^{15} \text{ molecule/cm}^2$  about  $1.5 \times 10^{13}$  molecules will be desorbed from an area of  $1 \text{ mm}$  radius by a single laser pulse. This corresponds to about half of the molecules originally in this area.

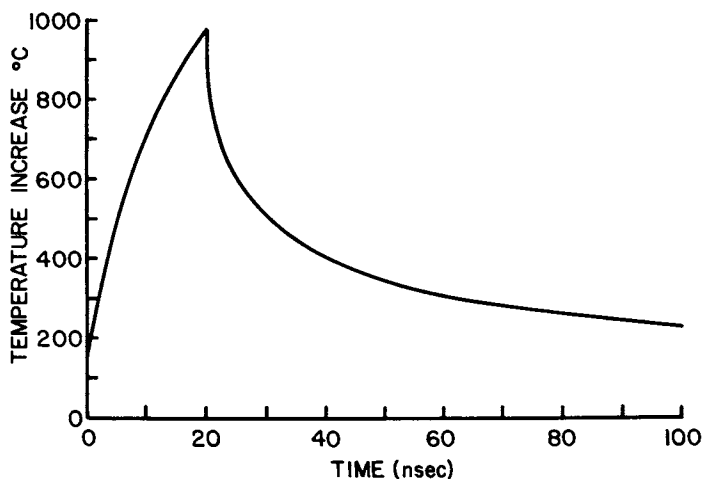


Figure 1. Calculated temperature increase under the center of the laser beam assuming the thermal parameters of bulk nickel and  $10\text{MW}/\text{cm}^2$  of absorbed power.

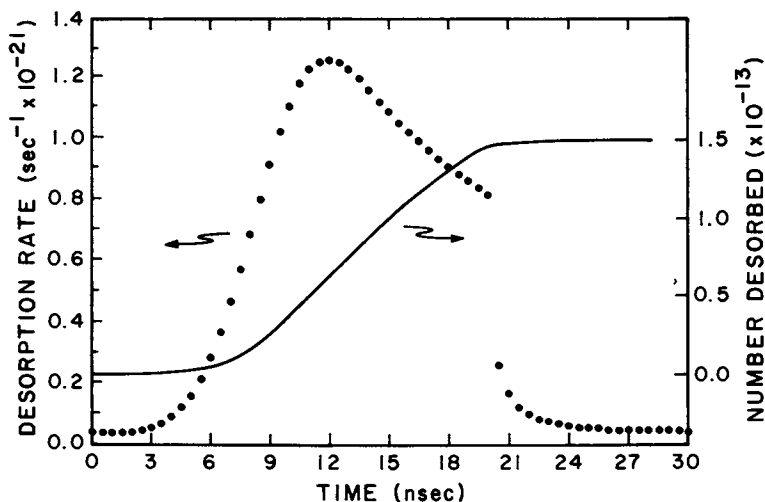


Figure 2. Plot of the desorption rate, molecules/sec, (solid circles) and the integrated number of molecules desorbed (solid line) for an adsorbate with a desorption activation energy of  $20\text{Kcal}/\text{mole}$  and a preexponential of  $10^{19}\text{sec}^{-1}$ . The temperature jump shown in Figure 1 was used for this calculation.

Of particular importance in the application of laser desorption to the study of chemistry on surfaces is what is to be expected for a situation in which the adsorbate has two (or more) competing thermally activated channels (eg. desorption versus decomposition). For illustrative purposes, consider the case of two competing channels, both of which obey simple first-order kinetics with constant preexponential factors and activation energies (see figure 3a). This scheme describes a reaction in which molecular adsorbate A can either react to form surface species B or directly desorb to give gas phase A. If the activation energy for desorption is greater than that for reaction ( $E_d > E_r$ ), the reaction channel will predominate in a conventional TPR experiment with a slow heating rate. In contrast, rapid laser heating can cause the branching ratio between reaction and desorption to be determined by the preexponential factors  $\nu_r$  and  $\nu_d$  rather than the activation energies. This occurs when the temperature increase is so fast that the activation energy terms in the rate expression approach unity before a significant amount of the lower energy reaction has occurred.

Figure 3b shows the calculated branching ratio as a function of heating rate for the specific case of  $\nu_r = 10^{10} \text{ sec}^{-1}$ ;  $E_r = 20 \text{ kcal/mole}$ ;  $\nu_d = 10^{13} \text{ sec}^{-1}$ ; and  $E_d = 35 \text{ kcal/mole}$ . Notice that under the typical heating rates of a thermal desorption experiment (10K/sec) the reaction proceeds predominantly via the lower energy channel, whereas at the more rapid heating rates the higher energy channel can dominate. Our model calculations assume that the internal degrees of freedom of the adsorbate are equilibrated with the instantaneous surface temperature. Recent calculations by Tully(5) indicate that internal degrees of freedom of the adsorbate will remain relatively cold during a fast surface temperature jump. This will lead to an even more pronounced depression of the reaction channel for systems that require thermal activation via internal degrees of freedom (ie. vibrations) of the adsorbate. It should be mentioned that preexponential factors for direct desorption can be expected to be large for many systems because of the increase in entropy going from an adsorbate with restricted translations to a gas phase molecule.

It is well known that a larger heating rate results in the desorption occurring at higher temperatures in a thermal desorption experiment (6). If it is necessary to desorb a large fraction of a monolayer to observe a signal, the peak temperatures required quickly exceed the threshold for surface damage, as the heating rate is increased. As a consequence, when extremely high heating rates are used, very little of the adsorbate (A) undergoes either channel (reaction or desorption). This is indicated in figure 3b where in addition to the channel branching ratio we have plotted the fraction of original adsorbate (A) which undergoes either of the two processes. Note that for the particular parameters used here only  $\approx 5\%$  of the adsorbate undergoes either process when a heating rate of  $5 \times 10^{10} \text{ K/sec}$  is used. The reason behind this phenomena is that at very high heating rates, the time scale of the temperature jump becomes short compared to reaction times. These considerations lead us to conclude that the high sensitivity of FTMS would be of critical importance for these experiments.

### FTMS and Laser Desorption Results

The usual method of detecting the desorbed molecules in TPR and laser desorption is with a quadrupole mass spectrometer placed a few centimeters from the surface of the crystal. The use of a quadrupole mass spectrometer limits the experiment in several respects. Since the resolution of a typical quadrupole is quite low, ions of the same nominal mass, such as  $\text{CO}^+$  and  $\text{C}_2\text{H}_4^+$ , cannot be distinguished. Also, since the quadrupole is a single-channel, scanning device, only a single mass is detected at a time. As a result, laser desorption experiments must be repeated many times to observe all the masses of interest.

Many of these limitations can be alleviated by the use of Fourier transform mass spectrometry (FTMS) (7-13). In FTMS, ions are stored in an analyzer cell which is situated between the pole caps of an electromagnet. The ions move in circular orbits perpendicular to the magnetic field with a cyclotron frequency  $\omega = qB/m$ , where  $m/q$  is the mass-to-charge ratio, and  $B$  is the magnetic field strength. When accelerated by a radio frequency (RF) pulse, the ions are detected by observing the coherent image currents induced in a pair of receiver plates. This phenomenon is illustrated in Figure 4. If, for instance, a packet of positive ions moves away from the first electrode and towards the second, the electric field of the ions induces electrons in the external circuit to flow through the resistor and accumulate on the second electrode. During the other half of the cyclotron orbit, the electrons leave the second electrode and accumulate on the first electrode as the positive ions approach. This flow of electrons in the external circuit is called an image current. It is an alternating current that has the same frequency as the cyclotron frequency of the ions that induced it, and the amplitude of the current is proportional to the number of ions. Thus, ions of different masses, each having a characteristic cyclotron frequency, create a composite signal, allowing simultaneous detection of all ions in the analyzer cell. Fourier transform analysis of the image current signal yields the mass spectrum.

During the last year we have built an FTMS instrument specifically designed for laser-induced thermal desorption from single-crystal surfaces. Figure 5 is a perspective drawing of the instrument. The chamber is pumped by a 150 l/s ion pump and has a base pressure of  $2.0 \times 10^{-10}$  torr. Gases are introduced through sapphire-sealed leak valves from a diffusion pumped gas manifold. A Pt(s)[7(111) x (100)] crystal is positioned in front of a hole in one of the plates of the analyzer cell. Ions formed by electron impact are trapped in the analyzer cell and detected by FTMS. An excimer laser, having a pulse width of 20 nsec, is used to desorb molecules from the Pt crystal.

Figure 6 shows the sequence of events in a laser desorption FTMS experiment. First, a focused laser beam traverses the analyzer cell and strikes the crystal normal to the surface. Molecules desorbed by the thermal spike rapidly move away from the crystal and are ionized by an electron beam which passes through the cell parallel to the magnetic field and 3 cm in front of the crystal. The ions are trapped by the combined effects of the magnetic field

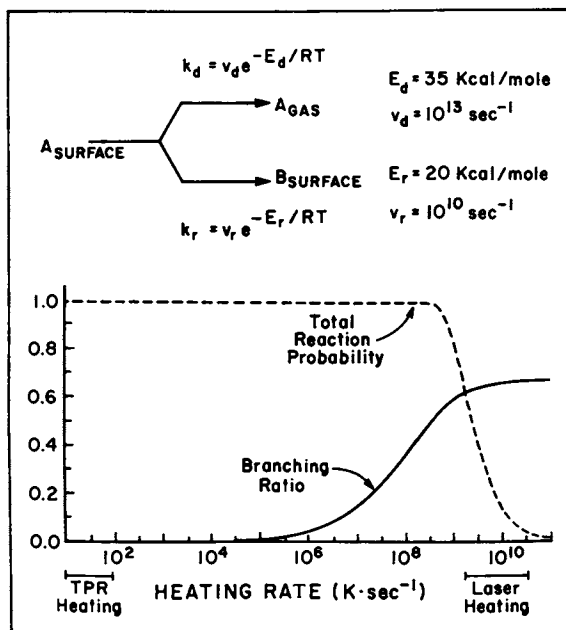


Figure 3. (a) Model reaction scheme showing direct desorption of adsorbate A competing with a surface reaction of A to form the surface species B. The kinetic parameters shown are those used to generate the curves. (b) Plot of the calculated branching ratio for desorption,  $\{A(\text{gas})\}/\{A(\text{gas})+B(\text{surface})\}$ , and the total reaction probability,  $\{A(\text{gas})+B(\text{surface})\}$  divided by the initial amount of adsorbate as a function of heating rate. A temperature jump of 1000 K and starting temperature of 300K is used for all heating rates.

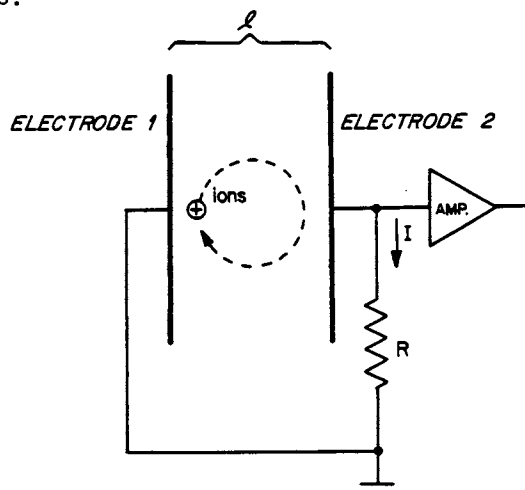


Figure 4. Ions undergoing coherent cyclotron motion induce image currents in the plates of the FTMS analyzer cell. Reproduced with permission from Ref. 18. Copyright 1985, North-Holland Physics Publishing.



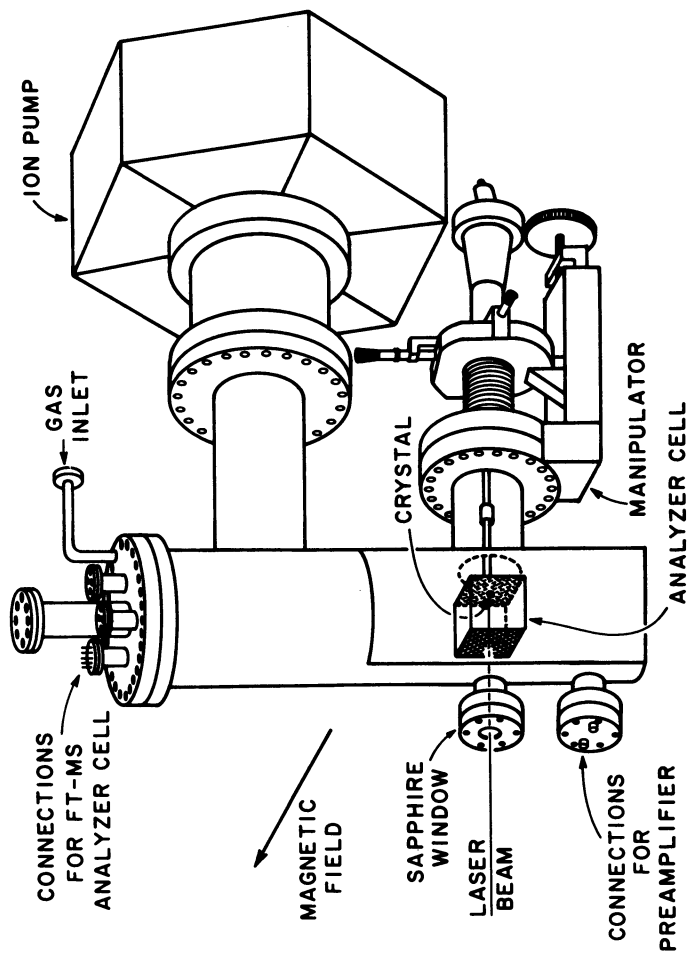


Figure 5. Perspective drawing of the laser desorption FTMS instrument showing the relative positions of the crystal, the laser beam, and the FTMS analyzer cell. Reproduced with permission from Ref. 18. Copyright 1985, North-Holland Physics Publishing.

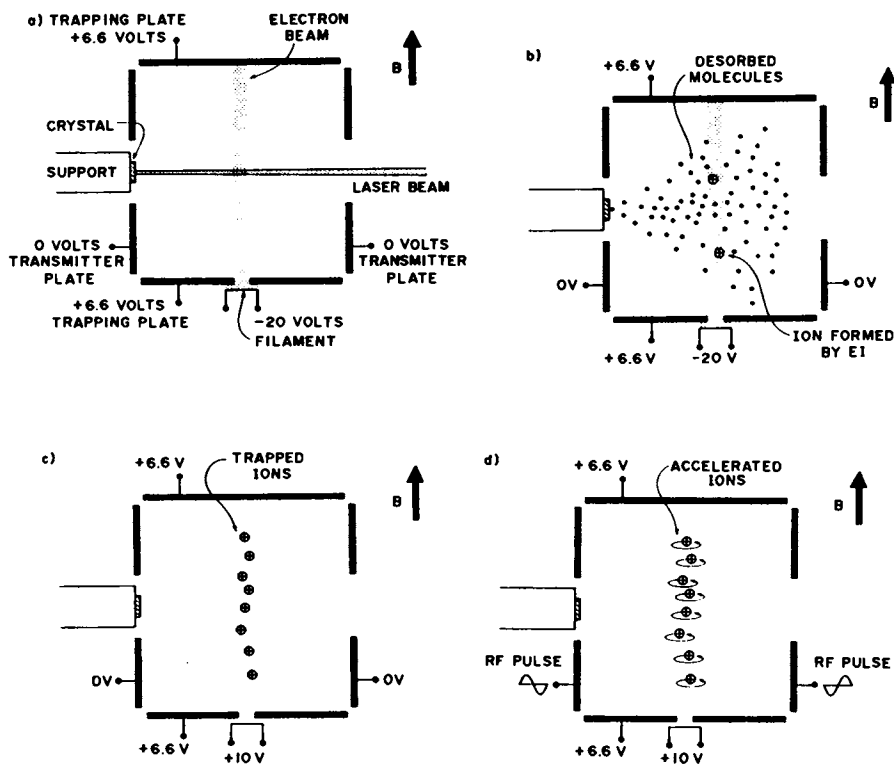


Figure 6. The sequence of events in a laser desorption FTMS experiment. (a) The laser beam enters the cell and strikes the crystal. (b) Some of the desorbed molecules are ionized by an electron beam. (c) Ions are trapped in the analyzer cell by the magnetic and electric fields. (d) Ions are accelerated by an RF pulse and the resulting coherent image current signal is detected. Reproduced with permission from Ref. 18. Copyright 1985, North-Holland Physics Publishing.

and electrostatic voltages applied to the cell plates. Desorbed molecules which are not ionized exit the analyzer cell through high transparency stainless steel mesh. The ions are detected, as discussed above, by RF acceleration followed by image current detection. Before the next laser pulse, all the ions are removed from the analyzer cell by changing the polarity of the voltages on the trapping plates.

Laser desorption FTMS is fundamentally different from SIMS because the desorption and ionization steps are separate. With FTMS, neutral atoms and molecules desorbed by the laser are ionized by the electron beam after they have moved about 3 cm away from the surface. As a result, complications introduced into SIMS spectra by gas-phase reactions above the surface are minimized because neutral-neutral reactions are typically two-orders of magnitude slower than ion-molecule reactions. We believe, therefore, that laser desorption FTMS spectra are representative of the species actually present on the surface.

Figure 7a demonstrates that FTMS can simultaneously detect ions over a broad mass range. This is the actual high resolution mass spectrum, not a stick plot. This spectrum was obtained when a mixture of CO, N<sub>2</sub>, C<sub>2</sub>H<sub>4</sub> and acetone was leaked into the chamber and ionized by the electron beam. The total sample pressure was 1.8 X 10<sup>-8</sup> torr. The magnetic field strength was 1.16 T and 10 scans were signal averaged.

The ultra-high mass resolution capabilities of FTMS are illustrated in Figure 7b. This spectrum was obtained by leaking a mixture of CO, N<sub>2</sub>, and C<sub>2</sub>H<sub>4</sub> into the chamber to a pressure of 1.8 X 10<sup>-9</sup> torr. The magnetic field strength and number of scans averaged were the same as for Figure 7a. Peaks for all three components are clearly resolved even though all have a nominal mass of 28 u. The mass resolution (m/Δm) is approximately 120000, which is over 1000 times greater than is available with a typical quadrupole mass spectrometer (The UTI-100C quadrupole mass analyser is typical of those used for most surface science experiments. The resolution obtainable with a UTI-100C quadrupole mass analyser is m/Δm = 2m (14)). These three peaks are also separated to baseline resolution in Figure 7a; however, they appear as one peak due to the wide mass range which is displayed.

Figure 7b also illustrates the high detection sensitivity of the FTMS instrument. We calculate that the CO<sup>+</sup> peak corresponds to approximately 5000 ions in the analyzer cell. In Figure 7a, the number of ions with m/z 43 was calculated to be approximately 20 million. A point to note is that in FTMS the sensitivity increases with resolution whereas it decreases with other mass spectroscopies.

Our first results for laser-induced thermal desorption of CO from a Pt crystal are shown in Figure 8. In this experiment, the crystal was cleaned by heating it in oxygen at 1100 K (1 X 10<sup>-6</sup> torr for 5 minutes) followed by annealing at 1300 K in vacuo to remove residual oxygen. The crystal was then exposed to 5L of CO at room temperature. Successive shots from the laser at the same spot are shown in Figures 8a,b,c. Most of the CO is desorbed by the first laser pulse, and after five pulses the CO<sup>+</sup> signal returns close to its background level. Figure 8d is a background spectrum showing CO<sup>+</sup> and N<sub>2</sub><sup>+</sup> signals due to residual CO and N<sub>2</sub> in the chamber.

American Chemical Society  
Library

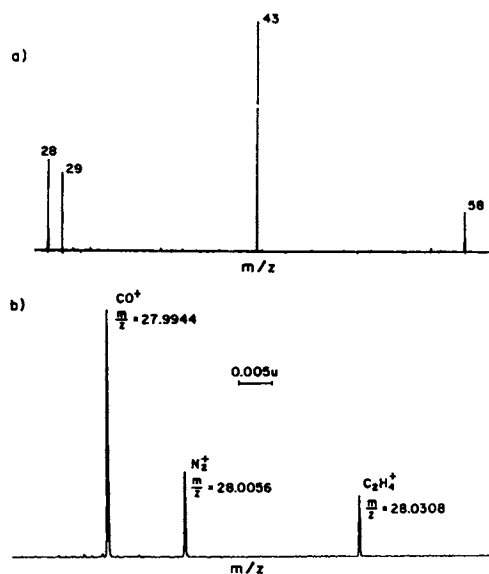


Figure 7. (a) FTMS mass spectrum obtained for a mixture of CO,  $\text{N}_2$ ,  $\text{C}_2\text{H}_4$ , and acetone. (b) High resolution FTMS mass spectrum of the mass 28 region showing  $\text{CO}^+$ ,  $\text{N}_2$ , and  $\text{C}_2\text{H}_4^+$ . Reproduced with permission from Ref. 18. Copyright 1985, North-Holland Physics.

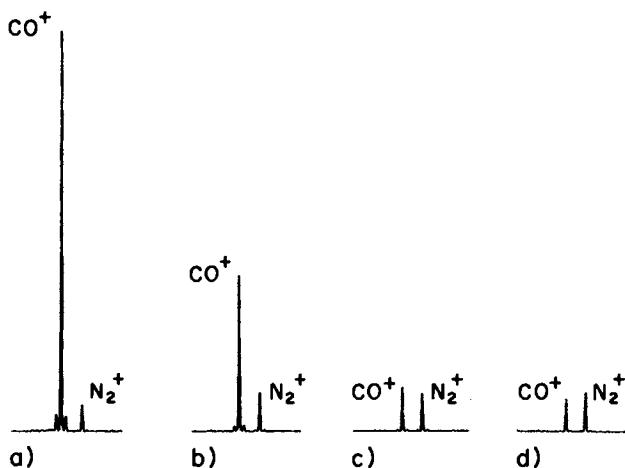


Figure 8. Laser desorption of CO from a Pt(s)[7(111) x (100)] surface following 5L exposure of CO at room temperature. In each case the mass spectrum in the region of  $28\mu$  is shown. (a) following the first laser pulse, (b) following the second laser pulse at the same spot, (c) following the fifth laser pulse at the same spot, (d) background spectrum of residual gas in the vacuum chamber (laser off). Reproduced with permission from Ref. 18. Copyright 1985, North-Holland Physics.

The  $N_2^+$  signal is relatively constant in the laser desorption spectra as expected.

At the low laser powers used here, ionization of the molecules was found to be due to the electron beam only. No ions were detected with the electron beam turned off and the laser beam positioned at a new spot on the crystal. At higher laser powers, we have observed direct desorption of Pt ions.

We have also carried out preliminary experiments in which we have detected the laser desorption of ethylene, cyanogen, methanol, and benzene from the Pt(s)[7(111) x (100)] surface. These spectra are shown in Figure 9. In the experiments involving ethylene, cyanogen, and methanol only neutral species are desorbed. In the case of benzene we observe the molecular parent ion in the absence of the electron beam. We believe that this is due to resonance multiphoton ionization of the benzene by the laser after desorption (resonance multiphoton ionization of benzene is very efficient with 249 nm radiation). These spectra are in marked contrast to the results of SIMS experiments which produce a wide variety of complex metal-adsorbate cluster ions. In the case of ethylene, our experiments were performed at 140 K, and under these conditions ethylene is known to be a molecular  $\pi$ -bonded species on the surface. In SIMS under these conditions the predominant species is  $CH_2^+$  (15), but in the laser desorption FTMS experiments neutral ethylene is the principal species detected at low laser power.

### Conclusions

We have described the use of FTMS as a detection method for laser desorption of molecular adsorbates from metal surfaces. FTMS provides several important characteristics for these experiments. The high sensitivity of FTMS can be used to great advantage. Since the ions are trapped in the analyzer cell, the signals can be monitored over several seconds if necessary. The broad mass range capabilities of FTMS allow single shot experiments even for more complex chemical systems. In addition to the advantages of FTMS which we have demonstrated, the technique should allow us to carry out a variety of new kinds of experiments. As a result of the proximity of the detector to the surface, FTMS has the potential of detecting desorbed molecules in a single pass through the electron beam, before wall collisions occur. This affords the possibility of looking at direct desorption of reactive intermediates which may exist during the course of a reaction on the surface. Another possibility is to use multiphoton ionization for the ionization of desorbed molecules (16,17). A two laser experiment could be employed whereby the first laser would desorb the molecules and a second laser would ionize them. Angular and velocity distributions of desorbed molecules could be obtained in this way since the ionization produced by the second laser can be spatially and temporally resolved.

### Acknowledgments

This work was supported by a Faculty Research Grant from the University of California, Irvine and the Petroleum Research Fund administered by the American Chemical Society. The excimer laser

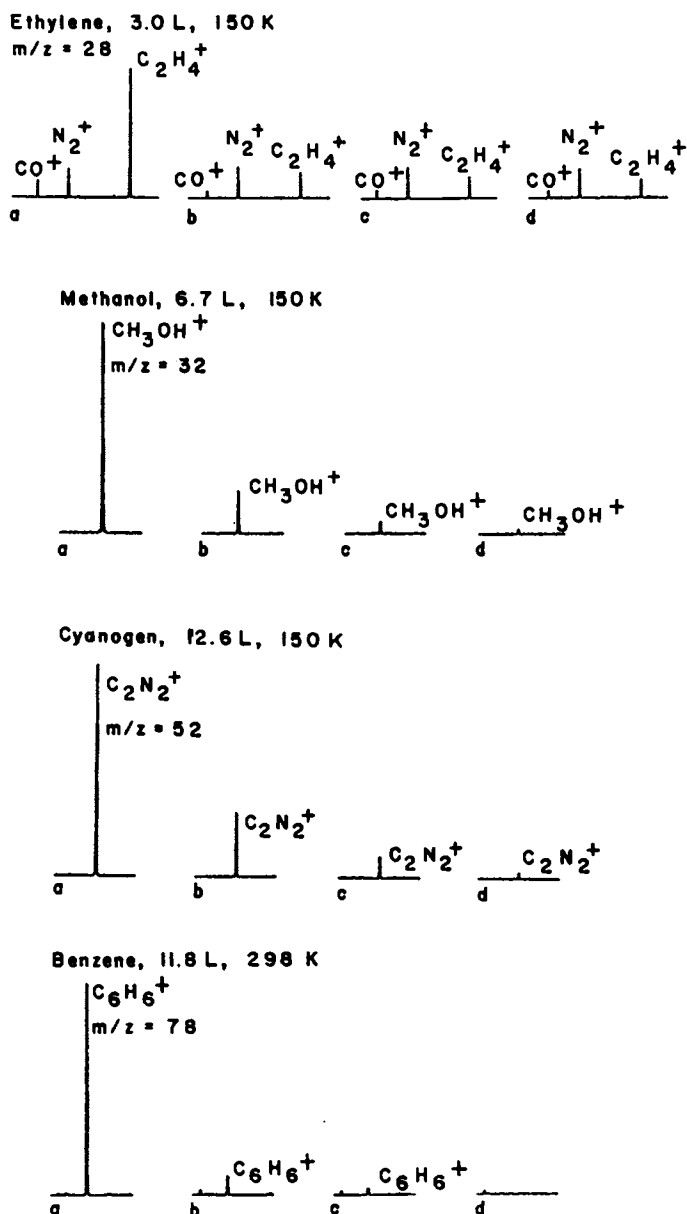


Figure 9. Laser desorption FTMS mass spectra recorded following successive shots of the laser. In each spectrum, (a) shows the results following the first laser pulse, (b) is the second laser pulse at the same spot, (c) is after the third laser pulse, and (d) is the background spectrum (laser off).

was loaned to us by Prof. F. S. Rowland. JCH would like to thank the Alfred P. Sloan Foundation for support in the form of an Alfred P. Sloan Foundation Fellowship.

#### Literature Cited

1. R. Viswanathan, D.R. Burgess, Jr., P.C. Stair, and E. Weitz, J. Vac. Sci. Technol. 1982, 20, 605.
2. R.B. Hall, and A.M. Desantolo, Surface Science 1984, 137, 421.
3. G. Wedler and H. Ruhmann, Surface Science 1982, 121, 464.
4. Ready, J.F. "Effects of High Power Laser Radiation"; Academic: New York, 1971.
5. R.R. Lucchese, J.C. Tully, J. Chem. Phys. 1984, 81, 6313.
6. P.A. Redhead, Vacuum 1962, 12, 203.
7. M.B. Comisarow, and A.G. Marshall, Chem. Phys. Lett. 1974, 25, 282.
8. C.L. Wilkins, Anal. Chem. 1978, 50, 493A.
9. R.T. McIver, Jr., Am. Lab. 1980, 12, 18.
10. C.L. Wilkins and M.L. Gross, Anal. Chem. 1981, 53, 1661A.
11. T.J. Francl, M.G. Sherman, R.L. Hunter, M.J. Locke, W.D. Bowers, R.T. McIver, Jr., Int. J. Mass Spectrom. Ion Phys. 1983, 54, 189.
12. E.B. Ledford, Jr., S. Ghaderi, R.L. White, R.B. Spencer, P.S. Kulkarni, C.L. Wilkins, and M.L. Gross, Anal. Chem. 1980, 52, 463.
13. R.L. White, E.C. Onyiriuka, and C.L. Wilkins, Anal. Chem., 1983, 55, 339.
14. UTI 100-C Operators Manual, UTI Corp.
15. J.R. Creighton, J.M. White, Surface Science 1983, 129, 327.
16. M.P. Irion, W.D. Bowers, R.L. Hunter, F.S. Rowland, and R.T. McIver, Jr., Chem. Phys. Lett. 1982, 93, 375.
17. F.M. Kimock, J.P. Baxter, N. Winograd, Surface Science 1983, 124, L41.
18. M.G. Sherman, J.R. Kingsley, D.A. Dahlgren, J.C. Hemminger, and R.T. McIver, Jr. Surf. Sci., 148 (1985) L25.

RECEIVED April 30, 1985

## Structure of Bimetallic Catalysts

### Application of Extended X-ray Absorption Fine Structure Studies

J. H. Sinfelt<sup>1</sup>, G. H. Via<sup>1</sup>, G. Meitzner<sup>1</sup>, and F. W. Lytle<sup>2</sup>

<sup>1</sup>Exxon Research & Engineering Company, Amundale, NJ 08801

<sup>2</sup>The Boeing Company, Seattle, WA 98124

The application of extended X-ray absorption fine structure (EXAFS) spectroscopy in the study of catalysts has been aided greatly by the availability of synchrotron radiation as a high-intensity source of X-rays. From an analysis of EXAFS data, it is possible to determine the number of neighboring atoms of a particular kind at a particular distance from an absorber atom. From EXAFS for each element of interest in a complex material, one can obtain information on the environments of the different types of atoms present. The application to bimetallic cluster catalysts provides a good illustration. Structural information is now available for a number of bimetallic systems, including various combinations of a Group VIII metal with a Group IB metal, and also combinations of two Group VIII metals. Both types of bimetallic cluster systems have attracted much interest in catalysis.

In recent years the utility of extended X-ray absorption fine structure (EXAFS) as a probe for the study of catalysts has been clearly demonstrated (1-17). Measurements of EXAFS are particularly valuable for very highly dispersed catalysts. Supported metal systems, in which small metal clusters or crystallites are commonly dispersed on a refractory oxide such as alumina or silica, are good examples of such catalysts. The ratio of surface atoms to total atoms in the metal clusters is generally high and may even approach unity in some cases.

The fine structure constituting EXAFS consists of oscillations in the X-ray absorption coefficient on the high energy side of an absorption edge, beginning at an energy of approximately 30 eV beyond the edge and extending over a range of 1000-1500 eV. The acquisition of EXAFS data has been aided greatly by the availability of high-intensity synchrotron radiation as an X-ray source. From an analysis of EXAFS data, one can determine the number of neighboring atoms of a particular kind at a particular distance from a given type of absorber atom. By determining EXAFS for each element of interest in a complex material, it is possible to obtain information on the environments of the different types of atoms present.

0097-6156/85/0288-0253\$06.00/0  
© 1985 American Chemical Society



We have found EXAFS to be a very effective method for obtaining structural information on bimetallic cluster catalysts (8,12-15,17). These types of catalysts, and bimetallic catalysts in general, have been the subject of extensive research in the EXXON laboratories since the 1960's (18-25). In this paper we present a brief review of the results of some of our EXAFS investigations on bimetallic cluster catalysts.

### Analysis of EXAFS Data

A photoelectron ejected from an atom as a result of X-ray absorption is characterized by a wave vector  $K$ , which is given by the equation:

$$K = (2mE)^{1/2}/\hbar \quad (1)$$

where  $m$  is the mass of the electron,  $\hbar$  is Planck's constant divided by  $2\pi$ , and  $E$  is the kinetic energy of the photoelectron. The EXAFS function  $\chi(K)$  is defined by the equation:

$$\chi(K) = (\mu - \mu_0)/\mu_0 \quad (2)$$

where  $\mu$  and  $\mu_0$  are atomic absorption coefficients characteristic of an atom in the material of interest and in the free state, respectively. The determination of  $\chi(K)$  from experimental EXAFS data has been discussed in detail elsewhere (7,9).

Theories of EXAFS (26,30) based on the scattering of an ejected photoelectron by atoms in the coordination shells surrounding the central absorbing atom give an expression for  $\chi(K)$  of the following form:

$$\chi(K) = \sum_j A_j(K) \sin[2KR_j + 2\delta_j(K)] \quad (3)$$

where the summation extends over  $j$  coordination shells. In this expression,  $R_j$  is the distance from the central absorbing atom to atoms in the  $j$ th coordination shell and  $2\delta_j(K)$  is the phase shift. The factor  $A_j(K)$  is an amplitude function for the  $j$ th shell, and is defined by the expression:

$$A_j(K) = (N_j/KR_j^2)F_j(K) \exp(-2K^2\sigma_j^2) \quad (4)$$

where  $N_j$  is the number of atoms in the  $j$ th shell,  $\sigma_j$  is the root mean square deviation of the interatomic distance about  $R_j$ , and  $F_j(K)$  is a factor accounting for electron backscattering and inelastic scattering (7,9). Key features in the analysis of EXAFS data include Fourier transformation of the data (26,31) and the application of an iterative least squares fitting procedure (7,9).

In the analysis of EXAFS data on bimetallic clusters, we consider two EXAFS functions, one for each component of the clusters (8,12-15,17). If the treatment is limited to contributions of nearest neighbor backscattering atoms, each of the functions will consist of two terms. For a bimetallic cluster composed of elements  $a$  and  $b$ , the EXAFS associated with element  $a$  is given by the expression:

$$\{\chi_1(K)\}_a = \{\chi'_1(K)\}_a^a + \{\chi'_1(K)\}_a^b \quad (5)$$

Similarly, for the EXAFS associated with element b

$$\{x_1(k)\}_b = \{x_1'(k)\}_b^a + \{x_1'(k)\}_b^b \quad (6)$$

In these expressions, the subscript outside the braces identifies the absorber atom, while the superscript identifies the backscattering atom. The contribution  $x_1'(k)$  of one type of backscattering atom to the total EXAFS function is given by the equation:

$$x_1'(k) = (N_1/KR_1^2)F_1(k) \exp(-2K^2\sigma_1^2) \sin[2KR_1 + 2\delta_1(k)] \quad (7)$$

where the subscript 1 signifies nearest neighbor atoms. The quantities in this equation have been defined in the discussion of equations 3 and 4.

### Ruthenium-Copper and Osmium-Copper Clusters

Ruthenium-copper and osmium-copper clusters (21) are of particular interest because the components are immiscible in the bulk (32). Studies of the chemisorption and catalytic properties of the clusters suggested a structure in which the copper was present on the surface of the ruthenium or osmium (23,24). The clusters were dispersed on a silica carrier (21). They were prepared by wetting the silica with an aqueous solution of ruthenium and copper, or osmium and copper, salts. After a drying step, the metal salts on the silica were reduced to form the bimetallic clusters. The reduction was accomplished by heating the material in a stream of hydrogen.

An X-ray absorption spectrum at 100°K showing the extended fine structure beyond the K absorption edge of ruthenium is given in Figure 1 for a silica supported ruthenium-copper catalyst containing 1.0 wt% ruthenium and 0.63 wt% copper (8). The copper to ruthenium atomic ratio in the catalyst is equal to one. The spectrum in Figure 1 is taken directly from our original paper (8), but the energy scale of the abscissa is different. It is now the actual energy of the X-ray photons, rather than the energy in excess of the threshold value (22.1 KeV) at the edge. The region of the plot in Figure 1 which constitutes EXAFS begins at an energy of about 30 eV beyond the edge and continues over an additional energy range of approximately 1000 eV.

When the ruthenium EXAFS for the ruthenium-copper catalyst is compared with the EXAFS for a ruthenium reference catalyst containing no copper, it is found that they are not very different. This indicates that the environment about a ruthenium atom in the bimetallic catalyst is on the average not very different from that in the reference catalyst. This result is consistent with the view that a ruthenium-copper cluster consists of a central core of ruthenium atoms with the copper atoms present at the surface.

If the degree of coverage of the ruthenium by the copper is very high, the copper atoms should be coordinated extensively to ruthenium atoms. It is emphasized that the ruthenium-copper clusters are of such a size (average diameter of 32Å by electron microscopy (33)) that the surface metal atoms constitute almost half of the total. Hence for a Cu/Ru atomic ratio of one, the number of copper atoms would correspond roughly to that required to form a monolayer on the ruthenium.

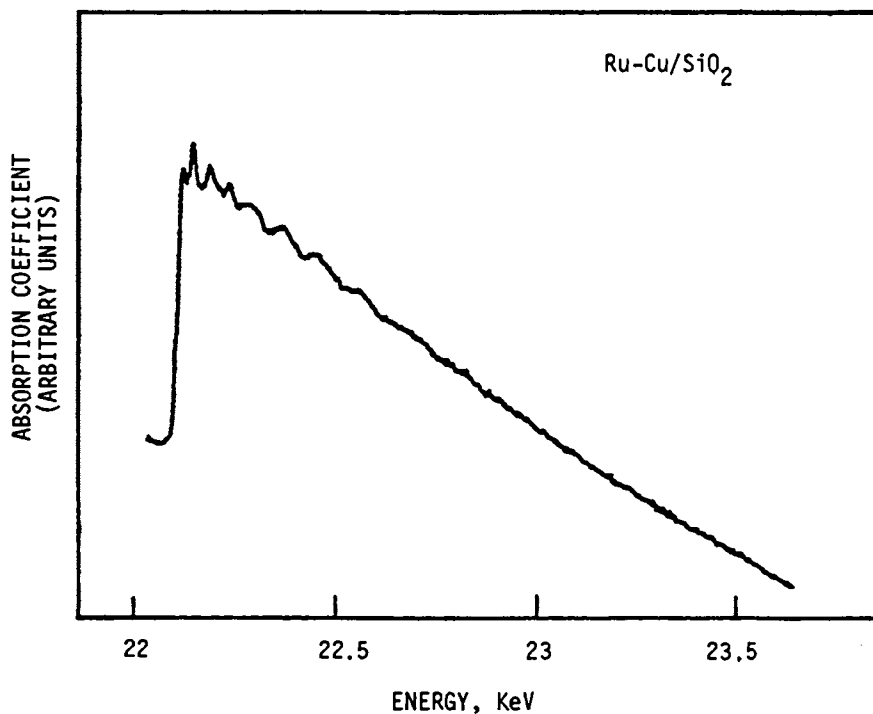


Figure 1. X-ray absorption spectrum of a silica supported ruthenium-copper catalyst at 100°K in the vicinity of the K absorption edge of ruthenium. Reproduced with permission from Ref. 8. Copyright 1980, American Institute of Physics.

The copper EXAFS of the ruthenium-copper clusters might be expected to differ substantially from the copper EXAFS of a copper on silica catalyst, since the copper atoms have very different environments. This expectation is indeed borne out by experiment, as shown in Figure 2 by the plots of the function  $K \cdot \chi(K)$  vs.  $K$  at 100°K for the extended fine structure beyond the copper K edge for the ruthenium-copper catalyst and a copper on silica reference catalyst (8). The difference is also evident from the Fourier transforms and first coordination shell inverse transforms in the middle and right-hand sections of Figure 2. The inverse transforms were taken over the range of distances 1.7 to 3.1Å to isolate the contribution to EXAFS arising from the first coordination shell of metal atoms about a copper absorber atom. This shell consists of copper atoms alone in the copper catalyst and of both copper and ruthenium atoms in the ruthenium-copper catalyst.

In Figure 3 the EXAFS envelope function derived from the extended fine structure beyond the copper K-absorption edge for the copper reference catalyst is compared with that for the ruthenium-copper catalyst (8). The envelope functions were obtained from the maxima and minima in the inverse transforms in Figure 2 and hence represent the first coordination shells of metal atoms about copper absorber atoms. The markedly different envelope function observed for the ruthenium-copper catalyst is a consequence of the copper atoms having ruthenium atoms in addition to copper atoms as nearest neighbors. The copper and ruthenium have very different electron scattering properties. The existence of bimetallic clusters containing both ruthenium and copper atoms is clearly indicated by the data in Figure 3.

This discussion of EXAFS on ruthenium-copper clusters has emphasized qualitative aspects of the data analysis. A quantitative data analysis, yielding information on the various structural parameters of interest, has also been made and published (8). Of particular interest was the finding that the average composition of the first coordination shell of ruthenium and copper atoms about a ruthenium atom was about 90% ruthenium, while that about a copper atom was about 50% ruthenium. Details of the methods involved in the quantitative analysis of EXAFS data on bimetallic clusters can be obtained from our original papers (8,12-15).

In the quantitative analysis of EXAFS associated with an absorption edge of either component of a bimetallic cluster catalyst, we consider two separate contributions to the EXAFS. These arise from the two different types of backscattering atoms constituting the local environment about an absorber atom. This is illustrated in Figure 4 for osmium-copper clusters dispersed on silica in a catalyst containing 2 wt% osmium and 0.66 wt% copper (12). The copper to osmium atomic ratio in the catalyst is equal to one. In all three fields of Figure 4, the solid line represents the EXAFS function for the osmium  $L_{III}$  edge due to backscattering from nearest neighbor atoms. It is derived from the experimental EXAFS function by inverting the Fourier transform of the function over a restricted range of distances. The range is chosen to include only nearest neighbor atoms about the osmium atoms in the clusters. The nearest neighbors, of course, include both osmium and copper atoms. The circles in the middle field (field B) of the figure represent the contribution to the osmium  $L_{III}$  EXAFS due to backscattering from nearest neighbor

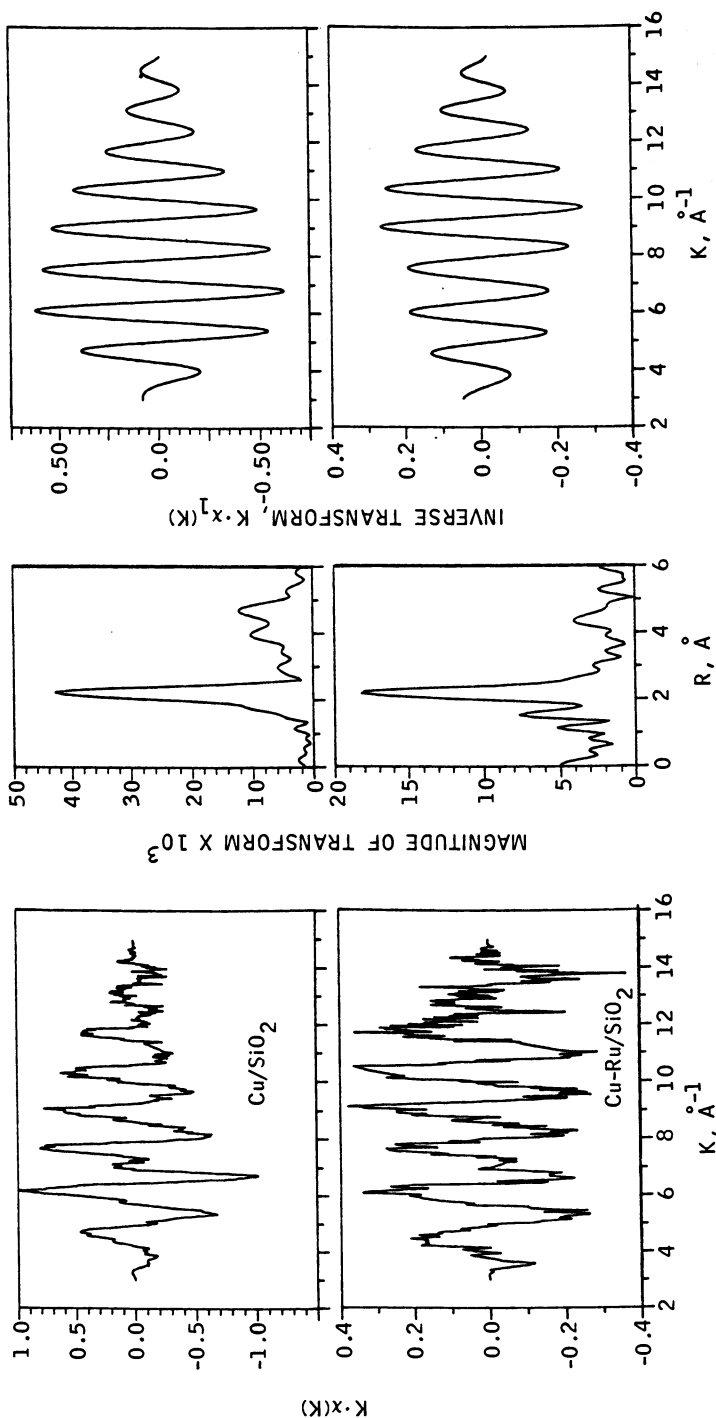


Figure 2. Normalized EXAFS data (copper K absorption edge) at 100°K, with associated Fourier transforms and inverse transforms, for silica supported copper and ruthenium-copper catalysts. Reproduced with permission from Ref. 8. Copyright 1980, American Institute of Physics.

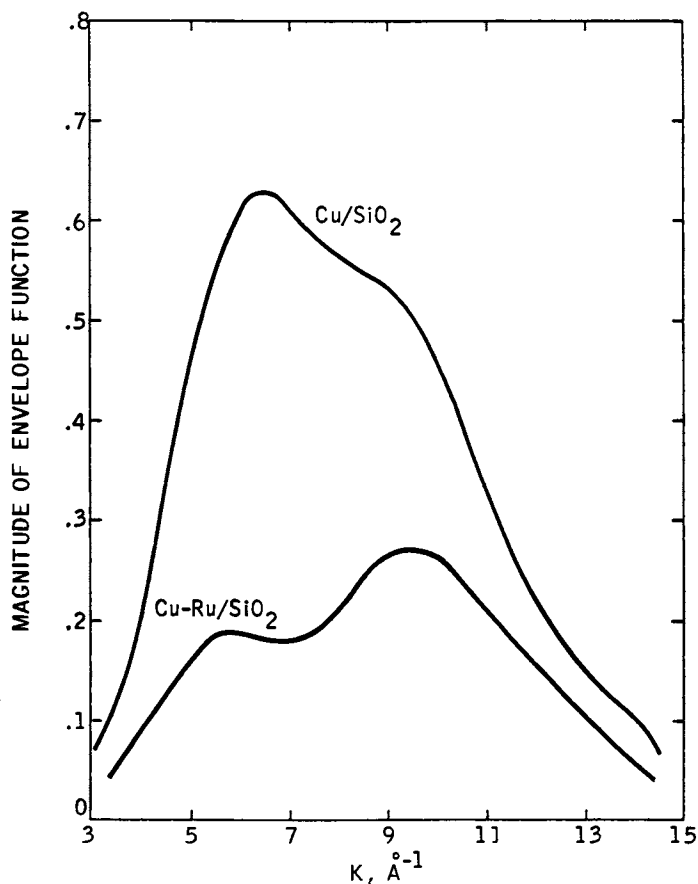


Figure 3. Comparison of EXAFS envelope functions derived from the inverse transforms in Figure 2 for silica supported copper and ruthenium-copper catalysts. Reproduced with permission from Ref. 8. Copyright 1980, American Institute of Physics.

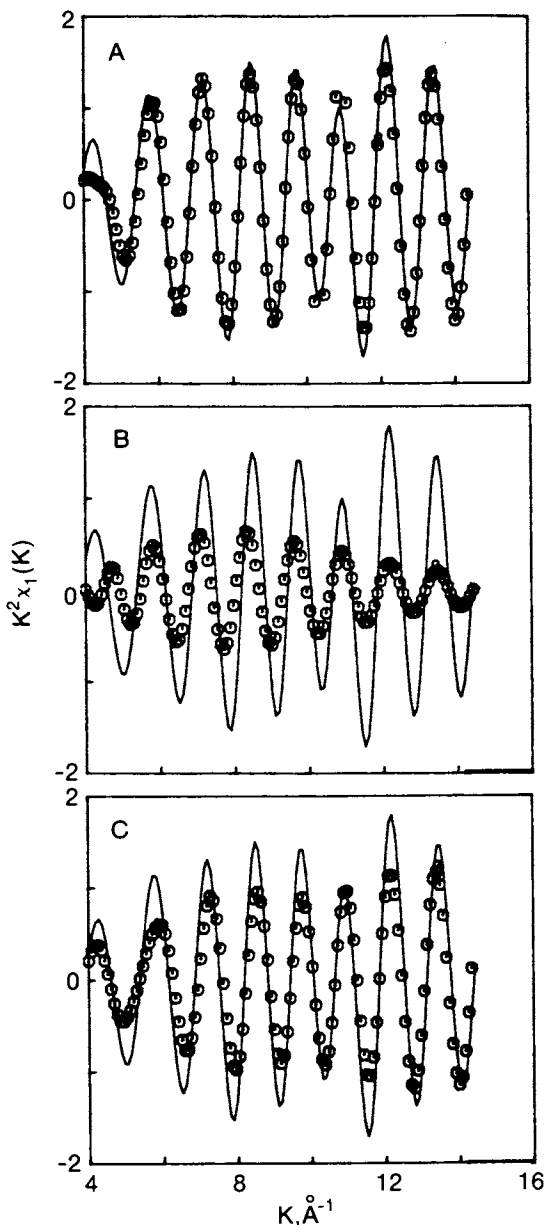


Figure 4. Contributions of nearest neighbor copper and osmium backscattering atoms (circles in fields B and C, respectively) to the EXAFS (solid line) associated with the osmium  $L_{III}$  absorption edge of a silica supported osmium-copper catalyst. The circles in field A represent the combined contributions resulting from the data analysis. Reproduced with permission from Ref. 12. Copyright 1981, American Institute of Physics.

copper atoms. The values are determined by means of an iterative least squares data fitting procedure. The circles in the lower field (field C) of the figure represent the contribution from nearest neighbor osmium atoms. In the upper field (field A) the circles represent the total EXAFS arising from the combined contribution of nearest neighbor osmium and copper atoms, as determined by the data fitting analysis. Comparison of the points with the solid line in the upper field provides a measure of the quality of fit obtained in a quantitative analysis of this type. Precisely the same type of analysis has also been made of the EXAFS associated with the K absorption edge of the copper in the osmium-copper clusters (12).

The results of the EXAFS studies on osmium-copper clusters lead to conclusions similar to those derived for ruthenium-copper clusters. That is, an osmium-copper cluster is viewed as a central core of osmium atoms with the copper present at the surface. The results of the EXAFS investigations have provided excellent support for the conclusions deduced earlier (21,23,24) from studies of the chemisorption and catalytic properties of the clusters. Although copper is immiscible with both ruthenium and osmium in the bulk, it exhibits significant interaction with either metal at an interface.

### Rhodium-Copper Clusters

The ruthenium-copper and osmium-copper systems represent extreme cases in view of the very limited miscibility of either ruthenium or osmium with copper. It may also be noted that the crystal structure of ruthenium or osmium is different from that of copper, the former metals possessing the hcp structure and the latter the fcc structure. A system which is less extreme in these respects is the rhodium-copper system, since the components both possess the face centered cubic structure and also exhibit at least some miscibility at conditions of interest in catalysis. Recent EXAFS results from our group on rhodium-copper clusters (14) are similar to the earlier results on ruthenium-copper (8) and osmium-copper (12) clusters, in that the rhodium atoms are coordinated predominantly to other rhodium atoms while the copper atoms are coordinated extensively to both copper and rhodium atoms. Also, we conclude that the copper concentrates in the surface of rhodium-copper clusters, as in the case of the ruthenium-copper and osmium-copper clusters.

Since ruthenium and rhodium are neighboring elements in the periodic table, a closer comparison of the properties of ruthenium-copper and rhodium-copper clusters is of interest (17). When we compare EXAFS results on rhodium-copper and ruthenium-copper catalysts in which the Cu/Rh and Cu/Ru atomic ratios are both equal to one, we find some differences which can be related to the differences in miscibility of copper with ruthenium and rhodium. The extent of concentration of copper at the surface appears to be lower for the rhodium-copper clusters than for the ruthenium-copper clusters, as evidenced by the fact that rhodium exhibits a greater tendency than ruthenium to be coordinated to copper atoms in such clusters. The rhodium-copper clusters presumably contain some of the copper atoms in the interior of the clusters.

The copper-copper interatomic distance in rhodium-copper clusters is substantially longer than in metallic copper (2.62-2.63Å vs. 2.556Å) and closer to the value (2.64Å) obtained for the rhodium-



copper interatomic distance in the clusters. This result may also be taken as an indication of a significant tendency of the copper to be present in the interior of the clusters as a consequence of its partial miscibility with rhodium.

We plan to make studies on palladium-copper, iridium-copper, and platinum-copper catalysts to extend our investigation of the effect of varying miscibility of the components on the structural features of the bimetallic clusters present. With these additional systems, the whole range from complete immiscibility to total miscibility of copper with the Group VIII metal will be encompassed.

### Platinum-Iridium Clusters

Bimetallic clusters of platinum and iridium can be prepared by coimpregnating a carrier such as silica or alumina with an aqueous solution of chloroplatinic and chloroiridic acids (22,34). After the impregnated carrier is dried and possibly calcined at mild conditions (250°-270°C), subsequent treatment in flowing hydrogen at elevated temperatures (300°-500°C) leads to formation of the bimetallic clusters.

An X-ray absorption spectrum at 100°K in the region of the L absorption edges of iridium and platinum is given in Figure 5 for a silica-supported platinum-iridium catalyst containing 10 wt% each of the individual metals (13). The X-ray absorption data in Figure 5 were obtained over a range of energies of the X-ray photons wide enough to include all of the L absorption edges of iridium and platinum. In the following discussion we will be concerned with the extended fine structure associated with  $L_{IIII}$  absorption edges.

The  $L_{IIII}$  absorption edges of iridium and platinum are 348.5 eV apart in energy. Since the extended fine structure associated with the  $L_{IIII}$  edge of iridium is observable to energies of 1,200-1,300 eV beyond the edge, there is overlap of the EXAFS associated with the  $L_{IIII}$  edges of iridium and platinum for a catalyst containing both of these elements. Separating the iridium EXAFS from the platinum EXAFS in the region of overlap is a key feature in the analysis of the data. A method for accomplishing this separation is described in our 1982 paper (13). To test the method, we obtained EXAFS data on platinum-iridium materials with known structural parameters. The materials included a physical mixture of platinum and iridium and a bulk alloy of platinum and iridium. The method worked very well in both cases, as demonstrated by the fact that results on interatomic distances were very close to the expected values.

Because of the similarity in the backscattering properties of platinum and iridium, we were not able to distinguish between neighboring platinum and iridium atoms in the analysis of the EXAFS associated with either component of platinum-iridium alloys or clusters. In this respect, the situation is very different from that for systems like ruthenium-copper, osmium-copper, or rhodium-copper. Therefore, we concentrated on the determination of interatomic distances. To obtain accurate values of interatomic distances, it is necessary to have precise information on phase shifts. For the platinum-iridium system, there is no problem in this regard, since the phase shifts of platinum and iridium are not very different. Hence the uncertainty in the phase shift of a platinum-iridium atom pair is very small.

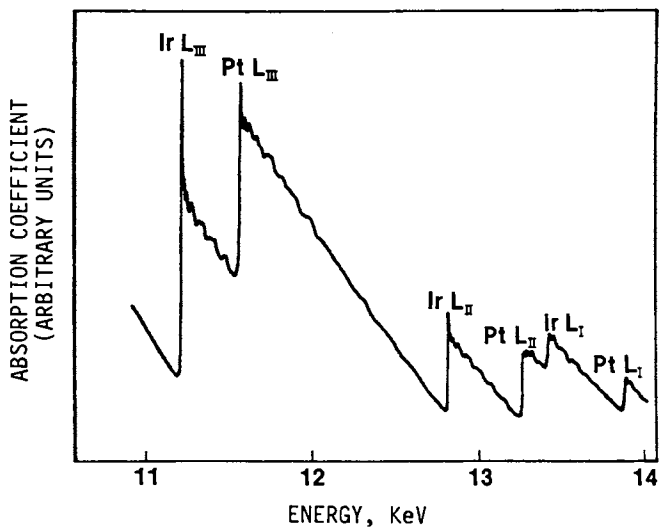


Figure 5. X-ray absorption spectrum of a silica supported platinum-iridium catalyst at 100°K in the region of the L absorption edges of platinum and iridium. Reproduced with permission from Ref. 13. Copyright 1982, American Institute of Physics.

From results on interatomic distances derived from analysis of EXAFS data, one can draw some conclusions about the structure of platinum-iridium clusters (13,17). If the clusters were truly homogeneous, the interatomic distance characteristic of the platinum EXAFS should be identical to that characteristic of the iridium EXAFS. When we analyze EXAFS data on the clusters, however, we do not find this simple result. We find in general that the distances are not equal. The data indicate that the clusters are not homogeneous; in other words, the environments about the platinum and iridium are different. We conclude that the platinum concentrates at the surface or boundary of the clusters. In the case of very highly dispersed platinum-iridium clusters on alumina, the clusters may well have "raft-like" two dimensional structures, with platinum concentrating at the perimeter.

### Iridium-Rhodium Clusters

Recently we reported EXAFS results on bimetallic clusters of iridium and rhodium, supported on silica and on alumina (15). The components of this system both possess the fcc structure in the metallic state, as do the components of the platinum-iridium system. The nearest neighbor interatomic distances in metallic iridium and rhodium are not very different (2.714Å vs. 2.690Å). From the results of the EXAFS measurements, we concluded that the interatomic distances corresponding to the various atomic pairs (i.e., iridium-iridium, rhodium-rhodium, and iridium-rhodium) in the clusters supported on either silica or alumina were equal within experimental error. Since the interatomic distances of the pure metals differ by only 0.024Å, the conclusion is not surprising.

There appears to be concentration of rhodium in the surface of the iridium-rhodium clusters, on the basis that the total number of nearest neighbor atoms about rhodium atoms was found to be smaller than the number about iridium atoms in both catalysts investigated. This conclusion agrees with that of other workers (35) based on different types of measurements. The results on the average compositions of the first coordination shells of atoms about iridium and rhodium atoms in either catalyst indicate that rhodium atoms are also incorporated extensively in the interiors of the clusters. In this respect the iridium-rhodium system differs markedly from a system such as ruthenium-copper (8), in which the copper appears to be present exclusively at the surface.

The EXAFS results suggested that the iridium-rhodium clusters dispersed on alumina differed in size and/or shape from those dispersed on silica, based on the result that the total coordination numbers of the iridium and rhodium atoms in the clusters were very different (7 and 5 in the alumina supported clusters vs. 11 and 10 in the silica supported clusters). These coordination numbers suggested that the clusters dispersed on alumina were smaller or that they were present in the form of thin rafts or patches on the support. The possibility of a "raft-like" structure in the case of the alumina supported clusters suggests an interaction between the metal clusters and the support which is much more pronounced for alumina than for silica. If the clusters on the alumina were present as rafts with a thickness of one atomic layer, one could have a situation in which the rhodium concentration at the perimeter of the raft was greater

than in the interior, analogous to the suggestion made for the platinum in very highly dispersed platinum-iridium clusters (13).

### Conclusions

Extended X-ray absorption fine structure (EXAFS) studies have been very useful for obtaining structural information on bimetallic cluster catalysts. The application to bimetallic systems is a particularly good one for illustrating the various factors which have an influence on EXAFS. Moreover, the applicability of EXAFS to this area has been very timely, in view of the enormous interest in bimetallic systems in both catalytic science and technology.

The results of the EXAFS studies on supported bimetallic catalysts have provided excellent confirmation of earlier conclusions (21-24) regarding the existence of bimetallic clusters in these catalysts. Moreover, major structural features of bimetallic clusters deduced from chemisorption and catalytic data (21-24), or anticipated from considerations of the miscibility or surface energies of the components (13-15), received additional support from the EXAFS data. From another point of view, it can also be said that the bimetallic catalyst systems provided a critical test of the EXAFS method for investigations of catalyst structure (17). The application of EXAFS in conjunction with studies employing chemical probes and other types of physical probes was an important feature of the work (25).

Investigations utilizing EXAFS have the very important feature of yielding information in an environment of the kind actually encountered in catalysis. We have recently demonstrated the feasibility of making measurements while a catalytic reaction is actually occurring. One can anticipate that measurements of this type will receive increased emphasis in the future. For studies of the structures of highly dispersed metal catalysts, EXAFS may well be the most generally applicable physical probe currently available.

### Literature Cited

1. Lytle, F. W.; Via, G. H.; Sinfelt, J. H. American Chemical Society, Division of Petroleum Chemistry Preprints 1976, 21(2), 366.
2. Lytle, F. W.; Via, G. H.; Sinfelt, J. H. J. Chem. Phys. 1977, 67, 3831.
3. Sinfelt, J. H.; Via, G. H.; Lytle, F. W. J. Chem. Phys. 1978, 68, 2009.
4. Bassi, I. W.; Lytle, F. W.; Parravano, G. J. Catalysis 1976, 42, 130.
5. Reed, J.; Eisenberger, P.; Teo, B. K.; Kincaid, B. M. J. Am. Chem. Soc. 1977, 99, 5217.
6. Friedman, R. M.; Freeman, J. J.; Lytle, F. W. J. Catalysis 1978, 55, 10.
7. Via, G. H.; Sinfelt, J. H.; Lytle, F. W. J. Chem. Phys. 1979, 71, 690.
8. Sinfelt, J. H.; Via, G. H.; Lytle, F. W. J. Chem. Phys. 1980, 72, 4832.
9. Lytle, F. W.; Via, G. H.; Sinfelt, J. H. In "Synchrotron Radiation Research"; Winick, H.; Doniach, S., Eds.; Plenum Publishing Corporation: New York, 1980; pp. 401-424.

10. Greigor, R. B.; Lytle, F. W. J. Catalysis 1980, 63, 476.
11. Joyner, R. W. J. Chem. Soc. Faraday Trans 1 1980, 76, 357.
12. Sinfelt, J. H.; Via, G. H.; Lytle, F. W.; Greigor, R. B. J. Chem. Phys. 1981, 75, 5527.
13. Sinfelt, J. H.; Via, G. H.; Lytle, F. W. J. Chem. Phys. 1982, 76, 2779.
14. Meitzner, G.; Via, G. H.; Lytle, F. W.; Sinfelt, J. H. J. Chem. Phys. 1983, 78, 882.
15. Meitzner, G. W.; Via, G. H.; Lytle, F. W.; Sinfelt, J. H. J. Chem. Phys. 1983, 78, 2533.
16. Via, G. H.; Meitzner, G.; Lytle, F. W.; Sinfelt, J. H. J. Chem. Phys. 1983, 79, 1527.
17. Sinfelt, J. H.; Via, G. H.; Lytle, F. W. Catalysis Reviews-Science and Engineering 1984, 26(1), 81.
18. Sinfelt, J. H.; Barnett, A. E.; Dembinski, G. W. U.S. Patent 3 442 973, 1969.
19. Sinfelt, J. H.; Barnett, A. E.; Carter, J. L. U.S. Patent 3 617 518, 1971.
20. Sinfelt, J. H.; Carter, J. L.; Yates, D. J. C. J. Catalysis 1972, 24, 283.
21. Sinfelt, J. H. J. Catalysis 1973, 29, 308.
22. Sinfelt, J. H. U.S. Patent 3 953 368, 1976.
23. Sinfelt, J. H.; Lam, Y. L.; Cusumano, J. A.; Barnett, A. E. J. Catalysis 1976, 42, 227.
24. Sinfelt, J. H. Accounts of Chemical Research 1977, 10, 15.
25. Sinfelt, J. H. "Bimetallic Catalysts: Discoveries, Concepts, and Applications"; John Wiley & Sons: New York, 1983.
26. Sayers, D. E.; Lytle, F. W.; Stern, E. A. Phys. Rev. Lett. 1971, 27, 1204.
27. Stern, E. Phys. Rev. B 1974, 10, 3027.
28. Ashley, C. A.; Doniach, S. Phys. Rev. B 1975, 11, 1279.
29. Lee, P. A.; Pendry, J. B. Phys. Rev. B 1975, 11, 2795.
30. Lee, P. A.; Beni, G. Phys. Rev. B 1977, 15, 2862.
31. Stern, E. A.; Sayers, D. E.; Lytle, F. W. Phys. Rev. B 1975, 11, 4836.
32. Hansen, M. "Constitution of Binary Alloys"; McGraw-Hill: New York, 1958, 2nd ed.; pp. 607, 620.
33. Prestridge, E. B.; Via, G. H.; Sinfelt, J. H. J. Catalysis 1977, 50, 115.
34. Sinfelt, J. H.; Via, G. H. J. Catalysis 1979, 56, 1.
35. Wong, T. C.; Brown, L. F.; Haller, G. L.; Kemball, C. J. Chem. Soc. Faraday Trans. 1 1981, 71, 519.

RECEIVED January 10, 1985

## Surface Chemistry and Catalysis on Some Platinum-Bimetallic Catalysts

V. Ponec

Gorlaeus Laboratories, State University of Leiden, P.O. Box 9502, 2300 RA Leiden, The Netherlands

Data accumulated in the last years on the Pt/Cu alloys, in particular on the 1) surface composition, 2) electronic structure, 3) adsorption properties, 4) catalytic behaviour and 5) various side effects, make a detailed discussion possible of the catalytic selectivity and mechanism of hydrocarbon reactions.

Alloys or multimetallic catalysts are not only commercially important but they are also an attractive object for scientific studies. In the recent past these studies helped to identify some factors which determine the activity and - mainly - the selectivity of metal catalysts (1-5).

It is convenient to classify the observed (or expected!) effects of alloying in two classes (4,6):

- 1) Geometrical effects, related to the number and geometrical arrangement of the surface metal atoms participating in the formation of the essential surface intermediates of the reaction in question. For these, number of atoms (ensemble size) appeared to be particularly crucial.
- 2) Effects related to the changes in the electronic structure of atoms after alloying or formation of bimetallics (electronic or ligand (4) effects).

The state of the knowledge is at the moment such that still in each particular case, the investigator should analyse and establish experimentally how important are, relative to each other, the effects 1) and 2) for the activity and the selectivity of a given multimetallic catalyst. It is an historical experience that when the explanation of the data is not immediately obvious, the authors offer as an "explanation" "an electronic (ligand) effect" (7). In this way it happened that the effect sub 1) has been most frequently proven to operate, while the effect sub 2) is the most frequently postulated one.

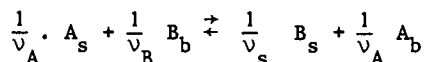
In this paper mainly the results on Pt/Cu will be reviewed and discussed. However, also some other Pt alloys will be mentioned briefly.

## Experimental

The main purpose of this paper is to draw conclusions from a rather long list of papers and dissertations published from Leiden. Therefore, for details on the techniques used (catalytic measurements, Auger spectroscopy, TPD, IR) as well as for details of catalyst preparation, the reader is kindly referred to the literature quoted.

## Results

Surface composition. The principle of surface segregation in ideal systems is easy to understand and to derive thermodynamically the equilibrium relations (surface concentration  $X_s$  as a function of the bulk concentration  $X_b$  at various temperatures) is also very easy (4,8). Even easier is a kinetic description which can also comprise some of the effects of the non-ideality (9). We consider an equilibrium between the surface(s) and the bulk(b) in the exchange like:



The equilibrium constant is obviously:

$$K = \left( \frac{1-X_s}{1-X_b} \right)^\alpha \cdot \frac{X_b}{X_s} \cdot F = K_A \cdot F$$

where  $X$  is the molar ratio of A,  $\alpha = \frac{v_A}{v_B}$ , and  $F$  comprises all activity coefficients.  $K_A$  can be written as  $\exp(-\Delta H_{\text{exchange}}/RT)$ .

The heat effects of segregation are usually calculated from the so-called broken bond model. It is assumed that each atom forms 8(bcc) or 12(fcc) bonds in the bulk of the metal and that the total cohesion energy (heat of sublimation) is equally distributed over these bonds. In the surface, the number of bonds not formed (broken) is correspondingly different according to the crystal face exposed. This reasoning already can explain why the metal with the lower sublimation energy tends to segregate in the surface (it is energetically less expensive not to form the weaker bonds) and why the segregation is more pronounced on the rougher (higher index) planes (there is a higher number of not formed bonds).

However, the reality is considerably more complicated than the ideal model. Non-ideality of the system causes that segregation extends over more than one layer. Further, when the size of the atoms is not equal one has to consider it in the calculations. This all has been done by A.D.van Langeveld (10), who made the following assumptions on the Pt/Cu system: i) segregation extends over the two outmost layers, ii) when the binding energy of pairs of atoms is  $\epsilon_{ij}$ , the non-ideality of an alloy AB is described by the parameter:  $\Omega(R_b) = \epsilon_{AB}(R_b) + \frac{1}{2}\{\epsilon_{AA}(R_b) + \epsilon_{BB}(R_b)\}$ , with  $R_b$  standing for the interatomic (bulk) distance, iii) the  $\epsilon_{ij}$ 's can be calculated from the corresponding sublimation energies  $\epsilon_{ij}$  and/or heat mixing, using a correction for the compression or expansion of the interatomic distances, when the alloy is formed from pure metals; this correc-

tion is calculated by using the "6-12" pair-potential, iv) the differences in the thermal (internal) entropy upon segregation are neglected and the configurational entropy is calculated as for ideal (random mixing) systems. The procedure is otherwise the same as developed by Williams and Nason (11), only the  $\Omega$ -parameters are obtained from the corresponding expressions and not by averaging as the authors (11) suggest.

Experimental determination of the surface composition in non-ideal systems, in which the gradients extend over several layers inwards the crystal is as difficult as the exact calculations. Therefore, one has to make again rather unpleasant assumptions. Van Langeveld (10) in his thesis first calculated the concentration in the first and the second surface layer of the alloys and when he saw the second layer differed only marginally from the bulk, he determined the surface concentration by AES, assuming that only the first layer is different from the bulk. In such cases the relevant equation is as follows:

$$\frac{I(A)}{I(B)} = R^* \cdot \frac{\rho^B}{\rho^A} \cdot \frac{N_1^A x_1 + (1-N_1^A) x_{\text{bulk}}}{N_1^B (1-x_1) + (1-N_1^B) (1-x_{\text{bulk}})}$$

where  $I(A)$  and  $I(B)$  are AES signals of A and B elements in the alloy, divided by the AES signal of the pure metal A or B, respectively;  $R^*$  the correction for back scattering,  $\rho$ - the planar densities,  $N_1$  the fraction of the total signal originating from the first layer and  $x_1$  and  $x_{\text{bulk}}$  the molar ratio of A in the outmost layer and in the bulk of the alloy. Result of determination of  $x_1 = f(x_{\text{bulk}})$  is compared in figure 1 with the calculated values (shaded area) and with some literature data. The agreement is not excellent but considering the approximations made, still satisfactory.

In conclusion, one remark. It is evident that the calculations describing the ideal case are rather far from reality. Further, it should be noticed, that it is absolutely incorrect, to take as a measure of surface concentration the AES signals (eventually normalized); that is to put  $N_1 = 1$ . Even for the signals most sensitive for the surface,  $N_1 \approx 0.5$ ! It is equally incorrect to say (what is very popular in the literature) that the AES signals characterize the average concentration over the free pathlength  $\lambda$  of the electrons monitored; the contribution of the deeper layer decreases exponentially and not linearly with the distances from the surface (8).

Electronic structure changes in the Pt/Cu system. We have no "our own" data on the electronic structure changes taking place upon alloying of Pt with Cu, but - fortunately - this system has been studied in great detail by other authors (12-14).

The basic information is the fact that formation of Pt/Cu alloys is rather exothermic (15) so that one would expect more pronounced changes in the electronic structure of Pt and Cu, than with, e.g. Pt/Au, Pt/Ag, (endothermic alloy formation) or Pt/Re, Pd/Ag, Pd/Au (moderately exothermic).

The best method available at the moment, to look at the electronic structure of transition metals and their alloys, is probably



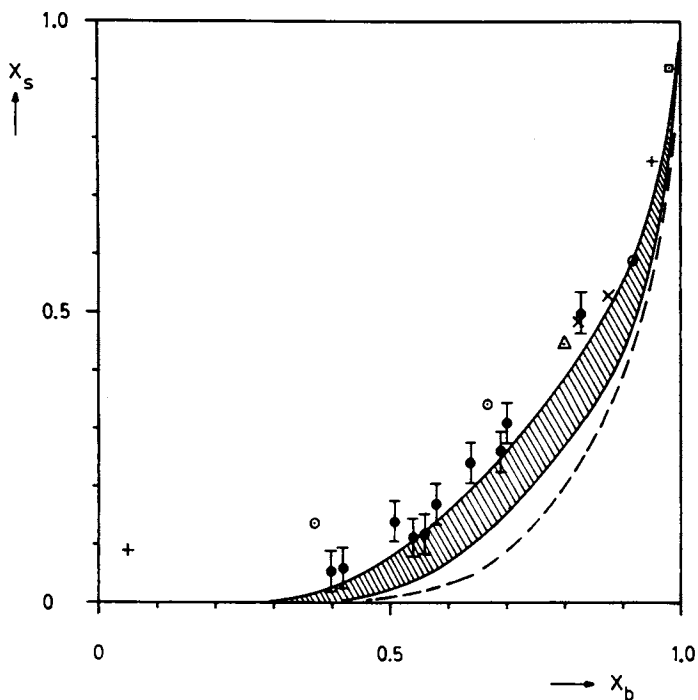


Figure 1. Surface Pt content as a function of the bulk content in Pt/Cu alloys. Shaded: predicted by theory for  $T = 300-1000\text{K}$  and non-ideal alloys. --- ideal alloys. Points  $\bullet$ , own data obtained by AES; other symbols - various data from the literature. (Reproduced with permission from Ref.10. North-Holland Publ.Co.)

the photon excited electron spectroscopy. With synchrotron radiation (10-150 eV) or with more classical sources of UV radiation, the valence bands can be studied in many details, while higher energy (X-ray) photons are suitable to check the behaviour of the core levels. Studied by these methods, Pt/Cu alloys offer the following picture:

- i) there is definitely no electron transfer (12-14) from Cu to Pt, as assumed in the old Rigid Band Theory and in its catalytical applications in the theory by Dowden (16).
- ii) Even for this rather strong-exothermically formed system of alloys, the changes in the electronic structure of Pt and Cu are surprisingly subtle. The 5d valence electrons of Pt can be considered as uninfluenced at all by alloying (12-14) and the valence (3d) and core levels (2p) electrons of Cu show a lower B.E. ( $B.E. = h\nu - E_{kin}$ ; relative to the Fermi energy). This lowering is more pronounced for the core levels, as one would expect if the effect were due to better screening of ionisation holes in alloys, than in pure Cu. Indeed, the effect is most likely due to the final state relaxation/screening (see the remark on p.7297 in ref.14).
- iii) There are strong indications that the valence band states show a strong mixing of Pt 5d and Cu 3d states (13,14). Further, some data have been interpreted as showing a lower degree of 3d/4s hybridization on Cu in alloys than in pure Cu metal (12).

Summarizing, the changes in the electronic structure of Pt and Cu atoms caused by alloying are rather marginal. At least, those which are observable by the electron spectroscopy.

#### How are the electronic structure changes reflected by adsorption?

It can be expected that the electronic structure changes would be reflected by the heats of adsorption of suitable chosen molecules. Indeed, Shek et al (17) report that one maximum in the thermal desorption profile of  $\overline{CO}$  shifts to lower temperatures when the Cu content of alloys increases. If the variations in the entropy changes upon adsorption can be neglected (probably - they can) this would indicate a lower heat of adsorption of CO on alloys than on Pt: from abt. 33 Kcal/mol on pure Pt, to 26 Kcal/mol for an alloy with abt. 20% Cu.

However, before we accept this conclusion as the definitive one, a word of caution is necessary. Due to the CO-CO interactions the heats of adsorption depend on the coverage  $\theta$ . Shek et al (17) compared Pt and alloys at a constant dosage and this could mean that the coverage of Pt was (at the same dosage) lower on Pt than on alloys, and consequently - the heat of adsorption higher. Shek et al report the above mentioned data for the (111) faces of Pt and alloys. They studied also the (110) faces, but there the effect of alloying is masked by the reconstruction of the surface upon CO-adsorption (18).

Alloys used by Shek et al (18) were prepared by dissolving adsorbed Cu layers into the bulk, by heating the sample. Complications with a varying roughness can not be excluded and it is known that such changes would change the heat of adsorption as well (19). In fact, such effect has been probably observed (20). It would be desirable to have data on monocrystals equilibrated or - better - grown at a much higher temperature. Unfortunately due to the side

effects of ordering it is not easy to produce the Pt/Cu monocrystals. Therefore, Noordermeer et al (21) studied a related system, which is easier to obtain, the PdCu (111) monocrystal plane. These authors come to the conclusion that alloying does not change the position of the CO-desorption peaks (see figure 2) and only the population of various states (peaks) vary.

Another way to monitor the expected changes in the metal electronic structure is to look at the adsorbed molecules, which are sensitive in their properties to the changes in the electronic structure of surface metal atoms. Such a molecule is CO and the frequency of the CO stretch vibrations ( $\nu(\text{CO})$ ) is a sensitive detector of the direct- and back-donation upon adsorption of CO. It has been reported, that  $\nu(\text{CO})$  decreases for the VIII group metal by alloying of Pd with Ag (22), Ni with Cu (23), but also when mixing Ni with Co (24). This has been first explained (25) as an indication for an increased backdonation due to an assumed electron shift  $\text{Cu} \rightarrow \text{Pt}$ ,  $\text{Cu} \rightarrow \text{Ni}$  and consequently  $\text{Pt}$  or  $\text{Ni} \rightarrow \pi^*(\text{CO})$ , but this explanation was rather unsatisfying (although widely spread and still being popular). Cobalt caused namely the same kind of effect as Cu and yet it could be hardly suspected of donating electrons to Ni. Indeed, it appeared that the reason for a lower  $\nu(\text{VIII grp.}, \text{CO})$  value with alloys is simply the dilution of the CO-layer. The following experiments elucidated the problem.

When CO is adsorbed on, say Pt, interaction of dipoles of individual molecules is repulsive, and it decreases the heat of adsorption and increases the  $\nu(\text{Pt}, \text{CO})$  frequency. This effect on frequency is a resonance effect; when a  $^{12}\text{CO}$  layer is diluted by  $^{13}\text{CO}$  or  $\text{C}^{18}\text{O}$ , etc., the interaction is much weaker (26,27).  $^{13}\text{CO}$  molecules in the full layer of  $^{12}\text{CO}$  simulate, thus, actually the empty sites. If Pt surface layer is diluted by Cu atoms, not covered by  $^{12}\text{CO}$ , or covered, but by  $^{13}\text{CO}$  vibrating at a different frequency, then the  $\nu(\text{Pt}, ^{12}\text{CO})$  value at  $\theta(\text{Pt}, \text{CO}) \rightarrow 1$  must be with Pt/Cu alloys lower than the corresponding value of  $\nu(^{12}\text{CO}, \text{Pt})$  on pure Pt. The question is - does alloying cause an effect additional to this decrease by dilution? The answer can be obtained when  $\nu(\text{Pt}, ^{12}\text{CO})$  is monitored at  $\theta(\text{CO}, \text{Pt}) \rightarrow 1$  as a function of  $x$ ,  $x = ^{12}\text{CO}/(^{12}\text{CO} + ^{13}\text{CO})$ , the molar ratio of  $^{12}\text{CO}$  in the adsorbed layer. One follows the  $\nu(\text{Pt}, ^{12}\text{CO})$  on pure Pt and on one or more alloys and extrapolates  $\nu$  to  $x \rightarrow 0$ . The remaining effect, i.e., the difference at  $x \rightarrow 0$  of  $\nu(\text{Pt}, ^{12}\text{CO})$  between pure Pt (or on other metal) and its alloys, is the maximum room left for possible electronic structure changes being reflected by the  $\nu(\text{Pt}, ^{12}\text{CO})$  frequency.

Toolenaar, Stoop et al performed such measurements, being inspired by earlier papers (26,27) and they have seen that with Pt/Cu the room for possible electronic structure effects was virtually zero (28) (see figure 3). Also with Pt/Re and with very strongly exothermic Pt/Sn alloys, the "residual" effect at  $x \rightarrow 0$  was rather small (29). The effect was only pronounced with Pt/Pb alloys, for reasons not known at the moment. However, even with Pt/Pb the maximum possible "electronic" effect was of a size comparable with that of the effect of varying CO-coverage. The conclusion is easy then: investigations using adsorbed CO as a detector did not reveal any appreciable change in the electronic structure of underlying metal Pt atoms.

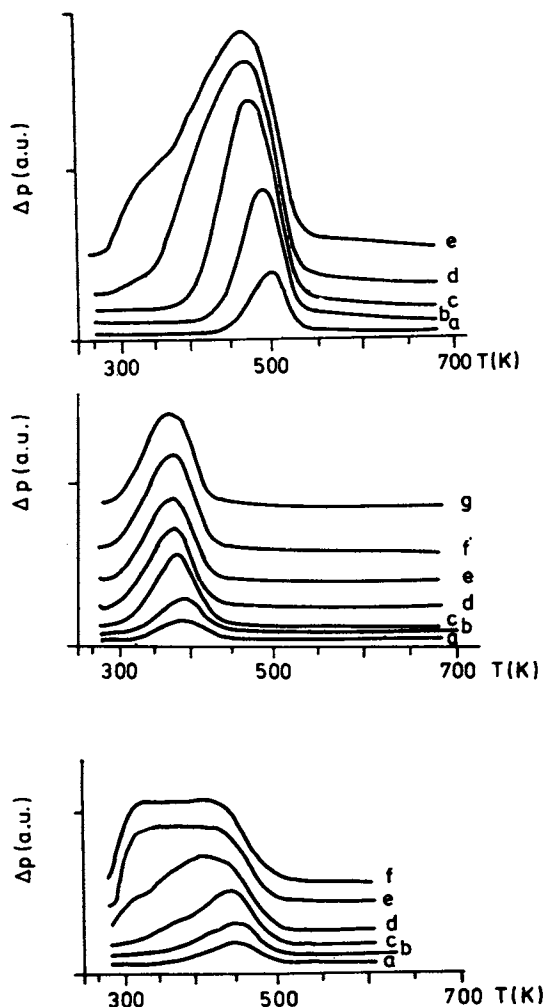


Figure 2. Above: thermal desorption of CO adsorbed on PdAg(111), exposures at 250K; 0.15, 8.3, 0.6, 1.5, 3.0 and 6 nbar.s. In agreement with the LEED and IR data, the peak and shoulders correspond to the multiple and single bound (on top and in the valleys adsorbed) CO. In the middle: thermal desorption of CO adsorbed on PdAg(111); exposures at 250K; 0.15, 0.3, 0.6, 1.2, 3.0, 6.0 and 12 nbar.s. In agreement with IR data, only the single bound CO is present in this strongly diluted ( $\approx 10\%$  Pd<sub>surf</sub>) alloys. Below: thermal desorption of CO adsorbed on PdCu(111); exposures at 250K; 0.15, 0.3, 0.6, 1.2, 3.0 and 6 nbar.s. On this Pd rich alloy (Pd<sub>surf</sub>  $\approx 70\%$ ) the same types of adsorption are present as on Pd. (ref.21) (Reproduced with permission from Ref.21. North-Holland Publ.Co.)

With Pt, the strongly prevailing type of CO adsorption is the "on top" adsorption. Only at very high coverages is some CO moved by mutual repulsions into a less favourable position, into the valleys. However, with Pd or with Ni, CO prefers at low coverages to be bound to several Pd or Ni atoms, sitting in the valley among several Pd or Ni atoms (multiply bound CO). When a second metal is introduced into Ni or Pd (Ag or Pt) the adsorption into the multiply bound CO state is suppressed, demonstrating that the number of available atoms (ensemble size) is critical for the way in which "C" of CO is bound to the surface (14). It can be reasonably expected that the same holds for "C" of hydrocarbons.

Catalytic effects of alloying of Pt with Cu. Catalytic effects are represented by figure 4. We observe that the selectivity for hydrogenolysis decreases and that of isomerization increases with increasing temperature. This can be formally ascribed to a difference in the activation energies of hydrogenolysis (cracking), isomerization and dehydrocyclization; the activation energy of isomerization should be then abt. 25 Kcal/mol higher than that of hydrogenolysis (30). Activation energy is found to be independent of the alloy composition: i.e., the curves of selectivities as functions of temperature, are only shifted in parallel to higher temperatures with a higher Cu-content.

Another piece of information available concerns the surface intermediates. By using the  $^{13}\text{C}$  labelling and by monitoring the reaction of a molecule which is an "archtype" for two types of complexes the following has been established (31-33): i) dilution of Pt by Cu increases the relative contribution to isomerization of the 5-C-intermediates (something like an adsorbed methylcyclopentane) in comparison with that of 3C-intermediates. ii) The contribution of various types of the 3C-( $\alpha\gamma$ ) and 2C-( $\alpha\beta$ ) intermediates to the overall reaction is independent of the Cu-content, but with Cu increasing, the proportion increases to which the 3C-( $\alpha\gamma$ ) intermediates are hydrogenolysed (as compared with their isomerization).

On some important side effects. When an alloy is brought into contact with a gas which shows a higher affinity for one of the alloy components, a gas induced segregation takes place. Such a process has been also found for the Pt/Cu alloys. The authors (34) established, that by hydrocarbon adsorption, Pt is preferentially covered by a carbon(aceous) layer, but under this layer the Pt concentration is higher than under vacuum (figure 5). However, this finding does not change principally the picture of the surface one had earlier.

While Pt is preferentially covered, and only at very high C-depositions also Cu may become partially covered, the presence of Cu exerts another important effect, namely on the behaviour of the carbon(aceous) layer. Auger spectra reveal (35) that Pt, more than other metals (Rh, Ni) which are good for hydrogenolysis, converts the surface carbon(aceous) layer in a highly unreactive (blocking, protective) graphite layer. However, dilution of Pt by Cu slows down this graphitization (figure 6) and, most likely, other metals might have a similar effect as well. This is certainly a point which must be considered in the discussion of the catalytic effects.

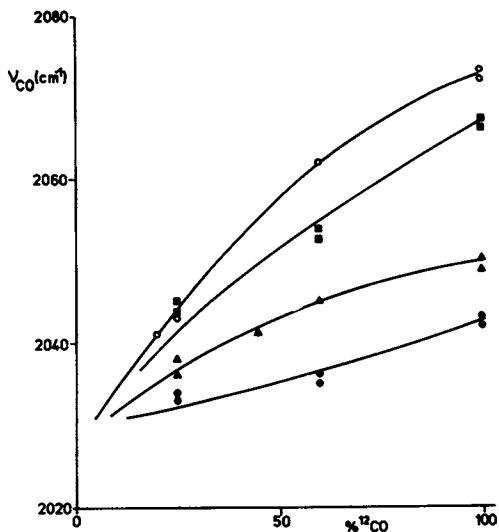


Figure 3. Wavenumbers of the high-frequency  $^{12}\text{CO}$  IR abs. band maxima of CO on Pt, as a function of  $x(^{12}\text{CO})$ . All samples of Pt/Cu on  $\text{Al}_2\text{O}_3$ , at  $\Theta(\text{CO}, \text{Pt}) \rightarrow 1$ .  $\circ$  Pt,  $\Delta$  Pt 76%  $\square$  Pt 42%  $\cdot$  Pt 31%, % - the average ( $\approx$  bulk) concentration. (Reproduced with permission from Ref.28. Acad.Press Inc.)

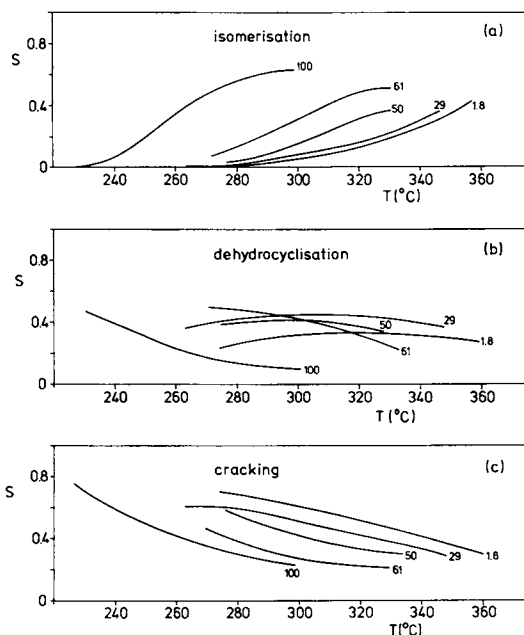


Figure 4. Selectivity in isomerization, dehydrocyclization and hydrogenolysis (cracking) of Pt/Cu alloys (on  $\text{SiO}_2$ ). Bulk composition of alloys (% Pt) indicated. (Reproduced with permission from Ref.30. Chem.Soc.London)

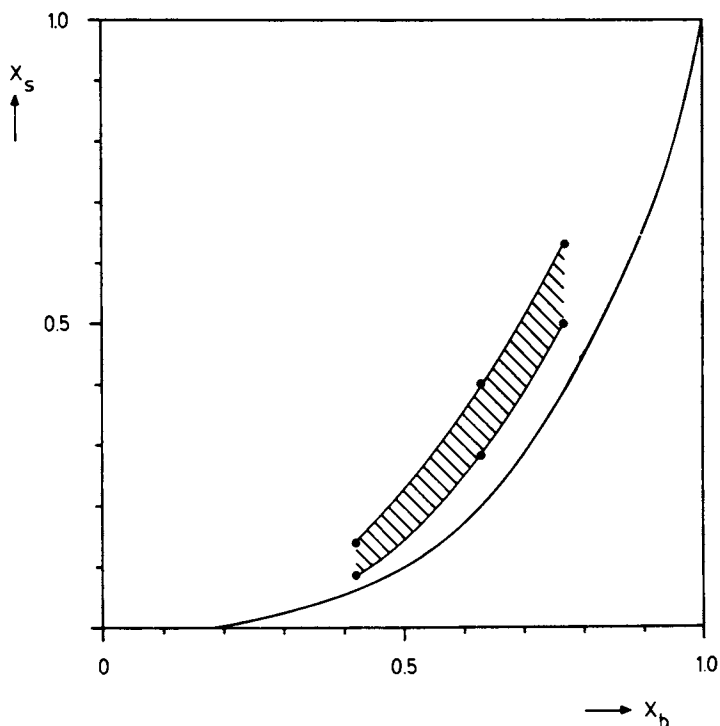


Figure 5. The molar fraction  $x_s$  of Pt in the topmost atomic layer of the alloy as a function of the bulk molar fraction of Pt- $x_b$ . Curved full line: the best fit through the experimental AES data for surfaces in vacuum. The shaded area indicates the range of the steady state molar fraction of Pt, estimated by using different growth-models for the carbon(aceous) layers, calculated for the topmost layer of Pt/Cu alloys in contact with ethene, at ambient temperature. (Reproduced with permission from Ref.34. North-Holland Publ.Co.)

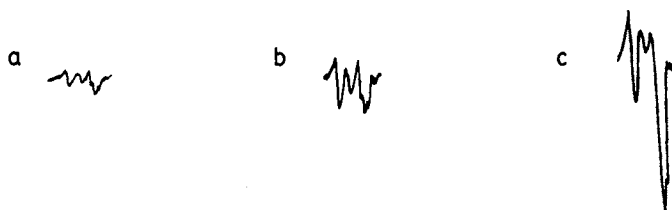


Figure 6. Characteristic part of the carbon KVV AES spectra after 55 min. exposure of  $2.10^{-8}$  nbar ethene at ambient temperature. Pt and C peak are not separated in these spectra; nevertheless the C-spectrum shows a pronounced graphite structure on pure Pt (c) and much more of the carbidic (or molecular) C on 42% (a) and 63% (b) Pt alloys. (Reproduced with permission from Ref.34. North-Holland Publ.Co.)

### Discussion

A decrease in the size of Pt ensembles achieved by alloying with a very inert second component like Ag or Au, leads to a decrease of hydrogenolytic selectivity (36-38). This is a common feature of various VIII group Ib alloys (1); at least when they are prepared in a well defined form (as, e.g., in (37)). However, a decrease of the Pt-ensemble size by alloying with Cu leads to an increase in the hydrogenolytic selectivity. This has been rationalized by assuming that Cu is - somehow - involved in the formation and conversion of the surface intermediates (30). The knowledge accumulated since the time this hypothesis has been formulated allows us to be a little bit more specific in suggesting the picture of the Pt/Cu working surfaces.

The three changes in the selectivities of Pt caused by Cu are, namely: i) the 3C-complexes are rather split than isomerized, at the given temperature, ii) The MCP-ring-opening produces more n-hexane than on pure Pt, and iii) the formation of 5C-surface complexes is promoted. These three changes are the same as changes caused by diminishing the Pt (pure Pt) particle size. What happens then by diminishing the particle size? The small Pt particles are less self-poisoned by the reaction, since it is more difficult to cover a curved (or stepped, with monocrystals) surface of small particles, as compared with large, flat planes (39). With very small particles, the reaction intermediates bound to the edge atoms find it more difficult to get the neighbouring metal atoms directly involved in the conversions of the intermediates, etc. On the other hand these neighbours have a better chance not to be covered by a continuous carbon(aceous) layer and they can intervene indirectly in the conversions of the intermediate, for example by mediating a free transport of H-atoms, from and to the intermediate. This is to be compared with the situation on the flat planes where a continuous carbon(aceous) layer can grow easily and where the neighbours of an uncovered Pt atom are most likely prevented from having any interference directly or indirectly with the conversion of the surface intermediates.

Consider now reactions of, say, n-hexane at increasing temperatures, i.e., at reversibly increasing coverage of the surface by a carbonaceous layer. It is certainly conceivable that when the surface is being progressively covered, the remaining isolated Pt atoms tend to isomerize hexane, rather than to split it by hydrogenolysis. Among other reasons, this is because the progress of dehydrogenation of intermediates and the final back-hydrogenation of the fragments, is slowed down by the carbonaceous layer (the same situation arises when Pt atoms are isolated by inert Ag or Au atoms). Further, the isolated VIII group atoms or the smallest ensembles of VIII group atoms usually show a promoted isomerization and a slowed down hydrogenolytic splitting and this could be an intrinsic property of the smallest ensembles. However, the situation is probably different with Cu. The Cu-H bond strength is sufficient to make a splitting of a C-H bond by a pair Pt-Cu, in principle, possible. Cu-atoms can further mediate a rather free transport of H-atoms to and from the intermediates, possibly promoting by that the C-H bond splitting and fragment hydrogenation.



More severe conditions, i.e., a higher T, is needed to exclude Cu from this kind of interfering and this situation would lead to a parallel shift of the selectivity curves to higher temperatures, exactly as observed experimentally (see figure 4). When the Pt/Cu catalysts are compared with Pt at the same temperature, an increased hydrogenolytic selectivity is observed. A metal like Re or Ir, when alloyed with Pt, can play a very similar role like Cu.

As mentioned above, when a Pt-atom is surrounded by Ag, Au, Sn, etc., that is, by atoms considerably less active than Cu, very well isolated Pt atoms or small Pt ensembles can be created, which, even without any assistance of the neighbouring Ag, Au, Sn, etc., will tend to isomerize hexane rather than to split it. However, when the alloys are not well homogenized, as is frequently the case with alloys on some supports, sufficient larger ensembles of Pt, but now more difficult to be selfpoisoned (like the smallest Pt particles), may coexist next to Au, Ag, Sn or their alloys and be responsible for higher hydrogenolytic selectivity (1). Such effects may be then easily misinterpreted as a consequence of an alloy - support (non specified!) electronic interaction.

#### Literature Cited

1. Ponec, V. Adv.Catal. 1983, 32, 149
2. Clarke, J.K.A. Chem.Rev. 1975, 75, 291
3. Sinfelt, J.H. Acc.Chem.Res. 1977, 10, 15
4. Sachtler, W.M.H.; van Santen, R.A. Adv.Catal. 1977, 26, 69
5. Ponec, V. Catal.Revs.Sci.Engn. 1975, 11, 1
6. Ponec, V.; Sachtler, W.M.H. J.Catal. 1972, 24, 250
7. Ponec, V. Proc.of the IXth Intl.Vacuum Congr.and Vth Intl.Conf. on Surf.Sci., Madrid, 1983, p.121
8. Kelley, M; Ponec, V. Progress in Surf.Sci. 1981, 11, 139
9. Ponec, V. In "Electronic Structure and Reactivity of Solid Surfaces"; Derouane, E.G.; Lucas, A.A., eds.; Plenum Press, 1976, p.537
10. van Langeveld, A.D.; Ponec, V. Applic.of Surf.Sci. 1983, 16, 405
11. Williams, F.L.; Nason, D. Surf.Sci. 1974, 45, 377
12. Kleimann, G.G.; Sundaram, V.S.; Barreto, C.L.; Rogers, J.D. Solid State Commun. 1979, 32, 919
13. Shek, M.L.; Stefan, P.M.; Lindau, I.; Spicer, W.E. Phys.Rev.B 1983, 27, 7277
14. Shek, M.L.; Stefan, P.M.; Lindau, I.; Spicer, W.E. Phys.Rev.B 1983, 27, 7288
15. Hultgren, R.; Desai, P.D.; Hawkins, D.T.; Gleiser, M.; Kelley, K.K. In "Selected Values of Thermodynamic Properties of Binary Alloys"; Amer.Soc.Metals, Ohio, 1973
16. Dowden, D.A. J.Chem.Soc. 1950, 242
17. Shek, M.L.; Stefan, P.M.; Lindau, I.; Spicer, W.E. Surf.Sci. 1983, 134, 438
18. Shek, M.L.; Stefan, P.M.; Lindau, I.; Spicer, W.E. Surf.Sci. 1983, 134, 399 and 427
19. Erley, W.; Ibach, H.; Lehwald, S.; Wagner, H. Surf.Sci. 1979, 83, 585
20. See the analysis of various data in ref.1 of this paper

21. Noordermeer, A.; Kok, G.A.; Nieuwenhuys, B.E. Surf.Sci. submitted paper for ECOS VI, England, 1984
22. Primet, M.; Mathieu, M.V.; Sachtler, W.M.H. J.Catal. 1976, 44, 324
23. Dalmon, J.A.; Primet, M.; Martin, G.A.; Imelik, B. Surf.Sci. 1975, 50, 95
24. Van Dijk, W.L. M.Sc.Thesis, Leiden, 1974
25. Blyholder, G. J.Phys.Chem. 1964, 68, 2772
26. Hammaker, R.M.; Francis, S.A.; Eischens, R.P. Spectrochim. Acta 1965, 21, 1295
27. Crossley, A.; King, D.A. Surf.Sci. 1977, 68, 528
28. Toolenaar, F.J.C.M.; Stoop, F.; Ponec, V. J.Catal. 1983, 82, 1
29. Bastein, A.G.T.M.; Toolenaar, F.J.C.M.; Ponec, V. J.Catal. in print
30. De Jongste, H.C.; Kuijers, F.J.; Ponec, V. Proc. Vith Congr. on Catal., London, 1976; Bond, G.C.; Tompkins, F.C.; Webb, G. eds.; Chem.Soc., London, 1976, Vol.2, p.915
31. De Jongste, H.C.; Ponec, V. Proc. VIIth Congr. on Catal., Tokyo, 1980; Seiyama, T.; Tanabe, K. eds.; Kadansha, Tokyo, 1981, Vol.1, p.186
32. De Jongste, H.C.; Ponec, V.; Gault, F.G. J.Catal. 1980, 63, 395
33. Botman, M.J.P.; De Jongste, H.C.; Ponec, V. J.Catal. 1981, 68, 9
34. Van Langeveld, A.D.; Van Delft, F.C.M.J.M.; Ponec, V. Surf.Sci. 1983, 134, 665
35. Van Langeveld, A.D.; Van Delft, F.C.M.J.M.; Ponec, V. Surf.Sci. 1983, 135, 93
36. Van Schaik, J.R.H.; Dessing, R.P.; Ponec, V. J.Catal. 1975, 38, 273
37. Sachtler, J.W.A.; Somorjai, G.A. J.Catal. 1983, 81, 77
38. Vogelzang, M.W.; Botman, M.J.P.; Ponec, V. Faraday Soc. Discussions, 1982, 72, 33
39. Lankhorst, P.P.; De Jongste, H.C.; Ponec, V. In "Catalyst Deactivation"; Delmon, B.; Froment, G.F. eds.; Elsevier, Amsterdam, 1980, p.43

RECEIVED March 20, 1985

## Determination of the Atomic and Electronic Structure of Platinum Catalysts by X-ray Absorption Spectroscopy

F. W. Lytle<sup>1</sup>, R. B. Gregor<sup>1</sup>, E. C. Marques<sup>2,4</sup>, V. A. Biebesheimer<sup>2,5</sup>, D. R. Sandstrom<sup>2,6</sup>, J. A. Horsley<sup>3</sup>, G. H. Via<sup>3</sup>, and J. H. Sinfelt<sup>3</sup>

<sup>1</sup>The Boeing Company, Seattle, WA 98124

<sup>2</sup>Department of Physics, Washington State University, Pullman, WA 99164

<sup>3</sup>Exxon Research & Engineering Company, Annandale, NJ 08801

X-ray absorption spectroscopy was used for *in situ* characterization of active, supported Pt catalysts. The extended fine structure (EXAFS) was used to determine bond distances, coordination number and disorder. The near edge (XANES) was used as an indication of electronic state. Significant results include, 1) a reversible change of shape of clean supported metal clusters as a function of temperature, 2) supported Pt clusters have more disorder or strain compared to the bulk metal, and 3) a clear determination of the bonds between the catalytic metal atoms and the oxygen atoms of the support.

X-ray absorption spectroscopy combining x-ray absorption near edge fine structure (XANES) and extended x-ray absorption fine structure (EXAFS) was used to extensively characterize Pt on Cabosil catalysts. XANES is the result of electron transitions to bound states of the absorbing atom and thereby maps the symmetry - selected empty manifold of electron states. It is sensitive to the electronic configuration of the absorbing atom. When the photoelectron has sufficient kinetic energy to be ejected from the atom it can be backscattered by neighboring atoms. The quantum interference of the initial

---

<sup>4</sup>Current address: Monsanto Company, St. Louis, MO 63166

<sup>5</sup>Current address: Fachbereich Physik, Freie Universität Berlin, Arnimallee 14, 1000 Berlin 33, Federal Republic of Germany

<sup>6</sup>Current address: The Boeing Company, Seattle, WA 98124

0097-6156/85/0288-0280\$06.00/0  
© 1985 American Chemical Society

electron wave state and backscattered wave produces a modulation of the absorption cross section, i.e., EXAFS. EXAFS data can provide information on bond distances, coordination numbers, disorder and types of ligand for the first few coordination spheres. Although both XANES and EXAFS depend upon a measurement of x-ray absorption cross section the electronic and structural information is due to electron transitions and/or scattering where the source of electrons is an atomic species within the sample. This element is chosen by the coincidence in energy of the x-ray probe and the absorption edge of interest. In this element specificity lies the power of the technique for catalyst characterization. Unlike most structural techniques, x-ray spectroscopy is not overwhelmed by the presence of the support. The support only appears in the data as it interacts with the atoms examined. A recent review by Lee, et al. has discussed the general use of the EXAFS technique and its limitations.(1) We have reviewed catalytic applications of both EXAFS and XANES.(2-3)

In the following, structural data are obtained for Pt atoms and their near neighbors on active catalysts under controlled conditions. XANES is used to indicate the direction and amount of d-electron flow between the Pt catalyst and its ligands, EXAFS to measure near neighbor structural parameters. We find EXAFS/XANES to be a sensitive and subtle indicator of small changes in the environment of catalytic atoms.

#### Experimental Methods

The preparation and characterization by chemisorption (H/Pt = 0.9 for 1 wt.% catalyst and 1.0 for 0.5 wt.% catalyst) of the catalysts have been described.(4) The data were obtained in the catalyst cell previously described (2) either by transmission measurements, measuring  $\ln I_0/I$ , or by the fluorescent EXAFS technique (5) measuring  $I_F/I_0$  where  $I_0$ ,  $I$  and  $I_F$  are the intensity of the incident x-rays, transmitted x-rays and, Pt L-fluorescent x-rays, respectively. For Pt at 0.5 - 1.0 wt.% concentration the transmission and fluorescent techniques are about of equal merit. The fluorescent EXAFS technique becomes advantageous for elements of lower atomic number or at lower concentration (to 10 ppm in favorable cases). The measurements were made at Stanford Synchrotron Radiation Laboratory. In all cases a

Si(220) double crystal monochromator was used with entrance slit (1 mm high 20 m from the source point) chosen to give a bandpass of 2 eV at the Pt  $L_{III}$  edge, 11,563.7 eV.<sup>(6)</sup> The operation of the catalyst cell allowed in situ reduction, chemisorption or catalysis while maintaining the temperature in the desired range from 1300 to 90 K. In practice once a desirable catalyst condition was achieved x-ray measurements often were taken at temperature and after quenching to 90 K in an attempt to minimize thermal smearing of the EXAFS data. For each measurement 2 to 3 scans were averaged over a total time of  $\sim$  40 minutes. Temperatures were measured and kept constant at the temperatures indicated to  $\pm 5^\circ\text{C}$ . An example of raw data for 2.5  $\mu\text{m}$  thick Pt foil at 298 K is shown in figure 1. The three L-edges of Pt are shown, with the zero of energy at 11,563.7 eV, the position of the  $L_{III}$  edge. Note the sharp XANES feature at the  $L_{III}$  edge in contrast with the  $L_{II}$  edge which will become more evident later when the graph is expanded.

#### EXAFS Data Analysis

We have described in detail our technique of data analysis.<sup>(2-4)</sup>

Basically, the EXAFS,  $\chi(K)$

$$\chi(K) = \sum_j A_j(K) \sin [2KR_j + \phi_j(K)] \quad (1)$$

$$A_j(K) = \left( N_j / KR_j^2 \right) F_j(K) \left( \exp -2K^2 \sigma_j^2 \right) \quad (2)$$

is Fourier transformed

$$\Phi_n(R) = (1/2\pi)^{1/2} \int_{K_{\min}}^{K_{\max}} K^n \chi(K) \exp [2iKR + \phi_j(K)] dK \quad (3)$$

to produce a radial structure function centered on the absorbing atom. We proceed by taking the inverse transform of the first neighbor peak and then extract the unknown functions  $F_j(K)$ , electron back-scattering and  $\phi_j(K)$ , the phase shift from a suitable reference material. For catalysts with the same bond, i.e., Pt-Pt, we include the phase shift in the forward transform. This greatly simplifies the peak structure.<sup>(7)</sup> Then by a least-squares fitting routine we evaluate  $N_1$ ,  $R_1$  and  $\Delta\sigma_1^2$ . We found for a 1% Pt catalyst Pt-Pt bonds:

$N_1 = 8 \pm 1.5$ ,  $R_1 = 2.77 \pm .01 \text{ \AA}$ , and  $\Delta\sigma_1^2 = .0018 \text{ \AA}^2$ . (4) For the 0.5% catalyst  $N_1 = 6 \pm 1.5$ ,  $R_1 = 2.77 \pm .01 \text{ \AA}$  and  $\Delta\sigma_1^2 = .003 \text{ \AA}^2$ . The  $\Delta\sigma_1^2$  is the increase in disorder over Pt metal at the temperature of measurement, 90 K.

In figure 2 Fourier transforms of Pt  $L_{III}$  EXAFS are shown for metallic Pt, 1% Pt on Cabosil, and 0.5% Pt on Cabosil all at 90 K. The effect of the phase shift on sharpening the transform peak is particularly evident for metallic Pt. Also note that the peaks are now at the correct radial distance, e.g., the measured versus (known) distances for the 1st through 5th coordination spheres are 2.769 (2.769), 3.948(3.917), 4.803(4.797), 5.537(5.539) and 6.172(6.193)  $\text{\AA}$ , respectively. Compared with the metal the Pt-Pt distances in the catalysts are identical within experimental error. The diminished magnitude of the transform is the result of the smaller average coordination number. In the catalyst transforms there is evidence of a smeared out Pt-O peak in the region from  $\sim 1.0 - 2.5 \text{ \AA}$ . Using a sequential Fourier filtering technique with appropriate phase shift (8) this region was further analyzed to produce the Pt-O peaks shown in the INSET to figure 2. For the 1% and 0.5% catalysts the bond distance is  $1.96 \pm .05 \text{ \AA}$  with Pt-O coordination numbers of  $\sim 0.5$  and 1.0, respectively. This means that the average Pt atom will have 0.5 (1.0) oxygen neighbors. This is evidence for interaction of the Pt atoms with the surface of the support and is also shown by the XANES and the temperature versus disorder study described in the following.

In a recent paper we used the temperature sequence of EXAFS measurements of the reduced catalyst in  $H_2$  to determine the temperature dependence of the disorder. (7) Comparable data was obtained for Pt metal over the same temperature range. The analysis proceeded by fitting the 1st coordination shell catalyst data to a 2-shell model in which the 1st shell was assumed to be that part of the Pt cluster with a full complement of near neighbors and would behave like bulk Pt. The remainder was assumed to be surface atoms and  $\Delta\sigma^2$  was allowed to vary to achieve the best fit to the data. The relative fraction of surface and bulk was assigned from the chemisorption measurement, i.e., 0.9 and 0.1, respectively. The results are given

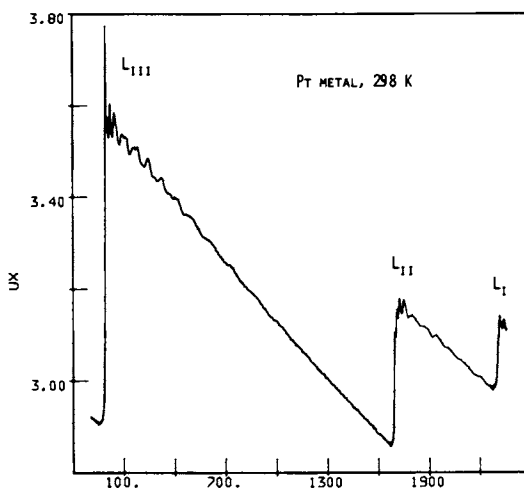


Figure 1. The L-absorption edges of 2.5  $\mu\text{m}$  thick Pt foil at 298 K. The zero of energy is defined by the Pt  $L_{III}$  edge at 11,563.7 eV.

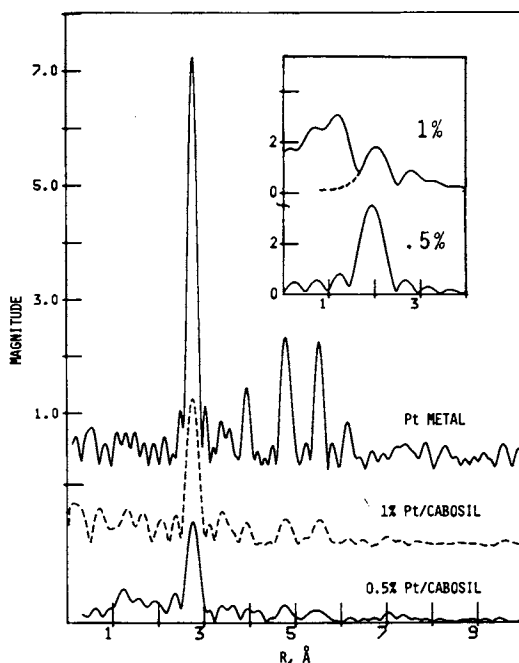


Figure 2. Phase adjusted Fourier transforms of Pt metal, 1% Pt/Cabosil catalyst in  $\text{H}_2$  and 0.5% Pt/Cabosil catalyst in  $\text{H}_2$ , all at 90 K. All are plotted to the same scale to emphasize the diminished magnitude because of the smaller average coordination numbers in the catalysts. The INSET shows the Pt-O peak area retransformed with the appropriate Pt-O phase shift. The artifact at low R is due to the EXAFS extraction procedure.

in figure 3 and show that the relative thermal motion of the surface atoms is significantly greater than in the bulk metal over the range from 100 - 800 K. This result is expected considering the partial coordination, hence lack of constraint of the surface atoms. A similar result has been found from LEED measurements on a Pt surface. (9) Significantly, the surface atom disorder when extrapolated to 0 K remains sizable. This static disorder or strain appears to be a result of the interaction of the Pt atoms with the support, a kind of epitaxy to the oxygen (or hydroxyl) surface of the support.

#### Analysis of XANES Data

The electronic dipole transitions at the Pt  $L_{III}$  ( $L_{II}$ ) edge(s) are from the  $2P_{3/2}$  ( $2P_{1/2}$ ) core level(s) to the empty 5d and 6s states ( $\Delta J = 0 + 1$ ); however, the transition to 6s has a much lower probability and is not expected to contribute measurably. In previous work (10) it was shown that the intensity of the peak at the  $L_{III}$  absorption edge was approximately proportional to the d-electron vacancies. A series of compounds of one element illustrated that the increase in the peak intensity of the compound compared with the pure element was proportional to an ionicity estimate of the number of 5d electrons removed from the element by formation of chemical bonds. (11) In this same work XANES sensitivity to interaction with the support and to  $O_2$  chemisorption was also demonstrated for Pt or Ir supported on  $Al_2O_3$ . Gallezot, et al. (12) demonstrated similar effects for Pt on zeolites. Mansour, et al. (13) investigated Pt on  $SiO_2$  and  $Al_2O_3$  as a function of  $H_2$  reduction temperature. All three studies (refs. 11-13) agreed that the increase in area of the peak at the Pt  $L$  edge(s) indicated that reduced, supported Pt was electron deficient compared with the bulk metal. (In that which follows this conclusion is shown to be over simplified. At high temperature Pt/ $SiO_2$  has more electrons than bulk Pt.) The most simple explanation is that Pt 5d electrons form bonds with available ligands on the support. Short, et al. (14) have used the same technique to explore the strong metal support interaction (15) (SMSI) of Pt on  $TiO_2$ . A small effect was noted in the EXAFS and XANES between the normal and SMSI catalyst conditions. An interesting result in light of references 11-13 was that the  $L_{III}$  edge peak was diminished in intensity and width compared



to bulk Pt in contrast with the particularly wide  $L_{III}$  peak observed on  $SiO_2$  or  $Al_2O_3$ . A serious caveat of all the above results (refs. 11-14) is that the catalyst was conditioned at a particular temperature and then cooled to room temperature or below for the x-ray measurement. As will be shown there is a significant temperature effect on the XANES of a Pt catalyst in  $H_2$  or He. Horsley (16) has shown how the  $L_{II,III}$  x-ray absorption edge resonances can be modeled by X $\alpha$ -SW molecular orbital calculations of a cluster composed of Pt or Ir and its first neighbors. Both chemical compounds and catalyst clusters were modeled and there was good agreement with experiment. Both Horsley (16) and Mansour, et al. (13) emphasized that the  $L_{II,III}$  edges must both be considered for a quantitative measure of total d-state occupancy.

The XANES region for the Pt  $L_{II,III}$  edges in Pt metal and the 0.5% catalyst is shown in figure 4. It is evident that there is an edge resonance ("white line") at the  $L_{III}$  edge which is much diminished at the  $L_{II}$  edge. The reason for this difference was first pointed out by Mott (17) and is based upon atomic dipole selection rules ( $\Delta J = 0 \pm 1$ ). In a Pt atom the empty 5d state has  $J = 5/2$  symmetry, hence a transition is expected at the  $L_{III}$  edge ( $J = 3/2$ ) but not at the  $L_{II}$  edge ( $J = 1/2$ ). Brown, et al. (18) discussed this problem in detail and concluded that in Pt metal the empty d-band is predominately  $J = 5/2$ . Mattheiss and Dietz (19) (MD) investigated the problem with a more accurate relativistic model which included hybridization of the 5d with the broad 6s and 6p bands. Their result differs in detail but generally substantiates the result of Brown, et al. (18) Mansour, Cook and Sayers (20) have applied the MD result to Pt catalysts, developing a procedure to determine changes in d-electron occupancy.

MD (19) determined the equations for dipole transitions including the splitting of the final d-states due to spin-orbit coupling. These results were then applied to relativistic tight binding energy band calculations for Pt and Au where the appropriate electron symmetries had been projected out. Selected emission and absorption data were shown to be in agreement with calculations. Pertinent to the present work is the result

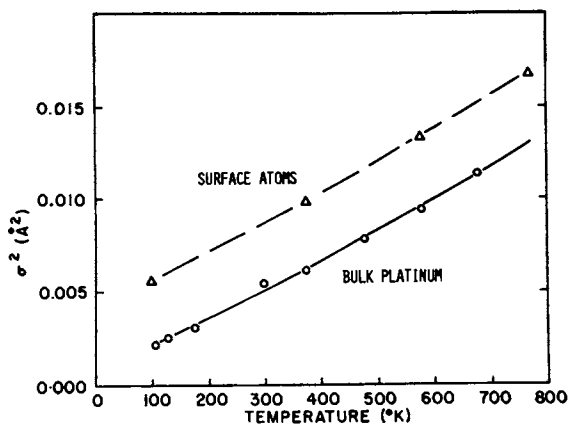


Figure 3. Comparison of relative mean squared thermal motion for bulk and surface Pt atoms as a function of temperature. The triangles mark the catalyst surface atoms, the circles are for bulk Pt.

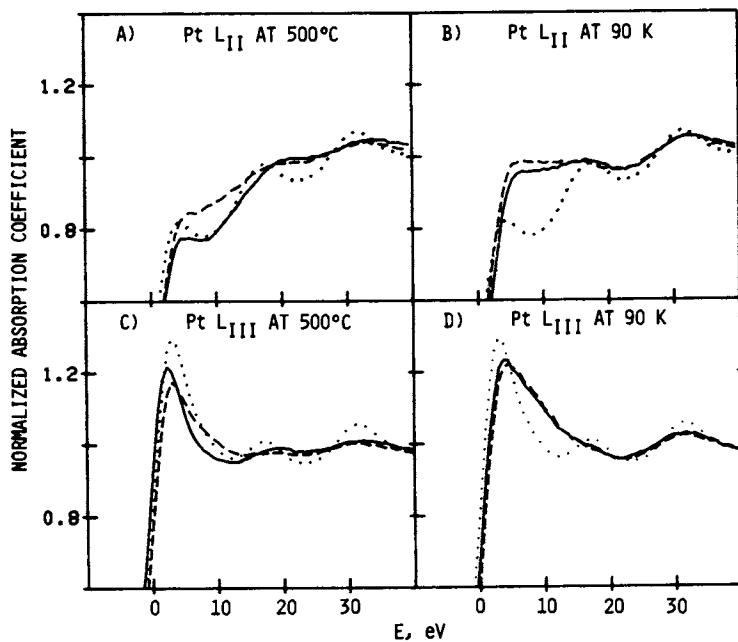


Figure 4. Comparison of Pt metal (.....)  $L_{II,III}$  spectra with 0.5% Pt/Cabosil in  $H_2$  (-----) and He (——) at 773 K and 90 K.

$$A(L_{III}) = Cw_{L_{III}} \left( \frac{R^{2p_{3/2}}}{d} \right)^2 \left( 6h_{5/2} + h_{3/2} \right) / 15 \quad (4)$$

$$A(L_{II}) = Cw_{L_{II}} \left( \frac{R^{2p_{1/2}}}{d} \right)^2 \left( h_{3/2} \right) (2) / 3 \quad (5)$$

where  $A(L)$  is the area of the L-edge resonance;  $h_{5/2,3/2}$  are the number of 5d-electron holes of indicated symmetry; and the factor (2) is due to the double degeneracy of the  $L_{III}$  transition compared to  $L_{II}$  and must be included when both edges are normalized to unit edge jump as is done here. The projected density of states curve for Pt in reference 19 shows that the shape of the  $J = 5/2$  and  $J = 3/2$  curves are virtually identical with  $(J = 5/2) \approx 3X (J = 3/2)$ . This is the reason for the greater strength of the  $L_{III}$  edge resonance. As shown by Horsley (16) the transition to the d-band, the edge resonance, may be convolved with an arc tangent to produce the kind of absorption curves observed in Pt  $L_{II,III}$ . In the Pt density of states curves the Fermi surface at  $E_F$  cuts the curves in a region of maximum slope. This would make the  $L_{II,III}$  transitions very sensitive to changes in  $E_F$ , i.e., electron flow to or from the catalyst clusters. By this discussion we have attempted to show that the Pt  $L_{II,III}$  edge resonances may be considered as images of their respective d-bands (broadened by the appropriate lifetime and resolution functions) and will discuss the catalyst data in terms of a d-band model.

The differences between the Pt  $L_{II,III}$  XANES of the catalyst in  $H_2$  and He and bulk Pt as a function of temperature is shown in figure 4. (There is no measurable difference in Pt metal over this temperature range.) There is a continuous, reversible change for the catalyst XANES shown in A or C (773 K) to that shown in B or D (90 K) as shown in Figure 6.

The data was taken as follows: The catalyst was reduced in flowing  $H_2$  at atmospheric pressure to a maximum temperature of 773 K and then cooled in  $H_2$ , taking data at  $\sim 100$  degree intervals to a low temperature of 90 K. It was then heated back up to 773 K in  $H_2$ . At 773 K a purified He flow at atmospheric pressure was initiated and repeated data scans were taken at 773 K until the sample equilibrated as shown by the data. The sample was then cooled in flowing He taking data as

before. Under these conditions we believe the catalyst to be below sintering temperature (this was proved by cycling the catalyst) and to consist of naked Pt clusters in He or with chemisorbed H when in  $H_2$  atmosphere over most of the temperature range with some equilibrium for Pt-H bonds at the temperatures where H desorbs.

In comparison to Pt metal there are significant differences in the unfilled catalyst d-states at both temperatures. At high temperature the d-band is slightly narrower than bulk Pt, at low temperature it is much broader. The extra x-ray absorption in the 5-15 eV interval shown in figure 4 D) was the basis for the earlier conclusion (11-13) that Pt/SiO<sub>2</sub> is electron deficient. Although the  $L_{II}$  and  $L_{III}$  edges appear to be very different from each other this is merely the result of mixing the different  $L_{II}$  and  $L_{III}$  edge resonance intensities with the onset (the arctangent curve) of the absorption edge. The difference spectra in figure 5, where the appropriate Pt metal edge has been subtracted, show that the changes relative to Pt for both edges are very similar. Allowing for the factor of 2 multiplier in the  $L_{II}$  edge the relative difference amplitudes are of the expected magnitude, i.e.,  $L_{III} > L_{II}$ . We can conclude that the  $J = 5/2$  and  $J = 3/2$  states in the catalyst are similar to each other as they are in Pt metal but they are significantly different from Pt metal.

What are the electronic and structural implications of that conclusion? We have considered the following possibilities to explain the data:

1. A change in the Fermi energy due to electrons flowing to and from the Pt clusters would correspondingly change that part of the d-band available for the edge resonance. The edge narrowing with increasing temperature implies electron flow to the Pt clusters as Pt-O bonds to the support are broken. This effect cannot explain the extra absorption at 5-15 eV with decreasing temperature if the d-band of the cluster is similar to bulk Pt. There are no sharp peaks in the density of states located at appropriate energies.
2. Could a change in shape of the small Pt clusters produce sufficiently large changes in the density of states to cause the effect? One of us (Horsley) has made preliminary multiple

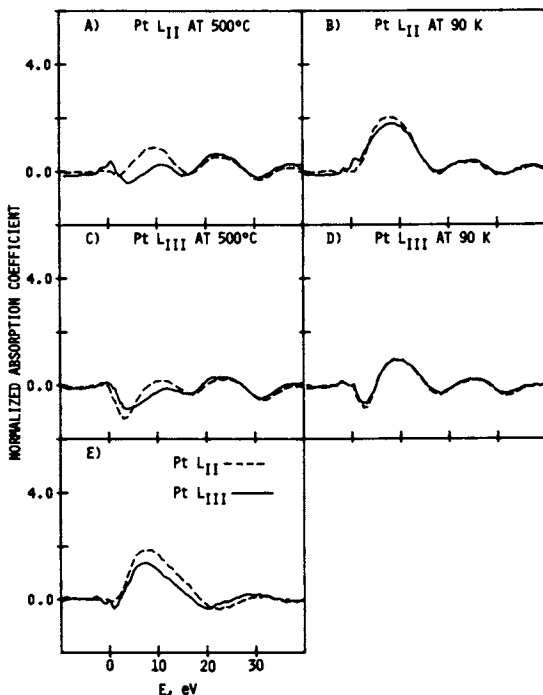


Figure 5. Difference spectra of the data in figure 4 where Pt metal  $L_{II,III}$  has been subtracted appropriately from the catalyst data. In E) the difference areas Cat. (He, 773 K) - Cat. (He, 90 K) are shown.

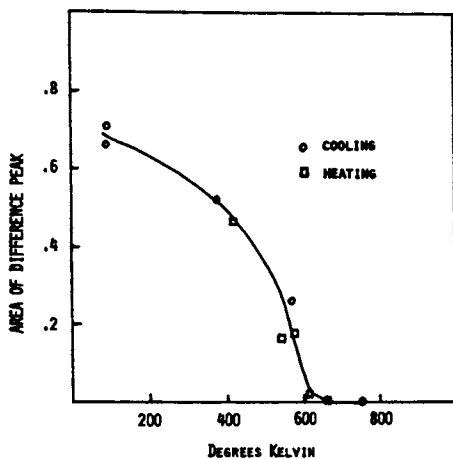


Figure 6. Area of the first peak in difference curve of the Pt  $L_{III}$  edge versus absolute temperature for 1% Pt on Cabosil in  $H_2$ . The high temperature measurement (773 K) was subtracted from each of the other spectra.

scattering X $\alpha$  calculations to investigate this question. For Pt clusters corresponding to 13 atom spheres, two-layer, and mono-layer rafts no changes were observed in the d-states that would cause the effect.

3. The low temperature EXAFS data showed Pt-O bonds to the support. If those bonds broke with increasing temperature would that cause the effect? (The thermal smearing of the EXAFS at high temperature makes it impossible to investigate the bonds directly.) One of us (Horsley) has made preliminary calculations which show that the Pt 5d-orbitals interact with the O 2p-orbitals to create a hybrid orbital with bonding and anti-bonding states below and above the Pt d-band, respectively. The increased x-ray absorption at low temperature is due to transitions to the empty anti-bonding orbitals. At high temperatures the Pt-O bonds to the support begin to be broken because of the increased thermal motion, hence the orbitals disappear. Presumably, at higher temperatures all the bonds would break and the clusters would become mobile, thereby providing a model for agglomeration and sintering.

It has been shown by electron microscopy (21) and EXAFS (22) that highly dispersed supported metal catalysts consist of a mix of sphere-and-raft-like shapes. We believe that as Pt-O bonds break (or form) the raft-like clusters curl up (or flatten out) on the support. The bonds to the support are the driving force for raft-like dispersion. The high temperature difference between H<sub>2</sub> and He may be due to a similar anti-bonding resonance between the Pt(5d) and H(1s) orbitals, the width of the resonance arising from an interaction with the Pt 5-P band. (23) In a UPS study of highly dispersed Pt/SiO<sub>2</sub> Ross, et al. (24) investigated the filled bonding orbitals below the Pt d-band and found a large increase in the density of states. This would confirm, in part, our explanation. The narrower edge resonance in He at high temperature is not explained by these bonding arguments. The effect is experimentally significant and may be a true density of states effect caused by the small cluster size.

### Conclusions

The new results of this study include a clear demonstration of Pt-O bonds to the support at low temperature in either He or H<sub>2</sub>. As the temperature is raised above 600 K the Pt-O bonds break and the Pt raft-like clusters curl up to be more sphere-like. Concurrently with this bond-breaking and change in shape, electrons flow to the Pt d-band. At temperatures above 600 K there is a d-electron surplus in the Pt clusters compared to bulk Pt, i.e., they are more noble than Pt. This may be a significant result since practical applications of Pt-containing catalysts are in the temperature range where these changes occur.

### Acknowledgment

The work at Boeing and WSU was supported by NSF grant CHE 8219605. The x-ray measurements were made at the Stanford Synchrotron Radiation Laboratory which is supported by DOE.

### Literature Cited

1. Lee, P. A., Citrin, P. H., and Kincaid, B. M., *Rev. Mod. Phys.* 53 769 (1981).
2. Lytle, F. W., Via, G. H., and Sinfelt, J. H., "X-ray Absorption Spectroscopy: Catalyst Applications" in *Synchrotron Radiation Research*, H. Winick and S. Doniach Eds., Plenum (1980), p. 401.
3. Sinfelt, J. H., Via, G. H., Lytle, F. W., *Catal. Rev.* 26, 81 (1984).
4. Via, G. H., Sinfelt, J. H., and Lytle, F. W., *J. Chem. Phys.* 71 690 (1979).
5. Jaklevic, J., Kirby, J. A., Klein, M. P., Robertson, A. S., Brown, G. S., and Eisenberger, P., *Sol. St. Comm.* 23, 679 (1977).
6. Bearden, J. A. and Burr, A. F., *Rev. Mod. Phys.* 39, 125 (1967).
7. Marques, E. C., Sandstrom, D. R., Lytle, F. W., and Greegor, R. B., *J. Chem. Phys.*, July 15 (1982).
8. Lytle, F. W., Greegor, R. B., Marques, E. C., Sandstrom, D. R., Via, G. H., and Sinfelt, J. H., "Structural Genesis of Pt on SiO<sub>2</sub>: Determination by X-ray Absorption Spectroscopy," presented at *Advances in Catalytic Chemistry II*, Salt Lake City, Utah, May 1982. *J. Chem. Phys.* (submitted). The procedure

is as follows: Apply the Pt-Pt phase shift (derived from Pt metal) to the 1st forward transform of PtO<sub>2</sub>. This will partially smear the Pt-O peak. Then take the back transform of this smeared Pt-O peak. Extract a new phase shift from this back transform using the known Pt-O distance, 2.07 Å. This phase shift can now be used on the catalysts to focus the Pt-O peak region.

9. Lyon, H. B. and Somorjai, G. A., *J. Chem. Phys.* 44, 3707 (1966).
10. Lytle, F. W., *J. Catal.* 43, 376 (1976).
11. Lytle, F. W., Wei, P. S. P., Gregor, R. B., Via, G. H., and Sinfelt, J. H., *J. Chem. Phys.* 70, 4849 (1979).
12. Gallezot, P., Weber, R., Dalla Betta, R. A., and Boudart, M., *Z für Naturfor* 34A, 40 (1979).
13. Mansour, A. N., Cook, J. W., Sayers, D. E., Emrich, R. J., and Katzer, J. R., *J. Catal.* (submitted).
14. Short, D. R., Mansour, A. N., Cook, J. W., Sayers, D. E., and Katzer, J. R., *J. Catal.* (submitted).
15. Tauster, J. J., Fung, S. C., and Garten, R. I., *JACS* 100, 170 (1978).
16. Horsley, J. A., *J. Chem. Phys.* 76, 1451 (1982).
17. Mott, N. F., *Proc. R. Soc. Lond.* 62, 416 (1949).
18. Brown, M., Pierls, R. E., and Stern, E. A., *Phys. Rev.* B15, 738 (1977).
19. Mattheiss, L. F., and Dietz, R. E., *Phys. Rev.* B22, 1663 (1980).
20. Mansour, A. N., Cook, J. W., and Sayers, D. E., "Quantitative Technique for Determination of the Number of Unoccupied d Electron States in a Pt Catalyst from the L<sub>II,III</sub> X-ray Absorption Edge Spectra," *J. Chem. Phys.* (to be published).
21. Prestridge, E. B., Via, G. H., and Sinfelt, J. H., *J. Catal.* 50, 115 (1977).
22. Gregor, R. B., and Lytle, F. W., *J. Catal.* 63, 476 (1980).
23. Louie, S. G., *Phys. Rev. Lett.* 42, 476 (1979).
24. Ross, P. N., Kinoshita, K., and Stonehart, P., *J. Catal.* 32, 163 (1973).

RECEIVED April 17, 1985



## The Effect of Support-Metal Precursor Interactions on the Surface Composition of Supported Bimetallic Clusters

H. Miura, S. S. Feng, R. Saymeh, and R. D. Gonzalez<sup>1</sup>

Department of Chemistry, University of Rhode Island, Kingston, RI 02881

The effect of precursor-support interactions on the surface composition of supported bimetallic clusters has been studied. In contrast to Pt-Ru bimetallic clusters, silica-supported Ru-Rh and Ru-Ir bimetallic clusters showed no surface enrichment in either metal. Metal particle nucleation in the case of the Pt-Ru bimetallic clusters is suggested to occur by a mechanism in which the relatively mobile Pt phase is deposited atop a Ru core during reduction. On the other hand, Ru and Rh, which exhibit rather similar precursor support interactions, have similar surface mobilities and do not, therefore, nucleate preferentially in a cherry model configuration. The existence of true bimetallic clusters having mixed metal surface sites is verified using the formation of methane as a catalytic probe. An ensemble requirement of four adjacent Ru surface sites is suggested.

It has generally been assumed that the most important consideration in the surface enrichment of one metal in preference to another in a supported bimetallic cluster is based on differences in the enthalpies of sublimation of the metals which comprise the cluster. In most cases, the surface composition is enriched in the metal having the lower enthalpy of sublimation (1).

The role played by the support of influencing the surface composition of supported bimetallic clusters has only recently begun to receive some attention. Miura, *et al* (2) have shown that the nature of the support can play an important role in determining not only the surface composition of the supported bimetallic clusters but also the morphology of the particles. For silica-supported Pt-Ru

<sup>1</sup> Author to whom correspondence should be directed.

bimetallic clusters, a cherry model structure having an inner core consisting primarily of Ru (85% Ru) was observed. The composition of this inner core did not depend significantly on the overall Ru composition of the bimetallic catalyst. When Pt-Ru bimetallic clusters were supported on alumina, the Ru content of the inner core was observed to increase monotonically with the overall concentration of Ru in the catalyst. In another study involving porous supports, Haller, *et al* (3) have observed marked differences in the activity of ethane hydrogenolysis over a series of Cu-Ru bimetallic catalysts. These differences could be related to changes in the texture of the support.

The possibility that metal precursor-support interactions could have a strong influence on the dynamics of the bimetallic nucleation process cannot be ruled out and has already been alluded to in previous work performed in this laboratory (1-2). Because  $\text{H}_2\text{PtCl}_6 \cdot 6\text{H}_2\text{O}$  is much more weakly adsorbed on the surface of silica than  $\text{RuCl}_3 \cdot 3\text{H}_2\text{O}$ , bimetallic clusters with an inner core of Ru can be attributed to the nucleation of the mobile phase (Pt) atop Ru surface sites. On alumina, differences in the relative adsorptivities of the metal precursor phases are less pronounced (4). This results in bimetallic clusters which have a more homogeneous internal structure as opposed to the cherry model configuration observed on silica (2). These results suggest that the dynamics of the metal nucleation process are an important variable which may override thermodynamic effects based on enthalpies of sublimation.

In order to pursue these ideas in more detail, metal precursors which would be expected to interact via an ion exchange mechanism with the hydroxyl protons of silica were used to prepare the supported bimetallic clusters. We therefore report on the preparation of silica-supported Ru-Rh and Ru-Ir bimetallic clusters using  $\text{RuCl}_3 \cdot 3\text{H}_2\text{O}$ ,  $\text{RhCl}_3 \cdot 3\text{H}_2\text{O}$  and  $\text{IrCl}_3 \cdot 3\text{H}_2\text{O}$  as metal precursors.

In order to verify the presence of bimetallic particles having mixed metal surface sites (i.e., true bimetallic clusters), the methanation reaction was used as a surface probe. Because Ru is an excellent methanation catalyst in comparison to Pt, Ir or Rh, the incorporation of mixed metal surface sites into the structure of a supported Ru catalyst should have the effect of drastically reducing the methanation activity. This observation has been attributed to an ensemble effect and has been previously reported for a series of silica-supported Pt-Ru bimetallic clusters (5).

### Experimental Procedures

Apparatus and Procedure. The apparatus and procedure were identical to those outlined in ref. 2. Surface composition measurements were based on an  $\text{O}_2$ -CO titration technique described by Miura and Gonzalez (5-6). The ratio of surface metal/ $\text{O}_2$ /CO was 1/1/1 on Ru-silica, 1/0.5/1.75 on Rh-silica, 1/0.5/2.0 on Pt-silica and 1/0.5/1.6 on Ir-silica. These titration ratios were found to be independent of surface composition. Surface compositions determined by the  $\text{O}_2$ -CO titration method have been verified using a variety of experimental techniques (2,5-6).

Metal dispersions were obtained by the dynamic pulse method using either  $\text{H}_2$ , CO or  $\text{O}_2$  chemisorption at 298 K (7).

Catalyst Preparation. The silica-supported samples used in this

study were prepared by impregnation. Initially, the appropriate weight of  $\text{RuCl}_3 \cdot 3\text{H}_2\text{O}$ ,  $\text{RhCl}_3 \cdot 3\text{H}_2\text{O}$  and  $\text{IrCl}_3 \cdot 3\text{H}_2\text{O}$  (Strem Chemical) was dissolved in an amount of doubly deionized water sufficient to ensure the complete wetting of the support. The solutions were mixed with Cab-O-Sil (grade M-5, Cabot Corp., Boston, MA), or Alon-C (Cabot Corp.) until a slurry having the consistency of a thin paste was formed. The surface area and the average pore size of Cab-O-Sil, as reported by the manufacturer, are  $200 \text{ m}^2/\text{g}$  and  $14.0 \text{ nm}$ , respectively. The slurry was dried in a vacuum desiccator at room temperature for one or two days and stirred regularly during the drying process to retain uniformity. The dried catalyst was then ground into a fine powder before use. Total metal loadings were  $0.3 \text{ mmoles of metal/g}$  of catalyst for both the monometallic and the bimetallic catalysts.

#### Determination of Metal Precursor Mobilities During Pretreatment.

Relative precursor mobilities were obtained by premixing the silica- or alumina-supported metal catalysts with pure silica (Cab-O-Sil, grade M-5, Cabot Corp.) or pure alumina (Alon C, Cabot Corp.) in a 1:2 ratio prior to pretreatment. The catalyst and silica were ground together using a mortar and pestle for at least 0.5 hr. before they were placed in the Pyrex microreactor for pretreatment. The procedure was similar to that used by Sarkany and Gonzalez (8). A large increase in dispersion following pretreatment was explained by considering the migration of the metal precursor from the catalyst to the additional silica support during pretreatment.

Pretreatment was as follows: The temperature was increased from 298 to 493 K at 10K/min in flowing He (25 ml/min); the carrier gas was switched to  $\text{H}_2$  and the temperature was increased from 493 to 673K at 10K/min; reduction for 2 hr. in flowing  $\text{H}_2$  was followed by flushing in He and cooling to room temperature. Oxygen impurities in the He carrier gas were reduced to the p.p.b. range through the use of a Supelco oxygen gas purifier backed by a 13-X molecular sieve maintained at 160K. Further purification was obtained by inserting an  $\text{MnO}$  trap in the line.

Methanation Studies. Turnover frequencies for methane formation were measured at either 493 or 498 K by a procedure which was identical to that in ref. 5. Hydrogen and CO were premixed to a  $\text{H}_2/\text{CO}$  ratio of 3.

### Results

Surface Composition Measurements. The surface composition and metal dispersion for a series of silica (Cab-O-Sil) supported Ru-Rh bimetallic clusters are summarized in Table I. Surface enrichment in Rh, the element with the lower heat of sublimation, was not observed over the entire bimetallic composition range. In fact, to within the experimental limit of error of the measurements, surface compositions and catalyst compositions were nearly equal. A small local maximum in the dispersion was observed for the catalyst having a surface composition of 50% Rh.

Table I. Catalyst Composition<sup>(a)</sup> and Surface Composition for Silica-Supported Rh-Ru Bimetallic Catalysts

| Catalyst               | Catalyst Composition Rh/Ru | Dp <sup>(b)</sup> % | Surface Composition Rh/Ru |
|------------------------|----------------------------|---------------------|---------------------------|
| Rh/SiO <sub>2</sub>    | 100/0                      | 25                  | 100/0                     |
| Rh-Ru/SiO <sub>2</sub> | 75/25                      | 21                  | 69/31                     |
| Rh-Ru/SiO <sub>2</sub> | 50/50                      | 23                  | 51/49                     |
| Rh-Ru/SiO <sub>2</sub> | 27/75                      | 19                  | 18/82                     |
| Ru/SiO <sub>2</sub>    | 0/100                      | 11                  | 0/100                     |

(a) metal loading = 0.3 m. moles of metal/g of catalyst.

(b) measured using CO chemisorption (CO/M = 1).

The corresponding data for a similar series of silica-supported Ru-Ir catalysts are shown in Table II.

Table II. Catalyst Composition and Surface Composition for Silica-Supported Ru-Ir Bimetallic Catalysts

| Catalyst               | Catalyst Composition Ir/Ru | Dp <sup>(a)</sup> (%) | Surface Composition |
|------------------------|----------------------------|-----------------------|---------------------|
| Ir/SiO <sub>2</sub>    | 100/0                      | 61                    | 100/0               |
| Ir-Ru/SiO <sub>2</sub> | 75/25                      | 28                    | 86/14               |
| Ir-Ru/SiO <sub>2</sub> | 40/60                      | 14                    | 45/55               |
| Ir-Ru/SiO <sub>2</sub> | 25/75                      | 15                    | 27/73               |
| Ir-Ru/SiO <sub>2</sub> | 10/90                      | 12                    | 5/95                |
| Ru-SiO <sub>2</sub>    | 0/100                      | 11                    | 0/100               |

(a) measured using both O<sub>2</sub> and CO chemisorption.

As was the case for the silica-supported Ru-Rh bimetallic catalysts, there was no significant surface enrichment in either metal over the entire range of bimetallic catalyst compositions. Metal dispersions were observed to decrease as the concentration of Ru was increased. This same trend was observed for the Ru-Rh catalysts and was in marked contrast to observations on silica-supported Pt-Ru catalysts (2). In this case a large increase in dispersion was obtained as a result of bimetallic clustering in the cherry model configuration.

A word should be said regarding the use of O<sub>2</sub> chemisorption to measure Ru-Ir metal dispersions. The stoichiometry of the CO adsorption on Ir (CO/Ir<sub>(s)</sub>) was taken from the literature to be 0.5 (9-10). The measured CO/O<sub>2</sub> chemisorption ratio on Ir was determined using the dynamic pulse method and found to be 1.56. These results give

an  $O_2/Ir_{(s)}$  chemisorption ratio of 0.32, in excellent agreement with an  $O_2/Ir_{(s)}$  ratio of 0.33 reported by Falconer, *et al* (9). The stoichiometry of the  $O_2/Ru_{(s)}$  chemisorption ratio has been reasonably well established and is close to one (5). On the assumption that these stoichiometries are preserved in the Ir-Ru bimetallic clusters, metal dispersions can readily be obtained from a knowledge of the surface composition.

The surface-catalyst composition data for the silica-supported Ru-Rh and Ru-Ir catalyst are shown in Figure 1. A similar plot for the series of silica-supported Pt-Ru bimetallic catalysts taken from ref. (2) is included for comparison purposes. Enthalpies of sublimation for Pt, Ru, Rh and Ir are 552, 627, 543, and 648 KJ/mole. Differences in enthalpies of sublimation ( $\sim 75$  KJ/mole) between Pt and Ru and between Rh and Ru are virtually identical, with Pt and Rh having the lower enthalpies of sublimation. For this reason surface enrichment in Pt for the case of the Pt-Ru/SiO<sub>2</sub> bimetallic clusters cannot be attributed solely to the lower heat of sublimation of Pt. Other possibilities must also be considered.

**Precursor Mobility Experiments.** The mobility of the metal precursor during catalyst pretreatment is, of course, a strong function of the interaction between the metal precursor and the support. Because  $H_2PtCl_6$  is adsorbed as the  $PtCl_6^{2-}$  anion, it interacts only weakly with the hydroxyl groups of silica. Ru, Rh, and Ir, on the other hand, are adsorbed as cations and readily exchange with the acidic hydroxyl groups on silica. The relative surface mobilities of the metal precursors during pretreatment can readily be studied by using the dilution technique described in the experimental section. A large increase in dispersion following pretreatment would be indicative of weak metal precursor-support interactions. Small increases in dispersion, on the other hand, suggest strong metal precursor-support interactions. The results for the catalysts studied are shown in Table III.

Table III. Effect of Dilution on the Dispersion of Supported Metal Catalysts

| Catalyst                                       | Dispersion % | Increase in % Dispersion |
|--|--------------|--------------------------|
| 6% Pt/SiO <sub>2</sub> (a)                     | 28           | 54                       |
| 6% Pt/SiO <sub>2</sub> :SiO <sub>2</sub> (1:2) | 43           |                          |
| 6% Pt/Al <sub>2</sub> O <sub>3</sub>           | 57           | 38                       |
| 6% Pt/Al <sub>2</sub> O <sub>3</sub> (1:2)     | 79           |                          |
| Ru/SiO <sub>2</sub> (b)                        | 11           | 27                       |
| Ru/SiO <sub>2</sub> :SiO <sub>2</sub> (1:2)    | 14           |                          |
| Rh/SiO <sub>2</sub>                            | 24           | 25                       |
| Rh/SiO <sub>2</sub> :SiO <sub>2</sub> (1:2)    | 30           |                          |
| Ir/SiO <sub>2</sub>                            | 61           | 27                       |
| Ir/SiO <sub>2</sub> :SiO <sub>2</sub> (1:2)    | 78           |                          |

(a) measured using H<sub>2</sub> adsorption.

(b) measured using CO adsorption.

(c) measured using CO and O<sub>2</sub> adsorption.

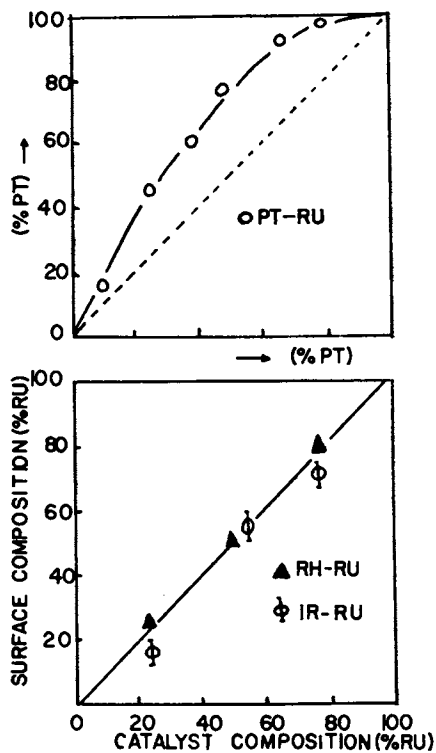


Figure 1. Catalyst composition, surface vs. bulk. Reproduced with permission from Ref. 2. Copyright 1984, Academic Press.

From the results it is evident that  $\text{Ru}^{3+}$ ,  $\text{Rh}^{3+}$  and  $\text{Ir}^{3+}$  interact strongly with the support and do not migrate extensively from their primary adsorption sites during pretreatment.  $\text{PtCl}_6^{2-}$ , on the other hand, interacts rather weakly with the support and is observed to migrate extensively during the initial stages of the pretreatment in flowing He. When alumina (Alon-C) was used as a support, differences in the surface mobility of  $\text{PtCl}_6^{2-}$  and  $\text{Ru}^{3+}$  during catalyst pretreatment were not nearly as large as those observed on silica. This suggests a stronger interaction between  $\text{PtCl}_6^{2-}$  and support on alumina than on silica. No redispersion was observed following reduction to the metallic state. An additional feature which undoubtedly contributes to the extensive desorption-readsorption phenomena observed in the case of  $\text{PtCl}_6^{2-}$  is the high solubility of  $\text{PtCl}_6^{2-}$  in  $\text{H}_2\text{O}$ . Because  $\text{PtCl}_6^{2-}$  is weakly adsorbed, the distribution of  $\text{H}_2\text{PtCl}_6$  between  $\text{H}_2\text{O}$  and the  $\text{SiO}_2/\text{H}_2\text{O}$  interface is highly favorable to  $\text{H}_2\text{O}$ , and the resulting complex is therefore highly mobile. Water is, of course, present during the initial pretreatment due to: (1) dehydroxylation of the support, and (2) the waters of hydration.

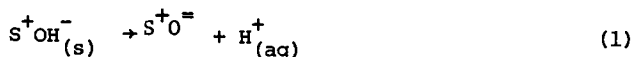
Methanation Studies. Because the most effective way to determine the existence of true bimetallic clusters having mixed metal surface sites is to use a demanding catalytic reaction as a surface probe, the rate of the CO methanation reaction was studied over each series of supported bimetallic clusters. Turnover frequencies for methane formation are shown in Fig. 2. Pt, Ir and Rh are all poor CO methanation catalysts in comparison with Ru which is, of course, an excellent methanation catalyst. Pt and Ir are completely inactive for methanation in the 493-498K temperature range, while Rh shows only moderate activity.

All of the supported bimetallic catalysts studied show a sharp drop in methanation activity when the Ru/M ratio falls below four. (M = Ir, Pt, Rh). These results are suggestive of a geometric effect which requires a minimum ensemble size consisting of at least 4 Ru atoms. Reaction rates obtained using mechanical mixtures prepared by mixing the appropriate weights of reduced catalysts are also shown for the case of the Ir-Ru/ $\text{SiO}_2$  catalysts. The linear drop off in rate is further evidence of the existence of mixed metal surface sites and the absence of mass transfer effects.

### Discussion

The results of this study suggest that the dynamics of the nucleation process are of the utmost importance in determining the structure and the surface composition of supported bimetallic clusters. Because the surface mobility of the metal phase during pretreatment is strongly influenced by the nature of the precursor-support interaction, it is useful to consider this interaction in some detail.

The possibility exists that a surface hydroxyl group on silica can itself function as a proton donor (12),



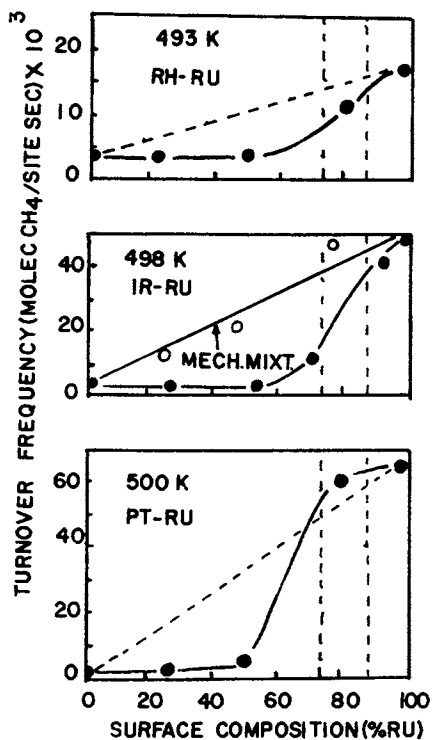
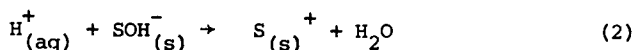


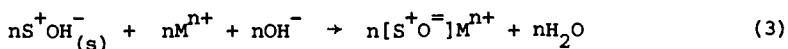
Figure 2. The dependence of the reaction rate for methane formation on surface composition.



or in the case of an amphoteric oxide such as alumina, as a hydroxyl donor,



The oxides are cation exchangers in an environment which generates a negative surface charge (equation 1) and anion exchangers in an environment which generates a positive surface charge. When the surface is only protonated, i.e., no metal ions are adsorbed, exchange can be brought about by contacting it with the appropriate metal ions.

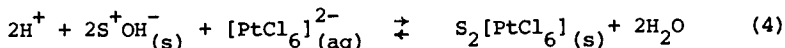


the pH dependence of this exchange is obvious. However, if the pH is too high, the metal may precipitate out as the hydroxide.

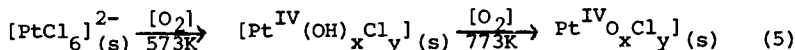
Because the hydroxyl groups on silica are more acidic than those on alumina, cations such as  $\text{Ru}^{3+}$ ,  $\text{Rh}^{3+}$  and  $\text{Ir}^{3+}$  should exchange according to the mechanism suggested in equation (3). For this reason,  $\text{Ru}^{3+}$  and  $\text{Rh}^{3+}$  should be strongly adsorbed on silica, as suggested by their relatively low mobility under the influence of the He pretreatment. Pt, on the other hand, must adsorb on silica as the  $\text{PtCl}_6^{2-}$  anion and cannot exchange with surface protons. It is therefore weakly adsorbed on silica and, because of its solubility in  $\text{H}_2\text{O}$ , is free to migrate freely on the support during the pretreatment. After it is reduced to the Pt(0) state, it will no longer migrate.

The net result of this effect is one in which the mobile Pt phase preferentially nucleates atop the relatively immobile Ru phase to form supported Pt-Ru/SiO<sub>2</sub> bimetallic clusters having the cherry model structure observed by Miura, *et al* (2). On the other hand, because Ru, Ir and Rh are adsorbed cationically on the surface of silica, desorption-readsorption from primary to secondary sites during pretreatment occurs only to a limited extent. For this reason the resulting bimetallic clusters, Ru-Ir/SiO<sub>2</sub> and Ru-Rh/SiO<sub>2</sub>, do not show significant surface enrichment in either metal even though the enthalpy of sublimation of Rh is significantly lower than that of Ru (11). The enthalpies of sublimation of Ru and Ir, on the other hand, are about the same.

Metal precursor-support interactions in the case of alumina are quite different. The nature of the  $\text{H}_2\text{PtCl}_6\text{-Al}_2\text{O}_3$  interaction is still open to question. However, recent "in-situ" ultraviolet studies (13-14) suggest the following:



The  $[\text{PtCl}_6]^{2-}$  formed appears to be stable on drying at temperatures up to 393K. The subsequent chemistry of the  $[\text{PtCl}_6]^{2-}_{(\text{s})}$  species as determined from ultraviolet spectroscopy is as follows:



Either the  $[\text{Pt}^{\text{IV}}(\text{OH})_x\text{Cl}_y]_n(\text{s})$  or the  $[\text{Pt}^{\text{IV}}\text{O}_x\text{Cl}_y]$  can readily be reduced to  $\text{Pt}(\text{O})$  by  $\text{H}_2$  at  $473\text{ K}$ . The chlorine evolved is readily incorporated into the alumina support. However, silica does not scavenge chloride ions to the same extent as does alumina.  $[\text{PtO}_2]_n(\text{s})$  prepared by the oxidation of  $\text{Pt}(\text{O})$  from a chloride-free source can readily be converted into the  $[\text{Pt}^{\text{IV}}\text{O}_x\text{Cl}_y]$  following treatment with  $\text{HCl}(\text{g})$  (14).

Because both  $[\text{PtCl}_6]^{2-}(\text{s})$  and  $\text{Ru}^{3+}$  are more equally adsorbed on alumina, the mobility of the Pt-precursor phase relative to the Ru-precursor phase is reduced. The data in Table III show that the increase in dispersion following dilution with pure alumina (Alon-C) is moderate with respect to that observed on silica. However, the redispersion of Pt is still substantially greater than that of Ru. The experimental results of Miura, *et al* (2) are in agreement with these redispersion experiments. The cherry model structure observed for Pt-Ru/ $\text{Al}_2\text{O}_3$  was more poorly defined than that observed for the Pt-Ru/ $\text{SiO}_2$  clusters.

A comment regarding the dispersion of the Ru-Rh/ $\text{SiO}_2$  and the Ru-Ir/ $\text{SiO}_2$  is in order. For the case of the supported Pt-Ru catalysts, increases in dispersion as a result of clustering were very large (2). This effect was particularly noticeable for bimetallic particles which conform to the cherry model. Evidently, the formation of an inner core enriched in one of the two metals, followed by an outer layer enriched in the other metal, inhibits further crystal growth. For the alumina-supported Pt-Ru bimetallic clusters, the effect, although present, is considerably smaller.

In the present study, the cherry model does not apply. For this reason, the increase in dispersion observed due to clustering is small.

The methanation studies shown in Figure 2 confirm the presence of bimetallic clusters which have mixed metal surface sites. There is one more point which merits a final comment. Turnover frequencies for methane formation for all of the bimetallic catalysts studied show a sharp drop in reaction rate for Ru/M ratios which are less than four, where M is Pt, Ir or Rh. These results are suggestive of an ensemble requirement of about four adjacent Ru atoms. These results are in striking agreement with the proton-induced reduction of CO to  $\text{CH}_4$  on a series of homonuclear and heteronuclear metal carbonyls (15). These authors showed that a minimum cluster size of four active metal atoms was required to catalyze the formation of  $\text{CH}_4$ . For the reaction between  $[\text{Fe}_4(\text{CO})_{13}]^{2-}$  and  $\text{HSO}_3\text{CF}_3$ , Whitmire and Shriver (16) identified an intermediate consisting of a carbon atom bound to four Fe atoms in a "butterfly" configuration. The ensemble requirement of four appears, therefore, to have an analog in the homogeneous reaction between polynuclear transition metal carbonyls and hydrogen in strongly acidic solutions.

### Conclusions

The following conclusions emerge as a result of this study:

- (1) When  $\text{RuCl}_3 \cdot 3\text{H}_2\text{O}$ ,  $\text{RhCl}_3 \cdot 3\text{H}_2\text{O}$  and  $\text{IrCl}_3 \cdot 3\text{H}_2\text{O}$  are used as metal precursors, the resulting silica-supported bimetallic clusters are not significantly enriched in either metallic component.
- (2) The surface dynamics of metal precursor-support interactions dur-

ing catalyst pretreatment can override thermodynamic effects in influencing the morphology of supported bimetallic clusters.

(3) Methanation studies suggest the presence of mixed metal surface sites with a Ru ensemble requirement of about four.

#### Acknowledgments

Acknowledgment is made to the Donors of the Petroleum Research Fund, administered by the American Chemical Society, for the support of this research. We also wish to acknowledge the support of the National Science Foundation which provided funds for the equipment used in this research under Grants #DMR 78-18917 and CPE-7920155.

#### Literature Cited

1. Gonzalez, R.D. Applications of Surf. Sci., 1984, 19, 113.
2. Miura, H.; Suzuki, T.; Ushikubo, Y.; Sugiyama, K.; Matsuda, T.; Gonzalez, R.D. J. Catal. 1984, 85, 331.
3. Haller, G.L.; Resasco, D.E.; Wang, J. J. Catal. 1983, 84, 477.
4. Maatman, R.W.; Prater, C.D. Ind. Eng. Chem. 1957, 49, 253.
5. Miura, H.; Gonzalez, R.D. J. Catal. 1982, 74, 216.
6. Miura, H.; Gonzalez, R.D. J. Phys. Chem. 1982, 86, 1577.
7. Sarkany, J.; Gonzalez, R.D. J. Catal. 1982, 76, 75.
8. Sarkany, J.; Gonzalez, R.D. I & EC Prod. Res. and Development, 1983, 23, 548.
9. Falconer, J.L.; Wentreck, P.R.; Wise, H. J. Catal. 1976, 45, 248.
10. Brooks, C.S. J. Colloid Interface Sci. 1970, 34, 419.
11. Gates, B.C.; Katzer, J.R.; Shuit, G.C.A. Chemistry of Catalytic Processes. McGraw-Hill Book Co., New York, 1979, 198.
12. Anderson, J.R. Structure of Metallic Catalysts, 1st ed., Academic Press, New York, 1975, 181.
13. Lieske, H.; Lietz, G.; Spindler, H.; Volter, R. J. Catal. 1983, 81, 8.
14. Lietz, G.; Lieske, H.; Spindler, H.; Volter, R. J. Catal. 1983, 81, 17.
15. Drezdson, M.A.; Whitmire, K.H.; Bhattacharyya, K.H.; Hsu, A.A.; Wen-Liang; Nagel, C.C.; Shore, S.G.; Shriver, D.F. J. Am. Chem. Soc., 1982, 104, 5630.
16. Whitmire, K.; Shriver, D.F. J. Am. Chem. Soc. 1980, 102, 1456.

RECEIVED June 21, 1985

## Surface Characterization and Methanation Activity of Catalysts Derived from Binary and Ternary Intermetallics

M. Houalla<sup>1,2</sup>, T. A. Dang<sup>1</sup>, E. L. Eddy<sup>2</sup>, C. L. Kibby<sup>2</sup>, L. Petrakis<sup>1,2</sup>, and D. M. Hercules<sup>1</sup>

<sup>1</sup>Department of Chemistry, University of Pittsburgh, Pittsburgh, PA 15260

<sup>2</sup>Gulf Research & Development Company, Pittsburgh, PA 15230

The surface properties of three types of methanation catalysts obtained by oxidation of selected intermetallics were examined in relation to their CO conversion activity. The first type ( $\text{Ni}_x\text{Si}_y$ ,  $\text{Ni}_x\text{Al}_y$ ) which corresponds to active phase-support in the conventionally prepared catalyst is little affected by the oxidation treatment. The surface Ni is oxidized and relatively more abundant in the active solids. The second type (active phase-promoter; ex:  $\text{Ni}_x\text{Th}_y$ ) is extensively decomposed on oxidation. The transformation of these alloys is accompanied by a surface enrichment in Ni. The overall behavior of the third type [mixed active phase-promoter; ex:  $(\text{Ni}_x\text{Fe}_{5-x})\text{Th}$ ] is similar to the second. Preferential segregation of Fe, as compared to Ni, occurs on oxidation. A close correlation between CO conversion rate and surface Ni content has been observed.

Industrial type methanation or Fisher-Tropsch Catalysts consist of three components: 1) an active phase (Ni, Co, Fe, Ru, Rh), 2) a promoter (Th, La, K), and 3) a high surface area carrier ( $\text{SiO}_2$ ,  $\text{Al}_2\text{O}_3$ ,  $\text{TiO}_2$ ). These supported catalysts are conventionally obtained by co-impregnation or sequential impregnation of the support with a solution containing the active phase or the promoter salt followed by drying, calcination, and reduction. Recently a new class of "supported" catalysts has been developed at the University of Pittsburgh (1-4). They are formed by reaction of synthesis gas or  $\text{O}_2$  with a binary intermetallic compound (ex:  $\text{A}_x\text{B}_y \xrightarrow[\text{CO}/\text{H}_2]{2} \text{A}/\text{BO}_2$ , A = Ni, Co, Fe, and B = Si, Ti, Th, and Ce). The transformed materials exhibit high specific activity in methanation, ammonia synthesis, and ethylene hydrogenation reactions. The similarity between the industrial methanation catalysts and catalysts obtained by decomposition of various intermetallics is striking. Most catalysts obtained by decomposition of a binary alloy involve an associative combination of

0097-6156/85/0288-0305\$06.00/0

© 1985 American Chemical Society

an active phase (Ni, Co) with the carrier (ex.  $\text{Ni}_x\text{Si}_y$ ,  $\text{Ni}_x\text{Ti}_y$ ) or the promoter (ex.  $\text{Ni}_x\text{Th}_y$ ,  $\text{Ni}_x\text{La}_y$ ,  $\text{Ni}_x\text{Ce}_y$ ,  $\text{Co}_x\text{Th}_y$ ). The purpose of the present work is twofold: first, to outline the results of our recent study of the surface structure of binary intermetallics, representative of the two types of alloys described above (e.g.,  $\text{Ni}_x\text{Si}_y$  and  $\text{Ni}_x\text{Th}_y$ ) and second, to extend this study to ternary alloys. The ternary system considered here is derived from a given intermetallic highly active in synthesis gas conversion (e.g.,  $\text{ThNi}_5$ ) by partial substitution of Ni by Fe. Ternary systems are of interest because 1) they provide a means to tailor the selectivity of the final catalyst for a given product. For example, in the  $\text{CeNi}_{5-x}\text{Cu}_x$  system Ni promotes methanation, whereas Cu is known to catalyze the formation of oxygen-containing products (e.g.,  $\text{CH}_3\text{OH}$ ), and 2) in ternary intermetallics such as  $\text{ThNi}_x\text{Fe}_{5-x}$ , the ratio  $(\text{Ni}+\text{Fe})/\text{Th}$  is maintained constant. With binary systems such as  $\text{Ni}_x\text{Th}_y$ , the wide range of Ni/Th ratios involved leads to large changes in the BET surface areas of the decomposed intermetallics, which complicates the interpretation of spectroscopic and activity data.

Surface and bulk characterization were carried out using electron spectroscopy for chemical analysis (ESCA or XPS) and x-ray diffraction (XRD). The results will be discussed in relation to methanation activity.

### Materials

Binary and ternary intermetallics were prepared by induction melting of the component metals in a water cooled copper boat under a flow of purified argon. The systems considered here are the following:  $\text{Ni}_x\text{Si}_y$  ( $\text{Ni}_5\text{Si}_2$ ,  $\text{Ni}_2\text{Si}$ ,  $\text{Ni}_3\text{Si}_2$ , and  $\text{NiSi}_2$ ),  $\text{Ni}_x\text{Th}_y$  ( $\text{Ni}_5\text{Th}$ ,  $\text{Ni}_2\text{Th}$ ,  $\text{NiTh}$ , and  $\text{Ni}_3\text{Th}_7$ ), and  $\text{ThNi}_x\text{Fe}_{5-x}$  ( $x = 0, 1, 2, 3, 4$ , and  $5$ ). All were obtained in single phase form, as evidenced by x-ray diffraction results. Two types of materials will be examined in this study: untreated, noted as  $(\text{Ni}_x\text{Th}_y)_u$ ,  $(\text{Ni}_x\text{Si}_y)_u$ , or  $(\text{ThNi}_x\text{Fe}_{5-x})_u$ , refer to the alloys ground in air and sieved through 45 mesh; and oxidized, abbreviated hereafter as  $(\text{Ni}_x\text{Th}_y)_o$ ,  $(\text{Ni}_x\text{Si}_y)_o$ , or  $(\text{ThNi}_x\text{Fe}_{5-x})_o$ , designate the alloys which were treated with oxygen for 20-24 hours at relatively high temperatures [ $450^\circ\text{C}$  for  $(\text{Ni}_x\text{Si}_y)_o$  systems and  $350^\circ\text{C}$  for the remaining systems].

### Physico-Chemical Characterization

X-ray diffraction (XRD) measurements were carried out using a Diano XRD-6 powder diffractometer with  $\text{CuK}\alpha$  radiation.

ESCA measurements were performed with an AEI ES200 spectrometer equipped with an Al anode ( $1486.6\text{ eV}$ ) and operated at 12 kV and 22 mA with a base pressure of  $4 \times 10^{-8}$  torr. The Ni  $2p_{3/2}$ , Ni 3p, Fe  $2p_{1/2}$ , Fe  $2p_{3/2}$ , Th  $4f_{7/2}$ , Si 2p, O 1s, and C 1s regions were scanned. More experimental details are given elsewhere (5).

In the case of a homogeneous binary alloy, A<sub>x</sub>B<sub>y</sub> (A: Ni, B: Si, Th) the ESCA intensity ratio of two peaks ( $I_A/I_B$ ) is related to the atomic ratio  $n(A)/n(B)$  in the alloy, as shown in the following Equation (6):

$$\frac{I_A}{I_B} = \frac{n(A) \cdot \sigma(A) \cdot \lambda(A) \cdot D(A)}{n(B) \cdot \sigma(B) \cdot \lambda(B) \cdot D(B)}$$

where  $\sigma(A,B)$  represents the photoelectron cross sections of A and B levels taken from Scofield (7);  $\lambda(A,B)$  is the escape depth of A or B photoelectrons;  $D(A,B)$  stands for the detector efficiencies for the A and B photoelectrons, which according to the design of the AEI instrument varies linearly with kinetic energy (8).

### Methanation Activity

CO conversion data relative to  $(Ni_xSi_{1-x})_y$  and  $(ThNi_xFe_{5-x})_y$  series were taken from ref. (3) and (9), respectively. Catalytic measurements were obtained for oxygen treated Ni-Th intermetallics. Prior to each run, a sample mixture (50 mg catalyst + 50 mg ground quartz) was reduced in  $H_2$  at 275°C for 16 hours. CO hydrogenation was carried out at 275°C using  $H_2/CO$  ratio  $\approx 9$ . More experimental details are given elsewhere (10).

### Surface and Bulk Characterization of Binary Alloys $(Ni_xSi_{1-x})_y$ and $(Ni_xTh_{1-x})_y$

Untreated Alloys. As previously noted, the untreated alloys were ground in air prior to any surface or bulk analysis. Examination of the ESCA spectra relative to Ni 2p<sub>3/2</sub>, Si 2p, and Th 4f<sub>7/2</sub> indicates that the surface Ni is essentially in the metallic state (BE = 852.5 eV) in all  $(Ni_xSi_{1-x})_y$  alloys and in a mixed state (Ni, NiO) in  $(Ni_xTh_{1-x})_y$  samples. Si is partially oxidized. The extent of oxidation seems to increase with increasing Ni content. Conversely, Th is present exclusively as ThO<sub>2</sub>.

Ni surface concentrations determined from ESCA are plotted as a function of bulk Ni content in Figures 1 and 2. In the case of homogeneous alloys the points should fall on the 45° diagonal line. It can be seen that in both  $(Ni_xSi_{1-x})_y$  and  $(Ni_xTh_{1-x})_y$  series the surfaces of the alloys are nickel-poor, as compared to the bulk. Similar observations have been made in the case of NiAl<sub>y</sub> (11,12) and CoTh<sub>y</sub> (13) alloys. Surface enrichment in Si or Th is to be expected because of the higher heats of formation of SiO<sub>2</sub> and ThO<sub>2</sub> compared to NiO (-210, -292, and -58.4 kcal/mol, respectively). This would lead to a higher chemical affinity of Si and Th toward the ambient gas and consequently an increased driving force of Si and Th for segregation.

Oxidized Alloys. The most striking difference between the  $(Ni_xSi_{1-x})_y^u$  and  $(Ni_xTh_{1-x})_y^u$  alloys can be readily seen in Tables I and II which show the nature of phases present, as identified by XRD, following oxygen treatment at 450°C and 350°C, respectively. Thus, whereas  $(Ni_xTh_{1-x})_y$  intermetallics are extensively transformed to Ni, NiO, and ThO<sub>2</sub> upon oxidation,  $(Ni_xSi_{1-x})_y$  alloys are little affected by oxygen treatment. Only in the case of Ni<sub>5</sub>Si<sub>2</sub> was unequivocal evidence found for the formation of a separate Ni phase. Similar behavior was observed for NiAl<sub>y</sub> and CoSi<sub>y</sub> alloys (3). Similarly, the relative ease of decomposition of  $(Ni_xTh_{1-x})_y$  alloys in O<sub>2</sub> atmosphere is equally observed in the alloys which consist of a chemical union of a Group VIII metal with rare earth or actinide elements known as

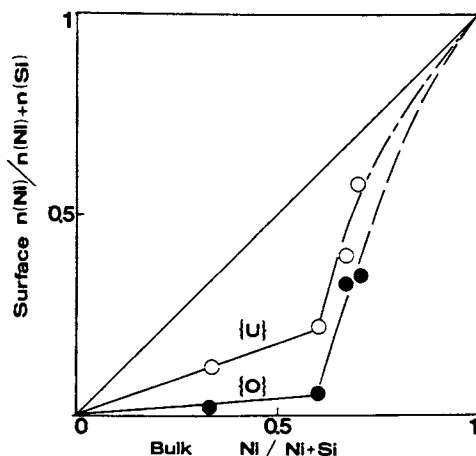


Figure 1. Variation of the surface composition of  $Ni_xSi_y$  alloys as a function of bulk Ni content (relative standard derivation of  $\pm 10\%$ ).

(O): untreated alloys

(●): oxidized alloys

Reproduced from Ref. 5. Copyright 1983, American Chemical Society.

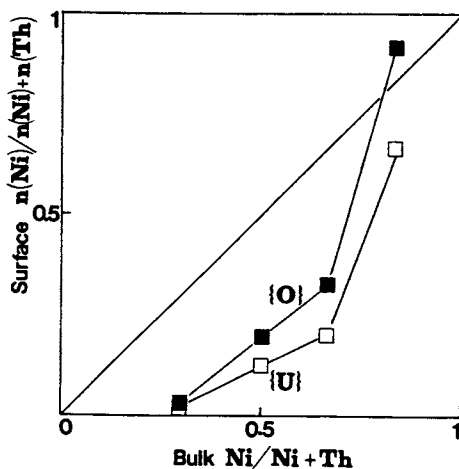


Figure 2. Variation of the surface composition of  $Ni_xTh_y$  alloys as a function of bulk Ni content (relative standard derivation of  $\pm 10\%$ ).

(□): untreated alloys

(■): oxidized alloys

Reproduced with permission from Ref. 10. Copyright 1984, Academic Press.

promoters of Fisher-Tropsch reactions (e.g.,  $\text{Ni}_x\text{La}_y$ ,  $\text{Ni}_x\text{Ce}_y$ ,  $\text{Co}_x\text{Th}_y$ ,  $\text{Fe}_x\text{Th}_y$ , etc.) (14).

Table I. Nature of Phases Present in  $(\text{Ni}_x\text{Si}_y)_o$  Series as Identified by X-ray Diffraction<sup>y</sup>

| $(\text{Ni}_x\text{Si}_y)_o$ | $(\text{NiSi}_2)_o$ | $(\text{Ni}_3\text{Si}_2)_o$ | $(\text{Ni}_2\text{Si})_o$      | $(\text{Ni}_5\text{Si}_2)_o$          |
|------------------------------|---------------------|------------------------------|---------------------------------|---------------------------------------|
| Crystalline phases present   | $\text{NiSi}_2$     | $\text{Ni}_3\text{Si}_2$     | $\text{Ni}_2\text{Si}$ modified | $\text{Ni}_5\text{Si}_2 + \text{NiO}$ |

Table II. Nature of Phases Present in  $(\text{Ni}_x\text{Th}_y)_o$  Series as Identified by X-ray Diffraction<sup>y</sup>

| $(\text{Ni}_x\text{Th}_y)_o$ | $(\text{Ni}_3\text{Th}_7)_o$           | $(\text{NiTh})_o$                      | $(\text{Ni}_2\text{Th})_o$             | $(\text{Ni}_5\text{Th})_o$             |
|------------------------------|--|--|--|--|
| Crystalline phases present   | $\text{Ni}, \text{NiO} + \text{ThO}_2$ | $\text{Ni}, \text{NiO} + \text{ThO}_2$ | $\text{Ni}, \text{NiO} + \text{ThO}_2$ | $\text{Ni}, \text{NiO} + \text{ThO}_2$ |

Surface characterization of  $(\text{Ni}_x\text{Si}_y)_o$  and  $(\text{Ni}_x\text{Th}_y)_o$  systems further illustrates the difference in their behavior. ESCA spectra of Ni  $2p_{3/2}$  levels indicate that in the case of silicon rich alloys ( $\text{NiSi}_2$ ,  $\text{Ni}_3\text{Si}_2$ ) the surface Ni remains in the metallic state upon oxidation (5). Substantial surface oxidation occurs, however, at high Ni content ( $\text{Ni}_2\text{Si}$ ,  $\text{Ni}_5\text{Si}_2$ ) (5). Conversely, ESCA analyses show that the surface Ni of  $(\text{Ni}_x\text{Th}_y)_o$  samples consists exclusively of NiO. The evolution of the surface compositions of  $(\text{Ni}_x\text{Si}_y)_o$  and  $(\text{Ni}_x\text{Th}_y)_o$  alloys upon oxidation is equally different. It is clear from Figures 1 and 2 which compare the surface composition of  $(\text{Ni}_x\text{Si}_y)_o$  and  $(\text{Ni}_x\text{Th}_y)_o$  samples determined from ESCA data to those of the untreated alloys that oxidation induces surface Ni depletion in the  $\text{Ni}_x\text{Si}_y$  system and surface Ni enrichment in the case of  $\text{Ni}_x\text{Th}_y$  alloys. In principle, because of the higher heat of formation of  $\text{SiO}_2$  and  $\text{ThO}_2$  compared to NiO, oxidation of  $(\text{Ni}_x\text{Si}_y)_o$  and  $(\text{Ni}_x\text{Th}_y)_o$  alloys should lead, in both cases, to Si and Th segregation. This has been indeed the case for  $\text{Ni}_x\text{Si}_y$  alloys. Their observed behavior is in accordance with previous studies of the oxidation of metal silicides (15,16) which show that Si is preferentially oxidized and migrates to the surface to form a passivating  $\text{SiO}_2$  layer, thus inhibiting further oxidation of the intermetallics. The opposite trend observed for the  $\text{Ni}_x\text{Th}_y$  system can be, tentatively, ascribed to their extensive transformation under oxidation conditions. Indeed, in accordance with the data relative to  $\text{Ni}_x\text{Si}_y$  system, mild oxidation of  $\text{Ni}_2\text{Th}$  (100°C, 1 h) brings about a significant surface enrichment in Th illustrated by a decrease in  $n(\text{Ni})/n(\text{Th})$  atomic ratio from 2 to 0.97 (Table III). More drastic conditions (200°C, 20 minutes) caused the bulk intermetallic to decompose into Ni and  $\text{ThO}_2$ , as observed by x-ray diffraction; under these conditions the atomic Ni/Th ratio



began to increase ( $Ni/Th = 2.9$ ). Higher oxidation temperature ( $350^\circ C$ , 8 hours) resulted in further decomposition of the intermetallic, as well as a further increase in the atomic ratio ( $n(Ni)/n(Th) = 13.2$ ).

Table III. Variation of the Surface and Bulk Composition of  $Ni_5Th$  Alloy as a Function of Oxidation Conditions

| Treatment                                       | Untreated | In Air at $100^\circ C$ for 60 min. | In Air at $200^\circ C$ for 20 min. | In Air at $350^\circ C$ for 60 min. | In Air at $350^\circ C$ for 480 min. |
|---|-----------|-------------------------------------|-------------------------------------|-------------------------------------|--------------------------------------|
| (Surface)<br>$n(Ni)/n(Th)$<br>from<br>ESCA data | 2.0       | 0.97                                | 2.9                                 | 6.0                                 | 13.2                                 |
| Phases<br>present<br>from<br>XRD data           | $Ni_5Th$  | $Ni_5Th$                            | $Ni_5Th$ ,<br>$Ni_5ThO_2$           | $Ni_5Th$ ,<br>$Ni_5ThO_2$           | $Ni$ , $ThO_2$                       |

#### Surface and Bulk Characterization of Ternary Alloys ( $ThNi_xFe_{5-x}$ )

Untreated Alloys.  $ThNi_xFe_{5-x}$  alloys ( $x = 0, 1, 2, 3, 4,$  and  $5$ ) are all structurally isomorphous. They all have the hexagonal  $CaCu_5$  structure with  $P_6/MMM$  symmetry.

As observed in the case of  $(Ni,Th)_x$  alloys, ESCA spectra relative to  $Ni\ 2p_{3/2}$ ,  $Fe\ 2p_{3/2}$ , and  $Th\ 4f_{7/2}$  levels indicate the presence of  $(Ni, NiO)$ ,  $(Fe, Fe_2O_3)$ , and  $ThO_2$  as major surface species. The percent of surface  $NiO$  increased with increasing bulk  $Ni$  content, whereas the fraction of  $Fe_2O_3$  in the total surface  $Fe$  did not vary significantly with bulk  $Fe$  concentration (85%). A plot of the surface atomic ratios  $n(M)/n(Th)$  ( $M = Fe, Ni$ ) calculated from ESCA data versus bulk  $Ni/Th$  content (Figure 3) shows that the surface of  $(ThNi_xFe_{5-x})_u$  alloys is poor in  $Ni$  and  $Fe$ , as compared to the bulk (17).<sup>x</sup> Preferential segregation of  $Fe$ , as compared to  $Ni$ , can be clearly seen in Figure 4 which shows the variation of the surface ratio  $n(Ni)/n(Ni)+n(Fe)$  versus the bulk  $Ni/(Ni+Fe)$  content. The observed surface composition of the untreated alloys is in accordance with the relative heat of formation of  $ThO_2$ ,  $Fe_2O_3$ , and  $NiO$  ( $-292$ ,  $-100$ , and  $-58$  kcal/at g).

Oxidized Alloys. Ternary intermetallics undergo extensive transformation when they are treated in air for 24 hours at  $350^\circ C$ . XRD data indicate the presence of  $NiO$ ,  $Fe_2O_3$ , and  $ThO_2$ . The presence of  $Ni-Fe$  alloy could not be confirmed by XRD because of the small difference in the various structures involved ( $Fe, Ni, NiFe$ ). However, evidence for the formation of  $Ni-Fe$  alloy has been obtained from the observed values of Curie temperatures determined from thermomagnetic analysis performed on these intermetallics (9).

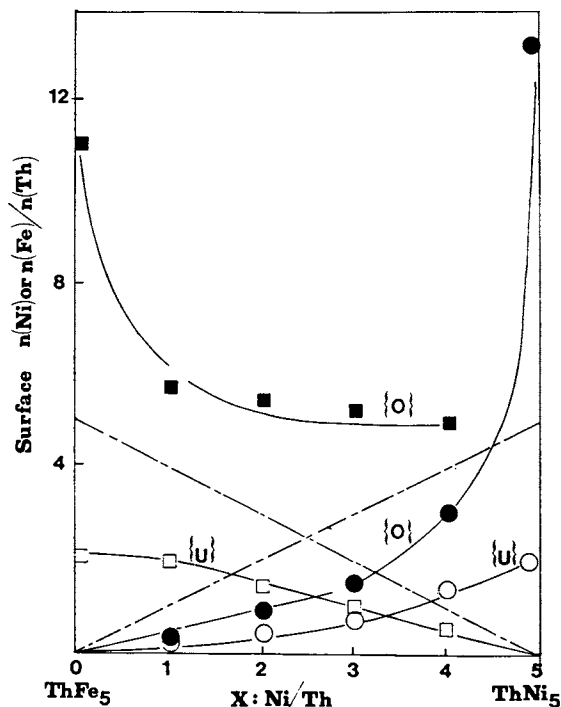


Figure 3. Variation of the surface composition of  $\text{ThNi}_x\text{Fe}_{5-x}$  alloys as a function of bulk Ni/Th ratio (relative standard deviation of  $\pm 10\%$ ). Reproduced from Ref. 17. Copyright 1984, Amer. Chem. Society.

- (O):  $n(\text{Ni})/n(\text{Th})$ ; untreated alloys
- (●):  $n(\text{Ni})/n(\text{Th})$ ; oxidized alloys
- (□):  $n(\text{Fe})/n(\text{Th})$ ; untreated alloys
- (■):  $n(\text{Fe})/n(\text{Th})$ ; oxidized alloys

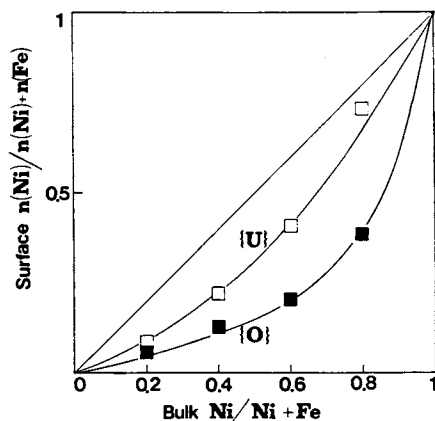


Figure 4. Variation of the surface ratio  $n(\text{Ni})/n(\text{Ni})+n(\text{Fe})$  as a function of bulk Ni/Ni+Fe content in  $\text{ThNi}_x\text{Fe}_{5-x}$  alloys.

- (□): untreated alloys
- (■): oxidized alloys

The salient features of surface analysis by ESCA of the oxidized ternary alloys are in general agreement with the results in the case of the binary Ni-Th system. NiO, Fe<sub>2</sub>O<sub>3</sub>, and ThO<sub>2</sub> are the predominant species present. Surface enrichment in Ni and Fe were observed upon oxidation. Preferential segregation of Fe, as compared to Ni, is conspicuously shown in Figure 4.

#### Correlation Between Surface Structure and CO Conversion Activity

Before any attempt to establish a correlation between the surface structure of the oxidized alloys and their CO conversion activity one must stress that the surface composition of the samples under reaction conditions may not necessarily be identical to that determined from ESCA data. Moreover, surface nickel content estimates from ESCA relative intensity measurements are at best semi-quantitative. This can be readily rationalized if one takes into consideration ESCA finite escape depth, the dependence of ESCA intensity ratio  $I_{Ni}/I_{Si}$  or  $I_{Th}$  on the bulk nickel content, the relative BET surface areas of Ni and SiO<sub>2</sub> (or ThO<sub>2</sub>) and on the location of Ni with respect to SiO<sub>2</sub> (or ThO<sub>2</sub>). Finally, assuming an ideal situation where the variation of ESCA intensity ratio  $I_{Ni}/I_{Si}$  indeed reflects the changes in surface Ni content, a linear correlation between rate and surface Ni concentration is not necessarily obtained. This can be easily visualized if one takes into account that most often the active sites are only a small fraction of the active phase exposed and that some reactions are strongly affected by the size of the active metal particle.

Binary Alloys. The reported methanation activity (3) of the oxidized alloys, expressed as the amount of CO consumed/g, is plotted in Figure 5B as a function of their nickel content. The activity of (NiSi<sub>2</sub>)<sub>o</sub> was not measured in ref. (3). However, because of the stability of the untreated alloy, its reported activity can be considered as representative of that relative to the oxidized form. One can readily note the close correlation between the observed variations of the catalytic activity and the evolution of surface nickel concentration (Figure 5A). However, the dramatic difference between the activity of nickel rich alloys [(Ni<sub>5</sub>Si<sub>2</sub>)<sub>o</sub> and (Ni<sub>2</sub>Si)<sub>o</sub>] and silicon rich intermetallics [(Ni<sub>3</sub>Si<sub>2</sub>)<sub>o</sub> and (NiSi<sub>2</sub>)<sub>o</sub>] far exceeds that expected, solely on the basis of the observed variation in surface nickel content estimated from ESCA data. This can be partially ascribed, as noted above, to the dependence of ESCA intensity ratio  $I_{Ni}/I_{Si}$  on the relative BET surface areas of Ni and SiO<sub>2</sub> and on the location of Ni with respect to SiO<sub>2</sub>. There is also another characteristic feature of the surface of nickel rich alloys [(Ni<sub>5</sub>Si<sub>2</sub>)<sub>u</sub>, (Ni<sub>2</sub>Si)<sub>u</sub>] reportedly active in methanation when compared with those of the inactive Ni-Si intermetallics [(Ni<sub>3</sub>Si<sub>2</sub>)<sub>u</sub>, (NiSi<sub>2</sub>)<sub>u</sub>]. Upon oxidation only the active alloys present ESCA spectra characteristic of Ni<sup>2+</sup> in an oxidic environment, thus indicating the partial decomposition of the intermetallic.

Comparison of the surface analysis and methanation activity of (Ni-Th)<sub>o</sub> alloys (Figure 6) shows that there is some interdependence between the surface concentration of Ni and activity; high Ni surface concentration generally results in greater methanation activity.

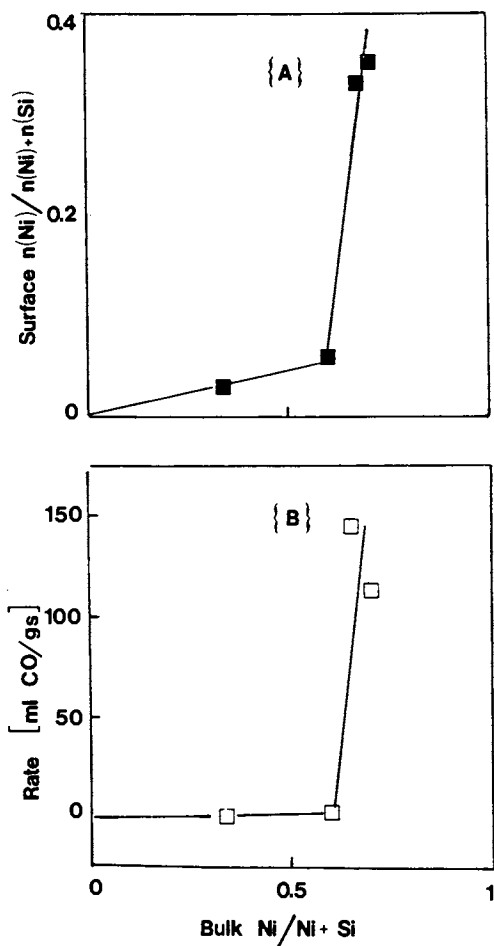


Figure 5: Correlation between surface composition and CO conversion activity of oxidized  $\text{Ni}_x\text{Si}_y$  alloys  
 (A): Variation of the surface nickel abundance  $n(\text{Ni})/n(\text{Ni})+n(\text{Si})$  as a function of bulk nickel content in oxidized  $\text{Ni}_x\text{Si}_y$  alloys.  
 (B): Variation of CO conversion activity of oxidized  $\text{Ni}_x\text{Si}_y$  alloys as a function of nickel content.

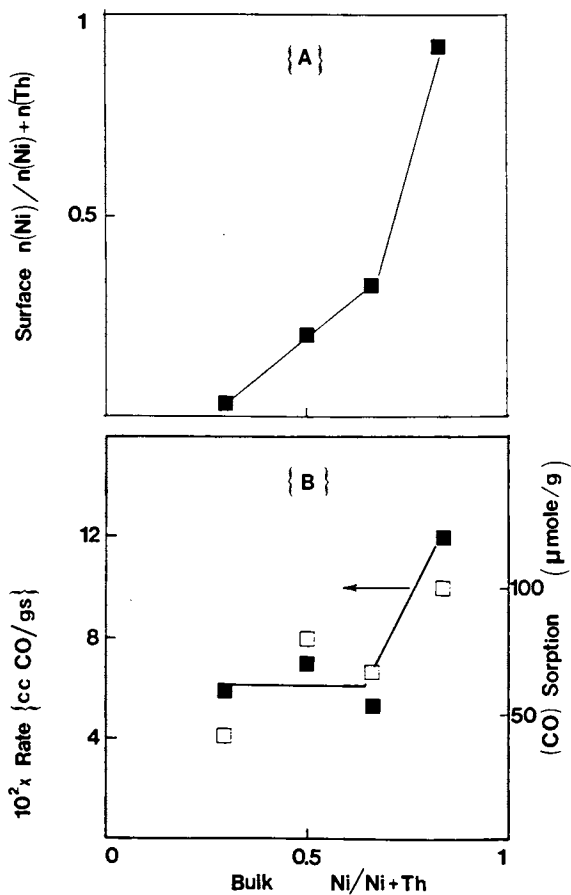


Figure 6: Correlation between surface composition and CO conversion activity of oxidized Ni-Th alloys  
 (A): Variation of surface nickel abundance  $n(\text{Ni})/n(\text{Ni})+n(\text{Th})$  as a function of bulk nickel content.  
 (B): Variation of CO conversion activity (■) and CO sorption capacities (□) as a function of bulk nickel content.

However, Figure 6 indicates that a significantly better correlation exists between the CO conversion rate and the CO sorption data. The lack of correlation between Ni surface concentration, as determined from ESCA data and CO chemisorption measurements, can tentatively be interpreted by considering that, as a result of oxygen treatment, a large fraction of Ni in Th-rich catalysts is encapsulated within the porosity of  $\text{ThO}_2$  particles and cannot be detected by ESCA. The texture of  $\text{ThO}_2$  is probably spongy and can be penetrated by hydrogen as well as  $\text{CO}$ . Thus, Ni under this permeable  $\text{ThO}_2$  layer is readily attainable and can chemisorb  $\text{CO}$ .

**Ternary Alloys.** The variations of CO conversion rate as a function of Ni content in  $(\text{ThNi}_x\text{Fe}_{5-x})_2\text{O}_7$  catalysts are compared in Figure 7 to Ni surface concentration as determined from ESCA data. It is evident

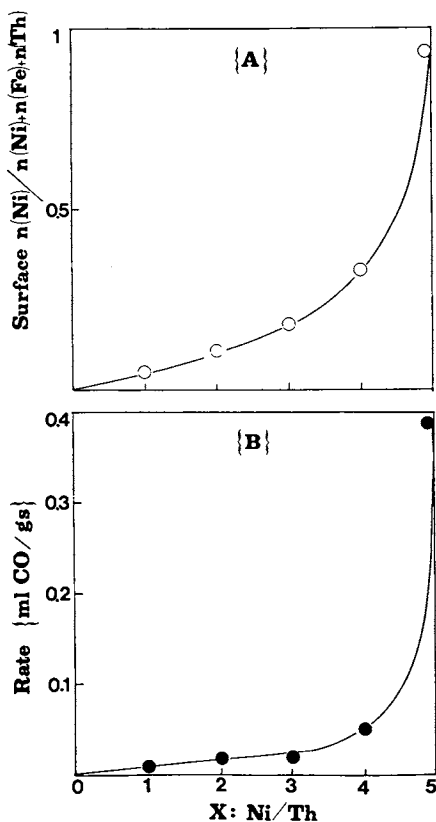


Figure 7: Correlation between surface nickel abundance  $n(\text{Ni})/n(\text{Ni})+n(\text{Fe})+n(\text{Th})$  and CO conversion activity of oxidized  $\text{ThNi}_x\text{Fe}_{5-x}$  alloys.  
 (A): Variation of surface nickel abundance  $n(\text{Ni})/n(\text{Ni})+n(\text{Fe})+n(\text{Th})$  as a function of bulk Ni/Th content.  
 (B): Variation of CO conversion activity as a function of bulk nickel content.

that CO conversion rate follows closely the changes in surface Ni content. Such a simple correlation is presumably due to the extremely low activity of the Fe phase and the constancy of the ratio Fe+Ni/Th in the various samples which limits the variation of the BET surface areas of the treated materials and, consequently, enhances the reliability of surface composition measurements from ESCA intensities data.

#### Acknowledgments

This work was supported by the National Science Foundation under Grant CHE-8020001.

#### Literature Cited

1. Wallace, W. E., Chemtech. 1982, 752-754.
2. Imamura, H. and Wallace, W. E., J. Catal. 1980, 65, 127-132.
3. Imamura, H. and Wallace, W. E., J. Phys. Chem. 1979, 83, 2009-2012.
4. Chin, R. L., Elattar, A., Wallace, W. E., and Hercules, D. M., J. Phys. Chem. 1980, 84, 2895-2898.
5. Houalla, M., Kibby, C. L., Petrakis, L., and Hercules, D. M., J. Phys. Chem. 1983, 87, 3689-3693.
6. Penn, D. R., J. Electron Spectrosc. Relat. Phenom. 1976, 9, 29-40.
7. Scofield, J. H., J. Electron. Spectrosc. Relat. Phenom. 1976, 8, 129-137.
8. Barrie, A. in "Handbook of X-ray and Ultra-Violet Photoelectron Spectroscopy", Briggs, D., Ed.; Heyden: London, p. 116.
9. France, J., Ph.D. Thesis, University of Pittsburgh, Pittsburgh, 1982.
10. Dang, T. A., Petrakis, L., Kibby, C. L., and Hercules, D. M., J. Catal. 1984, 88, 26-36.
11. Storp, S., Berresheim, K., and Wilmers, M., Surface and Interface Analysis 1979, 1, 96.
12. Klein, J. and Hercules, D. M. Anal. Chem. 1981, 53, 754-758.
13. Houalla, M., Dang, T. A., Kibby, C. L., Petrakis, L., and Hercules, D. M., to be published.
14. Imamura, H. and Wallace, W. E. J. Phys. Chem. 1980, 84, 3145-3147.
15. Grunthaner, P. J., Grunthaner, F. J., Scott, D. M., Nicolet, M. A., and Mayer, J. W. J. Vac. Sci., Technol. 1981, 19, 641-648.
16. Abbati, I., Rossi, G., Gallinari, L., Braicovich, L., Lindau, I., and Spicer, W. E. J. Vac. Sci. Technol. 1982, 21, 409-412.
17. Dang, T. A., Petrakis, L., and Hercules, D. M. J. Phys. Chem. 1984, 88, 3209-3215.

RECEIVED March 5, 1985

## Secondary Ion Mass Spectroscopic Studies of Adsorption and Reaction at Metal Surfaces Correlations with Other Surface-Sensitive Techniques

C. R. Brundle, R. J. Behm, P. Alnot, J. Grimblot, G. Polzonetti, H. Hopster, and K. Wandelt  
IBM Research Laboratory, San Jose, CA 95193

The use and limitations of SIMS ion intensity distributions to provide quantitative and chemical state information for adsorption and reaction of small molecules at metal surfaces is discussed. We concentrate on well-defined surfaces where there is sufficient information on the adsorption system from other surface sensitive techniques to test the information content of SIMS.

Several years ago, Secondary Ion Mass Spectroscopy (SIMS) seemed to be showing considerable promise for studying adsorption at metal surfaces (1). Though static SIMS is now widely used for studying organic films (2-5) and angular-resolved static SIMS (6,7) is being used in successful but limited studies for the determination of adsorption geometries on well-defined surfaces, the general promise of the technique in using cluster ion intensities for chemical and bonding analysis in adsorption studies has not been fully born out. Two factors were most important in the early promise of the technique. They were the direct chemical specificity of the mass spectrometric analysis and the often extreme surface sensitivity of the technique. For the latter, it is possible in favorable cases to detect much less than 1% overlayer concentrations. For the former, it is *sometimes* possible to make straightforward statements about the chemical identity of the adsorbate and its manner of bonding to the substrate. The problems that have led to the technique being less than generally applicable are strongly correlated with the above two advantages. Though SIMS can be extremely surface sensitive, it is hard to make it a quantitative analysis technique because the sensitivity, or secondary ion yields, vary enormously with the changing *chemical* nature of the surface species. The reason is that most species ejected from the surface during the SIMS process are neutrals, but only that small fraction which is positive or negative ions is detected. The fractions which escape as ions depend strongly on the charge distributions in the bonds being broken and the work functions at the surface. Thus the yield of Ni<sup>+</sup> species from a Ni surface can increase four orders of magnitude in the presence of adsorbed

0097-6156/85/0288-0317\$06.00/0  
© 1985 American Chemical Society



oxygen atoms (8). The yield of O containing cluster ions can vary at least two orders of magnitude depending on the chemical nature of the oxygen at the surface (chemisorbed atomic, oxide, physisorbed or  $H_2O$ , etc.). The question of determining the chemical nature of the adsorbate and its bonding characteristics to the surface involves somehow relating the distribution of molecular cluster ions removed from the surface by sputtering to the original bonding situation before the ion impact. Often a rich variety of cluster ions are observed. For instance, for CO adsorbed on Ni(100),  $Ni^+$ ,  $Ni_2^+$ ,  $Ni_3^+$ ,  $NiCO^+$ ,  $Ni_2CO^+$  and  $Ni_3CO^+$  can all be observed (8). The temptation is to draw conclusions concerning the adsorption situations based on the "dominant" cluster ion(s). In the Ni/CO situation, for instance, increased  $Ni_2CO^+/NiCO^+$  ratios under different CO adsorption situations have been over-simplistically taken as an indication that CO was moving from an ontop to bridge-bonded situation (9,10). Unfortunately, the SIMS process is far too complex and the "scrambling" effect of energetic ion impact too great for such simple correlations to have any general validity, though in specific cases, they may be correct. The more fundamental approach of calculating ejected cluster distributions for different adsorbate sites by classical trajectory collision methods (6,7) has more validity but is partly flawed by the fact that it related to the neutrals not the ions and also involves some empirical pair-interactions. In addition these studies suggest that the ejected molecular ions consisting of combinations of substrate atoms and adsorbate atoms/molecules,  $M_xAds_y^z$ , are always formed by recombination of neutral and ionized particles just above the surface. There is experimental evidence, however, that this is not always the case and that some such species are formed by direct emission of intact units (11,12). In any case, the trajectory calculation approach seems to have been used much more successfully in determining adsorbate geometries by comparison to angle-resolved experimental SIMS than to experimental cluster ion distributions.

We have adopted the approach that because of the large and poorly understood variations in ion yields and cluster ion distributions with variation in chemistry, it is necessary to empirically characterize these effects by using well-defined adsorbate situations which are simultaneously monitored by other, better understood, surface sensitive techniques such as LEED, XPS and thermal desorption. We report here some of the progress made to this end. Most of the work discussed is our own, but in some cases, we re-interpret other authors' SIMS results in the light of a better understanding of the adsorption situations to which those results refer. The object of this paper is to illustrate what correlations can and cannot be safely made between observed SIMS behavior and the nature of the adsorbate/substrate interaction. In doing this, we use a variety of adsorbate/substrate situations. One major class is the dissociative adsorption of oxygen followed by the onset of oxidation. Work on Ni(100) and W(100) is discussed. A second class is to follow the changes in SIMS on increasing coverage and, therefore, changing geometric and bonding conditions for CO adsorption on Ni(100). A third class is adsorption at alloy surfaces. The final class is low temperature molecular adsorption, followed by reactions and/or desorptions on raising the temperature.

## Experimental

Our SIMS data is taken using a VGQ8 quadrupole with unit mass resolution between 0-300 amu and a differentially pumped argon ion gun used in a defocused mode. A current of  $1-2 \times 10^{-9}$  A in a  $\sim 0.5$  cm<sup>2</sup> spot area is used. The SIMS system is mounted on a UHV spectrometer which also has XPS, UPS, LEED and thermal desorption capabilities (13). Heating is achieved by electron bombardment from a filament mounted on the manipulator behind the sample. Cooling is achieved by circulating liquid N<sub>2</sub> or He. Temperatures of 25K can be reached. The samples used, Ni(100), Cu(17%) Ni(83%) (100) and (111) and Ag(111) were oriented within 1° and cleaned *in situ* by standard heating and Ar<sup>+</sup> ion sputtering procedures.

SIMS Cluster Ion Characterization During Oxygen Adsorption and Oxidation. For heavy oxidation, that is essentially bulk oxide films, the oxidation state of the metal can be determined from the positive and negative SIMS intensity distributions (1). Though similar attempts have been made to characterize the nature of the surface during the early stages of oxygen interactions (14,15), we now know from the extensive information available from other techniques that such interpretations are incorrect. We use the by now well-characterized W(100)/O and Ni(100)/O systems as examples.

For W(100)/O, Benninghoven *et al.* (14) made some conclusions concerning the different stages of the reaction based on the behavior of the O<sup>+</sup>, W<sup>+</sup>, WO<sup>+</sup>, O<sup>-</sup>, WO<sub>2</sub><sup>-</sup> and WO<sub>3</sub><sup>-</sup> SIMS intensities as a function of exposure. They concluded that at <1L exposure, only dissociative adsorption occurred and was characterized by W<sup>+</sup> and O<sup>-</sup> emission. Between 1 and 10L, WO<sub>2</sub><sup>-</sup> emission was observed and considered to be representative of a "monomolecular W-O structure" on the surface. Above 10L, WO<sup>+</sup> emission was observed and it was suggested that 3D oxidation was occurring.

The above suggested sequence of reaction stages is now known not to represent the reaction stages for the majority oxygen species. There is a great deal of evidence (16) to show that, over the whole range of exposures at 300K up to saturation under UHV conditions, the majority species adsorption products are overlayer atomic oxygen only. Yu (17) repeated the SIMS measurements, but with the additional important factor, the determination of total O coverage by AES. Only the O<sup>+</sup> SIMS signal was found to be linear with coverage over the complete adsorption range. We have replotted his data for the other ion intensities as a function of coverage in Figure 1.

The O<sup>-</sup> and WO<sub>2</sub><sup>-</sup> intensities are shown before and after annealing to 1300K. This process is now known to reconstruct the surface (16). The following facts can be deduced from Yu's work. First, since the relationship of O<sup>+</sup> SIMS intensity to total O coverage is independent of annealing, the O<sup>+</sup> secondary ion yield is clearly independent of the drastic geometric and electronic structure effects brought about by reconstruction. On the other hand, the O<sup>-</sup> and WO<sub>2</sub><sup>-</sup> plots have obvious linear segments with breaks at discrete coverages and are strongly affected by the reconstruction process. Clearly, the bonding and/or geometric environment is important in determining the O<sup>-</sup> and WO<sub>2</sub><sup>-</sup> yields.

Second, W<sup>+</sup>, WO<sup>+</sup> and WO<sub>2</sub><sup>+</sup> and WO<sub>3</sub><sup>+</sup> are observed in small quantities at low coverages, but there is no linear relationship with coverage. The signals, however, increase very rapidly near saturation. Indeed, they continue

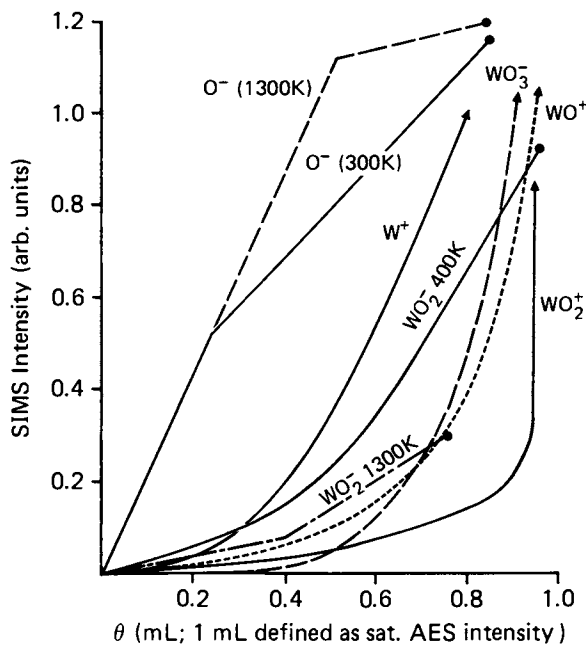


Figure 1. (a) SIMS intensities *versus*  $\theta$  for W(100)/O<sub>2</sub> derived from Ref. 17. Curves ending in an arrow signify that the signals are still rising rapidly even though  $\theta$ , as determined by AES, has saturated; (b) reconstruction of W(100)/O surface occurring above  $\sim 650\text{K}$ .

increasing rapidly with exposure even when the O AES signal has ceased to increase (particularly  $\text{WO}_2^+$ ).

There are two possible explanations for this behavior: (1) the signals come from the oxygen of *minority* species, such as incipient oxide nuclei, which continue to grow with exposure even though total coverage barely changes; (2) the high yields occur above a critical *local* O coverage. This could include case (1) but is not restricted to minority species. For example, a patch with 1 ML O coverage might have zero  $\text{W}^+$ ,  $\text{WO}^+$  and  $\text{WO}_3^-$  intensities but a slight increase in coverage may change the bonding and geometric relationship such that *all* the O atoms in the patch became "active" for  $\text{W}^+$ ,  $\text{WO}^+$  and  $\text{WO}_3^-$  emissions. In the W(100) case, we cannot really distinguish between possibilities (1) and (2). In the Ni(100) case discussed below, we have clear evidence that it is, indeed, oxide species which lead to the high yields of certain cluster ions.

Hopster and Brundle (8) correlated the SIMS intensities during the Ni(100)/ $\text{O}_2$  interactions with coverage (XPS), chemisorbed overlayer order (LEED) and the onset of oxidation (XPS of the Ni 2p levels). The data are replotted in Figure 2. The downward arrows indicate the known coverage at which NiO nucleation begins as documented by a large variety of other techniques (8). Several points become clear from these correlations. First, the positive ion intensities are clearly proportional to the chemisorbed O coverage and oxide oxygen does *not contribute* over the early exposure range. Then the signals reach a maximum at the end of the chemisorption stage. Second, there is no dependency of these positive ion yields on the ordering of the chemisorbed O (*i.e.*, no break in the curve associated with switching from  $\text{p}(2 \times 2)$  to  $\text{c}(2 \times 2)\text{O}$ , as was suggested by Fleisch *et al.* (18) in a study which did not have the benefit of LEED measurements). Third, the negative ion signals are proportional to the amount of oxidation and have very little or zero contribution from chemisorbed O. This general behavior is also found for Ni(110) and Ni(111) (19), with the additional factor that after saturation coverage was reached (AES determined), the  $\text{Ni}^+$  and  $\text{Ni}_2^+$  signals started to increase again with exposure. This further increase could represent elimination of defects in the NiO bilayer (19), or the uptake of small amounts of O on this bilayer. What it does *not* represent is oxide thickening as was originally concluded from comparable SIMS work on polycrystalline Ni which did not utilize an independent coverage measurement (20).

Our conclusion then for the oxygen interactions with metals is that because of the specific association of cluster ion intensities with particular types of oxygen rather than total coverage, the technique is *not suitable for monitoring coverages or kinetics* in an independent manner. Once it is established which type of oxygen a particular cluster ion is representative of, then that ion may, in favorable circumstances, be used for quantification. In the case of Ni, it seems that the negative ions are very sensitive to the initiation of oxide nucleation. In the case of W(100), the  $\text{WO}_3^-$ ,  $\text{WO}^+$  and  $\text{WO}_2^+$  ions may fill a similar role.

**Coverage and Secondary Ion Yield Relationship for Ni(100)/CO.** We showed above the enormous variation in yields that occurred on going from adsorption to oxide nucleation. In the case of Ni(100)/CO, one can perform more subtle bonding changes by changing the CO coverage. Below  $\theta \sim 0.4$  ML, no ordered LEED structure is formed, and vibrational spectroscopy (HRELS) indicates

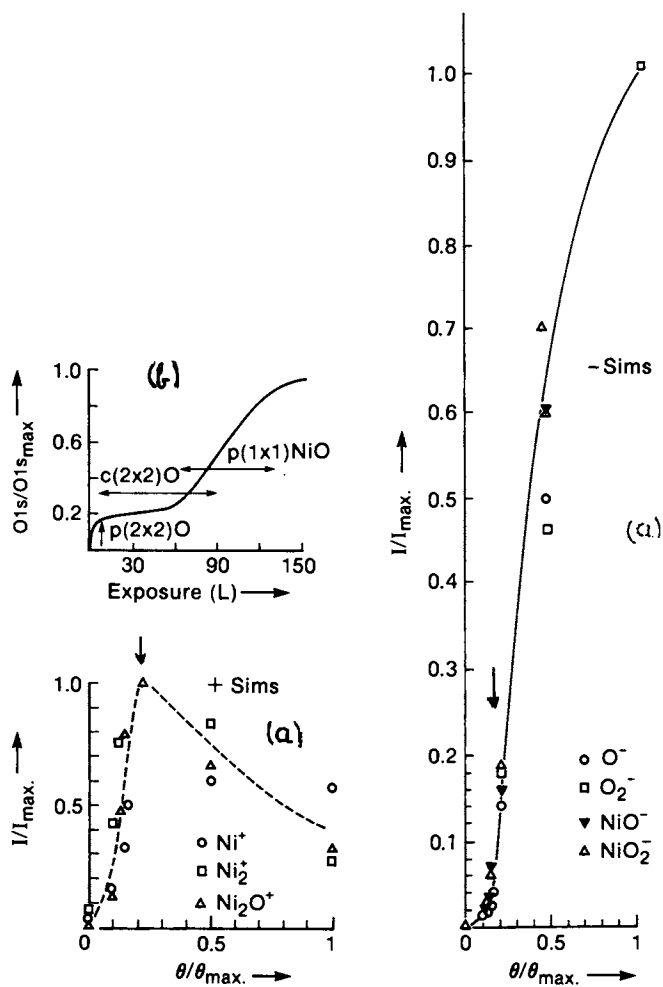


Figure 2. (a) SIMS intensities versus  $\theta$  for Ni(100)/O<sub>2</sub>, Ref. 8; (b) schematic of the different interaction stages of Ni(100)/O<sub>2</sub>.

that both bridge-bonded and linear-bonded CO are present (21). Between 0.4 and 0.5 ML, a  $c(2 \times 2)$  CO overlayer is formed which is known (22) to have linearly bonded CO. At saturation coverage (0.68 ML, 77K), a hexagonal LEED pattern is formed. Both the LEED and the vibrational spectra are consistent with this being an out-of-registry compression of the basic  $c(2 \times 2)$  structure, such that a range of CO bonding sites between linear and bridge bonding are formed.

In the table, we show the positive SIMS intensities for the above three situations, which were also monitored by XPS for CO coverage and LEED for structural condition. In addition, we also show the intensities for the 0.5 ML situation where the CO molecule has been deliberately dissociated to C and O atoms by an electron beam. This process was also monitored by XPS, which confirmed that the CO had, indeed, dissociated (from C(1s) and O(1s) chemical shifts) and that the total coverage was now  $\sim 0.25$  ML (C(1s) and O(1s) intensities). Several informative points can be gathered from the table:

(1) The observation or absence of CO containing clusters does directly signify the presence or absence of *molecular* CO on the surface. Note that after dissociation of the CO, but with atomic C and O still on the surface, the intensity of CO containing cluster goes to zero.

(2) The yields vary considerably with coverage; that is, the SIMS intensities are *not* proportional to coverage. In particular, the increase in coverage from 0.5 to 0.68 ML (36% increase) causes an approximately fourfold increase in intensities. One might at first suspect that this is associated directly with the change in bonding geometry accompanying the coverage change (linearly bonded CO converting to a range of bonding situations between linear and bridge-bonded). Looking at the yields for the low-coverage ( $\sim 0.25$  ML) CO situations, however, this seems unlikely, since there are bridge-bonded CO's present at low coverage, yet the secondary ion yields are weak. The effect then appears to be a local coverage one, rather than being directly traceable to geometry changes. Of course, an increase in the local coverage and therefore CO/Ni ratio must imply some electronic structure/bonding changes, and in fact we know that the CO in the out-of-registry 0.68 ML hexagonal structure has a lower heat of adsorption than does the 0.5 ML registered  $c(2 \times 2)$  structure. It is possible then that there is a correlation between the SIMS intensities and bonding, even though there is no direct correlation to geometric structure.

In early SIMS work on the Ni/CO system, it was suggested that the  $\text{Ni}_2\text{CO}^+/\text{NiCO}^+$  ratio was related to the relative amount of bridge and linearly bonded CO present (9,10). From our above discussion, we would anticipate that this is a very unlikely suggestion and the table bears this out. Again, the  $\text{Ni}_2\text{CO}^+/\text{NiCO}^+$  ratio appears to be a function of *coverage*, but shows no correlation with the known linear and bridge-bonding behavior of CO.

Brown and Vickermann (23) have recently revisited the Ni(100)/CO data. They relate the ratio  $\text{NiCO}^+ / (\text{NiCO}^+ + \text{Ni}_2\text{CO}^+)$  to the relative amounts of linearly bonded CO and bridge bonded CO on the empirical basis that CO in a linear M-CO site will give  $9/10\text{th MCO}^+$  and  $1/10\text{th M}_2\text{CO}^+$  and that CO in a bridge-bonded site will give  $5/10\text{th MCO}^+$  and  $5/10\text{th M}_2\text{CO}^+$ . Over their low to high exposure adsorption range (they have no way of knowing actual LEED structures since LEED was not monitored) the above ratio changes from 0.78 to 0.91. In other data by Fleisch *et al.* (24), it varies

from 0.84 to 0.94, and in our data (Table) at 0.2 ML coverage where both the bridge-bonded and linear-bonded species are present (21) the ratio is 0.86, and at a  $\theta$  of 0.5 ML where only linear-bonded CO is present it is 0.91. However, at a  $\theta$  of 0.68L, at which coverage a range of structures between linear and bridge is present the ratio does not decrease but stays constant or even increases again slightly to 0.92. Clearly in our data, which is directly correlated against LEED structure and coverage, the small variations in  $MCO^+/(MCO^+ + M_2CO^+)$  do not correlate with structural change. Also it seems to us to be a little unreasonable to try and make something of such a small relative change when the absolute intensities, which vary by a factor of 10 over this coverage range, are ignored.

Our conclusion then, from this work, is that though the chemical speciation capability of SIMS is quite clear, quantification is still not easy, even for a system where the bonding changes with coverage are much more subtle than those encountered on going from  $O_{ad}$  to oxide nucleation. In addition, except when angle-resolved effects are specifically included, there is no direct relationship between the CO bonding site and the  $Ni_2CO^+/NiCO^+$  SIMS intensity ratio, or the  $NiCO^+/NiCO^+ + Ni_2CO^+$  ratio.

Brown and Vickerman (23) also present new data on Ru(001)/CO and Ni(111)/CO in which coverage has been calibrated using TDS. In the Ni(111)/CO data they find a much stronger variation of  $MCO^+/(MCO^+ + M_2CO^+)$ , 0.5 to 0.8, with increasing  $\theta$  which appears to correlate with conversion of bridge to linear CO species, as determined from literature HRELS data over the same exposure range. This data looks much more convincing than the Ni(100)/CO data but again it is difficult to see how effects on the  $MCO^+/(MCO^+ + M_2CO^+)$  ratio of changes in coverage, heat of adsorption, and changes in dipole or work function can be separated from geometric effects.

**Reaction at Cu/Ni Alloy Surfaces.** The Cu/Ni alloy system is one which involves strong surface segregation of Cu. Thus, Cu(17%)/Ni(83%) has 70% Cu in the top  $\sim 4\text{\AA}$  at a clean (100) surface and 65% Cu at a clean (111) surface, as determined by low angle XPS (25). CO adsorbs only at Ni sites at 300K, as determined by UPS. This preferential adsorption results in some back-segregation of Ni to the surface (25). For oxygen reaction, there also is preferential oxidation of Ni and back-segregation to the surface, but the system is more complex than for CO because adsorption will take place at Cu sites also and eventually the Cu component will oxidize. We have monitored the changes in SIMS cluster ion intensities for these systems while monitoring CO and O coverage and Cu and Ni surface concentrations by XPS. The strong, but well-characterized, chemical specificity of the systems offers an ideal case to test the useful information content of SIMS cluster ion intensities.

We refer the readers to the original paper for the results and just list the main conclusions here:

(1) SIMS intensities from the "clean" Cu/Ni surfaces cannot be used to determine Cu/Ni surface concentrations, or relative change in concentration from one surface to another. This is because trace impurities (of very low but unknown concentration) preferentially bond to Ni sites and therefore the Ni containing SIMS cluster ions are preferentially enhanced, leading to an erroneously high determination of Ni concentration.

(2) Since CO at 300K bonds only to Ni sites, preferentially enhancing Ni containing SIMS cluster yields, a comparison of intensities from one composition surface to another during CO adsorption does provide a measure of the *relative* Ni concentrations in the two surfaces, *e.g.*, the SIMS cluster ion intensities do correctly indicate that the (111) surface of the bulk 17/83 Cu/Ni crystal has more Ni at the surface than the (100) surface. An advantage of SIMS measurements of this kind is that the information refers strictly to the top layer, whereas the XPS information even at grazing angle looks several layers deep.

(3) For oxygen interactions, similar interpretations as for CO can be offered in the chemisorption stage, but the onset of oxidation complicates the SIMS data at high exposures. At very high exposures, it is possible to detect the onset of Cu oxidation by a sudden rise in the, by then, very low  $\text{Cu}^+/\text{Ni}^+$  ratio.

Coadsorption and Decomposition Reactions. The final area we discuss are cases where there are coadsorbed species present, which may react, and cases where molecular adsorption converts to dissociative (or associative) products.

We have already discussed an example of the last case, the dissociation of CO on Ni(100). It was mentioned in the context of demonstrating that CO containing SIMS clusters signified the presence of molecular CO on the surface. As can be seen from the table, however, the yields of the C containing and O containing clusters after dissociation of CO are low compared to those of the CO containing cluster, and on the basis of the SIMS data above, one might have been led to believe desorption rather than dissociation of CO had occurred.

Though the secondary ion yields for the CO containing clusters is much higher than for the C and O containing clusters, the yield for  $\text{H}_2\text{O}$  containing clusters following  $\text{H}_2\text{O}$  adsorption is even higher. Thus, a 1:1 mixture of  $\text{H}_2\text{O}$  and CO adsorbed on the Ni(100) surface at 77K (XPS determined) gives a  $\text{Ni}(\text{H}_2\text{O})^+/\text{Ni}(\text{CO})^+$  ratio of 30 (8). In fact, small traces of  $\text{H}_2\text{O}$  are always detectable by SIMS for the adsorption at low temperature of  $\text{H}_2$ ,  $\text{O}_2$ , CO and  $\text{CO}_2$  on Ni(100) (8) and for NO,  $\text{N}_2\text{O}$  and  $\text{N}_2$  on Ag(111) (26) even when the quantity there is below the detection limits of XPS. Conversion of  $\text{H}_2\text{O}$  to OH by reaction with  $\text{O}_{\text{ads}}$  is easily observed by SIMS. In the case of Ni(100)/ $\text{O}_2$ , this removed a point of contention concerning the assignment of a second O(1s) XPS peak of  $\sim 1 \frac{1}{2}$  eV higher BE than the main peak. Suggestions that it represented molecular  $\text{O}_2$ , NiO as opposed to  $\text{O}_{\text{ads}}$ , or one geometric arrangement of  $\text{O}_{\text{ads}}$  as opposed to another, *etc.*, had all been made. SIMS unambiguously showed (27) that the high BE O(1s) was representative of OH by correlating  $\text{OH}^-$  SIMS signal intensities with it. The reaction between residual  $\text{H}_2\text{O}$  and  $\text{O}_{\text{ads}}$  to give  $\text{OH}_{\text{ads}}$  was the cause.

The Ag(111)/NO system turns out to be rather complex for adsorption at 20K despite the fact that at 300K virtually no adsorption occurs, and one might therefore expect that at low temperature only physisorption and condensation would occur. In fact, condensed NO exists as  $(\text{NO})_2$  dimers (28), and a complex set of reactions leading to O, NO,  $\text{N}_2\text{O}$  and  $\text{NO}_2$  species takes place when the temperature is raised as determined by combined XPS and TPD measurements (29). Following the SIMS cluster behavior during the reactions shows that several of the reaction species can be identified from the SIMS molecular clusters.



Rabalais and coworkers (30) have reported on the SIMS of NO on Ni(100) as a function of temperature. They were not able to go to low enough temperature to observe (NO)<sub>2</sub> condensation, but they did observe that the decomposition of NO to N and O fragments with temperature increase was accompanied by a decrease of NO containing clusters and an increase in N and O containing clusters. This result is, therefore, rather similar to that mentioned in this paper earlier for CO dissociation on Ni(100) (8).

### Conclusions

By combining measurements on SIMS cluster ion intensities with parallel XPS, LEED and TPD studies for well-defined adsorption systems, we have been able to provide some guidance concerning in which areas the SIMS ion intensities can give useful quantitative and chemical information. Though there are cases where the cluster ion intensities can be used for quantitative analysis, it is not easy to know for which system this is true. In general, it seems most productive to use static SIMS as a means for tracking minority species which cannot be monitored by conventional means, or to distinguish chemical species, such as OH from O, where other techniques fail. It also seems very promising for adsorption at binary alloy surfaces where preferential reactions with one component may be occurring.

Table. Intensities (Arbitrary Units)  
of SIMS Clusters for the Ni(100)/CO System

| Surface Condition                            | Ni <sup>+</sup> | NiCO <sup>+</sup> | Ni <sub>2</sub> CO <sup>+</sup> | Ni <sub>2</sub> C <sup>+</sup> | Ni <sub>2</sub> O <sup>+</sup> | $\frac{\text{NiCO}^+}{\text{Ni}_2\text{CO}^+}$ | $\frac{\text{NiCO}^+}{\text{NiCO}^+ + \text{Ni}_2\text{CO}^+}$ |
|--|-----------------|-------------------|---------------------------------|--------------------------------|--------------------------------|--|--|
| "Clean"                                      | 0.3             | -                 | -                               | -                              | -                              | -  | -  |
| 0.2 ML, 300K                                 | 9.3             | 3.1               | 0.5                             | -                              | -                              | 6.2  | 0.86   |
| c(2x2) overlayer,<br>0.5 ML                  | 40.0            | 20.0              | 2.0                             | -                              | -                              | 10.0   | 0.91   |
| Hexagonal overlayer,<br>77K, 0.68 ML         | 230.0           | 110.0             | 10.0                            | -                              | -                              | 11.0   | 0.92   |
| 0.25 ML of C<br>and 0.25 ML of O<br>~0.05 CO | 3.0             | 0.6               | -                               | 0.2                            | 0.1                            | -  | -  |

### Literature Cited

1. Benninghoven, A. In "Chemistry and Physics of Surfaces"; Vanselow, R.; Tong, S. Y.; Eds., C. R. C. Press: Cleveland, Ohio, 1977; p. 207.
2. Benninghoven, A.; Ed. "Ion Formation from Organic Solids," Vol. 25, Springer Series in Chemical Physics; Springer-Verlag: Berlin, 1983.
3. Day, R. J.; Unger, S. E.; Cooks, R. G. Anal. Chem. 1980, 52, 557A.
4. Cotton, R. J. J. Vac. Sci. Tech. 1981, 18, 737.
5. Busch, K. L.; Cooks, R. G. Science 1982, 218, 805.
6. Winograd, N.; Garrison, B. J. Acc. Chem. Res. 1980, 13, 400.
7. Garrison, B. J.; Winograd, N. Science 1982, 216, 805.

8. Hopster, H.; Brundle, C. R. J. Vac. Sci. Tech. 1979, 16, 548.
9. Barber, M.; Vickerman, J. C.; Wolstenholme, J. J. Chem. Soc. Farad. Trans. I 1976, 72, 40.
10. Barber, M.; Bordoli, R.; Wolstenholme, J.; Vickerman, J. C. Proc. Seventh Int. Vac. Congr., Vienna, 1977, p. 933.
11. Yu, M. L. Phys. Rev. B. 1981, 24, 5625.
12. Yu, M. L. Appl. Surf. Sci. 1982, 11/12, 196.
13. Brundle, C. R. IBM J. Res. 1978, 22, 235.
14. Benninghoven, A.; Loebach, E.; Plog, C.; Trietz, N. Surf. Sci. 1973, 39, 397.
15. Müller, K. H.; Beckmann, P.; Schemner, M.; Benninghoven, A. Surf. Sci. 1979, 80, 325.
16. Brundle, C. R.; Broughton, J. Q. In Vol. 3B of "The Chemical Physics of Solid Surfaces and Heterogeneous Catalysis," King, D. A.; Woodruff, P.; Eds., to be published.
17. Yu, M. Surf. Sci. 1978, 71, 121.
18. Fleisch, T.; Winograd, W.; Delgass, W. N. Surf. Sci. 1978, 78, 161.
19. Rieder, K. H. Appl. of Surf. Sci. 1978, 2, 76.
20. Müller, A.; Benninghoven, A. Surf. Sci. 1974, 41, 493;  
Müller, K. H.; Beckmann, P.; Schemmer, M.; Benninghoven, A. Surf. Sci. 1979, 80, 325.
21. Andersson, S. Proc. Seventh Int. Vac. Congr., Vienna, 1977, p. 1019.
22. Andersson, S.; Pendry, J. B. Phys. Rev. Lett. 1979, 43, 363.
23. Brown, A.; Vickerman, J. C. Surf. Sci. 1982, 117, 154.
24. Fleisch, T.; Ott, G. L.; Delgass, W. N.; Winograd, N. Surf. Sci. 1979, 81, 1.
25. Wandelt, K.; Brundle, C. R. Phys. Rev. Lett. 1981, 46, 1529.
26. Brundle, C. R.; Behm, R. J.; Grimblot, J.; Polzonetti, G.; Alnot, P., to be published.
27. Brundle, C. R.; Hopster, H. In "SIMS II," Benninghoven, A.; Evans, C. A.; Powell, R. A.; Shimuzu, R.; Storms, H. A.; Eds., Vol. 9, Springer Series in Chemical Physics; Springer Verlag: Berlin, 1979.
28. Nelin, C. J.; Bagus, P. S.; Behm, J.; Brundle, C. R. Chem. Phys. Lett. 1984, 105, 58.
29. Behm, R. J.; Brundle, C. R.; Grimblot, J.; Polzonetti, G., to be published.
30. Rabalais, J. W. Nucl. Instr. Methods 1981, 191, 323.

RECEIVED June 21, 1985

## Electron Microscopy and Diffraction Techniques for the Study of Small Particles

J. M. Cowley

Department of Physics, Arizona State University, Tempe, AZ 85287

Recent advances in electron microscopy with instruments having a resolution of  $2\text{\AA}$  or better provide the possibility of atomic-scale imaging of small particles and, in favorable cases, atom positions can be determined with an accuracy approaching  $0.1\text{\AA}$ . The scanning transmission electron microscope provides complementary information through the use of special detector configurations and the possibilities for obtaining microdiffraction patterns and microanalysis signals from very small specimen regions,  $10\text{\AA}$  or less in diameter. Examples are given of the analysis of supported catalyst systems using electron beams of about  $10\text{\AA}$  in diameter to obtain diffraction patterns from individual metal particles of comparable diameter.

Advances in the design of transmission electron microscopes, combined with the use of accelerating voltages higher than the  $100\text{keV}$  of the older high resolution instruments, have provided the very important improvements of the resolution limit which allow the atom positions in many inorganic solids to be distinguished. Point-to-point resolutions of  $2\text{\AA}$  or better approached by some of the older million volt microscopes and achieved by some of the newer instruments should allow meaningful images of the atom configurations in small regions of thin specimens to be interpreted quantitatively and reliably. Developments of the special detector configurations for scanning transmission electron microscopy (STEM) have made it possible to perform selective imaging making use of known characteristics of the specimen, such as composition or crystallinity, to answer more specific questions. The techniques of microdiffraction have advanced to the stage that diffraction patterns from regions  $10\text{\AA}$  or less diameter can be obtained readily. This can provide information on the structures of individual small particles or regions within small particles, thus complementing in an important way the information from the selected area electron diffraction and X-ray diffraction methods which refer to averages over very large numbers of individual particles.

0097-6156/85/0288-0329\$06.00/0  
© 1985 American Chemical Society

In addition, use of the scanning principle allows microanalysis of very small specimen regions to be performed by detection of either the characteristic X-rays emitted or the characteristic energy loss peaks in the energy spectrum of transmitted electrons.

In this review an attempt will be made to assess the current capabilities of these techniques in their application to the study of small metal and oxide particles which are of interest in relation to catalysis. Some examples will be given of recent applications and some suggestions will be made concerning probable directions for future developments.

### Transmission electron microscopy (TEM)

For many years it has been possible to detect single heavy atoms as small black (or white) spots in TEM images. Also it has been possible to detect detail due to diffraction effects in crystals on a scale of  $1\text{\AA}$  or better even with electron microscopes having a nominal "point-to-point" resolution of  $3\text{--}4\text{\AA}$  (1,2). However with such microscopes the interpretation of image detail on this scale in terms of structure is possible only for very special cases of extended, perfect thin crystals of very simple structure and is not possible for small crystals or crystals with defects. The practical use of electron microscopes as a means for deriving the atom arrangements in small particles or other thin specimens had to wait for the development of electron microscopes having a point-to-point resolution around  $2\text{\AA}$  or better since the interatomic distances in projections of the structures of metals, semiconductors, oxides and other materials tend to be  $1.5\text{--}2\text{\AA}$  for even the most favorable orientations. The required resolution has been attained by use of microscopes having higher accelerating voltages than the  $100\text{keV}$  which has been conventional in the past.

Interpretation of the images is still not straightforward even when there seems to be a simple one-to-one correspondence between black (or white) dots in the image and atom positions. Especially when quantitative data on interatomic distances is to be derived, detailed calculations based on many-beam dynamical theory (3) must be applied to derive calculated images for comparison with experiment. For this purpose the experimental parameters describing the imaging conditions and the specimen thickness and orientation must be known with high accuracy.

A recent example of a successful analysis comes from the studies of small gold particle by Marks and Smith (4,5) using the  $600\text{keV}$  Cambridge microscope, (see also their article in this volume). With the incident beam parallel to the (110) face of a gold crystal, in [100] direction, the configuration of atom rows extending about  $50\text{\AA}$  in the beam direction could be seen clearly, showing the  $2\times 1$  surface reconstruction, which had previously been postulated from LEED results. Displacements of the gold surface atoms from the bulk lattice positions could be determined with an accuracy of about  $0.1\text{\AA}$ . These displacements, derived by comparison with calculated images

were distinctly different from those suggested by the positions of the black dots associated with the atom rows in the images.

An extreme case of the apparent distortion of structures due to the complications of the imaging process is shown in figure 1, an image of the corner of a cubic crystal of MgO smoke viewed along the [001] direction, parallel to the edge of the cube. The image was obtained with JEM 200CX microscope by Dr. T. Tanji in our laboratory. The 2Å square grid corresponding to the 200 and 020 lattice periodicities is visible in the bulk of the crystal. In the small crystal projecting from the top of the large crystal and at the corner of the large crystal the lattice planes appear to be bent, curving away from the crystal face by 1 or 2Å. There may, of course, be some slight displacements of the atoms present, but these large apparent displacements are almost certainly the result of an artifact produced by dynamical diffraction processes.

Determinations of projected atom positions are much more difficult for atoms in the interior of the particle if the atoms are not conveniently aligned in straight rows in the direction of the incident electron beam. For the immediate future only the most favorable cases will be studied but with the application of anticipated improvements of resolution to the 1.5Å level or better and the means for more accurate and automated measurement of the necessary instrumental parameters, the detailed study of configurations of atoms in small particles should become generally feasible.

In the meantime a great deal of more qualitative but highly significant information on small particles should flow from the high resolution instruments now available.

#### Scanning transmission electron microscopy (STEM)

While STEM instruments have not shown the same resolution or picture quality as the fixed beam TEM instruments for bright-field imaging, they have important advantages derived from the flexibility with which different detector systems may be arranged to obtain a variety of image signals. Also the fact that multiple images from different detectors can be produced as parallel electronic signals in serial form allows great flexibility in on-line image processing. Early work by Crewe and associates (6,7) established the benefits of STEM for dark-field imaging and for images using combinations of signals from inelastic and elastic scattering. These, and other means involving special detector configurations, have increasingly been applied to the special problems of imaging small heavy-atom particles supported on, or embedded in, light-atom material.

The Z contrast method, involving signals from inelastically and elastically scattered electrons, has been shown to be effective for the study of supported catalyst particles (8). Later, advantage was taken of the fact that heavy atoms scatter more strongly to higher angles than light atoms and it was shown that heavy atom particles could be revealed more readily if the images were obtained only with electrons scattered to high angles, of the order of  $10^{-1}$  radians (9). Unless the scattering angle is sufficiently large, the remaining

signal still shows some contrast due to crystallinity of the light atom material, with maxima or minima of intensity from small regions giving strong diffraction effects.

A further refinement of the method has been made in which only those electrons were used which were scattered to higher angle regions of the diffraction pattern where crystalline reflections were weak or absent. Then a difference signal was obtained from electrons scattered to very high angles and those scattered to high angles (10). The signal levels from such a scheme are low but the discrimination between heavy and light atoms can be very good if the specimen is not too thick.

For most studies of catalyst particles the electron microscopy is done on very thin specimens and the use of high angle scattering for dark field imaging is feasible. When circumstances require the use of thick specimens these techniques are not so effective but even then the choice of specific detector configurations can enhance the contrast of small particles. It has been shown, for example, that the visibility of small particles on thick supports can be improved considerably by using a detector displaced from the normal bright field imaging position so that it lies on the edge of the central spot (the directly transmitted beam) in the detector plane (11).

Figure 2 shows two STEM images of small gold particles on a crystal of MgO. For the image on the left, the detector was central in the beam spot containing the directly transmitted electrons, as for normal bright field imaging. The other image was obtained with the detector displaced so that it was just at the edge of the central beam spot, giving an image produced partly by the directly transmitted electrons and partly by electrons deflected by elastic and inelastic scattering processes. In this, the small gold particles are seen much more clearly.

### Microanalysis

When the fine electron beam of a STEM instrument passes through a specimen, it generates secondary radiation through inelastic scattering processes. When inner shell electrons of the atoms are excited, the secondary radiation signals may be characteristic of the elements present and so provide a basis for the microanalysis of the small specimen regions which are irradiated.

Firstly, the energy losses of the incident electrons which produce the inner shell excitations may be detected as peaks in electron energy loss spectroscopy (EELS). The electrons transmitted by the specimen are dispersed in a magnetic field spectrometer and the peaks, due to K, L and other shell excitations giving energy losses in the range of 0-2000eV, may be detected and measured.

Secondly, the characteristic X-rays, emitted as the electrons displaced from the inner shells of the atoms are replaced, can be detected by use of an energy-sensitive detector placed close to the specimen. An account of the application of both the energy dispersive spectroscopy (EDS) of the emitted X-rays and EELS to the

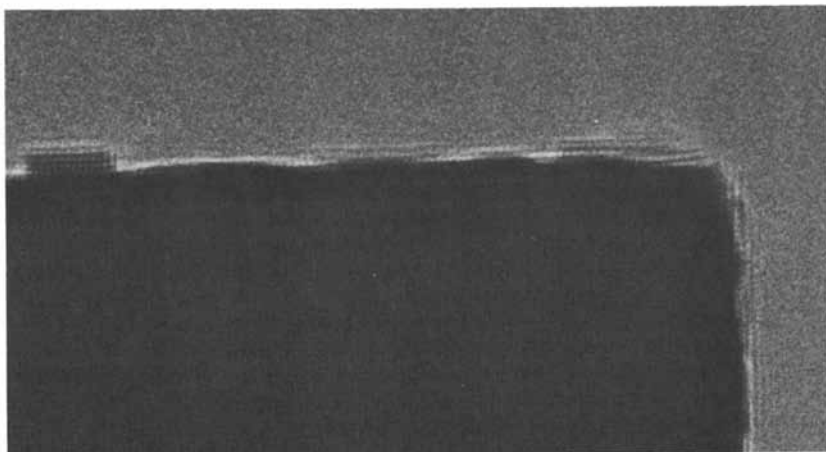


Figure 1. High resolution Electron Micrograph of a cubic MgO crystal viewed in [100] direction showing square net of 2 Å fringes and apparent bending of atom planes at edges. Courtesy of Dr. T. Tanji.

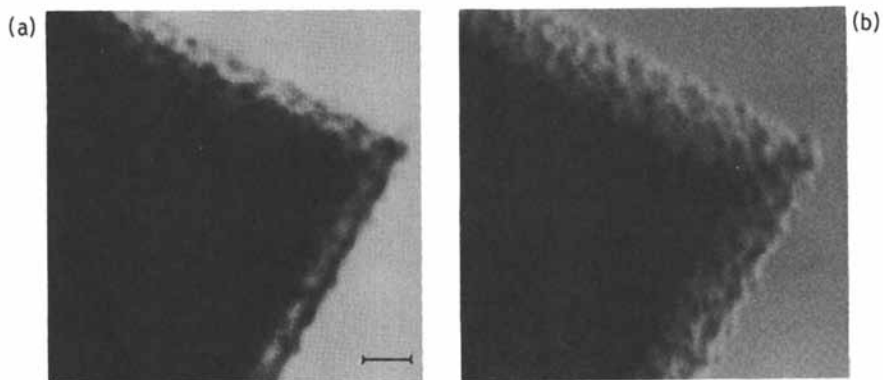


Figure 2. (a) Bright field STEM image of small gold crystals on a large MgO smoke crystal. Marker indicates 100 Å. (b) As for (a) but with a displaced detector.

study of the composition of small particles of interest in catalysis is given by the article of Lyman in this volume. In each case the analysis may be done of very small specimen regions of diameter less than  $100\text{\AA}$ . The limitations on size of particle which may be analysed, or on the percentage of a particular element present in any sample area, are determined in each case by the signal strength. The relevant parameters include the intensity of the incident beam, the scattering cross section for inner shell excitations, the detection efficiency and the ratio of signal to background. In general the detection efficiency is high for EELS but the background levels of the signals are also high. For X-ray EDS the detection efficiency is not so good but the signals show lower background levels. Each technique has its own particular areas of strength and weakness.

A third signal, dependent on the nature of the elements present, is given by the Auger electrons, emitted as an alternative to X-rays when the energy of an inner shell excitation is dispersed. Because the emitted electrons are of relatively low energy (0-2000eV) and so have only limited penetration through solids, Auger electron spectroscopy (AES) and the corresponding scanning imaging technique (SAM: scanning Auger Microscopy) have been thought of as surface analysis techniques to be applied to bulk samples. Currently, however, instruments are being built to combine AES with STEM imaging in the transmission or reflection mode. With a projected spatial resolution of  $50\text{\AA}$  or less, AES and SAM may well take their place as major tools for the investigation of the composition and surface modifications of small particles. Particularly for light elements, the cross sections for the production of Auger electrons may be greater than for X-rays and the collection efficiencies may also be greater.

#### REM electron microscopy (REM)

In recent years the technique for imaging with diffracted beams, obtained in the RHEED mode with an incident beam at grazing incidence to the flat surface, has been shown to be effective as a means for studying surface structure and surface reactions (12,13). While it is desirable to use a microscope having an ultra-high vacuum specimen environment if surface reactions are to be studied, some valuable determinations of structure can be made with a conventional instrument. In each case single atom steps on the surface give good contrast, dislocations intersecting the surface are clearly visible and a number of other interesting surface features have been seen and explored. In the case of the regular arrays of steps seen on vicinal surfaces of gold crystals, a resolution of better than  $10\text{\AA}$  has been demonstrated (14). This technique has been applied most effectively for the study of extended surfaces of bulk samples and the implications for the knowledge of surfaces of small particles are, at best, indirect. The equivalent type of imaging using the scanning mode, is more directly relevant.

#### Scanning reflection electron microscopy (SREM)

By use of a scanning transmission electron microscope, with the incident beam grazing the crystal surface, the structural features on surfaces have also been revealed with a resolution of  $10\text{\AA}$  or better



(15). This technique has been applied effectively to examine details of surfaces of particles  $1\mu\text{m}$  or less in diameter. It has been used, for example, to detect the ordering in linear arrays of small gold particle,  $20\text{\AA}$  in diameter, on the surfaces of MgO crystals (16). The extraordinary result is that the gold particle(s) apparently are aligned on surface steps which are inclined to each other, and to the [100] crystal edge directions, at angles of only 2 or 3 degrees.

As in the case of STEM, the main benefit arising from the use of the scanning mode is that the incident electron probe can be stopped or controlled in its motion and a variety of detector types and configurations can be used to obtain particular signals, giving information beyond that obtained in the normal imaging modes.

When the scan of the incident beam is stopped at a chosen part of the image, a diffraction pattern can be obtained from the selected region which may have a diameter as small as the image resolution of  $10\text{\AA}$  or less. Also electron energy loss analysis of the scattered electrons may allow deductions concerning the energy states of very small surface regions. The most striking results obtained in this way come from experiments in which an electron beam of  $10\text{\AA}$  diameter is made to traverse the vacuum just outside the face of a small crystal (17-19). In this way the surface excitations can be examined with no complication from scattering or excitations of the bulk crystal. The main features of the energy loss spectra have been shown to be in essential agreement with the deductions from the known dielectric constant of MgO, but there are indications of effects due to surface states appearing within the band gap of the bulk crystal and to surface channelling phenomena (17). Experiments have also been conducted to investigate the form of the potential field extending from the crystal into the surrounding vacuum by detection of the deflection of electrons passing close to the crystal surface (20).

#### Microdiffraction in a STEM instrument

The diffraction pattern obtained in the detector plane when the beam scan in a STEM instrument is stopped at a chosen point of the image comes from the illuminated area of the specimen which may be as small as  $3\text{\AA}$  in diameter. In order to form a probe of this diameter it is necessary to illuminate the specimen with a convergent beam. The pattern obtained is then a convergent beam electron diffraction (CBED) pattern in which the central spot and all diffraction spots from a thin crystal are large discs rather than sharp maxima. Such patterns can normally be interpreted only by comparison with patterns calculated for particular postulated distributions of atoms. This has been attempted, as yet, for only a few cases such as on the diffraction study of the planar, nitrogen-rich defects in diamonds (21).

Diffraction patterns having relatively well-defined sharp spots can be obtained from small unit-cell crystals with an incident beam of diameter  $10\text{-}15\text{\AA}$ . Such patterns have been used in the study of the structures of small metal particles (22). For particles  $10\text{-}20\text{\AA}$  diameter the electron beam can illuminate the whole of the particle

so that any structural features such as twin or faults can be revealed. For larger particles, in the 20-50Å size range, the diffraction pattern may be seen to change as the beam is moved across the particle.

For the smaller particles which include only a few tens or hundreds of atoms, any twinning or faulting reduces the range of ordering to the extent that the pattern can not be interpreted in the same way as a pattern from an extended crystal. The individual single-crystal regions may contain only two or three atomic planes. Interpretation can be made only by calculation of patterns from postulated models for the configurations of atoms (22).

This technique has been applied, for example, to test the theoretical prediction that for small particles of face-centered cubic metals the equilibrium state will be a multiply-twinned form with preference for configurations in which either five or twenty tetrahedrally shaped single crystal regions are related by twinning on (111) planes (23). For particles of gold in a polyester film, formed by co-sputtering (24), it was shown that in the size range of 30-50Å approximately half were multiply twinned but in the size range of 15-20Å a much smaller proportion of the particles could be identified as such. Most were single crystals or had at most one or two twin planes.

It is not necessarily to be concluded that, in general, the proportion of small metal particles having the multiplicity twinned form decreases as the size is decreased. The evidence concerning particles formed in other ways shows a great deal of variability. For example 20Å gold particles epitaxed on MgO (100) faces are almost invariably single crystals when formed by indirect evaporation on faces not exposed to the direct flux of incident gold atoms (16), although gold particles formed on MgO (100) faces by direct deposition from the source are in random orientation, usually with (111) planes parallel to the surface, and are frequently twinned or multiply twinned. Particles of Pd on single-crystal  $\alpha$ -Al<sub>2</sub>O<sub>3</sub> faces were sometimes twinned and sometimes not for different regions of the same specimen. In agglomerates of pure Pt particles, individual particles in the 100Å size range showed a relatively high incidence of twinning and multiple twinning but Pt particles in the size range of 15-30Å, supported on alumina or silica substrates gave mostly single-crystal patterns.

The extent to which small particles of Pd and Pt show evidence of oxidation after exposure to air is also highly variable. It is difficult to confirm the evidence of X-ray diffraction and EXAFS (25) that most particles in the 15-20Å size range consist entirely of oxide. We have found that such particles usually give single crystal patterns attributable to the metals. There is, however, considerable evidence that, in the case of Pt on alumina, the Pt crystals have a well-defined epitaxial relationship with the crystallites (20-50Å diameter) of the nominally "amorphous" alumina substrate.

Similar observations of epitaxial relationships have been observed for small crystals of Ru and Au on MgO (26). Figure 3(a)

for example, shows the pattern of the MgO crystal substrate in [111] orientation, obtained with an incident beam of diameter approximately  $10\text{\AA}$ . The additional hexagonal array of spots of figure 3(b) comes from a crystal of Ru about  $15\text{\AA}$  in diameter, aligned in a parallel orientation. Figure 3(c) shows the spots from an Au crystal, about  $20\text{\AA}$  in diameter, seen in an approximate [110] direction with one set of (111) planes almost parallel to MgO (220) planes, with some indication that it is accompanied by a small Ru crystal aligned as for Figure 3(b).

The STEM images obtained when the incident beam, used to obtain microdiffraction patterns such as in Figure 3, is scanned over the specimen will have a resolution no better than the beam diameter of about  $10\text{\AA}$ , as in Figure 4(a). This is usually sufficient to allow the particles in question to be located and identified in images subsequently obtained with better resolution, using larger objective aperture, such as Figure 4(b). The resolution of the STEM instrument is currently limited to about  $3\text{\AA}$  but this is sufficient to provide considerable information on the particle morphology and to allow some correlation with more detailed images now possible with the best TEM instruments.

#### Statistical information from single crystal patterns

The possibility of obtaining single crystal diffraction patterns from regions of very small diameter can obviously be an important addition to the means for investigating the structures of catalytic materials. The difficulty arises that data on individual small particles is usually, at best, merely suggestive and at worst, completely meaningless. What is normally required is statistical data on the relative frequencies of occurrence of the various structural features. For adequate statistics, it would be necessary to record and analyse very large numbers of diffraction patterns.

The powder patterns obtained by X-ray diffraction and selected area electron diffraction do represent averages over very large numbers of particles but the averaging over size, orientation and imperfection of crystals removes much of the important information, especially that on the correlations of properties, e.g. the orientational relationship of adjacent crystal regions or the dependence of twinning on size.

In order to take advantage of the capabilities of the microdiffraction method it thus seems necessary to find some alternative to the laborious compilation of vast numbers of analyses of individual results. One alternative which we have explored is to use our automatic digital data collection equipment (25) in combination with a pattern recognition device (26). In our system the small electron probe of the STEM instrument is scanned over a chosen area of a specimen and the microdiffraction patterns from each successive probe position are viewed by a low light-level TV camera and displayed on a video screen. A set of detectors is arranged such that when a diffraction pattern which includes a particular array of spots appears on the screen, a signal is generated to stop the scan and record the diffraction pattern in digital form in the computer

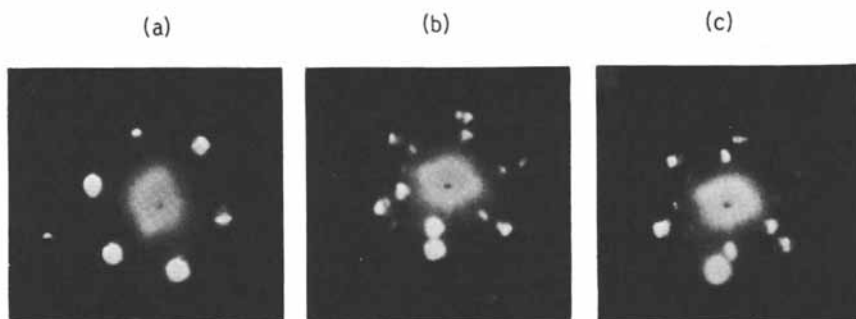


Figure 3. Microdiffraction patterns obtained with an electron beam of diameter about  $10\text{\AA}$  from particles of Ru and Au on a MgO support. (a) MgO crystal. (b) Ru crystal,  $15\text{\AA}$  in diameter, on MgO. (c) Au crystal,  $20\text{\AA}$  in diameter, on MgO.

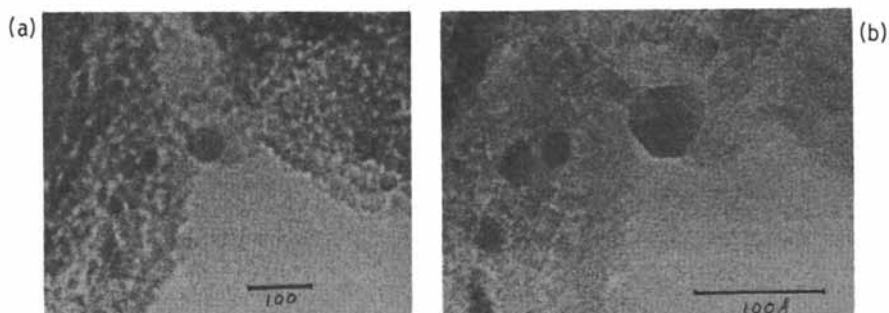


Figure 4. STEM images of Au particles on a MgO support. (a) Image taken with the small objective aperture used for microdiffraction; (b) Image obtained with larger objective aperture showing better resolution.

memory. It is then possible to perform digital correlation analysis of all such patterns recorded and derive answers to specific questions such as, for example, if a small metal particle has a particular orientation, is there evidence that neighboring parts of the metal particle or of the supporting material have a tendency to occur in a similar or related orientation?

There are many variants of this system which can be envisaged as means by which the current possibilities for automation in data collection can be applied for specific purposes. There are considerable dangers in this approach in that it may be all too easy to build in restrictions which predetermine the results. These dangers, however, are not likely to be worse than those normally encountered in electron microscopy or single crystal diffraction where the one particularly "good-looking" picture is taken as being "typical" of a sample.

It is felt that the use of electron microbeam methods offers the basis for a revolutionary new approach to the study of catalyst particles. Some results can be obtained immediately but to realise the full potential of the method a considerable amount of further exploration of data collection and data analysis methods will be needed.

#### Acknowledgment

The author wishes to thank Dr. J.B. Cohen for supplying samples of Pt and Pd on alumina and silica and Drs. J. Schwank and A.K. Dayte for samples of Ru and Au on magnesia and silica. This work was supported by the US Department of Energy under Contract DMR-76ER02995 and has made use of the resources of the ASU Facility for High Resolution Electron Microscopy, supported by NSF grant DMR 8306501.

#### Literature Cited

1. Hashimoto, H.; Endoh, H.; Tanji, T.; Ono, A.; Watanabe, E.; J. Phys. Soc. Japan 1977, 42, 1073.
2. Izui, K.; Furuno, S.; Ono, A.; J. Electron Microscopy 1977, 26, 129.
3. Cowley, J.M.; Diffraction Physics, 2nd Edit. North Holland Publ. Co., 1981.
4. Marks, L.D.; Surface Sci. 1984, 139, 281-98.
5. Marks, L.D.; D.J. Smith; Ultramicroscopy (1984) In Press.
6. Crewe, A.V. in "Electron Microscopy in Material Science;" U. Valdre, Ed.; Academic Press, New York, 1971, p. 62.
7. Langmore, J.P.; Wall, J.; Isaacson M.; Optik 1973, 38, 335.
8. Brown, L.M. in Developments in Electron Microscopy and Analysis 1978; D.L. Misell Ed.; Institute of Physics, Bristol, England 1977 p. 14.
9. Treacy, M.M.J.; Howie, A.; Pennycook, S.J. in Electron Microscopy and Analysis, 1979, (T. Mulvey, Ed.) Institute of Physics, Bristol, England 1980, p. 261.
10. Butler, J.H.; Turner, P.S.; Cowley, J.M. 1984 In preparation.
11. Cowley, J.M.; J. Electron Microscopy Techniques 1984, 1, 83.

12. Osakabe, N.; Tanishiro, Y.; Yagi, K.; Honjo, G.; Surface Sci. 1981, 109, 353.
13. Hsu, Tung; Cowley, J.M.; Ultramicroscopy 1983, 11, 239.
14. Hsu, Tung; Ultramicroscopy 1983, 11, 167.
15. Cowley, J.M. in Microbeam Analysis 1980, D.B., Wittry, Ed., San Francisco Press, San Francisco 1980, p. 33.
16. Cowley, J.M.; Neumann, K.D.; Surface Sci. 1984, In press.
17. Cowley, J.M., Surface Sci. 1982, 114, 587.
18. Marks, L.D. in Electron Microscopy and Analysis, 1981, M.J. Goringe, Ed.; Institute of Physics, Bristol, England 1981, p. 259.
19. Batson, P.E.; Ultramicroscopy 1983, 11, 299.
20. Tan, C.S.; Cowley, J.M.; Ultramicroscopy 1983-4, 12, 333-44.
21. Cowley, J.M.; Osman, M.A.; and Humble, P.; Ultramicroscopy 1984, In press.
22. Monosmith, W.B.; Cowley, J.M.; Ultramicroscopy 1983-4, 12, 177.
23. Allpress, J.A.; Sanders, J.V.; Surface Sci., 1965, 7, 1.
24. Roy, R.A.; Messier, R.; Cowley, J.M.; Thin Solid Films 1979, 79, 207.
25. Cohen, J.B., These proceedings.
26. Datye, A.K.; Schwank, J. in Proceedings of 8th International congress on catalysis, Berlin, 1984. In press.
27. Strahm, M.; Butler, J.H.; Rev. Sci. Instr. 1981, 52 840.
28. Monosmith, W.B.; Cowley, J.M.; Ultramicroscopy 1983, 12, 51.

RECEIVED March 11, 1985

## Atomic Imaging of Particle Surfaces

L. D. Marks<sup>1,3</sup> and David J. Smith<sup>2,4</sup>

<sup>1</sup>Department of Physics, Arizona State University, Tempe, AZ 85287

<sup>2</sup>High Resolution Electron Microscope, Department of Metallurgy, University of Cambridge, Cambridge CB2 3RQ, England

High resolution electron microscopy has recently demonstrated the capability to directly resolve the atomic structure of surfaces on small particles and thin films. In this paper we briefly review experimental observations for gold (110) and (111) surfaces, and analyse how these results when combined with theoretical and experimental morphological studies, influence the interpretation of geometrical catalytic effects and the transfer of bulk surface experimental data to heterogeneous catalysts.

During the last twenty years, small metal particle systems, often model catalysts or commercial heterogeneous catalysts, have been extensively studied by electron microscopy. The primary objective has been to characterise their chemical and structural nature, with the intention of eventually understanding the nucleation and growth of small clusters as well as heterogeneous catalysis. In the process, essentially the whole range of electron microscope imaging techniques have been used. Conventional bright field and dark field techniques are illustrated by the classic work of Ino (1), and Ino and Ogawa (2). More sophisticated dark field techniques have also been developed which give improved particle contrast, such as selected zone dark field (3), annular dark field (4), and weak beam dark field (5). Other approaches, primarily using a scanning transmission instrument, have also been developed which produce analytical information (e.g. 6-8). Some recent reviews of these techniques can be found elsewhere (9-12) and reference should be made to the article by J.M. Cowley in these proceedings.

All of these methods suffer from one serious shortcoming - the spatial resolution is relatively poor ( $\sim 10\text{\AA}$ ) and information about the catalytically interesting region of the particle, namely the surface structure, is then not available. One particular technique, high resolution electron microscopy, has for many years been slowly

<sup>3</sup>Current address: Department of Materials Science and Ipatieff Laboratory, Northwestern University, Evanston, IL 60201

<sup>4</sup>Current address: Center for Solid State Science, Arizona State University, Tempe, AZ 85287

0097-6156/85/0288-0341\$06.00/0  
© 1985 American Chemical Society

progressing towards this goal. Although useful results were obtained using the technique to unravel complicated particle structures (13-17), surface information remained unavailable except for a few unusually favorable circumstances (e.g. 18).

As a result of technical improvements (19) to the Cambridge High Resolution Electron Microscope (20), we have recently succeeded in directly resolving the atomic structure of surfaces on small particles and thin films (21-27). This has included the first direct observation of a surface reconstruction, the so-called missing row model (28) of the  $2 \times 1$  (110) gold surface (see Figure 1 and 21,22), effects due to elastic and plastic deformations at surfaces (see Figures 2 and 3 and 23,26) and details of surface steps and faceting (see Figures 4,6 and 21,27). In this paper we briefly describe the principle of the technique, review these observations, and consider their implications with respect to geometrical effects, linking the experimental data with theoretical analyses.

### Basis of the Technique

The technique employs a beam of swift (~500kV) electrons grazing the surface of interest. Provided that the beam is accurately aligned along a crystal zone axis, and that the electron-optical imaging system is adequate, then images are obtained which appear to show the atomic surface structure in profile (see Figure 1).

Interpretation of these images is both complicated and simple. With any electron microscope technique, the final image is the result of a complicated diffraction and lens aberration process and it is necessary to avoid the trap of naive interpretation, that seeing is believing. It is generally accepted that detailed calculations are required to confirm image interpretations, particularly for high resolution imaging, but also for other techniques. Fortunately, in most cases, high resolution images are faithful representations of the surface structure. The reasons for this are discussed in detail in 25,29,30, and can be summarised thus. With swift electrons and a heavy element, the electron waves channel (e.g. 30-32) down the atomic columns (for a crystal zone-axis orientation) with minimal cross-talk between adjacent columns. With optimal imaging conditions, primarily depending on the objective lens defocus, the spherical aberration and the damping effects of the microscope instabilities balance each other out (25,29). The final image is then an accurate local representation of the object, and it is correct to believe what is seen. Monolayer sensitivity and, with some care, limited sensitivity to chemical impurities can be achieved (25). When these conditions are not met an averaged (over the object) image is obtained rather than a local one and measurement of, for instance, surface relaxations is well nigh impossible.

### Results

Gold (110). The gold (110) surface has been observed to undergo a  $2 \times 1$  reconstruction, with every other surface column missing, as shown in Figure 1. This particular image is from a particle of approximately  $300\text{\AA}$  in radius, and elements of the reconstruction were also observed on smaller particles ( $\sim 100\text{\AA}$  in radius). One interesting feature of the reconstruction is a  $20 \pm 5\%$  expansion at the top of



the corrugated structure which becomes apparent in careful, digital comparisons of experimental and calculated images (22). This expansion has recently been confirmed by X-ray grazing incidence diffraction and ion scattering experiments (33,34).

Gold (111). The main feature of the gold (111) surface is that the surface mesh expands relative to the bulk - there is a tangential surface pressure (23,26,35). This behaviour manifested itself during an electron beam induced etching of contaminant carbon layers (by water vapour) as a "hill and valley" reconstruction, as shown in Figure 2. This is a roughening mechanism which provides space for an expansion to occur which is eventually accommodated by surface dislocations, essentially misfit dislocations to accommodate the surface pressure (see Figure 3). It is important to recognise here that the nature of the specimen used for electron microscopy differs from the bulk surfaces studied by, for instance, LEED. With a bulk surface we might expect some manifestation of the surface expansion other than a hill and valley roughening.

It is interesting to consider this surface as if it were an epitaxial system, that is a monolayer of gold epitaxed on a gold (111) surface. With any epitaxial system, provided that the misfit between the adsorbate and the substrate is small, the adatoms are elastically strained to the substrate surface mesh yielding pseudomorphic growth (for a review see, for instance, 36). For an infinite surface the strain is purely homogeneous, but with a finite adsorbed layer there is some buckling due to the implicit boundary condition of no tractions at the edges of the layer (37,38). This buckling also appears in some of the earlier analyses of surfaces using simple Morse potentials (e.g. 39) since these have an inbuilt expansive surface pressure. If the misfit between the adsorbate and the substrate is sufficiently large, it becomes energetically favorable to nucleate misfit dislocations to relieve the strains. Numerical calculations by Snyman and Snyman (40) for the case of a (111) layer on a (111) substrate show that Shockley partial dislocations and stacking faults are a low energy mechanism for this strain relief, correlating with the case of silver epitaxed on gold (111) (40). These calculations are in excellent agreement with our results.

Benzene on Gold (111). One chemically interesting event seen on the gold (111) surface was the formation of a benzene monolayer during the etching of the initial carbon contaminant layer by water vapour (25,26). This is a flat  $\pi$ -bonded layer, with a benzene to benzene spacing of 7.3 (+0.2) $\text{\AA}$ , and is shown in Figure 4. It is interesting to connect this observation with the mechanism of the etching process, which is probably similar to that of the water-gas reaction. We would hypothesise that the carbon acts as a temporary sink for the hydrogen during the etching with the initial reaction products being hydrocarbons and carbon monoxide. With various cracking reactions taking place under the electron beam, benzene can be one of many reaction products. Since benzene is probably relatively radiation resistant, particularly when  $\pi$ -bonded to a metal which can act as an energy sink, it could be a favored metastable product. There could also be some catalytic effect from the gold substrate.

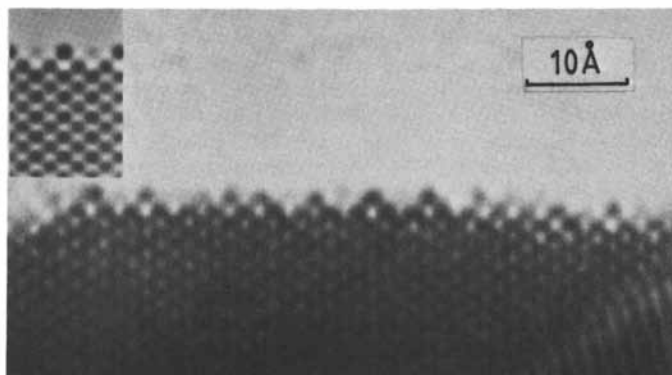


Figure 1. Area of rough gold (110) 2x1 reconstruction, with a numerical calculation inset - see 22. Atomic columns are black.

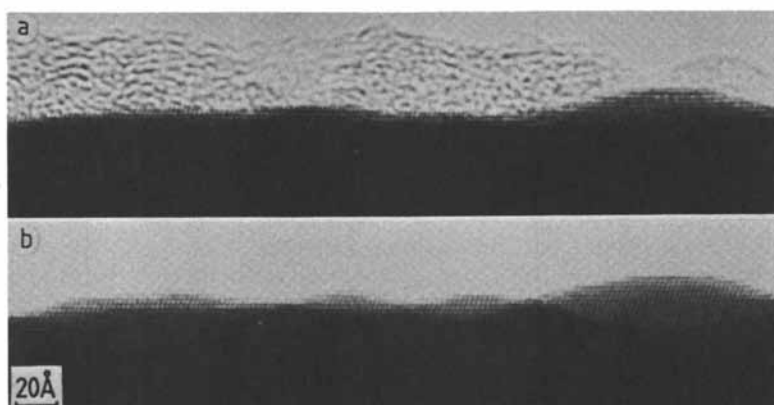


Figure 2. Hill and valley roughening of a gold (111) surface in a) before roughening (carbon covered) and b) following carbon removal.

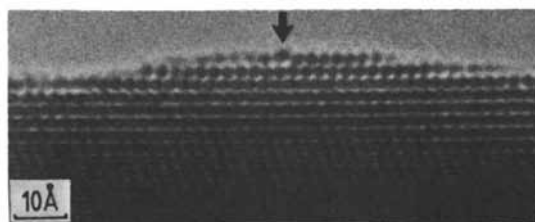


Figure 3. Area of clean gold (111) surface showing a surface Shockley partial dislocation (arrowed) - see 26. Atomic columns are black.

### Geometric Effects

There are a number of concepts concerning the structure of small particles which have a bearing upon geometrical catalytic effects (e.g. 41-43). These follow both from the surface imaging results, and a detailed experimental (13-15) and theoretical (44-47) study of particle morphologies.

Finite size effects. It is well known that, as the size of an atomic cluster drops, the relative proportion of edge and surface atoms increases. However, calculations of the relative fraction of these different surface sites have to date made one important assumption, namely that the external morphology of the particle remains constant. This assumption is not in fact valid; edge atoms for example have a higher intrinsic energy than surface atoms, so it is possible that a morphological change could occur which would minimise the number of edge atoms.

Detailed calculations (47) show that effects from the edge atoms are present and that there is also a stronger effect which can be linked to sphere packing. The number of atoms on a particular face, or in the cluster, deviates substantially from the continuum value (parameterised in terms of the surface area and cluster volume respectively) when the particles are small. This introduces further large edge-like terms in the total particle energy which will drive substantial morphological changes. For instance, for a simple broken bond model of an fcc particle restricted to having only (111) and (100) faces, the fraction of (100) surface drops markedly as the cluster size decreases as shown in Figure 5. This effect only occurs when the cluster energy is minimised with respect to its morphology.

It is also possible to have discrete microfacetting in small particles. For a large (essentially continuum) crystal, vicinal surfaces are important, their role being well understood through the Wulff construction (e.g. 48-50). However, the unit cell of a vicinal surface is large, and there may be insufficient space on a small particle. Only small unit mesh surfaces can be accommodated, and this can lead to microfacetting, a possible example being shown in Figure 6. We note that there is a likely catalytic particle size effect here in the disappearance of vicinal surfaces.

Boundary Conditions. The implicit boundary condition of small surface area can affect surface reconstructions and chemisorption. Surface steps, for example, are important for reconstructions (e.g. 51), and can determine the particular domain that occurs (e.g. 52). An example of a structural effect is on the gold (111) surface where there is an in-plane tangential surface pressure (23,26,35). On extended surfaces, a hill-and-valley roughening occurs to accommodate the expansion, as described earlier. In contrast, small particles accommodate the pressure by a surface buckle (26). We would expect similar behaviour when there is chemisorption involving interactions between the adsorbed molecules.

Gas-Particle effects. The gas environment and chemical impurities, such as promoters or poisons, can strongly influence the total particle morphology (49,50,53,54). Effects can occur via morphological changes which may eliminate or promote certain

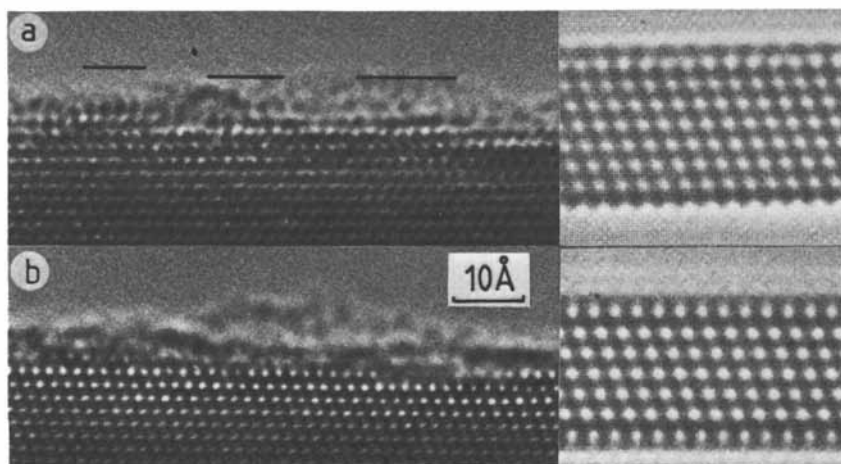


Figure 4. Area of benzene covered gold (111) surface, for two different objective lens defoci as required for unique image interpretation (see 24, 25). In a) the gold atomic columns are black, in b) white. Moiré fringes, rather than any true structural image, result from the benzene monolayer. Simulations (right) have benzene overlay on top surface only.

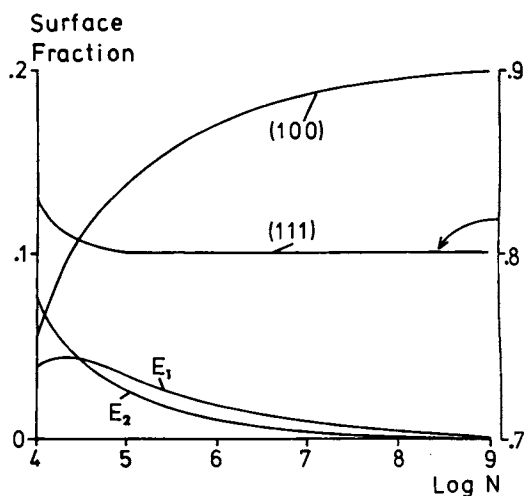


Figure 5. Relative fraction of the different surface atoms as a function of Log N, where N is the number of atoms, for a (111) and (100) faceted f.c.c. crystal when the surface morphology is equilibrated. E<sub>1</sub> refers to the edges between the (100) and (111) faces, E<sub>2</sub> to the edges between two (111) faces. The (111) curve is drawn using the axes to the right.

(catalytically important) facets. (For a review of effects on large surfaces see 12, 49 and 50). This is equivalent to the blocking of an enzyme via a conformational change, rather than a direct attack upon the active site.

One example of this type of process arises in gold particles. When grown in UHV, the stable structures are in the form of non-crystallographic particles called multiply twinned particles or MTPs (1, 2, 13, 15, 44-46, 55 and see Figure 7). In-situ experiments by Yagi et al (56), who observed the formation of MTPs both during growth and following coalescence, demonstrated that these particles are thermodynamically preferred when small (see also 44). However, specimen catalysts produced by Avery and Sanders (56) did not show significant concentrations of MTPs, which would appear to contradict the stability results of Yagi et al (56).

The difference can probably be attributed to the effects of trace water vapour, which experimentally inhibits gold MTP formation (26 and Figure 8), and which we suspect was present during the preparation of Avery and Sanders. The theoretical explanation is through the change in surface free energy and tangential surface pressure with contaminants, since both affect the energy balance between MTPs and single crystals (46). The surface pressure term is probably dominant, with the surface expansion upon the clean gold

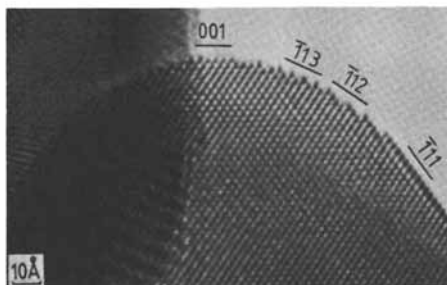


Figure 6. Microfaceted region of a gold crystal, with the facet indexing marked. The atomic columns are black.

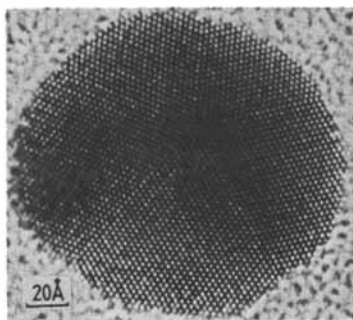


Figure 7. A decahedral MTP of gold showing white atomic columns, supported on an amorphous carbon film - see 15. An explanation of the complicated faceting of MTPs is given in 45.

American Chemical Society  
Library

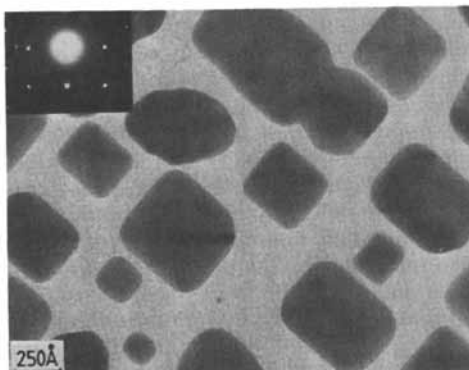


Figure 8. Image and diffraction pattern from an (100) epitaxial specimen of gold prepared in an unbaked UHV evaporator by deposition onto KCl and then transfer onto amorphous carbon. Here water vapour was the dominant residual gas (determined by mass spectrometry). The particles are square pyramidal single crystals.

(111) surface (23,26) presumably being suppressed by water adsorption, thus favoring single crystal formation. There are good theoretical reasons (35) for believing that similar effects can occur in other systems.

### Conclusions

We have discussed here, very briefly, some recent observations of small particle surfaces and how these relate to geometrical catalytic effects. These demonstrate the general conclusion that high resolution imaging can provide a direct, structural link between bulk LEED analysis and small particle surfaces. Apart from applications to conventional surface science, where the sensitivity of the technique to surface inhomogeneities has already yielded results, there should be many useful applications in catalysis. A useful approach would be to combine the experimental data with surface thermodynamic and morphological analyses as we have attempted herein. There seems no fundamental reason why results comparable to those described cannot be obtained from commercial catalyst systems.

### Acknowledgments

The authors would like to thank Drs. A. Howie, V. Heine, E. Yoffe, R.F. Willis, J.M. Cowley and J.A. Venables for advice and comments during the course of this work. We acknowledge financial support from the SERC, U.K. and L.D. Marks also acknowledges support on Department of Energy (USA) Grant No. DE-AC02-76ER02995.

Literature Cited

1. Ino, S.; J. Phys. Soc. Japan 1966, 21, 346.
2. Ino, S.; Ogawa, T.; J. Phys. Soc. Japan 1967, 22, 1369.
3. Heinemann, K.; Poppa, H.; Appl. Phys. Letts. 1972, 20, 122.
4. Freeman, L.A.; Howie, A.; Treacy, M.M.J.; J. Microsc. 1977, 111, 165.
5. Yacamán, M.J.; Ocana, T.; Phys. Stat. Sol. (a) 1977, 42, 571.
6. Treacy, M.M.J.; Howie, A.; Wilson, C.J.; Phil. Mag. A 1978, 38, 569.
7. Pennycook, S.J.; J. Microsc. 1981, 124, 15.
8. Pennycook, S.J.; Howie, A.; Shannon, M.D.; Whyman, R.; J. Molecular Catalysis 1983, 20, 345.
9. Howie, A.; Marks, L.D.; Pennycook, S.J.; Ultramicroscopy 1982, 8, 163.
10. Lyman, C.E. In "Catalytic Materials, Relationship Between Structure and Reactivity", American Chemical Society, Washington D.C., 1983, p. 311.
11. Treacy, M.M.J. *ibid.*, p. 367.
12. Baird, T. In "Catalysis"; The Royal Society of Chemistry: London, 1982; Vol 5, p. 172.
13. Marks, L.D.; Smith, D.J.; J. Crystal Growth 1981, 54, 425.
14. Smith, D.J.; Marks, L.D.; J. Crystal Growth 1981, 54, 433.
15. Marks, L.D.; Smith, D.J.; J. Microscopy 1983, 130, 249.
16. White, D.; Baird, T.; Fryer, J.R.; Freeman, L.A.; Smith D.J.; Day, M.; J. Catal. 1983, 81, 119.
17. Smith, D.J.; White, D.; Baird, T.; Fryer, J.R.; J. Catal. 1983, 81, 107.
18. Sanders, J.V.; Chemica Scripta 1978/79, 14, 141.
19. Smith, D.J.; Camps, R.A.; Freeman, L.A.; Hill, R.; Nixon, W.C.; Smith, K.C.A.; J. Microscopy 1983, 130, 127.
20. Smith, D.J.; Camps, R.A.; Cosslett, V.E.; Freeman, L.A.; Saxton, W.O.; Nixon, W.C.; Ahmed, H.; Catto, C.J.D.; Cleaver, J.R.A.; Smith, K.C.A.; Timbs, A.E.; Ultramicroscopy 1982, 9, 203.
21. Marks, L.D.; Smith, D.J.; Nature 1983, 303, 316.
22. Marks, L.D.; Phys. Rev. Letts. 1983, 51, 1000.
23. Marks, L.D.; Heine, V.; Smith, D.J.; Phys. Rev. Letts. 1983, 52, 656.
24. Smith, D.J.; Marks, L.D.; Proc. 7th Int. Conf. High Voltage Electron Microscopy, 1983, p. 53.
25. Marks, L.D.; Surf. Sci. 1984, 139, 281.
26. Marks, L.D.; Smith, D.J.; Surf. Sci. 1984, 143, 587.
27. Smith, D.J.; Marks, L.D.; submitted to Ultramicroscopy.
28. Noonan, J.R.; Davis, H.L.; J. Vac. Sci. Tech. 1979, 16, 587.
29. Marks, L.D.; Ultramicroscopy 1983/84, 12, 237.
30. Marks, L.D.; Submitted to Acta Cryst.
31. Berry, M.V.; J. Phys. C 1971, 4, 697.
32. Cowley, J.M.; "Diffraction Physics", 2nd edition, North-Holland: Amsterdam, 1981.
33. Robinson, I.K.; Kuk, Y.; Feldman, L.C.; Phys Rev. B 1984, 29, 4762.
34. R.J. Culbertson, private communication.
35. Heine, V.; Marks, L.D.; in preparation

36. van der Merwe, J.H.; Ball, C.A.B. In "Epitaxial Growth"; Matthews, J.W., Ed.; Academic Press: New York, 1975; Part B, p. 493 (see also other articles in both Parts A and B).
37. Neidermeyer, R.; Thin Films 1968, 1, 25.
38. Snyman, J.A.; van der Merwe, J.H.; Surf. Sci. 1974, 42, 190.
39. Wynblatt, P.; in Interatomic Potentials and Simulation of Lattice Defects, (Ed Gehlen, Beeler and Jaffee, Plenum Press, New York, 1972) pp. 633.
40. Snyman, J.A.; Snyman, H.C.; Surf. Sci. 1981, 105, 357.
41. van Hardeveld, R.; Montfoort, V.; Surf. Sci. 1966, 4, 396.
42. Burton, J.J.; Catal. Rev. Sci. Eng. 1974, 9, 209.
43. Andersson, J.R. "Structure of Metallic Catalysts": Academic Press: London, 1975.
44. Marks, L.D.; J. Crystal Growth 1983, 61, 556.
45. Marks, L.D.; Phil Mag A 1984, 49, 81.
46. Howie, A.; Marks, L.D.; Phil Mag. A 1984, 49, 95.
47. Marks, L.D.; Submitted to Surf. Sci.
48. Linford, R.G.; In "Solid State Surface Science"; Green, M., Ed; Marcel Dekker: New York, 1973; Vol. 2, p.1.
49. Flytzani-Stephanopoulos, M.; Schmidt L.D.; Prog. Surf. Sci. 1979, 9, 83.
50. Drechler, M.; In "Surface Mobilities on Solid Materials", Binh, V.T., Ed; Plenum Press: New York and London, 1983; p. 405.
51. Chabai, Y.J.; Rowe, J.E.; Christman, S.B.; Phys. Rev. B. 1981, 24, 3303.
52. Krueger, S.; Monch, W.; Surf. Sci 1980, 99, 157.
53. Lacmann, R.; Springer Tracts in Modern Physics 1968, 44, 1.
54. Metois, J.J.; Spiller, G.D.T.; Venables, J.A.; Phil Mag A 1982, 46, 1015.
55. Buttet, J.; Borel, J.P.; Helv. Phys. Acta, 1983, 56, 541.
56. Yagi, K.; Takayanagi, K.; Kobayashi, K.; Honjo, G.; J. Crystal Growth, 1975, 28, 117.
57. Avery, N.R.; Sanders, J.V.; J Catal. 1970, 18, 129.

RECEIVED March 20, 1985



## Microanalysis of a Copper-Zinc Oxide Methanol Synthesis Catalyst Precursor

P. B. Himelfarb<sup>1</sup>, G. W. Simmons<sup>1</sup>, K. Klier<sup>1</sup>, and M. José-Yacamán<sup>2</sup>

<sup>1</sup>Center for Surface and Coatings Research and Department of Chemistry, Lehigh University, Bethlehem, PA 18015

<sup>2</sup>Instituto de Física Universidad Nacional Autónoma de México, Apdo. Postal 20-264, México 20 DF, México

The naturally occurring mineral aurichalcite has been used as a model for the methanol synthesis catalyst precursor that is formed by coprecipitation from aqueous copper and zinc nitrate solution by the addition of alkali carbonate. The chemical and morphological transformations that occur in both materials upon calcination and subsequent reduction have been monitored by transmission electron microscopy, selected area electron diffraction, and X-ray powder diffraction. The treatments did not change the platelet morphology of these samples, but produced platelets that were porous and polycrystalline, in contrast to the original single crystal materials. Calcination of the mineral and synthetic samples yielded ZnO crystallites in crystallographic registry, oriented with major zone axes of  $[10\bar{1}0]$  and  $[30\bar{3}1]$ . The preferred orientations of ZnO were in epitaxial registry to the original aurichalcite orientation having a  $[10\bar{1}]$  zone axis, such that, the aurichalcite  $[040]$  and  $[202]$  axes were aligned with the ZnO  $[\bar{1}2\bar{1}0]$  and  $[0002]$  axes, respectively. In the reduced materials, the Cu(211) planes were parallel to the ZnO(10 $\bar{1}0$ ) planes such that the Cu $[\bar{1}11]$  axis was aligned with the ZnO $[0002]$  axis.

The coprecipitated precursor of the most active binary Cu/ZnO methanol synthesis catalyst (1) has recently been shown to be a single phase hydroxy carbonate,  $(\text{Cu}_{0.3}\text{Zn}_{0.7})_5(\text{CO}_3)_2(\text{OH})_6$ , aurichalcite (2). In the present investigation, the natural aurichalcite mineral of composition  $(\text{Cu}_{0.4}\text{Zn}_{0.6})_5(\text{CO}_3)_2(\text{OH})_6$ , which consisted of large, thin platelets having dimensions on the order of micrometers, was used as a model compound for following the chemical, structural, and morphologic changes during catalyst preparation. The phase distributions and morphology of the synthetic and mineral samples were compared

throughout the preparation procedures. Although the precipitated precursors and the natural mineral gave rise to essentially identical catalysts, the larger platelet dimensions of the natural mineral provided an ideal morphology for studying the genesis of the final Cu/ZnO catalyst by transmission electron microscopy (TEM). Techniques of x-ray diffraction (XRD), selected area electron diffraction (SAD), and dark field and bright field imaging in the TEM were used to characterize the mineral during and after calcination and after reduction.

### Experimental

Copper ore containing a deposit of aurichalcite was obtained from Wards Natural Science Establishment. The mineral aurichalcite crystallites were gently scraped from the ore and rinsed in ethanol prior to use. The synthetic precursor was prepared by coprecipitation from a mixture of 1M Cu and 1M Zn nitrate solutions, such that a Cu/Zn mole ratio of 30/70 was prepared, by dropwise addition of 1M Na<sub>2</sub>CO<sub>3</sub> at 90°C until the pH increased from approximately 3 to 7. Calcination and reduction of the mineral were performed as in standard catalyst preparation procedures, which have been described in detail earlier (1).

A Philips EM 400T transmission electron microscope which included a scanning transmission mode was used in the electron microscopic characterization studies. Samples were prepared by dispersing the aurichalcite mineral in ethanol and placing a drop of the dispersion on a carbon-coated titanium or copper grid. For reduced specimens exposure to air was minimized by preparing and transporting samples in a nitrogen filled glove bag. Energy dispersive X-ray analysis (EDS) for the identification of elements and quantitative analysis was carried out in the manner described in reference (3). Powder diffraction patterns were obtained with a Philips XRG 3100 X-ray generator coupled with an APO 3600 control unit using CuK<sub>α</sub> radiation. Scans were conducted with a step size of 0.01° in 2θ and a counting time of 1.2 sec.

### Results

Representative TEM micrographs and SAD patterns of the mineral and synthetic aurichalcite are given in Figures 1 and 2, respectively. The SAD patterns were indexed to a [101] zone axis, as described in reference (2). The unit cell parameters of the mineral and synthetic aurichalcite are given in Table I together with the Cu/Zn ratios. The XRD data and Zn/Cu ratio are also given for a reference aurichalcite specimen reported in the literature (4). All d-spacings in the mineral and synthetic aurichalcite matched the literature values within the lattice volume changes (<2%) reported in Table 1. Over 30 XRD peaks were used in the XRD comparisons. The XRD analysis established that the structure of the mineral and synthetic aurichalcite was essentially identical. The only distinguishing features were the higher Cu content and the 1.6% smaller unit cell volume of the mineral sample compared to the synthetic sample.

The aurichalcite mineral was calcined in air at 350°C for 4 hours according to the standard catalyst preparation procedure used earlier for the precipitated precursor (1). XRD showed that aurichalcite and

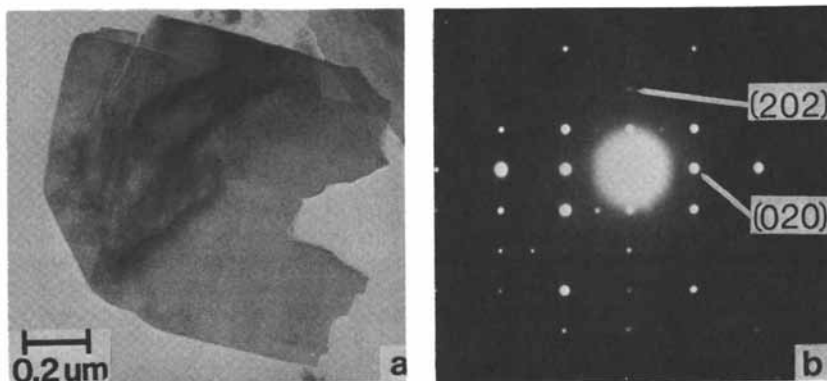


Figure 1. Electron micrographs of mineral aurichalcite,  $(\text{Cu}_{0.4}\text{Zn}_{0.6})_5(\text{CO}_3)_2(\text{OH})_6$ . (a) Bright field image. (b) Selected area diffraction pattern close to a  $[10\bar{1}]$  zone axis.

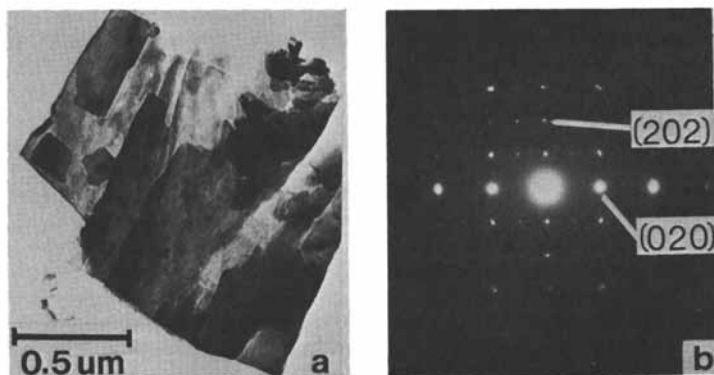


Figure 2. Electron micrographs of synthetic aurichalcite,  $(\text{Cu}_{0.3}\text{Zn}_{0.7})_5(\text{CO}_3)_2(\text{OH})_6$ . (a) Bright field image. (b) Selected area diffraction pattern close to a  $[10\bar{1}]$  zone axis.

ZnO were present after this calcination, see Figures 3a and 3b. The XRD pattern of CuO was not resolved because the CuO reflections overlapped with undecomposed aurichalcite. XRD patterns of the synthetic sample calcined in a similar manner clearly showed the presence of both CuO and ZnO and no evidence for the aurichalcite structure (1). The mineral sample was therefore recalined at a higher temperature of 400°C, after which no traces of aurichalcite were observed, and both the CuO and ZnO reflections were identified as seen in Figure 3c. The higher temperature needed for the complete transformation of mineral aurichalcite to CuO and ZnO, as compared to the synthetic sample, is most likely a result of the larger size and thickness of the mineral platelets.

Table I. Unit Cell Dimensions and Zn/Cu Ratios in Aurichalcite Samples

| Aurichalcite Sample    | $a_o$ (nm) | $b_o$ (nm) | $c_o$ (nm) | Unit Cell Volume (nm) <sup>3</sup> | Zn/Cu (atomic)   |
|------------------------|------------|------------|------------|------------------------------------|------------------|
| Mineral                | 2.678      | 0.641      | 0.527      | 0.9047                             | 1.4 <sup>a</sup> |
| Synthetic              | 2.721      | 0.641      | 0.527      | 0.9191                             | 2.2 <sup>a</sup> |
| Reference <sup>b</sup> | 2.72       | 0.641      | 0.529      | 0.9223                             | 2.4              |

<sup>a</sup> Analysis of sample by Galbraith Laboratories, Inc.

<sup>b</sup> ASTM #17-743.

An electron micrograph and a SAD pattern of the aurichalcite mineral calcined at 400°C are given in Figure 4. The overall platelet dimensions were maintained but the platelets became porous and appeared polycrystalline. The SAD pattern showed several preferred orientations of ZnO crystallites. The most intense ZnO diffraction spots were indexed to a  $[10\bar{1}0]$  zone axis. Also, weaker spots were observed that corresponded to 60° rotations of this diffraction pattern about the  $[10\bar{1}0]$  zone axis, which indicated that some of the crystallites were mutually rotated by this angle. The majority of the additional ZnO diffraction spots corresponded to zone axes of  $[n0n1]$ , where  $n$  is an integer in the range  $1 < n < 6$ . Two weak patterns corresponding to the zone axes  $[0001]$  and  $[\bar{4}5\bar{1}0]$  were also observed. The major orientation of ZnO previously found in the calcined synthetic aurichalcite sample had a zone axis of  $[10\bar{1}0]$  (3) and additional diffraction spots corresponding to a  $[30\bar{3}1]$  zone axis have been observed (5).

All diffraction spots in the aurichalcite mineral calcined at 400°C (Figure 4b) could be attributed to ZnO, except for four weak spots with a d-spacing of 0.192 nm. These spots matched well the  $\text{CuO}\{\bar{1}12\}$  reflections with a reported value of  $d = 0.195$  nm (6). Crystalline CuO was found to be present at this stage by XRD, as seen from Figure 3c.

Aurichalcite mineral calcined at 350°C was analyzed in greater detail because it contained both aurichalcite and ZnO phases, and thus represented an intermediate state in the calcination process.

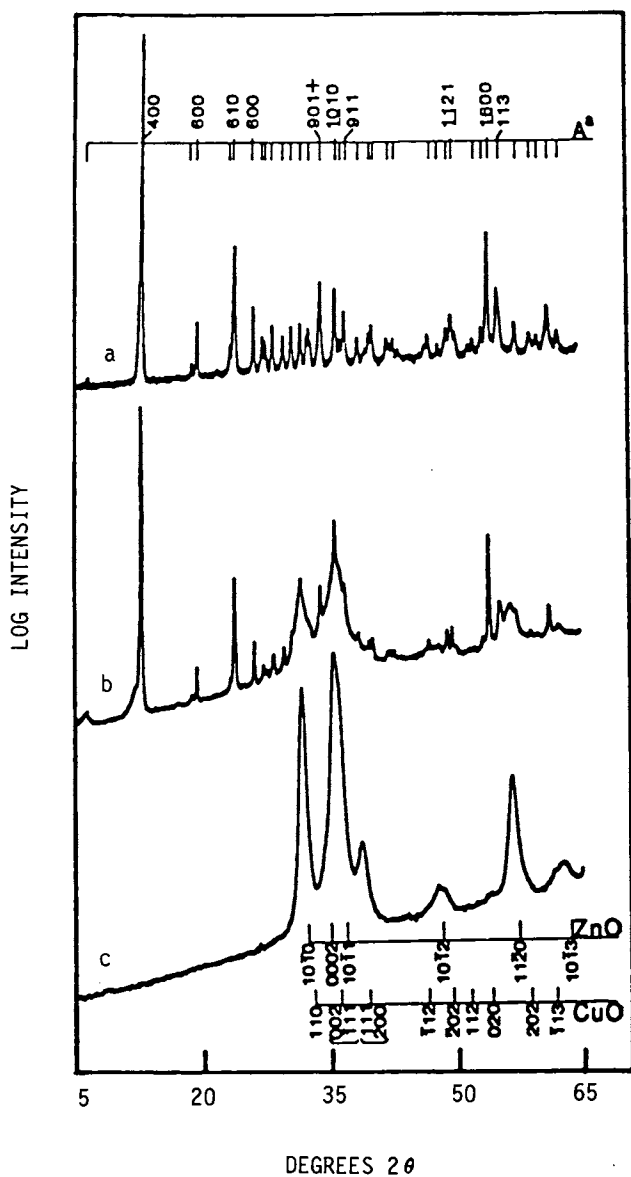


Figure 3. X-Ray diffraction spectra of the natural aurichalcite mineral (a), mineral aurichalcite calcined at 350°C for 4 hours (b), and the sample in (b) recalcined at 400°C for 4 hours (c).

An SAD pattern of the mineral sample calcined at 350°C is given in Figure 5a. The orientation of ZnO was the same as in the mineral sample calcined at 400°C, as follows from the comparison of Figures 5a and 4b. The diffraction pattern from the aurichalcite phase in Figure 5a was similar to the patterns obtained from the uncalcined specimens in Figures 1b and 2b. An epitaxial relationship between aurichalcite and ZnO is apparent from the alignment of the diffraction spots in Figure 5a. This result suggests that the decomposition of aurichalcite and subsequent formation of ZnO proceed along defined crystallographic directions common to both aurichalcite and ZnO. The epitaxial relationships are represented schematically in Figure 5b for ZnO orientations with zone axes  $[10\bar{1}0]$  and  $[30\bar{3}1]$ . All the ZnO diffraction spots were aligned to the aurichalcite spots in the common directions.

The calcined aurichalcite mineral was reduced as in standard catalyst preparation (1), until no water produced by the reduction of CuO was observed in the exit gas. Electron micrographs of the reduced sample are given in Figures 6a and 6b with the corresponding SAD pattern in Figure 6c. The platelets remained intact after reduction and were porous and polycrystalline. The preferred orientations of ZnO in the reduced sample were the same as those observed in the calcined samples. A spot pattern produced from Cu(211) planes was identified, which was in epitaxial registry with the ZnO(10 $\bar{1}$ 0) planes such that the Cu[ $\bar{1}11$ ] axis was parallel to the ZnO[0002] axis. This feature was also observed earlier in the reduced synthetic aurichalcite sample (3,5). Also, weak diffraction spots were observed that corresponded to 60° rotations of the Cu(211) plane, indicating that some of the crystallites were mutually rotated by this angle. This rotation was coincident to the 60° rotations of the ZnO(10 $\bar{1}$ 0) planes as previously identified. The Cu appeared to be in epitaxial registry only with the ZnO(10 $\bar{1}$ 0) orientation, even though other ZnO preferred orientations were present. Some metallic Cu was randomly oriented as shown by the Cu diffraction rings in Figure 6c.

Dark field imaging was used to estimate the Cu and ZnO particle sizes and distributions in the reduced specimens. The dark field images from the platelet in Figure 6a using the Cu( $\bar{1}11$ ) and ZnO(0002) diffraction spots are shown in Figures 6d and 6e, respectively. The Cu and ZnO crystallites were highly dispersed and uniformly distributed throughout the platelets, and both were approximately 5 nm in dimension. The copper particle sizes in the specimen obtained by the calcination and reduction of the synthetic aurichalcite showed that the majority of crystal sizes were in the 3-10 nm range (5). Dark field images of ZnO in the calcined mineral aurichalcite samples showed that the ZnO particles were similar in size and distribution to those in the reduced sample. Thus the orientation and particle size of ZnO were unchanged during the reduction process.

### Discussion

Combined analyses by XRD and TEM showed that the aurichalcite mineral was sufficiently similar to the synthetic aurichalcite to be used as a model compound, to study the microstructural changes occurring during the catalyst preparation procedures. Calcination of the mineral and synthetic samples led to highly preferred orientations of ZnO. ZnO electron diffraction patterns with  $[10\bar{1}0]$  and  $[30\bar{3}1]$  zone

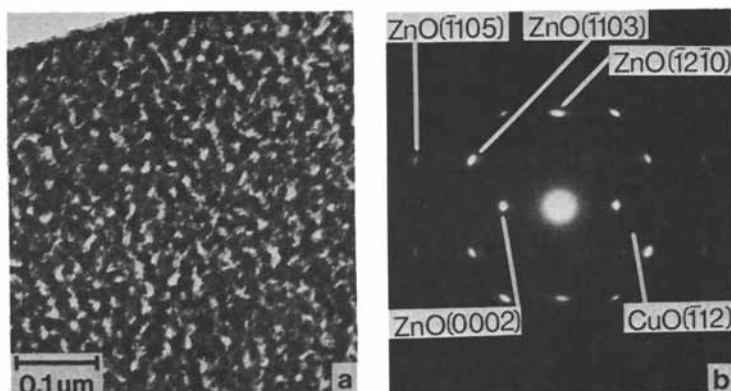


Figure 4. Electron micrographs of mineral aurichalcite calcined at 400°C for 4 hours. (a) Bright field image. (b) Selected area diffraction pattern showing ZnO orientations with zone axes of  $[10\bar{1}0]$ ,  $[30\bar{3}1]$  and  $[50\bar{5}1]$ . See text for other ZnO orientations.

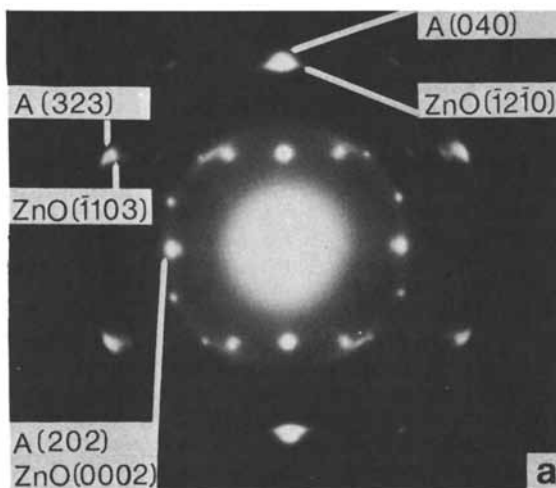


Figure 5a. Mineral aurichalcite calcined at 350°C for 4 hours. Selected area electron diffraction pattern showing ZnO orientations with zone axes of  $[10\bar{1}0]$  and  $[30\bar{3}1]$ . See text for other ZnO orientations. An aurichalcite pattern close to a  $[10\bar{1}]$  zone axis is also present.

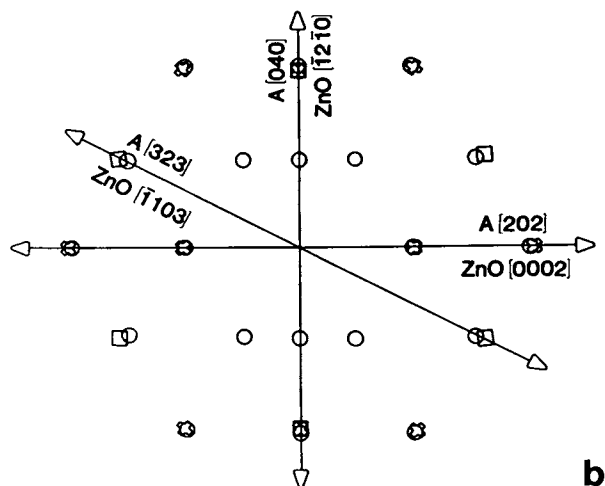


Figure 5b. Mineral aurichalcite calcined at 350°C for 4 hours. Schematic diagram showing epitaxial registry and similarities of d-spacings for the most intense aurichalcite and ZnO diffraction spots.  $\square$  = ZnO with  $[30\bar{3}1]$  zone axis,  $\circ$  = ZnO with  $[10\bar{1}0]$  zone axis, and  $\circ$  = aurichalcite near  $[10\bar{1}]$  zone axis. A = aurichalcite.

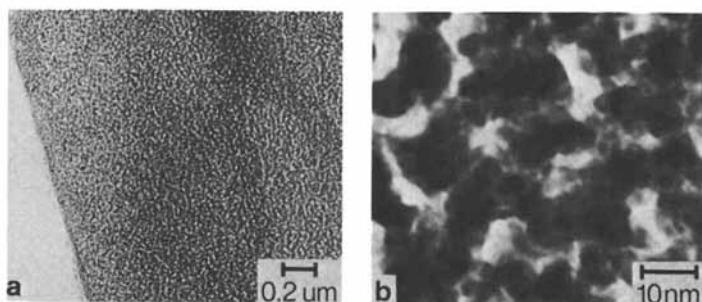


Figure 6a and b. Electron micrographs of mineral aurichalcite calcined at 350°C for 4 hours and reduced in a 2%  $H_2/N_2$  gas mixture. (a) and (b): bright field images.



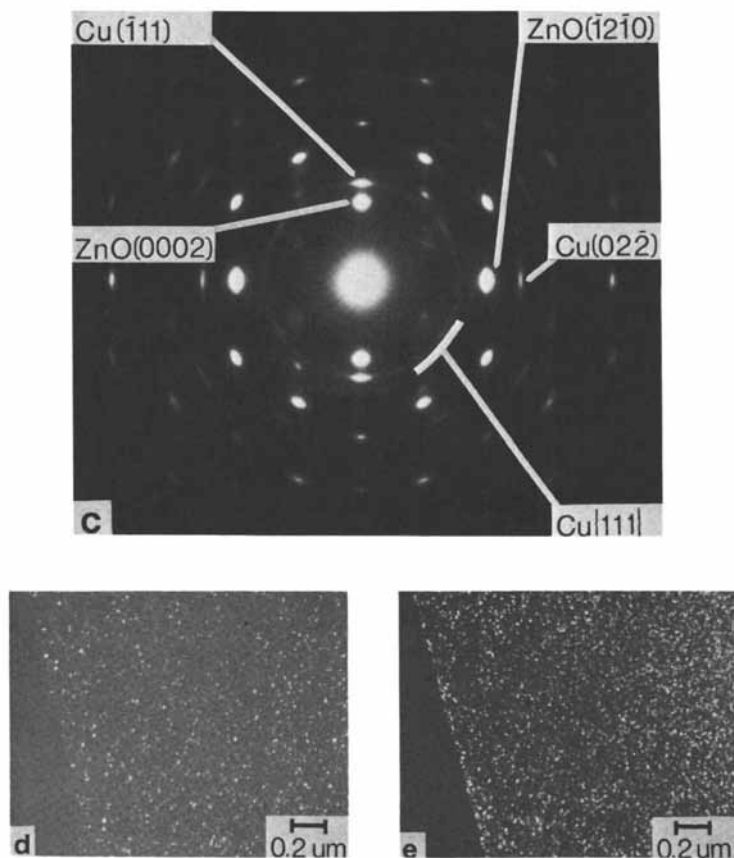


Figure 6c, d, and e. Electron micrographs of mineral aurichalcite calcined at 350°C for 4 hours and reduced in a 2% H<sub>2</sub>/N<sub>2</sub> gas mixture. (c) Selected area diffraction pattern showing a ZnO orientation with a [1010] zone axis. See text for other ZnO orientations. A Cu pattern with a [211] zone axis and randomly oriented Cu identified by the diffraction rings are shown. (d) Dark field image from Cu(111) diffraction spot. (e) Dark field image from ZnO(0002) diffraction spot.

axes were observed in the calcined synthetic and mineral aurichalcite. Additional ZnO patterns in the calcined aurichalcite mineral corresponded to zone axis of  $[n0n\bar{1}]$  for  $1 < n < 6$ . In terms of reciprocal lattices, these patterns arise by rotation of the  $(10\bar{1}0)$  reciprocal lattice layer about the  $[\bar{1}2\bar{1}0]$  axis. All ZnO diffraction spots were in epitaxial registry with aurichalcite diffraction spots, as was shown by the intermediate calcination state. Thus, the orientation of ZnO appears completely defined by the crystallography of aurichalcite.

Overall platelet dimensions of mineral aurichalcite did not appear to change during calcination, but became polycrystalline and porous. By dark field imaging in the TEM, the ZnO particles were observed to be uniformly and highly dispersed. The porosity can be accounted for by the approximately threefold increase in density of Zn atoms upon decomposition of aurichalcite to ZnO. For this density change to occur with a constant overall platelet volume, pores must form.

In summary, large ( $>1\mu\text{m}$ ) single crystal platelets of aurichalcite produced highly dispersed Cu and ZnO particles with dimensions on the order of 5 nm, as a result of standard catalyst preparation procedures used in the treatment of the precipitate precursors. The overall platelet dimensions were maintained throughout the preparation treatments, but the platelets became porous and polycrystalline to accommodate the changing chemical structure and density of the Cu and Zn components. The morphology of ZnO and Cu in the reduced catalysts appear to be completely determined by the crystallography of aurichalcite.

#### Acknowledgments

This research was supported by the U.S. Department of Energy through the Pittsburgh Energy Technology Center (Grant No. DE-FG22-80PC30265) and by the National Science Foundation (Grant INT-82-2842).

#### Literature Cited

1. Herman, R. G., Klier, K., Simmons, G. W., Finn, B. P., Bulko, J. B., *J. Catal.*, **56**, 407 (1979).
2. Himelfarb, P. B., Simmons, G. W., Klier, K., Herman, R. G., "Precursors of the Copper-Zinc Oxide Methanol Synthesis Catalysts," *J. Catal.*, in press.
3. Mehta, S., Simmons, G. W., Klier, K., Herman, R. G., *J. Catal.*, **57**, 339 (1979).
4. ASTM # 17-743.
5. Dominguez, E., J. M., Simmons, G. W., Finn, B. P., Bulko, J. B., *J. Mol. Catal.*, **20**, 369 (1983).
6. ASTM #5-0661.

RECEIVED June 21, 1985

## Characterization of Catalysts by Analytical Electron Microscopy

C. E. Lyman<sup>1</sup>

Central Research & Development Department, Experimental Station,  
E. I. du Pont de Nemours & Company, Wilmington, DE 19898

Analytical electron microscopy permits structural and chemical analyses of catalyst areas nearly 1000 times smaller than those studied by conventional bulk analysis techniques. Quantitative x-ray analyses of bismuth molybdates are shown from 10nm diameter regions to better than +5% relative accuracy for the elements Bi and Mo. Digital x-ray images show qualitative 2-dimensional distributions of elements with a lateral spatial resolution of 10nm in supported Pd catalysts and ZSM-5 zeolites. Fine structure in  $\text{CuL}_{2,3}$  edges from electron energy loss spectroscopy indicate whether the copper is in the form of Cu metal or Cu oxide. These techniques should prove to be of great utility for the analysis of active phases, promoters, and poisons.

Analytical electron microscopy (AEM) permits elemental and structural data to be obtained from volumes of catalyst material vastly smaller in size than the pellet or fluidized particle typically used in industrial processes. Figure 1 shows three levels of analysis for catalyst materials. Composite catalyst vehicles in the 0.1 to 10mm size range can be chemically analyzed in bulk by techniques such as electron microprobe, XRD, AA, NMR, IR, etc. The chemical and physical changes within 3mm of the surface of the pellet or fluidized bead can be studied by surface analysis techniques such as AES, XPS, ISS, SIMS, RBS, etc. However, these techniques may not detect important phenomena taking place on the surface of or within the interior of individual 1nm- to 1 $\mu$ m-diameter inorganic particles that are synthesized specifically for their catalytic activity. AEM is an extremely useful technique for analysis of the individual heterogeneous catalyst particle and its relationship to various supporting materials. Structural and chemical analyses can be obtained from specimen regions nearly 1000 times smaller than those studied by conventional bulk analysis techniques. This high lateral spatial

<sup>1</sup>Current address: Department of Metallurgy and Materials Engineering, Lehigh University, Bethlehem, PA 18015

resolution of analysis down to about 2nm is a consequence of both the very thin specimens used and the specialized equipment employed. In general, AEM should be used in conjunction with the other techniques mentioned for complete catalyst characterization.

Several previous studies have demonstrated the power of AEM in various catalyst systems (1-11). Often AEM can provide reasons for variations in activity and selectivity during catalyst aging by providing information about the location of the elements involved in the active catalyst, promoter, or poison. In some cases, direct quantitative correlations of AEM analysis and catalyst performance can be made. This paper first reviews some of the techniques for AEM analysis of catalysts and then provides some descriptions of applications to bismuth molybdates, Pd on carbon, zeolites, and Cu/ZnO catalysts.

### Analytical Electron Microscopy Techniques

Analysis of individual catalyst particles less than 1 $\mu$ m in size requires an analytical tool that focuses electrons to a small probe on the specimen. Analytical electron microscopy is usually performed with either a dedicated scanning transmission electron microscope (STEM) or a conventional transmission electron microscope (TEM) with a STEM attachment. These instruments produce 1 to 50nm diameter electron probes that can be scanned across a thin specimen to form an image or stopped on an image feature to perform an analysis. In most cases, an electron beam current of about 1 nanoampere is required to produce an analytical signal in a reasonable time.

Elemental analysis of thin specimens in the AEM can provide a 1000-fold improvement in spatial resolution of analysis over conventional electron microprobe analysis. The electron microprobe analyzes characteristic x-rays produced within a teardrop-shaped volume 1-5 $\mu$ m beneath the surface of a polished section of bulk material. Thus, the best spatial resolution of analysis that can be achieved is on the order of 1 $\mu$ m. By removing the teardrop-shaped electron diffusion region, the spatial resolution can be improved to 1-20nm in special cases where the specimen thickness, electron accelerating voltage, beam diameter, and average specimen atomic number are optimum. Figure 2 shows some of the signals available in the AEM. Imaging signals such as transmitted electrons (bright-field images), Bragg-diffracted electrons (dark-field images), backscattered primary electrons, secondary electrons, cathodoluminescence (light), heat, and specimen current are all available in an AEM if proper detectors are installed. Analytical signals (12,13) such as electron energy loss electrons, characteristic x-rays, backscattered electrons, Auger electrons, optical light emission (cathodoluminescence), and electron diffraction have been used in various instruments to analyze inorganic materials. Many of these analytical signals can be used to form qualitative images or maps of the location of certain elements and phases. Elemental imaging with the AEM is important for the analysis of catalysts because the location of active phases, promoters, and poisons may not be evident from the normal electron image alone.

Once an area of interest in the thin specimen is located, quantitative analysis of the volume penetrated by the electron beam

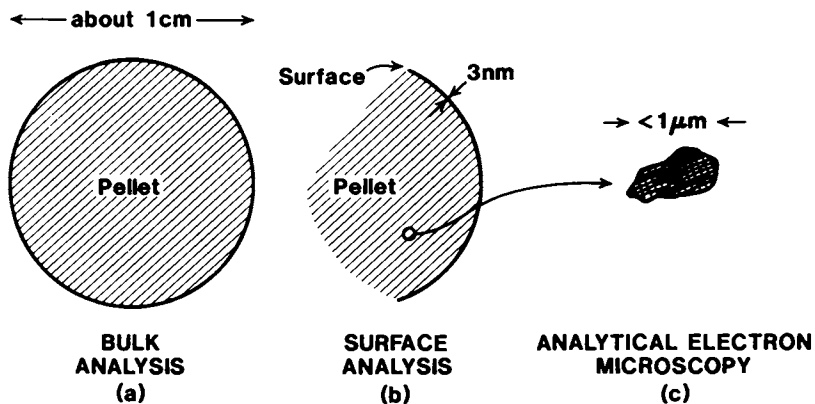


Figure 1. Three levels of analysis for catalyst materials, a) bulk analysis of an entire catalyst pellet, b) surface analysis and depth profiling from the surface inward, c) analytical electron microscopy of individual catalyst particles too small for analysis by other techniques.

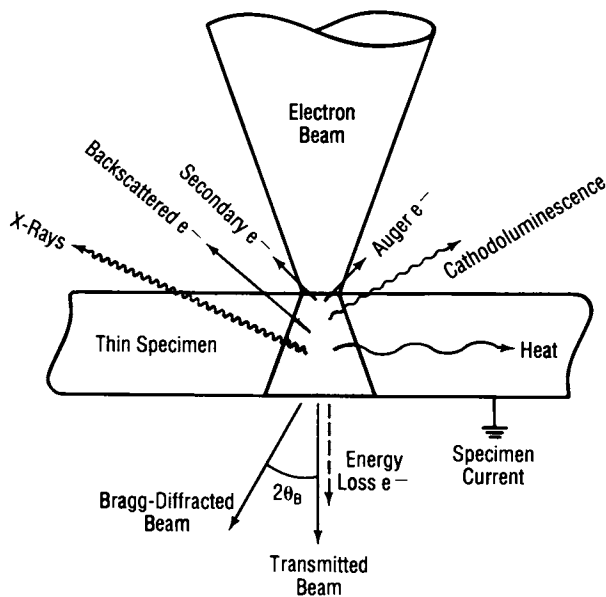


Figure 2. Signals generated in a thin specimen by a focused electron beam in an analytical electron microscope.

can be obtained by several methods. For thin specimens, x-ray emission spectroscopy (XES) and electron energy loss spectroscopy (EELS) are the major analytical modes for chemical analysis. These techniques analyze a through-section cylindrical volume under the electron probe which is broadened somewhat due to beam spreading in the thin specimen (13). Diffraction methods in the AEM are important complementary techniques for phase analysis but will not be discussed in this paper.

For XES, quantification techniques have been developed by Cliff and Lorimer (14) for correcting the background-subtracted x-ray intensity ratio of two elements,  $I_A/I_B$ , by a sensitivity factor known as the Cliff-Lorimer k-value, to yield the elemental ratio  $C_A/C_B$ . Absorption [ACF] and fluorescence [FCF] correction factors are required when the sample is thick or if the mass absorption coefficients of emitted x-rays are greatly different (15). Thus, for a thin specimen (generally <100nm thick), the composition ratio of two elements can be written:

$$\frac{C_A}{C_B} = k_{AB} \frac{I_A}{I_B} [\text{ACF}][\text{FCF}]$$

The factor  $k_{AB}$  can be measured from known standards on a particular microscope or can be calculated. The factors [ACF] and [FCF] can often be neglected in specimens meeting the thin-film criterion (15). One great advantage of x-ray analysis in the AEM is the straightforward manner in which profiles of elemental composition across catalyst particles can be determined. The accuracy of the analysis is on the order of +5% relative. The major limitation of this technique is electron scattering and Bremsstrahlung generation by the primary electron beam at the analysis area causing the generation of spurious x-rays from regions outside the analysis area (16).

Electron energy loss spectroscopy (EELS) is a useful complementary analysis mode especially for the light elements lithium to fluorine which cannot be detected by conventional Si x-ray detectors sealed with Be windows. EELS also finds application (13) in thickness measurement, detection of atomic band structure and specific atomic environments, and for elimination of the spurious signals generated outside the analysis area that plague x-ray analysis. However, a difficulty with the EELS technique is the requirement of very thin specimens (<50nm at 100kV). For EELS quantification (17) more spectrum analysis is required than in XES, but semi-quantitative analysis (+20% relative) is often possible with currently available electron spectrometers. New developments in hardware such as parallel detection at many points in the energy loss spectrum simultaneously (18) and higher accelerating voltages (300-400kV), allowing use of thicker specimens (13), will improve this technique in the future. The use of EELS in the present paper is qualitative in nature but shows the power of the technique in determining the chemical environment of a particular element.

### Specimen Preparation

In a bulk method of analysis there is little need for concern over the number of results necessary to achieve a representative

sampling of the catalyst material. Unfortunately, as seen from Figure 1, the volume of material analyzed in AEM is usually so small ( $10^{-25} - 10^{-20} \text{ m}^3$ ) that careful attention must be paid to analyzing enough areas of the sample (usually 20-100). It is also important that these analyses are performed on areas containing the active catalyst rather than just the support, binder, or filler.

The primary consideration for all AEM analysis is that the specimen be thin (generally  $<1\mu\text{m}$ ). Many catalysts can be simply ground in a mortar and pestle and dispersed on a carbon coated electron microscope grid either dry or in a suitable liquid. If a liquid suspension is used in preparing the specimen, it is important that all elements of interest are insoluble in that liquid. Only particles thin enough to meet AEM thin-film criteria (15) should be analyzed quantitatively. Scraping surface particles from a catalyst pellet for specimen preparation may be more useful than grinding the entire pellet.

Thin sections cut with a diamond knife microtome can be of great advantage in locating regions of catalyst where important chemical or structural changes take place during reaction. Comparison of equivalent areas of fresh and deactivated catalyst can be a difficult problem if the catalyst support does not have a uniform microstructure as in carbon supports produced from plant materials. Even when specimen selection and preparation are adequate, it may be difficult to know upon which image features to place the electron beam to solve the problem at hand.

#### Digital Imaging Using X-ray Signals

Analysis of catalyst materials using digital x-ray images of elements in an AEM offers a method of quickly finding significant areas for analysis. Indeed, important elements acting as promoters or poisons may not be located at obvious image features at all. Low resolution elemental images (spatial resolution about  $1\mu\text{m}$ ) formed by collecting characteristic x-rays as an electron beam is scanned across solid specimens in an SEM or microprobe have been available for many years (12). High resolution elemental images (spatial resolution  $<10\text{nm}$ ) using x-ray signals in the AEM may now be obtained with commercial equipment (19). The general scheme for digital x-ray imaging is to position the electron beam with a computer on an image pixel (small division of a digital image), count x-rays for selected elements over a specified dwell time, move to the next pixel, and repeat this cycle for  $64 \times 64$ ,  $128 \times 128$ , or  $256 \times 256$  pixels. Digital x-ray maps may take 1 hour or more to produce in order to find subtle differences in elemental distribution. In the present work, a Vacuum Generators VG HB501 STEM with an  $2\text{mm}$  electron beam carrying about  $1\text{nA}$  probe current was used. For this setup, at least a  $0.1 \text{ sec}$  dwell-time is required to produce x-ray peaks of adequate peak-to-background ratio for a reasonable elemental x-ray image. Thus, for thin sections and particles about  $100\text{nm}$  thick,  $128 \times 128$  x-ray images can be obtained within 28 minutes. Since entire digital x-ray images can be mathematically divided on a pixel-by-pixel basis, ratio images can be formed showing changes in elemental ratios even when thickness changes exist across a particle.

## Results and Discussion

Bismuth Molybdates. Synthesis of the  $\text{Bi}_2\text{Mo}_2\text{O}_9$  phase was by precipitation from a solution of bismuth nitrate and ammonium molybdate. The resulting amorphous precipitate was filtered, vacuum dried, and calcined in air at  $500^\circ\text{C}$ . This phase has been suggested to be the active phase in the catalyst used for acrylonitrile synthesis (20, 21). Particles of  $\text{Bi}_2\text{Mo}_2\text{O}_9$  were ground and dispersed dry on a carbon-coated Cu grid. Figure 3a shows the dispersion of particles. The thin film-criterion (15) for this compound was found to be about  $0.8\mu\text{m}$ . If particles less than this thickness are measured, the absorption and fluorescence corrections can be neglected to an error of about 10%. Thus, the measured x-ray intensity ratios  $\text{BiL}/\text{MoK}$ , could be corrected to yield atomic ratios by application of the Cliff-Lorimer k-value measured on bismuth molybdate phases of known composition ( $k=0.398$ ). This k-value was measured in terms of the atom ratio of the elements in Bi/Mo/O stoichiometric compounds rather than in terms of wt% from a secondary analytical technique as is often the case. However, even though a beam current of  $1\text{nA}$  was scanned in a raster across an entire particle, the x-ray signal from  $0.1\mu\text{m}$ -thick particles was so small that 100-200 seconds were required to accumulate 1000 counts in the MoK peak. Generally, for a single accurate analysis in an AEM, 10,000 counts are required to reduce the random error to 1%. However, since one of the objectives of the present analysis was to detect impurity phases, many particles had to be measured, and a 10% random error had to be accepted along with an error of the same order due to the neglect of absorption and fluorescence corrections. Figure 3 also shows histograms giving the number of analyses yielding a particular Bi/Mo atomic ratio. Figure 3b shows the distribution of analyses obtained by measuring "particle 19" 24 times. Figure 3c shows the distribution obtained by measuring 24 separate particles within the same field of view. The fact that many particles must be measured is evident. Particle 4 in Figure 3c does not fall on the distribution for  $\text{Bi}_2\text{Mo}_2\text{O}_9$ . Figure 4 shows analyses of  $10\times 10\text{nm}$  regions of particle 4 and clearly reveals the presence of two phases. Despite the compromises employed in these analyses, bismuth molybdate phases have been identified to within about 4% of the correct stoichiometric compounds on the basis of a single measurement in each analysis area.

Pd on Carbon. The catalyst analyzed here is a commercial hydrogenation catalyst with 5% Pd supported on activated carbon (Alfa). The catalyst was ground in a mortar and pestle and dispersed dry onto a carbon coated Cu grid. While x-ray spectra from heavy metal particles down to  $2\text{nm}$  in diameter can be obtained (4) by manually directing the electron beam to the particle, digital images of Pd particles at high resolution have not been obtained previously.

The objective here was to obtain a high resolution digital image of Pd using the background-subtracted  $L_{\alpha}$  peak of Pd and to assess the limit on x-ray image resolution and detection sensitivity imposed by the spurious x-ray problem mentioned earlier. Figure 5a shows an annular dark-field image of Pd particles on carbon ranging in size from  $2\text{-}10\text{nm}$  in diameter. The



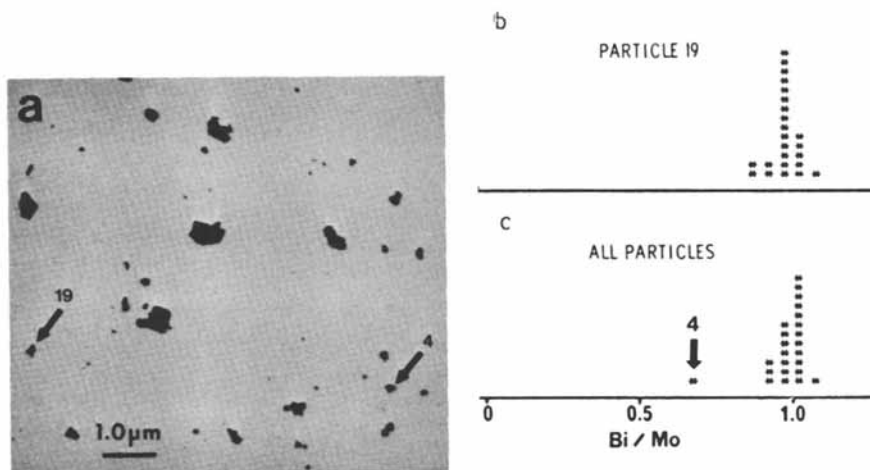


Figure 3. Analysis of bismuth molybdate  $\text{Bi}_2\text{Mo}_2\text{O}_9$ : a) bright-field STEM image showing dispersion of submicron particles, b) comparison between the analysis of the same particle 24 times (particle 19 in Fig. 3a) and c) the analysis of 24 separate particles.

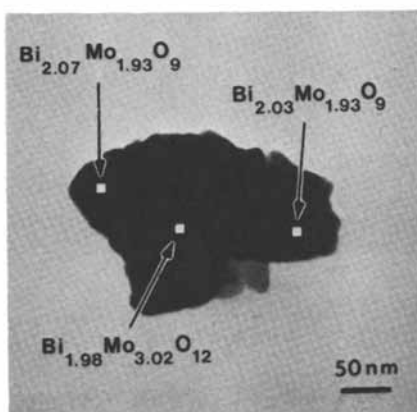


Figure 4. Phase analysis of particle 4 of Figure 3a. This particle did not fall on the  $\text{Bi}_2\text{Mo}_2\text{O}_9$  distribution in Figure 3b because it was composed of more than one phase.

original 128x128 pixel PdL $\alpha$  x-ray image obtained with a dwell time of 0.1 second showed only noisy images of the largest Pd particles. The raw data contained only 5 PdL $\alpha$  counts in the pixel with the maximum number of counts. One or two counts of background from spurious Pd x-rays reaching the detector from areas of the specimen away from the analysis area could be seen over the entire image. However, using several image processing steps (multiplication, addition, subtraction, 9-point smoothing) the original noisy Pd x-ray image was transformed into Figure 5b. In the processed x-ray image, the shapes and sizes of Pd particles as small as 4nm can be seen (note arrowed particle). To produce this result, an unusually small virtual objective aperture of 75 $\mu$ m was used in the VG HB-501 which improved image resolution, reduced further the instrumental spurious x-rays (the so-called 'holecount'), and reduced the beam current onto the specimen to about 0.2nA. This low beam current caused the low nominal x-ray count rate of only 50cps even from 10nm Pd particles.

Zeolite ZSM-5. Analysis of the aluminum distribution in ZSM-5 crystals has been examined by several workers (22-27). Depending upon the preparation method for this material, the Si/Al ratio in various regions within individual crystals may vary considerably. Except for using large crystals suitable for electron microprobe examination (24) or comparing surface and bulk measurements (22), AEM appears to be the only method available to assess the distribution of Al within the crystal. Digital x-ray imaging of both silicon and aluminum is possible if the Si/Al is not too high and if the x-ray detector energy resolution is adequate to separate these adjacent peaks cleanly. Spectral processing such as deconvolution of overlaps, while useful in single point analyses is more difficult to use for digital x-ray imaging in reasonable times. The Si-to-Al ratio was 49.5 for the present ZSM-5 specimen, and the details of preparation were reported earlier (28). Again, a 128x128 digital x-ray image was generated using a 0.1 sec dwell time per pixel. The region of interest for the x-ray peaks was adjusted to a slightly lower energy range for the AlK $\alpha$  peak and slightly higher energy for the SiK $\alpha$  peak. The spectrum background was subtracted before the x-ray counts were stored for each pixel. Figure 6a shows a STEM bright-field image of a 100nm thick section through a ZSM-5 particle. Figure 6b shows a digital x-ray image of the Al distribution within the ZSM-5 crystal. From this Al x-ray image, it is clear that the thickness of the Al enriched outer layer of the particle is about 600nm. Previous work could only show a line profile to indicate the Al distribution in ZSM-5 crystals (24,28).

Cu/ZnO Catalyst. Low-pressure syntheses of methanol from CO and H $_2$  are based on copper-zinc oxide catalyst formulations. There have been conflicting reports (8, 29-31) as to the nature of the Cu species in these systems, e.g. Cu $^{+1}$ , Cu $^{+2}$ , or Cu $^0$ . The work of Leapman et al. (32) showed that the fine structure of the CuL $_{2,3}$  edge in the electron energy loss spectrum can be used to distinguish copper metal from CuO. Lyman et al. (33) assessed the usefulness of this effect in the analysis of Cu in a ZnO catalyst. The specimen was prepared by the recipe used at Lehigh University (34) to produce 30wt% CuO/70wt% ZnO material that was subsequently

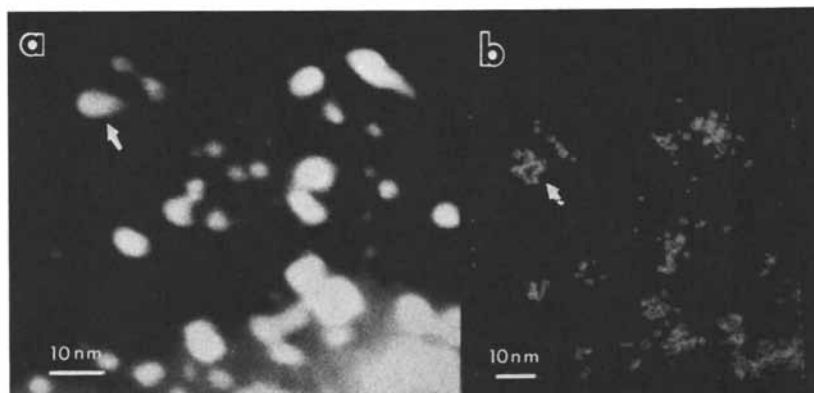


Figure 5. Pd supported on carbon: a) annular dark-field STEM image revealing particles as small 2nm, b) processed digital x-ray image showing that Pd particles 4nm and larger can be imaged using Pd x-rays alone.

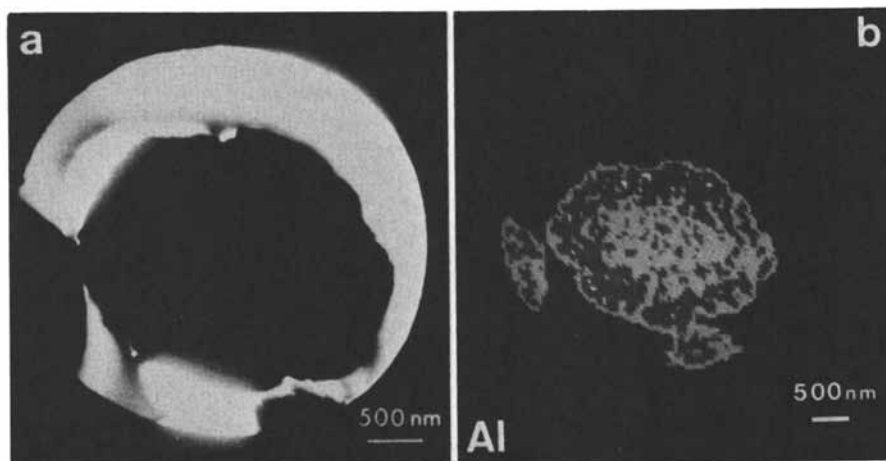


Figure 6. Digital x-ray imaging of zeolite ZSM-5 (Si/Al=49.5) thin section: a) bright-field STEM image, b) Al x-ray image smoothed by averaging each pixel with its 8 nearest neighbors. The darker shading within the particle indicates higher Al content. The circular field is due to the image of the selected area diffraction aperture.

reduced in  $H_2$  to produce an active catalyst. The ZnO network characteristic of this catalyst was suspended over a hole in a carbon support film and EELS spectra were taken at 3eV energy resolution with a 2nm electron beam scanned in a 4x4nm raster over the feature of interest. To reduce electron beam damage, the range of energy loss scanned by the spectrometer was deliberately limited to 840-1090eV including just the Cu and ZnL<sub>α</sub> edges. Only 5 spectrometer scans through this energy range were made providing a compromise between electron beam damage to the specimen and signal-to-noise ratio. Figure 7 shows the qualitative EELS analysis of two areas in the ZnO containing Cu. The area indicated as a metal particle in Figure 7a shows the CuL<sub>2,3</sub> near edge structure (Figure 7b) as two ledges indicating a filled 3d band for Cu metal (32). The particle analyzed was about 2nm in diameter. The copper oxide particle shown in Figure 7a was about 20nm in size. Figure 7c shows that this particle has the Cu near edge spectrum characteristic of CuO with a "white line" at the energies of the L<sub>3</sub> and L<sub>2</sub> absorption edges. In CuO the copper band structure is perturbed to create additional energy levels for excited electrons to reside short of escaping the Cu atom completely (32). The CuO particle was probably an artifact resulting from air handling since x-ray diffraction of this specimen immediately following synthesis indicated only Cu metal in addition to ZnO. In some areas of Figure 7a pure ZnO was observed. Unfortunately, the question of which species of copper is present could not be answered conclusively in this preliminary investigation since the electron beam used was intense enough to reduce the copper-oxide spectrum to the copper metal spectrum. However, the EELS technique has the advantage that it avoids the problem of spurious x-ray generation from areas not under the electron beam. These spurious x-rays can be generated by primary electron scattering or Bremsstrahlung generation at the analysis area and will show up in the Cu x-ray spectrum of the analysis area even though they were generated elsewhere. While instrumental difficulties prevented a definite conclusion as to the active Cu species in this system, this experiment points the way for more conclusive analyses of this type in the future.

### Conclusion

Analytical electron microscopy (AEM) can use several signals from the specimen to analyze volumes of catalyst material about a thousand times smaller than conventional techniques. X-ray emission spectroscopy (XES) is the most quantitative mode of chemical analysis in the AEM and is now also useful as a high resolution elemental mapping technique. Electron energy loss spectroscopy (EELS) while not as well developed for quantitative analysis gives additional chemical information in the fine structure of the elemental absorption edges. EELS avoids the problem of spurious x-rays generated from areas of the spectrum remote from the analysis area.

### Acknowledgments

The author is grateful to U. Chowdhry, E. F. Moran, and A. Ferretti for preparation of catalysts and to N. J. Long of VG Scientific, Ltd. for assistance in EELS analysis.

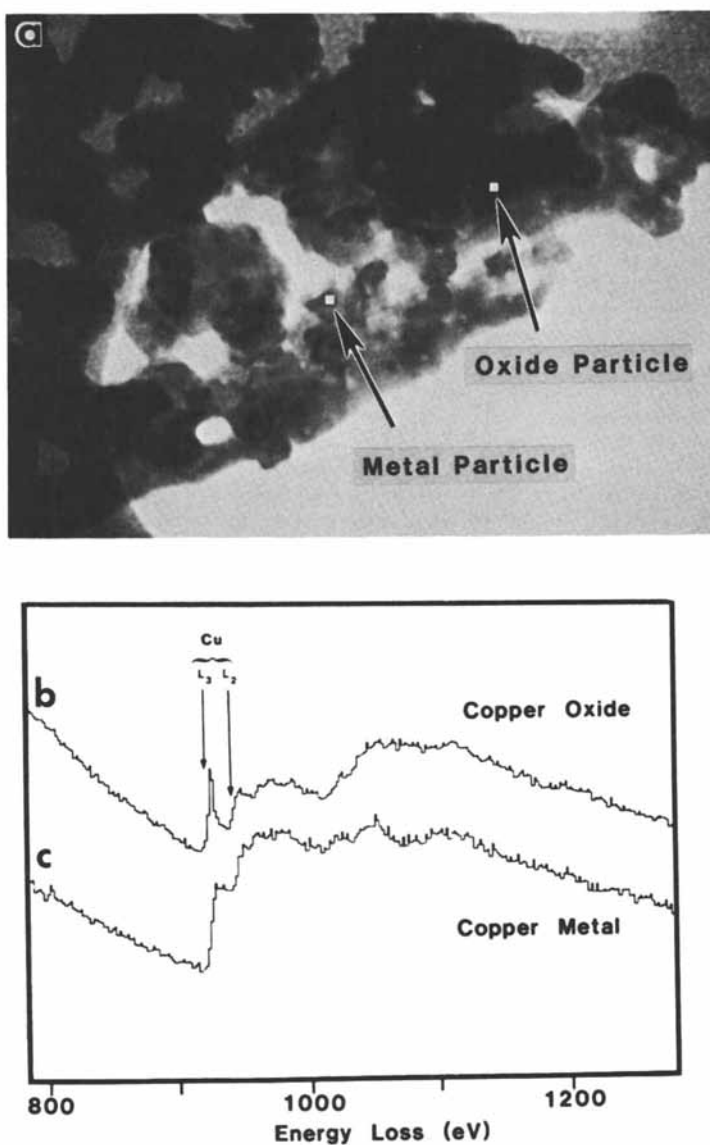


Figure 7. Electron energy loss spectroscopy (EELS) of a Cu/ZnO catalyst: a) bright-field STEM image showing a 20nm copper oxide particle and a small 2nm Cu metal particle on ZnO, b) and c) EELS spectra showing the distinction between copper atom environments on the basis of the near edge fine structure of the CuL edge.

Literature Cited

1. Delannay, F. Catal. Rev. Sci. Eng., 1980, 22, 141.
2. Mehta, S.; Simmons, G. W.; Klier, K.; Herman, R. G. J. Catal. 1979, 57, 339.
3. Cheetham, A. K.; Skarnulis, A. J. Anal. Chem., 1981, 53, 1060.
4. Dexpert, H.; Freund, E.; Lynch, J. in Lorimer, G. W.; Jacobs, M. H.; P. Doig Eds., "Quantitative Microanalysis with High Spatial Resolution", The Metals Society, London, 1981, 101.
5. Howie, A.; Marks, L. D.; Pennycook, S. J. Ultramicroscopy, 1982, 8, 163.
6. Schabes-Retchkiman, P.; Gomez, A.; Yacaman, M. J.; Ocana, T. Proc. 40th Annual Meeting Electron Microscopy Society of America, Claitor's Publishing, Baton Rouge, 1982, 666.
7. Lyman, C. E. J. Molecular Catalysis 1983, 20, 357.
8. Dominquez, J. M.; Simmons, G. W.; Klier, K. J. Molecular Catalysis, 1983, 20, 369.
9. Pennycook, S. J.; Howie, A.; Shannon, M. D.; Whyman, R. J. Molecular Catalysis, 1983, 20, 345.
10. Cowley, J. M.; Monosmith, W. B. Proc. of 41st Annual Meeting Electron Microscopy Society of America, 1983, 332.
11. Murrell, L. L.; Grenoble, D. C.; Baker, R.T.K.; Prestridge, E.B.; Fung, S. C.; Chianelli, R. R. J. Catal. 1983, 79, 203.
12. Goldstein, J. I.; Newbury, D. E.; Echlin, P.; Joy, D. C.; Fiori, C.; Lifshin, E. "Scanning Electron Microscopy and X-ray Microanalysis," Plenum, New York, 1981.
13. Williams, D. B. "Practical Analytical Electron Microscopy in Materials Science," Philips; Electronic Instruments Electron Optics Publishing, Mahwah, N.J., 1984.
14. Cliff, G.; Lorimer, G. W. J. Micros. (Oxford) 1975, 103, 203.
15. Goldstein, J. I.; Costley, J. L.; Lorimer, G. W.; Reed, S.J.B. Scanning Electron Microscopy/1977, Vol. I, IIT Res. Inst., Chicago, 315.
16. Bentley, J.; Zaluzec, N. J.; Kenik, E. A.; Carpenter, R. W. Scanning Electron Microscopy/1979, Vol. II, SEM, Inc., Chicago, 581.
17. Egerton, R. F. Phil. Mag. 1976, 34, 49.
18. Shuman, H. Ultramicroscopy 1981, 6, 163.
19. Lyman, C. E. Proc. 42nd Annual Meeting of Electron Microscopy Society of America, San Francisco Press, 1984, 654.
20. Gai, P. L. Proc. 4th Int. Conf. on Molybdenum Chemistry, Climax Molybdenum Co., 1982.
21. Matsuura, I.; Shut, R.; Hirakawa, K. J. Catal., 1980, 63, 152.
22. Derouane, E. G.; Gilson, J. P.; Gabelica, Z.; Mousty-Desbugnoit, C.; Verbist, J. J. Catal. 1981, 71, 447.
23. Suib, S. L.; Stucky, G. D.; Blattner, R. J. J. Catal. 1980, 65, 174.
24. von Ballmoos, R.; Meier, W. M. Nature (London), 1981, 389, 782.
25. Dwyer, J.; Fitch, F. R.; Qin, G.; Vickerman, J. C. J. Phys. Chem., 1982, 86, 4574.
26. Auroux, A.; Dexpert, H.; Leclercq, C.; Vedrine, J. Applied Catal. 1983, 6, 95.
27. Huges, A. E.; Wilshier, K. G.; Sexton, B. A.; Smart, P. J. Catal. 1983, 80, 221.

28. Lyman, C. E., Betteridge, P. W.; Moran, E. F. in "Intrazeolite Chemistry," ACS SYMPOSIUM SERIES No. 218, Stucky, G. D.; Dwyer, F. G. Eds., American Chemical Society, Washington, D.C., 1983, 199.
29. Matulewicz, E.R.A.; de Keijser, M. S.; Mol, J. C.; Kapteijn, F. Thermochemica Acta, 1984, 72, 111.
30. Friedrich, J. B.; Young, D. J.; Wainwright, M. S., J. Catal. 1983, 80, 14.
31. Okamoto, Y.; Fukino, K.; Imanaka, T., Teranishi, S., J. Phys. Chem. 1983, 87, 3747.
32. Leapman, R. D.; Grunes, L. A.; Fejes, P. L., Phys. Rev. B 1982, 26, 614.
33. Lyman, C. E.; Ferretti, A.; Long, N. J. in "Analytical Electron Microscopy 1984," San Francisco Press, in press.
34. Bulko, J. B. "Characterization of the Reactive Centers in Methanol Synthesis Catalysis," Ph.D. Thesis, Lehigh University, Bethlehem, PA., 1980.

RECEIVED March 20, 1985

## Multitechnique Characterization of Supported Metals

William Targos

Signal UOP Research Center, Des Plaines, IL 60016-6187

The scanning transmission electron microscope (STEM) was used to directly observe nm size crystallites of supported platinum, palladium and first row transition metals. The objective of these studies was to determine the uniformity of size and mass of these crystallites and when feasible structural features. STEM analysis and temperature programmed desorption (TPD) of hydrogen indicate that the 2 nm platinum crystallites supported on alumina are uniform in size and mass while platinum crystallites 3 to 4 nm in size vary by a factor of three-fold in mass. Analysis by STEM of platinum-palladium on alumina established the segregation of platinum and palladium for the majority of crystallites analyzed even after exposure to elevated temperatures. Direct observation of nickel, cobalt, or iron crystallites on alumina was very difficult, however, the use of direct elemental analysis of 4-6 nm areas and real time imaging capabilities of up to 20 Mx enabled direct analyses of these transition metals to be made. Additional analyses by TPD of hydrogen and photoacoustic spectroscopy (PAS) were made to support the STEM observations.

The use of highly dispersed metals at low concentration levels has found wide use in industry, particularly for electronic and catalytic uses. The desire to optimize the size and mass uniformity of these metal particles is of particular interest. Characterization of these materials is difficult especially when metal particle sizes are on the order of 5 nm or less and concentrations are below 1 wt-%. Development of highly sophisticated techniques in recent years has provided new approaches to understanding the physical and chemical properties of these materials. Electron microscopy has proven quite valuable in the acquisition of data and subsequent generation of information, which is necessary to understand the physical-chemical properties of individual nm-sized particles.

0097-6156/85/0288-0374\$06.00/0  
© 1985 American Chemical Society



Several groups (1-11) have been active in evaluating model supported systems, particle size distribution, sintering mechanisms, redispersion of metal particles, micro-structure of metal crystallites, and controlled atmosphere electron microscopy of metal particles. The majority of these studies have employed conventional transmission electron microscope (CTEM), high resolution electron microscope (HREM), or scanning transmission-transmission electron microscope (STEM-TEM) instruments. Although these instruments have, and will continue to provide valuable information concerning these complex systems, the application of the dedicated STEM, which is an instrument using a field emission source and designed to operate only in the scanning transmission mode, should provide new perspectives to this active area of research.

The STEM is ideally suited for the characterization of these materials, because one is normally measuring high atomic number elements in low atomic number metal oxide matrices, thus facilitating favorable contrast effects for observation of dispersed metal crystallites due to diffraction and elastic scattering of electrons as a function of Z number. The ability to observe and measure areas 2 nm in size in real time makes analysis of many metal particles relatively rapid and convenient. As with all techniques, limitations are encountered. Information such as metal surface areas, oxidation states of elements, chemical reactivity, etc., are often desired. Consequently, additional input from other characterization techniques should be sought to complement the STEM data.

### Experimental

Sample composition. The compositions for the majority of the samples characterized are listed in Tables I and II. In addition to these samples, characterization of a 0.65 wt-% Pt-0.1 wt-% Pd on alumina and 1 wt-% of either Co, Ni, or Fe on alumina was made.

Characterization methods. The 100 kV Vacuum Generator HB-5 STEM was used to microanalyze samples. The HB-5 has a KEVEX Si(Li) energy dispersive X-ray spectrometer (EDS) and micro area electron diffraction (MAED) capabilities in conjunction with simultaneous bright and dark field imaging capabilities. A more detailed explanation of the instrumental operation can be obtained in a publication by C. Lyman(12).

The TPD unit was constructed at the Signal UOP Research Laboratory. It includes a Carle 111 H gas chromatograph with Pd/Ag hydrogen separator, Leeds & Northrup temperature programmer, Bascom-Turner 8000 series recorder with data processing and storage capabilities and a custom designed quartz reactor.

The PAS was made by Princeton Applied Research and has a wavelength range of 200-2700 nm. The spectra were acquired on a signal/reference mode with carbon black as the reference. The scan rate was 50 nm/min, start 200 nm, end 1600 nm, frequency 40 Hz, 1 scan and a slit width of 2.0 nm.

Analysis of samples. For STEM analysis all samples were prepared using the tissue grinding method with suspension of the fine

particles in isopropanol. The particles were deposited on 180 mesh carbon coated nylon grids.

TPD experiments were conducted on platinum and palladium samples only. These samples were reduced in-situ in prepurified hydrogen at 500°C, purged with helium at 500°C prior to cooling to ambient conditions at which time hydrogen was added. The materials were purged with purified helium at ambient conditions to remove the non-adsorbed hydrogen before the TPD experiment proceeded. A programming rate of 7°C/min was used and the maximum temperature reached was 550°C. Approximately 0.5 g of 60-80 mesh sample was used.

The PAS studies were made on the transition metals under ambient conditions.

### Results and discussion

Supported platinum. The STEM and TPD data for platinum supported on alumina and silica are summarized in Table I. The platinum-silica samples show a high degree of variability in size and mass. This variability is indicative of the mobility of platinum on silica at elevated temperatures, i.e., 500°C. These samples were of little interest, because of their nonuniformity and will not be discussed further. Schmidt (2) and Baker (11) have elaborated on the platinum-silica mobility question and the strength of metal-support interactions. Sample C, Pt on alumina, was used as a reference for the H/Pt measurements, and beyond that is of little relevance in these discussions.

Samples A and B are of particular interest because they are composed of small, uniform platinum crystallites. The fact that these crystallites are on alumina limits the techniques available for their characterization. Sample A showed what appeared to be very thin platinum crystallites, which were barely observable by imaging techniques or measurable by EDS. An example of a bright field image and corresponding EDS analysis is shown in Figure 1. In order to obtain analyses of this type, focus variation at magnifications of 1 to 4 Mx was commonly used with EDS analysis at 20 Mx to confirm that the particle was platinum.

Table I. Platinum Crystallite Size and Dispersion Data

| Sample Code | Wt-% Pt | Support                                  | Crystallite Size (nm) | H/Pt    |
|-------------|---------|--|-----------------------|---------|
| A           | 0.07    | $\gamma$ -Al <sub>2</sub> O <sub>3</sub> | 2                     | 0.8-1.0 |
| B           | 0.65    | $\gamma$ -Al <sub>2</sub> O <sub>3</sub> | 3-4                   | 0.23    |
| C           | 0.65    | $\gamma$ -Al <sub>2</sub> O <sub>3</sub> | BD                    | 1.0     |
| D           | 0.65    | SiO <sub>2</sub>                         | 2-10                  | 0.16    |
| E           | 0.65    | SiO <sub>2</sub>                         | 25-50                 | 0       |
| F           | 0.07    | SiO <sub>2</sub>                         | 2.5-5.0               | BD      |
| G           | 0.07    | SiO <sub>2</sub>                         | 2-10                  | BD      |

BD - Below Detectable limits

Although detectability was pushed to the limit, the uniformity of the count rates from crystallite to crystallite suggests that this material was composed of platinum crystallites uniform in both size and mass. The high dispersion value obtained for this sample also suggests that the mass per crystallite may be in the 50-200 atom range assuming FCC packing. The TPD analysis had a wider variation than the normal  $\pm 5\%$  reproducibility observed for this method due to the low platinum loading.

Attempts to perform the MAED of these crystallites were unsuccessful because of the difficulty in observing the crystallites with the small objective apertures necessary to obtain reasonable MAED patterns, and the rapid mobility of these small crystallites in the stationary electron beam used in the MAED mode. Instrumental modifications are commercially available which might allow this measurement to be made.

Sample B provided platinum crystallites that were analyzed by both EDS and MAED. MAED of several 3 nm crystallites shows a wide variation of orientations with respect to the electron beam, however, many of the patterns match (111) and (110) orientations. An example of the MAED patterns observed is shown in Figure 2. The diffraction pattern was made with a 25  $\mu\text{m}$  objective aperture at a camera length of 2 m.

The majority of crystallites observed were 3 or 4 nm in size. In Figure 3, a bar graph illustrates the size range distribution and a comparison of mass variation for the 3 and 4 nm crystallite sizes. Although only thirty analyses were made, overall visual analysis confirmed the presence of hundreds of 3 to 4 nm platinum crystals with negligible numbers less or greater than these dimensions. It appears that slight variations in crystallite diameter and thickness have resulted in a fairly uniform number of platinum atoms per crystallite for the majority of the crystallites analyzed. In order to normalize count rates, the decrease in the field emission intensity was taken into account.

Although the H/Pt results are in reasonable agreement for the crystallite sizes observed and those predicted from FCC packing, the slight biasing to a lower H/Pt may be due to contamination or to the presence of a few large platinum crystallites which may have escaped observation during the general visual inspection. Most of the other H/Pt analyses appear in reasonable agreement with the sizes of the platinum crystallites observed and limits of detection of the TPD technique. All measurable TPD chromatograms for the supported platinum as well as palladium materials showed almost complete desorption of hydrogen before reaching a temperature of 350°C.

In addition to obtaining information about the size, relative mass, and structure of the platinum crystallites, the STEM can provide a qualitative evaluation of the metal distribution from support particle to support particle. In general, the distribution of platinum was more uniform on alumina than silica, however, optimal uniformity was not achieved. This observation was based on wide variations in Pt/Si and Pt/Al ratios measured by EDS.

Supported palladium. The STEM and TPD analyses as well as composition of the materials used is shown in Table II. Observation of palladium crystallites by STEM for sample H proved to be very difficult, whereas sample J proved to be relatively easy. In both cases

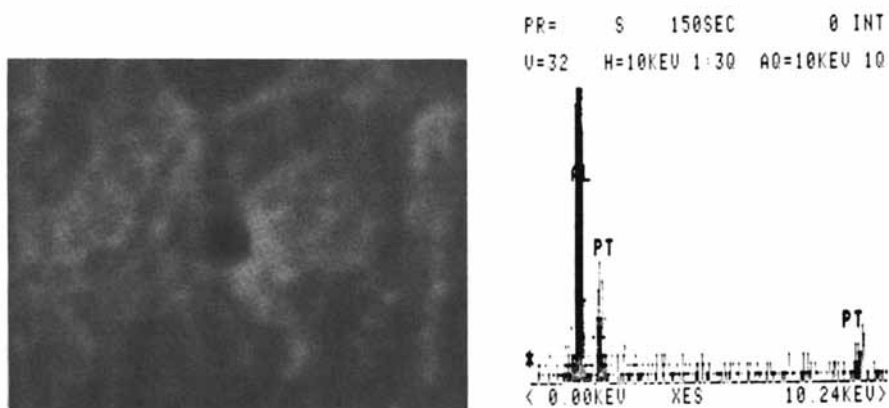


Figure 1. Example of a 2nm platinum crystallite at 4 Mx and corresponding EDS analysis at 20 Mx for 150 sec.

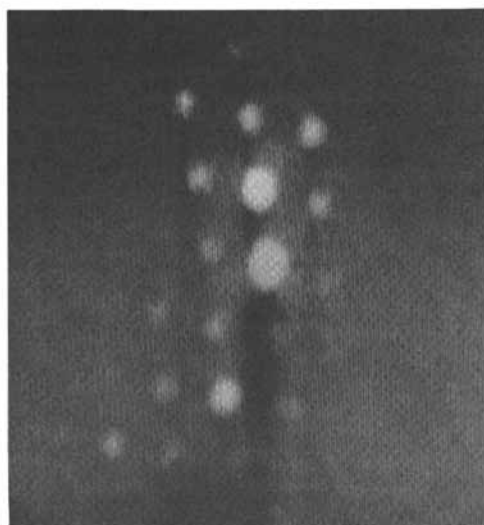


Figure 2. MAED pattern of a 3 nm platinum crystallite on  $\gamma$ -alumina (111) orientation.

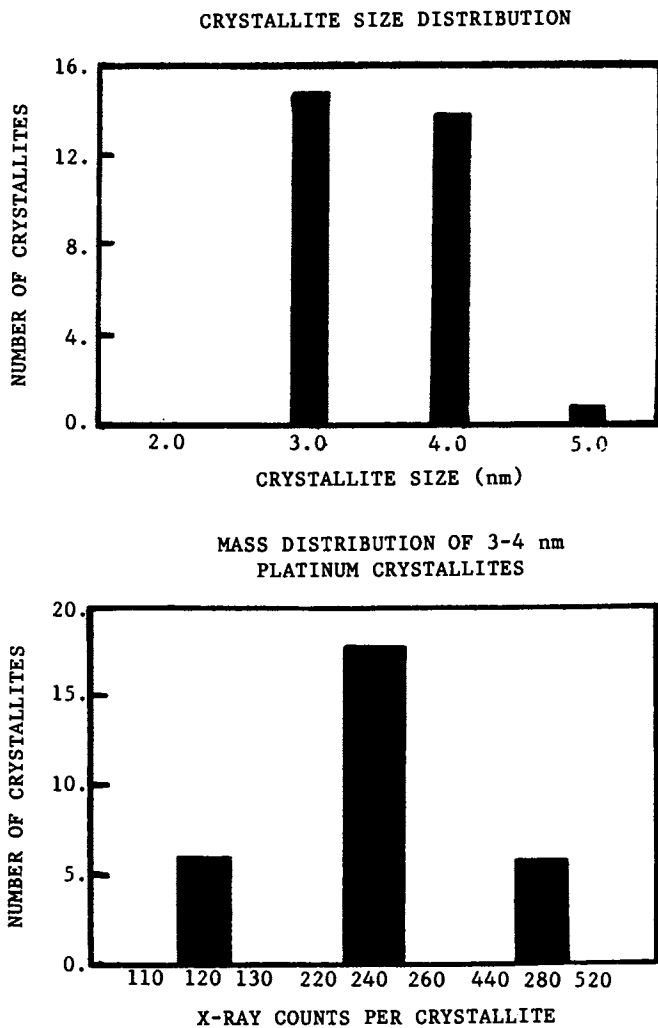


Figure 3. Size and mass distribution of platinum crystallites supported on  $\gamma$ -alumina.

the crystallites were not well defined and were very mobile in the electron beam during EDS analysis making accurate size and mass distribution measurements impractical.

Two approaches were taken to provide insight to the uniformity of these samples: 1) perform extensive visual inspection of the materials to ensure that no large palladium crystallites were present, which was the case for both samples, and 2) perform surface area measurements using hydrogen TPD to establish the relationship between the observed data by STEM and the estimated surface area from theoretical considerations.

Sample H was evaluated in this manner, and showed higher H/Pd ratios than anticipated, 0.6 versus 0.3 for the crystallites observed. This result would suggest that the palladium crystallites are thin, thus explaining the instability in the electron beam and lack of diffraction contrast.

Sample J showed a comparable result to sample H in that the observed crystallite size range did not correspond to the H/Pd ratio determined experimentally. The anticipated H/Pd ratio should be between 0.2 and 0.4 if these crystallites were uniform in all three dimensions. Although the palladium crystallites on Sample J were easier to observe and detect by EDS than those on sample H, their disorganized appearance and rapid dissociation in the presence of the electron beam suggest that they are also not very thick, possibly 1-2 nm. This would account for the higher H/Pd. It is also possible that because hydrogen is considerably more permeable in palladium than other noble metals and the crystallites observed appear more as disorganized clusters, additional hydrogen adsorption could be occurring on these crystallites which cannot be accounted for by a FCC crystal model. Finally, because of the difficulty in detecting palladium crystallites in the 2 nm size range, the possibility of adsorption contributions from undetected palladium which is well dispersed exists as another feasible explanation of why the H/Pd values are higher than anticipated.

One factor which should be noted for palladium, which also applies to the observation of the transition metals is that not all crystallites have the same efficiency for diffracting electrons, i.e., as the atomic number decreases, the extinction distance for the crystallite increases (13). Thus one would anticipate that as the mean atomic number decreases, the crystallites will have to be progressively larger to enable visual observation on a support such as alumina.

Table II. Palladium Crystallite Size and Dispersion Data

| Sample Code | Wt-%Pd, | Support                                  | Crystallite Size (nm) | H/Pd |
|-------------|---------|--|-----------------------|------|
| H           | 0.1     | $\gamma$ -Al <sub>2</sub> O <sub>3</sub> | 3-5                   | 0.6  |
| I           | 0.1     | SiO <sub>2</sub>                         | 4-20                  | 0*   |
| J           | 1.0     | $\gamma$ -Al <sub>2</sub> O <sub>3</sub> | 3-5                   | 0.5  |

\*Crystallites were greater than 25 nm after TPD analysis

Supported platinum-palladium. This aspect of the study focused on the characterization of platinum and palladium on alumina. The analytical capability of STEM is fully demonstrated in a problem of this type, because of the rapid manner in which crystallite composition can be analyzed. This study is especially interesting because of the use of platinum and palladium combinations in automotive catalysis.

The sample prepared contained 0.65 wt-% platinum and 0.1 wt-% palladium on  $\gamma$ -alumina. It was exposed to temperatures of 500°C under oxidizing and reducing atmospheres. The STEM analysis of this material showed crystallite sizes in the range of 3-5 nm. The composition of these crystallites was approximately 70% pure platinum, 15% pure palladium and the remainder a mixture of platinum and palladium of varying ratios. Two factors were involved in observing platinum: 1) the higher concentration, and 2) contrast phenomena associated with Z number and diffraction. The ratio of platinum to palladium crystallites observed, assuming equivalent number of atoms per crystallite, was in reasonable agreement to what would be expected based on concentration effects only. The fact that platinum and palladium only crystallites were numerous confirms that segregation was maintained at the elevated temperatures. The H/metal ratios from TPD studies for platinum and palladium on alumina, sample B, Table I, and sample H, Table II, would predict a H/Pt+Pd ratio of  $0.33 \pm 0.02$ . The actual experimental data showed a ratio of  $0.37 \pm 0.02$ . This result is in reasonable agreement and supports the STEM data which indicate that the majority of platinum and palladium crystallites are segregated.

Although the metal distribution was not uniform, there was no indication of large crystallites that might alter the interpretation of the results discussed above.

Supported transition metals. As mentioned previously, detection of transition metal oxides <4 nm on alumina by CTEM is virtually impossible because of the fundamental difficulty of providing sufficient contrast between support and crystallite (14, 15).

The STEM was used to image and analyze 4 nm areas of a transition metal on alumina. The samples contained 1 wt-% of Fe, Ni or Co on  $\gamma$ -alumina and were either in the chlorided state or oxidized state when analyzed by STEM and PAS. The PAS was used to confirm that the transition metals were present as chlorides on the support and, consequently, after oxidation showed a dramatic decrease in the chlorided species. In the case of cobalt, the tetrahedrally coordinated species was apparent after oxidation suggesting that a surface aluminate was formed. The iron and nickel did not show any of the characteristic bulk oxide transitions suggesting that a highly dispersed, possibly very thin metal oxide on alumina was present. An example of a PAS spectra for iron in the chlorided versus oxidized form is shown in Figure 4. Loss of the broad peak at 1000 nm signifies a loss of the chlorided species. Lack of additional absorption peaks in the 600 to 1200 nm range suggests that bulk iron oxides have not formed.

The STEM was used to evaluate the transition metals in the chloride and oxide forms. The following statements can be made about all of the materials investigated: 1) clusters 4-6 nm in size

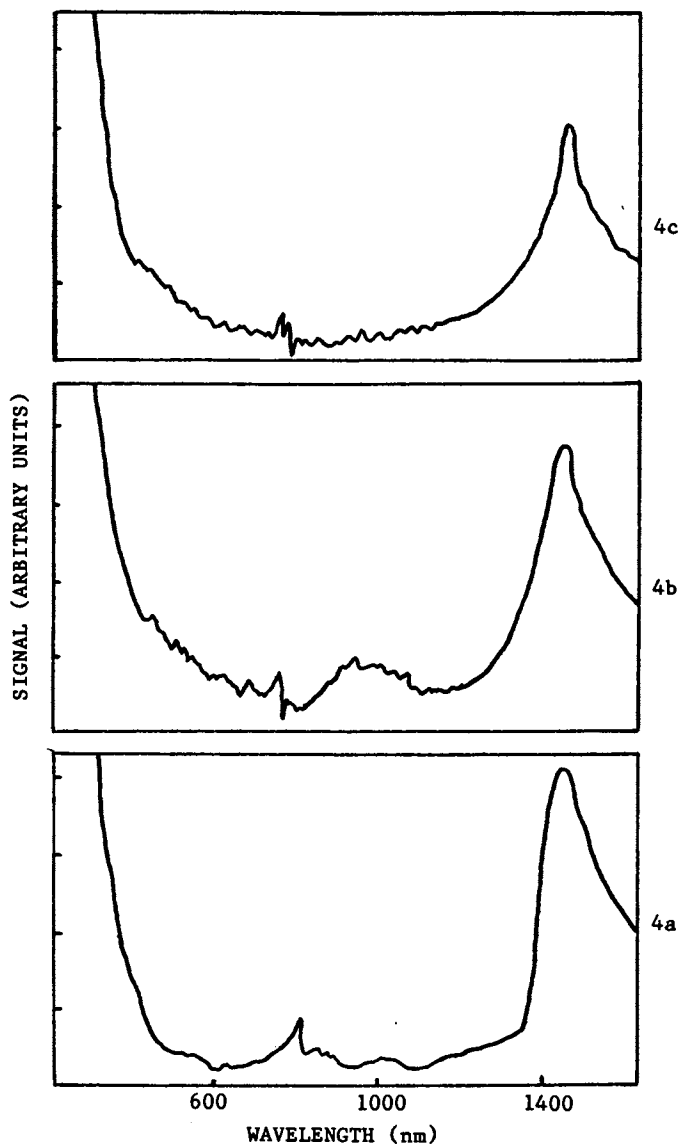


Figure 4. Example of PAS spectra; a)  $\gamma$ -alumina, b)  $\text{FeCl}_3$  on  $\gamma$ -alumina, and c)  $\text{FeCl}_3$  on  $\gamma$ -alumina after oxidation at  $500^\circ\text{C}$ .



containing Fe, Ni or Co were observed, 2) no one form, chloride versus oxide was easier to detect by EDS, and 3) the count rates were very low suggesting that the clusters were very thin. An example of iron-alumina EDS analysis in the chloride state is shown in Figure 5. It is difficult to estimate the number of atoms being analyzed. However, the fact that clusters of Co, Fe, or Ni could be vaguely distinguished from the alumina and microanalyzed to verify their presence is worth noting. The samples containing primarily metal chlorides do not show the appropriate stoichiometry of chloride to metal. This comes as no surprise based on STEM investigations at the Signal UOP laboratory of pure metal-chloride compounds that consistently show chloride to metal ratios 30 to 50% lower than theoretical values. The chloride-metal bond does not appear to be stable in the electron beam under the conditions selected for analysis. In the case of many pure compounds, reduction of the metal chloride to the metal is most likely occurring. However, in the case of supported metal chlorides, reaction of hydroxyls on the support with the metal chloride thus displacing some of the chloride ligands may also be a contributing factor to the lower chloride-metal ratios.

### Conclusion

The dedicated STEM provides a means of obtaining microanalytical information of supported metals not readily obtained by other instrumentation. The capability to observe and analyze some very highly dispersed metal particles on  $\gamma$ -alumina has been demonstrated and for the noble metals, verified by temperature programmed hydrogen desorption.

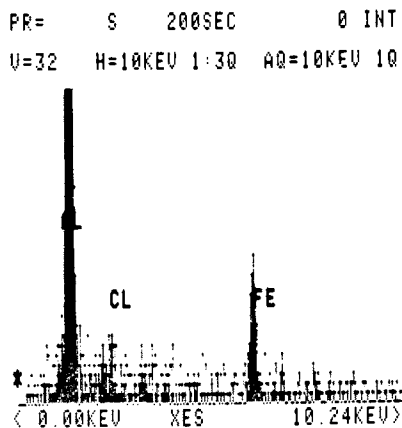


Figure 5. Typical EDS analysis of a 4nm cluster of Fe on  $\gamma$ -alumina in the chlorided form taken at 20 Mx for 200 sec.

This study has shown that reasonably uniform platinum crystallites can be made on  $\gamma$ -alumina, and that platinum and palladium can be segregated and maintained in that form for the most part even after exposure to high temperature oxidation-reduction conditions. Highly dispersed clusters of palladium, nickel, cobalt, and iron can be observed. Cluster size determination could not be accurately made because of the lack of contrast between the cluster and the support. The marginal detectability by EDS for these clusters enabled elemental identification to be made, however, mass uniformity determinations could not be made.

#### Acknowledgments

The author would like to thank G. Grieger for his assistance in obtaining and interpreting the platinum-alumina MAED patterns.

#### Literature Cited

1. Baker, R. T. K., Catal. Rev. Sci. Eng. 1979, 19 (2), 161-209.
2. Schmidt, L. D., and Chen, M., J. Catal. 1978, 55, 348.
3. Schmidt, L. D., and Wang, T., J. Catal. 1980, 66, 301.
4. Schmidt, L. D., Wang, T., and Chen, M., J. Catal. 1979, 60, 356.
5. Schmidt, L. D., and Chen, M., J. Catal. 1979, 56, 198.
6. Ruckenstein, E. and Chu, Y. F., J. Catal. 1978, 55, 281.
7. Yacaman, M. J., Gomez, A., Schabes-Retchkiman, P., and Ocana, T., Philos. Mag. A. 1983, 47, No. 2, 169.
8. Yacaman, M. J., and Dominguez, D. M., Surface Sci. 1979, 87, L263.
9. Yacaman, M. J., Dominguez, J. M., Vazquez, A. S., and Renouprez, A. J., J. Catal. 1982, 75, 101.
10. Harris, P. J. F., Boyes, E. D., and Cairns, J. A., J. Catal. 1983, 82, 127.
11. Baker, R. T. K., Prestridge, E. B., and Garten, R. L., J. Catal. 1979, 56, 390.
12. Lyman, C. E., J. Mol. Cat. 1983, 20, 357.
13. Delanay, F., Catal. Rev. Sci. Eng. 1980, 22, (1), 158.
14. Mustard, G., and Bartholomew, C. H., J. Catal. 1981, 67, 186.
15. Delanay, F., Catal. Rev. Sci. Eng. 1980, 22, (1), 162-164.

RECEIVED December 6, 1984

## Diffraction from Supported Metal Catalysts

J. B. Cohen, P. Georgopoulos, J. B. Butt, and R. L. Burwell, Jr.

Department of Materials Science and Engineering and Ipatieff Catalytic Laboratory,  
Northwestern University, Evanston, IL 60201

We review our work on techniques and methods for examining the diffraction patterns from supported Pt,Pd and alloy catalysts, as well as the results that have been obtained in the last decade with these procedures in our group.

X-ray diffraction has been employed for a very long time to attempt to characterize supported catalysts. For the most part, and until recently, only the width of a wide-angle peak has been employed. From the Scherrer equation, this width yields a "size". However, it has not been recognized that such a procedure faces many problems:

- 1) The measured "size" is not a size ( $D$ ), but a ratio of two moments in the distribution,  $\langle D^2 \rangle / \langle D \rangle$ .
- 2) The averages are volume averages, whereas the desired weighting for catalytic studies is by surface area. Furthermore, this difference in weighting has not always been recognized in making comparisons to results from electron microscopy.
- 3) Other factors contribute to broadening. Instrumental factors are particularly difficult to remove from the breadth, and the effects of local strain can only be approximated.

Instead of this methodology, we have chosen to use Fourier analysis of the entire peak shape. By this procedure all of the above problems are eliminated. In particular, we focus on the cosine coefficients of the Fourier series representing a peak. The instrumental effects are readily removed, and the remaining coefficient of harmonic number, ( $n$ ),  $A_n$ , can be written as a product:

$$A_n = A_n^{\text{size}} A_{n(\text{hkl})}^{\text{distortion}} \quad (1)$$

The first term is related to the (surface weighted) average size, whereas the second is a function of the microstrains. The first term is the same for all peaks, whereas the second depends on the interplanar spacing, "d", of the diffraction planes, and is proportional to  $1/d^2$ . The

two terms are readily separated by plotting  $2\kappa A_n$  for a given  $n$  vs.  $1/d^2$  for multiple orders of diffraction. The microstrains are obtained from the slope for each  $n$  and hence vs. distance normal to the diffraction planes. If there is no strain variation from point to point in a particle, the plot is horizontal. In other words, the coefficients for multiple orders superimpose. The initial slope of  $A_n^{\text{size}}$  vs.  $n$  yields the average size, whereas the second derivative is the size distribution (1). From the measured size in different crystallographic directions, and from the shape of the size distribution, information on particle shape can be obtained.

In principle, it is possible to fully automate the procedure (2) and software can be written to obtain the results to an operator specified precision, as the error equations are available. Unfortunately, this on-line procedure is sometimes difficult with catalysts because most supported metal catalysts contain only the order of one percent or less of metal, the peaks are broad due to the small size of the crystallites, and the large amount of support gives strong background scattering which has features of its own. Visual inspection of the data is often necessary prior to processing.

Tested analytical procedures are also available when only a single peak can be measured (3).

Other information that can be obtained from a wide-angle diffraction pattern includes the detection of stacking faults and microstrains, the lattice parameters, and the mean-square amplitude of vibration.

With a rotating anode X-ray generator or the new high-power sealed X-ray tubes for standard generators, it is possible to obtain suitable data for such analysis, down to about 40 percent metal exposed ( $\langle D \rangle \sim 25 \text{ \AA}$ ). With the intensity available at a synchrotron source, multiple peaks can be observed to ~60 percent metal exposed, and we have obtained interpretable patterns to ~80 percent metal exposed ( $\langle D \rangle \sim 13 \text{ \AA}$ ). At still smaller sizes, the pattern is so extended that analysis is better done by considering the scattering in terms of the radial density distribution, as is done for liquids or amorphous solids. (But this does not imply that the particles are indeed amorphous!) We have generally found that molybdenum radiation ( $0.7 \text{ \AA}$ ) is superior to Cu ( $1.5 \text{ \AA}$ ) because the penetration is deeper and hence the sampling is better. Also, the peaks are at lower angles and less broad.

The single-peak procedure is particularly useful with Pt and Pd catalysts supported on alumina, because the strong  $Al_2O_3$  reflections mask much of the scattering. Another procedure for examining such catalysts is via small-angle scattering. Brumberger and co-workers (4) have shown that it is possible to measure the surface area between support and catalyst, catalyst and air, and support and air, without pore-filling and with very simple procedures. With a rotating anode, and a position sensitive detector an entire pattern can be obtained and processed in a couple of hours. And the smaller the particles the more the scattering at small angles!

The wide range of wavelengths available at a synchrotron or storage ring permit the use of two additional methodologies. The atomic form factor changes drastically near an absorption edge for any of the electron shells. As a result of this, if the pattern is recorded at an energy very close but just below the L edge of Pt (or Pd), and also well below this edge, only the Pt scattering will change, not that of the silica or alumina support. By taking the difference, or still better yet, evaluating the derivative with respect to energy, the contribution of the support can be minimized. In addition, it can be shown that in such a difference, the

scattered intensity for Pt decreases much less with scattering angle than in the normal case, thus emphasizing higher order peaks. We show an example of this, in Fig. 1 from ref. 5, Pt on  $Al_2O_3$ . In the patterns for each wavelength the Pt peaks are largely obscured by those from  $Al_2O_3$ , but in the difference the metal peaks are quite clear. Note also the "flatness" of the background after the subtraction. We have used this procedure successfully down to sizes of 13-14 Å.

The shape of the edge itself examined by XANES (X-ray near-edge spectroscopy) can be employed to reveal information on d-band vacancy concentration vs. treatment. The oscillations at energies above the edge (EXAFS) can provide information on near-neighbor atom spacing and some limited information on the chemical environment. As we will show, the best way to use such tools is to use several at once, rather than only one.

It is true that these X-ray procedures are much less sensitive to sample preparation than chemisorption techniques. Nonetheless, it is desirable to use them in conjunction with such methods. In analysis of chemisorption data, it is necessary to make an assumption as to the number of gas molecules that attach to each atom in the catalyst. Careful X-ray studies can indicate the validity of such a number, and, as well, reveal whether the catalyst particles cluster. In this case, the X-ray size will be much smaller than that indicated by chemisorption. This can also be done by comparing X-ray and electron microscopy results. (6)

### Techniques.

It is often desirable to examine catalysts not in air, but rather after various treatments, or during a reaction, and without air exposure. Accordingly, we have developed a series of simple cells for wide-angle diffraction to accomplish these ends. (7,8) In the first of these, a large circular sample area of glass is covered with mica, and attached to long glass tubes, which can be connected to a gas train. The cell is easily placed on a diffractometer, and by tilting the cell the catalyst can be moved to these tubes for insertion in a furnace for treatment. A smaller version can be used to examine the pattern during a reaction. [The smaller size keeps the catalyst amount small enough for proper gas flow conditions.] Both types of cell can readily be tested for air leakage by examining the color of a powdered and reduced  $MnO/SiO_2$  vs. oxygen trap time.

We have also constructed a cell that permits close temperature control, even for exothermic reactions. In it, a sample can be heated to as high as 800°K, treated and then cooled to as low as 140°K, all in situ on the diffractometer (9).

### Results.

#### Pt Catalysts

In a series of studies of carefully prepared catalysts of Pt on silica gel (7,10-12) we have shown that the Pt particles are equi-axed, (and definitely not cuboidal as is often assumed) that the size (or percent metal exposed) agrees with results from hydrogen chemisorption, and that the particles are free of microstrain faults or twins, except when the average size is similar to the pore size of the support. In this latter case, the particles are elongated, and there is microstrain, probably due to differ-

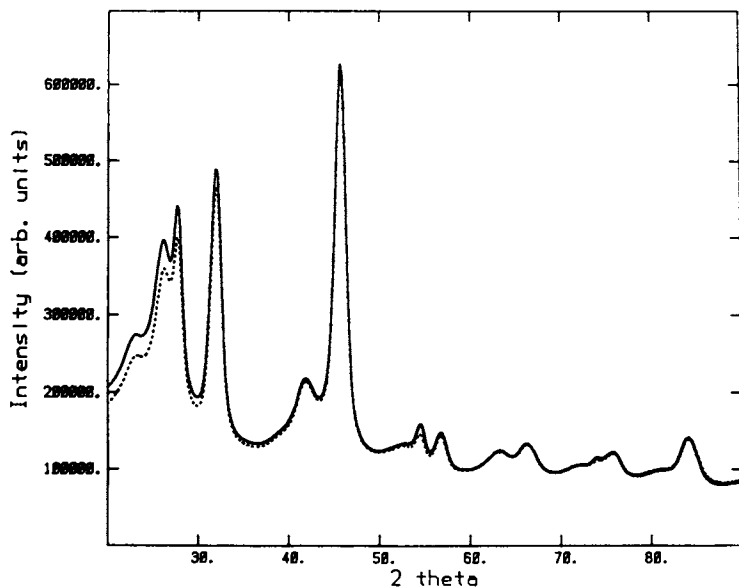


Figure 1a. Diffraction pattern, Pt on  $\text{Al}_2\text{O}_3$  (34. wt. pct.) 40 percent metal exposed. Incident beam energy, 11508 eV (solid line) and 11558 eV (dashed line).

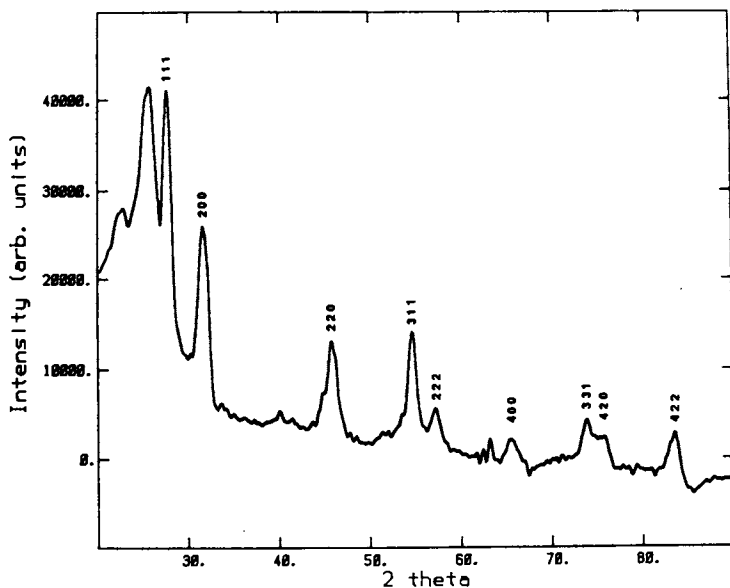


Figure 1b. Difference pattern. Reproduced with permission from Ref. 5. Copyright 1984, Academic Press.

ential contraction of the catalyst and support on cooling from the reduction treatment. The reactivity of these strained particles for methylcyclopropane hydrogenolysis is very high, a fact which we do not yet fully understand; it is possible that the microstrain is connected with this behavior. At least up to 60 percent metal exposed, even in air the particles are not heavily oxidized, and the lattice parameter is that of bulk Pt. The size distribution is sharper when the catalyst is prepared by ion-exchange, rather than impregnation, and the distributions suggest coalescence during preparation, not Ostwald ripening. The hydrogenolysis activity is proportional to the mean-square amplitude of vibration. As the size is reduced still further, for catalysts stored in air the Pt mass is slowly converted to (crystalline)  $Pt_3O_4$ , a process which is complete at ~80 percent metal exposed.

There is little contact area between the metal and support (10).

Reduction by hydrogen completely alters the chemical reactivity and its variation with size. At the same time, the Pt particle size is reduced. The mean-square amplitude of vibration follows this reactivity.

A study of the area of the  $L_{III}$  absorption edge resonance shows a correlation with chemical activity. This implies a correlation with the number of d-band vacancies. This occurred when Pt oxide was reduced by hydrogen or when the particle size was decreased (13).

#### Pd Catalysts (8,14)

The catalytic activity of Pd/SiO<sub>2</sub> of low percentage metal exposed (for methylcyclopropane (MCP) hydrogenolysis at 0°C) is less for catalyst cooled from 723°K in H<sub>2</sub>, than for the same material cooled in He. We have shown that this is due to hydride formation (when cooling in H<sub>2</sub>). The ease of hydride formation decreases with decreasing particle size up to ~30 percent metal exposed. Exposure to hydrogen results in nearly complete conversion to hydride, but purging with He (even at 0°C) reconverts the hydride to metal, although there is some induction period. Passing hydrogen plus MCP over the catalyst results in the conversion into hydride of a substantial portion of the catalyst originally present as palladium metal. The lattice parameter is the same as for bulk Pd, at least for particles of 45 Å or larger.

No hydride forms for very small particles. Yet when catalysts with such a small metal particle size are stored in air, they are converted to (crystalline) PdO. Reduction of this oxide with hydrogen produces Pd metal, not hydride.

#### Alloy Catalysts (9)

Co-Rh catalysts were prepared on silica gel by impregnation with a pentane solution of Rh<sub>2</sub>Co<sub>2</sub>(CO)<sub>12</sub>. After reduction at 823°K for 20 hours, there were diffraction peaks due to the Co-Rh alloy, but also peaks from the metals themselves.

#### Acknowledgments

Our research in this area was supported by DOE (Grant No. DE-AC02-77ERO4254). The X-ray measurements were performed either at the CHESS synchrotron facility, Cornell University, or in the X-ray Diffraction Facility of Northwestern University's Materials Research Center, supported in part by NSF under Grant No. DMR-MRL-76-80897.

Literature Cited

1. Pielaszek, J.; Cohen, J.B.; Burwell, Jr. R.L.; Butt, J.B. Jrnl. of Catalysis. 1983, 89, 479-481.
2. Schlosberg, W.H.; Cohen, J.B. Jrnl. Appl. Crystallogr. 1983, 16, 304-308.
3. Nandi, R.K.; Kuo, H.K.; Schlosberg, W.; Wissler, G.; Cohen, J.B.; Crist, Jr., B. Jrnl. Appl. Crystallogr. 1983, 17, 22-76.
4. Goodisman, J.; Brumberger, H; Cupelo, R. Jrnl. Appl. Crystallogr. 1981, 14, 305-308.
5. Georgopoulos, P.; Cohen, J.B. Submitted for publication.
6. Amelse, J.A.; Arcuri, K.B.; Butt, J.B.; Matyi, R.J.; Schwartz, L.H.; Shaprio, A. Jrnl. Phys. Chem.1981, 85, 708-711
7. Nandi, R.K.; Molinaro, F.; Tang, C.; Cohen, J.B.; Butt, J.B.; Burwell, Jr., R.L. Jrnl. Catal. 1982, 78, 289-305.
8. Nandi, R.K.; Pitchai, R.; Wong, S.S.; Cohen, J.B.; Burwell, Jr., R.L.; Butt, J.B. Jrnl. Catal. 1981, 70, 298-307.
9. Pielaszek, J.; Cohen, J.B. Adv. in X-ray Analysis, In Press
10. Uchijiima, T.; Herrmann, J.M.; Inouye, J.Y.; Burwell, Jr., R.L.; Butt, J.B.; Cohen, J.B.; J. Catal.1977, 50, 464-478.
11. Sashital, S.R.; Cohen, J.B.; Burwell, Jr., R.L.; Butt, J.B. Jrnl. Catal. 1977, 50, 479-493.
12. Otero-Schipper, P.H.; Wachter, W.A.; Butt, J.B.; Burwell, Jr., R.L. Jrnl. Catal1977, 50, 494-507.
13. Rorris, E. Ph.D. Dissertation, Northwestern University, Evanston, IL June 1983.
14. Nandi, R.K.; Georgopoulos, P.; Cohen, J.B.; Butt, J.B.; Burwell, Jr., R.L. Jrnl. Catal. 1982, 77, 421-431.

RECEIVED March 21, 1985



## Vibrational Analysis of Adsorbed Molecules

H. Ibach and J. E. Müller

Institut für Grenzflächenforschung und Vakuumphysik and Institut für Festkörperphysik,  
Kernforschungsanlage Jülich, D-5170 Jülich, Federal Republic of Germany

The principles of vibration analysis are outlined. The vibration spectrum of a surface species serves as a fingerprint rich enough in details to reveal the essentials of the structure and bonding of the species containing up to about 20 atoms. The analysis usually involves a comparison to spectra of free molecules or model compounds. Mode assignment is performed through the use of isotopes. Selection rules can be used to determine the point group of a surface species. Surface decomposition reactions are easily studied using the technique of vibration analysis. Recently, reliable calculations of the electronic structure of adsorbed species have become available. Calculated equilibrium geometries and frequencies provide an important connection between theory and experiment. Results of such calculations for  $\text{H}_2\text{O}$  and  $\text{NH}_3$  are presented and compared to experimental data.

Our understanding of the chemistry of molecules adsorbed on metals has greatly improved in recent years. Much of our present knowledge is owed to the advent of reliable tools to study the vibration spectrum of adsorbed species (1,2). Though vibration spectroscopy is not an exact method and the methodology does not follow a particular routine pattern, it yields important qualitative information on the structure, the adsorption sites and reaction paths of surface species, as we shall see. The purpose of this paper is to summarize the important principles in the analysis of vibration spectra from surfaces and to demonstrate the type of information which is obtained. Regarding the experimental technique we shall refer to electron energy loss spectroscopy (ELS) only in this paper. The reason is that this method provides for the largest amount of information on the entire vibration spectrum. It is suited for adsorption studies on single crystal surfaces as well as on real surfaces, as long as they are stable in vacuum. Other techniques, in particular infrared reflection absorption spectroscopy have a higher resolution in a limited spectral range. They frequently serve as a source of additional information on the details of the structure.

0097-6156/85/0288-0392\$06.00/0  
© 1985 American Chemical Society

On single crystal surfaces vibrational modes are in principle wavelike excitations with the wave vector parallel to the surface. For most molecules dispersion effects are small, however, and shall be disregarded in this paper which is more oriented towards the chemical aspects. However, dispersion of adsorbate modes has been measured recently (3).

The second part of the paper is devoted to some aspects of the current status of the theory of chemisorption. There, in particular, the adsorption of water and ammonia will be studied and discussed. Through the theory a qualitative understanding of the bonding of these molecules to surfaces is achieved which is in agreement with the experimental observations.

### Principles of the Vibrational Analysis

The Vibration Spectrum as a Finger Print. The methodology of vibrational analysis comprises a variety of different aspects. In some cases a well established path of logical routine is followed. In other cases the analysis works on analogies to a large group of known compounds and their vibration spectrum. We shall discuss the latter aspect first. Finger printing works with the notion that, by and large, the vibrational mode is associated with a particular bond within a molecule, be it in gas phase or adsorbed on the surface. This is, of course, a very approximate concept only, as in principle the vibrational mode is a property of the entire system and not a property of an individual bond. Yet, the comparison of vibrational spectra of a large number of molecules as well as dynamical calculations shows that, to a larger or lesser degree, the concept of a vibrational mode characterizing a bond can be used. Typical examples are the hydrogen stretching vibrations. Hydrogen has a significantly smaller mass than the atom which it bonds to (carbon, silicon, oxygen). Consequently its vibrational modes are rather localized to the hydrogen bond and their frequencies are little affected by the rest of the molecule. The frequencies are sensitive, however, to the orbital structure of the atom which hydrogen bonds to. Thus one can distinguish between  $sp$ ,  $sp^2$  and  $sp^3$  hybridized carbon atoms. This provides a sound basis for discriminating saturated and unsaturated hydrocarbons even on surfaces. Vibrational analysis of a large number of molecules in surface compounds has also shown that the carbon-carbon stretching vibration is characteristic of the bond and single, double and triple bonds can be distinguished.

When a molecule is adsorbed on a surface and a vibrational analysis is attempted one usually tries to rationalize the vibration spectrum in analogy to the well documented vibration spectra of free molecules. This renders a first guess. Frequently, also, the answer is provided as to whether the molecule decomposes upon adsorption or not. The simplest case there is the adsorption of diatomic molecules where the absence or presence of the characteristic stretching vibration decides upon the question of dissociation. For larger molecules and a more detailed analysis of the vibration spectrum, the comparison to the spectra of free molecule may not suffice. Here the comparison to organometallic compounds of known structure and vibration spectrum can be most helpful. A good example is provided with the analysis of the species formed from ethylene adsorbed on Pt(111)

(4) and Pd(111) (5) at room temperature. While it became clear very quickly that the species on the surface could not be acetylene as was assumed in the older literature, the precise nature of the species was debated for a while. The final answer came when the model compound  $CCH_3Co_3(CO)_9$ , named tricobalt-ethylidene-nonacarbonyl, was prepared and the vibration spectrum was studied (6). Figure 1 shows that the vibration spectrum of the surface species correlates very well with the spectrum of the model compound. This correlation also includes the symmetry assignment of the modes for which we shall describe the methodology shortly.

Isotopes. As we have seen, the frequency of modes contains important information on the nature of the bonding. While the information is qualitative it still serves for an educated first guess on the structure of the molecule. For the identification of the species in Figure 1, e.g., the assignment of modes reveals the  $1130\text{ cm}^{-1}$  mode as the C-C stretching vibration. This frequency is within the typical range of C-C single bond stretching frequencies, however, falls below the range of the typical C-C double bond frequencies ( $1500\text{--}1800\text{ cm}^{-1}$ ). Thus from the assignment it is clear that the species has the bonding characteristics of a saturated hydrocarbon. The question is, of course, how the correct assignment is achieved. Here studies of isotopes are indispensable. Upon total or partial deuteration one notices the CH vibrations to shift downwards by a factor of  $\sim 1.35$  while the C-C vibration changes very little. In a few cases, where a strong coupling between the C-C stretching vibration and the CH stretching vibrations of the same symmetry exists, larger shifts of the "CC" vibration can occur. Such shifts are, however, not completely arbitrary. The frequencies of modes within the same representation of the point group of the surface species follow the Teller-Redlich rule when atoms are displaced by isotopes. The Teller-Redlich rule also serves a useful purpose to check whether a proposed symmetry and the assignment of the mode according to the proposed symmetry is correct. An example is provided with the modes of  $C_2H_2$  and  $C_2D_2$  on Fe(110) (7). There it was shown by the Teller-Redlich analysis that the only symmetry of the species consistent with the spectra is  $C_1$ , that is, the structure is such that no element of symmetry exists. While this is somewhat disappointing to the theorist as it complicates the theoretical analysis of the bonding, the low symmetry finds a natural explanation in the structure of the lowest unoccupied orbital of acetylene.

Surface Point Groups and Selection Rules. The most important point groups of surface species are  $C_1$ ,  $C_3$ ,  $C_2$ ,  $C_{2v}$ ,  $C_{3v}$ ,  $C_{4v}$ . Except for  $C_2$ , examples are known for each of the point groups. The analysis of the point group of the surface species makes use of the fact that the spectroscopy implies particular selection rules. Here again the advantage of ELS over other vibration spectroscopies for structure analysis becomes obvious. ELS has the unique capability to employ different scattering mechanisms merely by observing under different scattering conditions. When spectra are observed in the directions of specular reflection ((00)-beam) dipole scattering is employed which means that only the totally symmetric vibrations are excited. Impact scattering is used when the spectrum is observed off the spe-

cular direction. Then, all even modes with respect to the scattering plane contribute to the spectrum provided the scattering plane is aligned along a plane of symmetry. In a general orientation of the scattering plane, all modes are excited. These selection rules allow the determination of the point group of the surface species in most cases.

A famous, yet simple example is CO. CO tends to adsorb in highly symmetric positions on low index surfaces, so that the point groups are  $C_{2v}$ ,  $C_{3v}$  and  $C_{4v}$ . The totally symmetric vibrations then are the CO stretching and the hindered translation of the molecule vertical to the surface (metal-carbon stretch). Consequently, these two modes are seen in dipole scattering. Another example is provided with ammonia Fe(110) (Figure 2), when the coverage is low (8). Again, only the totally symmetric vibrations appear, under the point group  $C_{3v}$ . Interestingly here, the point group  $C_{3v}$  is inconsistent with the symmetry of the substrate surface atoms ( $C_{2v}$ ). The direct product of  $C_{2v} \times C_{3v}$  contains only the irreducible representation of  $C_s$ . If the relevant point group of ammonia would be  $C_s$ , however, many more modes would appear. One must, therefore, conclude that the breaking of the molecular symmetry through the surface is negligible. This is best rationalized when the  $NH_3$ -molecule is adsorbed with the nitrogen atom bonded head on a surface atom (instead of bridging configurations) since then the symmetry of the adsorbed ammonia including the nearest neighbor surface atom is  $C_{3v}$ . We shall see later in the theoretical section that the proposed structure is in accordance with total energy calculations.

Controlled Reactions. Vibrational analysis of surface chemical reactions, decomposition reactions in particular, is also feasible. A number of decomposition reactions have been studied already. The simplest of these involve the dissociation of diatomic molecules such as CO,  $O_2$ ,  $H_2$ , and NO. Yet, also the decomposition of more complex organic molecules, which proceed via several steps with metastable intermediate compounds, has been investigated. Typically such an experiment is performed with the molecule adsorbed at low temperatures. The temperature is then raised up to a particular value for a particular time. Spectra are recorded at that temperature or with the sample cooled down again. The ethylidene species from Figure 1 represents such an intermediate. We have seen that the analysis of that species was finally confirmed through comparison to an appropriate organometallic compound. This, however, was the last step undertaken in order to confirm an already existing proposition. To arrive at a reasonable conjecture about the nature of an unidentified object on the surface, the method of preparation provides equally valuable hints. For the example discussed here, e.g., it was important to learn that the species could be grown from adsorbed ethylene, but also from coadsorbed acetylene and hydrogen. The species, therefore, had to have more than two hydrogen atoms, yet no more than four. Another example where the "history" was important is the methoxy species formed from the decomposition of methanol on many metal surfaces. There, the similarity of the spectrum of methoxy to methanol, except for the removal of the OH stretching vibration from the spectrum upon warming the sample to higher temperature, was the important clue (9).

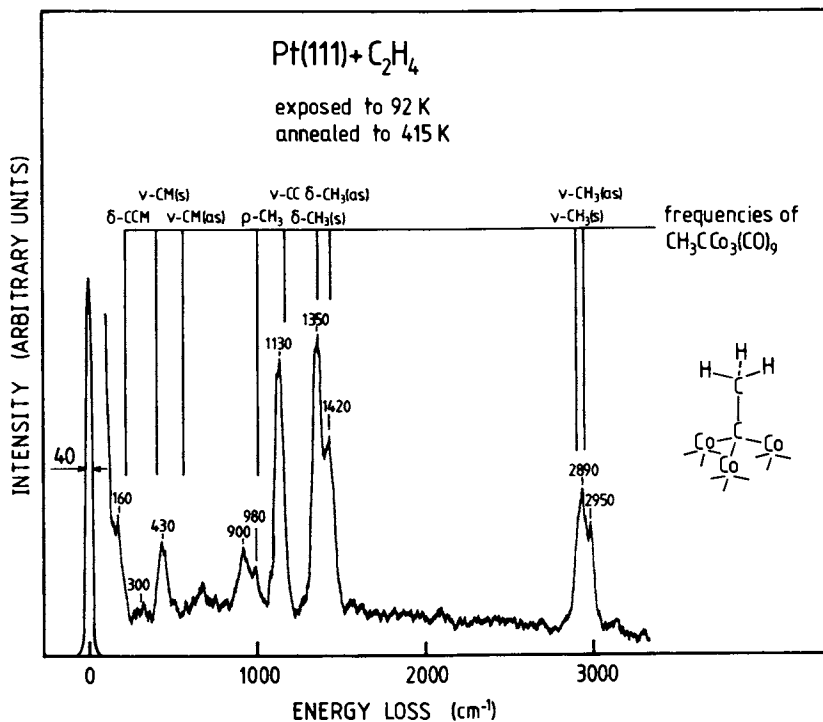


Figure 1. Off specular spectrum of CCH<sub>3</sub> on Pt(111) and model compound.

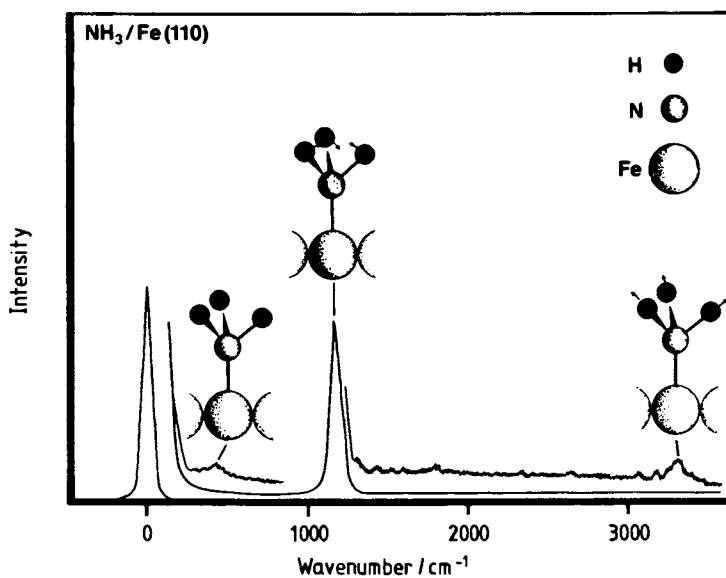


Figure 2. Dipole active modes of NH<sub>3</sub> on Fe(110).

### Electronic Structure Calculations

From a theoretical point of view, one is interested in the energy of a molecule as a function of its position and orientation on the surface. Such an energy map contains all the information about the chemical bond, mobility on the surface, as well as vibrational properties of the chemisorbed system. To perform a total energy calculation, two approximations are needed. First the surface must be modeled in some way, for which two methods are currently in use: the cluster (10,11) and the film (12) method. In the calculation described below the surface is represented by a 9-atom cluster. Second, the interacting many-electron problem must be simplified in order to treat systems of realistic size. The two approaches currently in use in surface calculations are the Hartree-Fock (HF) (11) and the Hohenberg-Kohn-Sham (HKS) (10,12) schemes, which treat the kinetic and potential energy exactly, but approximate the exchange and correlation energy in different ways. Both schemes yield results of useful accuracy (within 3 % for the equilibrium geometry and 15 % for the binding energy (13), whereby HF systematically underestimates and HKS overestimates the binding energies) and can provide valuable information about surface processes as we next show.

The Chemical Bonding. Here we describe an HKS calculation for  $H_2O$  and  $NH_3$  adsorbed on the aluminum (100) surface. Both molecules bind to the surface through their lone-pairs and show a definite preference for adsorption at the on-top site.  $H_2O$  adsorbs with the plane of the molecule tilted  $55^\circ$  away from the normal to the surface with a binding energy of 0.53 eV, while  $NH_3$  adsorbs straight up with a binding energy of 1.17 eV. The variation of the energy as the molecule moves along the surface is not trivial.  $H_2O$  remains rather mobile: at the bridge site, where it binds with its plane perpendicular to the bridge direction, the binding energy decreases to 0.25 eV, and at the hollow site the binding energy is 0.15 eV and the molecule shows almost no orientational energy. On the other hand,  $NH_3$ , which in the hollow site has a binding energy of 0.1 eV, is much less mobile.

The bonding is accompanied by a charge donation to the metal which produces a decrease of the work-function and affects also the vibrational properties of the molecule as we discuss below. The charge donation is 0.1 and 0.15 electrons for  $H_2O$  and  $NH_3$  respectively.

The molecules retain their essential character in all cases studied. This implies that the spontaneous dissociation observed under certain circumstances for  $H_2O$  must be a cooperative phenomenon involving more than one  $H_2O$  molecule.

The chemical interaction is schematically illustrated in Figure 3. The aluminum 3s function and a molecule lone pair (LP) with the appropriate symmetry make bonding and antibonding combinations which, however, are fully occupied and have no net bonding effect. The bonding is due to the mixing of aluminum 3p functions, which are unoccupied in the free metal surface. The occupation  $\beta$  of these functions produces a lowering  $\Delta E = \beta^2 (E_{3p} - E_{LP})$  of the lone pair orbital energy and a charge transfer  $\Delta Q = \beta^2$  to the metal. Since the

first unoccupied level of  $\text{H}_2\text{O}$  or  $\text{NH}_3$  lies much higher, the back-donation to the molecule is very suppressed. According to this argument, charge donation should be a characteristic of close shell systems interacting with simple metal surfaces. This is unlike the case of  $\text{CO}$ , where the polarization functions of the molecule contribute appreciably to the bonding.

$\text{H}_2\text{O}$  has two lone pairs, the  $\sigma$ -like  $3a_1$  at  $-9.1$  eV and the  $\pi$ -like  $1b_1$  at  $-7.3$  eV with respect to vacuum. At the on-top site, when the molecule is straight up, the relevant lone pair is the  $3a_1$ , and when the molecule lies flat on the surface the relevant lone pair is the  $1b_1$ . For an intermediate tilt both orbitals contribute to the bonding, but since the  $1b_1$  lies higher, there is a tendency for the molecule to tilt until for large enough tilt the H-Al repulsion takes over. This finite tilt angle is therefore a property of the  $\text{H}_2\text{O}$  molecule and is expected to be true for metals in general.

$\text{NH}_3$  has only one lone pair, the  $3a_1$ , at  $-5.9$  eV. This is higher than the  $\text{H}_2\text{O}$  lone pairs which explains the larger binding energy.

Vibrational Properties. Figures 4 and 5 show the variation of the energy  $E_B$  and the electric dipole moment  $\mu$  as a function of the relevant geometrical variables for  $\text{H}_2\text{O}$  and  $\text{NH}_3$  respectively. For the internal variables, the curves corresponding to the isolated molecules are also shown (dashed lines) for comparison. The oscillation frequencies  $\nu$  and dipole matrix elements  $M^2 = \langle \psi_1 | \mu | \psi_0 \rangle^2$  are also given and compared with those of the isolated molecules (in parenthesis) when appropriate. While the binding energies (and the oscillation frequencies) are quite reliable in cluster calculations, the calculated dynamical dipoles are systematically underestimated. Representing the surface by a finite size cluster leads necessarily to an incomplete formation of the image dipole ( $\approx 40\%$  for our  $\text{Al}_9$  cluster). However the calculated relative EELS intensities should be quite correct. We note that the values in Figures 4 and 5 apply to a single molecule interacting with a surface and should be compared only with low coverage experiments.

Hindered Translation (Figures 4a and 5a). The motion of the molecule normal to the surface characterizes the strength of the bonding to the surface.  $\text{NH}_3$  has a larger binding energy and therefore a larger oscillation frequency than  $\text{H}_2\text{O}$ . This mode lies quite low in energy loss because of the large associated effective mass. Experimentally, however, it may be hard to identify because it exhibits very small dipole matrix elements. Actually, for the simple model of a rigid dipole moving normally to a perfect metal surface, the dynamical dipole would be exactly zero. For a real surface there is a small, but finite dynamic dipole due to the charge transfer mechanism described above. This effect can be very dependent on the structure of the metal surface. The amplitude of this mode is thus a measure of the charge transfer or to the molecule. For instance calculations in smaller clusters exhibit a much larger charge transfer, suggesting that this mode would be enhanced at low coordinated sites or steps.

Hindered Rotation (Figure 4b). This mode characterizes the orientational energy associated with the bond. For  $\text{H}_2\text{O}$  the tilt energy is very small ( $\leq .1$  eV) until the protons get close to the surface and the Coulomb repulsion takes over abruptly, resulting in a

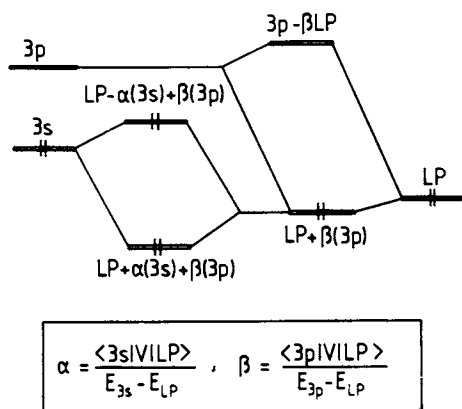


Figure 3. Bonding scheme of a molecule having a lone pair orbital to an s-metal.

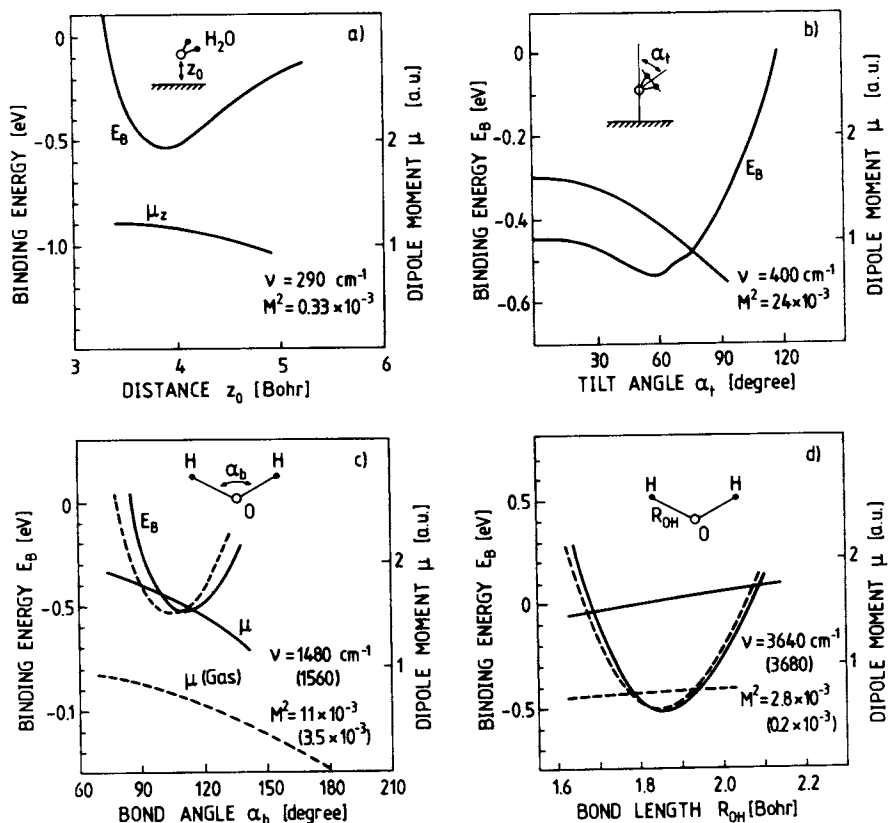


Figure 4. Total energy curves and dipole moments for H<sub>2</sub>O.



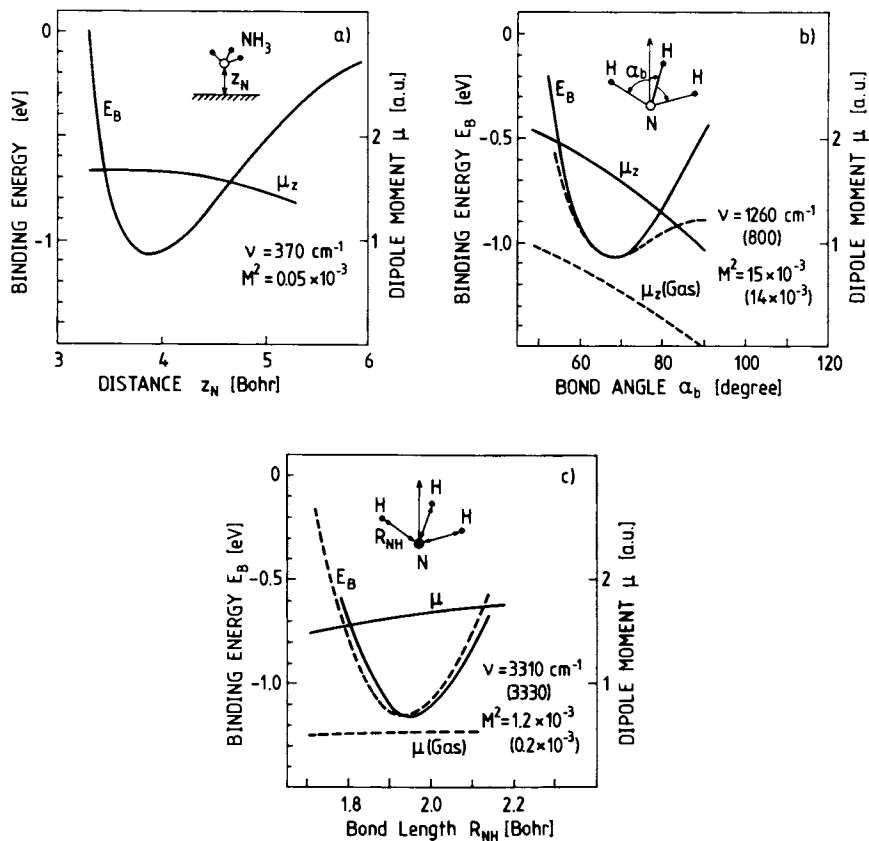


Figure 5. Total energy curves and dipole moments for  $\text{NH}_3$ .

very anharmonic energy variation. The mode has a very large zero-point motion, which together with the large dynamic dipole gives rise to a strong EELS signal (14). The dynamical dipole is approximately given by  $d\mu/d\alpha_t \approx 2\mu_M \sin\alpha_t$ , where  $\mu_M = 0.7$  a.u. (1 a.u.  $\approx 2.5$  Debye) is the permanent dipole of  $H_2O$  and the factor 2 (in our calculation only 1.4) is the enhancement due to the image. It has been observed that with the formation  $H_2O$  layers this mode stiffens and becomes even stronger (15).

For  $NH_3$  the orientational energy is quite large. However, since in the ground state the permanent dipole is perpendicular to the surface, the dynamical dipole for this mode is zero, so that the mode is EELS-inactive.

Internal Bend (Figures 4c and 5b). The internal modes are used to identify the adsorbed species, and a comparison with the isolated molecule values indicates to what extent the molecule is affected by the surface.

In the "scissors mode" of  $H_2O$ , the protons move parallel to the surface and the oscillation frequency is almost unaffected. For  $NH_3$ , on the other hand, the so called "umbrella mode" is drastically stiffened by the surface because the protons move against the surface and suffer a strong Coulomb repulsion. Here again the dynamical dipole moment is  $d\mu/d\alpha_b \approx 2\mu_M \sin\alpha_b$ . For  $NH_3$ , where  $\mu_M = 0.53$  a.u., the enhancement of the dynamic dipole by the surface is compensated by the smaller oscillation amplitude.

Internal Stretch (Figures 4d and 5c). In spite of an enhancement of the matrix elements by the surface, this mode shows a rather small intensity and essentially no change in frequency. The occurrence of a large peak shifted to lower frequencies must be interpreted in terms of hydrogen bonded networks (15).

#### Comparison Between Theory and Experiment

In Table I we compare calculated frequencies and matrix elements  $M^2$  (in parenthesis) for  $H_2O$  and  $NH_3$  on Al(100) with experimental values for the  $NH_3$ -Fe(110) and  $H_2O$ -Cu(100) systems, the data taken from (8) and (14). Only relative values of  $M^2$  are presented because of difficulties in determining the surface coverage. Even though we are comparing different systems, the good agreement found for the internal modes is an indication that these modes are rather independent of the substrate and therefore can be used to characterize the adsorbed species. The hindered modes, on the other hand are much more substrate specific. For instance,  $NH_3$  binds more strongly to Fe than to Al, and  $H_2O$  more weakly to Cu than to Al. Note that the tilted ground state geometry reduces the intensity of the internal  $H_2O$  modes by a factor  $\cos^2\alpha \approx 0.25$ , the internal stretch apparently below the limit of detection. The hindered rotation, on the other hand, is only observable in the tilted geometry. As mentioned above, this mode is forbidden by symmetry for  $NH_3$ , but observable with large intensity for  $H_2O$ . Finally, the hindered translation exhibits a small but finite amplitude both for  $NH_3$  and  $H_2O$ , indicating charge transfer, in this case from the molecule to the metal.

Table I. Comparison of calculated frequencies and matrix elements  $M^2$  (in parentheses) for  $H_2O$  and  $NH_3$  on  $Al(100)$  with experimental values for the  $NH_3-Fe(110)$  and  $H_2O-Cu(100)$  systems.

|                      | $H_2O-Cu$<br>(exp)      | $H_2O-Al$<br>(theory)   | $NH_3-Fe$<br>(exp)       | $NH_3-Al$<br>(theory)    |
|----------------------|-------------------------|-------------------------|--------------------------|--------------------------|
| Hindered translation | 121 $cm^{-1}$<br>(0.60) | 290 $cm^{-1}$<br>(0.33) | 429 $cm^{-1}$<br>(0.09)  | 370 $cm^{-1}$<br>(0.05)  |
| Hindered rotation    | 230 $cm^{-1}$<br>(26.0) | 400 $cm^{-1}$<br>(24.0) | -                        | -                        |
| Internal bend        | 1590 $cm^{-1}$<br>(2.7) | 1480 $cm^{-1}$<br>(2.7) | 1170 $cm^{-1}$<br>(15.0) | 1260 $cm^{-1}$<br>(15.0) |
| Internal stretch     | -                       | 3640 $cm^{-1}$<br>(0.7) | 3310 $cm^{-1}$<br>(1.2)  | 3310 $cm^{-1}$<br>(1.2)  |

Next we discuss the effect of deuteration on low frequency modes involving the protons. Because of the anharmonic variation of the energy as a function of tilt angle  $\alpha_t$  (Fig. 4b), the hindered rotations of  $H_2O$  and  $D_2O$  turn out to be qualitatively different. The first vibrational excited state of  $H_2O$  is less localized than that of  $D_2O$ , because of its larger effective mass. The oscillation frequency of the mode decreases by a factor 1.19 and the matrix elements by a factor 1.51 upon deuteration. Therefore, the harmonic approximation, which yields an isotopic factor 1.4 for both the frequency and the intensity, is quite inappropriate for this mode.

In Table II we compare the calculated frequency and matrix element  $M^2$  (in parenthesis) for the  $D_2O-Al(100)$  hindered rotation with experimental results for  $D_2O-Cu(100)$  (14). The experimental isotopic factor is 1.16 for the frequency and  $\approx 1.6$  for the matrix elements, in good agreement with our calculation. In Ref. 14, using the harmonic approximation, the anomalous isotopic factor for the frequency was interpreted as due to mixing with the hindered translation. However, as we have shown, the harmonic approximation is inappropriate in this case.

Table II. Comparison of calculated frequency and matrix element  $M^2$  (in parentheses) for the  $D_2O-Al(100)$  hindered rotation with experimental results for  $D_2O-Cu(100)$ .

|                   | $D_2O-Cu$<br>(exp)      | $D_2O-Al$<br>(theory)   |
|-------------------|-------------------------|-------------------------|
| Hindered rotation | 198 $cm^{-1}$<br>(16.0) | 337 $cm^{-1}$<br>(15.9) |

In concluding, we point out an essential role of vibrational spectra in theoretical studies. Total energy calculations yield quantities of much interest, like equilibrium geometries and binding energies, which are not accessible in a direct experimental way. Only the vibrational quantities can be meaningfully compared with experiment and provide a way to assess the adequacy of these calculations.

#### Literature Cited

1. For a general review see:  
Ibach H.; Mills, D.L. "Electron Energy Loss Spectroscopy and Surface Vibrations", Academic Press: New York, 1982.
2. Brundle, C.R.; Morawitz, M.; Eds. "Vibrations at Surfaces" Elsevier: Amsterdam, 1983.
3. Szeftel, J.M.; Lehwald, S.; Ibach, H.; Rahman, T.S.; Black, J.E.; Mills, D.L. *Phys. Rev. Lett.* (1983) 51, 268.
4. Steininger, H.; Ibach, H.; Lehwald, S. *Surf. Sci.* (1982) 117, 685.
5. Kesmodel, L.L.; Gates, J.A. *Surf. Sci.* (1981) 111, L747. and in (2) p. 307.
6. Shinner, P.; Howard, M.W.; Oxton, L.A.; Kettle, S.F.A.; Powell, D.B.; Sheppard, N. *J. Chem. Faraday Trans. 2* (1981) 77, 397.
7. Erley, W.; Baro, A.M.; Ibach, H. *Surf. Sci.* (1982) 120, 273.
8. Erley, W.; Ibach, H. in (2) p. 263 and Erley W., private communication.
9. Sexton, B.A. *Surf. Sci.* (1979) 88, 299.  
Demuth, J.E.; Ibach, H. *Chem. Phys. Lett.* (1979) 60, 395.  
Sexton, B.A. *Surf. Sci.* (1981) 102, 271.
10. See, for instance, Port, D.; Baerends, E.J. *Surf. Sci.* (1981) 109, 167.
11. See, for instance, Herman, K.; Bagus, P.S.; Brundle C.R.; Menzel, D. *Phys. Rev. B* (1981) 24, 7025.
12. See, for instance, Wimmer, E.; Freeman, A.J.; Hiskes J.R.; Karo, A.M. *Phys. Rev. B* (1983) 28, 3074 and  
Feibelman P.J.; Hamann, D.R. *Phys. Rev. Lett.* (1984) 52, 61.
13. Müller, J.E.; Jones, R.O.; Harris, J. *J. Chem. Phys.* (1983) 79, 1874.
14. Andersson, S.; Nyberg, C.; Tengstål, C.G. *Chem. Phys. Lett.* (1984) 104, 305.
15. Thiel, P.A.; Hoffmann, F.M.; Weinberg, W.H. *J. Chem. Phys.* (1981) 75, 5556.

RECEIVED March 28, 1985

## IR Spectroscopic Characterization of Adsorbed Species and Processes on Surfaces

John T. Yates, Jr., Patrick Gelin<sup>1</sup>, and Thomas Beebe

Surface Science Center, Department of Chemistry, University of Pittsburgh, Pittsburgh, PA 15260

The use of infrared spectroscopy as a probe of chemical and physical phenomena on surfaces extends back to the early work of Terenin in Russia(1) who first employed near-IR spectroscopy as a tool to observe surface OH groups on SiO<sub>2</sub>, working in the region of the second harmonic OH stretching mode. This work was extended dramatically in the 1950's by R. P. Eischens and coworkers, who first applied transmission IR spectroscopy to the study of species chemisorbed on supported metals of catalytic interest(2). Eischens found that the use of group vibrational frequency assignments was a powerful method for deducing general structural information about adsorbed surface species, building on spectra of compounds of known structure. Results of this body of work are summarized in three monographs (3-5). The infrared method is widely applied for surface studies in industry and academia today, a testament to the wide ranging utility of the method even after almost 30 years of use. In addition, a wide range of other types of surface vibrational spectroscopic methods have now been developed and are widely employed.

IR spectroscopy has several distinct advantages as a probe of surface species character, as listed below:

- Ability to work under high gas densities to study catalytic surfaces under working conditions.
- Ability to use high resolution to accurately characterize small shifts in oscillator frequencies, as well as to perform lineshape analysis.
- High sensitivity of species' vibrational frequency to bonding modes at surfaces.
- Strong correlation of the spectra of surface species with vibrational spectroscopy of molecules of known structure.

The first two advantages listed above allow an optical method like transmission or reflection IR spectroscopy to be used for studies which would be impossible for a widely used competitive technique, electron energy loss spectroscopy (EELS). EELS must

<sup>1</sup>Current address: CNRS Laboratories, Lyon, France

operate under ultrahigh vacuum conditions and does not possess the resolution inherent in the optical methods(6). Thus the examples selected for presentation in this paper could not have been done using the EELS technique.

Two examples of the application of transmission IR methods will be presented. The first, dealing with the chemisorption of CO on a Pd/SiO<sub>2</sub> catalyst surface, illustrates the first observation of a local stoichiometric surface species interconversion process which occurs among chemisorbed CO species at high CO coverages. Evidence for the operation of the local stoichiometric process has been obtained on 75Å Pd particles. These particles seem to show close similarities as well as to differ in some respects from a Pd(111) single crystal surface insofar as their interaction with CO is concerned.

The second example deals with the use of IR spectroscopy to study bonding details within a layer of physisorbed CO species on a SiO<sub>2</sub> surface. Here specific bonding of CO to polar SiOH<sup>δ+</sup> surface groups is observed; in addition, CO molecules having rotational freedom are produced at higher CO coverages, and the degree of rotational freedom allowed seems to be determined by the magnitude of shielding of the polar centers on the SiO<sub>2</sub> surface by CO species which bond to SiOH, and also participate as a dielectric screening medium.

### Experimental Methods

Commercial IR Spectrometer Developments. For the study of the IR spectrum of species present on high area surfaces, both grating and Fourier transform instruments are commonly employed. Both types of instruments now feature computer data acquisition techniques which permit enhancement of signal/noise ratios by multiple scan averaging methods. This feature, coupled with smoothing routines and background fitting procedures, has led to a significant enhancement of the quantitative aspects of IR surface spectroscopy. The data shown in this paper have been obtained at a resolution of 3-4 cm<sup>-1</sup> with a data acquisition time of from 0.4 - 1 sec/cm<sup>-1</sup>. Under these conditions, a background noise level of about 0.001 absorbance units is readily achieved, permitting the observation of weak absorption bands due to surface species.

IR Cell Developments. The design of cells for IR spectroscopy has taken many courses, depending upon the objectives of the research envisioned. For example, in the case of combining IR spectroscopy with surface kinetics measurements, the design of Vannice(7) is ideal; here, reactant gases flow through the porous pressed disk sample during IR measurements. Similar arrangements are employed by Bell using FTIR methods under reaction conditions (8).

Another variation in IR cell design which we have developed is shown in Figure 1. In this cell, three surface measurement objectives are readily achieved:

- Stabilization of surface species and reaction intermediates at cryogenic temperatures.
- Simultaneous adsorption studies on supported metals and on their support, where both have been treated with reactants in exactly the same manner.

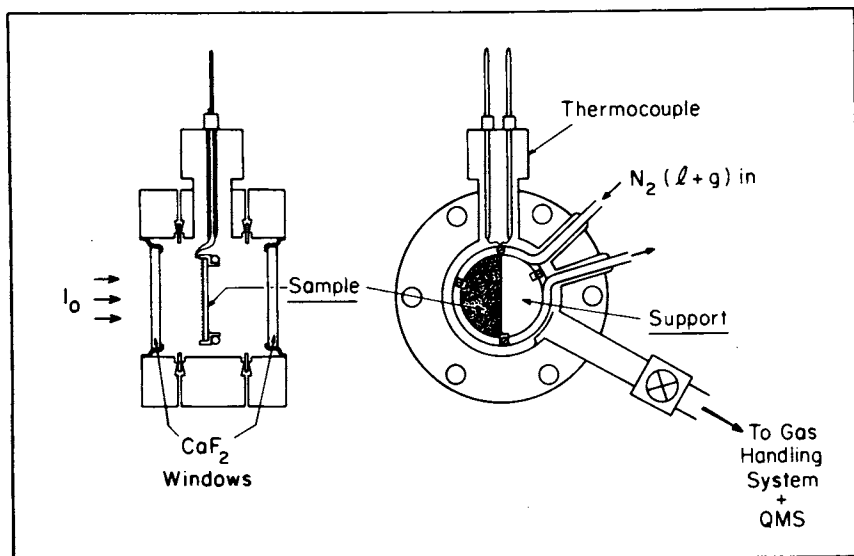


Figure 1. UHV cell for IR spectroscopy of adsorbed species.

- Measurement of surface species under high gas pressures, by means of complete cancellation of interfering gas phase spectra.

The ultrahigh-vacuum infrared cell, Figure 1, consists of a stainless steel body made from a double-sided conflat flange, 2-3/4" diameter, sealed by two CaF<sub>2</sub> windows in conflat flanges (available from Harshaw Chemical Co., Crystal and Electronic Products Dept., 6801 Solon, Ohio, 44139). This cell may be conveniently heated to 500K by being placed inside a small oven. Other cells, featuring internal electrical heating, may be operated at higher temperatures(9). The central body of the cell in Figure 1 contains a Cu support ring which may be cooled by circulation of liquid N<sub>2</sub> through tubing brazed to the copper. The temperature of the support ring is monitored by means of a 0.003" diameter chromel-alumel thermocouple. The temperature of the sample below room temperature may be controlled to  $\pm 1$ K by adjustment of the liquid-N<sub>2</sub> flow rate through the apparatus using the thermocouple signal for control of an electronic servosystem. We have shown experimentally that the adsorbant sample, supported on a circular CaF<sub>2</sub> plate clipped inside the Cu ring, reaches the temperature of the ring at all points to within about 1K(10).

Samples of high area powders and of supported metals may be applied to the CaF<sub>2</sub> support plate by a spraying technique, previously described in detail(11). In Figure 1, we show a "half plate" design in which a supported metal deposit, produced by H<sub>2</sub> reduction of metal ions held on the support, occupies one half of the plate while the pure support occupies the other half. Translation of the cell left and right permits the achievement of each of the three objectives listed above, using appropriate data subtraction procedures to remove contributions from gas phase species if present during measurements.

The cancellation of gas phase spectral features using the "half plate" design is far superior to methods involving a second gas cell placed in the reference beam. This is because the gas density and its rotational state population will differ in the two cells for different sample (and therefore gas) temperatures. For high sensitivity measurements, these effects can be difficult to handle using two cells.

### Experimental Results

The Chemisorption of CO on Pd/SiO<sub>2</sub> - Observation of Stoichiometric Species Interconversion Effects in the Chemisorbed CO Layer at High Coverages (12,13). It has long been recognized that bridging-CO readily forms upon chemisorption on both supported Pd(14-16) and on many Pd single crystal surfaces(17-21). At temperatures below 300K, or at high CO pressures, a terminal form of chemisorbed CO may also be populated, exhibiting a carbonyl stretching frequency near 2100 cm<sup>-1</sup>. This is shown in Figure 2, where spectrum a represents the stable IR species which remain on Pd/SiO<sub>2</sub> following CO saturation and evacuation at 300K. We see that several bridged-CO species exist together in the 1700 cm<sup>-1</sup> - 2000 cm<sup>-1</sup> region including a sharp high frequency bridged carbonyl band at 1979 cm<sup>-1</sup> (B<sub>1</sub>) which is most prominent. Upon cooling this surface to 80K and adding small quan-



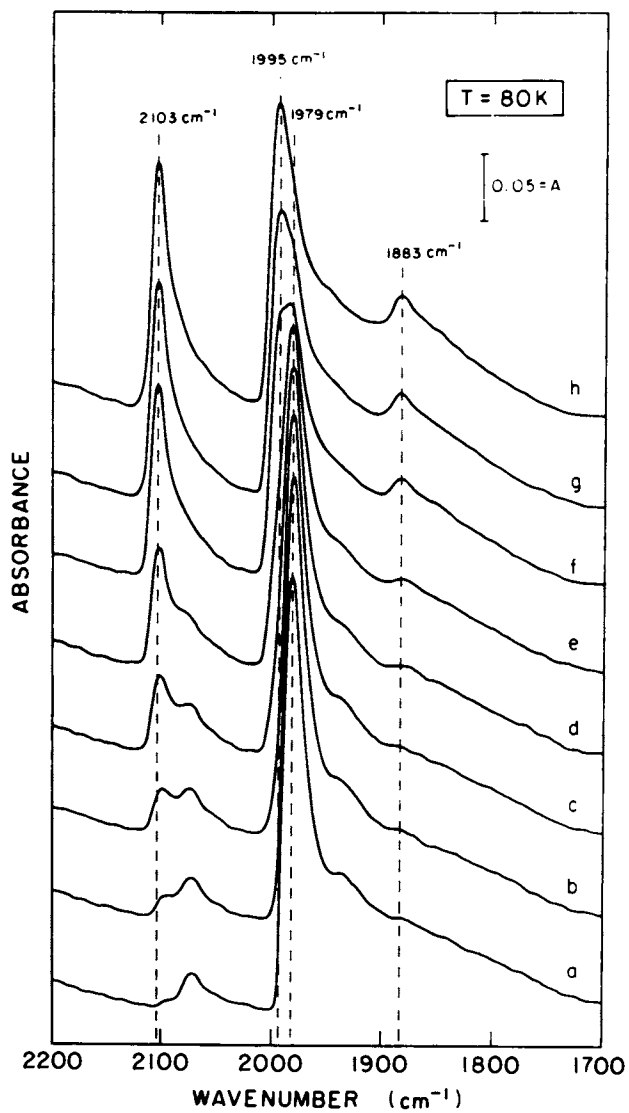


Figure 2. Additional CO adsorption on Pd/SiO<sub>2</sub> at low temperature.

titles of CO (spectra b-h) a terminal CO species (L) at  $2103\text{ cm}^{-1}$  develops; as the terminal  $2103\text{ cm}^{-1}$  CO species develops, systematic changes occur in the  $1979\text{--}1995\text{ cm}^{-1}$  region. In addition, a small band at  $1883\text{ cm}^{-1}$  is evident at the highest CO coverages.

Although the spectral developments shown in Figure 2 have been obtained by cooling the Pd/SiO<sub>2</sub> surface to 80K, we have shown that species L may also be formed at 300K at CO pressures of several hundred Torr. This behavior is consistent with species L having a fairly low heat of adsorption.

Subtraction of the spectra in Fig. 2 yields a set of difference spectra shown in Fig. 3. It may be seen that as the  $2103\text{ cm}^{-1}$  band develops at 80K, there is a loss of intensity at  $1979\text{ cm}^{-1}$  (B<sub>1</sub>) and a concomitant gain in intensity at  $1995\text{ cm}^{-1}$  (B<sub>2</sub>). These changes, as judged by the peak absorbances, are accurately linear functions of each other (Fig. 4), suggesting that a simple stoichiometric process occurs. It is also observed, Fig. 5, that the B<sub>1</sub> + B<sub>2</sub> conversion involves an isosbestic point. This strongly suggests that a simple stoichiometric process is involved, rather than some sort of frequency shift as a consequence of increasing CO coverage.

Further insight into the nature of the stoichiometric process has been obtained using isotopically labeled <sup>13</sup>CO (designated \*) as the species used to populate L\* - CO at 80K on top of a <sup>12</sup>CO layer produced at 300K. The results of this experiment are shown in Fig. 6, and a surprising feature is noted. The adsorption of L\* - CO induces the formation of L - CO. The <sup>12</sup>CO - L species produced by <sup>13</sup>CO adsorption can only arise from preadsorbed <sup>12</sup>CO-B<sub>1</sub> species.

Detailed investigation of this B<sub>1</sub> + L conversion suggests that about 2B<sub>1</sub> + 2L occur for each L\* - CO adsorbed. The stoichiometric relationship induced by L - CO adsorption causing 2B<sub>1</sub> + 2L is shown in Figure 7, where isotopically labeled CO has been employed in separate experiments as B<sub>1</sub> or as L. After a small correction is made for the experimentally determined difference in extinction coefficient for <sup>13</sup>CO(ads) compared to <sup>12</sup>CO(ads), it may be seen that the stoichiometry 2B<sub>1</sub> + L + 3L is closely verified.

A schematic one-dimensional model of the process is illustrated in Fig. 8. Here it is envisioned that the process 4B<sub>1</sub>+L + 3L+2B<sub>2</sub> is occurring. An electronic model suggests that this stoichiometric species conversion process may be due to the fact that the electron acceptor capacity of an ensemble of 2B<sub>1</sub> + L exceeds the donor capacity of the 3 Pd sites; a conversion to 3L reduces the total acceptor capacity of the CO ensemble to a point where the donor capacity of the 3 Pd sites is not exceeded. These processes are entirely reversible upon warming the Pd surface to 300K.

The average Pd crystallite size, measured by CO chemisorption uptake is about 75Å. The stoichiometric effect seen here is surprising for crystals of this size, and must indicate that a local picture of CO chemisorption applies to these small Pd crystals, in agreement with metal ensemble ideas of Sachtler(22). It is very instructive to compare the results shown above for Pd/SiO<sub>2</sub> surfaces with similar measurements made on Pd(111) using reflection IR methods(20). As shown in Fig. 9, a close similarity of CO species development occurs in comparing results with Fig. 2 for Pd/SiO<sub>2</sub>. In both cases, four carbonyl stretching bands are seen at saturation coverages, differing by only a few  $\text{cm}^{-1}$  in frequency in comparing

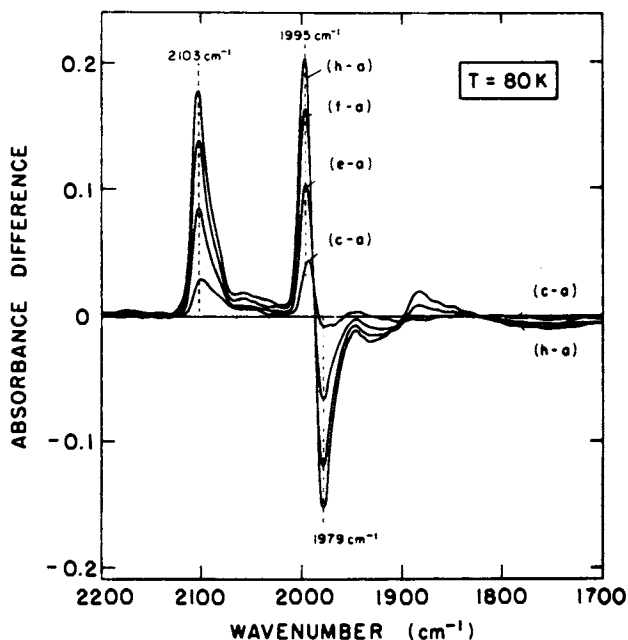


Figure 3. Difference spectra for CO chemisorption on Pd/SiO<sub>2</sub> at low temperature.

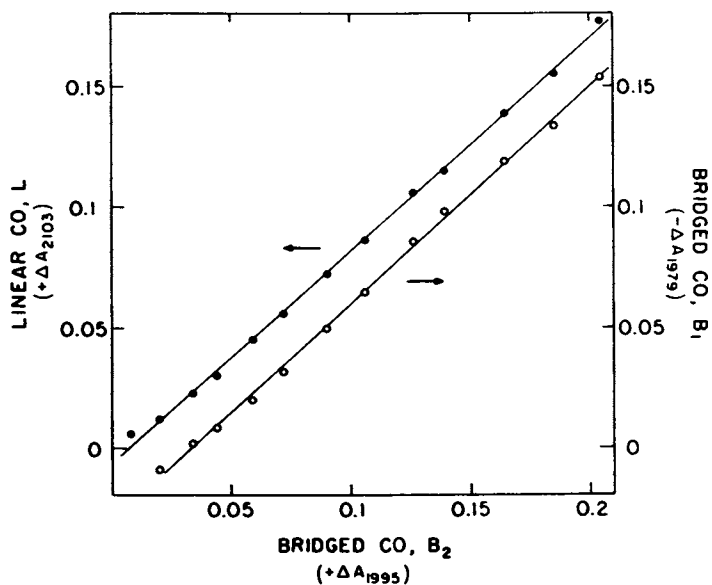


Figure 4. Evidence for stoichiometric interconversion of adsorbed CO species.

In Catalyst Characterization Science; Deviney, M., et al.; ACS Symposium Series; American Chemical Society: Washington, DC, 1985.

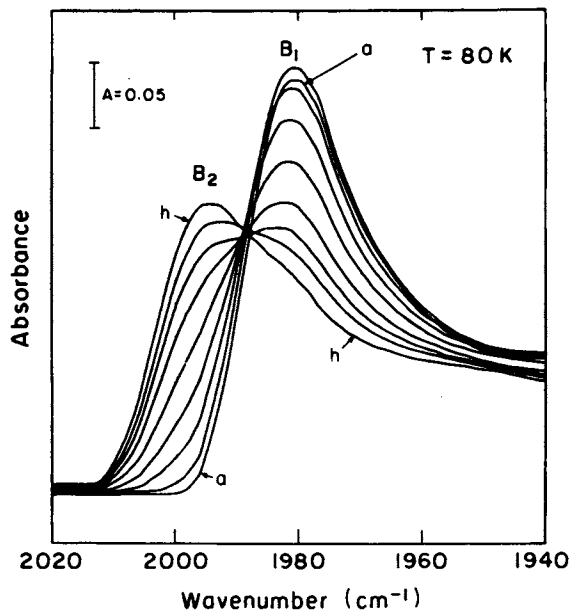


Figure 5. Expanded view of  $B_1 \rightarrow B_2$ -CO conversion as L-CO adsorbs.

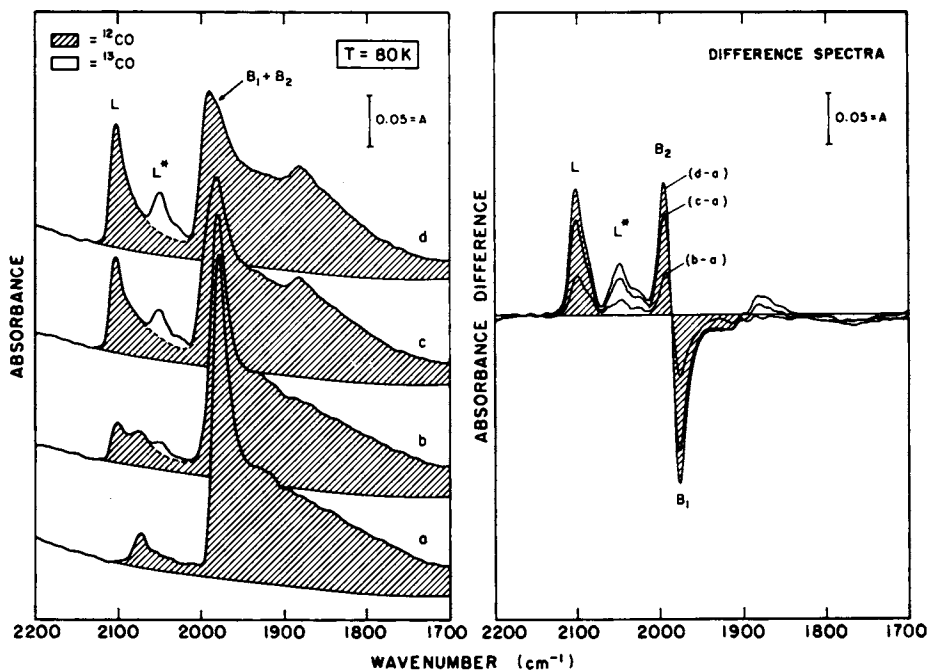


Figure 6. Direct evidence for bridged-to-linear CO conversion -- isotopic CO experiments.

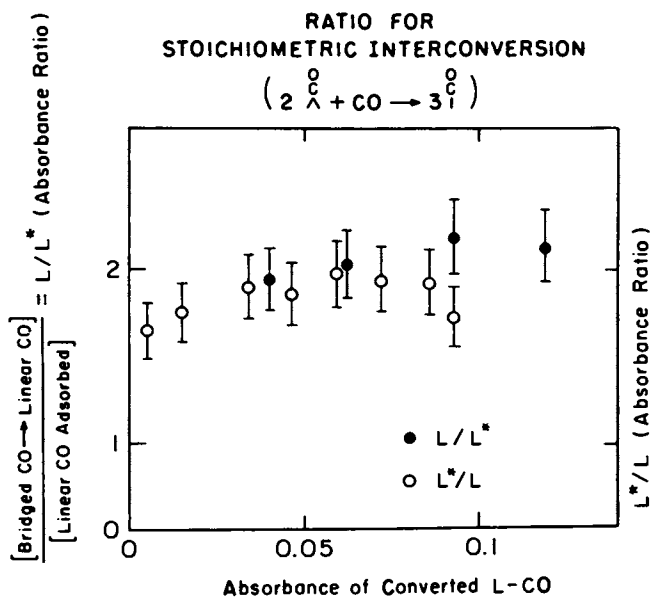


Figure 7. The stoichiometric relationship induced by L-CO adsorption causing  $2B_1 \rightarrow 2L$ .

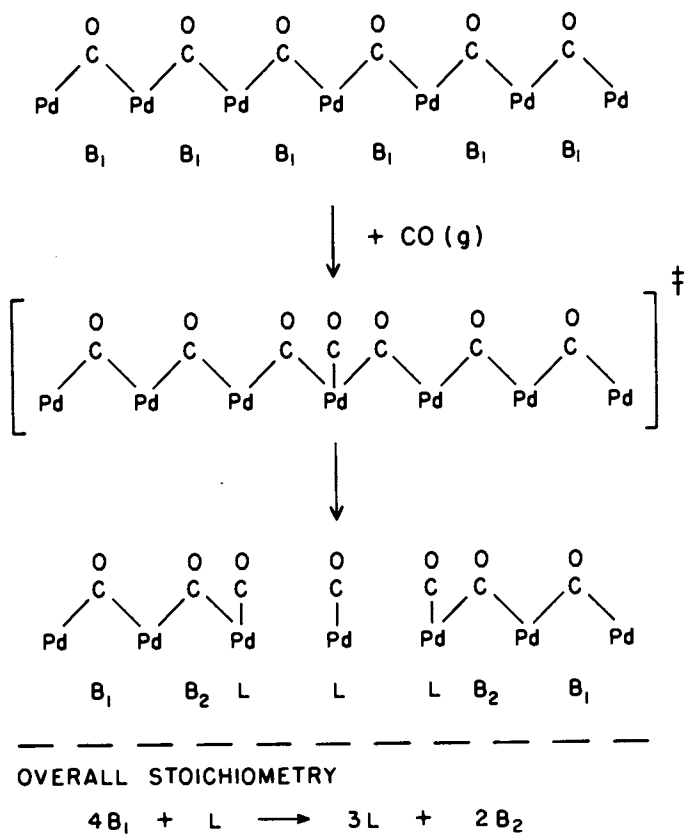


Figure 8. Schematic one-dimensional model for bridged-to-linear CO species conversion process.

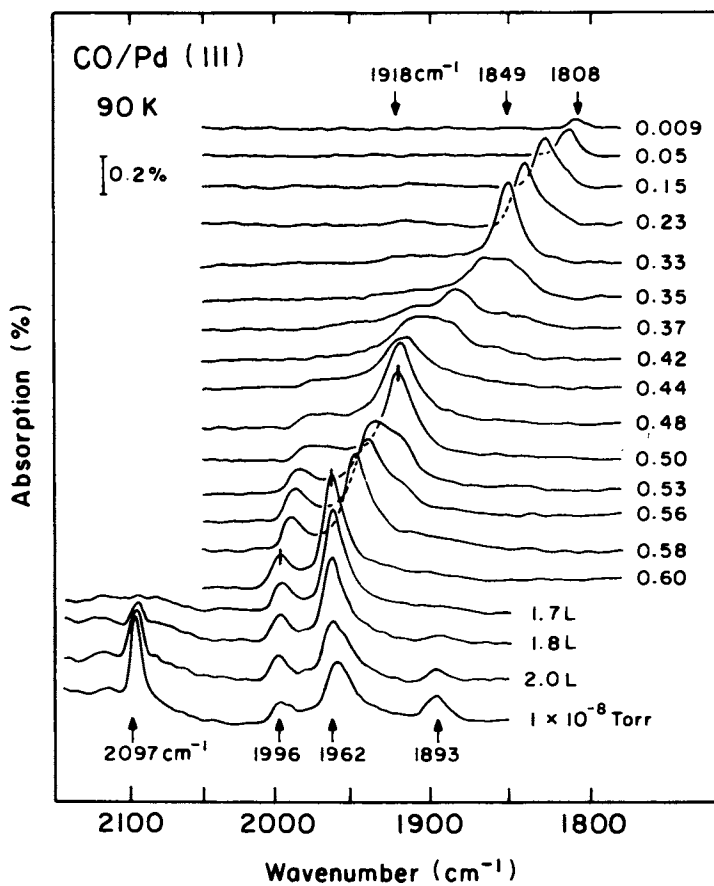


Figure 9. CO chemisorption on Pd(111).

Pd/SiO<sub>2</sub> with Pd(111). Also, the order of development of the 2103 cm<sup>-1</sup> band and the 1883 cm<sup>-1</sup> band (Fig. 2) resembles the behavior on Pd(111). However, Pd(111) shows little or no evidence for the stoichiometric 2B<sub>1</sub> + L + 3L process. This could be due to the presence of longer range order on the single crystal than on the Pd particles, leading to processes more akin to two dimensional phase transitions on the Pd(111) crystal surface, rather than a more local species conversion on the small metal crystallites.

We have studied the stoichiometric conversion process depicted in Fig. 8 at a temperature of 300K under high CO pressures. The conversion process is observed at 300K, but the B<sub>1</sub> + B<sub>2</sub> conversion is less sharp than at 80K, and appears to yield a shift in C-O frequency rather than a discrete conversion from one species to another. This is probably due to a thermal averaging effect involving CO conversion from one species to another at the higher temperature. Such effects have recently been reported from <sup>13</sup>CO + Pt/Al<sub>2</sub>O<sub>3</sub> using NMR techniques(23).

#### The Physical Adsorption of CO on SiO<sub>2</sub> - Observation of Bonding and

Dynamics of Physisorbed Species by IR Spectroscopy(10). We have utilized the particular design characteristics of the infrared cell in Fig. 1 to study the IR spectrum of physically adsorbed CO on SiO<sub>2</sub> surfaces under relatively high equilibrium CO pressures ranging from 10<sup>-5</sup> Torr to 800 Torr. This is accomplished by using 1/2 of the CaF<sub>2</sub> support plate to hold the SiO<sub>2</sub> sample; the second 1/2 plate remains uncovered. Subtraction of the spectra measured on the two sides permits an exact cancellation of the CO gas phase spectrum. Spectral developments in the carbonyl stretching region are shown in Fig. 10. Initially a band at 2157 cm<sup>-1</sup> (species A) develops with a small shoulder at 2140 cm<sup>-1</sup> (species B). As CO coverage increases the 2140 cm<sup>-1</sup> band overtakes the 2157 cm<sup>-1</sup> band and finally the 2157 cm<sup>-1</sup> band begins to shift to lower frequency and to diminish in intensity. Parallel studies of the behavior of the isolated - OH bonds on SiO<sub>2</sub> surfaces indicate that species A is in fact hydrogen-bonded to Si-OH groups with a bond energy of 2.7 kcal/mole<sup>-1</sup>; complete CO complexation may occur, producing an associated - OH band about 100 cm<sup>-1</sup> below the isolated Si-OH frequency as shown in Fig. 11. We believe that the most reasonable structural picture for the complex is SiOH...CO; here the 5σ (slightly antibonding) molecular orbital located primarily on the carbon end of CO donates charge to the proton, resulting in an increase in CO frequency compared to gas phase CO.

A deconvolution procedure to separate carbonyl spectra of species A and species B has been performed, and it has been shown that species B is associated with rotational wings above and below 2140 cm<sup>-1</sup>. These wings indicate that species B undergoes librational and rotational motions; it is undoubtedly very much like CO(ℓ), as shown by the comparison made in Fig. 12. Here the spectrum of a freely rotating CO(g) molecule at 80K is compared to CO(ℓ), also at 80K. In the liquid, the P and R rotational fine structure becomes broadened into rotational wings. In addition, the missing Q branch in CO(g) is observed in CO(ℓ) at about 2140 cm<sup>-1</sup>. Ewing(24) has postulated that the width of the Q branch in CO(ℓ) is due to the population of low-lying librational modes for CO molecules in their



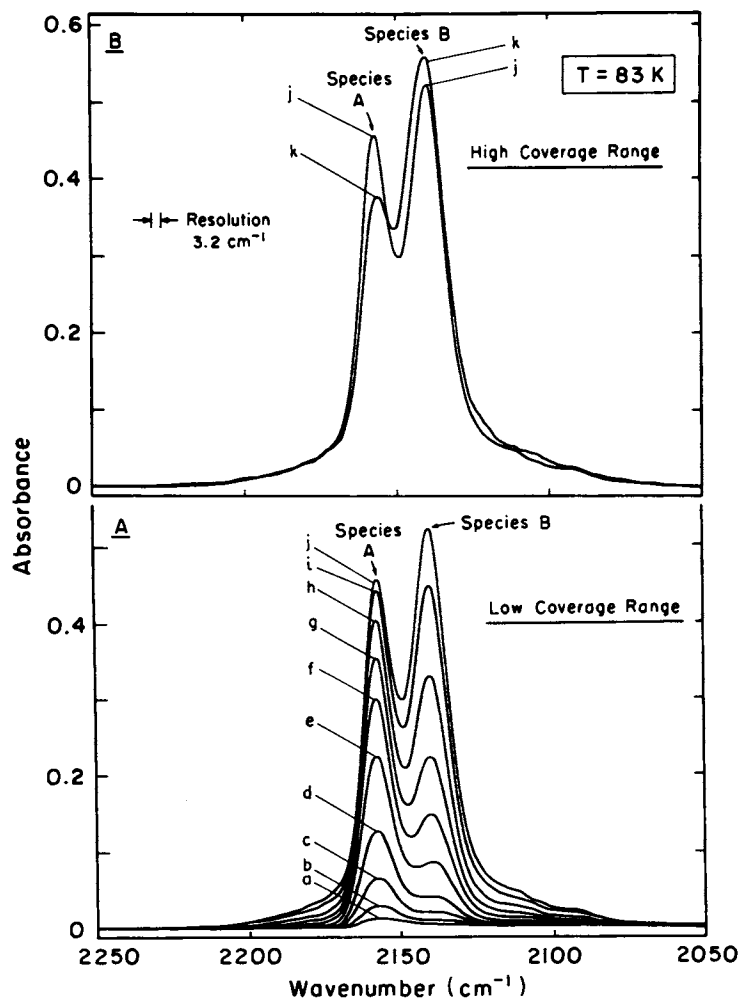


Figure 10. Development of IR spectra for two physisorbed CO species on  $\text{SiO}_2$  for increasing  $P_{\text{CO}}$ .

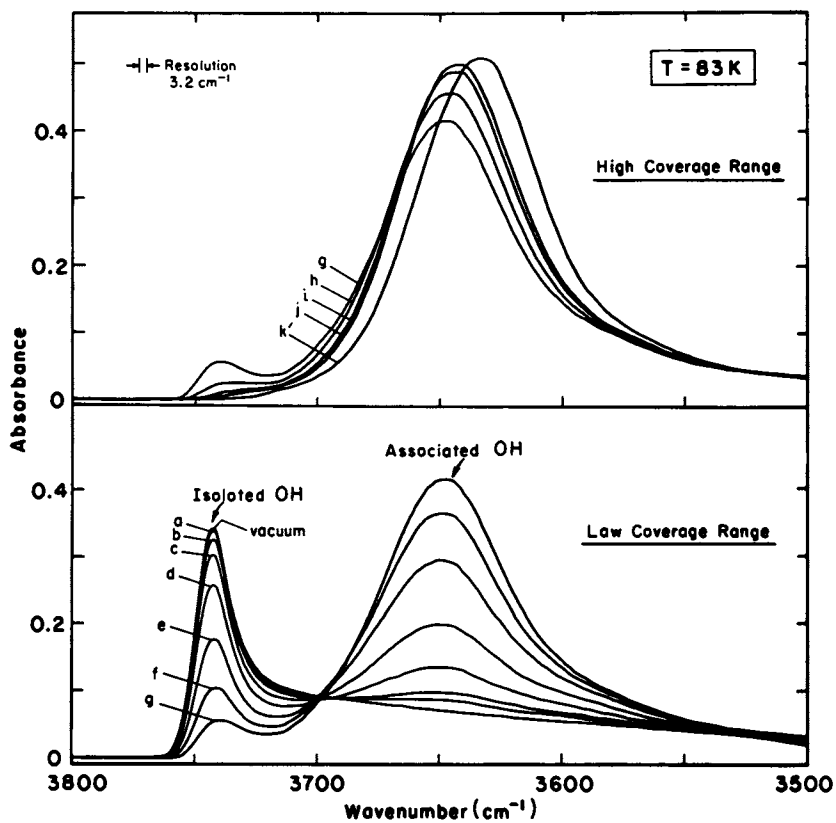


Figure 11. Influence of CO physisorption on surface SiOH groups.

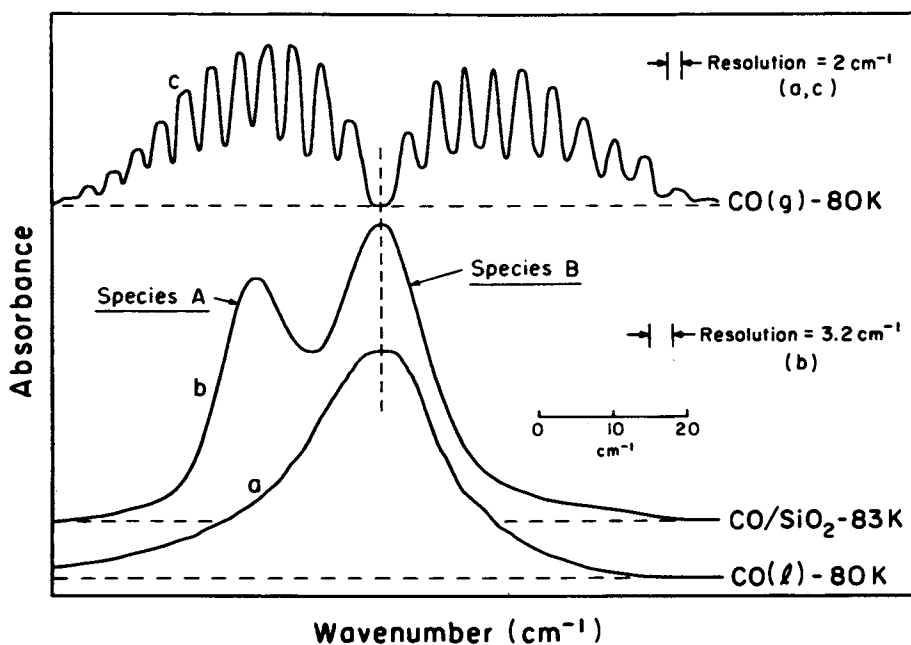


Figure 12. IR lineshape comparison for various states of CO.

liquid cages. Above rotational quantum number  $j = 4$ , the CO molecules rotate at energies above the rotational barrier present in the liquid, and these slightly hindered rotors contribute intensity to the wings.

It is instructive to examine the relative wing intensity to the central band intensity for CO species B as a function of increasing CO coverage in this physisorption system. A plot of both the P and R wing intensities relative to the intensity of the center band is shown in Fig. 13 over the full range of physisorbed CO coverage. It is observed that the relative intensity in the wings rises throughout the full range of coverage, but that this occurs in two stages. In the first stage at low  $P/P_0$  values, SiOH $^{\delta+}$ ...CO complexes are being formed in addition to small quantities of species B. The average electrostatic field due to free OH groups on the surface is decreasing due to hydrogen bond formation at the polar centers, and, on the average, an enhancement of the freedom of rotation of the CO dipoles forming species B will occur as CO coverage increases. At about  $P/P_0 = 0.03$ , all free OH groups have been complexed, and a short region of constant relative wing intensity is reached. Above  $P/P_0 = 0.03$ , liquid-like CO begins to fill the surface appreciably and these CO molecules act as a dielectric screen between SiOH...CO polar groups and additional CO rotors.

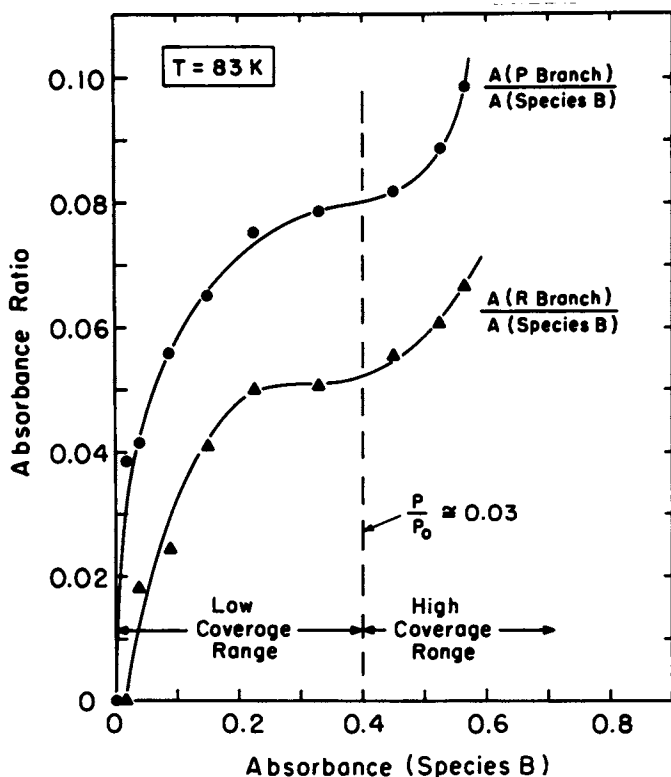


Figure 13. Relative CO rotor absorbances for increasing coverage.

Thus in this second stage, the relative wing intensity begins again to increase as species B grows in coverage. In Fig. 12 a comparison of relative wing intensity for species B to that for CO( $\ell$ ) indicates that the hindrance to rotation present in the adsorbed layer exceeds that in a thick CO( $\ell$ ) layer.

### Summary

In this paper it has been shown that IR spectroscopy remains one of the most incisive tools for the study of both strong and weak bonding at surfaces. In addition to being able to study surface species structure in the chemisorbed layer, it is possible to obtain dynamical information about more weakly-bound adsorbates as they librate and rotate on the surface. These motions are controlled by local electrostatic forces due to polar surface groups on the surface.

The versatile IR method may be extended to extremes of both temperature and pressure as a probe of adsorption and reaction processes on surfaces. The extension of IR spectroscopy to the study of weakly-bound surface species at low temperatures opens up the possibility of stabilization of transient surface species which are involved in surface chemistry at high temperatures.

### Acknowledgments

The authors wish to acknowledge support of this work by the 3M Science Research Laboratory and the Corporate Research Laboratory. Special thanks go to Dr. Allen Siedle for helpful discussions regarding the donor-acceptor model for CO chemisorbed on Pd, and to Dr. Mark Albert for discussions regarding the hydrogen bonding of CO.

### Literature Cited

1. Yaroslavskii, N. G.; Terenin, A. N. Dokl. Akad. Nauk SSSR, 1949, 66, 885.
2. Eischens, R. P.; Pliskin, W. A. Adv. in Catalysis 1956, 9, 662.
3. Little, L. H. "Infrared Spectra of Adsorbed Species"; Academic, London, 1966.
4. Hair, M. L. "Infrared Spectroscopy in Surface Chemistry"; M. Dekker, New York 1967.
5. Sheppard, N.; Nguyen, T. T.; in "Advances in Infrared and Raman Spectroscopy"; 1978, Vol. 5, pg. 67.
6. Ibach, H.; Mills, D. L., "Electron Energy Loss Spectroscopy and Surface Vibration"; Academic Press, New York 1982.
7. Vannice, A.; Moon, S. H.; Twu, C. C.; Wang, S. Y. J. Phys. E: Sci Instru. 1979, 12, 849.
8. Hicks, R. F.; Kelner, C. S.; Savatsky, B. J.; Hecker, W. C.; Bell, A. T. J. Catalysis 1981, 71, 216.
9. Griffin, G. L.; Yates, J. T. Jr., J. Catal. 1982, 73, 396.
10. Beebe, T. P.; Gelin, P.; Yates, J. T., Jr., submitted, Surface Science.

11. Yates, J. T., Jr.; Duncan, T. M.; Worley, S. D.; Vaughan, R. W. J. Chem. Phys. 1979, 70, 1219.
12. Gelin, P.; Yates, J. T., Jr. Surface Sci. 1984, 136, L1-L8.
13. Gelin, P.; Siedle, A.; Yates, J. T., Jr. J. Phys. Chem., accepted.
14. Palazov, A.; Chang, C. C.; Kokes, R. J. J. Catal. 1975, 36, 338.
15. Eischens, R. P.; Francis, S. A.; Pliskin, W. A. J. Phys. Chem. 1956, 60, 794.
16. Vannice, M. A.; Yang, S. Y. J. Phys. Chem. 1981, 85, 2543.
17. Bradshaw, A. M.; Hoffman, F. Surface Sci. 1978, 72, 513.
18. Hoffman, F. M.; Bradshaw, A. M. Proc. 7th Int. Vac. Congress and 3rd Int. Conf. Solid Surfaces, Vienna, 1977; pg. 1177.
19. Ortega, A.; Hoffman, F. M.; Bradshaw, A. M. Surface Sci. 1982, 119, 79.
20. Ortega, A. Ph.D. Thesis, Free University of Berlin.
21. Madey, T. E.; Yates, J. T., Jr.; Bradshaw, A. M.; Hoffmann, F. M. Surface Sci. 1979, 89, 370.
22. Soma-Noto, Y.; Sachtler, W.M.H. J. Catalysis 1974, 32, 315.
23. Slichter, C. P., Paper EC-1, Detroit APS Meeting, Bulletin of American Physical Society, 1984 29, 332.
24. Ewing, G. E. J. Chem. Phys. 1962, 37, 2250.

RECEIVED June 21, 1985

## Computerized IR Studies of Cobalt-Molybdenum-Aluminum Oxide Hydrodesulfurization Catalysts

J. B. Peri

Research and Development Department, Amoco Oil Company, Naperville, IL 60566

Adsorbed CO and NO were used as probes to investigate the effects of Co concentration and sulfide on the nature and numbers of exposed metal sites on reduced catalysts containing 1 to 6 wt% Co and 8 wt% Mo on three alumina supports. Exposure of Mo ions decreased with increased Co concentration. Exposure of Co ions typically reached a maximum at 2-4% Co. Sulfide decreased exposure of all metal ion sites and increased exposure of reduced metals. Effects of preadsorbed pyridine and 2,6-lutidine, known poisons, on the exposure of metal sites, plus other evidence, indicate that active sites are pair sites which contain reduced Mo and/or Co atoms next to Co and/or Mo ions.

Hydrodesulfurization catalysts containing Mo and a Co "promoter" are important in petroleum refining, but their surface properties remain mysterious (1-8). Better understanding should aid in development of better catalysts. Most applicable physical-chemical surface techniques have been used for characterization of these catalysts (4-8). Many structural variations exist, depending on composition, preparation, and pretreatment. Commercial catalysts typically contain about 8 wt% Mo plus 2-3% Co on an alumina support. They are normally presulfided but, in any case, rapidly become sulfided in use. Infrared studies of adsorbed probe molecules such as CO and NO have long provided information on atoms exposed (coordinatively unsaturated) on the surface of high area catalysts, including, presumably, the sites which are active catalytically (5-9). With computerized spectrometers and such probes, exposed Co and Mo atoms can be independently characterized (5-8). Recent studies of Mo on alumina and silica supports (8,10) provide important background. Infrared studies of simple HDS reactions under reaction conditions are possible, but major problems exist in such work. Until the variables involved are better understood, reliance must be placed mainly on studies of catalysts before and after treatments

simulating actual pretreatment or reaction conditions. The present work was undertaken to improve understanding of these variables.

### Experimental

Catalysts were normally prepared by double impregnation of the alumina support, first with ammonium paramolybdate solution to give 12 wt% MoO<sub>3</sub> (8% Mo) after 500°C calcination, then with cobalt nitrate solution. An "incipient wetness" technique was used to prepare catalysts containing 1 to 6 wt% Co on three alumina supports, Cyanamid Aero 1000, Aero 100, and Filtrol 90. Properties of the aluminas and other chemicals used have been described (5,8). A commercial catalyst (Nalco 477) containing 2.4% Co and 8.7% Mo was used in experiments involving adsorption of nitrogen bases. The pyridine was B & A reagent grade; the 2,6-lutidine, supplied by Aldrich Chemical Co., was redistilled. Both were dried with Linde 5A sieve and distilled under vacuum before use.

The Beckman 4260 spectrometer--Wang 2200VP computer system and general procedures used in infrared study of pressed disks have also been described (5,8). Catalysts were typically reduced by heating in 50 Torr of hydrogen for 1 hr. after evacuation for 15 min. at the reduction temperature, usually 500°C. The Filtrol 90 alumina, which contained 3.5% sulfate as an impurity, gave hydrogen sulfide during reduction to sulfide catalysts prepared on this support (8). Subsequent investigation of other sulfiding procedures justified the validity of this simple approach as a first approximation to normal sulfiding in its effects. The Nalco 477 catalyst was presulfided in flowing hydrogen sulfide (.5%) in hydrogen for 1 hr. at 300°C and reduced in hydrogen at 500°C before final evacuation.

### Results

The Nature of Exposed Co in CoMo Catalysts. Figure 1 shows typical original spectra for NO adsorbed on 2% Co/alumina. Spectra were recorded after reduction at 600°C, after admission of 8 Torr of NO, and again after 5 min. evacuation at 50°C. With the pure alumina the main NO/Co bands were 10 to 20 wavenumbers higher in frequency than those observed when using alumina with sulfate impurity.

Weakly held NO also gave a band near 1980 cm<sup>-1</sup> and strongly-held NO exhibited a shoulder near 1930 cm<sup>-1</sup> not seen on Co/sulfated-alumina.

Figure 2 shows spectra, after background subtraction in absorbance, for <sup>14</sup>NO, <sup>15</sup>NO, and a 50-50 mixture of the two adsorbed on 2% Co/Aero 1000 alumina prerduced at 600°C. Spectra were recorded after admission of 7 Torr of NO and again after 5 min. evacuation. Spectrum d was obtained by subtraction of 1/4 the sum of spectra a and b from spectrum c. Such subtraction, as previously discussed for NO held on Mo ions (5,8), should remove contributions from bands arising from (<sup>14</sup>NO)<sub>2</sub> and (<sup>15</sup>NO)<sub>2</sub> species leaving only those from possible (<sup>14</sup>NO)(<sup>15</sup>NO) species. The position of the bands



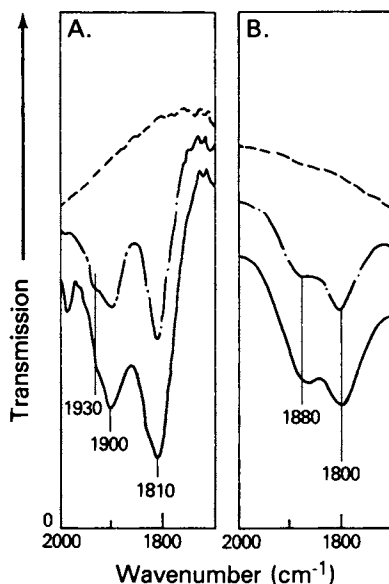


Figure 1. Spectra of NO adsorbed on 2% Co/alumina. Supports were as follows: A. Aero 1000. B. Filtrol 90. Spectra: upper (dashed), background; lower (solid) after addition of NO; middle (dot-dash), after 5 min. evacuation.

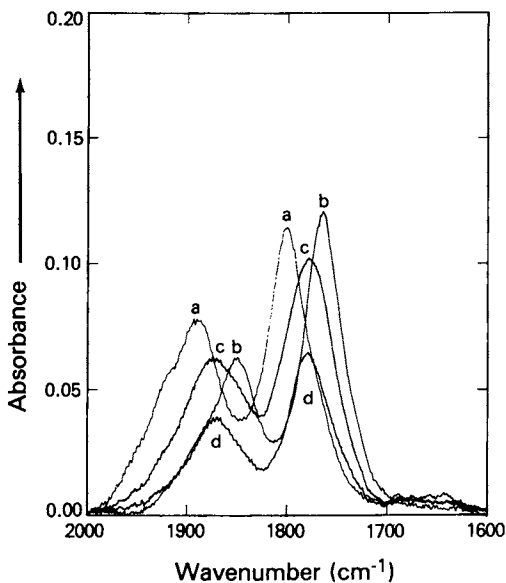


Figure 2. Spectra of NO isotopes adsorbed on 2% Co/Aero 1000 alumina. Spectrum a,  $^{14}\text{NO}$ ; b,  $^{15}\text{NO}$ ; c, 50-50 mixture of  $^{14}\text{NO}$  and  $^{15}\text{NO}$ ; d, after "correction" of c.

of spectrum d, halfway between those of spectra a and b, is understandable only if, as for NO on Mo ions, most of the exposed Co holds two NO molecules, either as dimer or as a dinitrosyl (5,8).

Because Co is evidently not reduced on pure alumina under the conditions used, as indicated by bands for adsorbed CO (shown below), the sites which hold NO are probably  $\text{Co}^{2+}$  ions. As will be seen, the NO bands observed with Co alone on alumina are quite similar to those for NO held on Co in the presence of Mo. In the absence of Mo, however, less exposure of Co is observed. Apparently at least some sites which could otherwise stabilize more-fully coordinated Co are preferentially filled by Mo ions when Mo is also held on the alumina.

Effects of Addition of Co to Mo/Alumina Shown by NO Bands. Figure 3 shows typical spectra for NO on CoMo catalysts containing from 1 to 6 wt% Co prepared by double impregnation of Aero 1000, a pure alumina. The three main bands between 1700 and 1900  $\text{cm}^{-1}$  represent NO adsorbed on Co and Mo ions exposed on the surface after reduction. The band near 1880 shows NO on Co ions, while that near 1710 arises from NO on Mo ions. The central band, near 1800, contains contributions from NO on both Co and Mo ions. By subtraction of a fraction of the absorbance bands for NO on 8% Mo/alumina sufficient to remove the 1710 band, the bands arising from NO on Mo could be eliminated, leaving bands from NO on Co or on other sites different from those normally seen on Mo/alumina.

As shown in Figure 4, these residual bands are similar to bands normally seen for NO on Co/alumina. On Co/alumina, however, a weak band or shoulder would appear at 1920-30  $\text{cm}^{-1}$ . This band may show NO held on ionic Co stabilized on the surface in incomplete octahedral or other special sites. When Mo is also present these sites are apparently no longer available to hold Co ions, probably because they are filled by Mo ions. The slightly negative "bands" seen near 1700  $\text{cm}^{-1}$  probably reflect slight changes in frequencies or shapes of NO bands caused either by direct interaction of Co with Mo ions or by partial occupation by Co of sites that would otherwise be filled by Mo ions.

Figure 5 shows relative intensities of both NO/Co and NO/Mo bands taken from the spectra of Figures 3 and 4. The number of Co sites exposed apparently increases with Co concentration to a broad maximum at about 3% Co and then decreases. The number of exposed ionic Mo sites appears to decrease steadily with increasing Co.

Another series of catalysts was made by coimpregnation, with Co and Mo in the same solution, of Aero 1000 alumina. The spectra (not shown) of NO on these catalysts were quite similar to those shown above except that the bands were only about 65% as intense.

Figure 6 shows spectra of NO adsorbed on a similar series of catalysts having the same concentrations of metals on Filtrol 90 alumina which, as discussed, sulfides the catalyst during subsequent reduction. The effect of sulfide, as on Mo/alumina catalysts (8,10) and as later seen on CoMo catalysts after more-usual sulfiding, was mainly a marked reduction in the intensities of the NO bands. These were roughly a fourth as intense as those on unsulfided catalysts on

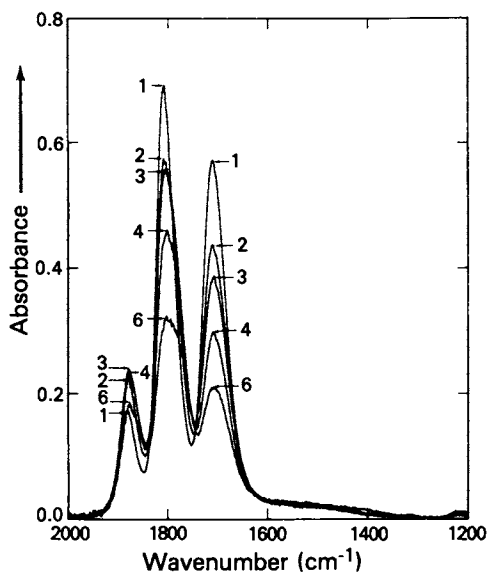


Figure 3. Spectra of NO adsorbed on Co + 8% Mo/Aero 1000 alumina catalysts. Concentrations of Co (wt%) are indicated on spectra.

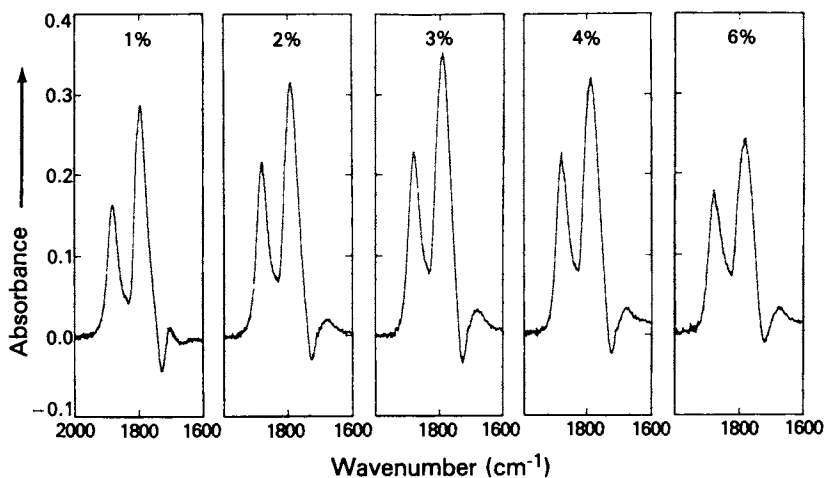


Figure 4. Spectra of NO adsorbed on Co in the presence of Mo obtained by subtraction of NO/Mo bands from the spectra of Figure 3.

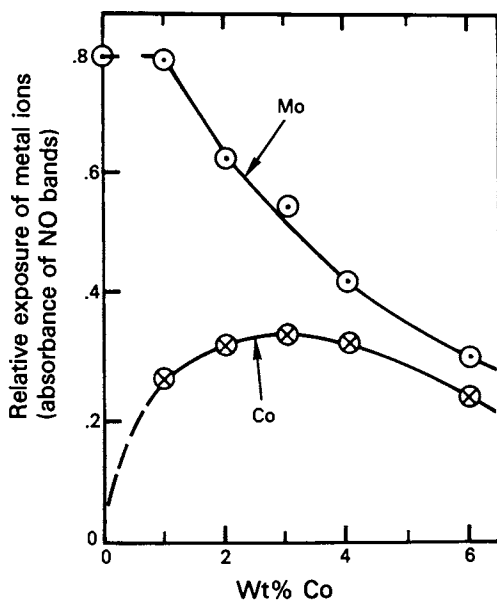


Figure 5. Apparent relative exposure of  $\text{Co}^{2+}$  and  $\text{Mo}^{4+}$  ions on reduced Aero 1000 alumina-supported CoMo catalysts as a function of Co concentration.

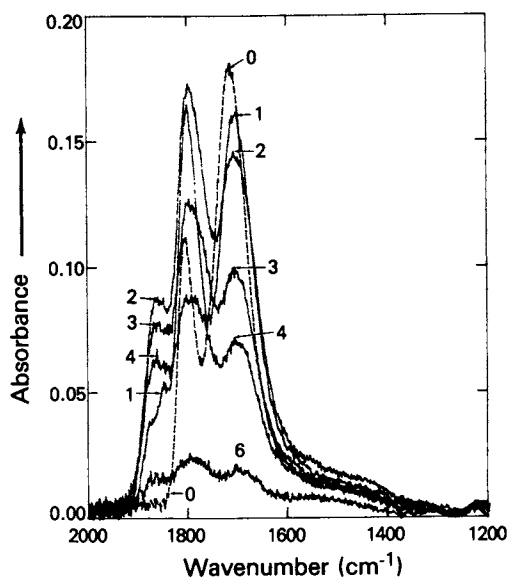


Figure 6. Spectra of NO on Co + 8% Mo/Filtrol 90 alumina. Concentrations of Co (wt%) are indicated on spectra.

pure alumina. They were also slightly lower in frequency and somewhat broader than those seen in the absence of sulfide (Figure 3), evidently reflecting greater heterogeneity of exposed metal sites.

Figure 7 shows bands, obtained like those of Figure 4 by fractional subtraction of the NO bands obtained in the absence of Co. These residual bands did not resemble the bands of NO/Co seen in the absence of Mo as well as did those obtained for the Aero 1000 series. Greater variety in site types, reflecting sulfide neighbors or increased metal-metal interaction, evidently exists on sulfided catalysts.

Plots of the relative intensities of the NO/Co and NO/Mo bands for catalysts made with Filtrol 90 are shown in Figure 8. The features are similar to those of Figure 5. As before, exposure of Co apparently increased to a maximum, at 2% in this case, and decreased at higher Co concentrations. Exposure of Mo again decreased steadily.

#### Effects of Addition of Co to Mo/Alumina Shown by CO Bands.

Figure 9 shows CO adsorbed on CoMo catalysts made on two alumina supports. Most of the CO was weakly-held, being largely removed by evacuation for 5 min. at 50°C. Depending on the extent of sulfiding during reduction, various bands were obtained. In the absence of sulfide, as previously seen on Mo/alumina catalysts (8), only Mo (4+) or Co (2+) ions appear to be exposed after reduction, giving CO bands near 2190  $\text{cm}^{-1}$ . When sulfiding occurs before or during reduction Mo and Co are exposed in lower oxidation states, or even as fully reduced metal atoms. Typically on sulfided samples a strong band, apparently arising from CO on metal sites that are slightly electropositive, is seen around 2100  $\text{cm}^{-1}$ . In Figure 9 this band lies near 2120  $\text{cm}^{-1}$ . On catalysts more-heavily presulfided by more-usual procedures the band was seen nearer 2100  $\text{cm}^{-1}$ . With more Co or with only very slight sulfiding, as seen when Aero 100 alumina was used as the support, CO bands were also seen near 2050  $\text{cm}^{-1}$ , showing the presence of fully-reduced metallic sites, probably Co. Such sites were not seen in the absence of sulfide. The major effect of sulfiding seemed to be the marked increase in electropositive ( $\text{Mo}^{\delta+}$  or  $\text{Co}^{\delta+}$ ) atoms exposed on the surface.

The Effects of Preadsorbed Nitrogen Bases on the Exposure of Co and Mo Sites. Marked differences exist in the poisoning effects of different nitrogen compounds on hydrodesulfurization activity. Such differences between alkylpyridines appear to result from differences in stereochemistry (11). Pyridine is a more effective poison than 2,6-lutidine. To learn whether such poisons selectively block certain exposed metal sites, infrared study was made of NO and CO adsorbed after adsorption and progressive desorption of these nitrogen compounds on a presulfided commercial CoMo catalyst (Nalco 477) reduced at 500°C. Contrary to expectation, because NO

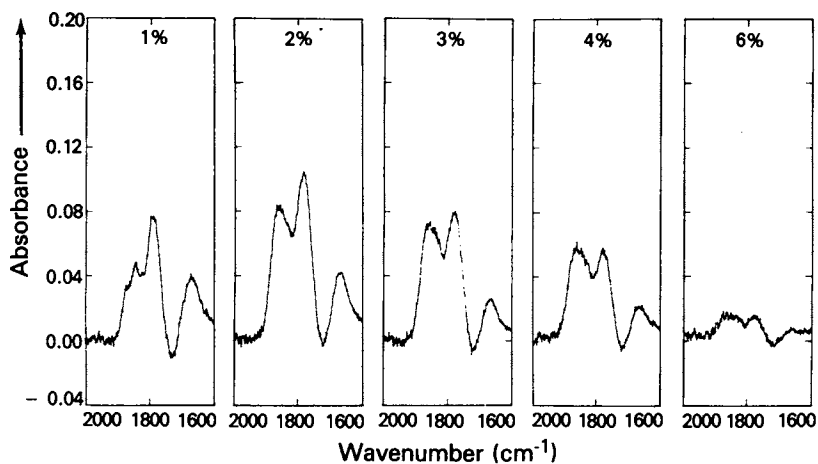


Figure 7. Spectra of NO adsorbed on Co on sulfided CoMo/alumina obtained by subtraction of NO/Mo bands from the spectra of Figure 6.

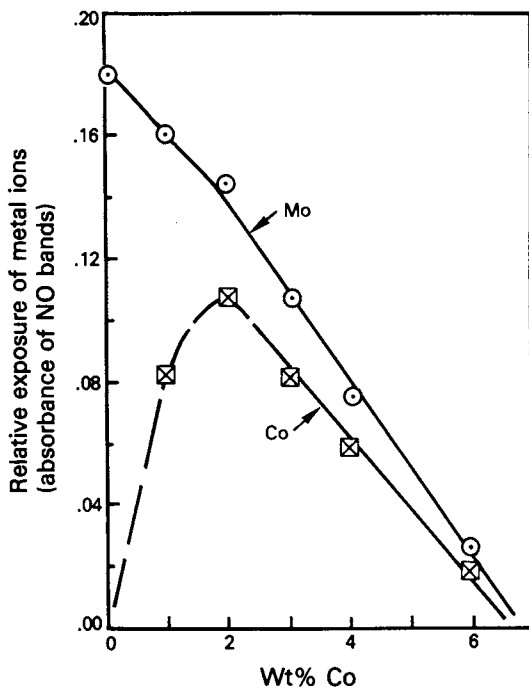


Figure 8. Apparent relative exposure of  $\text{Co}^{2+}$  and  $\text{Mo}^{4+}$  ions on reduced Filtrol 90-supported CoMo catalysts as a function of Co concentration.

poisons certain reactions on Mo/alumina catalysts (6,12,13), no major differences were seen in the blocking of sites for adsorption of NO. Both bases were held strongly by the ionic metal sites and were desorbed to approximately the same extent by heating in vacuum at progressively increased temperatures.

Adsorption of CO showed greater differences in the abilities of the nitrogen bases to block metallic sites. In these experiments excess nitrogen base was added, after presulfiding, reduction, and evacuation and then progressively desorbed by heating in vacuum at progressively higher temperatures with intervening additions of CO.

As indicated in Figure 10, pyridine was much more effective than 2,6-lutidine in blocking the "acidic" metal sites which normally adsorb CO to give a band near  $2100\text{ cm}^{-1}$ . Pyridine was, in fact, apparently held more strongly than 2,6-lutidine on the entire range of slightly electropositive sites on which CO would otherwise give bands in the region from 2050 to 2100 wavenumbers.

### Discussion

Although not pinpointing active sites for hydrodesulfurization, results of this study restrict the range for speculation on their nature and numbers. Review of the many hypotheses which have been proposed can be found elsewhere (1-4).

Promotional effects of sulfide can evidently be explained, because exposure of reduced metals is increased on reduced sulfided catalysts. The role of cobalt is less clear. It is normally not fully reduced. It apparently does not promote greater exposure of Mo in any form detected, either in the presence or absence of sulfide. On the contrary, it evidently only decreases the concentration of exposed Mo atoms, although, at concentrations typically used, most Mo atoms are unaffected by Co. Either some property of Co alone or some local cooperative effect of adjacent Co and Mo must explain promotion. Simple mechanical mixtures will not give the synergism observed, however (1-4).

Cooperative effects involving paired Co and Mo sites thus seem to offer the most likely explanation for promotion by Co. Paired ionic Co and Mo sites might reasonably reach a maximum concentration where maximum exposure of Co ions is observed, although the numbers of such paired sites might be considerably lower than that of exposed Co ions. When catalysts are sulfided and reduced additional types of exposed metal sites become possible members of pair sites, however. Ionic Co and Mo sites on sulfided catalysts appear similar to those on unsulfided catalysts, but less numerous. Despite this, the catalytic activity is increased by sulfiding. Greater efficiency for sulfided ionic sites has previously been postulated to explain higher activity of sulfided Mo/alumina (4), but evidence was not then available to show the substantial exposure of  $\text{Mo}^{\delta+}$  on sulfided and reduced catalysts (8).

At least one member of an active pair should probably exist to a greater extent on sulfided than on unsulfided catalysts. Exposed reduced metal sites, either slightly electropositive or uncharged, shown by infrared to exist appreciably only on reduced sulfided catalysts, thus appear to be likely members of active pair sites.

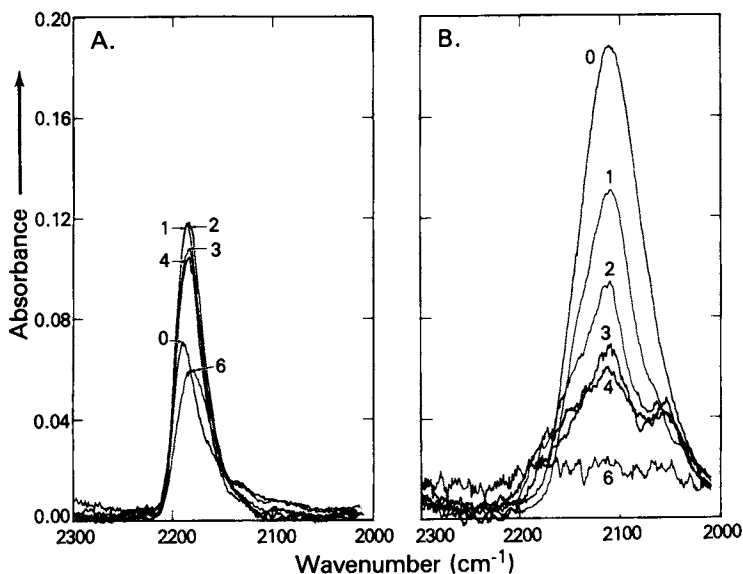


Figure 9. Spectra of CO adsorbed on Co+ 8% Mo/Al<sub>2</sub>O<sub>3</sub> catalysts supported on (A.) Aero 1000 alumina and (B.) Filtfol 90 alumina. Co concentrations as indicated on spectra.

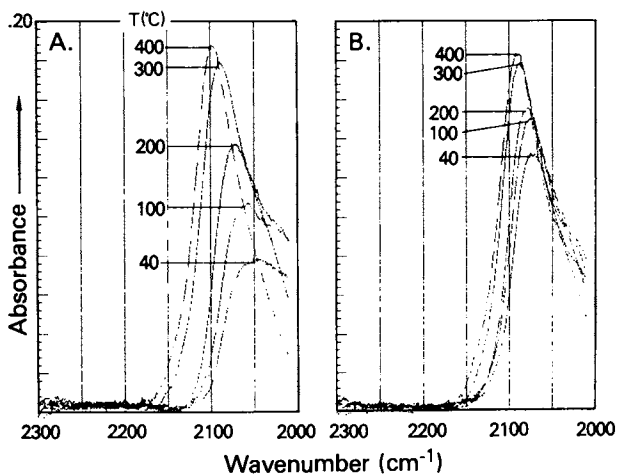


Figure 10. Spectra of CO adsorbed on CoMo/Al<sub>2</sub>O<sub>3</sub> after partial desorption of preadsorbed nitrogen base. A. CO spectra (8 Torr) after desorption of preadsorbed pyridine at the temperatures indicated on the spectra. B. CO spectra as above after progressive desorption of 2,6-lutidine.



On Mo/alumina catalysts the reduced metal pair member would necessarily be Mo, probably slightly electropositively charged. When Co is also present the reduced metal could be either Mo or Co. The spectra show, however, that the (electropositive) Mo sites giving a CO band near  $2120\text{ cm}^{-1}$  decrease in number as Co is added (Figure 9). The reduced metal component of a possible active pair site is thus probably more fully reduced than these sites.

An exposed Mo ion seems likely as the other member of an active pair site. Such ions have been postulated as active sites on

Mo/alumina (4). Exposed  $\text{Co}^{2+}$  ions could also serve as members of active pairs, however. This possibility gains some support from the observation that optimum Co concentrations on CoMo catalysts maximize exposure of  $\text{Co}^{2+}$  (and possibly of  $\text{Co}^{6+}$ ) but not of fully-reduced Co. The common feature in all these pair sites could be exposed, reduced, slightly electropositive metal atoms directly adjoining metal cations.

Figure 11 shows schematically how such sites may be formed on Mo/alumina or CoMo/alumina catalysts. The pair site contains a reduced metal next to an acidic metal cation, either Co or Mo. Presumably this dual site can remove S, leaving an olefin or aromatic molecule attached to the cation. This is then hydrogenated by hydrogen from the reduced metal component of the site.

The nature of such sites seems consistent with the behavior shown in the pyridine and lutidine poisoning experiments. The acidic nature of the reduced metal sites which hold the nitrogen bases seems established. Difference in the extent to which the exposed metal cation is accessible to the nitrogen atom of the organic nitrogen base could explain the selective poisoning seen with different substituted pyridines. Presumably the cations in an active pair are somewhat less accessible than most exposed Co and Mo cations, which, because they normally hold two NO molecules, are probably exposed in incomplete tetrahedral sites.

The activity shown by unsupported Mo sulfide or Co molybdate catalysts (4) is not inconsistent with the nature of the active sites postulated. The essential pair members and interactions could all exist on unsupported catalysts. Either Co or Mo alone can cause desulfurization. The support serves mainly to increase the amount of exposed Co and Mo in some desirable configuration.

### Conclusions

Although much progress has been made toward understanding the nature and probable catalytic behavior of active sites on CoMo/alumina catalysts, much obviously remains to be accomplished. Detailed explanation of the acidic character of the reduced metal sites evidently most important in HDS, and presumably in related reactions, must await the increased understanding which should come from studies of simplified model catalysts using advanced surface science techniques. Further progress of an immediately useful nature seems possible from additional infrared study of the variations produced in the exposed metal sites as a result of variations in preparation, pretreatment, and reaction conditions.

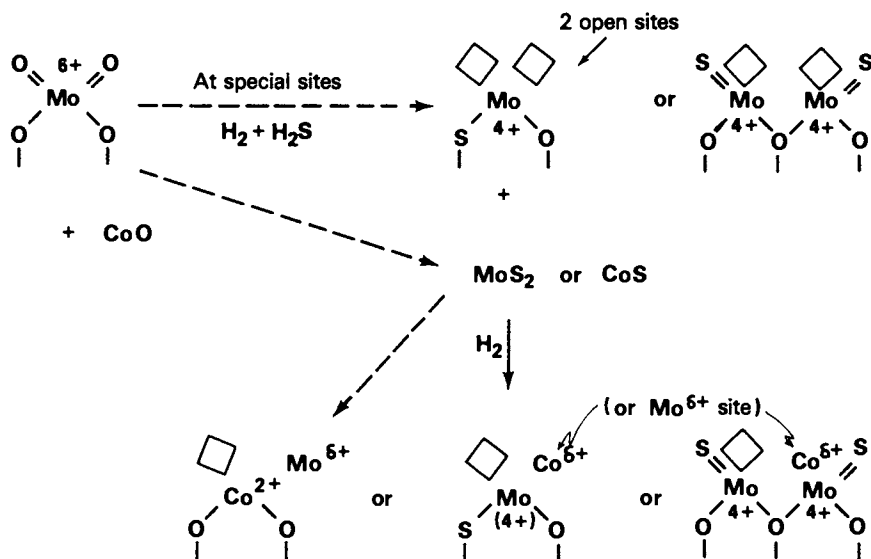


Figure 11. Possible formation of active pair sites on  $CoMo/Al_2O_3$  catalysts.

More effective utilization of the metals in HDS catalysts certainly seems possible, because only a very small fraction of the metal content appears to be usefully exposed on the surface.

#### Literature Cited

1. Gajardo, P.; Declerck-Grimee, R.I.; Delvaux, G.; Olodo, P.; Zabala, J. M.; Canesson, P.; Grange, P.; Delmon, B. "Second International Conference on The Chemistry and Uses of Molybdenum, Oxford, 1976"; Climax Molybdenum Company Ltd., London (1977); pp. 150-154.
2. Declerck-Grimee, R. I.; Canesson, P.; Friedman, R. M.; Fripiat, J. J. J. Phys. Chem. 1978, 82, 889.
3. Delmon, B. "Recent Approaches To The Anatomy and Physiology of Cobalt Molybdenum Hydrodesulfurization Catalysts"; in preprints of Third International Conference on the Chemistry and Uses of Molybdenum, Univ. of Michigan, Ann Arbor, 1979 (Climax Molybdenum Company).
4. Ratnasamy, P.; Sivasanker, S. Catal. Rev.-Sci. Eng. 1980, 22 (3), 401.
5. Peri, J. B. Prepr. Div. Pet. Chem., Am. Chem. Soc. 1978, 23, 1281.
6. Hardee, J. R.; Hightower, J. W. J. Catalysis 1983, 83, 182.
7. Topsoe, N. Y.; Topsoe, H. J. Catalysis 1983, 84, 386.
8. Peri, J. B. J. Phys. Chem. 1982, 86, 1615.
9. Peri, J. B. In "Infrared Spectroscopy in Catalytic Research"; J. R. Anderson and M. Boudart, Eds.; CATALYSIS-SCIENCE AND TECHNOLOGY Vol. 5, Springer-Verlag, Berlin, Heidelberg, New York, 1984; pp. 172-220.
10. Valyon, J.; Hall, W. K. J. Catalysis 1983, 84, 216.
11. Gutberlet, L. C.; Bertolacini, R. J. I. & E.C. Product Research & Development 1983, 22, 246.
12. Lo Jacono, E. A.; Hall, W. K. J. Catalysis 1980, 64, 150.
13. Howe, R. F.; Kemball, C. J. Chem. Soc., Faraday Trans. 1 1974, 70, 1153.
14. Kazusaka, A.; Howe, R. F. J. Catalysis 1980, 63, 447.

RECEIVED March 27, 1985

## Fourier Transform IR Studies of Surface Adsorbates and Surface-Mediated Reactions

David D. Saperstein<sup>1</sup> and William G. Golden<sup>1</sup>

IBM Instruments, Inc., San Jose, CA 95110

Recent work in our laboratory has shown that Fourier Transform Infrared Reflection Absorption Spectroscopy (FT-IRRAS) can be used routinely to measure vibrational spectra of a monolayer on a low area metal surface. To achieve sensitivity and resolution, a pseudo-double beam, polarization modulation technique was integrated into the FT-IR experiment. We have shown applicability of FT-IRRAS to spectral measurements of surface adsorbates in the presence of a surrounding infrared absorbing gas or liquid as well as measurements in the UHV. We now show progress toward in situ measurement of thermal and hydration induced conformational changes of adsorbate structure. The design of the cell and some preliminary measurements will be discussed.

Vibrational spectroscopic studies of heterogeneously catalyzed reactions refer to experiments with low area metals in ultra high vacuum (UHV) as well as experiments with high area, supported metal oxides over wide ranges of pressure, temperature and composition [1]. There is clearly a need for this experimental diversity. UHV studies lead to a better understanding of the fundamental structure and chemistry of the surface-adsorbate system. Supported metals and metal oxides are utilized in a variety of reactions. Their study leads to a better understanding of the chemistry, kinetics and mechanisms in the reaction. Unfortunately, the most widely used technique for determining adsorbate molecular structure in UHV, EELS [2], is incompatible with non-UHV environments, and the photon techniques, IR and Raman, are not usually of sufficient sensitivity to measure routinely a monolayer on a low area metal.

Our goal is to bridge the gap between studies of well-characterized surfaces in UHV and studies of high pressure, complex, heterogeneously catalyzed reactions. To achieve this goal, we

<sup>1</sup>Current address: San Jose Research Laboratory, IBM Corporation, San Jose, CA 95193

have been investigating several FT-IR techniques to study adsorbate-gas or adsorbate-liquid interfaces. Fourier Transform Infrared Reflection Absorption Spectroscopy (FT-IRRAS) combines an FT-IR with the grazing angle, reflection-absorption experiment [3] and can be used to measure the vibrational spectrum of a monolayer on a metal surface [4,6,9,10,13-16,19]. Using a double modulation, pseudo-double beam approach to enhance the dynamic range of FT-IRRAS, we have shown monolayer and sub-monolayer sensitivity for adsorbates on low area metals [4]. These studies were performed with most of the FT-IR beam path open to air to show our spectral discrimination of the surface adsorbates from the isotropic gas. Figure 1 shows the spectrum of six monolayers of cadmium arachidate on Ag, deposited by a Langmuir-Blodgett technique [5], taken with this equipment. The inset, a single beam spectrum, shows the level of water vapor and carbon dioxide that is effectively eliminated. Using this technique with appropriate optical modifications, we have shown that spectra of carbon monoxide chemisorbed on Pt in UHV can be measured with sub-monolayer sensitivity [6]. The expected dipole-dipole shift in frequency with coverage [7] is also observed. With techniques adapted from FT-IR evolved gas analysis, we have also shown the applicability of the FT-IR to follow reactions catalyzed by supported metal oxides in real time [8].

These studies lay the groundwork for in situ investigations of adsorbates on low area metal surfaces undergoing a physical or chemical change. By combining FT-IRRAS techniques with a temperature controlled cell which can accommodate gas flow over the surface, we are able to produce spectral changes of Langmuir-Blodgett films induced by heat [12] or hydration. The use of this reaction cell is a complement to the experiments which translate [11] a well defined surface between reaction zone and UHV analysis. At this writing we have completed some preliminary measurements, which we report below, using the fixed polarizer technique to assess system performance.

### Experimental Section

FT-IRRAS has been described elsewhere. For details of the appropriate experiment, the reader should refer to ref. 9 for the conventional fixed polarizer, grazing incidence experiment, to ref. 4 or 10 for the polarization modulation addition and to ref. 4 for the polarization/double modulation technique. In order to study low area metal surfaces under reaction conditions, a cell was designed [18] for continuous, in situ, grazing angle IR analysis, fig 2. The sample can be heated or cooled; the chamber can be used at reduced or elevated pressure with or without a gas flowing. The cell can be moved perpendicular to the optical path enabling the light to be reflected from the sample or transmitted only through the gas. It can be used with either fixed polarizer or polarization modulation techniques. Two thermocouples are used to measure cell temperature reproducibly. One is placed directly behind the sample; the other is placed in contact with the outer cell wall 1.5 cm beyond the edge of the sample.

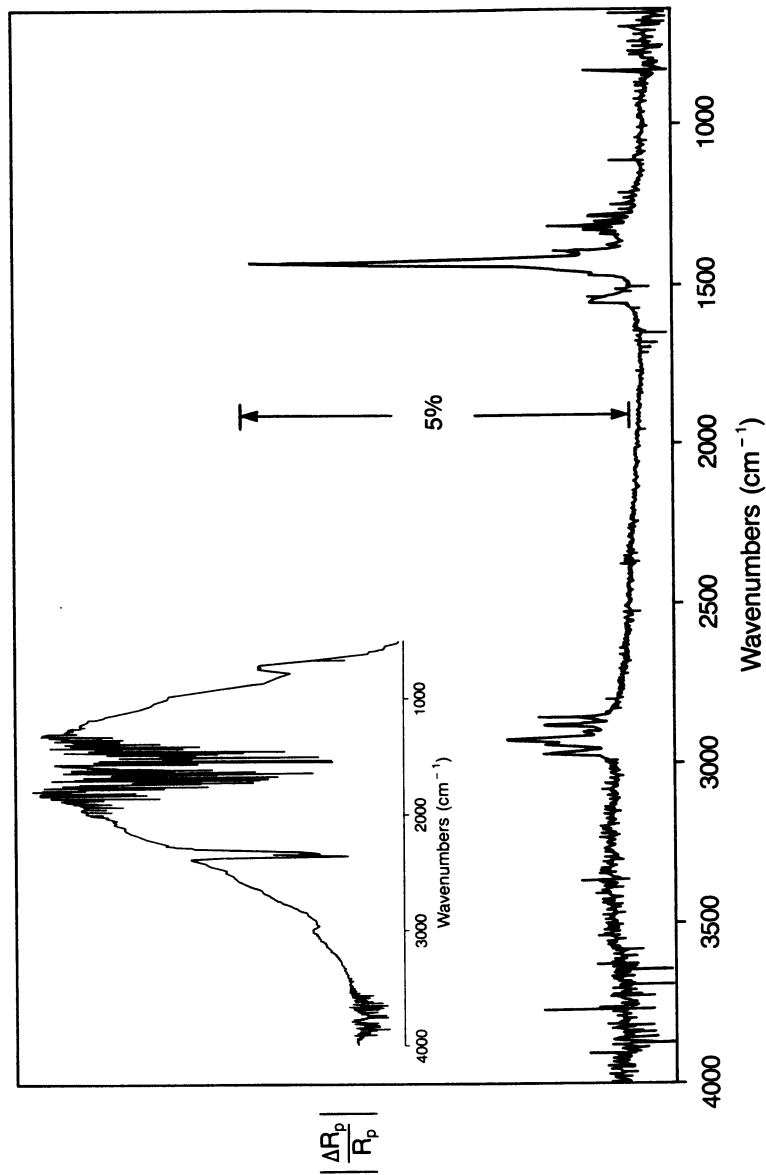


Figure 1. FT-IRRAS double modulation spectrum of six monolayers of Cadmium Arachidate on silver. The inset shows the background water vapor and carbon dioxide present in the measurement. IBM Instruments IR/90 series.

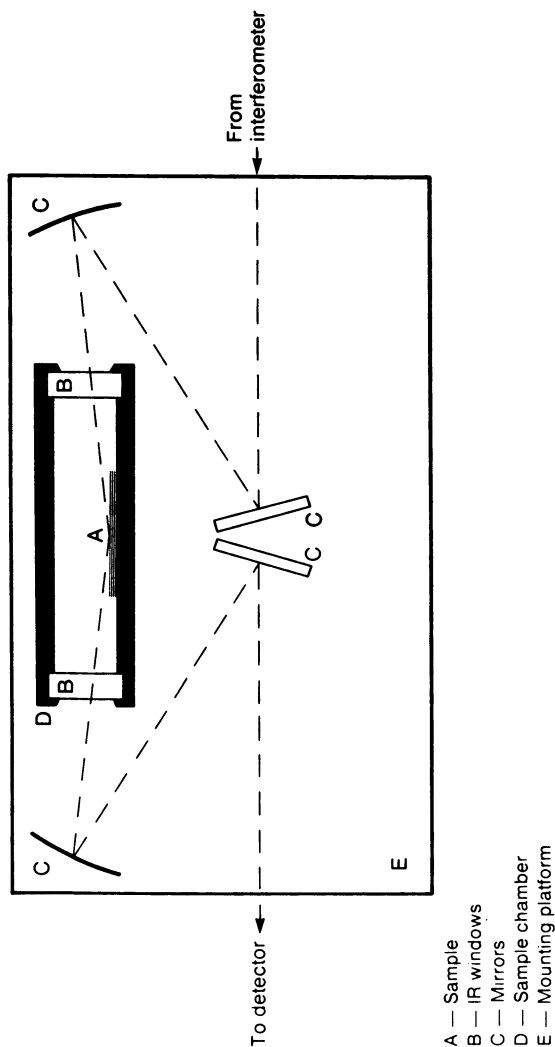


Figure 2. Optical schematic of the chamber for grazing angle measurements. Heaters and one thermocouple are located directly behind the sample (A). Gas inlet and outlet are near the IR transmitting windows (B). The mirrors (C) can be rotated and tilted to maximize signal and eliminate stray light. The entire cell (D) can be translated to change the angle of incidence.

For the work reported here, an IBM Instruments IR/85 with an MCT detector and a gold on silver bromide wire grid polarizer is used. Typically the resolution is set 4  $\text{cm}^{-1}$  with a 1000 scans (6 minutes) or more co-added to reduce the noise signal-to-noise. The polarizer is placed between the interferometer and the cell. When the light at grazing incidence to the sample is polarized parallel (p) to the plane of reflection, defined by the incoming and outgoing light rays, the electric vector perpendicular to the metal is enhanced near the surface [3]. A vibration of a molecule adsorbed on the metal can be observed with p-polarized light if a component of its dipole moment is normal to the metal. When the light is polarized perpendicular (s) to the plane of reflection - parallel to the surface, the electric vector changes by 180 degrees upon reflection and is essentially zero near to the surface [3]. Vibrations of monolayers adsorbed on low area metals are not generally observed with s-polarized light. Away from the surface, the p-polarized and s-polarized components are attenuated to the same extent by an isotropic medium.

Cadmium arachidate [ $\text{Cd}(\text{OOC}-\text{C}_{18}\text{H}_{36}-\text{CH}_3)_2$ ] samples are prepared by a Langmuir-Blodgett (L-B) dipping technique [5] (courtesy of Dr. John Rabolt, IBM Research, San Jose, CA.). The metal films, 0.2 microns thick, are evaporated on to clean glass slides prior to L-B monolayer deposition.

### Results and Discussion:

The study of model monolayers offers the opportunity to test instrument sensitivity. In the case of cadmium arachidate on silver, it is possible to observe a change in the spectrum corresponding to a phase change [12] around 115 degrees C. This spectral change is quite dramatic exhibiting a sizeable increase in both the methylene C-H and the asymmetric carboxylate stretching intensities. Figures 3a-j show a series of spectra, 3000 to 1000  $\text{cm}^{-1}$ , of 2 monolayers of cadmium arachidate on silver in which the sample was first heated to 155 deg C and then cooled to 30 deg C. These monolayers are oriented like a bilayer with the polar carboxylate head of the first monolayer proximate to the metal. The second monolayer is reversed with its methyl group tail proximate to the tail of the first monolayer, and its head pointed away from the metal. Fig. 4a-j shows the same data in expanded form for the C-H stretching region, 3000 to 2800  $\text{cm}^{-1}$ . The observed behavior is not unexpected [13-15] and is reviewed below. At the lowest temperatures, 30 to 75 deg C, we observe changes in the methyl C-H asymmetric stretches, 2960 to 2935  $\text{cm}^{-1}$ , possibly indicating orientational changes in the tail groups. At higher temperatures we observe increases in the methylene band intensities, e.g. 2920 and 2850  $\text{cm}^{-1}$ , which show increasing disorder in the hydrocarbon chain. Only at temperatures above 115 deg C, do we observe substantial intensity increases in the asymmetric carboxylate stretch at 1550  $\text{cm}^{-1}$ . Cadmium arachidate monolayers which are cooled after heating to 125 deg C or more show a partial reordering of the head, carboxylate, and backbone,



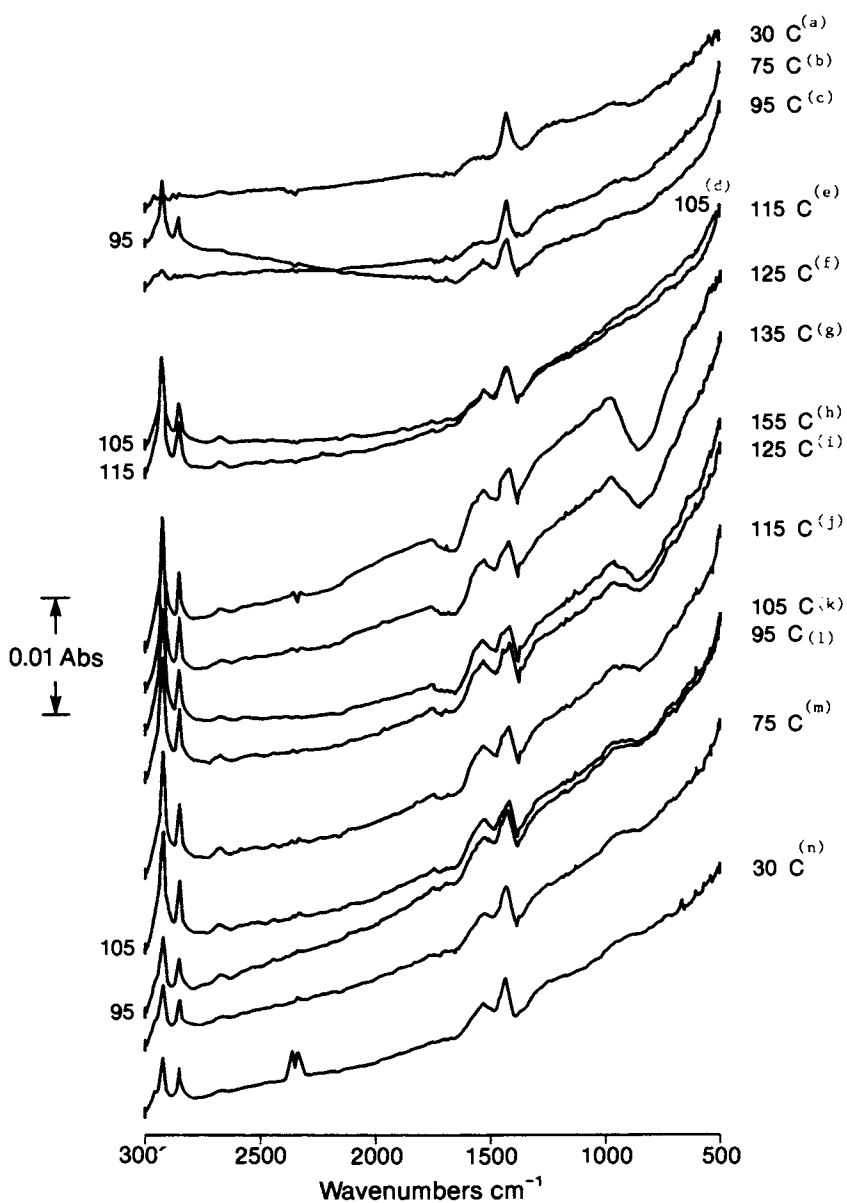


Figure 3. 2 L-B monolayers of cadmium arachidate on Ag. P polarization. Resolution = 4  $\text{cm}^{-1}$ . 4000 spectra co-added. Ratioed to Ag reference mirror. 3000 - 1000  $\text{cm}^{-1}$ .

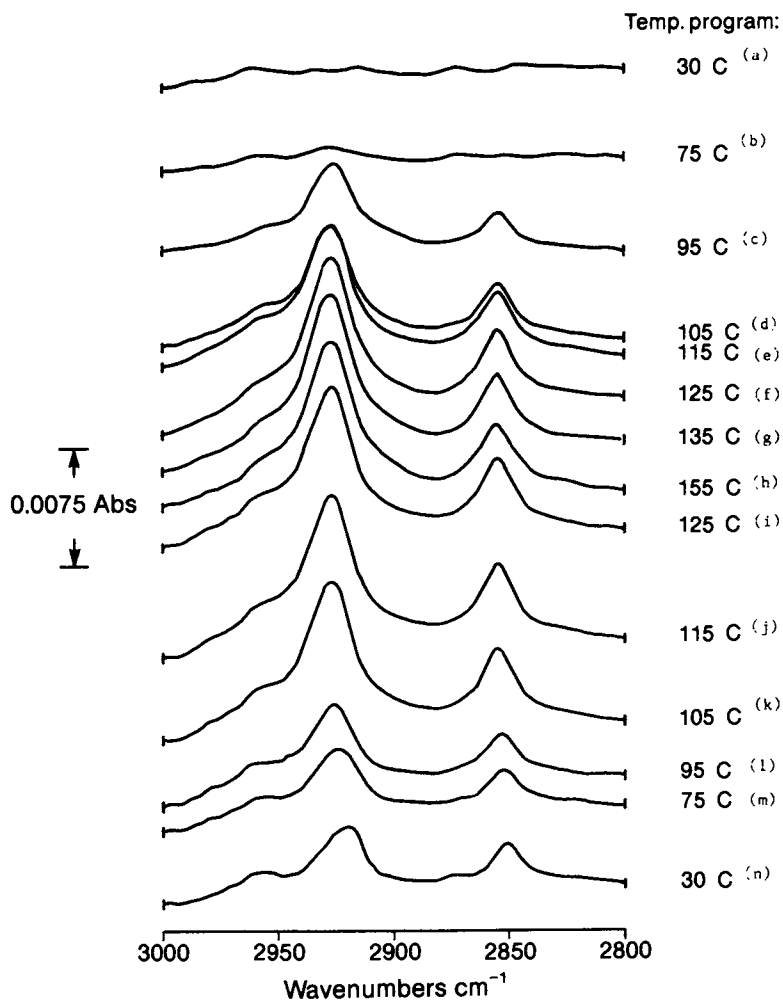


Figure 4. Same data as fig. 3; 3000-2800  $\text{cm}^{-1}$  region expanded.

methylenes, as evidenced by a decrease in the intensity of the bands at 1550, 2925 and 2850  $\text{cm}^{-1}$ .

The intensity changes are believed [3,13-15,19] to arise from the geometry of the monolayer with respect to the metal. Vibrations which lie parallel to the plane of the metal are not observed because they are perpendicular to the electric vector near the metal surface. When the cadmium arachidate monolayers are made by the L-B technique, the long axis, backbone, is near normal to the metal surface [4]. In this configuration the carboxylate symmetric stretch is observed because it has a component perpendicular to the metal, and the asymmetric carboxylate stretch is reduced by more than a factor of ten because it is nearly parallel to the plane of the metal. The planes formed by the H-C-H atoms of the methylene groups also lie nearly parallel to the plane of the metal. Hence, the intensities of the asymmetric and symmetric stretches and the in-plane bend are reduced sizeably from measurements made of the bulk material [13]. The methyl groups, when most tightly packed, have two C-H bonds parallel to the plane of the metal and one out of the plane. Of the three methyl C-H bonds only the C-H stretching vibration out of the plane of the metal will contribute significantly to the ordered monolayer spectrum. Any change in orientation of a bond of the carboxylate, methylenes or methyl groups from in the plane to out of the plane of the metal will cause a large increase in the measured IR absorption or the appropriate vibration.

The change observed for the L-B films are summarized in figure 5 in which the integrated band areas for the asymmetric and symmetric carboxylate are plotted against  $1/T$  for 2 and 6 monolayers on Ag. These plots show that the intensity of the carboxylate stretch, 1430  $\text{cm}^{-1}$  is nearly constant over the range of the experiment, whereas the intensity of the asymmetric carboxylate shows a sizeable increase in the temperature range 105 to 125 deg C. After the films are cooled below 105 deg C, the asymmetric carboxylate band intensities decrease to about 1/2 their maximum value. This cycle of intensity changes is also observed for films which are heated and cooled more than once. The ratio of the areas of the symmetric carboxylate stretching bands for the 6 monolayer film with respect to the 2 monolayer film is 2.6  $\pm$  0.4, i.e. within experimental error of the expected value of 3. The corresponding ratios for the asymmetric bands are temperature dependent showing a value of 1 at 30 deg C before heating, 4 at temperatures above 125 deg C and above and 2.7 - very close to the value measured for the symmetric case - after cooling below 105 deg C. The relative ratios, symmetric to asymmetric, vary by more than a factor of ten from the ordered monolayers (ca. 5) to the disordered bulk (ca. 0.5 [20]). The results for the 2 and 6 monolayers show 3  $\pm$  1 and 10  $\pm$  5 at 30 deg C, 0.8 and 0.6 at temperatures above 115 deg C, and 1.3 and 1.3 after cooling below 105 deg C, respectively. Although our data are preliminary and not fully understood (the observed trends may arise from small differences in sample preparation), they do highlight the need for measurements in situ because the results obtained on the melts show more disorder than the melted samples after cooling. It is

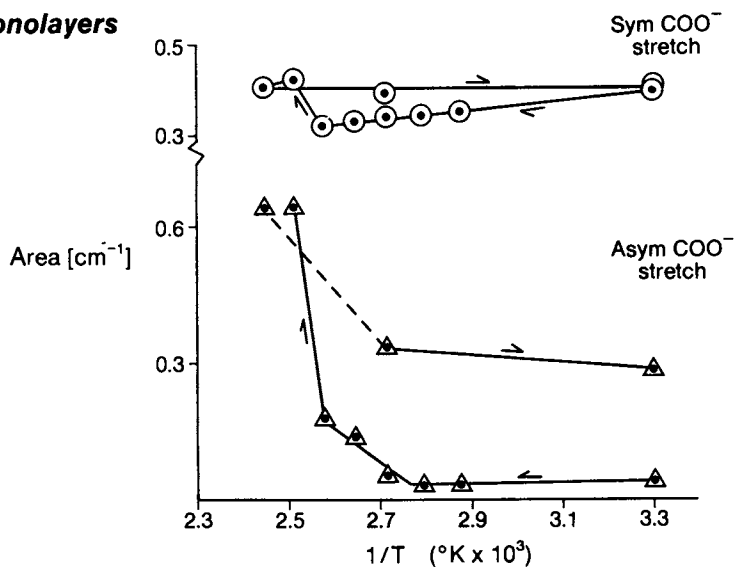
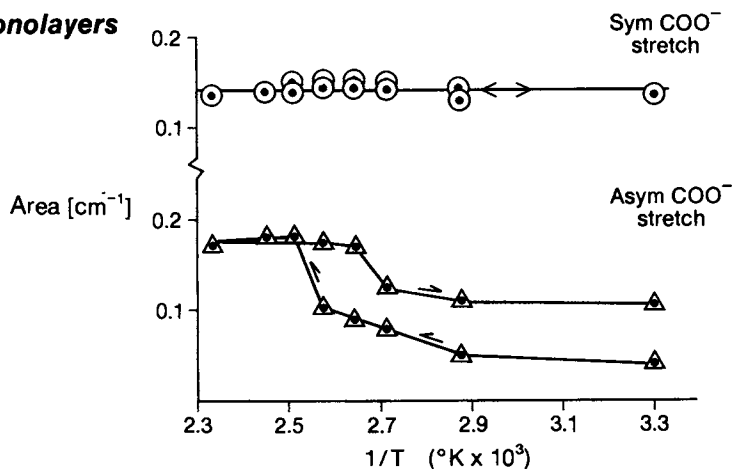
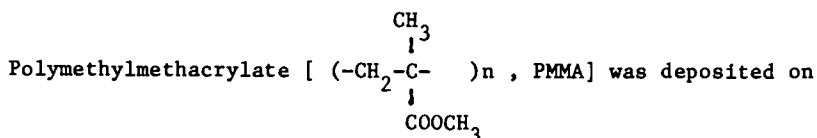
**6 Monolayers****2 Monolayers**

Figure 5. Integrated band areas vs.  $1/T$  for 2 and 6 monolayers of cadmium arachidate on Ag. Comparison of asymmetric ( $1630 - 1490 \text{ cm}^{-1}$ ) and symmetric ( $1490 - 1380 \text{ cm}^{-1}$ ) bands.

intriguing to hypothesize [12] that a single monolayer will exhibit less disorder (larger ratio) than the 2 monolayer sample. Tests of this hypothesis are in progress.



chromium from solution to form a 180 Å film (samples courtesy of Dr. J. Rabolt). Figure 6a-f shows a heating and cooling cycle for this film. The spectral changes are not as dramatic as that observed for the L-B film because solution deposited PMMA films are generally disordered with respect to the metal [6]. The very small spectral changes observed, e.g. intensity at 1175 compared to 1190  $\text{cm}^{-1}$ , are in the C-O single bond stretching bands and indicate conformational changes in the ester side chains [16].

The ability to measure changes in an L-B film due to the presence of water vapor is shown in fig. 7a-g and 8a-g. In this experiment the spectra of 2 monolayers of cadmium arachidate on Ni (tail to tail) are recorded in the presence of 11 torr of water vapor in nitrogen at 30 deg C and compared with the spectra obtained with dry nitrogen. The difference between cadmium arachidate on nickel and on silver is expected to be small because both films are prepared with the same water bath L-B technique prior to transfer to the metal [16]. In both the hydrated and anhydrous experiments, the gas is swept continuously through the cell to maintain constant pressure. Figures 7a-g show a sequence of dry and wet L-B film spectra in the C-H stretching region 3000 to 2800  $\text{cm}^{-1}$ . The spectra, a, c, e, and g of the anhydrous bilayer show the typical bands of fresh, unheated arachidate monolayers. The in situ spectra, b, d, and f, of the hydrated bilayer show noticeable changes to the methyl asymmetric stretching bands. Figure 8a-g shows the same sequence of spectra for the symmetric carboxylate, 1430  $\text{cm}^{-1}$ , and the symmetric methyl bend, 1380  $\text{cm}^{-1}$ . While there is little, if any difference between the carboxylate stretching band position or intensity for the hydrated or anhydrous film, there is a reproducible, 10  $\text{cm}^{-1}$ , shift in peak maximum for the methyl bend. These observations are consistent with the packing of the monolayers [13-15] where the carboxylate and the methylene groups are packed more tightly than the methyls. The water is presumed to sit in the region between the monolayers forcing conformational and, hence spectral, changes in the methyl positions. It is interesting also to compare fig 7b (d or f) with fig 4b which shows a dry two monolayer sample on Ag heated to 75 deg C. Both show a collapse of the 2935 and the 2920 bands to a single band and show shifts to higher frequency for the symmetric methylene C-H stretch. From these similarities, one might hypothesize that a hydrated arachidate film will melt at a different temperature than an anhydrous film. This has been observed for micellular lipids [17]. A test of this hypothesis is in progress.

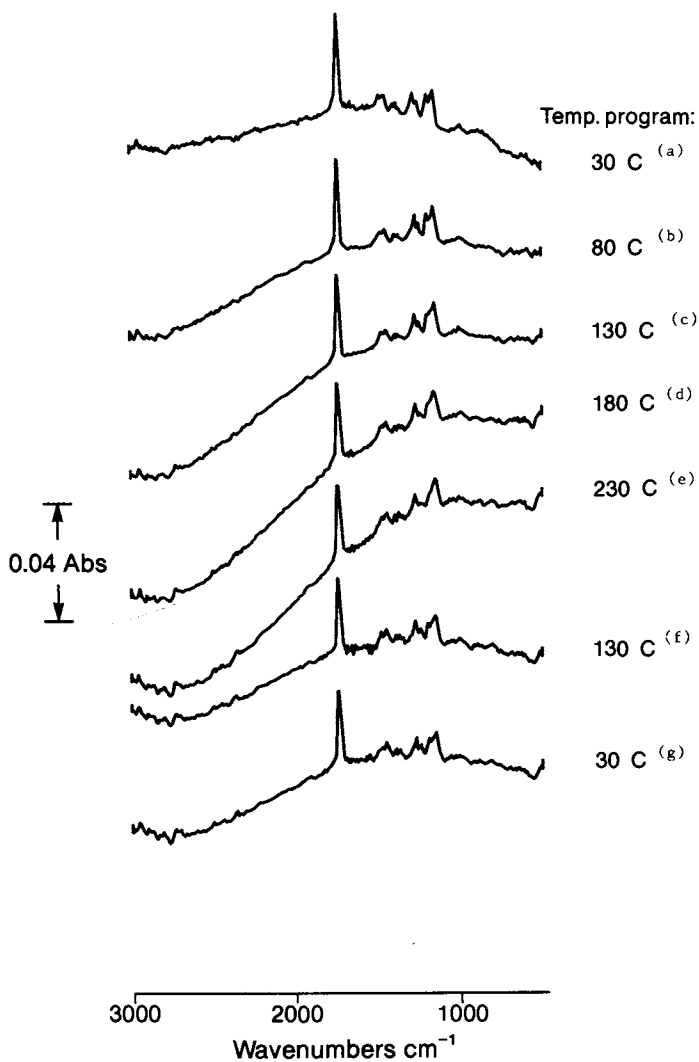


Figure 6. PMMA on Cr - solution deposition. P polarization; 180 Å layer [16]; Resolution = 4  $\text{cm}^{-1}$ ; 3000 - 1000  $\text{cm}^{-1}$ . Ratioed to Cr reference mirror. 4000 scans co-added.

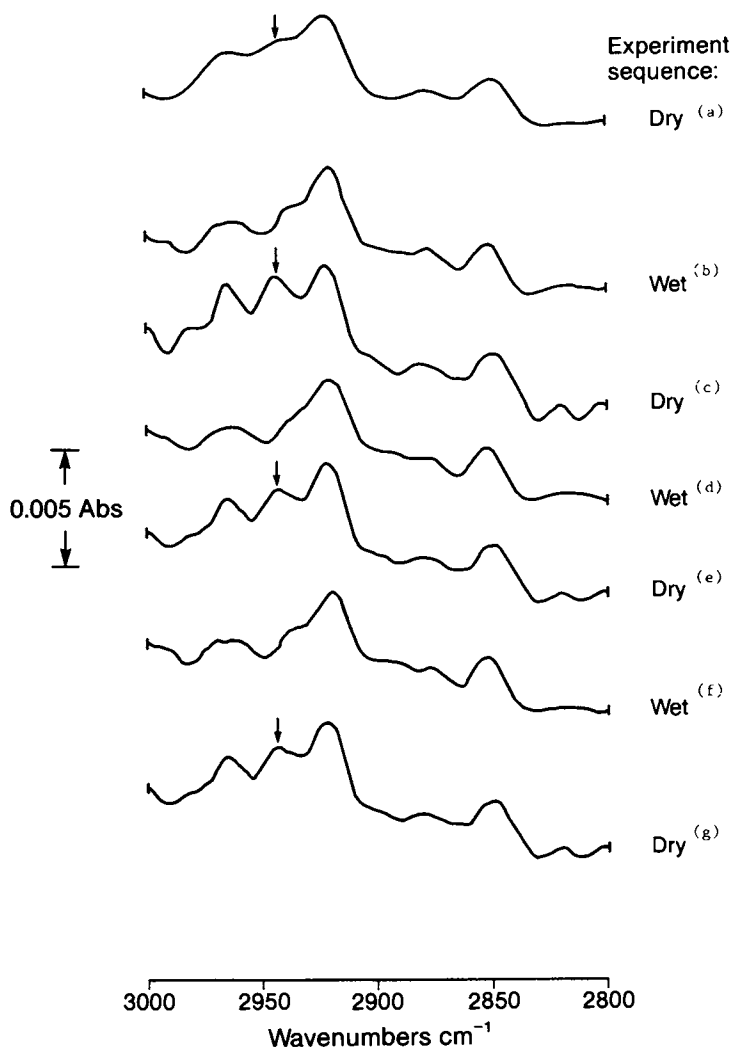


Figure 7. 2 L-B monolayers of cadmium arachidate on Ni. P polarization. 4000 spectra co-added. Ratioed to Ni reference mirror. Resolution ca. 10  $\text{cm}^{-1}$ ; 3000 - 2800  $\text{cm}^{-1}$ .

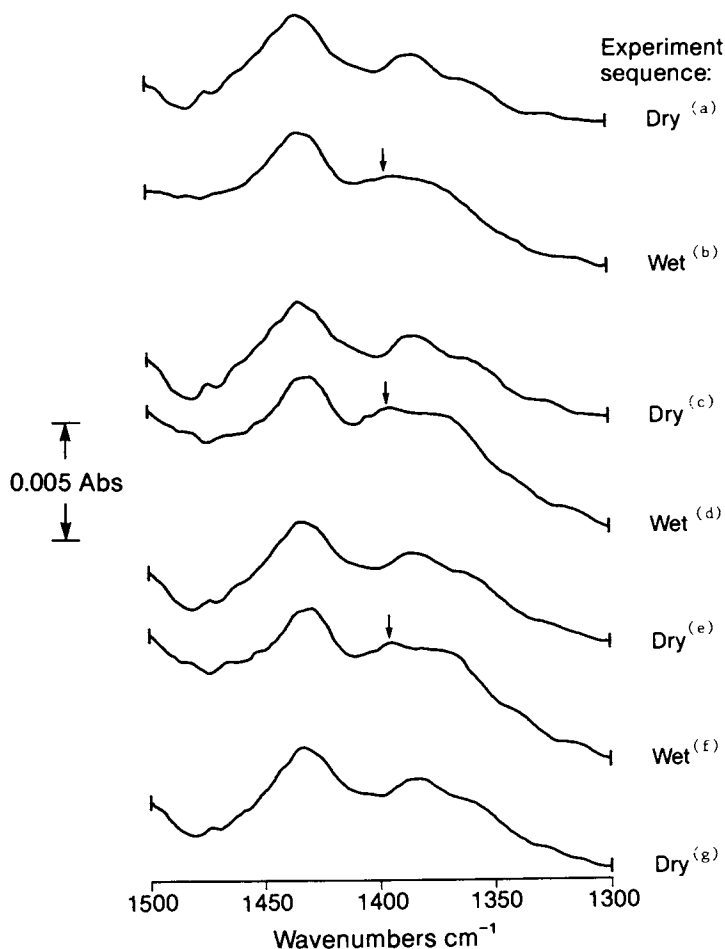


Figure 8. 2 L-B monolayers of cadmium arachidate on Ni. P polarization. 4000 spectra co-added. Ratioed to Ni reference mirror. Resolution ca. 10  $\text{cm}^{-1}$ ; 1500 - 1300  $\text{cm}^{-1}$ .

### Conclusion

To achieve surface selectivity in our studies of low area metal catalyzed reactions, we have developed FT-IRRAS techniques for the in situ study of surface adsorbates. With these methods, we are making progress toward examination of complex reactions. Preliminary results using fixed polarizer FT-IRRAS to study the melting and hydration of cadmium arachidate on low area metals show that both irreversible and reversible conformational changes can be

American Chemical Society  
Library



measured. Studies aimed at measuring the effect of hydration on the order to disorder transitions in cadmium arachidate are presently underway.

#### Literature Cited

1. C. B. Duke, J. Elec. Spec. 29, 1 (1983).
2. H. Ibach, ed., "Electron Spectroscopy for Surface Analysis" (Springer-Verlag, Berlin, 1977); H. Ibach, Surface Science 66, 56, 1977.
3. R. G. Greenler, J. Chem. Phys. 44, 310 (1966).
4. W. G. Golden, and D. D. Saperstein, J. Elect. Spect. 30, 43 (1983).
5. G. L. Gaines, "Insoluble Monolayers at Liquid-Gas Interfaces", (Interscience, New York, 1966).
6. W. G. Golden, D. D. Saperstein, M. W. Severson, and J. Overend, J. Phys. Chem. 88, 754 (1984).
7. R. P. Eischens, S. A. Francis and W. A. Pliskin, J. Phys. Chem. 60, 194 (1956); G. Blyholder, J. Phys. Chem. 68, 2772 (1964).
8. D. D. Saperstein, Abstract, ACS 187th National Meeting, St. Louis; D. D. Saperstein, Appl. Spect. 37, 279 (1983).
9. W. G. Golden, D. S. Dunn, and J. Overend, J. Phys. Chem. 82, 843, (1978); F. Hoffman and A. M. Bradshaw, Surf. Sci. 72, 513 (1977); J. D. Fedyk and M. J. Dignam in "Vibrational Spectroscopies for Adsorbed Species," A. Bell and M. Hair, eds., (American Chemical Society, Washington, D.C., 1980) and references therein; P. Hollins and J. Pritchard, "Vibrational Spectroscopy for Adsorbed Species", A. Bell and M. Hair, eds. (American Chemical Society, Washington, D.C., 1980); A. Crossley and D. A. King, Surf. Sci. 68, 528 (1977); M. D. Baker and M. A. Chesters in "Vibrations at Surfaces", R. Caudano et al, eds., (Plenum Press, New York, 1982).
10. A. E. Dowry and C. Marcott, Appl. Spect. 36, 414 (1982).
11. See for example: A. L. Cabrera, N. D. Spencer, E. Kozak, P. W. Davies and G. A. Somorajai, Rev. Sci. Instrum. 53, 1888 (1982); W. Erley, P. H. McBreen, and H. Ibach, J. Catalysis 84, 229 (1983).
12. J. Rabolt, private communication.
13. J. F. Rabolt, F. C. Burns, N. E. Schlotter and J. D. Swalen, J. Chem Phys. 78, 946 (1983).
14. D. L. Allara and J. D. Swalen, J. Phys. Chem. 86, 2700 (1982); P. A. Chollet, Thin Solid Films 52, 343 (1978).
15. W. G. Golden, C. D. Snyder and B. Smith, J. Phys. Chem 86, 4675 (1982).
16. J. F. Rabolt, M. Jurich, and J. D. Swalen, Appl. Spect., in press.
17. T. J. O'Leary and I. W. Levin, J. Phys. Chem. 88, 1790 (1984).
18. Manufactured to our design and specifications by Barnes Analytical, Division of Spectra-Tech, Stamford, CT.
19. N. Sheppard and J. Erkelens, Appl. Spect. 38, 471 (1984).
20. Values obtained by Rabolt et al, ref. 13; shown in their fig 1.

RECEIVED December 6, 1984

## IR Photoacoustic Spectroscopy of Silica and Aluminum Oxide

J. B. Benziger, S. J. McGovern, and B. S. H. Royce

School of Engineering and Applied Sciences, Princeton University, Princeton, NJ 08544

The application of infrared photoacoustic spectroscopy to characterize silica and alumina samples is reported. High quality infrared photoacoustic spectra illuminate structural changes between different forms of silica and alumina, as well as permit adsorbate structure to be probed. Adsorption studies on aerosil suggest adsorbed species shield the electric fields due to particle-particle interactions and induce changes in the vibrational spectra of the adsorbates as well as in the bulk phonon band. It is shown that different forms of aluminum oxides and hydroxides could be distinguished by the infrared spectra. Lastly, more complete infrared spectra of water and CO<sub>2</sub> adsorption were obtained and were able to distinguish different types of surface carbonates.

High surface area silica and alumina have been extensively studied utilizing a variety of spectroscopic techniques. Infrared spectroscopy has been particularly important as a surface probe and several excellent reviews have been published (1-3). Most infrared studies have been performed by transmission techniques using thin pressed discs in the region where silica and alumina are infrared transparent, typically in the regions above 1400 cm<sup>-1</sup> and between 500 and 1000 cm<sup>-1</sup> for silica and above 1200 cm<sup>-1</sup> for alumina. Attention has primarily focused on high frequency vibrations such as OH and CH stretching and bending modes. Features resulting from bonding to the surface and the surface structure itself have been inferred from changes observed in other parts of the spectrum.

Several of the problems associated with transmission techniques may be overcome utilizing photoacoustic detection. In particular, changes in the spectral region where silica and alumina are strong absorbers may be observed by photoacoustic spectroscopy. Additionally, infrared photoacoustic spectroscopy can examine the broadband absorption due to hydrogen bonding and mobile charge carriers, which are indistinguishable from scattering effects present in transmission spectra. Infrared photoacoustic spectroscopy

0097-6156/85/0288-0449\$06.00/0  
© 1985 American Chemical Society

of the structure of silicas and aluminas, and adsorption of simple molecules on these materials will be examined in this paper.

### Background

The spectroscopic application of the photoacoustic effect from solids was revived by Rosencwaig and Gersho (4), who recognized that the absorption of modulated light would cause a periodic heating of a solid sample, resulting in a periodic heating and cooling of the gas near the solid surface. This temperature variation results in a pressure variation whose amplitude depends on the optical absorption coefficient,  $\alpha_a$ , and the thermal diffusion length of the sample,  $\mu_s$ . The photoacoustic signal generated is proportional to the absorption coefficient provided the product of the absorption coefficient and the thermal diffusion length is less than one:

$$1 > \alpha_a \mu_s \quad (\text{photoacoustic})$$

Useful information from transmission spectroscopy is obtained when the product of the absorption coefficient and the sample thickness,  $l$ , is less than one:

$$1 > \alpha_a l \quad (\text{transmission})$$

Porous materials, such as silica and alumina, have thermal diffusion lengths of approximately  $10^{-5}$  m, which is much less than the typical thickness of pressed discs. The small thermal diffusion length gives photoacoustic spectroscopy a larger dynamic range than transmission methods when applied to powdered samples. An additional advantage is the ease of sample preparation, since photoacoustic spectroscopy uses powdered samples with no special preparation required.

Transmission spectroscopy is further complicated by scattering and reflection of the infrared radiation. Even with discs 0.1 mm thick the optical throughput is typically less than 5% making it difficult to obtain good signal to noise. Furthermore, light scattering can cause spectral distortion. With photoacoustic spectroscopy light scattering by micron size particles is of secondary importance. It redistributes the photon energy resulting in a slight enhancement of the photoacoustic signal (5,6), but has a negligible effect on the spectra as a photoacoustic signal cannot be generated without true absorption.

Transmission spectroscopy offers two significant advantages over photoacoustic spectroscopy of powders. First, transmission spectroscopy is not susceptible to external acoustic disturbances. Commercial spectrometers must be modified for vibrational isolation in order to obtain good photoacoustic spectra. Secondly, transmission spectroscopy can use solid state detectors with very fast response times, whereas photoacoustic spectroscopy is much slower, with spectra taking a few minutes to collect as compared to a few seconds for transmission spectra when both are taken with an FTIR.

The main advantages and disadvantages of transmission and photoacoustic spectroscopies are summarized in Table I. The advantages

of the photoacoustic method suggest it could be a useful routine analytical technique for catalyst samples.

TABLE I. A Comparison of Transmission and Photoacoustic Spectroscopies

|                           | Transmission  | Photoacoustic  |
|---------------------------|---|--|
| Detected Signal           | $I_T = I_0 \exp[-(\alpha_a + \alpha_s)l] - I_R$                                 | $PA \sim I_0 \alpha_a f(\alpha_s)$<br>$1 \leq f(\alpha_s) \leq 4$                  |
| Sample Preparation        | Pressed Disc of Mull  | Loose Powder   |
| Effect of Scattering      | Can Cause Spectral Distortion   | Negligible   |
| Spectrum Acquisition Time | Seconds   | Minutes  |
| Spectral Region Probed    | Limited to 4000-1200 $\text{cm}^{-1}$ from Absorption by Lattice Modes of Solid | 4000-400 $\text{cm}^{-1}$<br>Only Spectral Limitations are Imposed by Spectrometer |
| Special Problems          | Reflection Losses Result in Low Optical Throughput Limiting Signal to Noise     | Highly Susceptible to Airborne Noise and Building Vibrations                       |

### Experimental

Experiments were carried out in a Bomem DA3.002 FTIR using a specially built photoacoustic cell described elsewhere (7). The cell was equipped to allow *in situ* sample heating in vacuum or under a controlled atmosphere at temperatures up to 400 C. The spectra shown were obtained at room temperature in flowing hydrogen. A mirror velocity of 0.05 cm/s was used with 200 scans coadded for each spectrum. The spectra were transformed at 8  $\text{cm}^{-1}$  resolution using raised cosine apodization. The interferogram was phase corrected and numerically filtered by the convolution method with 256 coefficients. The spectra were normalized against a graphite reference spectrum obtained in the same cell. The total data acquisition time for each spectrum was approximately 15 min.

The interferometer assembly has been modified to provide acoustic isolation from both building vibrations and airborne noise (7). These improvements have greatly enhanced the signal to noise. The spectra presented here show a signal to noise ratio in excess of 500 for silica samples and in excess of 100 for the alumina samples; the differences are due to different sample porosities. No smoothing of the spectra has been performed, and all spectra reported are direct reproductions of the plotter output from the spectrometer.

## Results

Silica - Photoacoustic spectra of a variety of silica samples are shown in Figure 1. Figure 1a is of an aerosil sample (ALFA Chemicals #89376) that had been dried at 350 C for 4 hr and cooled to room temperature in flowing hydrogen. This sample is comprised of 60 A particles of silica with a nominal surface area of 400 m<sup>2</sup>/g. The large absorption feature between 1000 and 1200 cm<sup>-1</sup> is due to the transverse and longitudinal lattice vibrations (8). These features are broadened due to the amorphous structure of the aerosil, and the small particle size (9). Other lattice vibrations occur at 812 cm<sup>-1</sup> and 468 cm<sup>-1</sup>. Overtones of the fundamental lattice vibrations occur at 1625, 1860 and 2004 cm<sup>-1</sup>. The remaining features in the spectrum are due to surface groups. Surface hydroxyl groups give rise to an OH stretching band at 3744 cm<sup>-1</sup>. The long tail on the OH stretching band that extends from 3700 to 3400 cm<sup>-1</sup> is due to a small amount of residual water adsorbed on the surface. Hydrogen bonding interactions cause the peak to be broad.

The spectrum of the same aerosil sample before drying is shown in Figure 1b. The only noticeable difference from the dried sample is a broader band due to adsorbed water. The changes due to the adsorbed water are more clearly seen in the difference spectrum shown in Figure 2a. In Figure 2, positive features indicate absorptions by the sample with adsorbed water that are not present in the dried sample and negative features indicate absorption by the dried sample that are absent in the wet sample. In the OH stretching region a broad peak due to hydrogen bonded water is centered at 3400 cm<sup>-1</sup>. The adsorbed water influences the hydroxyl groups causing a slight blue shift, which results in the positive peak at 3756 cm<sup>-1</sup> and a negative peak at 3740 cm<sup>-1</sup>. The OH bending mode of the adsorbed water is seen at 1626 cm<sup>-1</sup>. There are three hindered rotations of adsorbed water that give rise to the three bands at 600, 538 and 468 cm<sup>-1</sup>. The absorption band at 764 cm<sup>-1</sup> appears to be due to the OH bending mode of adsorbed hydroxyl groups (10). Lastly, there are changes in the silica phonon spectra due to water adsorption that give rise to both positive and negative features in the difference spectrum around 1000 cm<sup>-1</sup>. The negative feature at 1008 cm<sup>-1</sup> appears to be due to an Si-OH stretching mode. This feature is red shifted to 926 cm<sup>-1</sup> when water is adsorbed. The band between 1050 and 1200 cm<sup>-1</sup> overlaps with the silica phonon band and may be due to a change in the bulk phonon spectrum due to surface effects (11).

Figure 1c shows the spectrum of aerosil that has been slurried in water and then dried at 100°C. This treatment initiates gel formation, so that the sample is no longer a chain of silica particles held together by electrostatic forces, but a porous network held together by siloxane linkages. The most obvious features in this spectrum are an increase in the water adsorption features at 3400 cm<sup>-1</sup> and 1632 cm<sup>-1</sup>. In addition, a band at 976 cm<sup>-1</sup> is evident, that was much less obvious in the spectra of the other two silica samples. This feature is due to siloxane bridges formed during gel formation (10,12).

The spectrum in Figure 1d is for a crystalline form of silica, silicalite (Union Carbide S-115, see ref. 13). The structure is comprised of twelve silica tetrahedra linked into five pentasil groups and one hexasil group. This building block is repeated

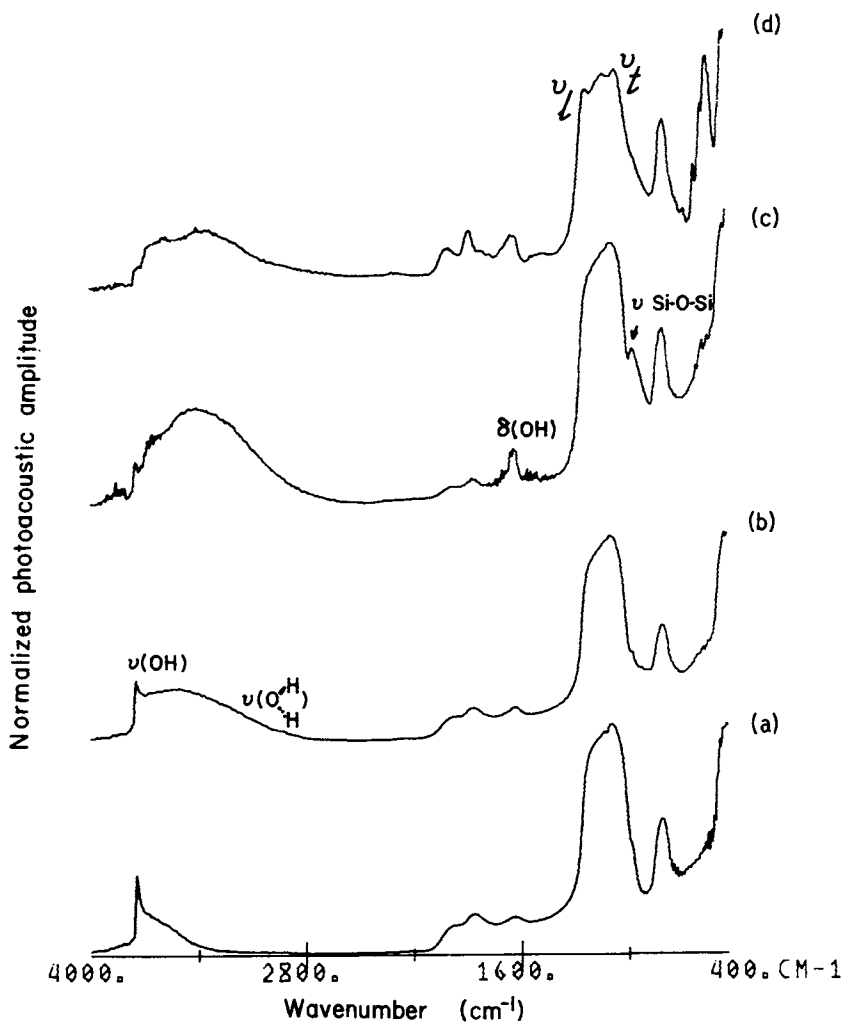


Fig. 1. Infrared spectra of silicas. a) Aerosil dried at 350°C, b) Aerosil as received, c) Aerosil slurried in water and dried at 100°C, d) Silicalite as received.

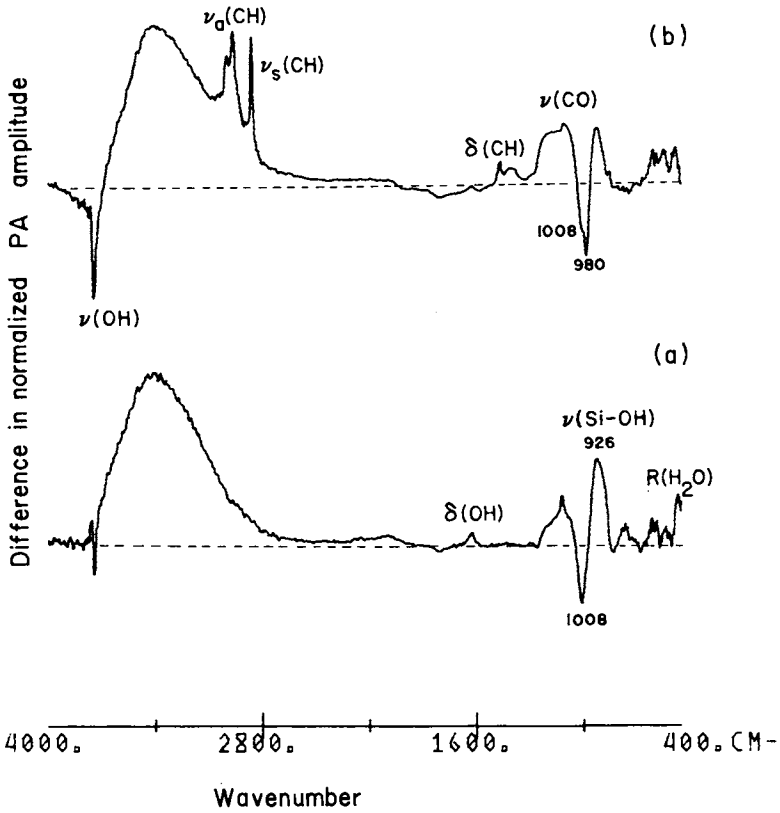


Fig. 2. a) Difference spectra between 1b - 1a (as received aerosil - dried aerosil), b) Difference spectra for methoxylated silica (methoxylated silica - dried silica).

forming a zig-zag channel structure. This material is distinct from the other silica samples as the crystalline structure does not have surfaces that are terminated with hydroxyl groups. This is evident in the infrared spectrum which shows a broad band due to adsorbed water, but no significant feature at  $3750\text{ cm}^{-1}$  due to surface hydroxyl groups. The remainder of the spectrum also shows some significant differences. Being a crystalline material, the longitudinal and transverse optical modes are seen as well defined peaks at  $1228$  and  $1072\text{ cm}^{-1}$  respectively. The broad feature between the two peaks appears to be due to the small particle size which gives rise to a distribution of modes. The other two bulk phonon modes at  $800$  and  $460\text{ cm}^{-1}$  are slightly red shifted relative to the amorphous silica. There is also an absorption feature at  $560\text{ cm}^{-1}$ , not observed with the other samples, that is due to the ring structure formed by silica tetrahedra. This is a characteristic band observed in zeolites where similar structures exist (14).

An aerosil sample was methoxylated at  $400^\circ\text{C}$  to examine the effect of surface composition on the infrared spectrum. The difference spectrum between the methoxylated silica and the dried silica is shown in Figure 2b. Comparing this with the difference spectrum for hydroxylated silica (2a) several changes are apparent. First, the band due to the hydroxyl stretches at  $3744\text{ cm}^{-1}$  is diminished and replaced by bands at  $2958$  and  $2856\text{ cm}^{-1}$  due to the asymmetric and symmetric CH stretching modes of the adsorbed methoxy. The CH bending modes are also evident at  $1464$  and  $1404\text{ cm}^{-1}$ , as is the loss of the OH bending mode at  $760\text{ cm}^{-1}$ . A band at  $1112\text{ cm}^{-1}$  superimposed on the changes of the phonon band is due to the CO stretch of the adsorbed methoxy, and a band at  $852\text{ cm}^{-1}$  appears to be the result of the Si-OCH<sub>3</sub> stretch. The remaining features are due to the adsorbed water, a broad OH stretch at  $3400\text{ cm}^{-1}$ , the OH bending mode at  $1626\text{ cm}^{-1}$ , and the three water librations at  $597$ ,  $546$ , and  $478\text{ cm}^{-1}$ . As the replacement of the hydroxyl groups was not quantitative, the loss features at  $1008\text{ cm}^{-1}$  and the positive deviations at  $926\text{ cm}^{-1}$  due to the Si-OH stretches are still evident. There is an additional loss at  $980\text{ cm}^{-1}$ , which is due to the Si-OH groups that have been replaced by surface methoxys. The nature of the two different frequencies for Si-OH stretching will be addressed further below. Lastly, the changes in the phonon band due to adsorbed water remain almost the same between methoxylated and hydroxylated silica.

**Alumina** - Alumina forms a variety of oxides and hydroxides whose structures have been characterized by X-ray diffraction (16). From the catalytic viewpoint  $\gamma$ -alumina is the most important. This is a metastable phase that is produced from successive dehydration of aluminum trihydroxide (gibbsite) to aluminum oxide hydroxide (boehmite) to  $\gamma$ -alumina, or from dehydration of boehmite formed hydrothermally.  $\gamma$ -alumina is converted into  $\alpha$ -alumina (corundum) at temperatures around  $1000^\circ\text{C}$ .

The infrared spectra for various aluminum oxides and hydroxides are shown in Figure 3. Figure 3a is  $\alpha$ -alumina (Harshaw A13980), ground to a fine powder with a surface area of  $4\text{ m}^2/\text{g}$ . The absorption between  $550$  and  $900\text{ cm}^{-1}$  is due to two overlapping lattice modes, and the low frequency band at  $400\text{ cm}^{-1}$  is due to another set of lattice vibrations. These results are similar to those obtained by reflection measurements, except that the powder does not show as



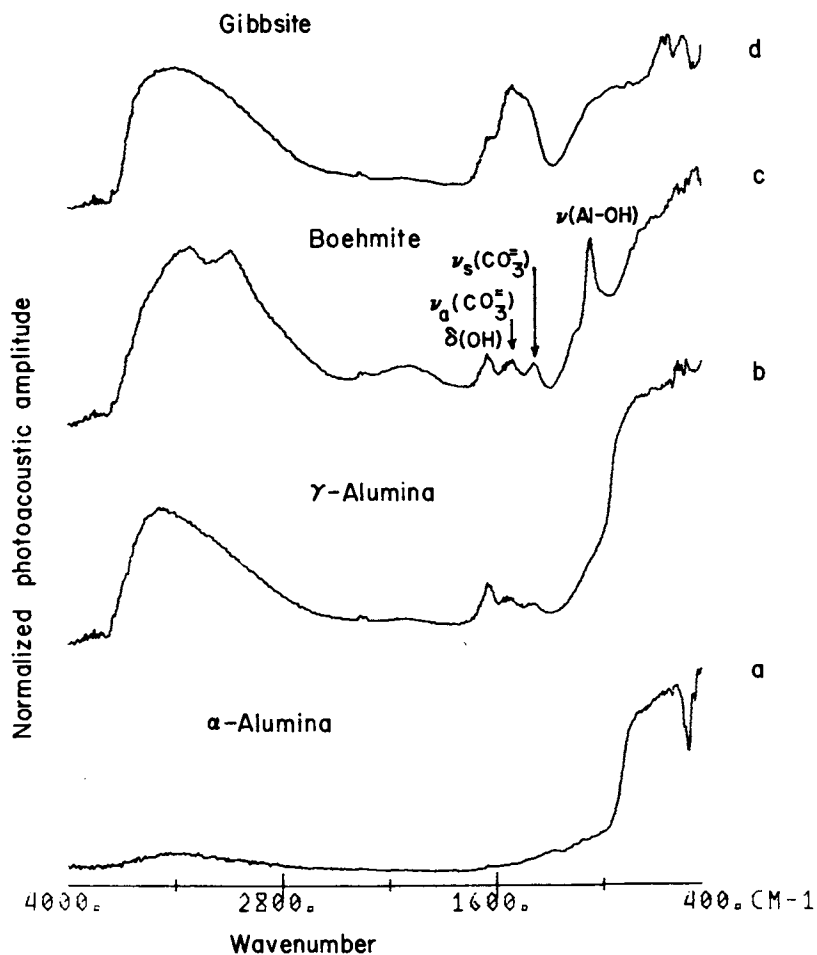


Fig. 3. Infrared spectra of aluminum oxides and hydroxides.  
 a)  $\alpha$ - $\text{Al}_2\text{O}_3$ ;  $4\text{m}^2/\text{g}$ , b)  $\gamma$ - $\text{Al}_2\text{O}_3$ ;  $234\text{m}^2/\text{g}$ , c)  $\text{AlOOH}$  (Boehmite);  $325\text{m}^2/\text{g}$ , d)  $\text{Al}(\text{OH})_3$  (gibbsite).

much band splitting as was observed by reflection from single crystals (17). There is also a very weak and broad band at  $3400\text{ cm}^{-1}$  due to water adsorbed on the alumina surface. As the surface area is low this band is not expected to be very strong.

Figure 3d is the infrared spectrum of gibbsite (Aldrich 23,918-6), which is the precursor of most aluminum oxides. The spectrum shows a broad band due to OH stretches at  $3400\text{ cm}^{-1}$ , a feature centered around  $1510\text{ cm}^{-1}$  due to carbonate, and a shoulder at  $1632\text{ cm}^{-1}$  due to OH bending of water. The Al-OH or Al-O stretching modes give rise to a broad band that begins to absorb strongly at  $1250\text{ cm}^{-1}$  and extends to below  $400\text{ cm}^{-1}$ . There are smaller absorption bands at 668, 634, and  $556\text{ cm}^{-1}$  superimposed on the broad Al-O band which appear to be due to bending modes of carbonates. Since gibbsite is produced by precipitation from a basic solution buffered with sodium carbonate (18) the high water and carbonate contents observed are not unexpected.

Dehydration of gibbsite under pressure in moist air produces boehmite (aluminum oxide mono-hydrate). An infrared spectrum of boehmite (Kaiser substrate grade alumina) is shown in Figure 3c. When the gibbsite is dehydrated a structural collapse occurs with a large increase in surface area. The boehmite sample has a nominal surface area of  $325\text{ m}^2/\text{g}$ . The infrared spectrum of the boehmite shows distinct structure in the OH stretching region, with two peaks located at  $3090$  and  $3320\text{ cm}^{-1}$ . There are three features at 1648, 1516 and  $1392\text{ cm}^{-1}$  that are due to adsorbed water and carbonate, which are removed upon heating the boehmite to  $350^\circ\text{C}$  in hydrogen. The lattice vibrations begin to absorb strongly below  $1200\text{ cm}^{-1}$ . An additional feature at  $1072\text{ cm}^{-1}$ , characteristic of boehmite, is the result of the Al-OH stretch. Both the OH stretches and the Al-OH stretch have been previously identified by transmission studies of boehmite single crystals (19).

Further dehydration of boehmite at  $600^\circ\text{C}$  produces  $\gamma$ -alumina, whose spectrum is shown in Figure 3b. There is a loss in surface area in going from boehmite to  $\gamma$ -alumina. The sample shown here has a surface area of  $234\text{ m}^2/\text{g}$  (this sample was obtained from Harshaw #A23945; the calcined Kaiser substrate gave an identical infrared spectrum). The  $\gamma$ -alumina sample shows two major differences from  $\alpha$ -alumina. First, there is a more intense broad absorption band at  $3400\text{ cm}^{-1}$  due to adsorbed water on the  $\gamma$ -alumina. Second, the  $\gamma$ -alumina does not show splitting of the phonon bands between 400 and  $500\text{ cm}^{-1}$  as was observed for  $\alpha$ -alumina. The  $\gamma$ -alumina is a more amorphous structure and has much smaller crystallites so the phonon band is broader. The  $\gamma$ -alumina also shows three features at 1648, 1516 and  $1392\text{ cm}^{-1}$  due to adsorbed water and carbonate.

The features due to adsorbed water and carbonates observed on the boehmite and  $\gamma$ -alumina deserve further attention as they differ from results published by previous investigators. Figure 4 shows a series of difference spectra for adsorption on  $\gamma$ -alumina. Spectra were taken after drying the  $\gamma$ -alumina at  $350^\circ\text{C}$ , cooling to room temperature and carrying out room temperature adsorption. The spectra are the difference of the sample before and after adsorption. Spectrum 4e is the spectrum for the as received alumina differenced with the dried alumina. The positive band at  $3400\text{ cm}^{-1}$  is due to adsorbed water, and the small negative feature at  $3740\text{ cm}^{-1}$  is due to isolated hydroxyls on the dried surface. Besides the three

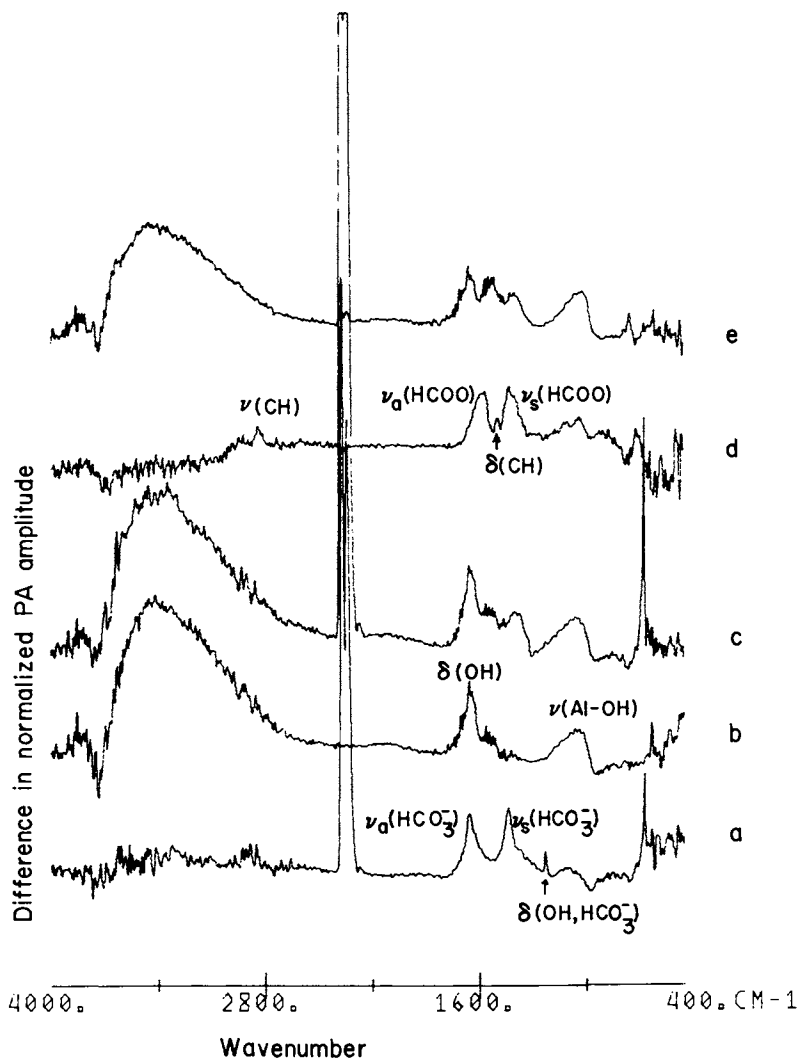


Fig. 4. Difference spectra of adsorbed species on  $\gamma$ -alumina (air exposure). a)  $\text{CO}_2$ ; b)  $\text{H}_2\text{O}$ ; c)  $\text{H}_2\text{O}$  followed by  $\text{CO}_2$ ; d) Methanol reacted with the alumina at  $350^\circ\text{C}$ ; e) As received  $\gamma$ -alumina (air exposure).

features previously noted at 1644, 1516 and 1392  $\text{cm}^{-1}$ , there are features at 1074  $\text{cm}^{-1}$  due to an Al-OH<sub>2</sub> stretch of coordinatively bound water, and small features at 748 and 628  $\text{cm}^{-1}$ . Spectrum 4a is for CO<sub>2</sub> adsorption. The gas phase CO<sub>2</sub> shows bands at 2346 and 668  $\text{cm}^{-1}$ ; bands at 1654, 1436 and 1228  $\text{cm}^{-1}$  are due to adsorbed bicarbonate species (20). There is a weak band at 3610  $\text{cm}^{-1}$  due to the OH stretch in the bicarbonate that is accompanied by small negative features at 3740  $\text{cm}^{-1}$  corresponding to the hydroxyl that reacted to form the bicarbonate. A weak band at 1050  $\text{cm}^{-1}$  is due to the C-O stretch in the bicarbonate. The bicarbonate bands disappear when the sample is exposed to water. After exposure of the  $\gamma$ -alumina sample to water several features are apparent in the infrared spectrum (Figure 4b) that were also apparent in the spectrum of the as received sample. An OH bending mode for adsorbed water appears at 1644  $\text{cm}^{-1}$ , as well as an Al-OH<sub>2</sub> stretching mode at 1058  $\text{cm}^{-1}$  and another feature at 628  $\text{cm}^{-1}$  that is probably due to a frustrated rotation of the adsorbed water. When the surface with adsorbed water is exposed to CO<sub>2</sub> additional features appear at 1536 and 1384  $\text{cm}^{-1}$ , as shown in Figure 4c. A small feature also starts to grow at 748  $\text{cm}^{-1}$ . These results suggest that a monodentate carbonate ligand is formed when CO<sub>2</sub> adsorbs on the alumina surface with water adsorbed. The features at 1536 and 1384  $\text{cm}^{-1}$  are due to the asymmetric and symmetric stretches respectively. The C-O stretching mode that occurs around 1050  $\text{cm}^{-1}$  coincides with the Al-OH<sub>2</sub> stretch. The feature at 748  $\text{cm}^{-1}$  corresponds to the out-of-plane deformation of the carbonate (2). A feature due to the planar deformation appears as a high frequency shoulder on the water libration at 628  $\text{cm}^{-1}$ . A shoulder also forms on the water band at 3620  $\text{cm}^{-1}$ , which is also visible in the as received alumina. This is the position for the OH stretch in a bicarbonate. However there is no evidence for the OH bending mode at 1230  $\text{cm}^{-1}$ , suggesting that the carbonate interacts with adsorbed water, but does not react to form a bicarbonate species.

The carbonate can also be compared with adsorbed formate species prepared by reacting methanol with the alumina surface at 350°C (22). The spectrum for adsorbed formate, Figure 4d, shows the asymmetric carboxylate stretches at 1565 and 1440  $\text{cm}^{-1}$  respectively, the CH stretch at 2832  $\text{cm}^{-1}$ , and the CH bending mode at 1505  $\text{cm}^{-1}$ . The Al-OC stretching mode is seen at 1060  $\text{cm}^{-1}$ , and the out-of-plane deformation at 750  $\text{cm}^{-1}$ . The signal to noise ratio in the low frequency end of the spectrum is insufficient to see the planar deformation, which should occur around 630  $\text{cm}^{-1}$ . It should be noted that the carbonate and formate species are very similar, the main distinction being the vibrations associated with the CH bond.

### Discussion

The infrared photoacoustic spectra presented here complement and extend previous results from transmission infrared studies. As an extension of previous studies of silica the photoacoustic results presented here have identified features in the infrared spectra that coincide with bulk phonon modes between 1000 and 1200  $\text{cm}^{-1}$  and below 500  $\text{cm}^{-1}$ . The photoacoustic spectra of water adsorbed on aerosil

with hydroxylated and methoxylated surfaces shown in Figure 2 indicate water adsorption can perturb the phonon spectrum of the solid, and that there are differences in the surface hydroxyl groups. Adsorbed water causes a red shift in the Si-OH stretch from 1008 to 926  $\text{cm}^{-1}$ . The spectrum for methoxylated silica indicates that replacement of hydroxyl by methoxyl groups causes a decrease in intensity at 980  $\text{cm}^{-1}$ . These results suggest there may be two different surface hydroxyl groups.

An alternative explanation is that the surface groups are perturbed by particle-particle interactions. The particles are held together by electrostatic forces which give rise to significant electric fields at the points of contact (9,23). The electric fields can perturb the surface bonds and hence the vibrational frequencies. Water adsorption probably occurs by condensation near the points of contact, whereas methoxylation will occur more uniformly over the surface. Removal of water then exposes perturbed hydroxyls, with an Si-OH stretch at 1008  $\text{cm}^{-1}$ , whereas methoxylation replaces non-perturbed hydroxyls with an Si-OH stretch at 976  $\text{cm}^{-1}$ . The adsorbed water interacts with the hydroxyl groups on the silica surface resulting in a red shift in the Si-OH band to 926  $\text{cm}^{-1}$ . Besides affecting the surface properties of the silica the adsorbed water caused changes in the bulk phonon modes. These changes are probably due to a shielding effect of the electrostatic forces between particles. For small particles this shielding is expected to produce significant effects.

A noteworthy feature of the photoacoustic spectra shown in Figure 2 is the presence of water librations. These are frustrated rotations and have been observed for ice (24) by infrared spectroscopy, as well as for water adsorbed on Pt and Ag surfaces by electron energy loss spectroscopy (25-27). The three libration modes have been associated with the bands at 600, 538 and 468  $\text{cm}^{-1}$ , as this set of peaks occurs for water adsorbed on both the hydroxylated and methoxylated silica.

The results for the methoxylation of silica are a useful extension of the studies carried out by Morrow (15,28) in which the CH stretching and bending modes had been observed. The spectra recorded here are at higher resolution and the band splitting of the asymmetric stretch (indicating that it has  $C_s$  symmetry) is more pronounced. The spectrum also shows the C-O stretch at 1112  $\text{cm}^{-1}$  and the Si-O stretch at 852  $\text{cm}^{-1}$  that had not previously been observed. The C-O stretch intensity is diminished relative to the C-H features because it is superimposed on the phonon band where there is a change in the dominant mode of signal generation (6). The M-O band for the methoxy bond to the surface is at a higher frequency than has been observed on transition metals such as Ni and Cu (29,30). This is expected as the Si-O bond is a much stronger bond than that found on transition metals.

The results obtained for the various aluminum oxides and hydroxides indicate that infrared photoacoustic spectroscopy may be useful in characterizing structural transformations in these species. Very clear differences between  $\alpha$ -alumina and  $\gamma$ -alumina were noted in the region of the lattice vibrations. The monohydrate, boehmite, showed a very distinct Al-OH stretching feature at 1070  $\text{cm}^{-1}$  as well as characteristic structure in the OH stretching

region. The gibbsite sample examined showed very little structure in the region above  $3000\text{ cm}^{-1}$ , in contrast to results obtained by Fredrickson (19), though it was easily distinguished from the other samples examined. This difference is probably the result of sample preparation and impurities. Fredrickson prepared large pure crystals of gibbsite. The commercial sample used in the present study was probably prepared by the Bayer process (18) and contained excess water and carbonate.

A number of investigators have examined  $\text{CO}_2$  adsorption on alumina (20,31-37). Results presented here agree with the findings of Baumgarten and Zachos who clearly showed bicarbonate formation on an alumina sample dried at  $400\text{ C}$  (20). Exposure to water causes the bicarbonate to decompose with the  $\text{CO}_2$  being replaced quantitatively with water. However, carbonate formation was observed on the surface with adsorbed water. The band positions suggest that the  $\text{CO}_2$  adsorbs as a monodentate carbonate. Dehydration of the surface produces coordinatively unsaturated Al cations and coordinatively unsaturated anions. Depending on the dehydration temperature there are varying concentrations of coordinatively unsaturated ions and hydroxyl groups (38). The unsaturated cations behave as Lewis acids and adsorb electron donors, such as  $\text{CO}_2$  and  $\text{H}_2\text{O}$ . After  $\text{CO}_2$  adsorption at an Al cation the carbon can undergo nucleophilic attack by either an oxygen anion or a hydroxyl anion. At high degrees of dehydration the attack by the oxygen anion is the only possible reaction. This produces bridged carbonate species, with bands at  $1800$  and  $1200\text{ cm}^{-1}$ . This has been observed by Peri (37) and by Parkyns (31). When there are hydroxyl groups on the surface the preferred reaction path appears to be the formation of a bicarbonate. The difference spectra do not show any water, but the spectra for the alumina dried at  $350^\circ\text{C}$  shows that approximately 45 percent of the intensity in the OH band at  $3400\text{ cm}^{-1}$  remains.

### Conclusion

Infrared photoacoustic spectroscopy has significant potential to be useful as an analytic technique for characterizing catalyst samples. It offers ease of sample preparation and has a high dynamic range due to the small thermal diffusion lengths of high surface area materials. Commercial instruments need to be acoustically modified to obtain high quality infrared photoacoustic spectra. These modifications are not difficult and new spectrometers will become available that will be good for photoacoustic spectroscopy.

The results presented here for silicas and aluminas illustrate that there is a wealth of structural information in the infrared spectra that has not previously been recognized. In particular, it was found that adsorbed water affects the lattice vibrations of silica, and that particle-particle interactions affect the vibrations of surface species. In the case of alumina, it was found that aluminum oxides and hydroxides could be distinguished by their infrared spectra. The absence of spectral windows for photoacoustic spectroscopy allowed more complete band identification of adsorbed surface species, making distinctions between different structures easier. The ability to perform structural analyses by infrared spectroscopy clearly indicates the utility of photoacoustic spectroscopy.

### Acknowledgments

The authors thank the National Science Foundation (CPE-8217364) for support of this work. One of us (SJM) thanks Mobil Research and Development Corp. for their financial support.

### Literature Cited

1. Hair, M. L. In "Vibrational Spectroscopies for Adsorbed Species"; Bell, A. T.; Hair, M. L., Eds.; American Chemical Society: Washington, D.C., 1980; pp. 1-11.
2. Little, L. H. "Infrared Spectra of Adsorbed Species"; Academic: New York, 1966.
3. Knözinger, H. In "The Hydrogen Bond"; Schuster, P.; Zundel, G.; Sandorfy, C.; Eds.; North Holland: New York, 1976; pp. 1263-1364.
4. Rosencwaig, A.; Gersho, A. J. Appl. Phys. 1976, 47, 64.
5. Yasa, Z. A.; Jackson, W. B.; Amer, N. M. Appl. Optics 1982, 21, 21.
6. McGovern, S. J.; Royce, B. S. H.; Benziger, J. B. J. Appl. Phys. 1985, 57, 1710.
7. McGovern, S. J.; Royce, B. S. H.; Benziger, J. B., Applications of Surface Science 1984, 18, 401.
8. Scott, J. F.; Porto, S. P. S. Phys. Rev. 1967, 161, 903.
9. Clippe, P.; Evrand, R.; Lucas, A. A. Phys. Rev. B 1976, 14, 1715.
10. Boccuzzi, F.; Coluccia, S.; Ghiotti, G.; Morterra, C.; Zecchina, A. J. Phys. Chem. 1978, 82, 1298.
11. Zhizhin, G. N.; Vinogradov, E. A.; Maskalova, M. A.; Yakovlev, V. A. Appl. Spectrosc. Rev. 1982, 18, 171.
12. Kinney, J. B.; Staley, R. H. J. Phys. Chem. 1983, 87, 3735.
13. Flanigen, E. M.; Bennett, J. M.; Grose, R. W.; Cohen, J. P.; Patton, R. L.; Kirchner, R. M.; Smith, J. V. Nature 1978, 271, 512.
14. Flanigen, E. M. In "Zeolite Chemistry and Catalysis"; Rabo, J. A.; Ed.; American Chemical Society: Washington, D.C. 1976; pp. 80-117.
15. Morrow, B. A. J. Chem. Soc. Faraday I. 1974, 70, 1527.
16. Wefers, K.; Bell, G. M. "Oxides and Hydroxides of Aluminum"; Technical Paper No. 19; Alcoa Research Laboratories: East St. Louis, 1972.
17. Baker, A. S. Phys. Rev. 1963, 132, 1474.
18. MacZura, G.; Goodboy, K. P.; Koenig, J. J. In "Encyclopedia of Chemical Technology"; Wiley: New York, 1978; Vol. 2, pp. 218-244.
19. Fredrickson, L. D. Jr. Analytical Chemistry 1954, 26, 1883.
20. Baumgarten, E.; Zachos, A. Spectrochim. Acta 1981, 37A, 93.
21. Borello, E.; Dalla Gatta, G.; Fubini, B.; Morterra, C.; Venturello, G. J. Catalysis 1974, 35, 1.
22. Greenler, R. G. J. Chem. Phys. 1962, 37, 2094.
23. Ulrich, G. D. Chem. Eng. News 1984, 62(32), 22.
24. Bertie, J. E.; Whalley, E. J. Chem. Phys. 1964, 40, 1637.
25. Sexton, B. A. Surface Science 1980, 94, 435.

26. Ibach, H.; Lehwald, S. Surface Science 1980, 91, 187.
27. Stuve, E. M.; Madix, R. J.; Sexton, B. A. Surface Science 1981, 111, 11.
28. Morrow, B. A.; Thomson, L. W.; Wetmore, R. W. J. Catalysis 1973, 28, 332.
29. Demuth, J. E.; Ibach, H. Chem. Phys. Lett. 1979, 60, 395.
30. Sexton, B. A. Surface Science 1980, 88, 299.
31. Parkyns, N. D. J. Chem. Soc. (A) 1969, 1910.
32. Gregg, S. J.; Ramsay, J. D. F. J. Phys. Chem. 1969, 73, 1243.
33. Morterra, C.; Coluccia, S.; Ghiotti, G.; Zecchina, A. Z. Phys. Chem. 1977, 104, 275.
34. Peri, J. B. J. Phys. Chem. 1966, 70, 3168.
35. Little, L. H.; Amberg, C. H. Canad. J. Chem. 1962, 40, 1997.
36. Amenomiya, Y.; Morikawa, Y.; Pleizier, G. J. Catalysis 1977, 46, 431.
37. Peri, J. B. J. Phys. Chem. 1975, 79, 1582.
38. Peri, J. B. J. Phys. Chem. 1965, 69, 220.

RECEIVED April 24, 1985



## Carbon Monoxide Oxidation on Platinum: Coverage Dependence of the Product Internal Energy

D. A. Mantell<sup>1</sup>, K. Kunimori<sup>2</sup>, S. B. Ryal<sup>3</sup>, and Gary L. Haller

Department of Chemical Engineering, Yale University, New Haven, CT 06520

Time resolved FTIR emission spectroscopy is used to detect vibrationally excited gas phase  $\text{CO}_2$  from catalyzed CO oxidation on a Pt foil. A continuous  $\text{O}_2$  free jet and a pulsed CO jet ( $\approx 200 \mu\text{sec}$  FWHM) supply the reactants to the surface. The infrared emission of the  $\text{CO}_2$  product is analyzed with 30  $\mu\text{sec}$  time resolution using the time multiplexing capabilities of a commercial Fourier transform spectrometer. At low CO pressures the total signal parallels the time dependent flux to the surface with only minimal changes in the infrared spectra. At high CO pressures the reaction can be shut off as the oxygen on the surface is depleted. These IR spectra show large changes in internal energy of the product  $\text{CO}_2$ .

The oxidation of CO on group VIII metals is one of the most studied metal catalyzed reactions and many aspects of it are well understood(1,2). Reaction occurs by a Langmuir-Hinshelwood mechanism between chemisorbed molecular CO and atomic oxygen. However, the kinetics are complex because high coverage of CO inhibits oxygen dissociation but CO chemisorbs on top of an oxygen covered surface. At low surface concentration of both species, the reaction is limited by oxygen chemisorption and the rate is directly proportional to oxygen partial pressure. With high coverage of adsorbed oxygen atoms and low CO coverage, the reaction is directly proportional to CO partial pressure. At relatively high coverage of both species, the case for most practical applications of catalytic oxidation of CO, the rate is about first order in oxygen pressure and inverse first order in CO.

<sup>1</sup>Current address: Physics, B-268, National Bureau of Standards, U.S. Department of Commerce, Washington, DC 20234

<sup>2</sup>Current address: Institute of Materials Science, University of Tsukuba, Sakura-mura, Ibaraki 305, Japan

<sup>3</sup>Current address: Aerodyne Research, Inc., Billerica, MA 01821

In the case of CO oxidation on Pt, there have been performed several experiments which elucidate the dynamics of the reaction. Because the reaction between adsorbed CO and oxygen atoms is activated and CO<sub>2</sub> has only a van der Waals interaction with the surface, a part of the energy acquired to form the activated complex may be distributed among degrees of freedom of the product molecule. In the limiting case where no energy is exchanged with the surface during the desorption event and a complete analysis of its partitioning between translation, rotation, vibration and electronic energies in the product is available, it is in principle possible to construct a potential energy surface which would describe the molecular structure of the activated complex and the dynamics of the desorption event. While this ideal is not yet practical, we have made significant steps toward gaining this information for CO oxidation on Pt. Several investigations have found that CO<sub>2</sub> molecules leave the surface with angular distributions which are strongly peaked in the direction of the surface normal which implies excess translational energy(3-5). Time-of-flight analysis of CO oxidation on a polycrystalline Pt foil also demonstrates that the product leaves the surface with kinetic energy in excess of that expected if the molecule were in equilibrium with the surface(6). Infrared emission experiments show that the CO<sub>2</sub> product of CO oxidation is, moreover, vibrationally(7,8) and rotationally(7) hotter than the surface. In very recent experiments it has further been observed that the angular distributions (translational energy)(9) and vibrational energy of the product CO<sub>2</sub> (15) are strong functions of surface coverage. We will confirm here that this is the case for rotational and vibrational distributions. Because the activation energy for the surface reaction between adsorbed CO and adsorbed oxygen atoms depends on the coverage(4), this is not unexpected. Qualitatively one might anticipate that the product CO<sub>2</sub> would have less excess energy at high oxygen coverage because there is less of a barrier to reaction and therefore the activated complex would have less energy to dissipate. However, the matter is somewhat complicated by the fact that as the coverage increases, the heat of adsorption of both CO and O<sub>2</sub> decrease(4,10), but suffice it to say that at low coverage the activated complex is about 100 kJ above CO<sub>2</sub> in the gas phase and that this value increases as coverage increases.

In experiments using a steady-state mixed CO-O<sub>2</sub> molecular beam reacting on a Pt foil, we observed excess energy in all vibrations and rotation and large changes in the amount of excess energy in the symmetric stretch of desorbed CO<sub>2</sub> as a function of surface temperature(11,12). There was a strong suggestion that the latter was primarily due to changes in surface coverage which accompany a change in surface temperature rather than a direct coupling between the internal energy states and the surface temperature. In order to test this hypothesis, we initiated pulsed molecular beam experiments with time resolved-infrared emission spectroscopy of the desorbed product. A steady-state beam of O<sub>2</sub> was incident on a Pt foil and a second pulsed beam was simultaneously directed onto the foil. The CO pulses were 200 μs halfwidth at half maximum height with a 2000 μs pause between pulses(12). The 2000 μs pause is long enough such

that the surface coverage of oxygen could recover to its steady-state value at the given reaction temperature and the particular flux used in the oxygen beam. The number of CO molecules in the pulse could be easily varied by changing the stagnation pressure in the pulsed nozzle source. At low pressures the surface coverage of oxygen did not vary much from its steady state value while at high pressures we could effectively perform a titration of the surface oxygen as the pulse passed over the surface. The leading edge of the pulse reacted at the relatively high oxygen coverage but, since reaction removed oxygen faster than it could be replenished by adsorption (in part due to CO inhibition), toward the end of the pulse reaction occurred at very low oxygen coverage. The pulsed experiment allowed us to vary the coverage isothermally over a much larger range than would have been practical by varying the flux of a steady-state source.

Time-resolved infrared emission spectroscopy of the desorbed CO<sub>2</sub> pulse effectively provides a coverage-resolved picture of the vibrational and rotational energy distribution in the product CO<sub>2</sub>. The time-resolved spectroscopy is accomplished using a Fourier transform spectrometer and a computer algorithm which allows efficient data collection by varying the time of initiating the beginning of the repetitive event (pulse of CO) and the beginning of the mirror movement in the interferometer(13). To obtain an interferogram one requires the measurement of intensity as a function of mirror displacement. Practically, data is collected only at discrete intervals of mirror displacement. Thus, to obtain a spectrum at a given time in a repetitive event, one could collect one data point at the same time into the repetitive event at each of the discrete mirror positions. This would produce the interferogram which would Fourier transform into a frequency spectrum. This is very inefficient but the same thing can be accomplished by repeating the event throughout the movement of the interferometer mirror and taking data as rapidly as practical. The computer algorithm keeps track of all of the various relations between mirror position and time relative to initiation of the repetitive event. After data points have been collected at all combinations of time intervals into the repetitive event and mirror position with appropriate signal averaging to attain the required signal-to-noise ratio, the data is sorted point by point to construct interferograms, and thus spectra, at discrete times through the repetitive event. In our experiments, a total of 65 emission spectra of the asymmetric stretch of CO<sub>2</sub> were collected at 30 μs intervals across a CO pulse. The spectral resolution used was 8 cm<sup>-1</sup>.

Time-resolved Fourier transform infrared spectroscopy has been used surprisingly little considering the number of commercial spectrometers that are currently in laboratories and the applicability of this technique to the difficult time regime from a few μs to a few hundred μs. One problem with time-resolved Fourier transform spectroscopy and possibly one reason that it has not been more widely used is the stringent reproducibility requirement of the repetitive event in order to avoid artifacts in the spectra(14). When changes occur in the emitter source over the course of a

measurement in normal Fourier transform spectroscopic collection, they are averaged into every point and the Fourier transformed data gives the time-averaged spectrum. Because of the nature of the data collection and reconstruction algorithm, a time-resolved Fourier interferogram will contain data points collected at very different real times. When Fourier transformed, adjacent data points which exhibit intensity fluctuation due to evolution (irreproducibility) in the repetitive event will produce artifacts in the frequency spectrum. Since they are not molecular related frequencies, they will not always appear as emission bands but each will have some phase relative to the molecular emission frequency signals and these can look like absorption bands, emission bands, or something in between. By starting the data collection for sets of time-resolved spectra at slightly different points in the interferogram, we are able to control this phase. Adding transformed sets of time-resolved spectra with opposite phases of the artifacts removes the artifacts while the signal-to-noise of the molecular frequencies simply improves, as one would expect, proportional to the square root of the total measurement time. Extremely stringent reproducibility in the repetitive event is still required but a small and monotonic decay in the signal can be corrected (artifacts removed) by the approach outlined here. It should be noted that artifacts can be differentiated from molecular frequencies by their regular spacing as well as their phase. The spacing, position and phase of artifact frequencies all vary in a systematic fashion when the pulse frequency is changed while, of course, the molecular emission frequencies are constant.

At low enough CO pressures behind the pulsed nozzle the reaction rate scales linearly with CO pressure, i.e., we are in the regime of relatively high oxygen coverage where the reaction is first order in CO. Under these conditions the time-resolved spectra do indeed show that the CO<sub>2</sub> emission intensity matches the CO flux intensity in the pulse with only minimal changes in the spectrum shape as a function of time into the pulse. It is only at higher CO pressures where the reaction rate is not linear with CO pressure that there are large surface coverage induced changes in the emission spectra. In Figure 1 we show an example of a sequence of such spectra obtained on a 900K surface with about  $2 \times 10^{18}$  molecules/cm<sup>2</sup>-s steady-state O<sub>2</sub> flux and a CO flux about one order of magnitude larger at the peak intensity of the pulse. The integrated emission rises rapidly to a maximum rate, then decays as the surface becomes depleted of adsorbed oxygen, begins to increase as oxygen adsorption catches up to oxygen consumption by reaction, and finally decays again as the surface becomes depleted in CO at the end of the pulse. The double lobed band with a minimum between the lobes at 2143 cm<sup>-1</sup> is due to CO which adsorbed and desorbed vibrationally excited without reaction. From its intensity the relative transient CO coverage can be estimated. It reaches a maximum just where the CO<sub>2</sub> signal is maximum and then decays monotonically. The beginning of the recovery in oxygen coverage indicated by the increase in CO<sub>2</sub> signal after the 10th spectrum in the sequence of Figure 1 occurs when the CO coverage is about half of the maximum attained during the pulse. Analysis of the band width and centroid allows an esti-

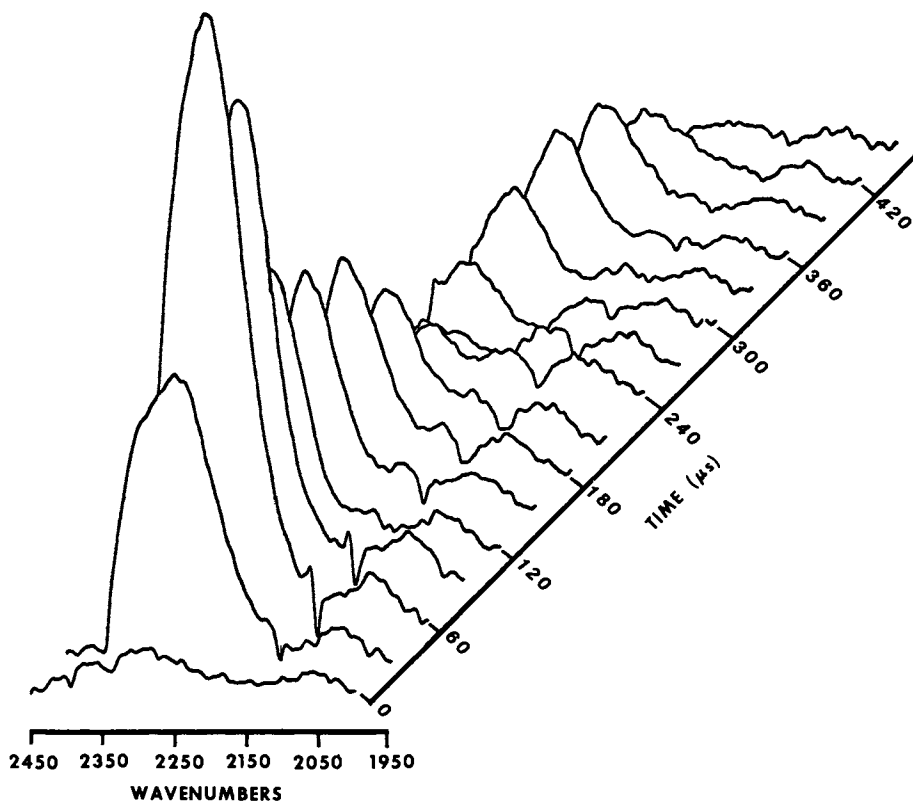


Figure 1. The infrared emission spectra of  $\text{CO}_2$  in the asymmetric stretch region and of  $\text{CO}$  as a function of 30  $\mu\text{s}$  intervals through a 200  $\mu\text{s}$  pulse. The surface temperature was 900K and the resolution was 8  $\text{cm}^{-1}$ .

mation of the rotational and vibrational temperatures. These are roughly 1600K, i.e., well above the surface temperature of 900K, for the spectra representing initial CO<sub>2</sub> desorption at high oxygen coverage. The vibrational temperature is, by necessity of the low resolution, some kind of average of the temperatures for asymmetric, symmetric stretches, and bending. Our high resolution, steady-state experiments indicate that these temperatures are all well above the surface temperature but they are not the same(7,11). With each successive time increment (30 μs) as the oxygen coverage on the surface is reduced the vibrational temperature changes very little but the rotational temperature drops rapidly to a value below the surface temperature. This drop in rotational temperature cannot be attributed to gas phase collisions since it drops even when the CO pressure is falling.

The vibrational temperature does not change appreciably until we reach spectrum 10 in the sequence shown in Figure 1, i.e., until oxygen depletion has nearly stopped the reaction. Our crude estimate of the vibrational temperature based on the centroid position and the assumption that all vibrational temperature are the same suggests that the vibrational temperature, like the rotational temperature, falls below the surface temperature. This cannot be the case because the emission intensity would be too low to detect in our system if the asymmetric temperature were in fact that low. Our interpretation is that symmetric stretch and bending have cooled to the point where they make very little contribution to the emission, i.e., reaction of CO on the Pt surface with very low oxygen coverage produces a CO<sub>2</sub> molecule with excess energy rather selectively channeled into asymmetric stretch. A possible interpretation is that the reaction coordinate of the activated complex is along the axis of the product CO<sub>2</sub>, i.e., a nearly linear activated complex exists at the top of the barrier. In such a linear activated complex, formation of the new C-O bond with concerted breaking of the Pt-O bond would mirror asymmetric stretch (not symmetric) and would not excite the bending mode. However, a more complete analysis of the reaction dynamics will require additional time-resolved experiments. In particular, improvement in the spectral resolution of the time-resolved spectra and detailed analysis of possible collision effect on rotational temperature are needed. These experiments are now in progress.

#### Literature Cited

1. Engel, T.; Ertl, G. Adv. Catal. 1979, 28, 1.
2. Engel, T.; Ertl, G. In "The Chemical Physics of Solid Surfaces and Heterogeneous Catalysis"; King, D. A.; Woodruff, D. P., Eds.; Elsevier: New York, 1982; p. 73.
3. Palmer, R. L.; Smith, J. N. J. Chem. Phys. 1974, 60, 1453.
4. Campbell, C.T.; Ertl, G.; Kuipers, H.; Segner, J. J. Chem. Phys. 1980, 73, 5862.

5. Matsushima, T. Surface Sci. 1983, 127, 403.
6. Becker, C. A. Cowin, J. P. Wharton, L. Auerbach, D. J. Chem. Phys. 1977, 67, 3394.
7. Mantell, D. A. Ryali, S. B. Halpern, B. L. Haller, G. L. Fenn, J. B. Chem. Phys. Lett. 1981, 81, 185.
8. Bernasek, S. L. Leone, S. R. Chem. Phys. Lett. 1981, 84, 402.
9. Segner, J. Campbell, C. T. Doyen, G. Ertl, G. Surface Sci. to be published.
10. Pacia, N. Cassuto, A. Pentenero, A. Weber, B. J. Catal. 1976, 41, 455.
11. Mantell, D. A. Ph.D. Thesis, Yale University, New Haven, CT, 1983.
12. Mantell, D. A. Ryali, S. B. Haller, G. L. Chem. Phys. Lett. 1983, 102, 37.
13. Murphy, R.E. Cook, F. H. Sakain, H. J. Opt. Soc. Am. 1975, 65, 600.
14. Garrison, A. G. Crocombe, R. A. Mamantove, G. Haseth, J. A. Appl. Spectrosc. 1980, 34, 399.
15. Brown, L. S. Bernasek, S. L. J. Chem. Phys. 1985, 82, 2110.

RECEIVED June 21, 1985

## The Role of Intercalates in Heterogeneous Catalysis

William Jones, John M. Thomas, D. Tilak B. Tennakoon, Robert Schlogl<sup>1</sup>, and Paul Diddams

Department of Physical Chemistry, University of Cambridge, Lensfield Road, Cambridge  
CB2 1EP, England

The intercalates of sheet aluminosilicates (clays) and of graphite are demonstrated to be efficient catalysts for a variety of reactions, and results obtained using several analytical techniques, including magic angle spinning NMR, are presented. For the clay family, Bronsted acidity is the principal source of activity with the relative concentration of protonated and non-protonated reactants being dependent upon the nature of the exchangeable cation. Using  $\text{FeCl}_3$  - graphite intercalates - formed using a photochemical procedure and subsequently reduced using K/naphthalide - an efficient catalyst for the production of acetylene from syngas has been produced.

The phenomenon of intercalation - whereby guest molecules are inserted between the sheets of a layered host matrix - is of interest for various reasons (1). From a structural viewpoint (2) the crystallographic arrangement of the guest molecules with respect to the host lattice is known to be considerably dependent upon *inter alia* stoichiometry, temperature and preparation procedures (3,4). The macroscopic stoichiometry of host and guest - as opposed to the microscopic domain-like composition now known to exist in, for example, certain graphite intercalates (5,6) - is, almost infinitely variable. For graphite intercalates such variation is generally accommodated by "staging" (7), whilst for sheet silicates interstratification and the insertion of one, two, three up to 10 or more sheets of guest between each pair of host layers (8,9), gives considerable scope for controlling local reactant (i.e. guest) concentrations.

This paper describes two broad types of intercalation compounds which are based on graphite on the one hand and sheet aluminosilicate (clay) hosts on the other. Taken together these provide a rich variety of examples of heterogeneously catalysed reactions. Appropriately cation exchanged clays, for example, act as efficient catalysts for a number of commercially important proton catalysed reactions (10-13) (see Table I). Graphite intercalates, whilst also capable of

<sup>1</sup>Current address: Institut für Physik, Universität Basel, Switzerland



effecting various organic reactions have, in particular, been reported to be efficient materials for syngas conversion and ammonia synthesis (see Table I) (14,15).

Table I. Typical reactions catalysed by clay and graphite intercalates

---

(a) By clays include (10) :

- (i) addition to alkenes of:-
  - water
  - alcohols
  - thiols
  - carboxylic acids
- (ii) elimination reactions of the type:-
  - water from alcohols to yield ethers
  - ammonia from amines to yield secondary amines
  - hydrogen sulphide from thiols to yield di-alkyl sulphides

(b) By graphite intercalates include (15) :

- fluorination of aromatic hydrocarbons
  - alkylation of nitriles and ketones
  - condensation of carbonyl derivatives
  - Fischer-Tropsch synthesis
  - ammonia synthesis
- 

For these systems, however, the small particle sizes involved (typically less than 5 microns) quite frequently require a variety of techniques to allow adequate characterization. For example, informative structural data (which might otherwise be obtained from 4-circle diffractometry) requires a combined analytical approach using high resolution electron microscopy, electron diffraction, powder X-ray diffraction and some spectroscopic technique to identify the species present. (SbCl<sub>5</sub>, for example, upon intercalation into graphite dissociates, yielding a variety of species, which we designate SbCl<sub>x</sub>, between the sheets (16,17) and organic amines are frequently protonated inside the layers of a clay particle (18,19)). Nevertheless a detailed picture of the intercalated material may be built up and indeed some of the techniques which will be subsequently mentioned (as well as others - e.g. Mossbauer spectroscopy) do allow some characterization of the catalysts under normal operating reaction conditions. We begin by outlining some relevant structural features of the guest matrices.

The principal building block of a sheet silicate is shown in Figure 1 and consists of two silica tetrahedra on either side of aluminium (pyrophyllite) or magnesium (talc) octahedra. Such structures are electro-neutral. Naturally occurring aluminosilicates, however, demonstrate a considerable variation in composition - with isomorphous replacement occurring both in the octahedral and tetrahedral manifolds. Table II gives typical examples of the replacements which may occur. In beidellite, for example, charge imbalance may result from substitution within the tetrahedral sheet - where Al<sup>3+</sup> has replaced Si<sup>4+</sup> - and this is a situation akin to that found in

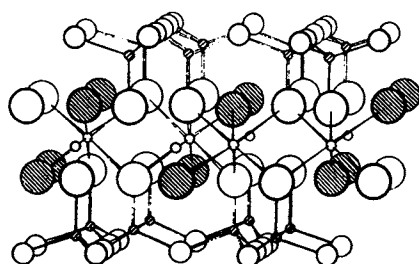
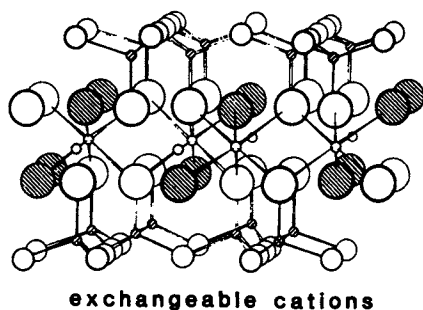


Figure 1. Schematic illustration of the structure of sheet aluminosilicates (After Brindley, G.W.; MacEwan, D.M.C. In "Ceramics - a symposium"; Green, A.T.; Stewart, G.H. Eds.; Br. Ceramic Society; 1953, 15).

zeolitic solids. In montmorillonite, on the other hand, the replacement is principally in the octahedral sheet ( $Mg^{2+}$  for  $Al^{3+}$ ).

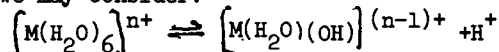
Table II. Idealised compositions of representative sheet aluminosilicates.

---

|   |   |
|---|---|
| <u>Reference Structures</u>                       |   |
| Pyrophyllite and talc carry no residual charge    | $\left[ Si_8 \right]^{IV} \left( Al_4 \right)^{VI} O_{20} (OH)_4$ <p style="text-align: center;"><u>PYROPHYLLITE</u></p> $\left[ Si_8 \right]^{IV} \left( Mg_6 \right)^{VI} O_{20} (OH)_4$ <p style="text-align: center;"><u>TALC</u></p> |
| <u>Structures with a cation exchange capacity</u> |   |
| Within octahedral layer for dioctahedral          | $M_x^+ \left[ Si_8 \right]^{IV} \left( Al_{4-x} Mg_x \right)^{VI} O_{20} (OH)_4$ <p style="text-align: center;"><u>MONTMORILLONITE</u></p>  |
| Within tetrahedral layer for dioctahedral         | $M_x^+ \left[ Si_{8-x} Al_x \right]^{IV} \left( Al_4 \right)^{VI} O_{20} (OH)_4$ <p style="text-align: center;"><u>BEIDELLITE</u></p>   |
| Within octahedral layer for trioctahedral         | $M_x^+ \left[ Si_8 \right]^{IV} \left( Mg_{6-x} Li_x \right)^{VI} O_{20} (OH)_4$ <p style="text-align: center;"><u>HECTORITE</u></p>  |

---

Whilst a rich variety of such materials occurs naturally, it is frequently advantageous to synthesise particular silicates so as to exclude certain impurity ions e.g. paramagnetic centres from samples prepared for study by MASNMR. But more important, perhaps, the charge imbalance resulting from this isomorphous substitution is compensated for by the presence of hydrated exchangeable cations within the interlamellar region. For small, highly charged ions pronounced polarization of the interlayer water may take place (see scheme) with the accompanying generation of protons. For a cation carrying a charge of  $n+$  we may consider:



These protons may then catalyse certain Bronsted reactions. One particularly effective interlamellar cation is known to be  $Al^{3+}$  (2).

### Experimental

(a) Clay as host. Naturally occurring montmorillonite samples of various origins have been used, with in each case  $Mg^{2+}$  replacement for the octahedral aluminium being the principal substitution. Other related materials used were synthetically prepared hectorite, Laponite XLG, provided by Laporte Chemicals (18) and beidellite prepared in these laboratories (19). (Magic angle spinning NMR along

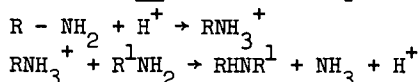
with other tests confirmed that the sample was beidellitic in character, vide infra.) Cation exchange capacity measurements, as well as cation exchange were completed in the usual way. The experimental instrumentation used has been described elsewhere (18,19).

(b) Graphite as host. Natural graphite crystals of two sizes (S40:2 mm; AF:1-2 micron) were obtained from Kropfmuhl, Bavaria (5). Intercalates of FeCl<sub>3</sub> were prepared by two methods - (a) from the vapour phase using the established "two-bulb" procedure and (b) by u.v. irradiation of CCl<sub>4</sub> dispersions. In both cases X-ray powder diffraction indicated that guest species were inserted between every graphite sheet i.e. that the material was nominally 1st stage. These FeCl<sub>3</sub> intercalates were then reduced by either high temperature hydrogen treatment or by reduction with a K/naphthalene mixture in THF at 0°C. The materials were then exposed to air prior to catalytic testing. Fuller details concerning preparation, elemental analyses and crystallographic data are described elsewhere (4,5).

### Results

(a) Clays. That the degree of local acidity within the interlayer region is very much dependent upon the identity of the exchangeable cation may be seen from IR studies of intercalated organic bases. Thin self-supporting clay films (appropriate for IR measurement) readily take up organic amines such as cyclohexylamine with displacement of the major fraction of the intercalated water. For the Na<sup>+</sup>-exchanged sample the majority of the amine is present in the unprotonated form - there being insufficient Bronsted acidity generated by the interlayer cation. When Al<sup>3+</sup> is the exchangeable cation, however, a major fraction of the intercalated amine becomes protonated (see Figure 2).

The balance between those molecules which are protonated and those which are not has emerged as an important function in determining the course of any reaction occurring within the interlamellar region. One carefully studied reaction is that of the elimination of ammonia from amines (21), a reaction proceeding by two simple steps



For R = benzylamine (B) and R<sup>1</sup> = cyclohexylamine (C) the amounts of BB and CC and of the BC cross product formed as the relative concentration of the reactants varies is shown in Figure 3. Clearly whilst for an approximately 50:50 reactant mixture the amount of CC formed has dropped to practically zero that of the cross product (BC) is still high. The interpretation suggests that the less basic amine is more readily intercalated and essentially remains unprotonated whilst the more basic amine, although present in much smaller concentration, removes nearly all of the available protons. Hence the major reaction is between protonated B and non-protonated C, yielding BC (23,23).

Clearly under such circumstances there is considerable scope for fine-tuning of selectivity if the relative amounts/ concentrations of the various species are taken into account. Analysis of another important clay-catalysed reaction (that of the esterification of acetic acid (24)) also demonstrates how variation of the exchangeable

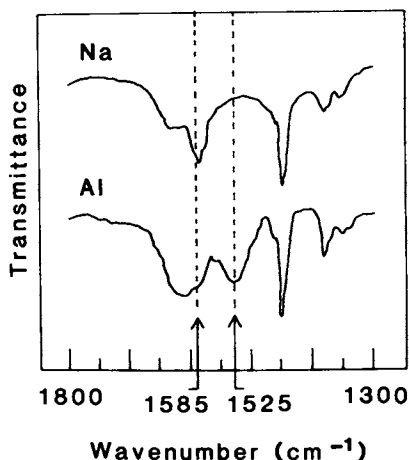


Figure 2. Infrared spectra of a Na<sup>+</sup> and Al<sup>3+</sup> exchanged clays following the uptake of cyclohexylamine. Absorptions at 1585 and 1525 cm<sup>-1</sup> are characteristic of the neutral and protonated amine species, respectively.

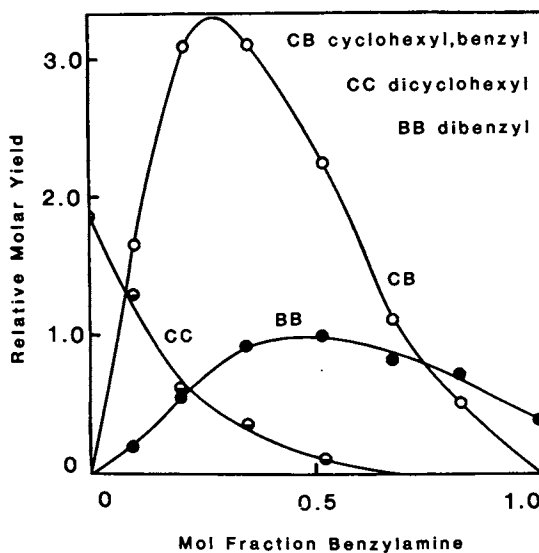


Figure 3. Relative molar yields of the secondary amines formed from reaction mixtures of cyclohexylamine (c) and benzylamine (B). See text.

cation may lead to changes in activity (as might be expected) but is also accompanied by pronounced changes in selectivity. In this particular reaction, however, it is unlikely that the relatively acid sensitive sheet silicates will remain unaffected by the presence of the acetic acid.

We alluded earlier to the variety of structural modifications which may be observed in sheet silicates. Clearly it is a matter of considerable importance to be able to determine if, for example, the aluminium content within a clay arises purely from octahedral substitution (as in montmorillonite) or whether there is some tetrahedral component (as in beidellite).  $^{27}\text{Al}$  MASNMR readily provides the necessary answers. Figure 4 illustrates the  $^{27}\text{Al}$  spectrum for a synthetic beidellite material with  $\text{Na}^+$  as charge balancing cation. Aluminium in two distinct chemical environments is observed, with chemical shifts corresponding to octahedrally and tetrahedrally co-ordinated aluminium. The associated  $^{29}\text{Si}$  spectrum for this sample is shown in Figure 4. The assignment given is such (see Table III) that the peak at -88ppm is associated with silicon linked (within the tetrahedral manifold) via oxygen to 2 silicons and 1 aluminium whilst the peak at -93ppm is associated with silica linked exclusively to other silicons (25-27). Using an analysis based on Loewenstein's rule and widely used in zeolite structural analyses (28) we have shown elsewhere (20) that for this particular synthetic beidellite the  $(\text{Si}/\text{Al})_{\text{tet}}$  ratio is 11.5 : 1.0. The octahedral cation lattice is believed to be entirely occupied by aluminium.

Table III.  $^{29}\text{Si}$  chemical shifts for some sheet silicates

|                                    | $\delta_{\text{Si}}$ (from TMS)           | ref. |
|------------------------------------|---|------|
| Pyrophyllite                       | -95.1                                     | (20) |
| Talc                               | -98.1                                     | (28) |
| Montmorillonite                    | -93.4                                     | (20) |
| Beidellite                         | -93 (OAl)<br>-88 (1Al)                    | (20) |
| Kaolinite                          | -91.5                                     | (28) |
| Synthetic<br>trioctahedral<br>clay | -95.1 (OAl)<br>-90.1 (1Al)<br>-85.5 (2Al) | (26) |

The use of the synthetic clay Laponite - which contains very little structural aluminium - is helpful in monitoring the nature of the interlamellar cation  $\text{Al}^{3+}$  - an exchangeable cation which generates high catalytic activity. Figure 5 illustrates the  $^{27}\text{Al}$  NMR spectrum obtained from  $\text{Al}^{3+}$  exchanged Laponite. Both octahedral and tetrahedral signals are observed (18). With increasing ageing of these materials there are clearly changes in the relative amounts of detectable tetrahedrally and octahedrally bound aluminium which is believed to arise from the formation of a polymeric hydroxy cation species.

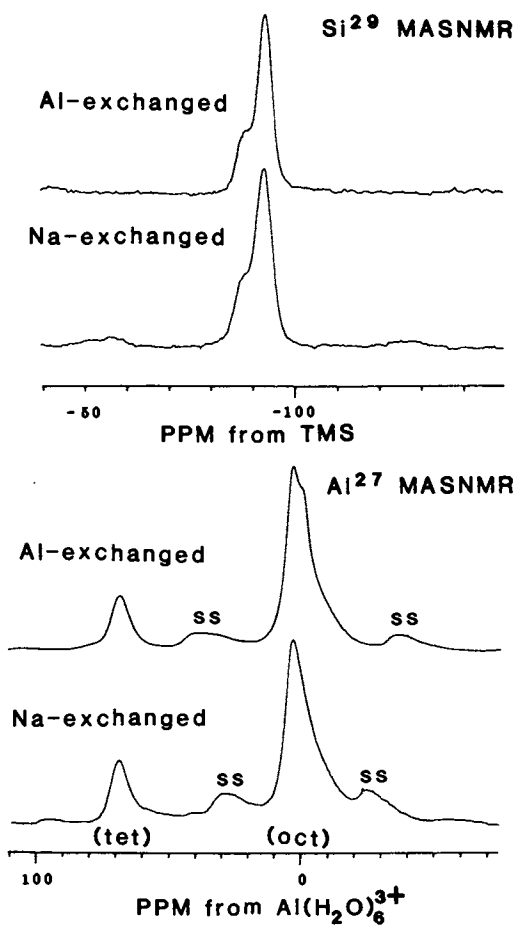


Figure 4.  $^{29}\text{Si}$  and  $^{27}\text{Al}$  MASNMR spectra for the  $\text{Na}^+$  and  $\text{Al}^{3+}$  exchanged forms of the synthetic beidellite sample.

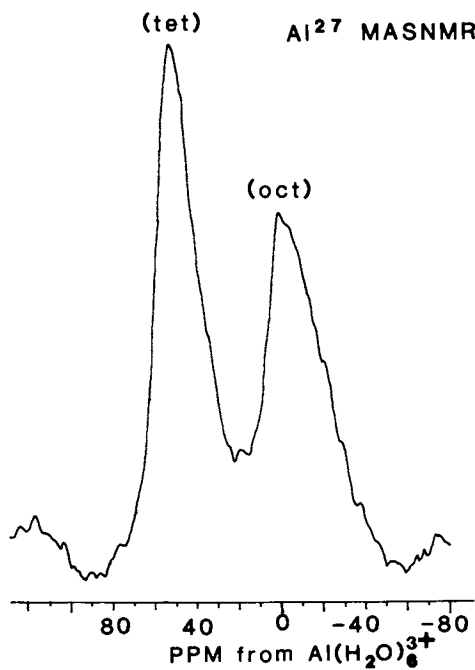


Figure 5.  $^{27}\text{Al}$  MASNMR spectra for an  $\text{Al}^{3+}$  exchanged sample of Laponite - the aluminium signal results entirely from material resulting from the cation exchange process.



(b) Graphite intercalation compounds. One of our interests in graphite intercalates as heterogeneous catalysts arose because it was felt that reactions proceeding between the graphite sheets may lead to particularly interesting selectivities during synthesis (29-31) e.g. circumvention of Schultz-Flory statistics in Fischer-Tropsch chemistry (32). Indeed it has frequently been assumed that for such intercalation compounds under catalytic conditions guest molecules (and presumably the active species) remain present between the graphite sheets. It has recently been shown however that  $\text{FeCl}_3$  intercalates of graphite are both air- and temperature-sensitive and that, for example, in the presence of water rapid de-intercalation takes place (33). It is unlikely, as a consequence, that under reaction conditions where water is a by-product and at operating temperatures of, for example,  $300^\circ\text{C}$  that the truly intercalated state will survive. As a consequence it is unlikely to be the intercalated state per se which is the active phase.

A strategy which evolved from this viewpoint, however, was the use of intercalation compounds as precursors for carbon (graphite) supported materials - where particle size might be controlled by the control of the 'domain size' for the inserted molecules and the method used for de-intercalation. In addition, the electronic properties of the support may be modified by the degree of residually intercalated material within the graphite sheets. Such a strategy clearly suggests that identical starting intercalation compounds may lead to very different types of catalysts, depending in particular upon the de-intercalation and reduction conditions (32).

First-stage intercalation compounds of  $\text{FeCl}_3$  were prepared and characterized by a variety of techniques (5,33). Two distinct preparation procedures were used: (see scheme): from vapour, using the established "two-bulb" method and from solution using U.V. light (see Experimental).

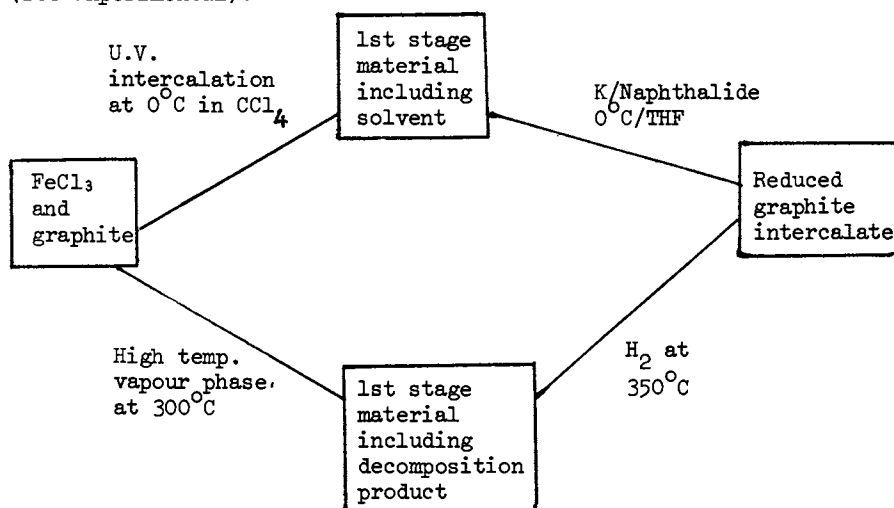


Table IV. Comparison of activities and selectivities for two reduced graphite intercalates<sup>1</sup>

| Operating Temperature (°C) | Time on Stream (hrs) | Catalyst A <sup>2</sup>   |                            | Catalyst B <sup>3</sup>   |                            |            |
|----------------------------|----------------------|---------------------------|----------------------------|---------------------------|----------------------------|------------|
|                            |                      | Conversion <sup>4</sup> % | Selectivity <sup>5</sup> % | Conversion <sup>4</sup> % | Selectivity <sup>5</sup> % |            |
| 100                        | 3                    | 1.18                      | 20 Ethane                  | 22.20                     | 96 Ethyne                  |            |
|                            |                      |                           | 17 Ethene                  |                           |                            |            |
|                            |                      |                           | 25 Propane<br>37 Butane    |                           |                            |            |
| 300                        | 24                   | 0.24                      | 94 Ethane                  | 19.7                      | 98 Ethyne                  |            |
|                            |                      | 3                         | 0.56                       | 74 Ethene                 | 0.20                       | 98 Propane |
|                            |                      |                           | 24                         | 0.27                      | 93 Propane                 | 0.30       |

<sup>1</sup> Using 300 mg of catalyst and a H<sub>2</sub>:CO feedstock ratio of 3:1. Flow rate was 7ml/min.

<sup>2</sup> Prepared from vapour phase and hydrogen reduction.

<sup>3</sup> Prepared from solution and K/Naphthalide reduction.

<sup>4</sup> Conversions are number of carbon atoms appearing in hydrocarbons vs number of carbon atoms in CO.

<sup>5</sup> Only major components are given.

Subsequently the intercalates - without prior exposure to air - were reduced either by hydrogen gas or using potassium naphthalide in THF. (34) Clearly the choice of intercalation and reduction temperature will control the nature of the final product. These materials were then exposed to air. Some of the results obtained are given in Table IV. Clearly catalyst B in its high conversion and selectivity to acetylene demonstrates unique properties.

From these results there is evidence that it is possible to use well-defined graphite intercalates as precursors for deliberate de-intercalation, yielding a multiphasic supported material which is catalytically active.

#### Acknowledgments

We gratefully acknowledge financial support from the SERC, National Coal Board and B.P. Research (Sunbury). Discussions with Prof. H. Purnell and Dr. J. Ballantine (Swansea) and Drs T. Rayment and J. Klinowski are appreciated.

#### Literature Cited

1. Whittingham, M.S.; Jacobson, A.J. Eds.; "Intercalation Chemistry"; Academic Press, New York, 1982.
2. Thomas, J.M. In "Physics and Chemistry of Electrons and Ions in Condensed Matter"; Mott, N.F.; Yoffe, A.D.; Acrivos, J.V. Eds.; N.A.T.O. Davy A.S.I.; 1984, in press.
3. Thomas J.M.; Schlogl,R.; Jones, W.; Korgul, P., Carbon 1983, 21, 409.
4. Schlogl, R; Jones, W. J de Physique 1984, in press.
5. Schlogl, R; Bowen, P; Millward, G.R.; Jones, W; Boehm, H.P. J. Chem. Soc., Faraday Trans. 1 1983, 79, 1793.
6. Thomas, J.M.; Millward, G.R.; Schlogl,R; Boehm, H.P. Mater. Res. Bull. 1980, 15, 671.
7. Dresselhaus, M.S.; Dresselhaus, G. Adv Phys. 1981, 30, 139.
8. Brindley, G.W. In "X-ray Identification and Crystal Structure of Clay Minerals"; Mineralogical Society of Great Britain, London, 1961.
9. Theng, B.K.C. In "The Chemistry of Clay Organic Reactions"; Hilger, London, 1974.
10. Thomas, J.M. In "Intercalation Chemistry"; Whittingham, M.S.; Jacobson, A.J.; Eds.; Academic Press, New York, 1982, 56.
11. Pinnavaia, J.J. Science 1983, 220, 365.
12. Thomas, J.M. Phil. Trans. Roy. Soc. A 1974.
13. Tennakoon, D.T.B.; Thomas, J.M.; Tricker, M.J. J. Chem. Soc., Dalton 1974, 2211.
14. Boersma, M.A.M. In "Advanced Materials in Catalysis"; Burton, J.J.; Garten, R.L.; Eds; Academic Press, N.Y., 1977; p.67.
15. Setton, R.; Beguin, F.; Piroelle, S. Synthetic Metals 1982, 4, 299.
16. Jones, W.; Korgul, P.; Schlogl, R.; Thomas, J.M. J. Chem. Soc. Chem. Commun. 1983, 468.
17. Schlogl, R.; Jones, W.; Thomas, J.M. J. Chem. Soc. Chem. Commun. 1983, 1330.
18. Tennakoon, D.T.B.; Schlogl, R.; Rayment, T.R.; Klinowski, J.; Jones, W.; Thomas, J.M. Clay Minerals 1983, 18, 357.

19. Jones, W.; Tennakoon, D.T.B.; Thomas, J.M.; Williamson, L.J.W.; Ballantine, J.A.; Purnell, H.J. Proc. Indian Acad. Sci.(Chem. Sci) 1983, 92, 27.
20. Diddams, P.A.; Thomas, J.M.; Jones, W.; Ballantine, J.A.; Purnell, H.P. J. Chem. Soc., Chem. Commun. 1983, in press.
21. Ballantine, J.A.; Purnell, J.H.; Rayanakorn, M.; Thomas, J.M.; Williams, K.J. J. Chem. Soc. Chem. Commun. 1981, 9.
22. Ballantine, J.A.; Purnell, J.H.; Thomas, J.M. Clay Minerals 1983 18, 347.
23. Purnell, J.H.; Ballantine, J.A. J. Mol. Catalysis in press.
24. Ballantine, J.A.; Davies, M.; O'Neil, R.M.; Patel, I.; Purnell, J.H.; Rayanakorn, M.; Williams, K.J. J. Mol. Cat. 1984, 26, 57.
25. Klinowski, J.; Ramdas, S.; Fyfe, C.A.; Hartman, J.S. J.C.S. Faraday II 1982, 78, 1025.
26. Lipsicas, M.; Raythatha, R.H.; Pinnavaia, T.J.; Johnson, I.D.; Giese, R.F.; Costanzo, P.M.; Robert, J.-L. Nature, 1984, 309, 604.
27. Barron, P.F.; Frost, R.L.; Skjemstad, J.O.; Koppi, A.J. Nature 1983, 302, 49.
28. Magi, M.; Lippmaa, E.; Samoson, A.; Engelhardt, G.; Grimmer, A.-R. J. Phys. Chem. 1984, 88, 1518.
29. Vol'pin, M.E.; Novikov, Yu.N.; Lapkina, N.D.; Kastochkin, V.I.; Struchkov, Yu.T.; Kazakov, M.E.; Stukan, R.A.; Pavitskii, V.A.; Karimov, Yu.S.; Zvarikina, A.V. J. Am. Chem. Soc. 1975, 12, 486.
30. Parkash, S.; Hooley, J.G.; J. Catal. 1980, 62, 187.
31. Kikuchi, E.; Ino, T.; Morita, Y. J. Catal. 1979, 57, 24.
32. Jones, W.; Schlogl, R.; Thomas, J.M. J.Chem.Soc.Chem.Commun. 1984, 464.
33. Schlogl, R.; Jones, W.; J.Chem.Soc. Dalton Trans. 1984, 1283.
34. Schlogl, R.; Jones, W.; Thomas, J.M. Proc. Roy. Soc. A. 1984, in preparation.

RECEIVED March 11, 1985

## Dynamics of Benzene in X-Type Zeolites

Dennis L. Hasha, Virginia W. Miner, Juan M. Garcés, and Stephen C. Rocke

Analytical Laboratories, The Dow Chemical Company, Midland, MI 48640

Deuterium NMR is used to study the molecular mobility of benzene-d<sub>6</sub> in Na and Cs forms of zeolite X. The systems studied were prepared with loadings in the range 0.7 molecules/supercage to 5.6 and 5.0 molecules/supercage for (Na)X and (Cs,Na)X, respectively. It is observed that at a given temperature, benzene possesses more motional freedom in (Na)X than (Cs,Na)X at all loadings. Two benzene species which differ only in their rotational motion are observed. The low temperature benzene species undergoes rotation about the C<sub>6</sub>-axis; whereas, the motion of the high temperature form is more complex (i.e. molecular tumbling). Sample inhomogeneities result in the simultaneous observation of both species over a narrow temperature range. The position of this temperature range is dependent on loading and the cation. A third benzene species, which goes undetected by the NMR experiment due to an extremely short spin-spin relaxation time, is found to be present. It is estimated that the effect of the Cs<sup>+</sup> ions on benzene mobility can be reproduced by adding ~2.7 molecules/supercage to (Na)X. This is discussed in terms of both steric effects and specific ion-benzene interactions.

Deuterium NMR has recently been used to study molecular motion of organic adsorbates on alumina (1) and in framework aluminosilicates (2). The advantage of <sup>2</sup>H NMR is that the quadrupole interaction dominates the spectrum. This intramolecular interaction depends on the average ordering and dynamics of the individual molecules. In the present work we describe <sup>2</sup>H NMR measurements of deuterated benzene in (Na)X and (Cs,Na)X zeolite.

Laser Raman (3) and UV diffuse reflectance (4) measurements have shown that the cation/aromatic ring interaction becomes stronger as the size of the cation increases. The Laser Raman results were interpreted as being due to electrostatic fields within the

supercages of the zeolite (3). Since electrostatic forces decrease with increasing cation size (5), it has been argued that differences in mobility of toluene detected by  $^{13}\text{C}$  NMR are due to steric factors (6). However, in the zeolite, interaction between the aromatic ring and the cations at the  $S_2$  sites depends not only on the size of the cations but also on their location with respect to the six-member ring site and on their interaction with it. These factors could make the electrostatic interaction with benzene stronger for  $\text{Cs}^+$  than for  $\text{Na}^+$ . Our long-term goal is to understand the individual contributions of the specific ion and steric interactions to the motions of adsorbates in these systems. The preliminary results presented here indicate that both effects are important.

### Experimental

The zeolites used for our experiments were ion-exchanged in our laboratory. The (Na)X zeolite which was obtained from Union Carbide, has the dehydrated composition  $\text{Na}_{85}(\text{AlO}_2)_{85}(\text{SiO}_2)_{107}$ . Exchange of the (Na)X zeolite with four successive batches of 0.2M CsOH solution at 298°K produced a (Cs,Na)X zeolite with dehydrated composition  $\text{Na}_{44}\text{Cs}_{37}(\text{AlO}_2)_{81}(\text{SiO}_2)_{111}$ . Crystallinity of the zeolites was confirmed by X-ray diffraction and BET adsorption isotherm measurements. The zeolites were dried at 373°K for 1 hour then calcined at 728°K for 4 hours before being loaded with deuterated benzene. The benzene- $d_6$  (isotopic purity 99.8%) was obtained from Stohler Isotope Chemicals.

Loading was accomplished by exposing the activated zeolites to benzene- $d_6$  vapors. The extent of vapor adsorption was determined by the increase in weight of the zeolite. The samples were found to be extremely hygroscopic and thus kept in a vacuum desiccator until their use. After two or three temperature runs the samples began to adsorb water vapor. Therefore, only the data obtained for the first two variable temperature cycles are presented here. The samples studied are listed in Table I.

Wideline  $^2\text{H}$  NMR spectra were collected using a Bruker CXP 200 NMR spectrometer, operating at  $\omega_0/2\pi$  ( $^2\text{H}$ ) = 30.7 MHz. To obtain spectra void of spectrometer artifacts, the solid spin echo pulse sequence,  $\pi/2$  -  $\tau$  -  $\pi/2$  -  $\tau$  - echo, was used. Unless otherwise noted, the delay between pulses,  $\tau$ , was set at 30  $\mu\text{s}$ .

### Results & Discussion

The  $^2\text{H}$  NMR spectrum of polycrystalline benzene- $d_6$  below 110°K is represented by a quadrupolar powder pattern with splitting  $\Delta\nu_Q = 144\text{kHz}$  (7). At these temperatures the benzene molecules are rigidly bound in the solid. As the temperature is raised benzene begins to rotate about the  $C_6$ -axis. This motion can be detected by  $^2\text{H}$  NMR provided the correlation time associated with the motion is shorter than the inverse of the rigid quadrupole splitting; i.e.  $\tau_c = 1/\Delta\nu_Q(\text{rigid}) \sim 7 \mu\text{s}$ . When this condition is satisfied the motion is said to be fast on the NMR timescale. Motions which are considered fast produce averaging of the static quadrupole powder pattern. The resulting averaged spectrum yields information about the nature of the molecular motions present.

In Figure 1, deuterium spectra of benzene- $d_6$  in (Cs,Na)X at

Table I. Benzene-d<sub>6</sub> Loadings in Zeolite X

| (mg/g)                                  | molecules per supercage |
|---|-------------------------|
| C <sub>6</sub> D <sub>6</sub> /(Na)X    |                         |
| saturated                               | 5.6 (7)                 |
| 243                                     | 4.9                     |
| 219                                     | 4.4                     |
| 124                                     | 2.5                     |
| 86.3                                    | 1.8                     |
| 53.8                                    | 1.1                     |
| 33.3                                    | 0.7                     |
| C <sub>6</sub> D <sub>6</sub> /(Cs,Na)X |                         |
| saturated                               | 5.0 <sup>‡</sup>        |
| 119                                     | 3.1                     |
| 92.4                                    | 2.4                     |
| 52.8                                    | 1.4                     |
| 31.7                                    | 0.7                     |

<sup>‡</sup>Maximum loading (Na)X = 5.6 molecules/supercage (7). Replacement of Na<sup>+</sup> ions with 4.6 Cs<sup>+</sup>/supercage reduces supercage volume ~10%. Therefore, maximum loading (Cs,Na)X = (0.9)(5.6) = 5.0.

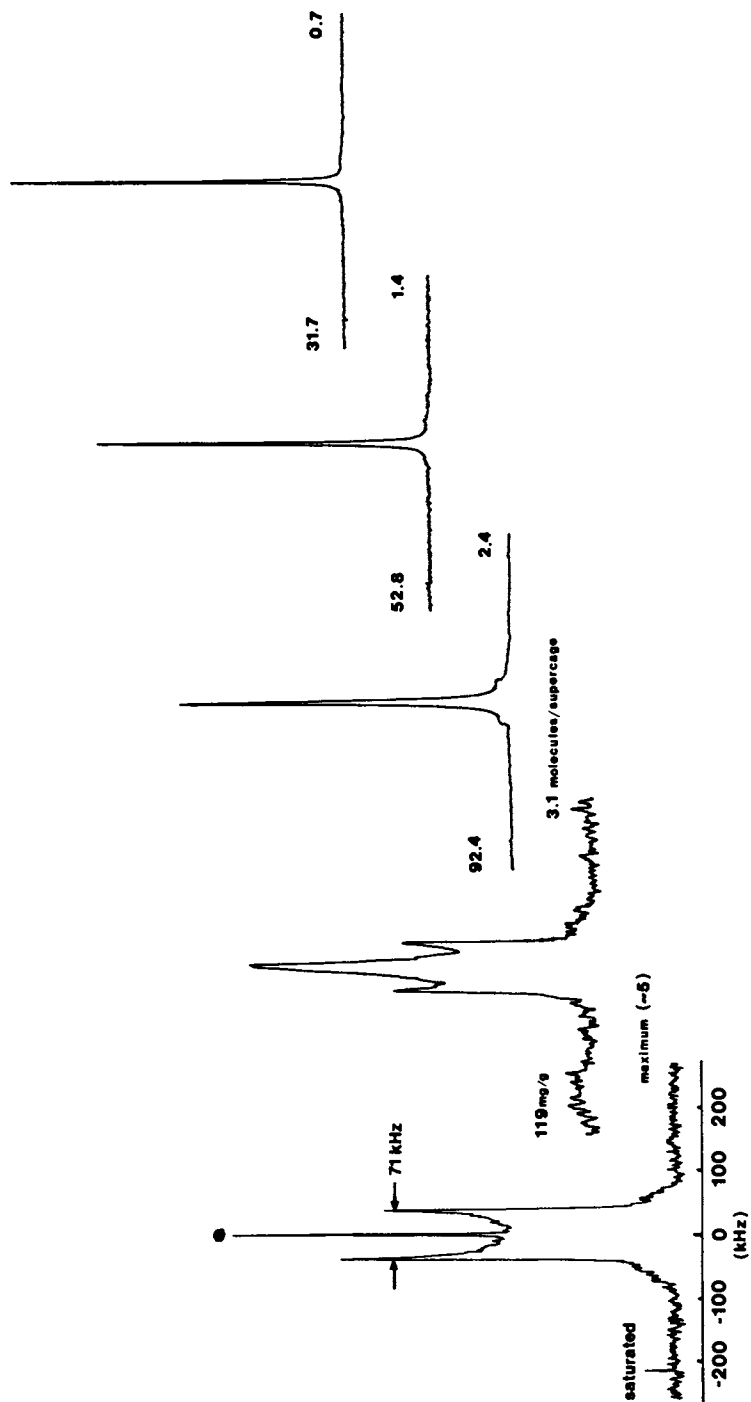


Figure 1.  $^2\text{H}$  NMR spectra of  $\text{C}_6\text{D}_6/(\text{Cs},\text{Na})\text{X}$  at room temperature. The spectral width is 500 kHz. Narrow resonance denoted with \* is due surface adsorbed benzene- $d_6$ .



room temperature for five different loadings are shown. At 0.7 and 1.4 benzene- $d_6$  molecules/supercage the linewidth at half height is  $\approx 5$  kHz indicating rapid molecular tumbling. As the loading increases, the spectra cannot be interpreted as arising from a single type of benzene. Instead, the spectra are due to two species; one producing a quadrupolar pattern with splitting of  $\nu_0 = 71$  kHz and the other a broadened singlet. The observation of two distinct patterns indicates that exchange between the two benzene species is slow on the NMR timescale. The magnitude of the splitting of the quadrupolar subspectrum is the value expected for an oriented benzene molecule experiencing fast reorientation about its  $C_6$ -axis. The linewidth of the broadened singlet increases from 7.9 kHz at 2.4 molecules/supercage to  $\approx 35$  kHz at 3.1 molecules/supercage. This broadening indicates that as the number of benzene molecules in the supercage increases their motional freedom is reduced. The concentration of the oriented benzene species increases as more molecules are added to the cavity. When the supercage becomes saturated all the benzene molecules are oriented and undergoing rapid  $C_6$  reorientation. The narrow resonance, denoted with the asterisk in the figure, is due to benzene molecules adsorbed on the surface of the zeolite. In the case of (Na)X, the deuterium spectra consist of a single narrow resonance ( $\Delta\nu_{1/2} \approx 520$  Hz) at loadings below  $\approx 2.5$  molecules/supercage (see Figure 2). It would appear that at these loadings the benzene molecules undergo nearly isotropic motion in (Na)X. Increasing the number of molecules in the cavity results in a broadening of the narrow resonance (4.4 kHz and 5.6 kHz at 4.4 and 4.9 molecules/supercage respectively). At maximum loading both benzene species are observed, with the oriented benzene being the minor component. From comparison of the spectra it is clear that benzene possesses more motional freedom in (Na)X than (Cs,Na)X at all loadings.

Lowering the temperature has a similar effect on the deuterium spectra as does increased loadings. In Figure 3, spectra for benzene- $d_6$ /(Na)X at 0.7 molecules/supercage over the temperature range 298 to 133°K are shown. It is observed that both benzene species are detected simultaneously between 228 and 188°K. Below this temperature the oriented benzene species becomes the predominant form. A similar situation occurs for polycrystalline benzene- $d_6$  in which two quadrupole patterns, one static and the other motionally narrowed due to  $C_6$  rotation, are observed to coexist at temperatures between 110 and 130°K (7). This behavior has been attributed to sample imperfections (8) which give rise to a narrow distribution in correlation times for reorientation about the hexad axis. For benzene in (Na)X and (Cs,Na)X such imperfections may result from the ion/benzene interaction, and a nonuniform distribution of benzene molecules and ions within the zeolite. These factors may also be responsible for producing the individual species. However, from the NMR spectra it is not possible to make this connection. Thus, the use of the term "species" to describe the quadrupole pattern and broadened singlet strictly represents molecules which possess different degrees of motional freedom.

From Figure 3 it is apparent that when both benzene species are present the signal to noise ratio (S/N) of the spectrum is greatly reduced. The spectra in Figure 3 are not normalized but displayed with the same vertical height. Thus the "observed" reduction in S/N

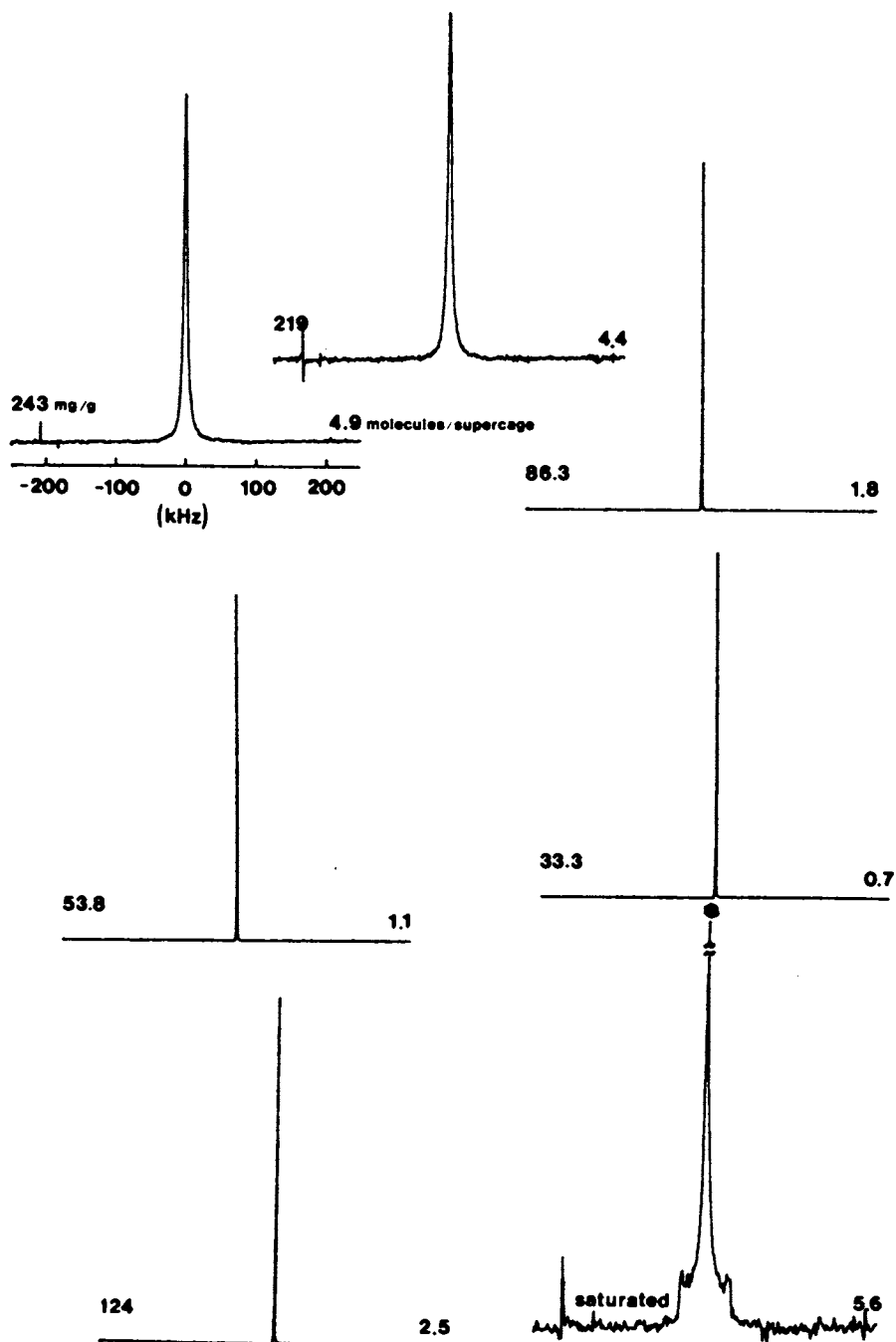


Figure 2.  $^2\text{H}$  NMR spectra of  $\text{C}_6\text{D}_6/(\text{Na})\text{X}$  at room temperature. SW = 500 kHz. \* denotes benzene- $\text{d}_6$  adsorbed on surface.

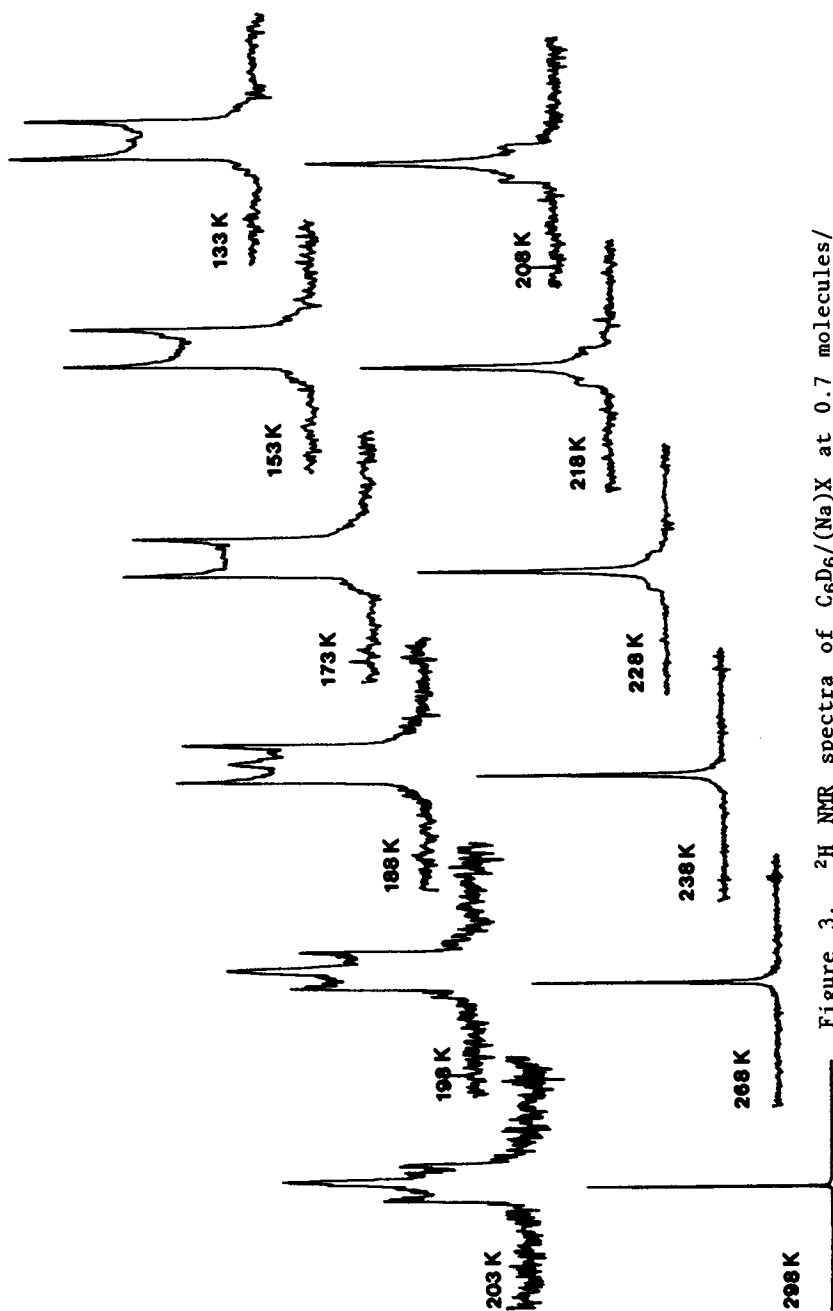


Figure 3.  $^2\text{H}$  NMR spectra of  $\text{C}_6\text{D}_6/(\text{Na})\text{X}$  at 0.7 molecules/supercage as a function of temperature. SW = 500 kHz. These spectra are not normalized but displayed with the same vertical height.

is actually a loss in signal intensity. As the temperature is lowered to temperatures below 188°K the signal intensity increases. This is due to the method of data collection. The solid spin echo sequence used to obtain the spectra is a two pulse sequence,  $\pi/2) - \tau - \pi/2) - \tau$ -echo. After the first  $\pi/2$ -pulse the magnetization dephases due to magnetic inhomogeneities of the system. The second  $\pi/2$ -pulse (rotated 90° with respect to the first pulse) causes a refocussing of the magnetization at  $2\tau$ . The height of the echo depends on the spin-spin relaxation time,  $T_2$ , and the rate of chemical exchange between the two benzene species.

The effect of  $T_2$  on the spectral intensity can be studied by varying the length of the time between pulses. In Figure 4 spectra for  $C_6D_6/(Cs,Na)X$  at 2.4 molecules/supercage and 283°K are shown as a function of  $\tau$ . As the delay increases the integrated intensity of the spectrum decreases. This loss of intensity does not occur at the same rate ( $\equiv 1/T_2$ ) for the two species. This rate is slower for benzene undergoing  $C_6$  rotation;  $T_2(C_6 \text{ rotation}) > T_2(\text{molecular tumbling})$ . Since the spin-spin relaxation time is inversely proportional to the correlation time associated with the motion, rotation about the  $C_6$ -axis for the oriented species is faster than the molecular tumbling of the species producing the broadened singlet;  $\tau(C_6 \text{ rotation}) < \tau(\text{molecular tumbling})$ . This is not a surprising result. Rotation about the  $C_6$ -axis is virtually unhindered; whereas, molecular tumbling in the supercages must take place by displacing neighboring molecules.

For a given species the spin-spin relaxation time decreases with decreasing temperature, with the rigid lattice value as the lower limit. Since the oriented benzene species, which is the low temperature form, has the longer  $T_2$  we would not expect the integrated intensity of the spectrum to decrease monotonically as the temperature is lowered. In fact, the signal intensity decreases, reaches a minimum and then increases when the temperature is reduced. This is shown more clearly in Figure 5. For benzene molecules which possess a natural  $T_2$  short compared to the delay between the pulses, complete dephasing occurs during  $\tau$ . Application of the second pulse does not produce an echo and these molecules go unobserved. Chemical exchange, which is actually a  $T_2$  process, also results in reduced signal intensity. Phase coherence is lost when a benzene molecule goes from "species I" to "species II" during the time of the experiment ( $2\tau$ ). The maximum reduction in signal intensity due to the exchange process occurs when the rate of the chemical exchange  $\cong 1/2\tau$ . It is observed that the minimum integrated intensity is observed when both species are detected simultaneously. For  $C_6D_6/(Na)X$  at 2.5 molecules/supercage this takes place at approximately 260°K. At this temperature, less than 50% of the benzene molecules are detected by the NMR experiment. These unobserved molecules constitute a third species. As the temperature is changed the number of undetected molecules decreases. At 220°K the integrated intensity is nearly 30% larger than the room temperature value. This is a result of the temperature dependence of the Boltzmann distribution, which produces an increase in available magnetization as the temperature is lowered.

The temperature range in which the two observed benzene species coexist, is shifted to lower temperatures for  $C_6D_6/(Na)X$  samples with fewer benzene molecules per supercage (see Figure 3 and 5). This is

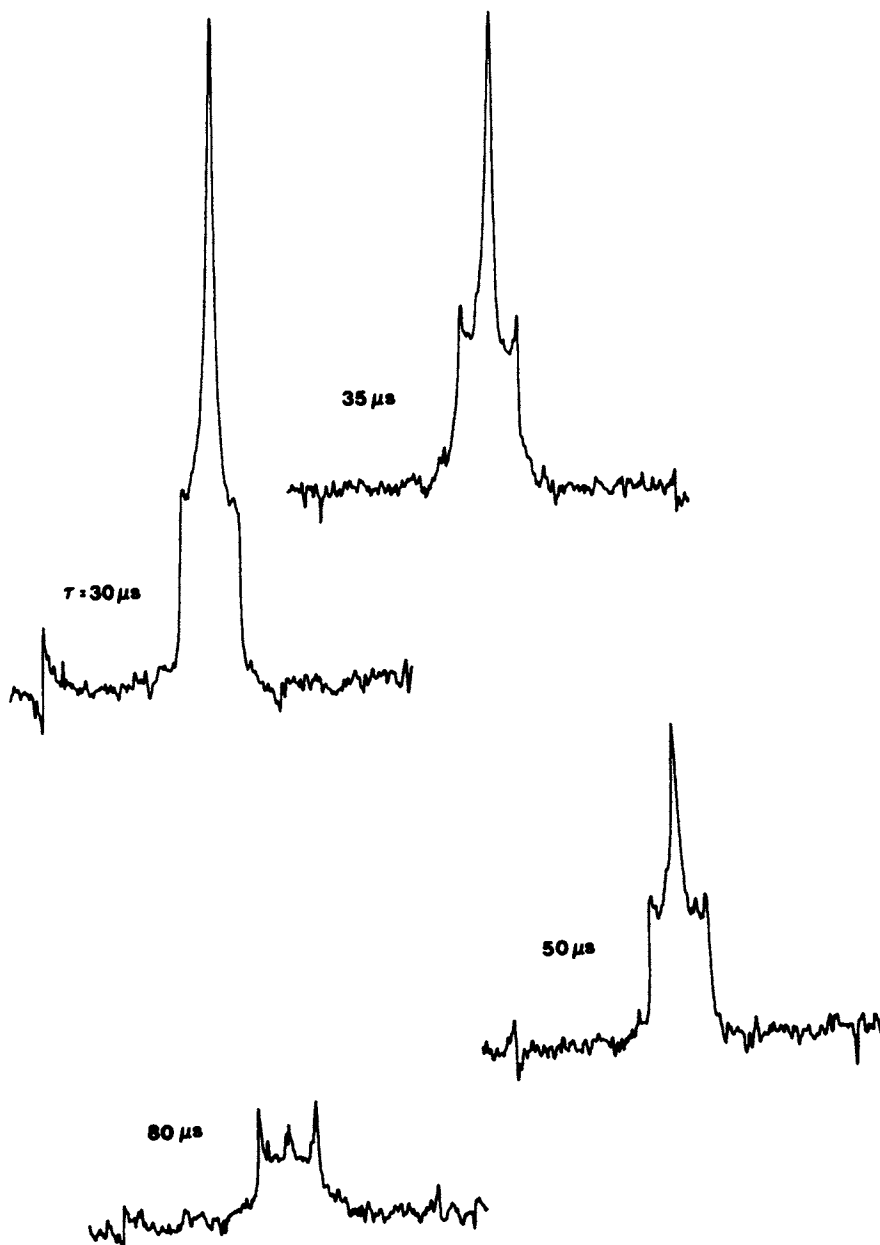


Figure 4. Dependence of the integrated intensity on the length between pulses,  $\tau$ , in the solid spin echo sequence.  $\text{C}_6\text{D}_6/(\text{Cs},\text{Na})\text{X}$  at 2.4 molecules/supercage and  $283^\circ\text{K}$ .  $\text{SW} = 500 \text{ kHz}$ .

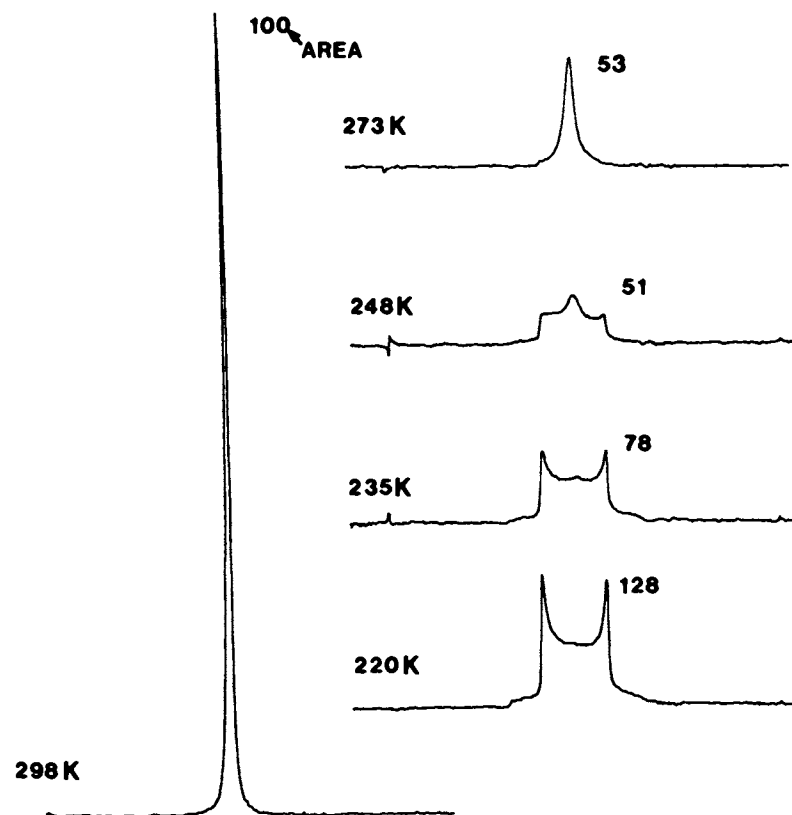


Figure 5. Dependence of the integrated intensity on temperature.  $C_6D_6/(Na)X$  at 2.5 molecules/supercage. SW = 500 kHz.

also true for  $C_6D_6/(Cs,Na)X$ . The temperature at which the system undergoes freezing out the molecular tumbling motion, is also dependent on the cation. For a given loading this transition shifts to lower temperatures for  $C_6D_6/(Na)X$  than for  $C_6D_6/(Cs,Na)X$ . The integrated intensity of the two subspectra yields a population ratio which is an equilibrium constant defining the motional state of the detected benzene molecules. The experimental conditions which produce the motional state described by equal populations of the two observed benzene species is shown in Figure 6 for (Na)X and (Cs,Na)X. The figure is actually a phase diagram of the motional state of benzene in the zeolite. The curves, which are linear, represent the coexistence lines separating the two observed benzene species. Moving to the low temperature side of the coexistence line gives rise to benzene molecules which undergo rotation about their  $C_6$ -axis. Moving in the other direction, produces benzene molecules capable of tumbling. The (Cs,Na)X coexistence line is shifted to higher temperatures with respect to the (Na)X line. Within experimental error, these two coexistence lines are parallel. Although the spectrum is extremely sensitive to changes in temperature, effects due to  $T_2$  mentioned earlier can dramatically alter the appearance of the spectrum. Since we are comparing the same motional state, differences observed in  $T_2$  for the two species are not expected to change substantially. Therefore, the estimated error of  $\pm 5^\circ K$  is not unreasonable.

The population ratio can be expressed as a Boltzmann distribution

$$(Na)X: \ln n'/n = -\Delta E_{Na}/RT ; (Cs,Na)X: \ln n'/n = -\Delta E_{Cs}/RT' \quad (1)$$

where  $\Delta E$  is the difference in energy between the two detected benzene species. It follows that for the same population ratio

$$\Delta E_{Na}/T = \Delta E_{Cs}/T' \quad (2)$$

Equations (1) and (2) hold for all points along the coexistence lines in Figure 6. At the lowest loading, 0.7 molecules/supercage,  $\Delta E_{Cs}/\Delta E_{Na} \cong 1.2$ . Since the two lines are approximately parallel this ratio is nearly constant for all loadings. In the temperature range 250 to 290°K, we can compare coexistence points for the two zeolites at the same temperature, such that  $\Delta E_{Cs} = \Delta E_{Na}$ . Comparison

of the curves shows that to reproduce the effect of  $Cs^+$  ions [there are 4.6  $Cs^+$  and 3.5  $Na^+$  ions per supercage for (Cs,Na)X] on the dynamics of benzene, an additional  $\sim 2.7$  molecules of benzene per supercage must be placed in the cavities of (Na)X. The volume of 2.7 additional benzene molecules is substantially greater than the  $\sim 10\%$  reduction in supercage volume resulting from substituting 4.6  $Cs^+$  ions for  $Na^+$ . This suggests that steric effects alone cannot explain the data, and that a specific ion/benzene interaction also contributes to the dynamics of benzene in zeolite X.

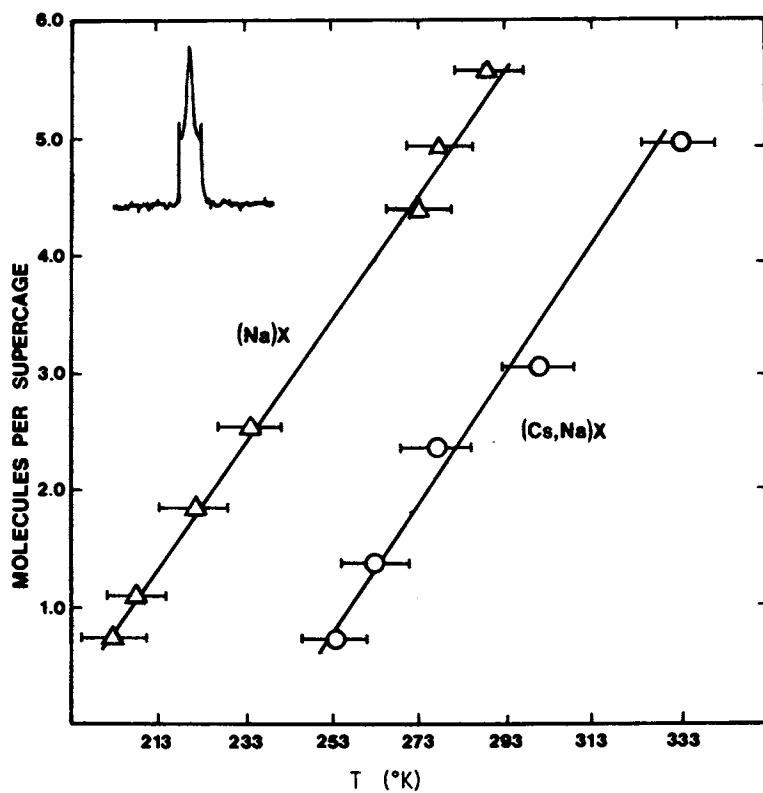


Figure 6. "Phase diagram of motional state of benzene". The experimental conditions which produce the motional state described by the inset spectrum.



Literature Cited

1. Gottlieb, H. E.; Luz, Z. J. Magn. Reson. 1983, 54, 257.
2. Eckman, R.; Vega, A. J. J. Am. Chem. Soc. 1983, 105, 4841.
3. Freeman, J. J.; Unland, M. L. J. Catal. 1978, 54, 183.
4. Unland, M. L.; Freeman, J. J. J. Phys. Chem. 1978, 82, 1036.
5. Barrer, R. M.; Gibbons, R. M. Trans. Faraday Soc. 1965, 61, 948.
6. Sefcik, M. D. J. Am. Chem. Soc. 1979, 101, 2164.
7. Rowell, J. C.; Phillips, W. D.; Melby, L. R.; and Panar, M. J. Chem. Phys. 1965, 43, 3442.
8. O'Reilly, D. E.; Peterson, E. M.; Scheie, C. E.; and Seyfarth, E. J. Chem. Phys. 1973, 59, 3576.

RECEIVED April 17, 1985

## Magnetic and Mössbauer Characterization of Iron-Zeolite and Iron and/or Ruthenium on Doped-Carbon Catalysts

L. N. Mulay<sup>1</sup> and Thomas Pannaparayil<sup>2</sup>

<sup>1</sup>Materials Science and Engineering Department, The Pennsylvania State University, University Park, PA 16802

<sup>2</sup>Department of Physics, The Pennsylvania State University, University Park, PA 16802

The basic characteristics of S.P. (superparamagnetic) clusters of well-known ferromagnetic metals and of ferrimagnetic insulators such as  $\gamma$ -Fe<sub>2</sub>O<sub>3</sub> and Fe<sub>3</sub>O<sub>4</sub> are succinctly outlined along with important features of <sup>57</sup>Fe Mössbauer spectroscopy. Selected examples of the magnetic and Mössbauer characterization of the Fe or Fe·Co/ZSM-5 system in the fresh, reduced, carbided and used catalysts are given, which indicated that Fe<sub>5</sub>C<sub>2</sub> is the active phase, which is then converted into Fe<sub>3</sub>C during the Fischer-Tropsch syngas reaction. Evidence for an interaction between Fe-oxide(s) and the Brönsted acid sites in H-Mordenites is also presented. Furthermore, characterization of boron-doped carbons by magnetic susceptibility is described, which yields band parameters such as the change in the Fermi level ( $E_F$ ) with boron doping. The behavior of S.P. Fe<sup>o</sup> on such carbons is also presented. Although a seven-fold change in  $E_F$  was found, no striking correlation between this change and the turnover frequencies ( $NC_1$  and  $NC_0$ ) could be established. Finally, the applicability of the magnetization measurements as a function of the [Field (H)/ Temperature (T)] for obtaining particle size distribution of the  $\gamma$ -Fe<sub>2</sub>O<sub>3</sub>/ZSM-5 system is illustrated. In this broad review of selected applications of magnetization and Mössbauer characterization, a comparison is given of the effects of Fe(NO<sub>3</sub>)<sub>3</sub> and Fe<sub>3</sub>(CO)<sub>12</sub> impregnation on the formation of S.P. species along with their practical significance in promoting the production of octane-range hydrocarbons.

0097-6156/85/0288-0498\$06.00/0  
© 1985 American Chemical Society

This contribution is concerned with the magnetic and Mössbauer characterization of (a) Fe/zeolite (mordenite) systems, and that of (b) Fe and/or Ru on boron-doped carbon substrates. Some correlations between the characterization and CO hydrogenation parameters will be pointed out. Because of limitations of space, we shall present salient features of these investigations. At the outset, it would be befitting to present a succinct background on the basic principles of magnetic and Mössbauer characterization.

### Background Information on the Principles of Magnetism and Mössbauer Spectroscopy

We shall invoke only those rudimentary principles, which have a direct bearing on our research for the benefit of non-magneticists. Ferromagnetic metals, such as Fe, Co, Ni, and insulators such as  $\gamma$ -Fe<sub>2</sub>O<sub>3</sub> and Fe<sub>3</sub>O<sub>4</sub>, show the well-known hysteresis curve, which stems from their domain structure. In their unmagnetized state, the unpaired electrons (spins) associated with each atom (or structural unit) have a net spontaneous magnetic "moment ( $\mu_s$ )" or magnetization ( $\sigma_s$ ); these are shown by the large arrows (Fig. 1). Saturation is shown by  $\sigma_s$ , the remanence by  $\sigma_r$ , and the reverse field necessary to bring  $\sigma_r$  to 0 is shown by  $H_c$ , the coercive force. Between the domains, a "Bloch wall" is formed, with spins curled up in a helical fashion. When an external field (H) is applied, the magnetic moments align "parallel" to the applied field, even at modest values ( $\sim 3000$  Oersteds) at room temperature, which happens to be below the Curie temperature ( $T_c$ ). This  $T_c$  is a critical temperature above which the magnetization ( $\sigma_s$ ) disappears and follows a paramagnetic behavior. Each domain consists of myriads of spins. One can imagine small clusters within each domain having different volumes ( $V_1, V_2, \dots V_i$ ). These subdomain particles, which consist of several thousand spins, are known as S.P. (superparamagnetic) clusters and have large magnetic moments of several thousand B.M. (Bohr Magnetons; one BM =  $eh/4\pi mc$ , where the symbols have their usual meaning [1,2]). When such S.P. clusters are well-dispersed on (or "within") a substrate (e.g., SiO<sub>2</sub>, carbon, zeolites, etc.), there is no magnetic interaction between their moments. Hence, the S.P. clusters behave in the same manner as "magnetically dilute" paramagnetic ions, such as Fe<sup>3+</sup> (<sup>6</sup>S<sub>5/2</sub> ion, with 5 d spins, which show an effective B.M. number ( $\mu_{eff}$ ) of  $\sqrt{5(5+2)} = 5.96$ ). Such ions can orient parallel and antiparallel to H, according to the Boltzmann statistics, independently of each other and experience thermal fluctuations. For paramagnetic ions, the susceptibility ( $\chi = \sigma/H$ ) and the  $\mu_{eff}$  are good parameters for interpretation of magnetic results. However, for the S.P. clusters with a giant B.M. number of  $\sim 10^4$ , the per gram magnetization ( $\sigma$ ) is a good parameter. The  $\sigma$  increases with increasing H, and with decreasing temperature (T). Therefore, it is customary to measure  $\sigma$  at constant H and varying T, and vice-versa. When the relative magnetization  $\sigma/\sigma_s$  (where  $\sigma_s$  is the saturation magnetization) is plotted as a function of H/T, one obtains an excellent superposition of data points, and there is no coercive force ( $H_c=0$ ); that is, there is no hysteresis, as in the bulk ferromagnetic material (Fig. 2). Hence, S.P. behavior may be regarded as a phenomenon intermediate between

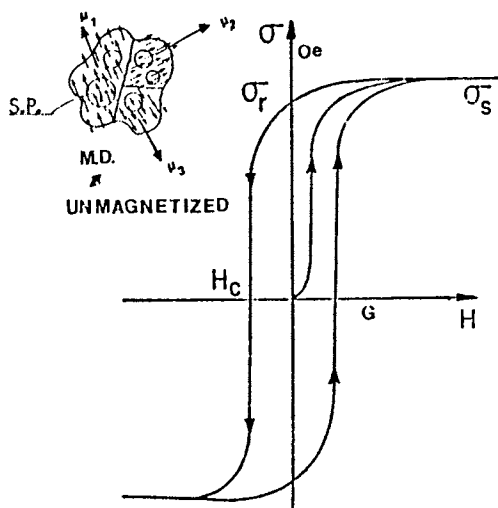


Figure 1. Schematic diagram of a hysteresis curve for a typical ferromagnet showing magnetization ( $\sigma$ ) as a function of the applied magnetic field ( $H$ ). Saturation magnetization is indicated by  $\sigma_s$ . Inset shows the multidomain structure and subdomain superparamagnetic clusters.

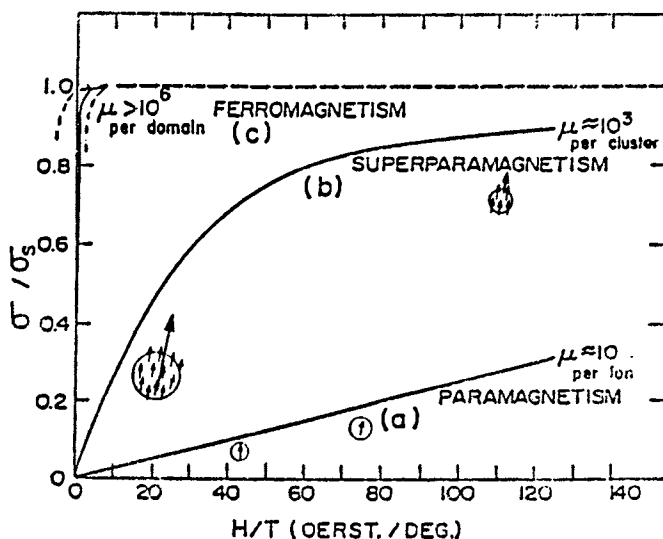


Figure 2. Plot of relative magnetization,  $\sigma/\sigma_s$ , as a function of  $H/T$ . (a) A paramagnetic system is characterized by an effective magnetic moment, with a Bohr Magnetron number  $\sim 10$  per ion, and by the absence of hysteresis. Paramagnetic saturation occurs at very high " $H/T$ "  $\approx 10^4$  Oe  $K^{-1}$ . (b) Langevin curve for S.P. clusters. (c) Part of a ferromagnetic hysteresis curve.

paramagnetism and ferromagnetism. For pure ferromagnetic materials, without mechanical strain, the  $H_C$  can be as small as 0.5 Oersteds. Hence, one can apply the classical Langevin function, first derived for the non-interacting paramagnetic spins, to the non-interacting (ideal) S.P. clusters. Thus,

$$\sigma/\sigma_s = \text{Coth}(\mu_c H/kT) - (kT/\mu_c)(H)$$

Here,  $\mu_c$  stands for the (giant) magnetic moment of the cluster which replaces the " $\mu$ " for single, isolated paramagnetic spins;  $k$  is the Boltzmann constant.

In the above equation, all quantities except  $\mu_c$  can be measured. The  $\mu_c$  can be derived for (ideal) S.P. clusters by a curve-fitting procedure (Cf ref. 3). The gist of obtaining the average volume  $\bar{v}$  of a S.P. cluster lies in the basic physics definition of  $\sigma_s$ , which for a S.P. system can be written as  $\sigma_s = \mu_c/\bar{v}$ . From the low-field (LF) and high-field (HF) approximations [4,5] of the Langevin function stated below, one can calculate the  $\bar{v}_{LF}$  for large clusters (which magnetically saturate easily at low values of  $H/T$ ) and  $\bar{v}_{HF}$  for small clusters (which saturate with difficulty at high values of  $H/T$ ). From the  $\bar{v}_{LF}$  and  $\bar{v}_{HF}$ , the average volume  $\bar{v}$  of clusters can be estimated by taking the arithmetic mean.

$$\bar{d}_{LF}^3 = \frac{18k}{\pi I_s} (\sigma/\sigma_s)/(H/T)$$

$$\bar{d}_{HF}^3 = \frac{6k}{\pi I_s} (1 - \sigma/\sigma_s)^{-1}/(H/T)$$

Here  $I_s$  is the spontaneous magnetization for the bulk material. For Fe,  $I_s$  is 1707 Gauss (or Oersted) at room temperature.

It should be stressed that below a critical (Blocking) temperature ( $T_B$ ) S.P. clusters will have a slow relaxation time ( $\tau$ ) at which their net moment will align so-to-speak "parallel" to  $H$ , and thus appear to behave as if they had an apparent "bulk-like" ferromagnetic behavior. This aspect will result in a hysteresis or an "apparent" ferromagnetic behavior. Conversely, above the  $T_B$ , the hysteresis will disappear and the clusters will show a unique curve with no hysteresis (Fig. 2).

In Mössbauer spectroscopy (recoil-free emission and resonance absorption of  $\gamma$ -rays) nuclear transitions are observed between the ground and low-lying excited nuclear states of natural isotopes such as  $^{57}\text{Fe}$  and  $^{119}\text{Sn}$  etc. The source nuclei ( $^{57}\text{Co}$  in the case of  $^{57}\text{Fe}$ ), embedded in a diamagnetic matrix with cubic symmetry and high Debye temperature, emit unsplit single-line. Quite frequently the nuclear state of the absorber is perturbed simultaneously by nuclear hyperfine interactions--electric monopole, magnetic dipole, and electric quadrupole interaction. Resonance absorption is achieved by superimposing a Doppler velocity on the source which gives rise to  $\gamma$ -rays with a variable range of frequencies.

Most valuable chemical information can be extracted from Mössbauer parameters such as the isomer shift ( $\delta$ ), the quadrupole splitting ( $\Delta E_Q$ ), the magnetic splitting ( $\Delta E_M$ ), and the asymmetry parameter ( $\eta$ ).

The isomer shift ( $\delta$ ) stems from the electric monopole (Coulomb) interaction between the nuclear charge and the S-electrons at the nucleus which shifts the nuclear energy levels. This interaction shifts the centroid of the absorption spectrum from the zero-velocity position (Fig. 2A). The S-electron density at the nucleus is affected very sensitively by the changes in the electronic structure of the valence shell by chemical influences such as changes of oxidation state, spin state, and in bonding, etc. In the case of  $^{57}\text{Fe}$  the isomer shift is very sensitive to the variations of the 3d-density near the nucleus which change the screening effect of the 3d- on the 3S-electrons. Isomer shift together with specific magnetization, therefore, provide valuable parameters to investigate the possibility of any metal-support interaction in Fe-supported catalysts.

Interaction of the nuclear quadrupole moment with the electric field gradient (EFG) produced at the nuclear site by extranuclear charges causes the splitting of the  $(2I + 1)$  fold degenerate energy levels of a nuclear state with spin quantum number  $I > 1/2$  into substates  $|I, \pm m_I\rangle$ . For  $^{57}\text{Fe}$  this interaction results in a typical two-line Mössbauer spectrum (Fig. 2A). The quadrupole splitting  $\Delta E_Q$  is dependent on the diagonal elements  $V_{xx}$ ,  $V_{yy}$ ,  $V_{zz}$  of the EFG-tensor. In principle, charges on distant ions which surround the Mössbauer atom in non-cubic symmetry and the anisotropic electron population in the molecular orbitals between the Mössbauer atom and coordinated ligands contribute to EFG. In a superparamagnetic system a high fraction of the Mössbauer atoms could be surface atoms, and since a surface represents a discontinuity with respect to the bulk, marked changes in the symmetry and strong EFG could be expected. In general, a higher value for  $\Delta E_Q$  may reflect a high state of dispersion achieved in a superparamagnetic system.

The hyperfine interaction between the nuclear magnetic moment of the Mössbauer atom and the internal magnetic field ( $H_{\text{int}}$ ) produced at the nuclear site by the atom's electrons splits the nuclear state with spin quantum number  $I$  into  $2I + 1$  non-degenerate substates  $|I, m_I\rangle$  and  $\gamma$ -ray transitions subject to selection rules  $\Delta I = 1$  and  $\Delta m_I = 0 \pm 1$  can be observed in Mössbauer spectrum (Fig. 2A). In magnetically ordered materials all factors contributing to  $H_{\text{int}}$  such as orbital term, dipolar term, Fermi contact term etc. are proportional to  $M_S$ , the spontaneous magnetization or sublattice magnetization. It should be noted that  $H_{\text{int}}$  will be different at structurally different Mössbauer atoms in polynuclear compounds. In a superparamagnetic system held above the Blocking temperature, the relaxation time of the clusters becomes shorter compared to the nuclear Larmor precession time and the time averaged magnetic hyperfine field seen by the Mössbauer spectrum (in the case of  $^{57}\text{Fe}$ ) collapses into a single line. Because nuclear transitions are observed, the Blocking temperature  $T_B'$  observed in Mössbauer spectroscopy is quite different from the  $T_B$  found from magnetization measurements [6]. The combined electric and magnetic hyperfine interactions result into an asymmetric magnetically split Mössbauer spectrum, as depicted in Fig. 2A ( $H_{\text{int}} \neq 0$ ,  $V_{zz} > 0$ ).

We shall now briefly describe the well-known temperature-independent Langevin diamagnetism of closed-shell ions, such as  $\text{K}^+$  and  $\text{Cl}^-$  in KCl and similar inorganics, such as  $\text{SiO}_2$ ,  $\text{Al}_2\text{O}_3$ , and the zeolites, as well as the covalent organic compounds. Since all such

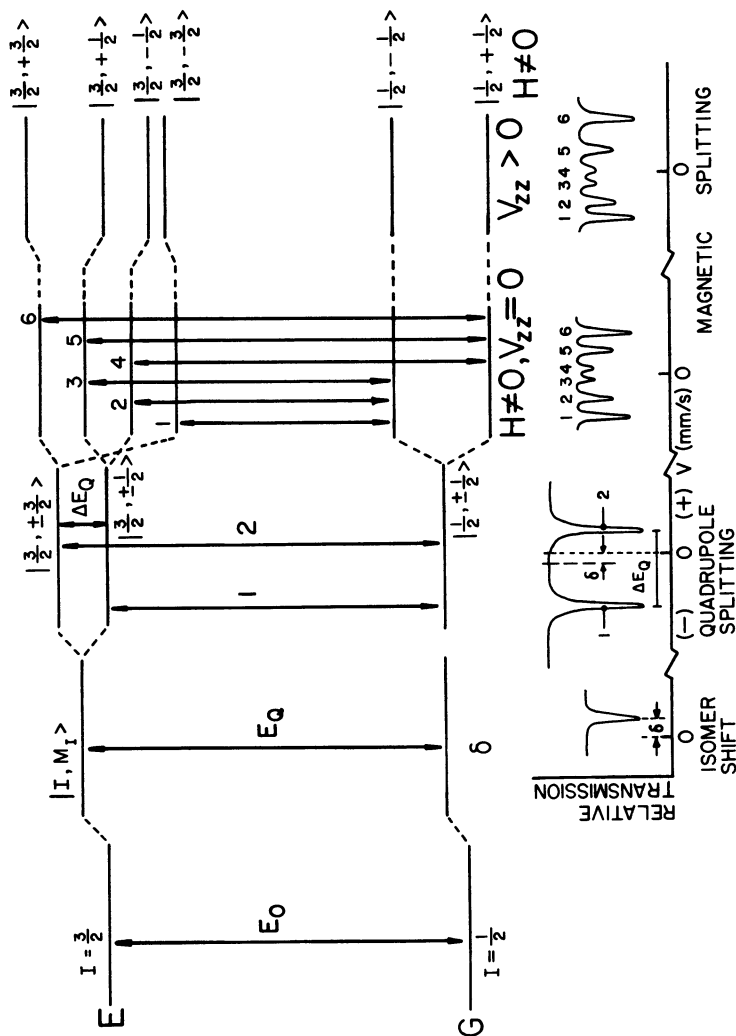


Figure 2A. Schematic diagram of Mössbauer parameters: isomer shift ( $\delta$ ), quadrupole splitting ( $\Delta E_Q$ ) and magnetic dipole splitting of the nuclear energy states of  $^{57}\text{Fe}$  leading to various hyperfine splitting in Mössbauer spectra.

(localized) spins in closed shells are paired up ( $\uparrow\downarrow$ ), there is no net magnetic moment (i.e.,  $\mu = 0$ ), and the  $\chi$  of such systems is independent of temperature. On the other hand, there is the temperature-dependent behavior, namely the Landau diamagnetism, which is not well-known to most chemists. In materials, such as graphite, graphitic carbons, or even in some disordered (amorphous) forms of carbon, there exist delocalized (or itinerant) electrons, which behave like a "free electron gas," whose  $\chi$  naturally depends on the temperature. Appropriate equations are given by Mulay et al. for the two systems [2a]. For the Landau diamagnetism, the effective mass ( $m^*$ ) of the electron is an important factor, whereas in the normal Langevin diamagnetism one takes into account the "rest mass" ( $m$ ) of the electron.

### Experimental

The magnetic susceptibilities ( $\chi$ ) or magnetization ( $\sigma = \chi \cdot H$ ) for the systems described here were measured by the in-situ Faraday method described by Mulay [1]. The Mössbauer Spectra were obtained with an Austin Associates spectrometer with a  $^{57}\text{Co}/\text{Rh}$  matrix source (50 mCi) and Nuclear data electronics. In-situ measurements were made, using a cell similar to that described by Delgass et al. [7].

### Results and Discussion

#### The Fe and Fe-Co/Zeolite Systems

The structure of ZSM-5 is shown in Fig. 3. The  $\chi$  vs T plots for the fresh sample obtained by  $\text{Fe}(\text{NO}_3)_3$  impregnation ( $\sim 11$  wt.% Fe) showed the Curie behavior ( $\chi = C/T$ ) from which a B.M. number of  $\sim 5.98$ , corresponding to that of an  $\text{Fe}^{3+}$  ion, was observed. On reduction, a S.P.-type curve (Fig. 2) was obtained with a  $\bar{v} \approx 5.0$  nm. As expected, the  $\bar{v}$  increased with increasing loading of Fe. Previous experience showed that loadings beyond  $\sim 20\%$  gave a ferromagnetic behavior and a decrease in catalytic activity for the F-T (Fischer-Tropsch) syngas reaction [3]. Typical thermomagnetic curves for  $\sim 11\%$  Fe loading in ZSM-5 (Fig. 4) showed that the  $\sigma_g$  for the reduced S.P. catalyst was lower (B.M. - 1.9) than for the bulk ferromagnetic Fe (2.2), and on carbiding, the  $\sigma$  decreased systematically. The  $T_C$  showed the carbided sample to be  $\text{Fe}_5\text{C}_2$  (Hägg carbide). The Fe-Co/ZSM-5 showed higher moments.

Typical Mössbauer spectra for the fresh, reduced, carbided and used Fe/ZSM-5 system are shown in a composite Fig. 5. Similar spectra were obtained for the Fe-Co/ZSM-5 system. The product distribution for the F-T reaction, using the Fe and Fe-Co systems, are shown in Table I. The gasoline range hydrocarbon yield increased from 75 to 94%, when the Fe-Co clusters were used in place of Fe only. In a typical CEMS (Conversion Electron Mössbauer Spectroscopy) of the Fe-Co system, no spectrum for  $^{57}\text{Fe}$  was observed even after one week; from this, it was concluded that in the Fe-Co clusters  $\text{Co}^0$  was predominantly in the "mantle" and  $\text{Fe}^0$  species were in their "core," in the parlance of metallurgy/geophysics. This model is sometimes referred to as the cherry model.

The ZSM-5 impregnated with  $\text{Fe}_3(\text{CO})_{12}$  was also studied by the same techniques. A brief summary of Fe-carbonyl vs  $\text{Fe}(\text{NO}_3)_3$  impregnation is given in Table II, which is self-explanatory.



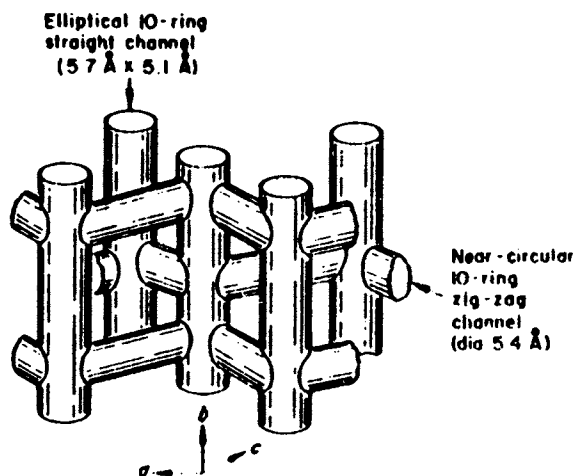


Figure 3. Possible model of the pore structure of ZSM-5 and Silicalite ("SiO<sub>2</sub>").

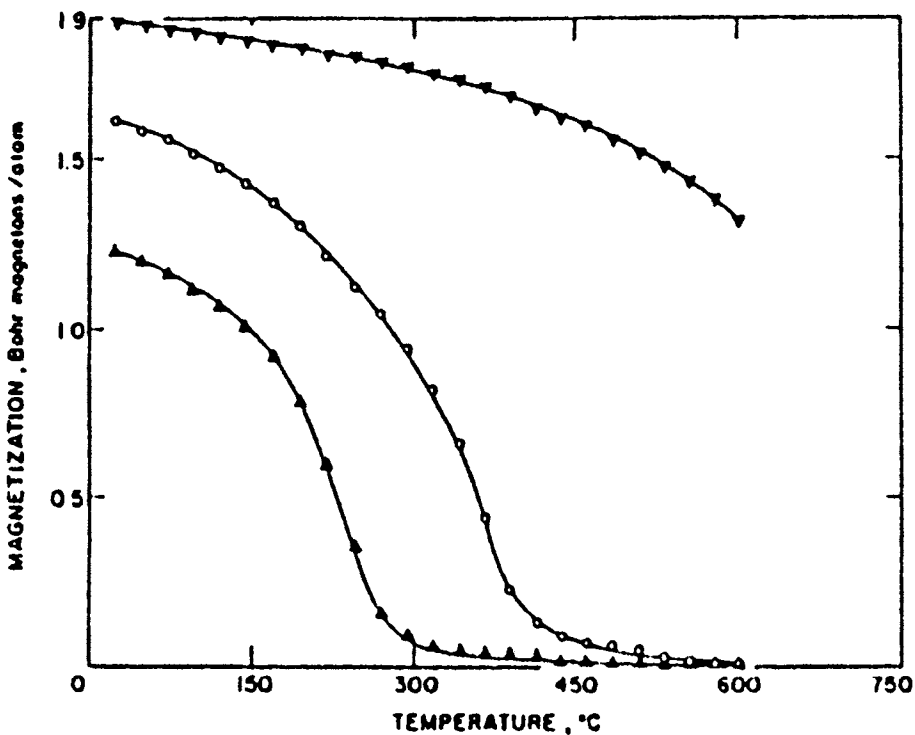


Figure 4. Magnetization (Bohr magnetons/iron atom) as a function of temperature for ZSM-5 (11.1% Fe) ( $H = 6300$  Oe; (▽) reduced; (Δ) carbided; (○) used).

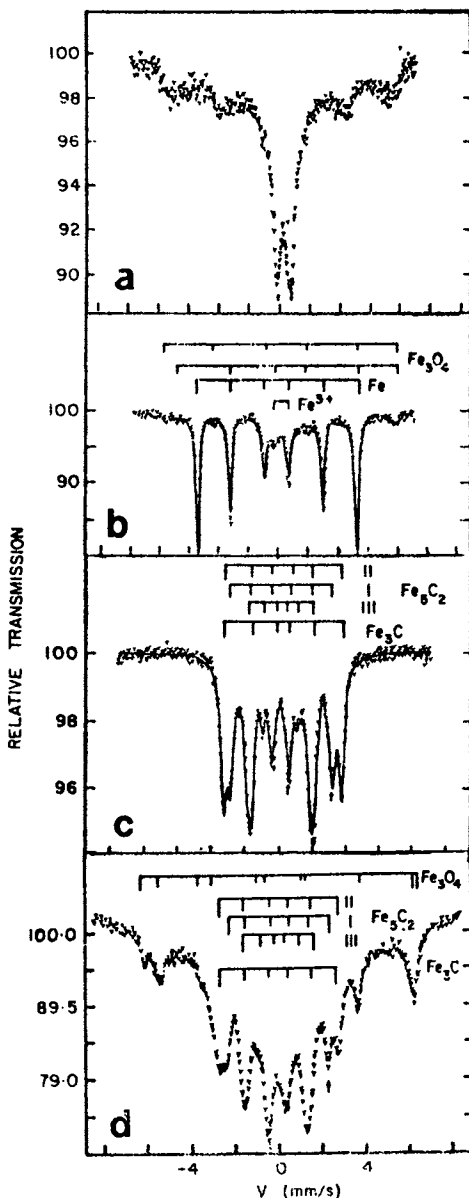


Figure 5. Mössbauer spectra (a) of "fresh" ZSM-5 impregnated with  $\text{Fe}^{3+}$  using  $\text{Fe}(\text{NO}_3)_3$  solution, (b) of reduced "Fe clusters" and unreduced  $\text{Fe}_3\text{O}_4$ , etc., (c) of carbided catalyst, and (d) of used catalyst. In (c) and (d) the Hägg carbide ( $\text{Fe}_5\text{C}_2$ ) shows a complex spectrum arising from three different sites occupied by Fe, whereas in Cementite ( $\text{Fe}_3\text{C}$ ) all sites are the same. Comparison of these spectra shows that the peaks for  $\text{Fe}_5\text{C}_2$  in (c) decrease and those for  $\text{Fe}_3\text{C}$  in (d) increase, suggesting a transformation from  $\text{Fe}_5\text{C}_2 \rightarrow \text{Fe}_3\text{C}$  during the F-T syngas reaction.

One of the recent advances in magnetic studies is that it enables not only the estimation of the average volume  $\bar{v}$  of clusters from the LF and HF approximations of the Langevin function, but also enables to compute particle size distribution based on an assumed function. By judiciously combining the parameters of the Langevin and of the "log normal" function, we obtained a particle (cluster) size distribution of  $\gamma$ -Fe<sub>2</sub>O<sub>3</sub> in ZSM-5. The essential features of such computation are shown in Fig. 6.

Subsequently, we studied the mordenite (Fig. 7) with varying ratios of SiO<sub>2</sub>/Al<sub>2</sub>O<sub>3</sub> in the range 12 to 60. These were impregnated with ~15 wt.% Fe using Fe<sub>3</sub>(CO)<sub>12</sub>. Decarbonylation yielded superparamagnetic dispersions of  $\gamma$ -Fe<sub>2</sub>O<sub>3</sub> (which were identified by Mössbauer Spectroscopy) in the range from 2.0 to 5.0 nm; the smallest clusters (1.8 nm) were obtained for a "ratio" = 17. Hydrogen chemisorption also revealed a similar trend in Fe dispersions. No samples, other than the one with a "ratio" = 60 and containing the largest particles, could be carbided under usual conditions. The acidity of the mordenite and the aromatics fraction in liquid hydrocarbons from syngas conversion also showed a maxima at a "ratio" = 17. From the plots of  $\sigma_s$  and the plots of the isomer shift ( $\delta$ ) for the Fe<sup>3+</sup> species (in the fresh sample), against the common axis of the "SiO<sub>2</sub>/Al<sub>2</sub>O<sub>3</sub>" ratios, a minimum was observed for  $\sigma_s$  and a maximum inflection for  $\delta$  was observed at the same ratio of 17 (Fig. 8). The  $\sigma_s$  result was explained on the basis of an interaction between the Brønsted acid sites and Fe<sup>3+</sup> species. The same type of interaction is believed to indirectly expand the s-wave function and to decrease the s-electron density at the <sup>57</sup>Fe nucleus, thus giving an increase in  $\delta$  at the same "SiO<sub>2</sub>/Al<sub>2</sub>O<sub>3</sub> ratio" of 17.

#### Fe on Boron-Doped Carbons

This work is based on the doctoral thesis of Prasad Rao [8]; it stemmed from the early work of Santiago, Mulay et al. (Cf. ref. 2a). Amorphous (disordered) carbons (Cabot Co.'s Monarch 700, CSX-203, etc.) were used after appropriate desulfurization. Some of these carbons were graphitized at high temperatures (2773 K). The above GMC samples were doped with boron in the range from 170 to 260 ppm. A few salient aspects of the research on these carbons and Fe/carbon catalysts will be presented in this section.

The GMC and boronated samples showed a Landau diamagnetism which changed over to almost the Langevin diamagnetism with progressive boron doping (8). The results were interpreted in terms of the equation

$$\chi = \chi_0 [1 - \exp(-T_0/T)]$$

where  $\chi_0$  is the limiting value of  $\chi$  at a cryogenic temperature (~80 K).  $T$  is the measurement temperature and  $T_0$  is the "degeneracy temperature," equal to  $kE_0$ , where  $k$  is the Boltzmann constant. According to a two-dimensional electron gas model for graphitic carbons (see ref. 2a),  $E_0$  is the energy "shift" from the Fermi level ( $E_F$ ), to the top of the valence band. Small values of  $T_0$  (~344 K) and consequently of  $E_0$  signify a more perfect graphite

Table I. Product Compositions from the Catalysts ZSM-5 (11.1% Fe) and ZSM-5 (5.6% Fe, 4.5% Co), in a Berty Reactor, Showing the Influence of Cobalt Addition to the Catalyst.  
Process Condition: H<sub>2</sub>/CO = 2, P = 21 Bar

| Catalyst  | ZSM-5<br>(11.1% Fe) | ZSM-5<br>(5.6% Fe, 4.5% Co) |
|---|---------------------|-----------------------------|
| Temperature   | 300                 | 280                         |
| CO Conversion, %  | 68.2                | 37.8                        |
| H <sub>2</sub> Conversion, %                            | 38.7                | 41.3                        |
| Space Velocity  | 1500                | 1400                        |
| <u>Product Composition (%)</u>                          |                     |                             |
| CO <sub>2</sub>   | 52.0                | 9.8                         |
| H <sub>2</sub> O  | 19.4                | 51.8                        |
| CH <sub>n</sub> + Oxygenates                            | 28.6                | 38.4                        |
| <u>Hydrocarbon and Oxygenate Composition (%)</u>        |                     |                             |
| C <sub>1</sub> -C <sub>4</sub> Hydrocarbons             | 83.1                | 74.3                        |
| C <sub>5</sub> + and Oxygenates                         | 16.9                | 25.7                        |
| <u>Composition of C<sub>5</sub>+ and Oxygenates (%)</u> |                     |                             |
| Aromatics   | 72                  | 10                          |
| Olefins   | 3                   | 46                          |
| Saturates   | 24                  | 37                          |
| Oxygenates  | 1                   | 7                           |
| % Gasoline Range (BP<204°C)                             | 75                  | 94                          |
| Research Octane No.                                     | 96                  | 81                          |

Source: V.U.S. Rao and R.J. Gormley, Hydrocarbon Processing 59(11), 139 (1980).

Table II. Summary of Results Obtained from Magnetic and Mössbauer Studies on ZSM-5 (Fe)

| Method of Impregnation | Carbonyl<br>Fe <sub>3</sub> (CO) <sub>12</sub>                      | Aqueous Ferric<br>Nitrate   |
|------------------------|---|---|
| Catalytic activity     | Very steady activity, low % of aromatics                            | Activity fluctuates with time, high % of aromatics initially                                  |
| Identified phases:     |   |   |
| As impregnated         | Superparamagnetic $\gamma$ -Fe <sub>2</sub> O <sub>3</sub> ; d=63 Å | Superparamagnetic $\alpha$ -Fe <sub>2</sub> O <sub>3</sub> ; d=100 Å                          |
| Reduced                | Nearly 80% of Fe in metallic form                                   | Nearly 80% of Fe in metallic form   |
| Carbided               | $\chi$ and $\epsilon$ carbides; and Fe <sub>3</sub> O <sub>4</sub>  | $\chi$ carbide  |
| Used                   | $\chi$ carbide and Fe <sub>3</sub> O <sub>4</sub>                   | $\epsilon$ and $\chi$ carbides; traces of $\theta$ carbide and Fe <sub>3</sub> O <sub>4</sub> |

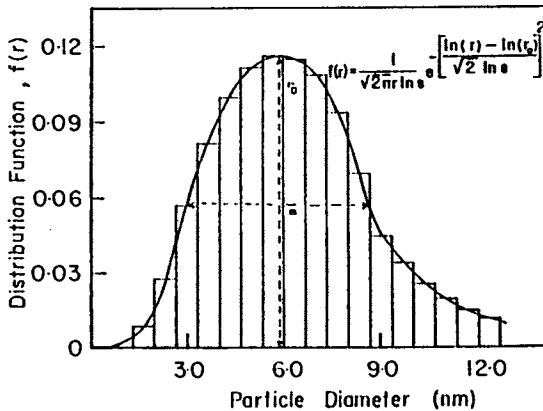
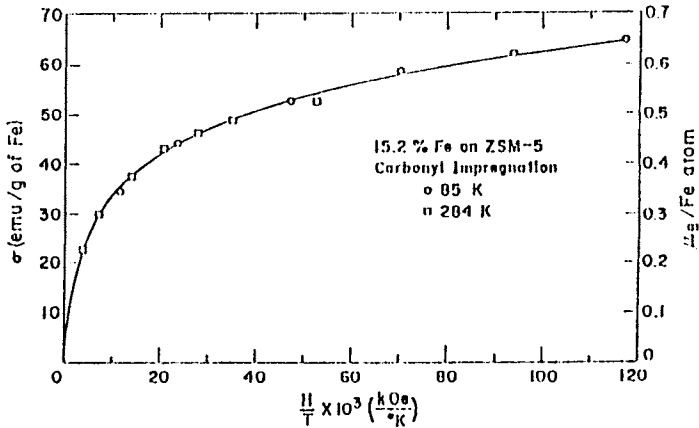


Figure 6. (a)  $\sigma$  vs  $H/T$  plots for the "fresh" ZSM-5 impregnated with  $\text{Fe}_3(\text{CO})_{12}$  and (b) the cluster (particle) size distribution for  $\gamma\text{-Fe}_2\text{O}_3$  obtained from (a), assuming a "log normal" distribution function.

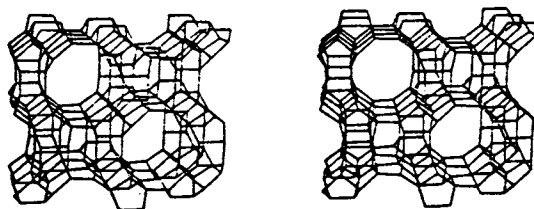


Figure 7. Structure of a typical sodium-mordenite  $[\text{Na}_3\text{Al}_8\text{Si}_{14}\text{O}_{96}] \cdot 24\text{H}_2\text{O}$  viewed along the  $[001]$  direction. The orthorhombic unit cell has the dimensions  $a = 1.81$ ,  $b = 2.05$ , and  $c = 0.75$  (nm). The "hydrogen form," obtained by exchanging  $\text{Na}^+$  ions with  $\text{H}^+$  (courtesy of Norton Co.), was used.

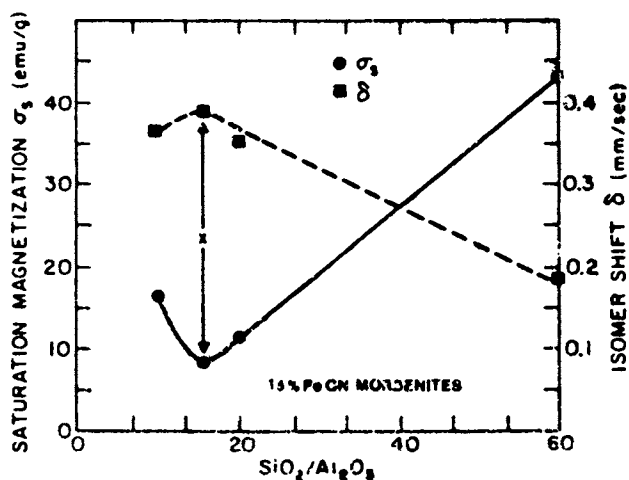


Figure 8. Saturation magnetization ( $\sigma_s$ ) and the Mössbauer isomer shift ( $\delta$ ) vs  $\text{SiO}_2/\text{Al}_2\text{O}_3$  ratio. The arrows show the ratio = 17, at which the acidity is highest.

with relatively more "metallic" character. The variation in the diamagnetic susceptibility ( $-\chi$ ) with boron concentration is shown in Fig. 9. The  $E_F$  values computed by using the equations mentioned above were plotted against the boron concentrations, and a trend similar to that of Fig. 9 was observed for  $E_F$ . Thus, a relative shift in  $E_F$  from  $-0.02$  to  $-0.14$  eV indicated that boron first entered the interstitial and some trigonal substitutional ( $sp^2$ ) sites in GMC and finally seem to have occupied practically all the substitutional sites; this behavior stemmed from the electron acceptor properties of boron. Other intricacies of the effects of boron doping are discussed in ref. 8. In addition, ESR (or EPR) spectroscopy (which is well-known to most chemists) was also employed to characterize the amorphous, GMC, and boron-doped (BGMC) carbons.

It should suffice to point out that the shifts in the 'g' value, the number of spin centers, the line widths, and analysis of the EPR Lorentzian-Spectra confirmed in general the interpretations deduced from the magnetic  $\chi$ -type characterization.

The undoped and boron-doped carbons were then used as supports for Fe, using the  $Fe(NO_3)_3$  solution impregnation technique to obtain a loading of  $\sim 5$  wt.% Fe. Mössbauer spectra for the fresh sample showed the presence of  $\alpha$ - $Fe_2O_3$  S.P. clusters (see the S.P. curve in Fig. 2). This oxide is antiferromagnetic with equal numbers of spins parallel and antiparallel in its two sublattices A and B, respectively, and as such cannot be magnetized permanently, whereas the ferrimagnetic materials, such as  $\gamma$ - $Fe_2O_3$  and  $Fe_3O_4$  with unequal numbers of spins at the "tet" and "oct" sites can be magnetized. The extent of reduction to the metallic S.P.  $Fe^0$  clusters depends not only on the reduction conditions (temperature,  $H_2$  flow rate, and total time), but also on the intrinsic nature of the oxide ( $\alpha$ ,  $\gamma$ ,  $Fe_2O_3$ ,  $Fe_3O_4$ ) etc., as well as on the nature of the substrate. The Mössbauer spectra for the Fe/carbon systems in general showed a six-line spectra with a central doublet arising from the  $Fe^0$  (reduced) clusters and a S.P. component (Fig. 2A).

A good S.P. behavior for  $Fe^0$  clusters was observed for the Fe/CSX-carbon catalyst over the entire range of 88-297 K (and H up to 8000 Oersteds). For other systems a S.P. behavior was observed from 196 to 443 K over the same range of H. For the Fe/CSX-carbon the average particle diameter ( $\bar{d}$ ) obtained from the LF and HF approximations of the Langevin function was found to be 3.9 nm, whereas the other Fe/carbons showed a larger  $\bar{d} \approx 5.5$  nm. No significant change in  $\bar{d}$  was observed when the boron doping was varied.

The kinetics of CO hydrogenation of various Fe/carbon catalysts was studied using an appropriate micro-reactor described by Jung et al. [9]. The kinetic studies showed that in the case of the boron-doped carbons, the observed changes in  $N_{C_1}$  and  $N_{CO}$  were not large, but did show a consistently increasing trend with increasing boron content. These results coupled with the  $E_F$  results are shown in Fig. 10. Arrhenius plots were drawn from the reaction rates measured at different temperatures for the CO hydrogenation reaction. Activation energies (E) ranging from 91 to 103 for  $E_{C_1}$  and from 101 to 114.6 for  $E_{CO}$  (in  $KJ\ mole^{-1}$ ), respectively, were calculated. Although it was tempting to ascribe a metal support

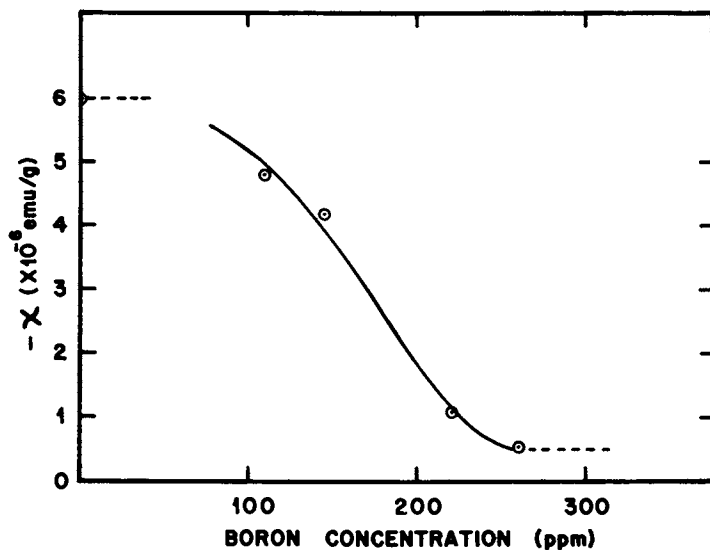


Figure 9. Variation of the diamagnetic susceptibility as a function of boron doping.

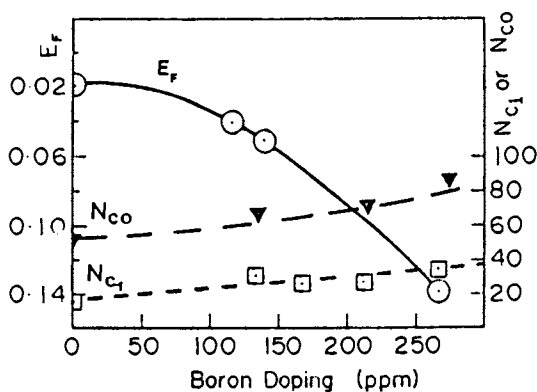


Figure 10. The variation in the Fermi level  $E_F$  [left hand scale] and the TOF for  $N_{CO}$  and  $N_{Cl}$  [right hand scale ( $\times 10^{-3} s^{-1} Fe_s^{-1}$ )], both as a function of boron doping.



interaction in the early phases of the work, which showed that the TOF values almost doubled with increasing boron content, a careful analysis of the overall results did not suggest a carbon-Fe interaction.

#### Fe and Fe<sub>2</sub>Ru on Carbons Using Fe<sub>3</sub>(CO)<sub>12</sub> and Fe<sub>2</sub>Ru(CO)<sub>12</sub>

High surface area carbon (CSX-203 desulfurized) was impregnated with Fe<sub>3</sub>(CO)<sub>12</sub> and subsequently reduced at 723 K for 16 h in flowing H<sub>2</sub> (30 cc/min). The magnetic and Mössbauer characterization was carried out on the decarbonylated (fresh) and reduced products. Typical results for a sample with a loading of 6.4 wt.% Fe are shown in Figs. 11 and 12.  $\sigma$  vs H/T plot for the fresh sample is shown in Figs. 11 and 12, respectively. A very good superposition of data points in Fig. 11 revealed that the metal species in the fresh sample was superparamagnetic. Using the data from the same figure, the average particle size was found to be 3.68 nm. A value of 59.5 emu/g·Fe indicated that the S.P. metal species in the fresh sample was  $\gamma$ -Fe<sub>2</sub>O<sub>3</sub>. The room temperature Mössbauer spectrum for the fresh sample (Fig. 13A) consisted of a well-resolved asymmetric quadrupole doublet ( $\delta = 0.3631$  mm/s,  $\Delta E_Q = 0.7966$  mm/s). The  $\delta$ -value is characteristic of high spin Fe<sup>3+</sup>. The relatively large value for  $\Delta E_Q$  for an Fe<sup>3+</sup> ion (<sup>6</sup>S<sub>5/2</sub> state) is again due to the very small particle size of the metallic species. The intensity asymmetry of the doublet could be attributed to the asymmetry in bonding at the surface Fe<sup>3+</sup> ions.

As can be seen from Fig. 12, there is a substantial ferromagnetic contribution to the magnetization of the reduced sample. The room temperature Mössbauer spectrum of the reduced sample (Fig. 13B,C) revealed a broad central line and four very weak outer lines. The outer lines appeared at the corresponding line positions in the magnetically split six-line spectrum of bulk iron (Fe<sup>0</sup>). The broad central line appeared to be superposition of four lines, a quadrupole doublet and two innermost lines of a magnetic six-line spectrum. Qualitatively, this spectrum indicated the presence of metallic iron in the superparamagnetic (corresponding to the quadrupole doublet) and ferromagnetic (corresponding to the sextet) forms. However, the Mössbauer spectrum of the reduced sample recorded at 4.2 K (Fig. 13D) was a well-defined sextet corresponding to a slow relaxation of S.P. particles.

The room temperature Mössbauer spectrum of the fresh sample Fe<sub>2</sub>Ru(CO)<sub>12</sub>/CSX-203 (Fe = 0.7 wt.%) exhibited a single quadrupole doublet ( $\delta = 0.3240$  mm/s,  $\Delta E_Q = 0.7334$  mm/s). From the  $\delta$ -value the Fe-species present was identified to be (superparamagnetic)  $\gamma$ -Fe<sub>2</sub>O<sub>3</sub>. The above Fe<sub>2</sub>Ru/C system when reduced in hydrogen showed only a single line in the room temperature Mössbauer spectrum with  $\delta = 0.1372$  (mm/s) which was ascribed to S.P. Fe<sup>0</sup>. A very low value of  $\sim 3$  emu/g·Fe was observed for the saturation magnetization ( $\sigma$ ) even at 80 K. This low value for  $\sigma$  and the non-zero value for  $\delta$  (with respect to bulk metallic iron) suggest the possibilities that (a) electrons from the Pauli paramagnetic Ru and/or (b) electrons from the carbon substrate entered the d-band of Fe.

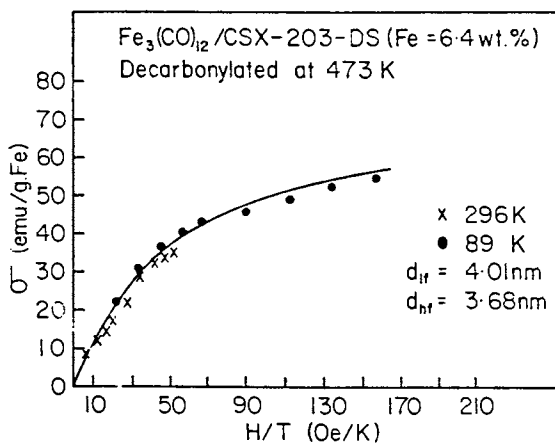


Figure 11.  $\sigma$  vs H/T plot for the fresh Fe<sub>3</sub>(CO)<sub>12</sub>/CSX-203 sample (Fe = 6.4 wt.%).

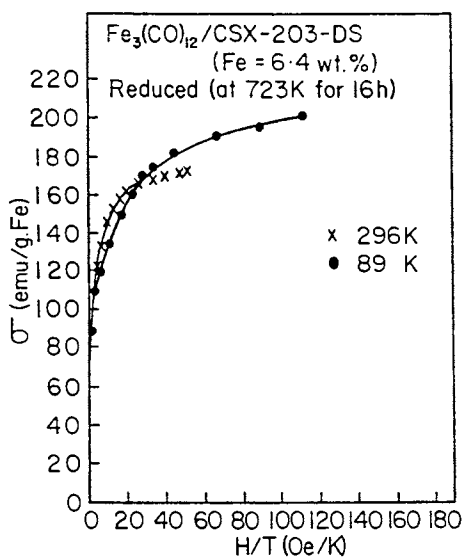


Figure 12.  $\sigma$  vs H/T plot for the reduced Fe<sub>3</sub>(CO)<sub>12</sub>/CSX-203 sample.

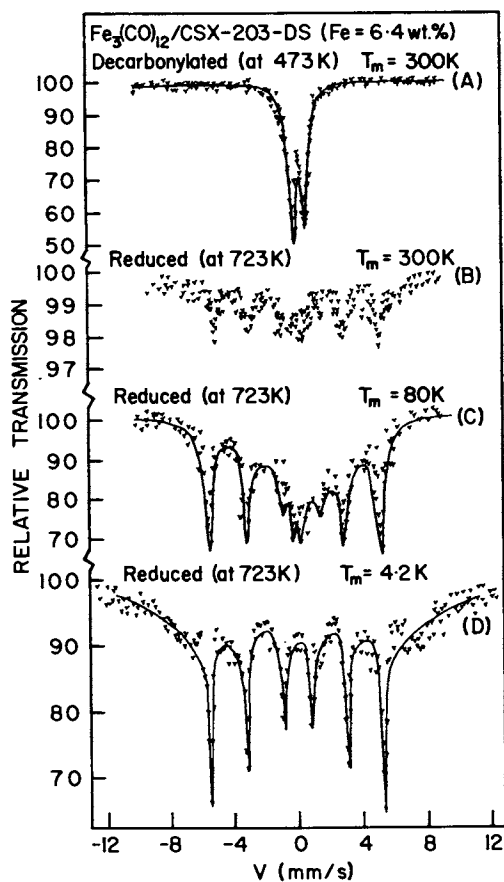


Figure 13. Mössbauer spectra for  $\text{Fe}_3(\text{CO})_{12}/\text{CSX-203}$  (a) in the decarbonylated (fresh) state at room temperature, (b) in reduced state at room temperature, (c) same at 80 K, and (d) same at  $\sim 4.2$  K.

### Conclusions

We have shown that the Fe or Fe-Co/Zeolite systems with  $\sigma$  vs H/T type results provide a unique probe for obtaining particle sizes ( $\bar{d}$ ) of the metal clusters, and can be extended for computing a particle-size distribution. In addition, electronic interactions between the Brönsted acid sites and the Fe species can be elucidated. Mössbauer spectroscopy has been shown to be a useful auxiliary technique for identifying various oxides and carbides of Fe and to discern which carbide and which type of bimetallic clusters are responsible for the enhancement of the gasoline range hydrocarbons in the F-T reaction. The carbonyls of Fe etc. gave a finer dispersion of particles and very steady catalytic activity and low fractions of aromatics. With the nitrate impregnation, the activity was found to fluctuate with an initial high fraction of aromatics. The magnetic susceptibility technique was used to obtain band structure parameters such as the degeneracy temperature  $T_0$  and the corresponding changes in  $E_F$ , for the boron-doped carbons. The  $NC_1$  and  $NC_0$  doubled with B-doping. Preliminary results on the Fe/carbon and  $Fe_2Ru$ /carbon showed the nature of electronic interaction between Fe and Ru.

### Acknowledgments

The authors sincerely appreciate the research carried out by former graduate students (now) Drs. C. Lo, M. Oskooie-Tabrizi, H.J. Jung, and A.V. Prasad Rao, under the direction of one of us (LNM), during the past five years. We are grateful to various research associates/collaborators, namely Drs. K.R.P.M. Rao (Bhabha Atomic Research Center, Bombay, India) and to Drs. B. Bernstein, R. Schehl, R. Diffenbach, and V.U.S. Rao (Pittsburgh Energy Technology Center, Pittsburgh, PA). We wish to thank our colleagues Profs. M.A. Vannice and P.L. Walker Jr. for their assistance in CO-hydrogenation with the various Fe/carbon catalysts and many helpful discussions. The research on the Fe, Fe-Co/Zeolites was supported by the U.S. Department of Energy and the work on the Fe/carbon catalysts was supported by the National Science Foundation, USA. The Government of India generously gave a fellowship to A.V. Prasad Rao.

### Literature Cited

1. L.N. Mulay, Magnetic Susceptibility, Wiley-Interscience, New York, NY (1966); Reprint Monograph, R.E. Krieger Publ. Co., Melbourne, FL (1980); see also L.N. Mulay, "Techniques for Magnetic Susceptibility," Ch. 7 in Physical Methods of Chemistry, A. Weissberger and W. Rossiter, eds., Wiley Interscience, New York (1972).
- 2a L.N. Mulay and E.A. Boudreaux, eds., "Theory and Applications of Molecular Diamagnetism," and
- 2b "Theory and Applications of Molecular Paramagnetism," Wiley-Interscience, New York, NY (1976). [These give a detailed discussion and factors for converting the classical Gaussian cgs-emu parameters to the mksA S.I. units.] Note: 2a is now available from Krieger Publishers; see ref. 1.
3. D.W. Collins and L.N. Mulay, IEEE-Mag-Trans 4, 470 (1968); see also L.N. Mulay (review) on "Mössbauer Spectroscopy and

- Superparamagnetism," p. 103 and "Philosophy of Research-Mössbauer Spectroscopy . . . etc.," p. 79 in "Mössbauer Methodology," Vol. 3, I.J. Gruverman, ed., Plenum Press, New York (1967); see also a paper by L.N. Mulay et al.; this describes "Superparamagnetism" in Proc. Am. Inst. Chem. Engrs. Conf. (Philadelphia, 1978), "Microfische No. 60" available from Am. Inst. Chem. Engrs., New York, NY.
4. H. Yamamura and L.N. Mulay, *J. Appl. Phys.* 50, 7795 (1979).
  5. P.W. Selwood, *Chemisorption and Magnetization*, Academic Press, New York (1975).
  6. M. Boudart, A. Delbouille, J.A. Dumesic, S. Khamamouna, and H. Topsøe, *J. Catal.* 37, 486 (1975).
  7. W.N. Delgass, L.Y. Cheng, and G. Vogel, *Rev. Sci. Instrum.* 47, 968 (1976).
  8. A.V. Prasad Rao, Ph.D. Thesis in Solid State Science, Aug. 1983, The Pennsylvania State University, University Park, PA.
  9. H.J. Jung, M.A. Vannice, L.N. Mulay, R.M. Stansfield, and W.N. Delgass, *J. Catal.* 76, 208 (1982).

#### Supplementary Literature Cited

- 1 V.U.S. Rao, R.J. Gormley, L.C. Schneider, and R. Obermyer, Preprints Div. of Fuel Chemistry, *ACS* 25, 119 (1980).
- 2 V.U.S. Rao and R.J. Gormley, *Hydrocarbon Processing* 59(11), 139 (1980).
- 3 G.T. Kokotailo, S.L. Lawton, D.H. Olson, and W.M. Meier, *Nature* 272, 437 (1978).
- 4 E.M. Flanigen, J.M. Bennett, R.W. Grose, J.P. Cohen, R.L. Patton, R.M. Kirchner, and J.V. Smith, *Nature* 271, 512 (1978).
- 5 F. Van der Woude and G.A. Sawatsky, *Physics Letters* 12C, 335 (1974).
- 6 W. Kundig, K.J. Ando, R.H. Lindquist, and G. Constabaris, *Czech. J. Phys.* 17, 467 (1967).
- 7 C. Kittel, "Introduction to Solid State Physics," Fifth Ed., John Wiley and Sons Inc., New York, NY (1980).
- 8 K.M. Sancier, W.E. Isakson, and H. Wise, Preprints, Div. of Petroleum Chemistry, *ACS* 23(2), 545 (1978).

RECEIVED March 28, 1985

## Characterization of Supported Iron Oxide Particles Using Mössbauer Spectroscopy and Magnetic Susceptibility

J. Phillips<sup>1</sup>, Y. Chen<sup>2</sup>, and J. A. Dumesic<sup>3</sup>

<sup>1</sup>Department of Chemical Engineering, The Pennsylvania State University, University Park, PA 16802

<sup>2</sup>Department of Chemistry, Nanjing University, Nanjing, China

<sup>3</sup>Department of Chemical Engineering, University of Wisconsin, Madison, WI 53706

The size and structure of iron oxide particles supported on Grafoil and used as water-gas shift catalysts were studied using magnetic susceptibility and Mössbauer spectroscopy. The use of a Mössbauer spectra modeling program which accounts for magnetic relaxation effects (both superparamagnetic and collective excitation) aided in the identification of the iron phase under reaction conditions (magnetite) and permitted a quantitative determination of particle size. The particle size determined using Mössbauer spectroscopy was in good agreement with that obtained using the well established magnetic susceptibility technique. It was also shown that the Grafoil supported particles sintered slowly under water-gas shift reaction conditions.

During recent decades, while significant advances have been made in understanding the behavior of supported metal catalysts, relatively little attention has been given to supported metal-oxide catalysts. Yet, supported oxide catalysts are potentially of great industrial significance, and work needs to be done in this area. The first requirement for the study of supported oxide catalysts is the development of techniques for measuring supported metal-oxide particle sizes and distributions. In this paper the applications of Mössbauer spectroscopy and magnetic susceptibility to the measurement of supported iron-oxide particle sizes are discussed. It is demonstrated that both methods give important particle size information.

### Theory

Mössbauer Spectroscopy. Small, single domain, ferro- or ferrimagnetic particles can show both collective magnetic excitation (precession of the magnetic moment) and superparamagnetic (relaxa-

0097-6156/85/0288-0518\$06.00/0

© 1985 American Chemical Society

tion of the magnetic moment) behavior. These modifications in the magnetic behavior of small particles produce significant changes in the resultant Mössbauer spectra. Thus, information about particle size (and shape) is contained in the Mössbauer spectra of small particles. This fact has been recognized for some time and many workers have attempted to analyze Mössbauer spectra to obtain information about particle size.

The early efforts were based exclusively on the analysis of superparamagnetic effects. In a series of papers Brown (1,2) and Aharoni (3,4) developed the theory for the relaxation of magnetic moments in single domain magnetic systems containing several equivalent low energy directions. They showed that in such systems there is a finite probability that the magnetization vector will spontaneously change directions. The energy barrier for this process is dependent on the origin of the magnetic anisotropy (e.g., magneto crystalline anisotropy, shape anisotropy, interface anisotropy, surface anisotropy). All of these anisotropy energy barriers are a function of particle size. (The origins and magnitudes of various anisotropies are discussed at length in reference 5.) The average lifetime  $\tau_R$  of a given state can be written:

$$\tau_R = (1/2f)\exp(\kappa v/kT) \quad (1)$$

where  $f^{-1}$  is of the order of  $10^{-9} - 10^{-11}$  sec,  $\kappa$  is the anisotropy energy constant (ergs/cm<sup>3</sup>) and  $v$  is the volume (cm<sup>3</sup>) of the magnetic particle. Brown showed that the preexponential factor is also a function of the anisotropy energy constants and temperature. In the limit of large anisotropy barriers ( $\kappa v \gg kT$ ) the preexponential factor can be written:

$$1/2f = \frac{M_s \pi^{1/2}}{2\kappa \gamma_0} (\kappa v/kT)^{-1/2} \quad (2)$$

where  $M_s$  is the saturation magnetization and  $\gamma_0$  is the gyromagnetic ratio. Thus, if the value of  $\tau_R$  can be obtained, then eq. (1) can be solved for  $\kappa v$ . It will be seen below that  $\tau_R$  can, in fact, be deduced from the shape of Mössbauer spectra.

The theory of the effect of magnetic relaxation on the shape of Mössbauer spectra has been discussed at length by Wickmann (6). Wickmann wrote the Mössbauer absorption intensities  $I(E)$  as a function of energy ( $E$ ) for a pair of equivalent, allowed transitions to be:

$$I(E) = \frac{k[(1+\tau\Gamma)P+QR]}{P^2+R^2} \quad (3)$$

where  $\tau = \tau_R$ ,  $\Gamma = \tau_N^{-1}$  (inverse of the natural lifetime of the nuclear excited state),  $k$  is a relative intensity factory (e.g. Klebsch-Gorden coefficient) and

$$P = \tau[\Gamma^2 - (\Delta - E)^2 + \delta^2] + \Gamma \quad (3a)$$

$$Q = \tau(\Delta - E) \quad (3b)$$

$$R = (\Delta - E)(1 + 2\tau\Gamma) \quad (3c)$$

where  $\Delta$  is the isomer shift and  $\delta$  is  $1/2$  the quadrupole splitting as conventionally defined. It can be shown that for  $\tau/\tau_N \gg 1$  the intensity equation reduces to the equation for a pair of Lorentzian lines with half widths equal to  $\Gamma$  and maximum values at  $E = \Delta + \delta$ . For  $\tau/\tau_N \ll 1$  the equation reduced to a Lorentzian line with a maximum value at  $E = \Delta$ . However, for intermediate values of  $\tau/\tau_N$  the line shapes are less well defined. There is no sharp transition from Zeeman split lines to a magnetically collapsed line. Wickmann shows that for  $\tau/\tau_N \sim 1$  the lines broaden considerably (see reference 6). In a typical Mössbauer spectrum of a magnetically split oxide the innermost pair of lines essentially merge when  $\tau/\tau_N \sim 1$ , creating a large peak in the center of the spectrum. Furthermore, the outer pairs of peaks also contribute significantly to the center peak of the spectrum for  $\tau/\tau_N \sim 1$ .

Mórup et al. (7) pointed out that the superparamagnetic model of magnetic behavior fails to explain several phenomena observed in the Mössbauer spectra of small magnetic particles (8). That is, it fails to explain the reduction in the hyperfine field and asymmetric line broadening which were reported by many workers (9,10). In order to explain the observed phenomena these workers postulated that the magnetization direction of small particles fluctuates around an energy minimum, which corresponds to a so-called 'easy direction' of magnetization. They described this effect as a "collective magnetic excitation". The average magnetization according to this model is:

$$M(V, T) = M(V = \infty, T) \langle \cos \theta \rangle_T \quad (4)$$

where

$$\langle \cos \theta \rangle_T = \frac{\int_0^{\pi/2} \exp\{-E(\theta)/kT\} \cos \theta \sin \theta \, d\theta}{\int_0^{\pi/2} \exp\{-E(\theta)/kT\} \sin \theta \, d\theta} \quad (5)$$

Furthermore, when  $\kappa v \gg kT$  the following approximation can be made:

$$\langle \cos \theta \rangle_T = 1 - kT/2\kappa v \quad (6)$$

This approximation is strictly valid only for systems of uniaxial symmetry, i.e., having two equivalent magnetic 'easy' directions. For systems with more equivalent directions (magnetite for example has eight)  $\kappa$  is a tensor. However, the scalar value of  $\kappa_0$  is a good approximation. Furthermore, Mórup and Topsøe (8) showed that the experimental results are linear in  $\kappa$  as suggested by eq. (6), and that the values of  $\langle \cos \theta \rangle$  computed on the basis of eq. (6) were nearly identical to those computed using the full expression, eq. (5), over a broad temperature range.



Mórup *et al.* independently measured particle size distributions for some of their samples using TEM (11). They used this distribution, and the shape and average particle sizes computed by X-ray line broadening, to computer-generate model Mössbauer spectra. They accounted for both collective excitation and superparamagnetic relaxation with the concomitant change in line shape (using the equations of Wickman (6)) in their computer program). The resulting spectra resembled quite closely the experimental spectra in all aspects. The values of the anisotropy energy constant they determined using this method were between  $1.3 \cdot 10^6$  and  $0.75 \cdot 10^6$  ergs/cm<sup>3</sup> for both unsupported (coprecipitated) and silica supported magnetite, values considerably larger than those reported elsewhere. Yet, these values are more consistent with the known values of shape and magneto-crystalline anisotropy constants than the values reported elsewhere (12-17). Furthermore, they report that the value of the anisotropy energy constant increases with decreasing particle size. This had been reported previously by Topsøe *et al.* (18) and was attributed to the effects of surface anisotropy. Further evidence that surface anisotropy has a significant effect on the value of  $\kappa$  for very small particles is available from other studies as well (19,20).

**Magnetic Susceptibility.** The magnetic moments of small, single domain, superparamagnetically relaxing particles tend to align parallel to an applied magnetic field (H). The energy of such a particle in an applied field is:

$$E = -M_{sp}vH\cos\theta \quad (7)$$

where  $M_{sp}$  is the spontaneous magnetic moment per unit volume of the particles,  $v$  is the particle volume, and  $\theta$  is the angle between the applied field and the particle magnetic moment. Measurements of particle volume can be extracted from measurements of the total magnetization as a function of the applied field in both the high and low field regimes. The various techniques are reviewed by Selwood (20). In particular, in the low field regime one can write the measured magnetic moment  $M$  for a group of uniform particles of total volume  $V$  as (21,22):

$$M = M_{sp} \cdot V (M_{sp} \cdot vH / 3kT) \quad (8)$$

where  $M_{sp}V$  is the saturation magnetization for the entire array of particles. In the event that there is a distribution of particle sizes, the measured magnetic moment can be written:

$$M = \frac{M_{sp}^2 H \sum N_p v_p^2}{3kT} \quad (9)$$

where  $N_p$  is the number of particles of volume  $v_p$ . It is assumed that  $M_{sp}$  is not a function of particle size. Thus, the measured magnetization is a function of the shape of the particle size distribution. When divided by the saturation moment,  $M_s$ , of the particle distribution, which is a function of the total volume only, eq. (9) becomes:

$$M/M_S = \frac{M_{sp} H_{EN} v_p^2}{3kT \frac{H_{EN} v_p}{M_{sp}}} \quad (10)$$

or,

$$\frac{\bar{v}^2}{\bar{v}} = \frac{3kT}{M_{sp} H} (M/M_S) \quad (11)$$

From this equation it is clear that a plot of  $M/M_S$  versus  $M_{sp}H/3kT$  will yield a line with slope  $\bar{v}^2/\bar{v}$ . The only unknown in this equation is the value of  $M_{sp}$ . Assuming that this does not change as a function of particle size (no dead layers) this can be determined for magnetite from the formula of Pauthenet (23):

$$M_{sp} = M_0(1 - 0.826 \cdot 10^{-6}T) \quad (12)$$

where  $M_0$  is the spontaneous magnetization at absolute zero. There is one difficulty in the actual application of this theory: the unknown effect of the superparamagnetic relaxation rate on the measured magnetization. This is discussed at length by Bean and Livingston (24). It is their contention that, any particle for which  $\tau_R$  is of the order of 100 seconds or less will behave like a large paramagnet in magnetic susceptibility experiments. This is equivalent to the criterion that  $k\nu < 25kT$ . Thus, according to Bean and Livingston, all measurements must be made above that temperature ( $T_{cm}$ ) for which  $k\nu < 25kT$  for the largest particles in the distribution. There is no analytical means of determining if all the particles in a given distribution are relaxing rapidly enough to fulfill this criterion. Thus, the value of  $T_{cm}$  is determined experimentally. That is, plots of  $M/M_S$  are plotted as a function of  $H/T$  using data collected at many temperatures. For all data taken at  $T > T_{cm}$  these plots collapse into a single curve.

### Experimental

Catalyst Production. Supported magnetite particles were produced on Grafoil (Union Carbide), a high surface area form of graphite. The nature of Grafoil and the reasons it is convenient to use in Mössbauer spectroscopy experiments are described elsewhere (25). Grafoil is also well suited for magnetic susceptibility experiments.

Two different methods were used to produce iron oxide ( $Fe_2O_3$ ) particles on Grafoil. One method was a simple impregnation-calcination based on the method of Bartholomew and Boudart (20). The exact method used is described elsewhere (27). The second method used was a two step process. First, metallic iron particles were produced on the Grafoil surface via the thermal decomposition of iron pentacarbonyl. This process is also described in detail elsewhere (25). Next, the particles were exposed to air at room atmosphere and thus partially oxidized to  $Fe_2O_3$ . Following the production of iron oxide particles (by

either technique) the samples were treated at 653 K in flowing 15%CO/85%CO<sub>2</sub> (mole fraction) at 650 K. This reduced the particles (28) to Fe<sub>3</sub>O<sub>4</sub>. In some cases, the samples were further treated under "standard" water-gas shift reaction conditions: 50% H<sub>2</sub>O, 45% CO and 5% CO<sub>2</sub> at 613 K and atmospheric pressure. Flowrates were maintained such that the CO conversion was kept to less than 7 percent.

Mössbauer Spectroscopy. All details of the Mössbauer spectroscopy studies are described elsewhere (25,27). This includes descriptions of the spectrometer, in situ cells, and the computer program used to analyze the Mössbauer spectra.

Magnetic Susceptibility. Magnetization as a function of applied field was determined at various temperatures according to the Faraday method. A Cahn model RG microbalance and an Alpha model 4800 magnet were used in this respect. A detailed description of the technique used can be found in reference 4.

### Results/Discussion

Mössbauer Spectroscopy. In Figure 1 are shown four Mössbauer spectra recorded under various conditions and after a progression of treatments of sample 1 (see Table I). The first spectrum (spectrum A) is a room temperature spectrum (in flowing helium) taken after the sample had been under water-gas shift conditions for three hours. The second spectrum (spectrum B) was recorded for 22 hours while the sample was under water-gas shift reaction conditions. Immediately following the collection of spectrum B the sample was cooled rapidly (5 minutes) to room temperature in flowing helium. At this point the sample had been under reaction conditions for a total of twenty-five hours. The third spectrum (spectrum C) was then recorded. Next, the sample was treated for an additional 40 hours under water-gas shift reaction conditions, and then cooled to room temperature in flowing helium. The fourth spectrum (spectrum D) was then recorded.

All three of the room temperature spectra (A, C and D), are characteristic of small magnetite particles. They all are composed basically of two juxtaposed sextuplets. Moreover, the sextuplets have about the same relative area ratio and the same magnetic hyperfine splitting found in bulk magnetite. (In Table II there is a complete listing of parameters for bulk magnetite and the parameters of spectra A-D for easy comparison). However, all have a central peak not present in magnetite. This peak arises from magnetic relaxation effects. The identity of the iron species which gives rise to spectrum B is not as readily apparent. However, it is clearly shown below that this is indeed the spectrum of small magnetite particles at 613 K.

In Figure 2, the Mössbauer spectrum of sample 2 (Table I) and a matching computer-simulated model spectrum are shown. This spectrum was recorded over a period of 30 hours while sample 2 was under a flowing CO/CO<sub>2</sub> (15:85) gas mixture at 613 K. Following the completion of the experiment, the average magnetite particle

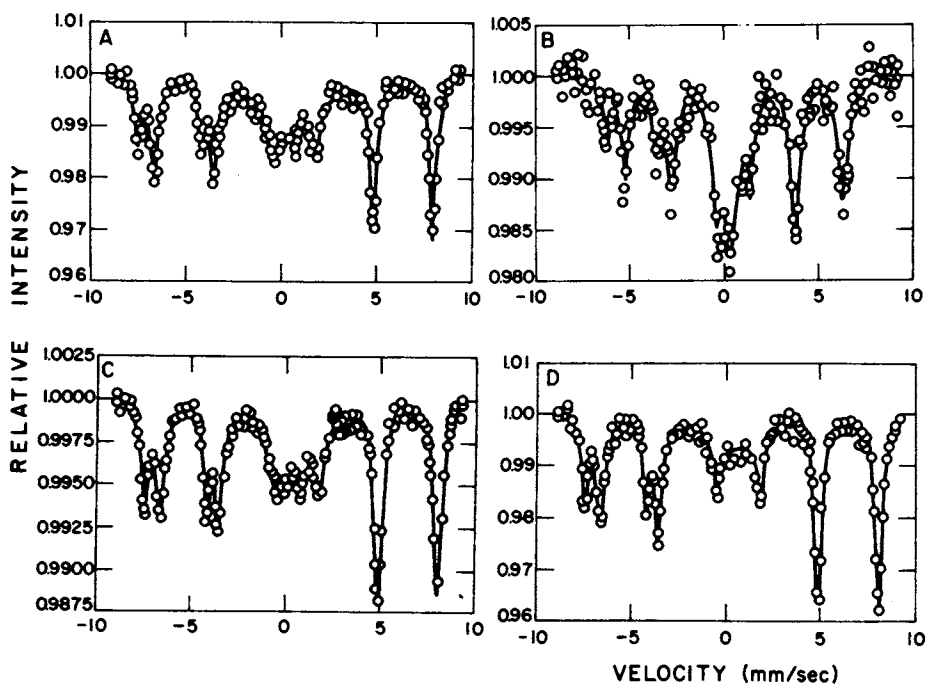


**Figure 1.** In Situ Mössbauer Spectra. A) Spectrum collected while the sample (sample 1) was at room temperature in flowing helium gas. The sample had been previously treated for 3 hours in water-gas shift synthesis gas at 613 K; B) Spectrum collected while the sample was at 613 K in flowing water-gas shift synthesis gas; C) Spectrum collected while the sample was at room temperature in flowing helium gas. The sample had been previously treated for 25 hours in water-gas shift synthesis gas at 613 K; D) Spectrum collected at room temperature in flowing helium gas. The sample had been previously treated for 65 hours in flowing water-gas shift synthesis gas at 613 K.

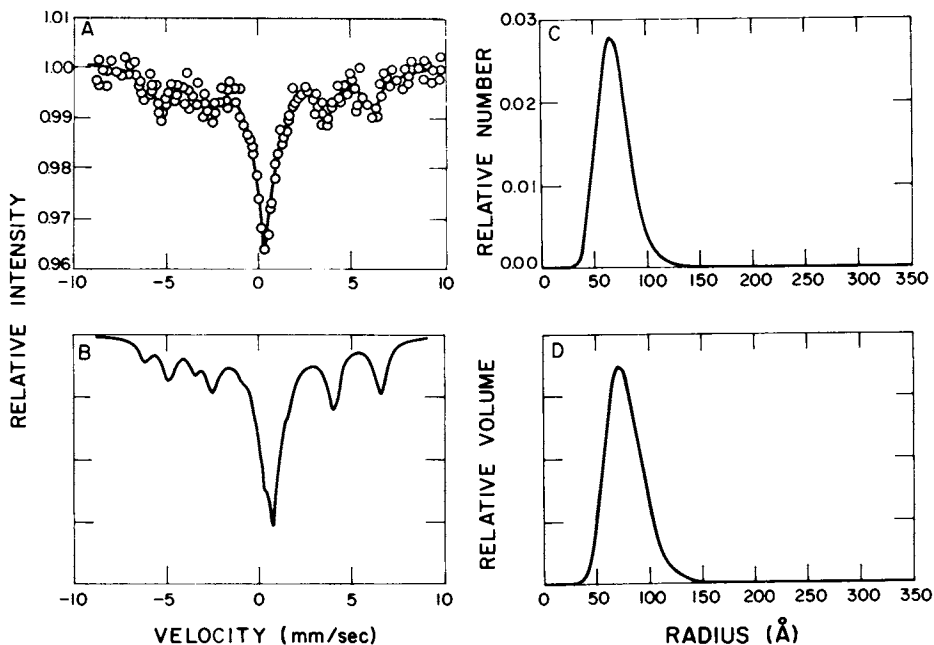


**Figure 2.** Mössbauer Spectrum and Corresponding Computer Simulation For Sample 2 Under Water-Gas Shift Reaction Conditions at 613 K. A) *In situ* Mössbauer spectrum of sample 2 at 613 K; B) Computer-simulated spectrum; C) Distribution of particle radii; D) Relative volume fractions as a function of radius (Å). For the computer simulation, the following parameters were used:  $\sigma=1.25$ , mean radius = 65Å,  $\kappa=8 \times 10^5$  ergs/cm<sup>3</sup>. The Klebsch-Gordon coefficients used were 3:3:1.

size of sample 2 was determined using magnetic susceptibility, as described below.

Following the example of Mórup *et al.* (7,8), the equations of Wickman were used to determine the effect of magnetic relaxation on line shapes and central peak area for small particles of magnetite. A log normal particle size distribution was employed, as described elsewhere (29-33):

$$f(x) = \frac{1}{(2\pi)^{1/2}} \cdot \frac{1}{\ln\sigma} \cdot \exp \left[ -1/2 \left[ \frac{\ln(x/\bar{x})}{\ln\sigma} \right]^2 \right] \quad (13)$$

where  $x$  is the particle diameter,  $\bar{x}$  is the statistical median of the diameter and  $\sigma$  is the (non-dimensional geometric) standard deviation. Indeed, it was determined from the modeling studies that while a log normal particle distribution (particle growth via coalescence) could describe the data very well, the distribution expected from Ostwald Ripening did not give satisfactory results. It was also assumed that the particles were hemispherical (volume =  $2/3\pi r^3$ ) rather than spherical. This assumption was made on the basis of the peak area ratios in each of the magnetite sextuplets. These area ratios were found to be very close to 3:3:1 (see Table II). The Klebsch-Gordon coefficients for randomly oriented magnetic moments are 3:2:1; however, these coefficients are 3:4:1 when all of the particle magnetic moments are aligned perpendicular to  $\gamma$ -ray direction. Thus, the peak area ratios measured are consistent with the notion that the magnetite particles are 'wetting' the Grafoil surface and thus have magnetic moments aligned with the Grafoil basal planes. This could be due to shape anisotropy or interaction anisotropy. The assumption of particle shape has no bearing on the average particle volume determined using the modeling technique. It only has an effect on the reported particle radii. Finally, temperature also plays a role in modeling the Mössbauer spectra of this paper. This is because as discussed in several papers (34-36), the magnetic moment of bulk magnetite changes as a function of temperature. Thus, the starting parameters for the computer-simulation of spectrum 1B were chosen to agree with the value of hyperfine fields at 613 K as measured by Riste and Tenzer, using neutron scattering measurements (36). In addition, the magnetic relaxation rate depends on temperature, as discussed in the Theory section of this paper.

The results of these modeling studies are shown in Figures 2 and 3. The value of  $\kappa$  (anisotropy constant) was chosen so that the average particle radius determined from the reduction in the average hyperfine field splitting due to collective magnetic excitations ( $\frac{\text{measured splitting}}{\text{bulk splitting}} = 1 - \frac{\kappa T}{2\kappa v}$ ) and values determined from the computer simulations were in close agreement. The value of  $\kappa$  determined on this basis was  $8 \times 10^5$  ergs/cm<sup>3</sup>. Also note, Figure 3A and 3B produced using the same particle size distribution and  $\kappa$  values, but at 300 K and 613 K respectively, reproduce the characteristic features of spectra 1A and 1B very well. Thus, this method of in situ particle size measurement has been shown to be both self-

Table I. Samples Used for Mössbauer Spectroscopy and Magnetic Susceptibility Studies

| Sample No.<br>(wt % Fe) | Total Weight                                  | Fabrication Method            | Figure(s) |
|-------------------------|---|-------------------------------|-----------|
| 1 (0.5)                 | 5.5 gm <sup>a</sup>                           | Fe(CO) <sub>5</sub> /oxidized | 1,3       |
| 2 (0.94)                | 4.4 gm <sup>a</sup><br>52.148 mg <sup>b</sup> | Impregnation/calcination      | 2         |
| 3 (0.6)                 | 10.106 mg <sup>b</sup>                        | Impregnation/calcination      | 4         |

<sup>a</sup>Used for Mössbauer Spectroscopy<sup>b</sup>Used for magnetic susceptibility

Table II. Mössbauer Spectral Parameters Obtained from Computer Fitting Spectra of Figure 1

| Spectrum (fig.) | Hyperfine Fields<br>(kOe) <sup>a</sup> |         | Relative Area of<br>Paramagnetic<br>Component (%) | Klebsch-Gordon<br>Coefficients |
|-----------------|--|---------|---|--------------------------------|
|                 | A-sites                                | B-sites |   |                                |
| 1A              | 480                                    | 456     | 21  | 3:2.7:1                        |
| 1B              | 397                                    | 356     | --  | --                             |
| 1C              | 481                                    | 456     | 21  | 3:3:1                          |
| 1D              | 485                                    | 458     | 17  | 3:3.3:1                        |
| Bulk Magnetite  | 492                                    | 461     | 0   | b                              |

<sup>a</sup>A-sites and B-sites correspond to iron cations in tetrahedral and octahedral sites, respectively.<sup>b</sup>Function of orientation, see text.

consistent and consistent with the theory of collective excitation.

Magnetic Susceptibility. A second objective of this study was to demonstrate that the values obtained from Mössbauer spectroscopy for the average particle size are consistent with those obtained using magnetic susceptibility. Thus, the average particle size of sample 2 (Table I) was measured first by computer simulation of the Mössbauer spectrum (see Figure 2) and then measured using the Langevin low field method. The mean particle radius obtained using the Mössbauer spectroscopy modeling was about 75Å. The value for  $\bar{v}^2/\bar{v}$  obtained from magnetization measurements at 663 K of the same sample was  $1.37 \cdot 10^{-18} \text{ cm}^3$ . This value represents  $\langle r^6 \rangle / \langle r^3 \rangle$ . Using the formula for the moments of a log-normal distribution:

$$\langle x^n \rangle = \bar{x}^n \exp(1/2 \cdot \bar{x}^n (\ln \sigma)^2) \quad (14)$$

we find that  $\langle r^6 \rangle / \langle r^3 \rangle = 1.96 \bar{r}^3$ , where  $\sigma = 1.25$ . Dividing the measured value of  $\bar{v}^2/\bar{v}$  by 1.96 and taking the cube root, we find that the measured value of the mean radius is 89Å. The agreement between the results of magnetic susceptibility and Mössbauer spectroscopy is very good (Table III).

A study of the rate of supported particle growth was also conducted using low-field magnetic susceptibility. The average radius of particles in sample 3 (see Table I) was measured after various lengths of time in CO/CO<sub>2</sub> (15:85) at 663 K. The first measurement was made after the sample had been heated for a total of 8 1/2 hours at 663 K. The second measurement was made after the sample had been treated for a total of 52 hours at 663 K. The average particle radius increased by only 15 percent during the additional 44 hours of high temperature treatment (see Table IV). The third measurement was made after the sample had been treated for a total of 146 hours at 663 K. The additional 94 hours of high temperature treatment resulted in an average increase in the particle radius of less than 15 percent. From these experiments we find that magnetite supported on Grafoil sinters slowly but steadily at 663 K.

Following the completion of the sintering study, a study was conducted to demonstrate that 663 K, the temperature at which all magnetic susceptibility measurements were taken, was indeed greater than  $T_{cm}$ . As discussed in the theory section, measurements were made at several temperatures until it was determined that plots of  $M/M_3$  versus  $H/T$  collapsed onto a single curve. It is clear from Figure 4 that  $T_{cm}$  must be less than 450 K. That is, for any temperature above 450 K the average particle size was measured to be nearly 200 Å in diameter. For smaller particles,  $T_{cm}$  will of course be an even lower temperature. This proves that all measurements made at 663 K were indeed accurate.

### Summary

In this paper the use of Mössbauer spectroscopy and magnetic susceptibility to measure the size of supported oxide catalyst



Table III. Particle Size Determined Using Both Mössbauer Spectroscopy and Magnetic Susceptibility Methods

| Sample | Figure <sup>a</sup> | Technique   | Avg. Particle Radius (Hemispheres)                 |
|--------|---------------------|---|--|
| 1      | 1A                  | Reduced Splitting <sup>b</sup><br>Simulation of Mössbauer Spectra | 85Å, 105Å <sup>c</sup><br>95Å, 115Å <sup>d</sup>   |
| 1      | 1B                  | Simulation of Mössbauer Spectra                                   | 95Å, 115Å <sup>d</sup>                             |
| 1      | 1C                  | Reduced Splitting <sup>b</sup>                                    | 90Å, 105Å <sup>c</sup>                             |
| 1      | 1D                  | Reduced Splitting <sup>b</sup><br>Simulation of Mössbauer Spectra | 100Å, 120Å <sup>c</sup><br>120Å, 140Å <sup>d</sup> |
| 2      | 2A                  | Simulation of Mössbauer Spectra<br>Magnetic Susceptibility        | 65Å, 75Å <sup>d</sup><br>90Å                       |

<sup>a</sup>See figure captions for description of sample treatment.

<sup>b</sup>Average size determined from the reduction in the hyperfine field according to the formula:

$$\frac{\text{measured splitting}}{\text{bulk splitting}} = 1 - \frac{kT}{2\kappa V} \text{ where } \kappa = 8 \times 10^5 \text{ erg/cm}^3$$

<sup>c</sup>A sites, B sites

<sup>d</sup> $\langle r \rangle$ ,  $\langle r^3 \rangle^{1/3}$

TABLE IV. Particle size versus Time in CO/CO<sub>2</sub> at 663 K as Measured Using Magnetic Susceptibility

| Total Time at 663 K (hrs) | Average Particle Radius |
|---------------------------|-------------------------|
| 8 1/2                     | 90Å                     |
| 52                        | 100Å                    |
| 146                       | 110Å                    |

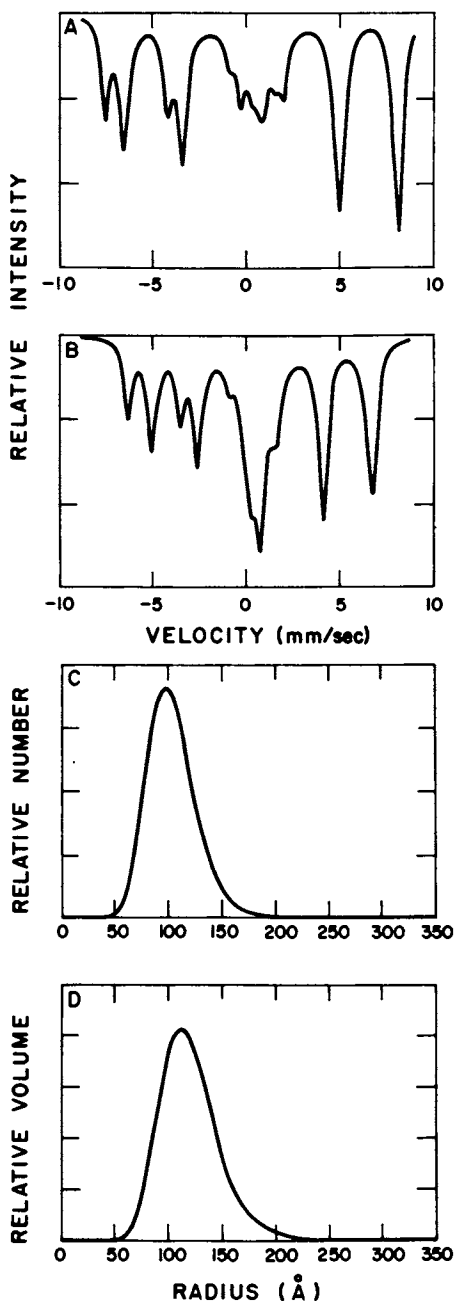


**Figure 3.** Computer Simulations of the Mössbauer Spectra of Figure 1. A) Simulation of Figure 1A; B) Simulation of Figure 1B; C) Distribution of particle radii; D) Relative volume fractions as a function of radius. For these simulations, the following parameters were used:  $\sigma=1.25$ , mean radius =  $95\text{\AA}$ ,  $\kappa=8 \times 10^5 \text{ ergs/cm}^3$ . The Klebsch-Gordon coefficients used were 3:3:1.

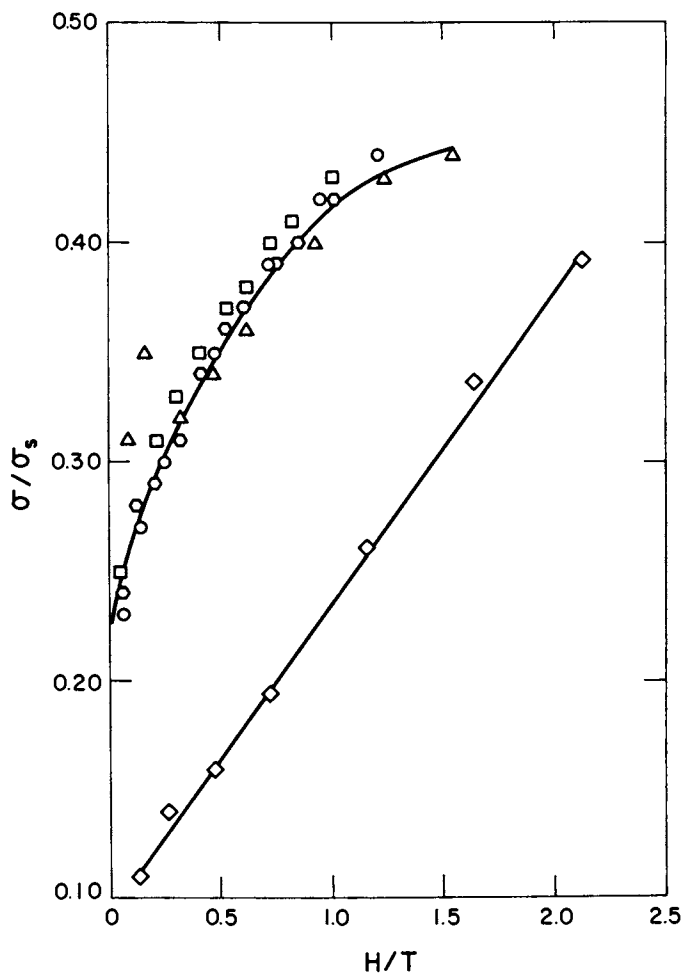


Figure 4. Plots of  $M/M_s$  versus  $H/T$  for Sample 3 at various temperatures.

- Measurements made while sample was at 660 K in a  $\text{CO}/\text{CO}_2$  atmosphere.
- Measurements made while sample was at 570 K in vacuum.
- Measurements made while sample was at 447 K in vacuum.
- Measurements made while sample was at 600 K in vacuum.
- Measurements made while sample was at 295 K in vacuum.

particles is discussed in theory and demonstrated in practice. Mössbauer spectroscopy is shown to be a particularly powerful technique because with the correct modeling equations, it can be used to measure the size and phase of catalyst particles under reaction conditions. It was also shown that the particle size determined using Mössbauer spectroscopy is in very good agreement with that obtained using the well established magnetic susceptibility technique.

Mössbauer spectroscopy and magnetic susceptibility were used to demonstrate that magnetite particles supported on a Grafoil substrate sinter very slowly under water-gas shift reaction conditions.

#### Literature Cited

1. W. F. Brown, Jr., Phys. Rev. 130, 1677 (1963).
2. W. F. Brown, Jr., J. Appl. Phys. 34, 1319 (1963).
3. A. Aharoni, J. Appl. Phys. 33, 1324 (1962).
4. A. Aharoni, Phys. Rev. 135A, 447 (1964).
5. S. Mørup, J. A. Dumesic and H. Topsøe, in "Appl. of Mössbauer Spectroscopy," (R. L. Cohen, ed.) Vol. 2, p. 1, Academic Press, N.Y. (1980).
6. H. H. Wickman in "Mössbauer Effect Methodology" 2, 39 (1966).
7. S. Mørup, H. Topsøe and J. S. Lipka, Jnl. de Phys. 37, C6-287 (1976).
8. S. Mørup and H. Topsøe, Appl. Phys. 11, 63 (1976).
9. A. M. Van der Kraan, Phys. Stat. Sol. 18A, 215 (1973).
10. T. Shinjo, T. Matsuzawa, T. Takada, S. Nasa and Y. Murakami, J. Phys. Soc. Japan 35, 1032 (1973).
11. L. Gerward, S. Mørup and H. Topsøe, J. Appl. Phys. 47, 822 (1976).
12. T. K. McNab, R. A. Fox and J. F. Boyle, J. Appl. Phys. 39, 5703 (1968).
13. W. Kündig, H. Bömmel, G. Constabaris and R. H. Lindquist, Phys. Rev. 142, 327 (1966).
14. W. Kündig, K. J. Ando, R. H. Lindquist and G. Constabaris, Czech. J. Phys. B17, 467 (1967).
15. W. Kündig and R. S. Hargrove, Sol. State Comm. 7, 223 (1969).
16. R. S. Hargrove and W. Kündig, Sol. State Comm. 8, 803 (1970).
17. P. Roggwiler and W. Kündig, Sol. State Comm. 12, 901 (1973).
18. H. Topsøe, J. A. Dumesic and M. Boudart, Jnl. de Phys. 35, C6-411 (1974).
19. S. Mørup, B. S. Clausen and H. Topsøe, J. Phys. Colloq. Paris 40, C2-78 (1979).
20. P. W. Selwood, "Chemisorption and Magnetization", Acad. Press NY (1975).
21. J. W. Cahn, Trans. AIME 209, 1309 (1959).
22. R. E. Dietz and P. W. Selwood, J. Chem. Phys. 35, 270 (1961).
23. R. Pauthenet, Ann. Phys. 7, 710 (1952).

24. C. P. Bean and J. D. Livingston, *J. Appl. Phys.* 30, 120S (1959).
25. J. Phillips, B. Clausen, J. A. Dumesic, *J. Phys. Chem.* 84, 1814 (1980).
26. R. H. Bartholomew and M. Boudart, *J. Cat.* 26, 173 (1972).
27. J. Phillips, Ph.D. Thesis, University of Wisconsin-Madison (1981).
28. A. Muan and E. F. Osborn, "Phase Equilibrium Among Oxides in Steelmaking", Addison-Wesley Pub. Co., Reading, MA (1965).
29. C. G. Granqvist and R. A. Burhman, *J. Appl. Phys.* 47, 2220 (1976).
30. C. G. Granqvist and R. A. Burhman, *Appl. Phys. Lett.* 27, 693 (1976).
31. C. G. Granqvist and R. A. Burhman, *J. Appl. Phys.* 47, 2200 (1976).
32. C. G. Granqvist and R. A. Burhman, *Sol. State Comm.* 18, 123 (1976).
33. C. G. Granqvist and R. A. Burhman, *J. Cat.* 42, 477 (1976).
34. G. A. Sawatsky, F. van der Woude and A. H. Morrish, *Phys. Rev.* 183, (1969).
35. F. van der Woude, G. A. Sawatsky and A. H. Morrish, *Phys. Rev.* 167, 533 (1968).
36. T. Riste and L. Tanzer, *J. Phys. Chem. Solids* 19, 117 (1961).

RECEIVED March 28, 1985

## In Situ Spectroscopic Studies of Oxygen Electrocatalysts Involving Transition Metal Macrocycles

Ernest Yeager, Daniel A. Scherson, and Cristian A. Fierro

Case Center for Electrochemical Sciences and The Chemistry Department, Case Western Reserve University, Cleveland, OH 44106

Some of the transition metal macrocycles adsorbed on electrode surfaces are of special interest because of their high catalytic activity for dioxygen reduction. The interaction of the adsorbed macrocycles with the substrate and their orientation are of importance in understanding the factors controlling their catalytic activity. *In situ* spectroscopic techniques which have been used to examine these electrocatalytic layers include visible reflectance spectroscopy; surface enhanced and resonant Raman; and Mossbauer effect spectroscopy. This paper is focused principally on the cobalt and iron phthalocyanines on silver and carbon electrode substrates.

Of special interest as  $O_2$  reduction electrocatalysts are the transition metal macrocycles in the form of layers adsorptively attached, chemically bonded or simply physically deposited on an electrode substrate (1-5). Some of these complexes catalyze the 4-electron reduction of  $O_2$  to  $H_2O$  or  $OH^-$  while others catalyze principally the 2-electron reduction to the peroxide and/or the peroxide elimination reactions. Various *in situ* spectroscopic techniques have been used to examine the state of these transition metal macrocycle layers on carbon, graphite and metal substrates under various electrochemical conditions. These techniques have included (a) visible reflectance spectroscopy; (b) laser Raman spectroscopy, utilizing surface enhanced Raman scattering and resonant Raman; and (c) Mossbauer spectroscopy. This paper will focus on principally the cobalt and iron phthalocyanines and porphyrins.

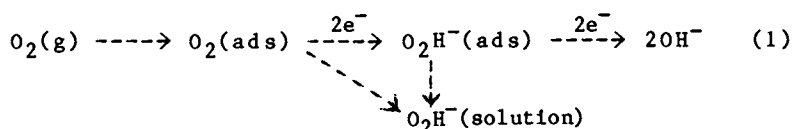
Before considering these catalysts, some background on the  $O_2$  reduction reaction will be reviewed (6).

The reduction of  $O_2$  is considered to proceed by two parallel pathways, namely, (A) a 2-electron process which generates peroxide and (B) a 4-electron pathway in which the presence of  $HO_2^-$  in the

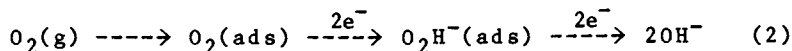
bulk of the solution phase cannot be detected. In the first case the reaction may be followed by the further reduction of  $\text{HO}_2^-$ , or the peroxide can undergo decomposition by a dismutation process to give  $\text{OH}^-$  and  $\text{O}_2$ . The peroxide pathway (A) has been found to be the predominant mechanism on graphite, gold, most transition metal oxides (e.g., NiO or spinels) and certain transition metal macrocycles such as cobalt tetrasulfonated phthalocyanine, Co-TsPc. The reduction of  $\text{O}_2$  on platinum, silver, palladium and a few other materials, including some transition metal macrocycles appears to follow a direct 4-electron pathway. The diagnostic criterion as to which pathways are involved with a given catalytic surface has involved almost invariably the rotating ring-disk electrode technique.

The reaction mechanisms associated with pathways (A) and (B) may share in common such adsorbed intermediates as peroxide, superoxide and their corresponding protonated forms. The distinction between pathways (A) and (B) can become therefore a matter of whether an intermediate such as peroxide ( $\text{HO}_2^-$ ) desorbs in significant quantities or not; for example,

(A) "Peroxide" pathway



(B) Direct 4-electron pathway



An understanding of the  $\text{O}_2$  reduction mechanisms is critically dependent on the identification of such adsorbed intermediates and the understanding of their interaction with various types of adsorption sites. Achieving such information has been severely hampered by the sparsity of *in situ* spectroscopic techniques with sufficient sensitivity to detect such adsorbed intermediates on most electrode surfaces. An attempt has been made to gain some insight as to how  $\text{O}_2$  interacts with such surfaces as platinum from *ex situ* spectroscopic studies using ultra high vacuum techniques (7) but extrapolation from the vacuum to the electrochemical environment suffers from considerable uncertainty. Consequently the models proposed for  $\text{O}_2$  reduction on metals and metal oxides must be regarded as rather speculative.

During the last two decades a variety of transition metal macrocycles have been shown to exhibit activity for  $\text{O}_2$  reduction in alkaline and acid media when adsorbed, chemically anchored or physically dispersed on electrode surface (1-5). This class of compounds provides a unique opportunity to examine in detail some of the factors involved in the activation and further reduction of  $\text{O}_2$ . These would include the effects associated with axial, peripheral

and ring substitutions, the nature of the metal center, and the degree of conjugation of the macrocycle ring. Furthermore, it has been possible under certain circumstances to synthesize stable  $O_2$ -macrocycle adducts (8) or to trap such species in inert gas matrices (9). This has facilitated the acquisition of structural and spectroscopic information which may be directly relevant to electrocatalysis as the adducts may be regarded as model intermediates in the reduction of  $O_2$ .

Of a number of transition metal macrocycles investigated, the dimetal Co-Co-4 face-to-face porphyrin (10) and the dicobalt bipyridal complex (11) have been found to catalyze the 4-electron reduction of  $O_2$  to  $H_2O$ . These complexes can form dioxygen bridges which can facilitate the cleavage of the O-O bond. The tetrasulfonated iron phthalocyanine (Fe-TsPc) adsorbed on graphite surfaces has also been found to catalyze the 4-e reduction (4,5). This compound is water soluble and proposed to form dioxygen bridged species in aqueous solutions. The question arises as to whether such dioxygen bridged species may also be found in the adsorbed layer.

Considerable progress has been made recently in the development of in situ spectroscopic techniques applicable to the study of transition metal macrocycles adsorbed at submonolayer coverages onto electrode surfaces. These have been aimed at gaining insight into the nature of the interactions of these compounds with the surface and with  $O_2$ . Most of the attention in the authors' laboratory has been focused on Fe- and Co-TsPc, although some preliminary results have already been obtained for some iron and cobalt porphyrins. The main conclusions obtained from these investigations will be outlined in the following sections.

#### UV-Visible Reflectance Spectroscopy

The molecular extinction coefficient for the prominent Q absorption bands in the UV-visible spectra of most macrocycles can reach values of  $10^4$ - $10^5$ . Hence, these compounds are excellent candidates for the study of the optical properties of molecules at submonolayer coverages. Fig. 1 gives the UV-visible reflectance spectra of Fe-TsPc adsorbed onto a highly oriented pyrolytic graphite (HOPG) and a Pt electrode in alkaline media<sup>12</sup>. The circles and triangles correspond to measurements taken in the absence and presence of  $O_2$ , respectively, without the macrocycles in solution. (Other conditions are specified in the figure caption.) Even though these compounds are highly soluble in water, the amount of material which desorbs from the surface during the experiments is negligible. The spectra for these compounds dissolved in the same electrolyte were found to be quite similar to those shown in Fig. 1. This suggests that the bonding to the substrate involves orbitals with little ring-character and that the macrocycle is most likely adsorbed in an edge-on fashion on the surface. The changes in the spectral features introduced by the presence of  $O_2$  were similar to those found in the solution phase. This provides evidence that the physicochemical characteristics of the adsorbed layer, such as aggregation and reactivity towards  $O_2$ , may not differ much from those of the species in the solution.



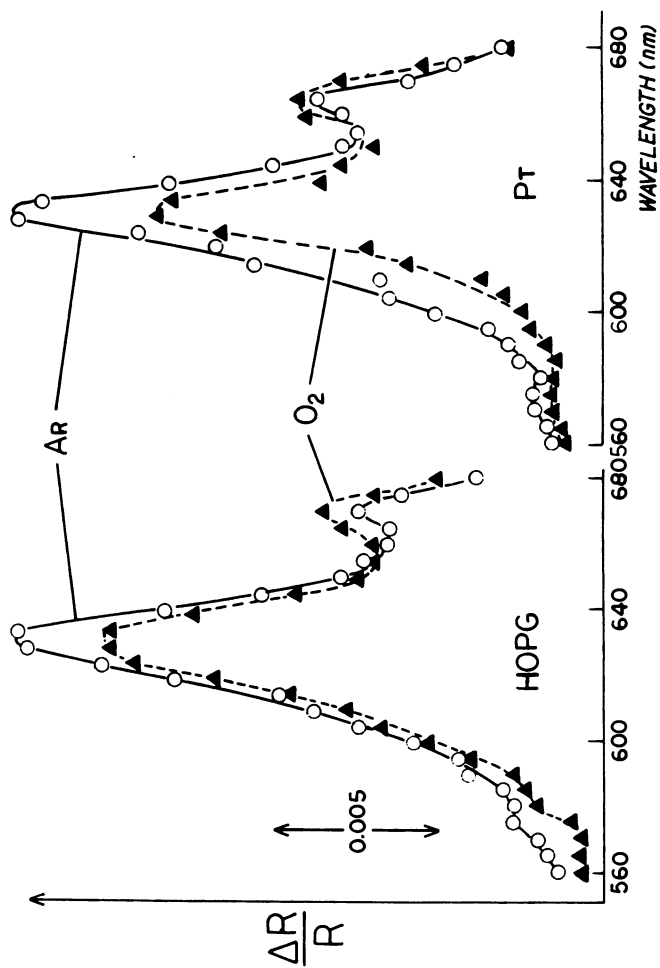


Figure 1. Reflectance spectra of Fe-TsPc in 0.1 M NaOH adsorbed on the basal plane of a highly ordered pyrolytic graphite (HOPG) electrode at 0.90 V vs.  $\alpha$ -Pd and on a Pt electrode at 0.70 V with Ar (O) and O<sub>2</sub> (▲) saturated solutions. Reproduced with permission from Ref. 12. Copyright 1979, Elsevier.

### Surface Enhanced Raman Spectroscopy (SERS)

Since its discovery, SERS has received attention both from theoretical and experimental viewpoints (13). The large enhancement has been observed only for certain metals such as Ag, Cu and Au. The enhancement mechanism is not quantitatively understood. Even so, very useful information concerning adsorbed species of some electrode surfaces can be obtained in-situ with this effect. With proper choice of laser radiation wavelength, advantage can be taken of the resonance Raman effect to further enhance the signals for the adsorbed transition metal. As an illustration, Fig. 2 shows the Raman spectra of adsorbed  $H_2^-$  and Fe-TsPc on silver in acid media in the absence of  $O_2$  at different potentials (14).  $H_2^-$ -TsPc exhibits very strong fluorescence when in the solution phase. This is quenched, however, when the molecules are adsorbed on this substrate, through a radiationless energy transfer due to the high number of available states in the metal. In all cases some changes in the relative intensity as well as in the position of few of the bands were observed as a function of the applied potential. A better description of these phenomena is given in Figs. 3 and 4. The first of these figures shows the frequency shift of the Raman band at  $612\text{ cm}^{-1}$  (associated with a deformation mode of the inner ring) for adsorbed Fe-TsPc on silver (14). A comparison of this curve with the corresponding cyclic voltammogram given in the same figure suggests that the shifts correlate with the peaks in the voltammetry. An illustration of the second effect mentioned above is given in Fig. 4 which shows the variations in intensity of the bands at  $1346$  and  $699\text{ cm}^{-1}$  for Fe-TsPc as a function of the applied potential at different pH values. A full quantitative understanding of these phenomena will most certainly require refined theoretical treatments which would include the effects of adsorption on the selection rules as well as account for possible distortions induced by the electric field on the metal surface.

Recently, the in situ Raman scattering from Fe-TsPc adsorbed onto the low index crystallographic faces of Ag was examined and the results obtained are shown in Fig. 5 (15). On the basis of the similarities of these spectra with those obtained for the macrocycle in solution phase, as well as the polarization behavior characteristics, it has been concluded that the most likely configuration is that with the macrocycle edge-on with respect to the surface. This is in agreement with conclusions reached from the UV-visible reflectance spectra. The preferred configuration, however, may depend on the particular macrocycle, as well as on the nature of the adsorption site.

### Mossbauer Effect Spectroscopy (MES)

Mossbauer effect spectroscopy, MES, is based on the ability of certain nuclei to undergo recoilless emission and absorption of  $\gamma$ -rays (16). The energy and multiplicity of the ground and excited states of a given nucleus are modified by the chemical environment. It is thus most often necessary to compensate for the differences in

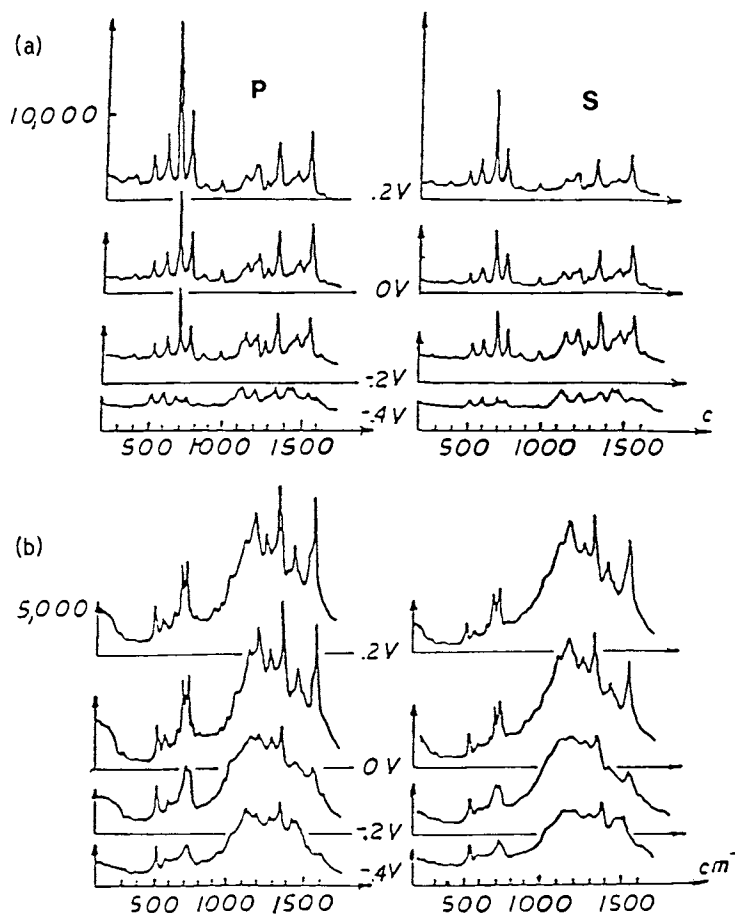


Figure 2. Surface-enhanced Raman spectra of Fe-TsPc (A) and H<sub>2</sub>-TsPc (B) adsorbed on a silver electrode at various potentials vs. SCE in 0.05 M H<sub>2</sub>SO<sub>4</sub>. Laser excitation line: 632.8 nm; output power: 20 mW; resolution: 5 cm<sup>-1</sup>; scanning time: 10 min/spectrum. P and S refer to depolarized and polarized light, respectively. Reproduced with permission from Ref. 14. Copyright 1983, Elsevier.

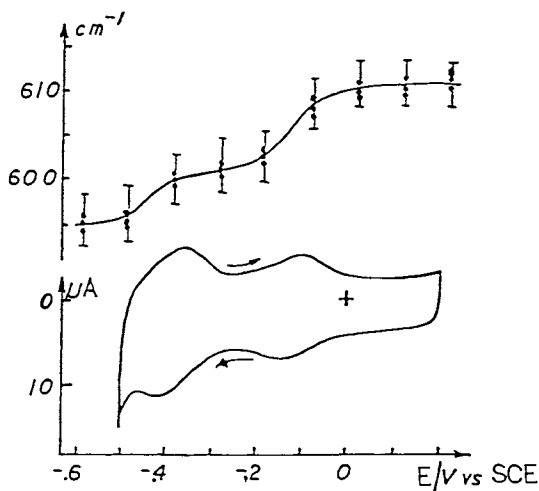


Figure 3. Frequency shift of the Raman band at  $612\text{ cm}^{-1}$  for Fe-TsPc adsorbed on a silver electrode as a function of the applied potential vs. SCE in  $0.05\text{ M H}_2\text{SO}_4$ . Laser excitation line:  $514.5\text{ nm}$ ; potential sweep rate:  $10\text{ mV s}^{-1}$ ; electrode area:  $0.27\text{ cm}^2$ . See caption Fig. 2.

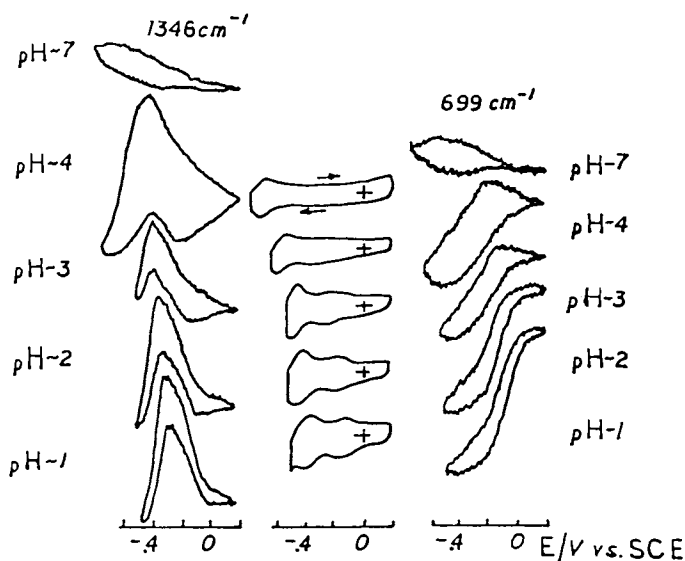


Figure 4. Intensity as a function of potential vs. SCE for two of the Raman bands ( $1346\text{ cm}^{-1}$  and  $699\text{ cm}^{-1}$ ) of Fe-TsPc adsorbed on a silver electrode at different pH values. These measurements were obtained at a potential scan rate of  $10\text{ mV s}^{-1}$ . See caption Fig. 2.

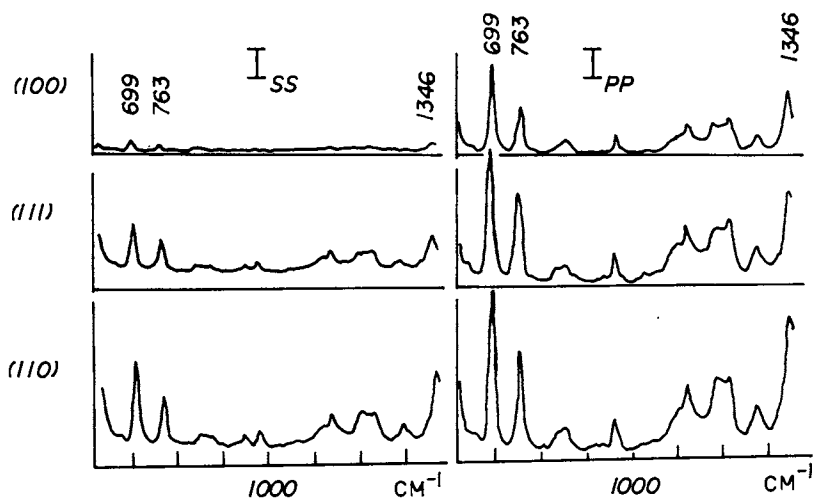


Figure 5. In situ Raman spectra for Fe-TsPc adsorbed on Ag(100), Ag(111) and Ag(110) at 0.2 V vs. SCE in 0.1 M HClO<sub>4</sub> Ar saturated aqueous solutions (15).

transition energy between emitter and absorber in order to bring about resonance. This is usually accomplished by varying the velocity of either the emitter or the absorber, a choice dictated mainly by the specific system under study. The resonance condition can be monitored by the use of detectors sensitive to  $\gamma$ -rays, X-rays or electrons which result from the de-excitation of the nucleus.

The recoilless fraction, that is, the relative number of events in which no exchange of momentum occurs between the nucleus and its environment, is determined primarily by the quantum mechanical and physical structure of the surrounding media. It is thus not possible to observe a Mossbauer effect of an active nucleus in a liquid, such as an ion or a molecule in solution. This represents a serious limitation to the study of certain phenomena; it allows, however, the investigation of films or adsorbed molecules on solid surfaces without interference from other species in solution. This factor in conjunction with the low attenuation of  $\gamma$ -rays by thin layers of liquids, metals or other materials makes Mossbauer spectroscopy particularly attractive for *in situ* studies of a variety of electrochemical systems. These advantages, however, have not apparently been fully realized, as evidenced by the relatively small number of reports in the literature (17).

The first *in situ* MES investigation of molecules adsorbed on electrode surfaces was aimed primarily at assessing the feasibility of such measurements in systems of interest to electrocatalysis (18). Iron phthalocyanine, FePc, was chosen as a model system because of the availability of previous *ex situ* Mossbauer studies and its importance as a catalyst for  $O_2$  reduction. The results obtained have provided considerable insight into some of the factors which control the activity of FePc and perhaps other transition metal macrocycles for  $O_2$  reduction. These can be summarized as follows:

(1) The Mossbauer spectra of FePc preadsorbed on Vulcan XC-72 carbon at loadings ranging from 3.5 up to 10% w/w exhibit only one doublet with a quadrupole splitting much smaller than that for bulk FePc. This doublet has been denoted as 2 and that corresponding to the bulk FePc as 1 in the referenced communications (18) (see Fig. 6). The dispersion method consisted in dissolving the FePc in pyridine to a concentration of  $10^{-3}$  M followed by the addition of the high surface area carbon in small quantities under ultrasonic agitation in an amount sufficient to obtain the desired catalyst to carbon fraction in the final product. Most of the solvent was then evaporated under vacuum with a water aspirator and later heated in flowing helium at 300 C, a temperature believed to be sufficient for the removal of pyridine either occluded in the sample or otherwise bound to FePc. At higher loadings (> 15% w/w) and using the same preadsorption procedure, doublets 1 and 2 are observed indicating a saturation of surface sites leading to the formation of FePc crystals.

(2) Significantly different ratios for the resonant absorption area, A, of the two doublets have been obtained for FePc preadsorbed at high loadings (> 15%) upon changing the available surface area of the carbon. Specifically, a higher value of  $A_2/A_1$  was found

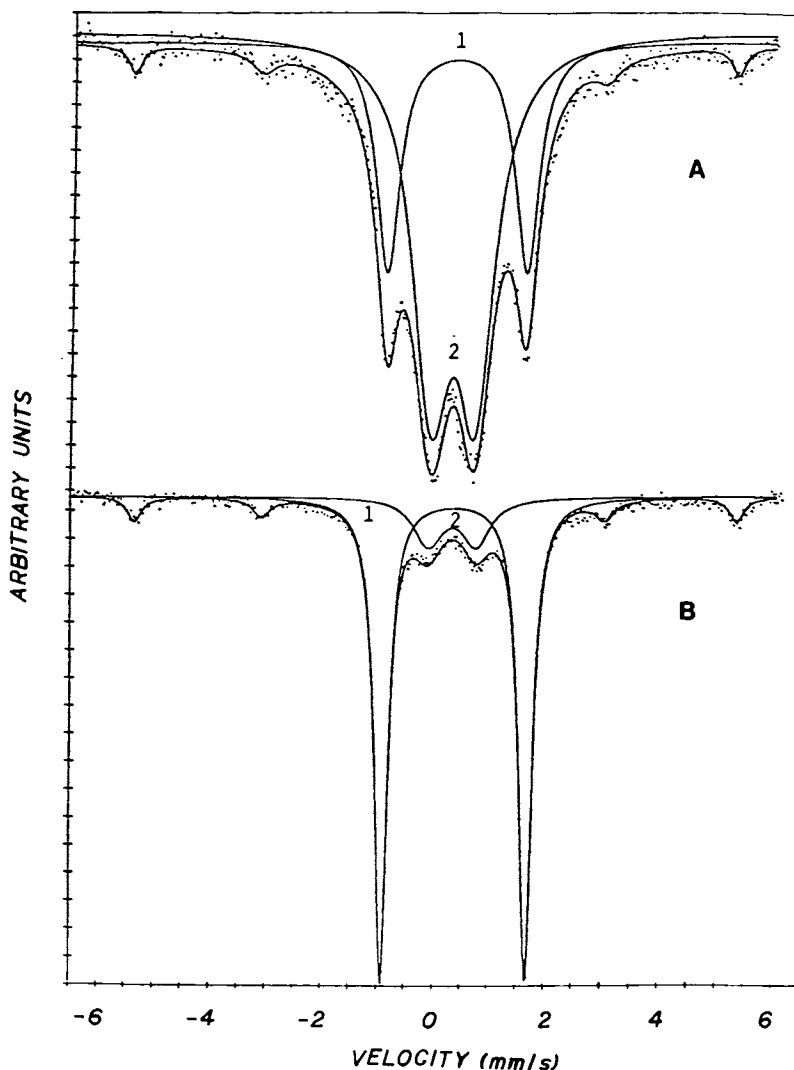


Figure 6. Ex situ Mossbauer spectra of 30% w/w FePc dispersed on high surface area carbons. Specimens prepared by mixing the carbon with an FePc solution in pyridine and subsequently removing the solvent by evaporation under vacuum. The samples were then heat treated at 420° C in a flowing He:H<sub>2</sub> (4:1) atmosphere. (A) RB carbon (1200 m<sup>2</sup>g<sup>-1</sup>) and (B) Vulcan XC-72 (250 m<sup>2</sup>g<sup>-1</sup>)(18).

for the same loading of FePc on RB carbon ( $1200 \text{ m}^2\text{g}^{-1}$ ) than for XC-72 ( $250 \text{ m}^2\text{g}^{-1}$ ) (17) (see Fig. 6).

These observations were regarded as providing evidence that doublet 2 corresponds to FePc preadsorbed at monolayer coverages on the carbon surface.

In an effort to gain further insight into the structural and electronic modifications introduced by the presumed adsorption of FePc onto high surface area carbon, cyclic voltammetry measurements were conducted with the material on XC-72 carbon exhibiting only the inner doublet in the Mossbauer spectrum. These experiments were performed with the catalyst-carbon sample in the form of a Teflon bonded porous coating spread into a very shallow ( $\sim 0.1$  mm deep) cylindrical cavity of an ordinary pyrolytic graphite rotating disk electrode. The cyclic voltammetry obtained is shown in Fig. 7. The Mossbauer spectrum of the material in dry form is given in Fig. 8. The voltammogram obtained is different from that of Fe-TsPc preadsorbed from aqueous solution at submonolayer coverages onto the same carbon (see Fig. 9).

The redox processes associated with the voltammetry for what was believed to be FePc adsorbed have been recently examined with *in situ* MES in 1 M NaOH (19). Two strikingly different spectra were obtained as a function of the applied potential, as shown in Fig. 10. The Mossbauer parameters associated with these spectral features were found to be very similar to those for a ferric (curve A) and a ferrous (curve B) hydroxide species (20). Furthermore, the literature (21) indicates that an iron metal electrode develops, upon repeated cycling in 1 M NaOH solution, a cyclic voltammogram with peak position almost identical to that shown in Fig. 7. It thus appears that the manner in which the samples were prepared leads to a partial or total degradation of the macrocycle involving the demetallation and further formation of an iron hydroxide species. This is a rather surprising finding as bulk FePc can be sublimed at temperatures as high as those employed during the removal of pyridine from the sample without undergoing decomposition. It should be mentioned that in a recent report (22) it has been claimed that a  $\mu$ -oxo form of FePc can be formed under certain circumstances which becomes thermally unstable at  $\sim 340$  C resulting in the destruction of the macrocycle. It is thus possible that the unexpected phenomenon found in the present study may be related to the formation of this  $\mu$ -oxo compound during the preparation of the samples prior to or during the heat treatment. Alternatively, the macrocyclic degradation may be associated with the presence of adventitious trace  $\text{O}_2$  in the heating system. A full investigation of such possibilities is currently under way in this laboratory.

This study illustrates the use of *in situ* MES as applied to the investigation of species involved in redox processes in porous electrodes. It is expected that a systematic utilization of this technique may enable the acquisition of microscopic level information of difficult accessibility with other spectroscopic methods, although limited to only Mossbauer active nucleus.

#### Acknowledgments

Support for this work has been provided by the Department of Energy, the Office of Naval Research, the Diamond Shamrock Corporation and



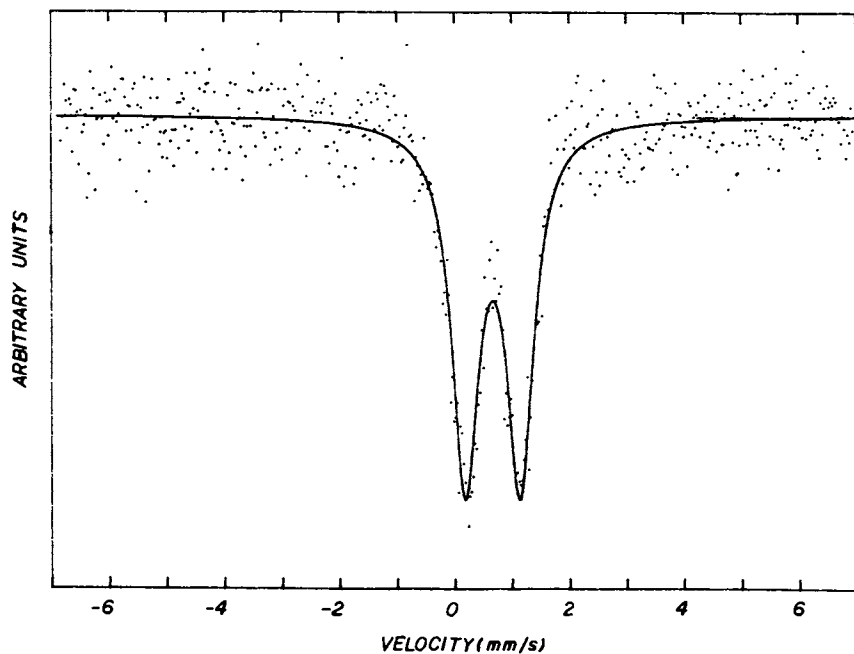


Figure 7. Cyclic voltammogram of 7% w/w FePc dispersed on Vulcan XC-72 carbon. The specimen was prepared by mixing the carbon with an FePc solution in pyridine and subsequently removing the solvent by boiling it off. The sample was then heat treated at 300°C in flowing He to remove coordinated pyridine. The cyclic voltammogram was obtained with the material in the form of a thin porous coating in 1 M NaOH at 25°C. Sweep rate: 5 mV s<sup>-1</sup> (19).

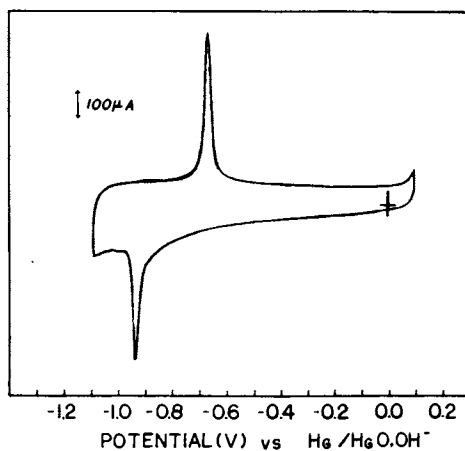


Figure 8. Mossbauer spectrum of 7% w/w FePc dispersed on a high surface area carbon (XC-72). The specimen was prepared in the same fashion as described in the caption Fig. 6. The spectrum corresponds to the dry material (19).

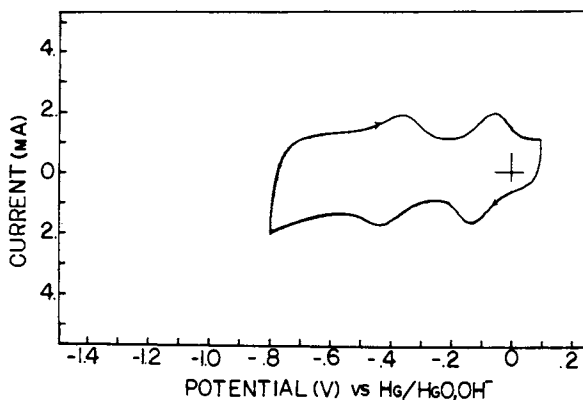


Figure 9. Cyclic voltammogram of Fe-TsPc adsorbed on Vulcan XC-72 at monolayer coverages. This measurement was obtained with the material in the form of a thin porous coating. Scan rate:  $50 \text{ mV s}^{-1}$ . Other conditions are the same as those in caption of Fig. 6.

American Chemical Society  
Library

1155 16th St., N.W.

In Catalyst Characterization Science, Deviney, M., et al.;  
ACS Symposium Series; American Chemical Society: Washington, DC, 1985.  
Washington, D.C. 20036

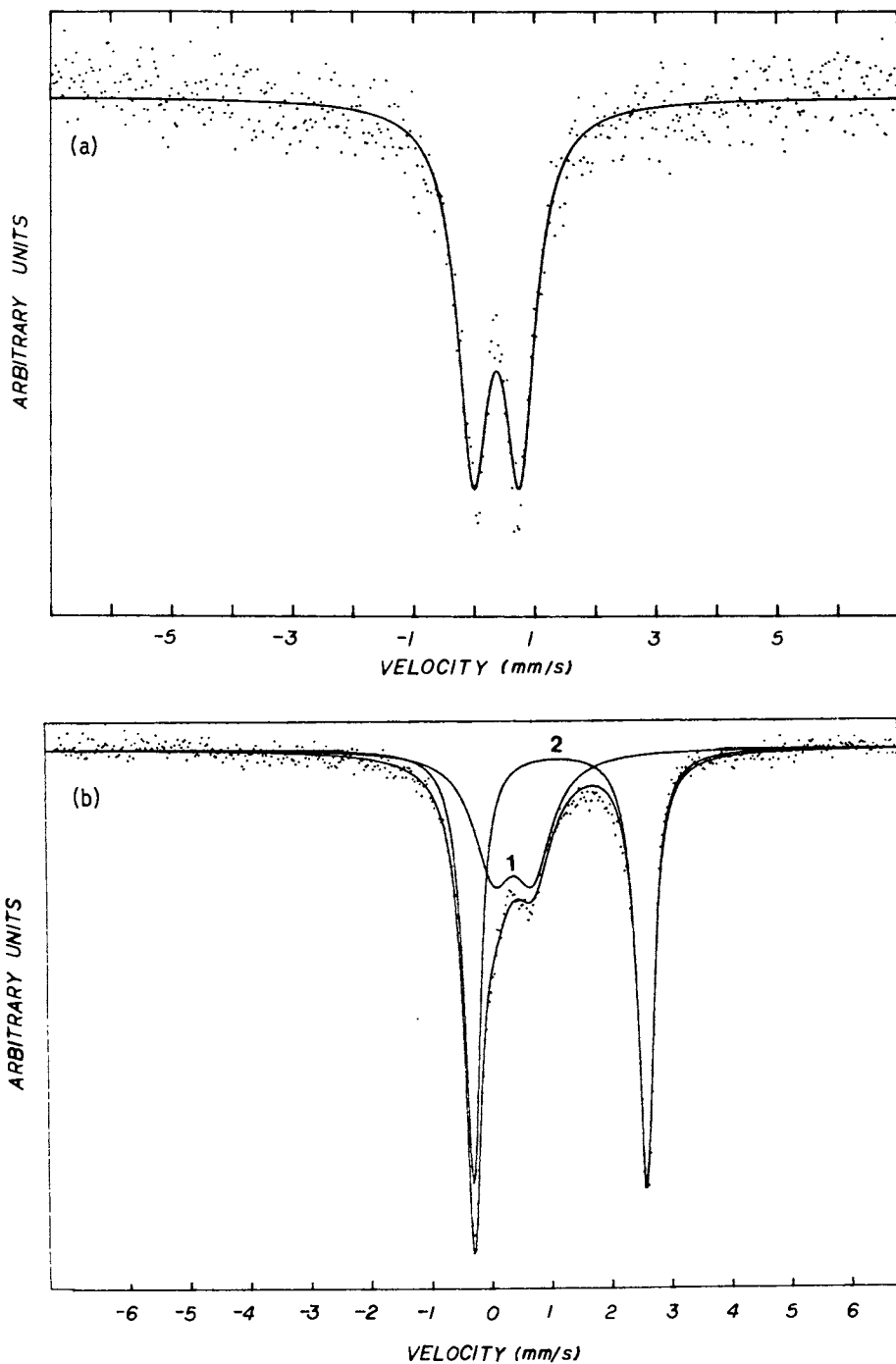


Figure 10. *In situ* Mossbauer spectra for a Vulcan XC-72 carbon electrode containing FePc obtained at 0.0 V vs. Hg/HgO, OH<sup>-</sup>, (Figure A) and at -1.05 V vs. Hg/HgO, OH<sup>-</sup>, (Figure B)(19).

the International Business Machines Corporation through a Faculty Development Award to one of the authors (D.S.). The Raman data in this paper have been obtained by Dr. B. Simic-Glavaski, S. Zecevic and R. Adzic. The authors express appreciation to them for their important contribution.

#### Literature Cited

1. Shigehara K.; Anson, F.C. J. Phys. Chem. 1982, 86, 2776.
2. Liu H.Y.; Weaver, M.J.; Wang, C.B.; and Chang, C.K. J. Electroanal. Chem. 1983, 145, 439.
3. Chang, C.K.; Liu, H.Y.; and Abdalmuhdi, I. J. Am. Chem. Soc. 1984, 106, 2725.
4. Zagal, J.; Sen, R.K.; and Yeager, E.B. J. Electroanal. Chem. 1977, 83, 207.
5. Zagal, J.; Bindra, P.; and Yeager, E.B. J. Electroanal. Soc. 1980, 127, 1506.
6. Tarasevich, M.; Sadowski A.; Yeager, E.B. In "Comprehensive Treatise of Electrochemistry"; Conway, B. E.; Bockris, J. O'M.; Yeager, E.B.; Khan, S.U.M.; White, R.E., Eds.; Plenum Press: New York, 1983; Vol. VII, p. 301.
7. Gland, J. L.; Sexton B. A.; and Fisher, G.B. Surf. Sci. 1980, 95, 587.
8. Collman, J. P.; Gagne, R. R.; Reed, C. A.; Robinson, W. T.; and Rudley, G. A. Proc. Nat. Acad. Sci. 1974, 71, 1326.
9. Watanabe, T.; Ama, T.; and Nakamoto, K. J. Phys. Chem. 1984, 88, 440.
10. Collman, J.P.; Denisevich, P.; Konai, P.; Marrocco, M.; Koval, C.; and Anson, F. C. J. Am. Chem. Soc. 1980, 102, 6027.
11. Sarangapani, S.; Urbach, F.; and Yeager, E. B. in preparation.
12. Nikolic, B. Z.; Adzic, R. R.; and Yeager, E. B. J. Electroanal. Chem. 1979, 103, 281.
13. "Surface Enhanced Raman Spectroscopy"; Chang, R.K.; Furtak, T. E., Eds.; Plenum Press: New York, 1982.
14. Simic-Glavaski, B.; Zecevic, S.; and Yeager, E. B. J. Electroanal. Chem. 1983, 150, 469.
15. Simic-Glavaski, B.; Adzic, R. R.; and Yeager, E. B. in preparation.
16. "Applications of Mossbauer Spectroscopy"; Cohen, R.L. Ed.; Academic Press: New York, 1980.
17. Scherson, D.; Yao, S. B.; Yeager, E. B.; Eldridge, J.; Kordesch, M. E.; and Hoffman, R. W. J. Electroanal. Chem. 1983, 157, 129.
18. Scherson, D.; Yao, S. B.; Yeager, E. B.; Eldridge, J.; Kordesch, M. E.; and Hoffman, R. W. J. Phys. Chem. 1983, 87, 932.
19. Scherson, D.; Fierro, C.; Gupta, S. L.; Tryk, D.; Yeager, E. B.; Eldridge, J.; and Hoffman, R.W. submitted to J. Electroanal. Chem.
20. O'Grady, W. E. J. Electrochem. Soc. 1980, 127, 555, and references therein.
21. Burke, L. D.; and Murphy, O. J. J. Electroanal. Chem. 1980, 109, 379.
22. Ercolani, C.; Gardini, M.; Monacelli, F.; Pennesi G.; and Rossi, G. Inorg. Chem. 1983, 22, 2584.

RECEIVED June 21, 1985

## IR Spectroscopy as an In Situ Probe for Molecular Structure in Electrocatalytic and Related Reactions

Alan Bewick and Maher Kalaji

Department of Chemistry, University of Southampton, Southampton, England

Techniques are described which obtain the IR absorption spectra of species, either adsorbed or free in the electrode/electrolyte solution interphase. Applications slanted towards topics relevant to electrocatalytic processes are discussed to illustrate the capabilities of the methods in probing molecular structure, orientation and interactions.

Data obtained using spectroscopic methods have had a profound influence on the development of many areas of chemistry. In most cases the value of these methods stems from their high sensitivity and molecular specificity which can lead directly to a quantitative assessment and a structural characterisation of the species present in a chemical system and possibly also to information on their interactions and reactions. High vacuum surface science provides a particularly spectacular example of the value of spectroscopic methods and the rapid progress that can be engendered by their intelligent deployment; thus the use of electron diffraction techniques to determine the long range atomic or molecular order on solid surfaces and adlayers in conjunction with UPS, XPS, EELS and IR reflection spectroscopy to characterise molecular structure and orientation have produced rapid advances in the understanding of surface chemistry and surface physics at the fundamental level. There has also been a direct technological benefit in the use of this information to improve catalytic processes and to develop new catalysts. It is a relatively simple step to remove the gas in a solid surface/gas phase system without seriously violating the structural integrity of the interface which can then be characterised using the high vacuum techniques. It would be expected, however, that only in very few cases will it be possible to remove the electrolyte from the electrode/electrolyte solution interface without producing major changes; thus the high vacuum methods have only limited applicability as ex-situ probes for the structure of the interface in electrochemical systems. Fortunately, the ease with which the electrode potential can be used to control and change, (i) the electrochemical potential of species in the electrical double layer, (ii) the free energy of adsorption/desorption processes and (iii) the rate constants

0097-6156/85/0288-0550\$06.00/0  
© 1985 American Chemical Society

for electron transfer processes, allows the small number of species in the electrode/electrolyte solution interphase to be distinguished from the overwhelming number in the bulk electrolyte in a manner which has enabled in-situ spectroscopic methods of investigation to be developed. These methods now include ESR spectroscopy (1), uv/visible reflection (2), transmission (3) and Raman scattering spectroscopies (4) and IR reflection spectroscopy (5,6,7,8,9). This paper will be restricted to a discussion of the latter.

### Experimental techniques

There are two major problems to be overcome in developing in-situ, external reflectance methods with submonolayer sensitivity towards adsorbates on smooth electrode surfaces. The first is to design a cell allowing sufficient radiation to emerge from it after passing twice through the electrolyte solution, the latter after being an aqueous solution. The second problem is to detect the very small absorbance change, usually in the range  $10^{-6}$  to  $10^{-2}$ , caused by the adsorbate in the presence of the overwhelming quantity of absorbing species in the total optical path. Use of a thin layer cell overcomes the first problem and adequate sensitivity is achieved by the marriage of electrochemical and spectroscopic techniques. The basic method has developed in two distinct directions: the first employs a grating spectrometer and is called electrochemically modulated infrared spectroscopy (EMIRS) (5); the second is subtractively normalized interfacial Fourier transform infrared spectroscopy (SNIFTIRS) (6). Both methods obtain the necessary sensitivity by modulating the electrode potential between two values which define two distinct states of the electrode surface; thus the chemistry to be observed is directly modulated and may be detected with great sensitivity by an appropriate form of synchronous detection. In the case of EMIRS, the modulation frequency is made sufficiently high compared to the wavelength scanning rate to enable a phase sensitive detection system to be used whereas, for SNIFTIRS, the electrode potential is held for a sufficient period at each potential to accumulate data from several interferometric scans and, after an adequate number, the two sets of data are ratioed.

### Cell design

Figure 1 illustrates a typical cell design containing the three electrodes required for control of the electrode potential and in which the thin layer of electrolyte, typically  $1\ \mu\text{m}$  to  $50\ \mu\text{m}$ , is produced by pushing the working electrode surface up to the surface of the IR window into the cell. The window can be a disc with parallel working surfaces or it can be prismatic to allow normal incidence of the radiation at the surfaces; the latter design minimises reflection losses at the air/window interfaces but it requires a longer pathlength in the window. The thin layer cell thus formed necessarily has a large value of uncompensated resistance due to the electrolyte layer. Typically, this leads to a time constant of the order of  $10^{-2}$ s for the charging of the double layer in response to a potential step. This factor together with the potential drop across the uncompensated resistance due to faradaic currents needs to be taken into account when designing experiments.

### Reflection/absorption at a metal surface

For a vibrating molecule to absorb radiation from an incident IR beam at the frequency of a particular normal mode it must be situated at a position of finite intensity and with an orientation such that there is a finite component of the dipole derivative  $du_1/dQ_1$  in the direction of the electric vector of the radiation field, where  $du_1$  is the change of dipole for the change of normal mode coordinate  $dQ_1$ . At a metal surface there is always a zero intensity for radiation having the electric vector parallel to the surface. As a result s-polarised radiation cannot interact with a molecule on a metal surface; p-polarised radiation has a finite intensity and can interact but the intensity of the resultant absorption band will depend upon the orientation of the molecule with respect to the surface, i.e. there is an apparent selection rule, the surface selection rule (10), which operates in addition to the normal selection rules for IR absorption. In EMIRS and SNIPTIRS measurements the "inactive" s-polarised radiation is prevented from reaching the detector and the relative intensities of the vibrational bands observed in the spectra from the remaining p-polarised radiation are used to deduce the orientation of adsorbed molecules. It should be pointed out, however, that vibrational coupling to adsorbate/adsorbent charge transfer (11) and also an electrochemically activated Stark effect (7,12,13) can lead to apparent violations of the surface selection rule which can invalidate simple deductions of orientation.

The surface active/surface inactive difference between p-polarised/s-polarised radiation has enabled an alternative modulation technique, polarisation modulation, to be developed (15,16). In electrochemical applications, it allows surface specificity to be achieved whilst working at fixed potential and without electrochemical modulation of the interface. It can be implemented either on EMIRS or on SNIPTIRS spectrometers and can be very valuable in dealing with electrochemically irreversible systems; however, the achievable sensitivity falls well short of that obtained with electrochemical modulation. It should also be noted that its "surface specificity" is not truly surface but extends out into the electrolyte with decreasing specificity to about half a wavelength.

### Information accessible

The EMIRS and SNIPTIRS methods provide the IR vibrational spectra (really the difference spectra - see later) of all species whose population changes either on the electrode surface or in the electrical double layer or in the diffusion layer in response to changing the electrode potential. Spectra will also be obtained for adsorbed species whose population does not change but which undergo a change in orientation or for which the electrode potential alters the intensity, the position or shape of IR absorption bands. Shifts in band maxima with potential at constant coverage  $(\partial\bar{\nu}_{\max}/\partial E)_\theta$  are very common for adsorbed species and they provide valuable information on the nature of adsorbate/adsorbent bonding and hence also additional data on adsorbate orientation.

In principle, therefore, these valuable techniques can provide all of the information needed to specify the molecular structure of the electrode/electrolyte solution interphase, the dynamics of adsorption/

desorption processes and the nature of reaction intermediates. In many cases, it will not be easy unambiguously to deduce quantitative molecular populations; this aspect has been neglected to date but will certainly command increasing attention in future.

It will be clear that EMIRS and SNIPTIRS spectra are difference spectra and can be somewhat complex (5). Typically they will contain positive absorption bands from species present in excess at potential  $E_1$  compared to potential  $E_2$  and negative absorption bands from species whose population changes oppositely with potential. In addition, bands which shift with potential will appear as a single bipolar band either with one lobe of each sign, figure 2, (or even more complex structures with three lobes).

### Electrocatalytic reactions

Electrocatalysis necessarily involves adsorption, often dissociative, and the characterisation of the molecular fragments produced is essential for an adequate understanding of the reaction pathways. Many of these reactions are important technologically; both the anodic and the cathodic reactions in fuel cells are good examples in this category. Hydrogen evolution and hydrogen oxidation are both of interest in this context. The exact characterisation of the adsorbed hydrogen atom involved in these reactions is not likely to stimulate technological progress but EMIRS studies have yielded information of considerable interest (16,17).

### Hydrogen adsorption

On platinum group metals, hydrogen adsorption/desorption is reversible and thus readily lends itself to investigation by EMIRS. The two kinds of adsorbed hydrogen on polycrystalline platinum, strongly adsorbed hydrogen ( $H_s$ ) formed at less negative potentials and weakly adsorbed hydrogen ( $H_w$ ) produced nearer the reversible potential for hydrogen evolution, are clearly distinguishable spectroscopically either using uv-visible (18) or infrared radiation (16). In the infrared, the formation of  $H_s$  substantially increases the reflectivity of the electrode and this is observed as a featureless negative absorption over a wide range of wavelength. When the electrode is covered with both  $H_s$  and  $H_w$ , absorption bands are observed superimposed on this baseline shift but, over the range  $4000\text{ cm}^{-1}$  to  $1250\text{ cm}^{-1}$ , these are all at the vibrational frequencies of hydrogen bonded water; no bands corresponding to Pt-H vibrations are observed. The bands all had the same sign: increased absorption when the metal was covered by  $H_w$ . Their assignment to vibrational modes of water associated with the adsorbed  $H_w$  were confirmed from isotopic shifts using  $H_2O/D_2O$  mixtures; examples are illustrated in figure 3. The difficult task of seeing this surface water through the large amount in the ambient electrolyte was facilitated by using the  $H_2O/D_2O$  mixtures to maximise energy throughput over the spectral region. Nine bands were clearly identified and measured from the range:  $\nu_1$ ,  $\nu_2$ ,  $\nu_3$ ,  $(\nu_2 + \nu_3)$ ,  $2\nu_3$ ,  $(2\nu_2 + \nu_3)$  for  $H_2O$ , HDO and  $D_2O$ . The relative intensities of these bands indicated a particular orientation for the water structure interacting with the adsorbed H atoms. Application of the surface selection rule leads to the model shown in figure 4(a) in which oriented water dimer units are hydrogen bonded to  $H_w$  on one side



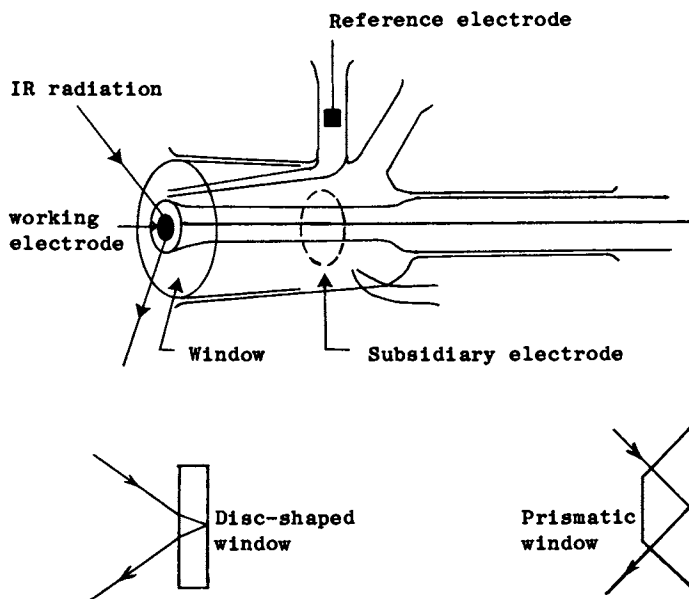


Figure 1. The IR spectroelectrochemical cell.

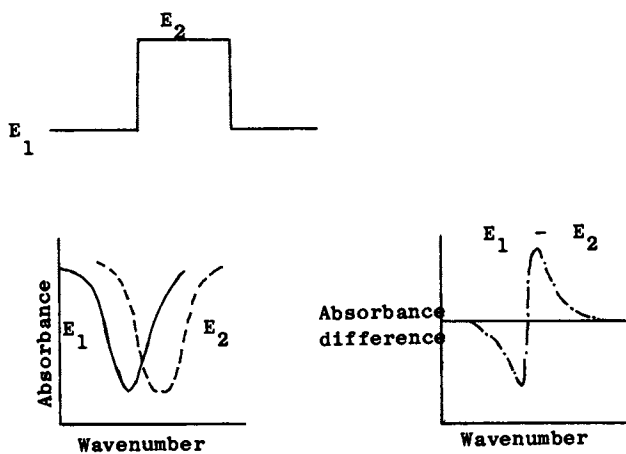


Figure 2. Origin of a bipolar difference band.

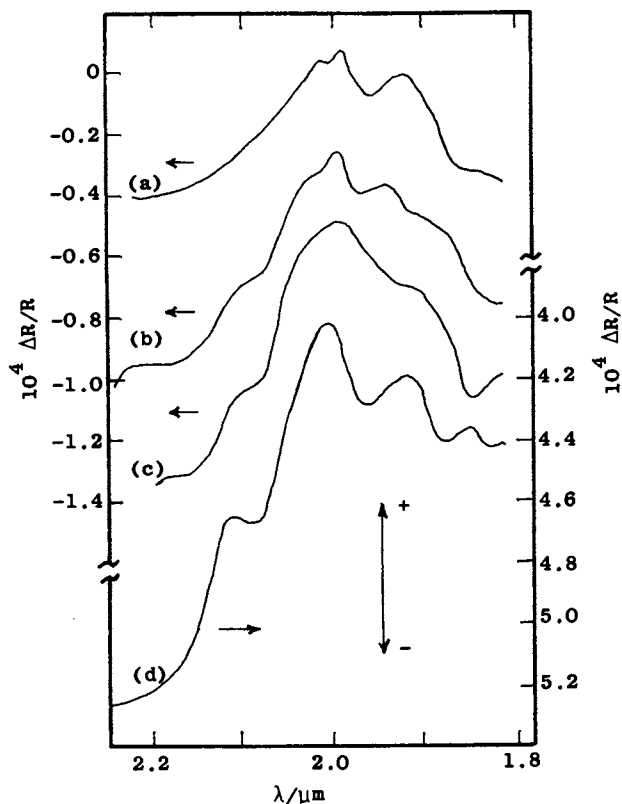


Figure 3. EMIRS spectra in the HDO  $\nu_2 + \nu_3$  region for 1M  $\text{H}_2\text{SO}_4$  containing 67% D. Modulation ranges: (a) 50-150 mV [NHE], (b) 50-200 mV, (c) 50-250 mV and (d) 50-450 mV.

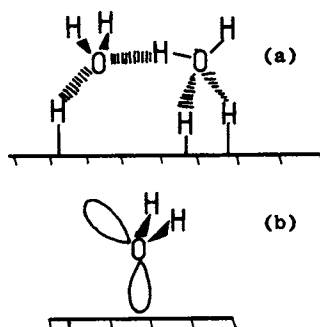


Figure 4. The structure and orientation of: (a) weakly bound hydrogen and its associated water on a Pt or Rh electrode; (b) water on the electrode surface at potentials in the double layer region.

and, on the other, to water molecules further out from the surface. Figure 4(b) shows the average water orientation assumed for a bare Pt surface at potentials in the double layer region; one lone pair orbital is assumed to be roughly normal to the surface. This orientation is in agreement with other electrochemical data and was used as the reference state for the EMIRS difference spectra.

### Electrocatalytic oxidations

Interest in fuel cells has stimulated many investigations into the detailed mechanisms of the electrocatalytic oxidation of small organic molecules such as methanol, formaldehyde, formic acid, etc. The major problem using platinum group metals is the rapid build up of a strongly adsorbed species which efficiently poisons the electrodes. Thus a substantial effort has been made by electrochemists to identify this species; use of non-spectroscopic techniques to evaluate the number of surface sites occupied by each molecule of poison and the number of electrons required in its oxidation to  $\text{CO}_2$  led to a consensus view that it was  $\text{:COH}$ . One of the first successful applications of EMIRS was an attempt to corroborate this conclusion (19); however, the spectroscopic data clearly identified CO as the poison and no evidence for COH could be obtained. Further detailed spectroscopic measurements using a variety of organic fuels ( $\text{CH}_3\text{OH}$ ,  $\text{HCHO}$ ,  $\text{HCOOH}$  and  $\text{CH}_2\text{OH}\cdot\text{CH}_2\text{OH}$ ) and electrode materials (Pt, Rh, Pd, Au) substantiated this finding as a general result in such systems (20,21,22). Examples of EMIRS spectra obtained from fully poisoned electrodes are shown in figures 5, 6 and 7. In every case, absorption bands are seen from one or more adsorbed CO species, the types and their exact vibration frequencies depending upon the nature of the metal. Thus, for example, Pt supports both linearly adsorbed CO, the band near  $2070\text{ cm}^{-1}$ , and also CO sitting in a higher coordination site with a vibration frequency near  $1850\text{ cm}^{-1}$ . On Pd bridge-bonded and more highly coordinated CO can be identified. These assignments have been made on the basis of the classification which has developed from gas phase adsorption of CO followed by the use of high vacuum spectroscopic techniques (23). There is a very close agreement between these data and the EMIRS spectra. Direct adsorption of CO on the electrodes from gas dissolved in the electrolyte gave almost identical spectra, at high coverage, to those obtained after organic oxidation. The same adsorbed CO species were obtained on Pt by reduction of  $\text{CO}_2$  (24). This was observed to take place only in the range of potentials where adsorbed hydrogen is formed, indicating that the reduction takes place indirectly via the adsorbed atomic hydrogen. In this case, it was noticed that the more highly coordinated adsorbed CO, seen near  $1850\text{ cm}^{-1}$ , was formed very readily, whereas it is formed directly from dissolved CO gas only after potential cycling of the electrode. There is evidence that this species is usually formed by reduction of  $\text{CO}_2$ ; it should be noted that, at non-poisoned electrodes, some  $\text{CO}_2$  is produced from the organic substrates at quite low potentials and many of these also form adsorbed hydrogen during their dissociative electro-sorption.

Adzic et al (25) have shown that partial coverage of the electrode by adsorbed Pb can substantially reduce the effects of poisoning, presumably by blocking the surface sites required by the adsorbed CO. This is nicely confirmed by spectroscopic measurements. Figure 8

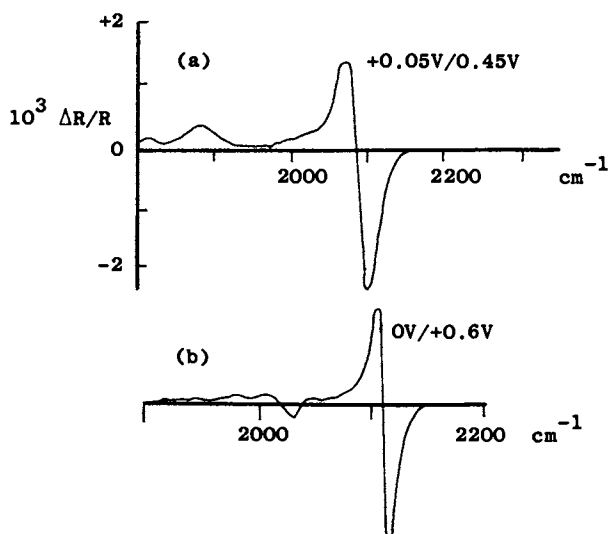


Figure 5. EMIRS difference spectra from (a) Pt in 1M  $\text{H}_2\text{SO}_4$  + 0.5M  $\text{CH}_3\text{OH}$  and (b) Pt in 0.25M  $\text{H}_2\text{SO}_4$  + 0.25M  $\text{HCOOH}$ .

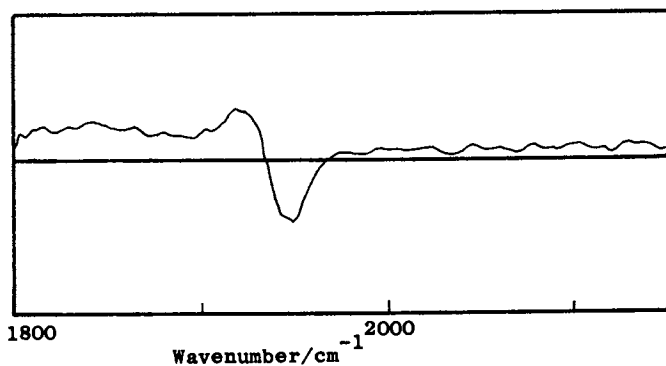


Figure 6. EMIRS difference spectrum from Pd in 1M  $\text{H}_2\text{SO}_4$  + 0.1M  $\text{HCHO}$ . Modulation between +0.25V and +0.65V.

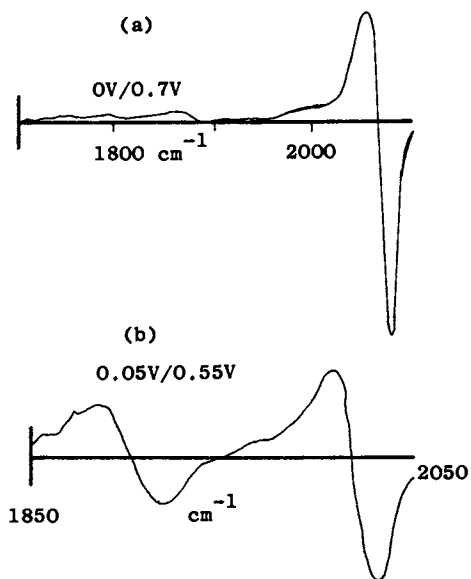


Figure 7. EMIRS difference spectra from (a) Pt in 0.5M HClO<sub>4</sub> + 0.1M HCHO and (b) Rh in 0.5M HClO<sub>4</sub> + 0.1M HCHO.

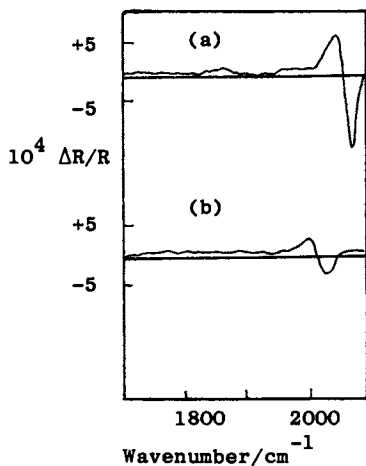


Figure 8. EMIRS difference spectra from Pt in 0.5M HClO<sub>4</sub> + 0.1M HCHO in the absence (a) and the presence (b) of deposited lead. Modulation between 0V and 0.25V.

gives EMIRS spectra obtained during the oxidation of HCHO on Pt in the absence and the presence of Pb. In this case, the Pb completely blocks the more highly coordinated CO and reduces the amount of the linearly adsorbed species. Other electrochemical measurements (26) have shown that each adsorbed Pb blocks three surface Pt sites. Another interesting correlation between catalytic activity and the extent of formation of adsorbed CO has been observed in measurements on Pt single crystal electrodes (27). The oxidation of HCOOH on Pt(111) occurs readily at low potentials and shows little sign of poisoning during electrochemical measurements (28); on Pt (100) the reaction is much faster on the non-poisoned surface but it rapidly becomes highly poisoned. The EMIRS spectra, figure 9, for these surfaces show very clearly the large difference in the formation of adsorbed CO. Both kinds of adsorbed CO are seen on the (100) surface with intensities rather higher than for polycrystalline surfaces. On Pt(111), the  $1850\text{ cm}^{-1}$  band is not observed and the  $2070\text{ cm}^{-1}$  band has a very small amplitude (note the difference in the absorbance scales); the broad absorbance at lower wavenumbers around  $1750\text{ cm}^{-1}$  might arise from the C=O stretch of an adsorbed reaction intermediate such as  $\cdot\text{CHO}$ .

#### Bonding and interactions in adsorbed CO layers

The close similarity between  $(\text{CO})_{\text{ads}}$  species formed, either directly or indirectly, on metal electrodes and the comparable species observed on the same metals following adsorption of CO from the gas phase has already been noted. There is, however, some effect due to the presence of the electrolyte. For example, an isolated CO molecule in the gas phase, an isolated CO molecule adsorbed onto a Pt surface from the gas phase, and an isolated  $(\text{CO})_{\text{ads}}$  on a Pt electrode at the point of zero charge give rise to bands attributed to C-O stretching fundamentals at 2143, 2064, and  $2030\text{ cm}^{-1}$ , respectively. Thus the metal/CO bonding produces a considerable weakening of the C-O bond, but there is appreciable further weakening in the presence of the aqueous electrolyte. This is evidence for significant interaction with solution species.

Quantitative comparisons between gas phase and electrochemical data need to take account of the electrode potential. The well known linear correlations between the electronegativity of a metal and its work function, and between the work function and the potential zero charge, imply that the electronegativity of the atoms in an electrode surface will depend upon the value of the electrode potential. Thus the electrode potential can be used to 'fine tune' the electronic properties of the electrode surface and thereby give a control over adsorbate/absorbent bonding and an ability to probe its character which is not available to gas phase studies. The strong variation with electrode potential of the observed vibrational frequency for  $(\text{CO})_{\text{ads}}$  is very apparent. The observed EMIRS bands owe their bipolar shape to this dependence. For all the cases studied, and it should be noted that these include adsorption on a gold electrode, the bands show that the C-O vibrational wavenumber increases as the electrode potential moves in a positive direction. In the case of linearly adsorbed CO on Pt, the variation is linear over a wide range of potential and  $d\nu/dE$  is  $+30\text{ cm}^{-1}\text{ V}^{-1}$  (14). The origin of this effect is almost certainly a reduction in the extent of back-bonding from the metal d-

orbitals to the  $\pi^*$  antibonding orbital of CO as the metal is made more positive and its effective electronegativity is increased. This will strengthen the C-O bond and weaken the Pt-C bond.

This explanation for the shift with potential is similar to that proposed by Blyholder (29) for the shift with coverage which had been observed for gas phase measurements. It is interesting to ask, therefore, whether the shift with potential at constant coverage  $(\partial\bar{\nu}/\partial E)_\theta$  and the shift with coverage at constant potential  $(\partial\bar{\nu}/\partial\theta)_E$  have a common explanation or whether they occur via different mechanisms. The latter coefficient is a result of those interactions in the adsorbed layer which affect the C-O vibrational frequency; the question, then, is whether these interactions are through-space, dipole-dipole interactions, or whether they occur via the metal surface and therefore include effects such as that proposed by Blyholder. Attempts to answer this question have centred on measurements at the gas/metal interface using  $C_{12}O/C_{13}O$  mixtures, and there has been considerable controversy over their interpretation (30,31). EMIRS measurements which are able separately to measure the effects of electrode potential and of coverage on the spectra from  $C_{12}O/C_{13}O$  mixtures have provided very useful new information (32). Figure 10 shows EMIRS spectra for  $(CO)_{ads}$  on Pt at saturation coverage as a function of the isotopic ratio. Only a single bipolar band is observed for all isotopic compositions and there are substantial changes in amplitude even though the total surface coverage is constant; these effects demonstrate the strong interactions in the layer. The appearance of only one band at intermediate isotopic compositions is an extreme example of intensity stealing by the higher energy vibrational modes. Measurements at lower coverage do, however, give spectra showing two bands at certain isotopic ratios. A major difference is observed between the effects of changing electrode potential at constant coverage and changing coverage at constant electrode potential: for a given isotopic ratio, the electrode potential changes only the position of the observed spectral bands without altering either their number or relative intensities, whereas varying the coverage can produce changes in all three of these characteristics. This strongly suggests that the origins of  $(\partial\bar{\nu}/\partial E)_\theta$  and  $(\partial\bar{\nu}/\partial\theta)_E$  are not the same. The  $d-\pi^*$  backbonding mechanism suggested for the former coefficient requires that it operates by changing the effective principal force constant  $f_1$ . On the other hand, the coverage dependence must be produced by mechanisms which alter either the interaction force constant,  $f_{11}$ , alone (as in through-space dipole-dipole coupling) or a combination of  $f_1$  and  $f_{11}$  (as in through-metal vibrational coupling). Thus the measurements outlined above suggest that the interaction effect, being essentially different in origin from the electrode potential effect, is dominated by dipole-dipole coupling. Further support for this conclusion comes from the results of model calculations for the vibrational modes of an array of coupled oscillators (32) using a model similar to that used by Moskovitz and Hulse (31). These calculations were carried out so as to reproduce the observed shifts with coverage and potential using several different combinations of  $f_{11}$  and the coverage dependence of  $f_1$ . The best fit to the experimental data was obtained for the model which derived the total coverage shift via the  $f_{11}$  term, i.e. a model which would correspond to dipole-dipole coupling but not to through-metal vibrational coupling.

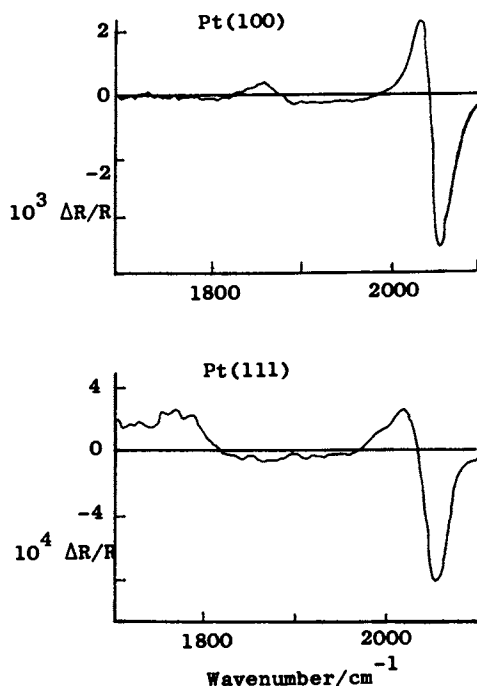


Figure 9. EMIRS difference spectra for CO adsorption on single crystal Pt electrodes.

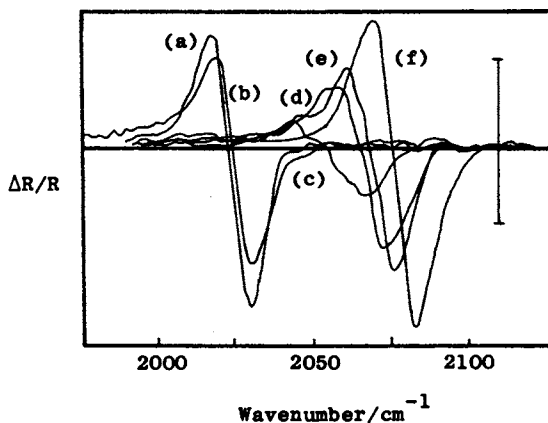


Figure 10. EMIRS spectra from Pt/1M H<sub>2</sub>SO<sub>4</sub> saturation with <sup>12</sup>C/<sup>13</sup>C, the isotopic ratio changing progressively from 100% <sup>13</sup>C in (a) to 100% <sup>12</sup>C in (f).



### Molecular Adsorption

The adsorption of intact molecules is encountered in many areas of electrochemistry. A complete description of the adsorbed state in terms of the orientation of the molecule, the way in which it bonds to the surface, the perturbation of the molecular structure caused by this additional bonding and the interaction between adjacent molecules is the ultimate goal of spectroscopic techniques. As more systems are studied by the EMIRS and SNIFTIRS methods, ways are being found to assess more of this information.

A straightforward case of molecular adsorption is that of benzonitrile on a gold electrode from an aqueous acid electrolyte. The EMIRS spectra (9,33) show a strong C≡N stretch band from the adsorbed molecule and weaker bands from the ring stretching modes with  $a_1$  symmetry. This indicates that the molecular axis in the adsorbed state is normal to the surface. The shift, on adsorption, of the C≡N stretch to higher wavenumber is in accord with bonding via the nitrogen atom, presumably in a Lewis base/acid coordination. The acid strength of the electrode would be expected to vary with the electrode potential, increasing with increasing positive potential. In the case of p-fluorobenzonitrile this effect appears to induce a change in orientation of the adsorbed molecule. At lower potentials it is oriented flat on the surface, bonding by the  $\pi$ -electron system, but at higher potentials it sits up and bonds via the nitrogen (34).

A SNIFTIRS study of the adsorption of p-difluorobenzene on platinum (35) showed a change of packing with concentration. The depletion of the solution produced by molecules adsorbing onto the electrode in adsorption/desorption cycles was clearly seen. Ten bands in the range  $3100\text{ cm}^{-1}$  to  $450\text{ cm}^{-1}$  were observed as a reduction in absorbance on adsorption; the positive going bands in figure 11. However, only two of these, the only two allowed by the surface selection rule for a molecule oriented flat on the surface (the  $b_{3u}$  modes) were seen as increased absorbances at frequencies shifted somewhat to lower wavenumber and clearly arising from the adsorbed state; the negative going bands. At higher concentrations of the solution, the need to pack more molecules onto the surface is satisfied by the tilting of the molecules at an angle to the surface. This is seen as the appearance of weak absorbances from the  $b_{1u}$  and  $b_{2u}$  modes of the adsorbed molecules.

A particularly interesting example of molecular adsorption is seen for acrylonitrile on gold under the same conditions as were used for the benzonitrile example discussed previously. The EMIRS spectra (13) for modulation over a range of potential where the adsorbate was at constant coverage contained two unipolar bands. Normally, only bipolar bands would be expected from an adsorbate at constant coverage arising from the effects of the shift  $(d\bar{\nu}/dE)_0$ . Moreover, these bands correspond to the C≡N and C=C stretches but with each shifted  $100\text{ cm}^{-1}$  to lower wavenumbers as would be expected for a molecule adsorbed flat and bonding via the  $\pi$ -electron system. However, the surface selection rule requires that these bands should be inactive from a molecule so oriented. In order to account for the appearance of these bands a vibronic coupling to the electrical field in the double layer was postulated (7) and this has been interpreted subsequently as a manifestation of the Stark effect (12,13). The frequency of the C≡N stretch band from the adsorbed molecule was seen to move markedly to

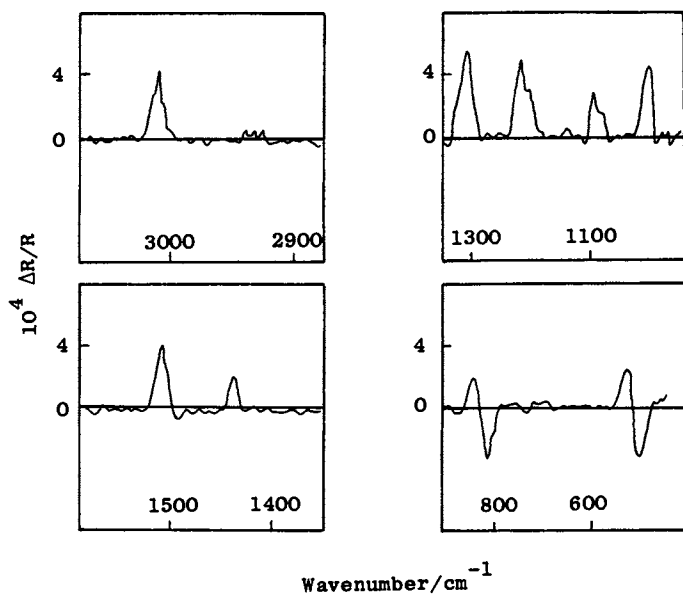


Figure 11. SNIPTIRS spectra from a Pt electrode in 1M  $\text{HClO}_4$  + 0.5 mM p-difluorobenzene. Modulation from +0.2V to +0.4V.

higher frequencies as the potential was made more positive. This indicates that bonding to the gold is predominantly by electron donation into the  $\pi^*$  antibonding orbital and not from the filled  $\pi$  orbital to the metal.

#### The Electrochemically Activated Stark Effect

The polarisability of a molecule will vary during vibrations which change the internuclear separations. Thus the vibrations of a molecule sitting in an electrical field will be coupled to the field via the polarisability. This should be particularly noticeable for a molecule adsorbed on an electrode surface where the field strength is typically in the range  $10^5$ - $10^8$  V cm<sup>-1</sup>. The dipole, perpendicular to the surface, induced in the molecule by the static electric field will fluctuate in step with the normal mode vibrations of the molecule. Thus the IR active modes will be determined by the matrix elements of the polarisability matrix and not by a combination of the surface selection rule and the normal IR selection rules i.e. all of the Raman active modes could become accessible. This effect has been formalized and its significance assessed in a discussion (12) which compares its magnitude for a number of different molecules. In the case of acrylonitrile adsorption discussed in the previous section, the intensity of the C≡N stretch band appears to vary with the square of the electric field strength as expected for the Stark effect mechanism.

#### Acknowledgments

The work discussed was supported in part by the Office of Naval Research, Washington and the U.K. Science and Engineering Research Council.

#### Literature Cited

1. Goldberg, I.B.; Bard, A.J. in "Magnetic Resonance in Chemistry and Biology"; Herak, J.N.; Adamic, K.J., Eds.; M. Dekker: New York, 1975.
2. McIntyre, J.D.E. in "Advances in Electrochemistry and Electrochemical Engineering"; Muller, R.H., Ed.; Wiley, 1973; Vol. 9, p.61
3. Heineman, W.; Hawkbridge, F.; Blount, H. in "Electroanalytical Chemistry", Bard, A.J., Ed.; M. Dekker: New York, 1984; Vol. 13, p.1.
4. Fleischmann, M.; Hill, I.R. in "Electrochemical Effects in Surface Enhanced Raman Scattering"; Chang, R.K.; Furtak, T.E., Eds.; Plenum Press: New York, 1982. Cooney, R.P.; Mahoney, M.R.; McQuillan, A.J. in "Advances in Infrared and Raman Spectroscopy", Clark, R.J.H.; Hester, R.E., Eds.; Heyden: London, 1982; Vol. 9, p.188.
5. Bewick, A.; Kunimatsu, K.; Pons, B.S.; Russell, J.W. J. Electroanal. Chem. 1984, 160, 47.
6. Pons, S.; Davidson, R.; Bewick A. J. Electroanal. Chem. 1984, 160, 63.
7. Bewick, A. J. Electroanal. Chem. 1983, 150, 481.
8. Pons, S. J. Electroanal. Chem. 1983, 150, 495.

9. Bewick, A.; Pons, S. in "Advances in Infrared and Raman Spectroscopy"; Clark, R.J.H.; Hester, R.E., Eds.; Wiley Heyden: London, 1985; Vol. 12, p.1.
10. Greenler, R.G. J. Chem. Phys. 1966, 44, 310.
11. Devlin, R.P.; Consani, K. J. Phys. Chem. 1981, 86, 2597.
12. Pons, S.; Karzeniewski, C.; Bewick, A. J. Phys. Chem., in press.
13. Bewick, A.; Gibilaro, C.; Pons, S. Langmuir, in press.
14. Russell, J.W.; Severson, M.; Scanlon, K.; Overend, J.; Bewick, A. J. Phys. Chem. 1983, 87, 293.
15. Seki, H.; Kunimatsu, K.; Golden, W.G. Appl. Spectroscopy, in press.
16. Bewick, A.; Russell, J.W. J. Electroanal. Chem. 1982, 132, 329.
17. Bewick, A.; Russell, J.W. J. Electroanal. Chem. 1982, 142, 337.
18. Bewick, A.; Kunimatsu, K.; Robinson, J.; Russell, J.W. J. Electroanal. Chem. 1981, 119, 175.
19. Beden, B.; Lamy, C.; Bewick, A.; Kunimatsu, K. J. Electroanal. Chem. 1981, 112, 343.
20. Beden, B.; Lamy, C.; Bewick, A. J. Electroanal. Chem. 1983, 148, 147.
21. Bewick, A.; Solumun, T. in preparation.
22. Bewick, A.; Solomun, T. J. Electroanal. Chem., submitted.
23. Sheppard, N.; Nguyen, R.R. in "Advances in Infrared and Raman Spectroscopy"; Clark, R.J.H.; Hester, R.E., Eds.; Heyden: London, 1978; Vol.5.
24. Bewick, A.; Beden, B.; Razaq, M.; Weber, J. J. Electroanal. Chem. 1982, 139, 203.
25. Spasojevic, M.C.; Adzic, R.R.; Despic, A.R. J. Electroanal. Chem. 1982, 139, 203.
26. Furuya, N.; Motoo, S. J. Electroanal. Chem. 1979, 100, 771.
27. Adzic, R.R.; Bewick, A.; Razaq, M. in preparation.
28. Adzic, R.R.; Tripkovic, A.V.; O'Grady, W.E. Nature, 1982, 296, 137.
29. Blyholder, G. J. Phys. Chem. 1964, 68, 2772.  
Blyholder, G.; Sheets, R.W. J. Catal. 1972, 27, 301.
30. Hammakar, R.A.; Francis, S.A.; Eischens, R.P. Spectrochim. Acta 1965, 21, 1295. Scheffler, M. Surf. Sci. 1979, 81, 562.
31. Moskovitz, M.; Hulse, J.E. Surf. Sci. 1978, 78, 397.
32. Bewick, A.; Razaq, M.; Russell, H.W. Surf. Sci., in press.
33. Bewick, A.; Hudec, J.; Razaq, M. in preparation.
34. Bewick A.; Hudec, J.; Pender, C., to be published.
35. Pons, S.; Bewick, A. Langmuir, 1985, 1, 141.

RECEIVED July 31, 1985

## Surface Spectroscopy of Platinum-Cadmium Sulfide-Perfluorosulfonate Polymer Systems

N. Kakuta, J. M. White, A. Campion, A. J. Bard, M. A. Fox, S. E. Webber, and M. Finlayson

Department of Chemistry, The University of Texas—Austin, Austin, TX 78712

Films on Pt/CdS/Nafion have been constructed for use in investigations of photoassisted  $H_2$  production from  $H_2O$ . These films were characterized using scanning electron microscopy, x-ray photoelectron spectroscopy and x-ray diffraction. Induction periods, observed in the photo-assisted  $H_2$  production, correlate with the extent of reduction of partially oxidized Pt to  $Pt^0$  as measured by the Pt(4f) binding energy changes. Two crystal forms of CdS (cubic and hexagonal) were detected by x-ray diffraction. The scanning electron micrographs show that samples dominated by the cubic form have a very rough surface compared to the hexagonal form. The S(2p) binding energies indicate that the surface of the hexagonal form is rich in sulfate ion, whereas the surface of the cubic form is dominated by sulfide ion.

Over the past several years, interest in photoassisted reactions involving semiconductors has expanded (1). Among the interesting relatively small bandgap materials is CdS (bandgap=2.4 eV). In operating systems, CdS has been stabilized with respect to photo-decomposition by the addition of sacrificial reagents (2). Recently, the cleavage of water in a colloidal CdS/Pt/RuO<sub>2</sub> system has been reported (3) and has led to increased interest in this system (4).

While these colloidal systems are very interesting, another approach with considerable promise involves localizing the photo-active species and other catalytic components in a polymer membrane. This has recently been accomplished for CdS in polyurethane (5) and Nafion (6). This kind of system lends itself to characterization using surface analytical techniques while at the same time preserving many of the small particle features of colloids. In this paper we examine how the CdS crystal structure and the state of the Pt in a CdS/Pt/Nafion system influences the rate of hydrogen generation in a system containing a sacrificial electron donor,  $S^{2-}$ . A detailed account of the photoassisted  $H_2$  production rates is given elsewhere (6b).

NOTE: Nafion is Du Pont's brand name for perfluorosulfonate polymers.

0097-6156/85/0288-0566\$06.00/0  
© 1985 American Chemical Society

### Experimental

Platinum was added to Nafion before incorporating CdS in order to avoid the reduction of CdS during the platinization process. Nafion (DuPont 117, 0.018 cm thick) films were soaked in  $\text{Pt}(\text{NH}_3)_2\text{I}_2$  (0.1 mM) solution for 4 hr. The amount of the Pt complex incorporated was determined by measuring the optical absorption change in the liquid phase. The films were subsequently reduced with  $\text{NaBH}_4$  (0.1 M) solution for one day to produce Pt metal dispersed throughout the polymer film. The amount of Pt was found to be about  $0.02 \text{ mg cm}^{-2}$ .

CdS was incorporated into these platinized films using two methods. In the first, the film was soaked in a  $\text{Cd}(\text{NO}_3)_2$  (0.5 M) solution for 1 hr, washed with water, soaked in boiling  $\text{HNO}_3$  (0.03 M, pH=2.1) solution, treated with bubbling  $\text{H}_2\text{S}$  for 10 min and finally washed with boiling water. The resulting films were bright orange.

In the second method, the preparation differed only in the  $\text{H}_2\text{S}$  treatment which was carried out at room temperature in distilled water. In both cases the amount of CdS incorporated was determined by polarographic reduction of  $\text{Cd}^{2+}$  to be  $1.3 \text{ mg cm}^{-2}$ .

The photodriven production of hydrogen was carried out using 1 cm x 1 cm films in a 10 ml Pyrex test tube containing 3 ml of 0.1 M  $\text{Na}_2\text{S}$  solution (pH=13). Prior to irradiation, these solutions were degassed by bubbling  $\text{N}_2$  through them. Irradiation was done with a 1 kW Xenon lamp. The light was filtered through water to remove most of the IR radiation. The amount of hydrogen formed was measured with a gas chromatograph.

The films were characterized using x-ray powder diffraction (XRD), x-ray photoelectron spectroscopy (XPS) and scanning electron microscopy (SEM). The photoelectron spectroscopy utilized a Vacuum Generators ESCA Lab II system with  $\text{Mg}(\text{K}\alpha)$  radiation. Binding energies (BE) were measured with respect to the surface C(1s) peak (284.5 eV) which was always present in these films. Scanning electron microscopy was done with a JEOL JSM-35C system.

### Results and Discussion

Pt/CdS/Nafion. Figure 1 shows the time dependence of the evolution of hydrogen for the irradiated films. The first preparation method gives the hexagonal form (7). In both cases x-ray linewidth analysis indicates particle sizes of 20 nm. The  $\text{H}_2$  generation rate is at least three times faster for the cubic form than for the hexagonal form. Generally speaking, the XRD and SEM analysis indicates small particles of CdS and Pt in intimate contact.

Figure 1 also shows an induction period during which the rate of  $\text{H}_2$  production accelerates. Although this effect is more pronounced for the hexagonal CdS sample, it is present in both. Further results, summarized in Fig. 2, emphasize this induction period. The curves labelled (1) and (2) involved repeated use of the same film. Between runs (1) and (2) the film was washed in boiling water. Clearly the rate of  $\text{H}_2$  evolution was significantly faster in the second run. Repeated experiments gave data superimposable on curve (2).

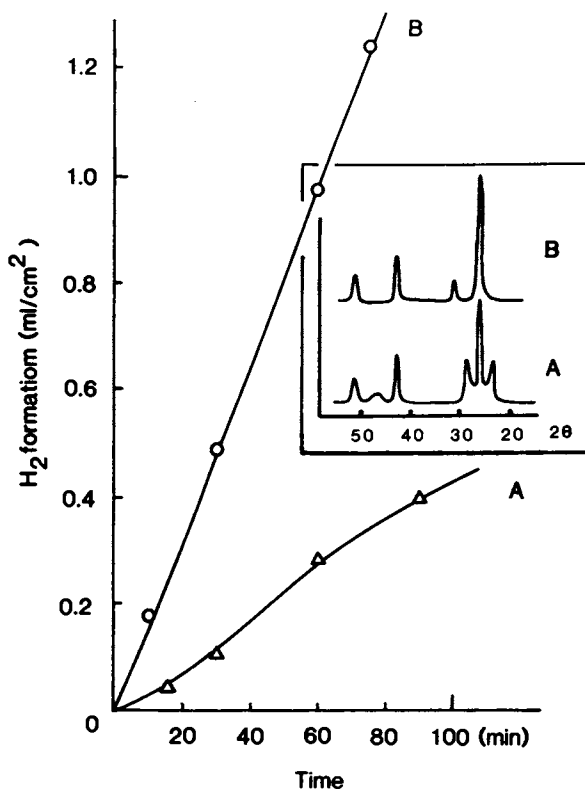


Figure 1. Comparison of H<sub>2</sub> generation from platinumized hexagonal CdS (curve A) and cubic CdS (curve B) in Nafion 117. The insert shows x-ray powder diffraction spectra of CdS in these films.

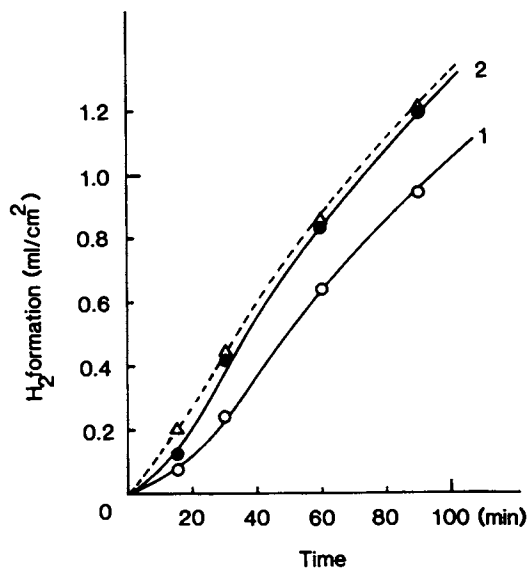


Figure 2. Time dependence of hydrogen production in a  $1 \text{ cm}^2$  Nafion film containing CdS ( $1.3 \text{ mg cm}^{-2}$ ) and Pt ( $0.02 \text{ mg cm}^{-2}$ ). Curves (1) and (2) are repeated runs with the same film. The dashed curve is for a different film pretreatment. See text for details.



In another experiment, a new film was pretreated by bubbling  $H_2$  at 1 atm and 300 K through the solution for 0.5 hr prior to the  $N_2$  treatment described above. The activity of this film is shown in Fig. 2, dashed curve. It is closer to (2) than (1), and the induction time is relatively short. This indicates that, during the initial stages of irradiation with a fresh film, the activity is enhanced by some process involving hydrogen.

Similar results have recently been reported by Aspnes and Heller (8). They proposed an autocatalytic model for photoactive systems involving metal/compound semiconductor interfaces. To explain induction times in CdS systems (9), they suggest that hydrogen incorporated in the solid lowers the barrier to charge transfer across the interface and thereby accelerates  $H_2$  production rates.

While our results follow the same trend and may involve similar effects, surface analysis using XPS indicates that the oxidation state of Pt is also significant. The Pt(4f) binding energy was 72.1 eV on fresh films. After irradiation in the manner described above, the BE dropped to 71.3 eV. For a Pt foil, the measured BE was 71.2 eV. We conclude that whole Pt was partially oxidized in the fresh films and that during the early stages of hydrogen production, it was reduced to  $Pt^0$ . This change in oxidation state is, we believe, related to the change in  $H_2$  production activity.

To investigate this further, we probed the state of Pt before CdS incorporation into the film. After Pt incorporation and reduction with  $NaBH_4$ , the Pt(4f) BE was 71.1 eV, indicating that  $Pt^{2+}$  complexes were completely reduced to  $Pt^0$ . Pt in films without CdS can be oxidized by boiling in nitric acid as indicated by the films becoming clear. Thus, the oxidized Pt species present in fresh CdS/Pt/Nafion films is formed at some point during the CdS incorporation process. Thus, while not excluding the process proposed by Aspnes and Heller (8), we consider the reduction of partially oxidized Pt as responsible, in part, for the observed induction period (10).

CdS/Nafion. Scanning electron microscopy (SEM) of the CdS films prepared by both methods revealed a striking difference in the surface roughness of cubic and hexagonal CdS in Nafion (Fig. 3). Examination of a cross-sectioned film by SEM did not show any morphological differences in the two crystal forms in the interior of the Nafion. X-ray fluorescence demonstrated that Cd was distributed throughout the Nafion, with a slightly higher concentration near the outer surface (Fig. 3).

The XPS of the Cd(3d) region shows (Fig. 4) that the cubic CdS film has a Cd( $3d_{5/2}$ ) BE of 405.6 eV, while the hexagonal CdS film has a peak at 406.4 eV. After  $Ar^+$  bombardment for a short time of the hexagonal CdS film, the peak position does not shift but the integrated intensity increases.

Figure 5 shows XPS for the S(2p) region. The cubic CdS film has peaks at 161.7 and 168.9 eV. Hexagonal CdS has only one peak at 169.6 eV which after  $Ar^+$  bombardment decreases in intensity and broadens. Based on a systematic comparison with binding energies reported on a variety of cadmium and sulfur compounds (11), we assign the Cd( $3d_{5/2}$ ) 405.6 eV peak to  $Cd^{2+}$  ion of CdS and the S(2p) 161.7 eV peak to  $S^{2-}$  ion of CdS.

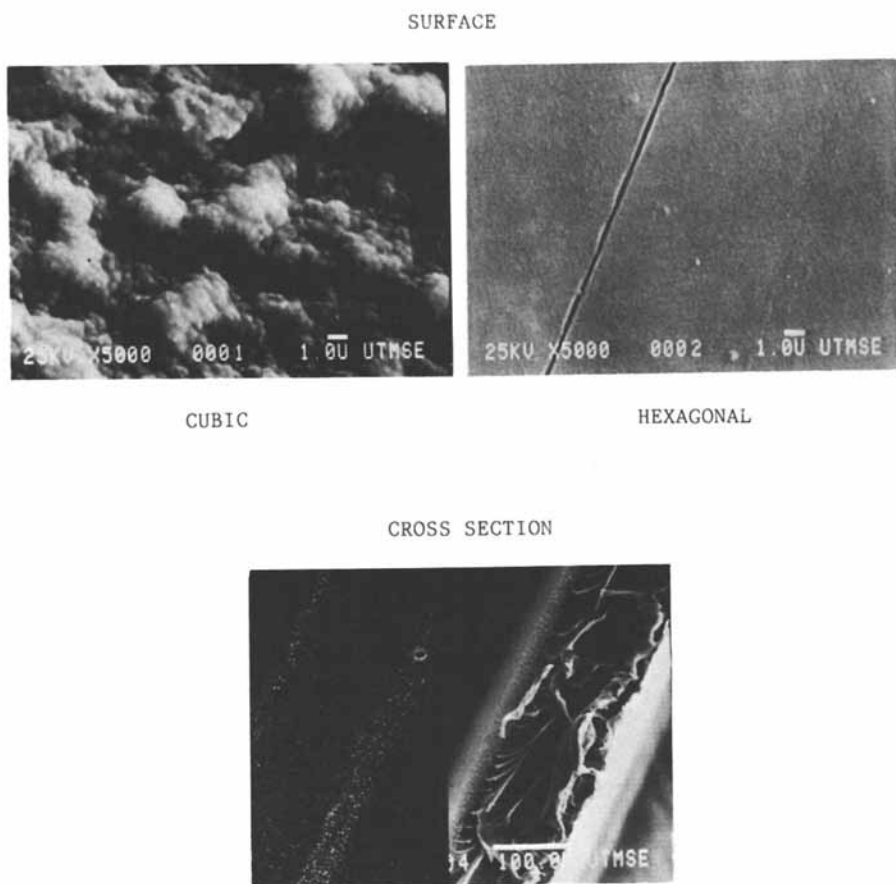


Figure 3. SEM photographs of hexagonal CdS/Nafion and cubic CdS/Nafion.

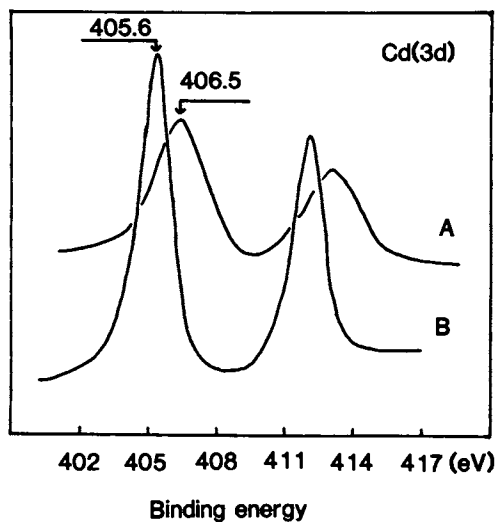


Figure 4. Cd(3d) XPS spectra of hexagonal CdS/Nafion (A) and cubic CdS/Nafion (B) films.

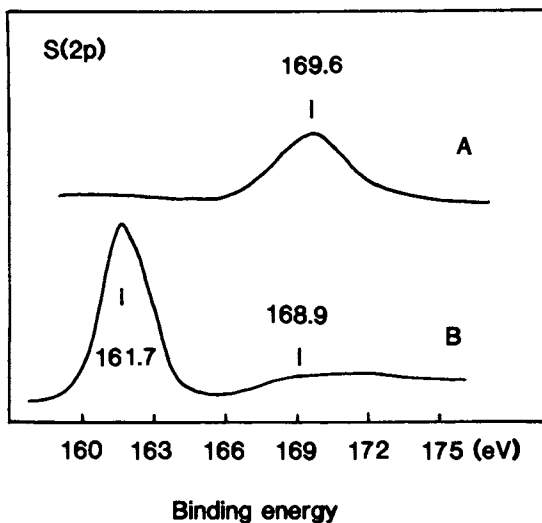


Figure 5. S(2p) XPS spectra of hexagonal CdS/Nafion (A) and cubic CdS/Nafion (B) films.

To elucidate the higher BE peaks [S(2p) 168.9, 169.6 eV], we examined the Nafion film itself because it has  $-\text{SO}_3^-$  cation exchange sites. Only C(1s) and F(1s) peaks were observed. No S(2p) peak was observed even after  $\text{Ar}^+$  bombardment. This result suggests that the surface concentration of cation exchange sites involving  $-\text{SO}_3^-$  is low. Sulfur located well below the surface would, of course, not be detected by XPS. We assign the higher BE S(2p) peak to a surface sulfate species (11).

The surface atomic ratios (Cd/F, S/F and C(nafion)/F) calculated from the XPS peak areas are listed in Table I. The results indicate that the cubic-CdS film has a higher surface concentration of CdS than the hexagonal film. In both, the C(1s)/F(1s) ratio is similar to Nafion itself.

The higher BE for the Cd(3d) peak for the film containing hexagonal CdS can be understood in terms of surface charging of the sample under x-ray irradiation. Since the surface of the hexagonal sample is not as rich in CdS as the cubic sample, we expect the Nafion to play a greater role in the former, and this would lead to a great surface charge. Shifts to higher BE and extensive broadening would then be expected, as observed. This conclusion based on XPS is consistent with the SEM data. We conclude that the surface density of CdS is higher for the cubic CdS and that the hexagonal CdS film surface contains a large amount of sulfate ion. One can speculate that the presence of sulfate may contribute to the lower activity of the hexagonal form for the photoassisted production of hydrogen.

Table I. XPS Peak Ratios

| (a)                          | $\alpha$ -CdS       | $\beta$ -CdS |
|------------------------------|---------------------|--------------|
| Cd(3d <sub>5/2</sub> )/F(1s) | 0.04                | 8.4          |
| S(2p)/F(1s)                  | 0.02 <sup>(b)</sup> | 1.6          |
| C(1s)/F(1s)                  | 0.1                 | 0.1          |

(a) Nafion F(1s) peak was used as standard.

(b) This peak was assigned to  $\text{SO}_4^{2-}$  species.

#### Acknowledgments

We acknowledge financial support of this work by the Gas Research Institute (Contract No. 5982-260-0756). NSF support of the x-ray photoelectron spectrometer by an equipment grant, CHE-8201179, is also acknowledged.

#### Literature Cited

- 1.a. Sato, S.; White, J. M.; *Chem. Phys. Lett.* 1980, 72, 83.
- b. Kawai, T.; Sakata, T.; *Chem. Phys. Lett.* 1980, 72, 87.
- c. Dunn, W. W.; Bard, A. J.; *Nov. J. Chim.* 1981, 5, 651.

- 2.a. Ellis, A.B.; Kaiser, S.W.; Wrighton, M.W. J. Am. Chem. Soc. 1976, 98, 6885.
- b. Inoue, I.; Watanabe, T.; Fugishima, A.; Honda, K. Bull. Chem. Soc. Jpn. 1979, 52, 1243.
3. Kalyanasundaram, K.; Borgarello, E.; Gratzel, M. Helv. Chim. Acta 1981, 64, 632.
- 4.a. Matsumara, M.; Sato, Y.; Tsubomura, H. J. Phys. Chem. 1983, 87, 3897.
- b. Kuczynski, J. P.; Milosavijevic, B. H.; Thomas, J. K. J. Phys. Chem. 1983, 87, 3368.
- c. Aruga, T.; Domen, K.; Naito, S.; Onishi, T.; Tamaru, K. Chem. Lett. 1983, 1037.
5. Meissner, D.; Memming, R.; Kastening, B. Chem. Phys. Lett. 1983, 96, 34.
- 6.a. Krishnan, M.; White, J. R.; Fox, M. A.; Bard, A. J. J. Am. Chem. Soc. 1983, 105, 7002.
- b. Mau, A. W.-H.; Huang, C.-B.; Kakuta, N.; Bard, A. J.; Campion, A.; Fox, M. A.; White, J. M.; Webber, S. E. J. Am. Chem. Soc. (in press).
- c. Kuczynski, J. P.; Milosavijevic, B. H.; Thomas, J. K. J. Phys. Chem. 1984, 88, 980.
7. Powder Diffraction File, ASTM, 1977.
8. Aspnes, D. E.; Heller, A. J. Phys. Chem. 1983, 87, 4919.
9. Borgarello, E.; Kalyanasundaram, K.; Gratzel, M.; Pelizzetti, E. Helv. Chim. Acta 1982, 65, 243.
10. Meyer, M.; Wallberg, C.; Kurihara, K.; Fendler, J. H. J. Chem. Soc., Chem. Commun. 1984, 90.
- 11.a. Outka, D. A.; Madix, R. J. Surface Sci. 1984, 137, 242.
- b. Furuyama, M.; Kishi, K.; Ikeda, S. J. Electron. Spectrosc. Relat. Phenom. 1978, 13, 59.

RECEIVED August 6, 1985

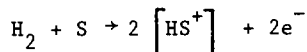
## New Catalysts and New Electrolytes for Acid Fuel Cells

P. N. Ross<sup>1</sup> and A. J. Appleby<sup>2</sup>

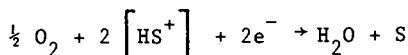
<sup>1</sup>Materials and Molecular Research Division, Lawrence Berkeley Laboratory, University of California—Berkeley, Berkeley, CA 94720

<sup>2</sup>Electric Power Research Institute, Inc. (E.P.R.I.), Palo Alto, CA 94303

In the phosphoric acid fuel cell as currently practiced, a premium (hydrogen rich) hydrocarbon (e.g. methane) fuel is steam reformed to produce a hydrogen feedstock to the cell stack for direct (electrochemical) conversion to electrical energy. At the fuel electrode, hydrogen ionization is accomplished by use of a catalytic material (e.g. Pt, Pd, or Ru) to form solvated protons,



At the cathode, air is reduced catalytically by reaction with solvated protons to generate the product water



In practical cells, the acid concentration is very high (>95%) and the solvated protonic species are not actually known, i.e.  $\text{H}_3\text{O}^+$  and  $\text{H}_4\text{PO}_4^+$  but probably very little  $\text{H}_9\text{O}_4^+$ . In order to maximize waste heat utilization, the cell stack operating temperature has been increased to the maximum value tolerated by the materials in current use, which is presently about 200°C. Catalysis is the key to the commercial viability of fuel cells, particularly the air cathode catalysis, as much more polarization occurs at the cathode than at the anode. Because of the severe operating conditions of the cell stack, the choice of catalytic materials is extremely limited. At present, the emphasis in cathode materials research is to find catalysts that provide improved kinetics over the integrated lifetime of the cell stack (ca. 40,000 hrs.). The baseline cathode material is Pt supported on a graphitized carbon black, usually at a weight loading of 10%, and a crystallite size of ca.  $3 \pm 0.5$  nm (i.e. about 30 percent exposed as measured by hydrogen chemisorption). At the end-of-life, we project that some Pt will be lost from the cathodes, and the crystallite size will have increased considerably, to 10-15 nm or more. The actual end-of-life conditions for the baseline catalyst are not known, since phosphoric acid fuel cell stacks have not yet been operated for the expected lifetime.

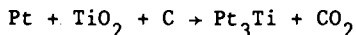
0097-6156/85/0288-0575\$06.00/0  
© 1985 American Chemical Society

Recent testing in phosphoric acid fuel cells has shown improved performance using promoted Pt on carbon catalysts in the air cathode. The promoters are oxides of the base transition metals, e.g., Ti (1), V (2), Cr (3), Zr (1), or Ta (1). The role of these promoters in the air cathode is unclear, and some have suggested that the active catalysts are alloys of the Pt with the transition metal (1,4) which form during heat-treatment of the oxide impregnated precursor. In the first section of this paper, we review the work from the Lawrence Berkeley Laboratory on the study of the mechanism of promotion of air cathode performance by these transition metal additives.

Phosphoric acid does not have all the properties of an ideal fuel cell electrolyte. Because it is chemically stable, relatively non-volatile at temperatures above 200°C, and rejects carbon dioxide, it is useful in electric utility fuel cell power plants that use fuel cell waste heat to raise steam for reforming natural gas and liquid fuels. Although phosphoric acid is the only common acid combining the above properties, it does exhibit a deleterious effect on air electrode kinetics when compared with other electrolytes (5) including such materials as sulfuric and perchloric acids, whose chemical instability at  $T > 120^\circ\text{C}$  render them unsuitable for utility fuel cell use. In the second part of this paper, we will review progress towards the development of new acid electrolytes for fuel cells.

### New Catalysts

All of the preparation procedures for the oxide promoted catalysts (1-4) shared one common feature, heat-treatment of the oxide impregnated Pt on carbon catalysts in an inert atmosphere at elevated temperature, usually around 900°C. If an "alloy" phase of Pt with the metal of the metal oxide is formed by this heat-treatment, thermal reduction would have to occur with carbon as reducing agent, e.g.



This reduction is thermodynamically favorable due to the very exothermic free-energy of formation of  $\text{Pt}_3\text{Ti}$  (6). However, such reduction reactions would require, in principle, the physical contact of three phases, which seems unlikely; it is more likely that it proceeds through a complex pathway involving a series of two-phase reactions. To understand these essential reduction reactions, we conducted a series of model studies of oxide overlayers on Pt surfaces. Because of the difficulty in characterizing supported multi-metallic catalysts, we decided to select just one of the bimetallic systems for detailed study, rather than attempt the characterization of the state of several different metal oxide promoters. We initially selected the Pt/ZrO<sub>2</sub> system because of the very strong inter-metallic bonding between Pt and Zr (7). However, following an initial study of the surface chemistry of ZrO<sub>x</sub> overlayers on Pt (8), we decided that the Pt/TiO<sub>2</sub> system was a more interesting choice. The Pt/ZrO<sub>2</sub> system had the major disadvantage that very high temperatures (1200°K) were required to cause reactions between the ZrO<sub>x</sub> and Pt(Zr) phases to occur, whereas in the Pt/TiO<sub>2</sub> system the analogous reactions occurred at ca. 500°K lower temperatures. We attributed this effect to the smaller metallic radius of Ti vs. Zr, noting that the radii of Ti, V, Cr and Ta are all much smaller than Zr.

### Surface Chemistry of TiO<sub>2</sub> Overlayers on Pt

Auger electron spectroscopy (AES) of TiO<sub>2</sub> overlayers on Pt(100) single crystal was used to follow the changes in surface composition with thermal annealing (9) in UHV. Generally the overlayers were ca. 4 monolayers thick, prepared by electron beam evaporation of Ti metal with simultaneous oxygen dosing. Above an annealing temperature of 600°K, the O/Ti and Ti/Pt AES ratios changed as a function of time, indicating reduction of the oxide overlayer and dissolution of Ti into the Pt bulk. It was not clear where the oxygen in the overlayer went, but since in most UHV systems [H<sub>2</sub>]/[H<sub>2</sub>O] >> 1 and/or [CO]/[CO<sub>2</sub>] >> 1, it is presumed to have left the surface as H<sub>2</sub>O or CO<sub>2</sub>. In the presence of a deliberately introduced reducing gas like H<sub>2</sub> or CO (typically 100 L dose), the O/Ti AES ratio decreased more rapidly than for thermal annealing, but the rate of the Ti/Pt AES ratio change was unaffected, indicating that Ti dissolution (solid state diffusion) was the slower step. Also, at temperatures above 900°K, the oxygen surface concentration went to essentially zero, indicating that at this temperature (and possibly at lower temperatures as well) titanium was dissolved into Pt as Ti metal, and not as "TiO" as reported by Gorty (10). The difference may be due to the polycrystalline nature of the Pt substrate used in (10) and grain boundary diffusion of "TiO" species. It was clear from the overlayer studies that with thermal annealing in reducing atmospheres, TiO<sub>2</sub> overlayers on Pt can be completely dissolved, forming Pt-Ti alloy surface phases of nominal composition Pt<sub>x</sub>Ti (3 ≤ x ≤ 8). Therefore, it seemed reasonable to conclude that similar reactions can occur in the supported TiO<sub>2</sub> impregnated catalysts, and that alloy phases are responsible for the enhanced catalysis.

### Surface Chemistry of Pt - Ti Alloys

The most recent work on the structure of the bulk alloys of composition Pt<sub>x</sub>Ti (3 ≤ x ≤ 8) is by Schryvers et al. (11). They reported that in the composition range between those for the ordered phases Pt<sub>8</sub>Ti and Pt<sub>3</sub>Ti there exists two long-period antiphase boundary structures based on the face-centered cubic structure. They suggest that due to strong ordering forces extending over several atomic separations (as exhibited by Pt<sub>8</sub>Ti) there is no composition in this range in which the alloy phase is a solid-solution (disordered). We have studied the surface properties of the model systems Pt<sub>3</sub>Ti extensively, including the surface composition and structure (12), the electronic properties (13), the reactivity of the surface towards oxygen (14), and small molecules adsorption on the surface (15). These studies have shown that while the Pt<sub>3</sub>Ti surfaces have very interesting properties for catalysis in reducing atmospheres, which may be related to the SMSI effect in CO/H<sub>2</sub> chemistry on Pt/TiO<sub>2</sub> (16), the reactivity of the Ti in the surface towards oxygen is very high, resulting in the formation of TiO<sub>x</sub> overlayers on a Pt enriched (relative to the bulk) surface layer. The stoichiometry and coverage by TiO<sub>x</sub> depend on the oxidation conditions. At 350°C in air, which is a common curing (of polymer binder) condition during electrode preparation, the surface becomes covered by a dense, compact multilayer of TiO<sub>2</sub>. Curiously, there is some evidence of proton conduction through this film when the surface is immersed in dilute acid



solution. However, under the conditions of use in phosphoric acid fuel cells, very concentrated hot acid, the  $TiO_2$  overlayers are dissolved rapidly, leaving an essentially pure Pt surface. These studies suggest that the electrocatalytic properties of  $Pt_3Ti$  in commercial fuel cells would be the same as pure Pt. There is the possibility that the Pt surface left after  $TiO_2$  dissolution is an atomically rough surface, and therefore the comparison to "pure Pt" would have to be made taking into account differences in morphology.

### Characterization of $TiO_2$ Promoted Pt Catalysts

Characterization studies of the oxide impregnated Pt on carbon catalyst are being conducted to determine the chemical state of the admetal as a function of heat treatment. Ultimately one wants to supplement these "dry" characterizations with characterizations of the "wet" state, i.e. as the catalyst exists in the fuel cell cathode. These characterization studies are still in progress, and we have no results published as yet. The techniques of x-ray diffraction (XRD), x-ray photoelectron spectroscopy (XPS), and extended x-ray absorption fine structure spectroscopy (EXAFS) are being used in combination. Each of the techniques "looks at" the catalyst in a different way and each provides a different kind of characterization. We are using XRD to indicate any phases present in crystalline form, XPS to determine the valence states of Ti, and EXAFS to determine the ligand coordination about the Ti atoms. In a supported catalyst both XPS and EXAFS are "integral" techniques, that is they sample all the Ti atoms present. Table I reports the binding energies for Ti (2p) in standard materials that represent the expected possible chemical states of the Ti.

Table I. XPS Binding Energies for Ti 2P<sub>3/2</sub> in Different Chemical States

| State             | B.E. *   | Chemical Shift |
|-------------------|----------|----------------|
| Ti                | 453.8 eV | ref.           |
| TiO               | 454.6    | +0.8           |
| TiC               | 454.7    | +0.9           |
| TiPt <sub>3</sub> | 454.9    | +1.1           |
| TiO <sub>2</sub>  | 458.5    | +4.7           |
| TiCl <sub>3</sub> | 459.4    | +5.6           |

\* Energy scale referenced to carbon 1S at 284.6 eV.

The +4 and +2 states are easily distinguished from the metallic state, but titanium in the ordered alloy  $Pt_3Ti$  has the nearly same chemical shift as in TiC which is also a possible reduction product. XPS alone would not be capable of reliably resolving the reduced state of Ti. But the backscattering cross-section of Pt is enormously greater than that of carbon, so the EXAFS coupled with XPS provides a clear discrimination of Ti in TiC and Ti in  $Pt_3Ti$  clusters too small to be observed in XRD patterns. A summary of the qualitative characterization heat-treated  $TiO_2$  impregnated Pt on carbon catalyst is given in Table II.

Table II. Characterizations of State of Ti as a Function of Heat-Treatment Temperature

| Sample                       | Method (characterization) |                       |                |
|------------------------------|---------------------------|-----------------------|----------------|
|                              | XRD(phases)               | XPS(valence)          | EXAFS(ligands) |
| TiO <sub>2</sub> impregnated | amorphous                 | +4                    | 0              |
| HT 700°C                     | "                         | +4                    | 0              |
| HT 900°C                     | TiC, Pt alloy             | +4, "+1" <sup>†</sup> | 0, Pt          |
| HT 1200°C                    | Pt <sub>3</sub> Ti        | " +1"                 | Pt             |

<sup>†</sup>" +1" is nominal oxidation state of Ti in Pt<sub>3</sub>Ti [13] or TiC.

Curiously, very little TiC was observed at any stage of the treatment; it does not appear to be an intermediate to alloy phase formation. A significant amount of alloy phase appears only at 900°C and above. At 1200°C, Pt<sub>3</sub>Ti is the predominant Ti phase present.

Fuel cell testing has indicated that the promotional effect of TiO<sub>2</sub> is observed after heat treating at 900°C; at 700°C the heat treatment had a small promotional effect that was not regarded as significant. Therefore, alloying may be essential to the promotional effect. However, a key element we are missing from the characterization mix is knowledge of the physical structure of the phases. Such structural characterization is possible by transmission electron microscopy (TEM) and such studies are in progress.

#### Current Status of New Catalysts

Based on the characterization studies and the behavior of the model systems, it appears that the promotion effect of oxides of Ti, V, Zr, Ta and Cr is probably not truly catalytic. The most probable mechanisms are changes in physical properties of the Pt catalyst in the "dry" state which result in improved electrode performance due to two effects: 1) a Pt crystallite shape/morphology effect, where the base metal oxide acts to impede Pt crystallite size growth (by coalescence) but allows surface diffusion to occur and equilibrium shapes to form during heat treatment; 2) the oxide acts as a "flux" for improving the wettability of the catalyst when fabricated into a gas diffusion electrode, resulting in higher catalyst layer effectiveness factors. Both of these effects have been discussed in the literature, but not with respect to how additives or promoters might relate to such effects. The effect of Pt crystallite shape/morphology on oxygen reduction activity has been discussed at length (17), and it is clear that metal oxides can have an indirect effect on oxygen activity via modification of shape/morphology. The effectiveness factor for the catalyst layer is known to be extremely sensitive to physical properties of the carbon, the Teflon dispersion, the use of wetting agents, the hydrophilicity of the SiC matrix, etc., and it is a difficult matter to determine truly catalytic effects from electrode structural effects. Watanabe et al. (18) have recently presented data showing that a novel electrode fabrication method enhanced the performance of "standard" Pt catalyst by

ca. 40 mV, which is about the same performance enhancement by metal oxides reported in References 1-4.

### New Electrolytes

Recent work has shown that use of concentrated trifluoromethane sulfonic acid (TFMSA) in place of concentrated phosphoric acid enhances the activity of standard Pt electrodes for oxygen reduction by 40 mV (which could improve the heat rate of first-generation fuel cells by 400 Btu/kWh) (19). It shows the real possibility that the catalytic activity of platinum-based catalysts in phosphoric acid can be improved under utility fuel cell conditions by the use of new electrolytes, especially fluorinated sulfonic or phosphoric acids. However, trifluoromethane sulfonic acid is much too volatile for practical use in utility fuel cells. Efforts to synthesize suitable non-volatile, stable fluorinated sulfonic acids to replace phosphoric acid have been moderately successful and are continuing. There has been some doubt about the kinetics of oxygen reduction in non-volatile, higher homologs of TFMSA, and whether the kinetic benefits are retained in the higher molecular weight acids. Recent work (20) has shown that, in the absence of impurities resulting from by-products of the synthesis, the kinetics in the higher acids are identical to those observed in TFMSA (at the same pH and temperature). The result allows some guarded optimism that the search for the optimum acid electrolyte will ultimately prove to be successful.

### Acknowledgment

This research was supported by the Assistant Secretary for Fossil Energy, Office of Fuel Cells, Advanced Concepts Division of the U.S. Department of Energy under Contract No. DE-AC03-76SF00098, and by the Electric Power Research Institute under Contract No. RP-1676-2.

### Literature Cited

1. Ross, P.N., EPRI Report EM-1553, September 1980; also The Electrochemical Society Proceedings Volume 80-2, Fall Meeting, Hollywood, FL, October 1980, 73-5.
2. Jalan, V., Landsman, D. and Lee, J., U.S. Patent 4 192 907, 1980.
3. Landsman, D. and Jalan, V., U.S. Patent 4 316 944, 1982.
4. Jalan, V. and Taylor, E., The Electrochemical Society Proceedings Volume 83-1, Spring Meeting, San Francisco, CA, May 1983, 1072-73.
5. Ross, P. and Andricacos, P., J. Electroanal. Chem., 1983, 154, 205.
6. Meschter, P. and Worrell, W., Met. Trans. A, 1977, 8A, 503.
7. Brewer, L. in "Phase Stability in Metals and Alloys," eds. P. Rudman, J. Stringer and R. Jaffee, McGraw-Hill, NY, 1967, pp. 39-53.
8. Bardi, U., Ross, P. and Somorjai, G., J. Vac. Sci. Technol. A, 1984, 2, 40.
9. Bardi, U. and Ross, P., J. Catalysis, in press.
10. Gorty, R., J. Catalysis, in press.

11. Schryvers, D., van Landuyt, J., van Tendeloo, G., and Amelinckx, S., Phys. Stat. Sol. (a), 76, 1983, 575.
12. Bardi, U. and Ross, P.N., Surf. Sci., 1984, 146, L555.
13. Derry, G. and Ross, P.N., Sol. State Comm., 1984, 52, 151.
14. Bardi, U. and Ross, P.N., J. Vac. Sci. and Technol. A, 1984, 2, 1461.
15. Bardi, U., Somorjai, G., and Ross, P.N., J. Catalysis, 1984, 85, 272.
16. Tauster, S., Fung, S., and Garten, R., J. ACS, 1978, 100, 170.
17. Ross, P., J. Electrochem. Soc., 1979, 126, 78, and references therein to previous work; also Ross, P.N., Paper No. 190, Fall Meeting of the Electrochemical Society, Los Angeles, CA, October 1979.
18. Watanabe, M., Tomikawa, M. and Motoo, S., Paper No. 410, Spring Meeting of the Electrochemical Society, Cincinnati, OH, May 1984.
19. Ross, P. J. Electrochem. Soc., 1983, 130, 882.
20. Striebel, K., Andricacos, P., Cairns, E., Ross, P. and McLarnon, F., Paper No. 410, Spring Meeting of the Electrochemical Society, Cincinnati, OH, May 1984.

RECEIVED April 1, 1985

## Carbonaceous Surfaces: Modification, Characterization, and Uses for Electrocatalysis

Dale H. Karweik, Ing-Feng Hu, Sue Weng, and Theodore Kuwana

Department of Chemistry, The Ohio State University, Columbus, OH 43210

Glassy carbon electrodes polished with alumina and sonicated under clean conditions show activation for the ferri-/ferro-cyanide couple and the oxidation of ascorbic acid. Heterogeneous rate constants for the ferri-/ferro-cyanide couple are dependent on the quality of the water used to prepare the electrolyte solutions. For the highest purity solutions, the rate constants approach those measured on platinum. The linear scan voltammetric peak potential for ascorbic acid shifts 390 mV when electrodes are activated. Such reduction in overpotential is the largest observed for a bare glassy carbon electrode. The presence of surface quinones may be indicative of activation but does not appear to mediate the heterogeneous electron transfer. XPS results support the presence of quinones as a minor constituent on the surface.

Although the initial use of glassy carbon as an electrode material indicated that it might be a viable substitute for platinum (1), subsequent investigations have shown that glassy carbon is quite complex as an electrode material. The conditions used to manufacture a particular sample of glassy carbon and the subsequent steps used to treat the surface for electrochemistry strongly influence its behavior, possibly even more so than with platinum. For example, the final heat treatment temperatures in the manufacture will produce different electrochemical properties, even with the same surface treatments (2-4) since the structure and electrical property of glassy carbon depends on the temperature, as indicated by the single crystal TEM patterns and by measurement of temperature dependent conductivity (5-6). On the other hand, it is also well established that the electrochemical properties of carbon-based electrodes are markedly affected by surface treatments.

Several methods have been applied to treat and activate glassy carbon surfaces for use as an electrode. The simplest one uses

alumina or diamond abrasives to polish the surface and to produce a reproducible surface state. Polishing has been often followed by sonication to remove polishing material and surface debris and by additional activation steps. These activation steps have included chemical (7), electrochemical (8), and thermal oxidations (9) as well as radio frequency plasma treatments (10). The overpotential for the oxidation of NADH and ascorbic acid can be reduced, for example, by the generation of an "oxidized" surface (8,9) via an oxygen radio frequency plasma, electrochemical or chemical oxidation. It has recently been reported that careful selection of electrode polishing conditions (11-12) or electrode heat treatments (9) also activates the observed heterogeneous electron transfer process and provides a more reproducible initial activity. Typical examples from our laboratory of such activation, using hydroquinone as a probe molecule, are shown in Fig. 1. Activation is indicated by the decrease in the separation between the peak anodic and cathodic potentials. In most cases, the activated surfaces have not been subjected to analysis by techniques (13) other than electrochemical ones. Thus, it is not possible to determine unambiguously what are the principal results of the pretreatments. The only clear consensus of opinion seems to be that surface pretreatment is necessary to produce reproducible and active electrodes (14).

Several mechanisms have been proposed to explain the activation of carbon surfaces. These have included the removal of surface contaminants that hinder electron transfer, an increase in surface area due to micro-roughening or build-up of a thin porous layer, and an increase in the concentrations of surface functional groups that mediate electron transfer. Electrode deactivation has been correlated with an unintentional introduction of surface contaminants (15). Improved electrode responses have been observed to follow treatments which increase the concentration of carbon-oxygen functional groups on the surface (7-8,16). In some cases, the latter were correlated with the presence of electrochemical surface waves (16-17). However, none of the above reports discuss other possible mechanisms of activation which could be responsible for the effects observed.

The purpose of this paper is: 1) to describe the electrochemistry of ferri-/ferro-cyanide and the oxidation of ascorbic at an activated glassy carbon electrode which is prepared by polishing the surface with alumina and followed only by thorough sonication; 2) to describe experimental criteria used to bench-mark the presence of an activated electrode surface; and 3) to present a preliminary description of the mechanism of the activation. The latter results from a synergistic interpretation of the chemical, electrochemical and surface spectroscopic probes of the activated surface. Although the porous layer may be important, its role will be considered elsewhere.

## Experimental

Electrode Preparation. Glassy carbon (GC-20, Tokai Carbon, Ltd., Japan) was polished successively with 600 grit, 1.0, 0.3, and 0.05  $\mu\text{m}$  alumina powder (Buehler Ltd., Chicago, IL) slurried with triple

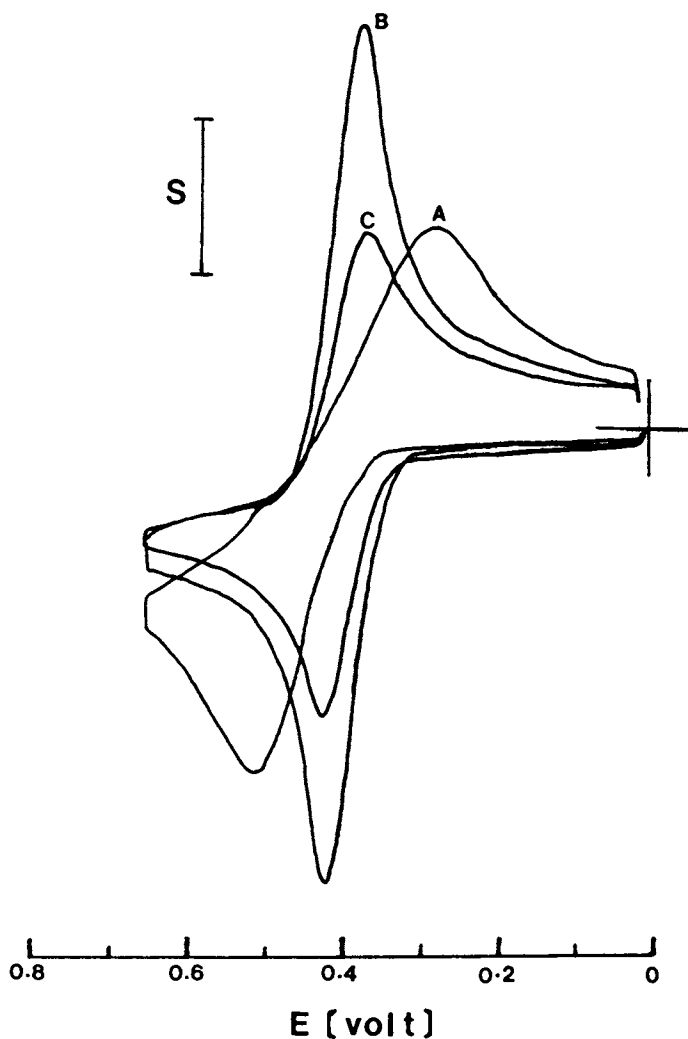


Figure 1. The redox behavior of 1,4-dihydrobenzene at a deactivated versus various activated glassy carbon electrodes.  
 A. Deactivated by final polishing on a polishing cloth.  $S = 50 \mu\text{A}$ .  
 B. Activated electrode in A by polishing with alumina.  $S = 50 \mu\text{A}$ .  
 C. Activated by heat treatment.  $S = 158 \mu\text{A}$ .

Scan rate = 100 mV/sec.

1 mM 1,4-dihydrobenzene in 0.1 M phosphate buffer with 0.15 M sodium perchlorate at pH 2.

distilled water on a glass optical flat. The last stages were continued until a mirror-like surface was obtained. The electrode and the optical flat were thoroughly cleaned several times during the polishing procedure with triple distilled water and between each polishing step. After polishing, the electrode was sonicated for a total of ca. 10 minutes with 3 to 4 changes of triple distilled water during sonication. The resulting "bare" glassy carbon electrode was used immediately to minimize the possibility of surface contamination and oxidation of the surface, which occurs on exposure to air (18).

Solutions. Solutions of ferricyanide (Baker Chemical Co., Phillipsburg, NJ) were prepared in 1.0 M KCl (Malinckrodt, Paris, KY). Ascorbic acid solutions were prepared in 0.1 M phosphate buffer adjusted to pH 2.0. All solutions were prepared with triple distilled water. Solution preparation precautions have been previously described (15).

Instrumentation. A conventional three electrode potentiostat was used for cyclic voltammetry studies. A PARC (Princeton Applied Research Corp., Princeton, NJ) Model 174A Polarographic Analyzer and a PARC Model 175 Universal Programmer were used for differential pulse (DPV) and square wave voltammetry (SWV). A PARC Model 128 Lock-In Amplifier was also used for the SWV. Data were recorded with an Omnigraphic Model 2000 (Houston Instruments Corp., Dallas, TX) X-Y recorder, a Tektronix Model 7613 Storage Oscilloscope (Tektronix, Beaverton, OR) or an Apple II+ microcomputer (Apple Computer Co., Cupertino, CA) equipped with an Ascope interface (Northwest Instrument Systems, Beaverton, OR). The potential of the working electrode was measured versus a KCl saturated Ag/AgCl reference electrode. The reference was constructed with a double junction consisting of Pt/cracked glass and Vycor glass (Dow Corning, Inc., Corning, NY) junctions to prevent AgCl leakage into the cell. The area of the working electrode was  $0.083 \text{ cm}^2$ .

The PHI Model 548 ESCA/ AES spectrometer (Physical Electronics Inc., Eden Prairie, MN) previously described (10,13) has been modified by the replacement of the original x-ray source with a PHI Model 1548 dual anode, 300W x-ray source. All binding energies are referenced to the Au 4f peak at 83.8 eV.

## Results And Discussion

Electrochemical Features The reversibility of the ferri-/ferro-cyanide redox couple and the position and definition of the current-potential wave for the oxidation of ascorbic acid were selected as probes to assess the extent of electrode activation. These probes were chosen because of their demonstrated sensitivity to the surface state of glassy carbon electrode (GCE) (7-8,15). The heterogeneous rate constant for ferricyanide has been shown to decrease by approximately an order of magnitude with the introduction of surface impurities. The overpotential for the oxidation of ascorbic acid has been reduced over 200 mV on activated GCE. In addition, these two probes offer distinctly different types of electrochemistry. The mechanism of the ferricyanide reaction



appears to involve only a simple outer-sphere electron transfer, while the ascorbic acid oxidation appears to proceed via an inner-sphere, adsorption mechanism. The simple outer-sphere reaction should avoid complications due to interactions with surface species and should provide information about the accessibility of the surface for electron transfer. The inner sphere mechanism might involve specific interactions with surface species and, therefore, should be more sensitive to electron transfer mediators on the surface.

The cyclic voltammograms of ferricyanide (1.0 mM in 1.0 M KCl) in Fig. 2 are illustrative of the results obtained for scan rates below 100 mV/s. The peak separation is 60 mV and the peak potentials are independent of scan rate. A plot of peak current versus the square-root of the scan rate yields a straight line with a slope consistent with a semi-infinite linear diffusion controlled electrode reaction. The heterogeneous rate constant for the reduction of ferricyanide was calculated from CV data (scan rate of 20 Vs<sup>-1</sup>) using the method described by Nicholson (19) with the following parameter values:  $D_0 = 7.63 \times 10^{-6}$  cm<sup>2</sup>s<sup>-1</sup>,  $D_r = 6.32 \times 10^{-6}$  cm<sup>2</sup>s<sup>-1</sup>,  $\alpha = 0.5$ , and  $n = 1$ . The rate constants were found to be dependent on the purity of the water used to prepare the electrolyte solutions. For example, the rates for three different water samples; i.e., double distilled, triple distilled from alkaline permanganate and filtered through a Barnsted Nanopure cartridge system, were 0.063 ( $\pm 0.005$ ), 0.104 ( $\pm 0.01$ ), and 0.14 ( $\pm 0.04$ ) cm s<sup>-1</sup>, respectively (15). The results indicate that the purity of the water affects the apparent rate of the electron transfer and that the rate constant for the highest purity water is nearly identical to those determined on clean platinum (20). These rates are the largest reported for glassy carbon. Chronocoulometry data show no evidence for adsorption of the ferricyanide on GCE (15) and are indicative of a simple outer-sphere electron transfer. The similarities in the rate constants for platinum and GCE are in agreement with Marcus rate theory, which predicts that the electron transfer rate of a simple outer-sphere reaction should be independent of the electrode material, provided a sufficient density of states with the appropriate energy exists on the electrode surface (21). It is reasonable to conclude that the improvement in the ferricyanide reversibility is, in part at least, a result of producing a clean, unblocked surface.

To determine the effects of cleanliness on the production of an activated surface, several variables, including the nature of the polishing surface, the type of polishing material and the quality of the water used to clean the surface, were examined. Whenever a commercial polishing cloth or pad was substituted for the glass plate, only deactivated electrodes could be produced with heterogeneous rate constants similar to those reported by Engstrom (8). Similarly, when commercial suspensions of alumina were employed rather than the corresponding powders suspended in triple distilled water, the electrodes showed surface deactivation. It is speculated that deactivation may be caused by organic surfactants used to treat the surface of the polishing cloths or to help stabilize the alumina suspension. Polishing with diamond suspensions produced even a more strongly deactivated electrode

surface. The deactivation is similar to that observed for poorer grades of water, as previously reported. Thus, it seems reasonable to conclude that cleanliness during preparation and use of GCE is absolutely essential to elicit and maintain activation.

The cyclic voltammograms of ascorbic acid (1.0mM in 0.1M phosphate buffer, adjusted to pH 2.0) in Fig. 3 show the difference between electrodes prepared as described and one which is deactivated by twenty, one minute chronocoulometry experiments at an applied potential of 0.70 V. There is a 390 mV shift in the oxidation peak potential from 0.66V to 0.27V coincident with activation. The resulting potential is at the thermodynamic potential for ascorbic acid and is nearly identical to that obtained on mercury (22). While this value is comparable to values reported for heat treated gc (9), it is less than that reported for chemically modified electrodes employing catechol-like mediators (23). A reduction in the overpotential, greater than that reported here, has not been observed on "bare" glassy carbon. The peak current of the CV is directly proportional to the square root of the scan rate indicating the electron transfer is semi-infinite linear diffusion limited. Peak shape suggests adsorption of ascorbic acid. Less than monolayer adsorption was, however, indicated by chronocoulometry. This level of adsorption is also present on deactivated electrodes and does not change the peak shape as shown in Fig. 3. Thus, the electrochemical data are consistent with an electrode reaction that is simply an irreversible electron transfer, which may proceed through, but is not limited by, surface adsorption. This is consistent with other reports concerning the electrochemistry of ascorbic acid (24). Such data do not distinguish between the mechanisms of activation, but do confirm the presence of an activated surface.

Molecular Characterization It has been reported that o-quinones oxidize ascorbic acid in homogeneous solutions (25). Surface quinones have also been reported to exist on activated carbon surfaces (16). However, cyclic voltammetry is not sufficiently sensitive to allow an unambiguous identification of the reversible wave ascribed to surface quinones (16). Therefore, differential pulse voltammetry (DPV) and square wave voltammetry were employed. A typical result for DPV in Fig. 4a shows the presence of two redox couples with peak potentials of 0.25 V and 0.19 V (10mV). Similar results have also been obtained with SWV. The relative intensities of the two peaks vary from sample to sample but are always present with activated electrodes. The similarities between the potentials found for the surface species and for the oxidation of ascorbic acid suggest that an ec catalytic mechanism may be operative. The surface coverage of the o-quinone is estimated to be the order of  $10^{-12}$  mol  $\text{cm}^{-2}$ . It is currently not possible to control the surface concentration of the o-quinone-like species or the oxygen content of the GCE surface.

The surface waves were simulated assuming the presence of two different functionalities, each undergoing a reversible two electron redox reaction. It was assumed that these surface functionalities were quinones in Nernstian equilibrium with the electrode potential before each DPV pulse. It was also assumed that the current during

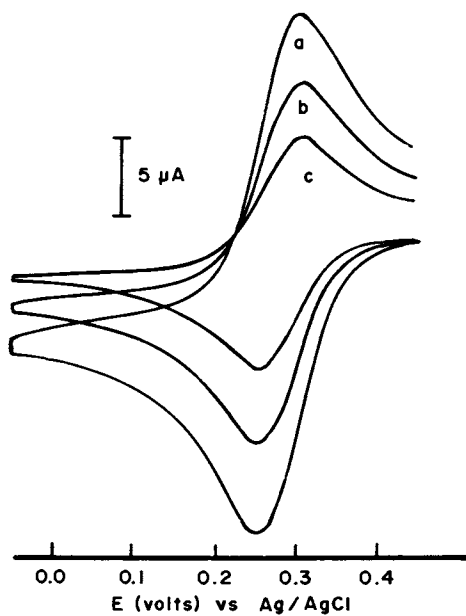


Figure 2. Cyclic voltammograms of ferri-/ferro-cyanide couple at an activated glassy carbon electrode at scan rates of a) 20, b) 50, and c) 100  $\text{mV s}^{-1}$ . See text for details.

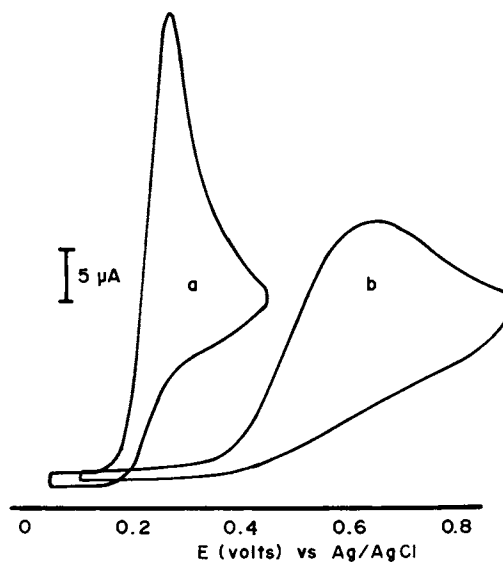


Figure 3. Cyclic voltammograms of ascorbic acid at a freshly polished, active (a) and a deactivated (b) glassy carbon electrode surface. See text for details.

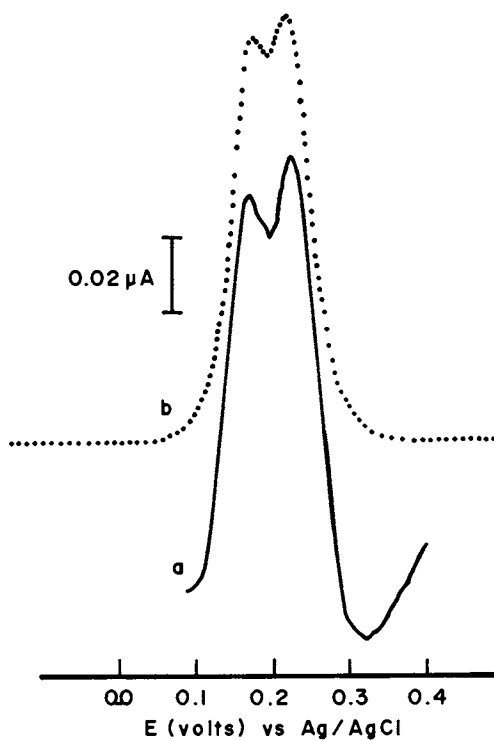


Figure 4. Differential pulse voltammetry of a freshly polished, activated glassy carbon surface (a) and a digital simulation of the DPV (b). The pulse frequency was 2 Hz with an amplitude of 10 mV. The DC scan rate was  $2 \text{ mV s}^{-1}$ .

the pulse was kinetically controlled and conformed to the Butler-Volmer relationship. Since diffusion is not involved, the current decay was assumed to be determined by electron transfer to surface species. Assuming that the surface reaction is pseudo-first order, an exponential decay of the surface concentration and hence, current should occur. The rate of decay was dependent on the value of the heterogeneous rate constant. The results of the simulation are shown in Figure 4b. If the DPV waves were simulated with two reactions, each involving only one electron, the waves could not be resolved with the two assumed  $E'$  values. A concentration ratio of 2:1 was used to produce the simulation shown in Figure 4b. The agreement between the simulated and experimental DPV waves, although not conclusive proof, does support the hypothesis of surface functionalities, like quinones, present on the polished gc surface.

The potential of one surface group (0.25 V) coincides closely to that found for o-naphthoquinone under similar solution conditions (26). The second wave is expected to be due to a similar o-quinone perhaps with a larger aromatic group attached, such as 13,14-picenedione. To investigate this hypothesis, the surface was reacted with o-phenylenediamine, as suggested first by Schreurs (26), for 6 hrs of refluxing in absolute ethanol. The derivatized electrode was then extracted in a Soxhlet for 1 hr with ethanol and dried under vacuum before examination. The electrochemistry of the derivatized surface showed a loss of the original DPV waves and the appearance of new waves at the same potential as found for the solution electrochemistry of naphthophenazine. Incomplete derivatization would preserve some presence of both the o-naphthoquinone- and the naphthophenazine-like peaks. Since both surface waves disappear upon derivatization to produce a corresponding pair of new phenazine-like waves, it appears that Schreurs' proposal is correct.

In an attempt to confirm the presence of quinones, the activated surfaces were subjected to XPS analysis. Based on previous experience (13), the C 1s region of the XPS spectrum was recorded for several sets of activated and deactivated electrodes. Unlike prior studies of radio frequency plasma oxidized surfaces, which showed distinct changes in the surface functional groups, no statistically significant differences were observed. No differences were evident in the O 1s regions which, as previously noted, was not surprising. Assuming that the o-quinone groups were minor species and masked by the larger quantity of other oxygen containing surface groups, the o-phenylenediamine derivatized electrodes were also subjected to XPS analysis. The XPS survey spectrum of a derivatized carbon surface in Fig. 5a shows the presence of C, N, and O as expected. The N 1s binding energy and the shape of the carbon peak indicates that the nitrogen is covalently bonded and is aromatic in character. This is supported by the high resolution spectra of the C 1s and N 1s regions which, shown in Fig. 5b, show the presence of different types of covalent carbon-heteroatom bonds (13) and aromatic N 1s binding energy position. The N 1s binding energy is quite unlike that of an amine, which would be present, if o-phenylenediamine were adsorbed rather than covalently bound (27). To confirm that the nitrogen XPS peak corresponded to a surface

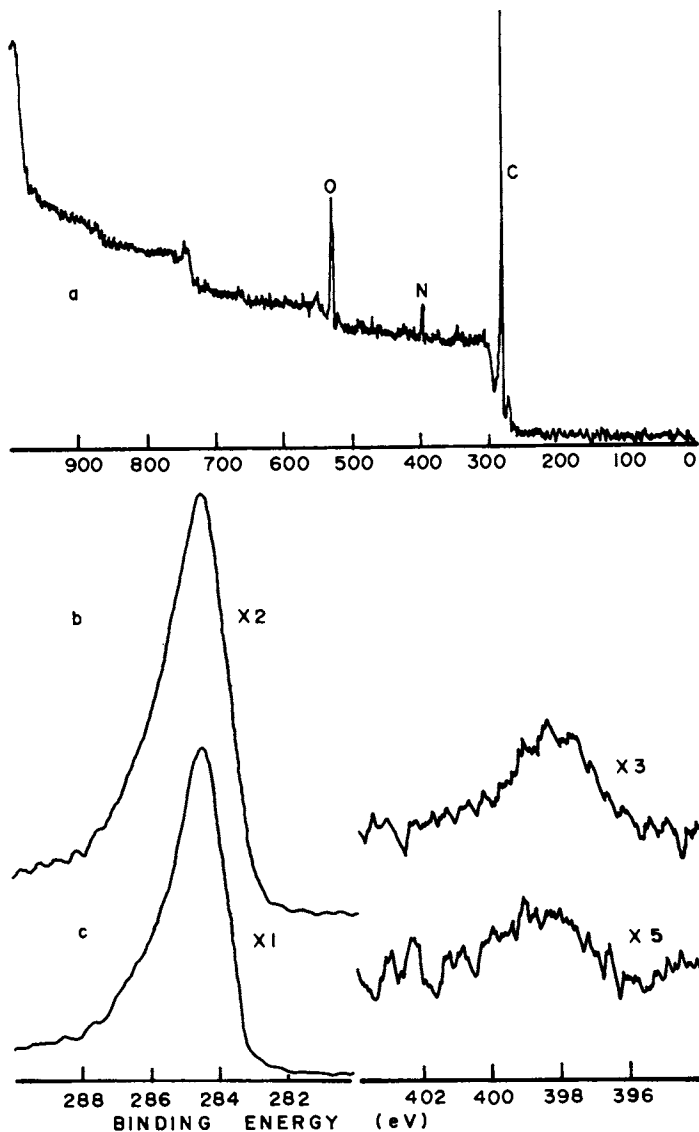


Figure 5. X-ray photoelectron survey spectrum (a) of an *o*-phenylenediamine derivatized glassy carbon surface. High resolution C 1s and N 1s spectra of a derivatized surface (b) and surface which was derivatized following reduction with  $\text{LiAlH}_4$  to destroy surface *o*-quinone functional groups (c). The spectrum were signal averaged for 90 min (a) and 20 min (b and c) and smoothed prior to display.

phenazine complex, a blank was run by first reducing the surface with  $\text{LiAlH}_4$  followed by derivatization. The results of the XPS scans of the C 1s and N 1s regions are shown in Fig. 5c. The N 1s peak is not evident in the survey scan when recorded to the same signal to noise ratio as in Fig. 4a. The surface concentration of nitrogen is reduced to near the limit of detection. Quantitation is difficult at this signal to noise level. The reduction in signal level corresponds to a decrease of the nitrogen concentration from approximately 3.6 A/o for the derivatized sample to slightly less than 1.0 A/o for the blank. Electrochemical results on the same blank samples indicate that there is a trace of phenazine on the surface. This may result from an incomplete reduction of the surface quinone by  $\text{LiAlH}_4$ . The XPS results confirm that the o-quinone-like oxygen is a minority species on the surface and that several other alcohol, phenol, ketone, and quinone functionalities may be present. Currently it is not possible to identify or control the nature and extent of each type of oxygen functionality. Correlations between the quantity and the electron transfer properties with respect to surface functionalities and the stability of the GC surfaces will be continued.

Attempts were made to determine whether surface o-quinones were responsible or coincident with the observed activation. Electrochemistry on electrodes derivatized with o-phenylenediamine or deactivated via  $\text{LiAlH}_4$  showed little evidence for activation with respect to the oxidation of ascorbic acid. However, the required chemical treatments of the electrodes surely contaminate the surface in addition to removing the functional groups. Therefore, these experiments do not distinguish between the possibilities of clean surface versus functional group activation. To resolve this issue, cyclic voltammograms corresponding to a scan rate of  $100 \text{ mV s}^{-1}$  were simulated (28) as simple, chemically irreversible electron transfer reactions without the inclusion of any catalysis via the o-quinone functionalities. A typical result is shown in Fig. 6. For the simulation it is assumed the electron transfer is completely irreversible and none of the products are electroactive. Literature values for the potential,  $\alpha n_a = 1.2$ , diffusion coefficient,  $D_o = 5.7 \times 10^{-6} \text{ cm}^2 \text{ s}^{-1}$ , and the heterogeneous rate constant ( $1.0 \times 10^{-2} \text{ cm s}^{-1}$ ) were used as adjustable parameters in the simulation (29). The electrode area, determined from chronocoulometry, was  $0.090 \text{ cm}^2$  to agree with the real CV. Although, the current following the potential reversal does not mimic the experimental CV exactly, there is a very close correspondence between the experimental (solid line) and simulated (circles) curves in Figure 6. Furthermore, the scan rate dependence is also in agreement. Although simulations does not provide conclusive proof, there is an indication that surface cleanliness may be the most important factor in this example. This is consistent with reports from other laboratories which have used other means to prepare active electrode surfaces without trying to produce activation through specific chemical modifications. In each case, it is easy to show that surface cleaning could be a major result of their activation procedure whether intentional or not. This is also consistent with mechanistic studies on platinum electrodes. Although there are cases, such as in the oxidation of  $\text{As(III)}$  by platinum oxides (30), the predominating observation is

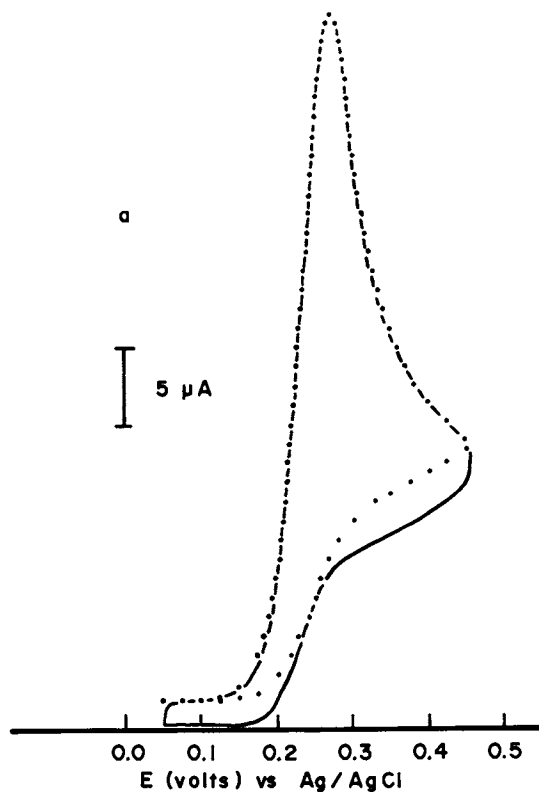


Figure 6. Simulated cyclic voltammogram for the oxidation of ascorbic acid without inclusion of ec catalysis by the surface quinone functionalities. Filled circles represent the simulated data and an experimental curve is shown with a line for comparison. A scan rate of  $100 \text{ mV s}^{-1}$  was assumed for experimental and simulated data.



that cleanliness is critical to Pt activation. Further studies are in progress which may be able to refine the description of GCE surface activation.

The presence of o-quinone surface waves seems, at the present time, to be coincidental to activation particularly in the case of ascorbic acid oxidation. On the other hand, its presence may serve as a criterion of cleanliness and activation. Thus, the surface waves at 0.250 and 0.190 are indicators or signatures for active GCE electrodes and should be used as diagnostic for a clean GCE surface as is the hydrogen fine structure for platinum (31). It is unfortunate that the o-quinone peaks do not appear to be proportional to the surface area as is the platinum fine structure.

### Conclusion and Comments

Activation of glassy carbon for the oxidation of ascorbic acid and the redox reaction of ferri-/ferro-cyanide can be obtained by polishing GCE surfaces with alumina abrasives followed by thorough sonication. Cleanliness with avoidance of impurity introduction during the polishing and in the electrolyte solution is a prerequisite for production and maintenance of activation. Although surface redox functionalities are found with activated GCE's, the experimental and simulation results indicate that they do not necessarily serve as mediators for electron transfer. However, these functionalities can serve as diagnostic "fingerprints" for a clean, active GCE surface.

It is instructive to consider what similarities might exist between glassy carbon and Pt. For example, is there a region of potential at which the double layer capacitance is independent of surface redox functionalities. On the other hand, such functionalities, like the adsorbed hydrogen waves on Pt, may serve as a marker of activity and also be quantitatively correlated to "active" sites. The similarities in the heterogeneous electron transfer rates for the ferri-/ferro-cyanide reaction at both "clean" GCE and Pt, however, downplay the role of such functionalities as redox mediators for GCE. Finally, it should be noted that we have not addressed the question of surface roughness. Thus, the rates for the ferri-/ferro-cyanide on GCE have not been normalized for "effective" area. Work is in progress in attempts to understand the conditions and mechanism(s) of activation at glassy carbon and other carbon electrodes.

### Acknowledgments

The authors would like to acknowledge support from National Science Foundation and The Ohio State University Material Research Laboratory. Helpful discussions with present and past members of the research group are also gratefully acknowledged.

### Literature Cited

1. Zittel, H.E.; Miller, F.J. Anal. Chem., 1965, 37, 200-3.
2. Bjelica, L.; Parsons, R.; Reeves, R.M. Proc. Electrochem. Soc., 1979, 1980, 80-3, 190-212.
3. Bjelica, L.; Parsons, R.; Reeves, R.M. Croat. Chim. Acta, 1980, 53, 211-31.

4. Gunasingham, H.; Fleet, B. Analyst, 1982, 107, 896-902.
5. Bose, S.; Saxena, R.; Bragg, R.H. Ext. Abstr. Progrm.-Bienn. Conf. Carbon, 1977, 13, 369-70.
6. Saxena, R.R. Department of Energy, Report 1976 LBL-5129.
7. Fujihira, M.; Osa, T. Prog. Batteries Sol. Cells, 1979, 2, 244-8.
8. Engstrom, R.C.; Strasser, V.A. Anal. Chem., 1984, 56, 136-41.
9. Stutts, K.J.; Kovach, P.M.; Kuhr, W.G.; Wightman, R.M. Anal. Chem., 1983, 55, 1632-4.
10. Miller, C.W.; Karweik, D.H.; Kuwana, T. in "Recent Advances in Analytical Spectroscopy"; Fuwa, K., Ed.; Pergamon Press: Oxford, England, 1982; 233-47.
11. Zak, J.; Kuwana, T. J. Electroanal. Chem., 1983, 150, 645-64.
12. Thorton, D.C.; Corby, K.T.; Spindel, V.A.; Jordan, J.; Robbat, A., Jr.; Ritstrom, D.J.; Gross, M.; Ritzler, G. Anal. Chem., 1985, 57, 150.
13. Karweik, D.H.; Miller, C.W.; Porter, M.D.; Kuwana, T. in "Industrial Applications of Surface Analysis"; Casper, L.A.; Powell, C.J. Eds.; ACS Symposium series No. 199, American Chemical Society: Washington, D.C., 1982; 98-119.
14. Van der Linden, W.E.; Dieker, J.W. Anal. Chim. Acta, 1980, 119, 1-24.
15. Hu, I.-F.; Karweik, D.H.; Kuwana, T. J. Electroanal. Chem., In Press.
16. Evans, J.F.; Kuwana, T. Anal. Chem., 1977, 49, 1632-35.
17. Evans, J.F.; Kuwana, T. Anal. Chem., 1979, 51, 358-365.
18. Rusling, J.F. Anal. Chem., 1984, 56, 575-8.
19. Nicholson, R.S. Anal. Chem., 1965, 37, 1351.
20. Goldstein, E.L.; Van der Mark, M.R. Electrochim. Acta, 1982, 27, 1079-85.
21. Marcus, R.A. J. Chem. Phys., 1965, 43, 679-701.
22. Dryhurst, G.; Kadish, K.M.; Scheller, F.; Renneberg, R. "Biological Electrochemistry"; Academic Press: New York, 1982; Vol. 1, 259.
23. Stutts, K.J.; Wightman, R.M. Anal. Chem., 1983, 55, 1576-9.
24. Karabinas, P.; Jannakoudakis, D. J. Electroanal. Chem., 1984, 160, 159-67.
25. Mattok, G.L. J. Chem. Soc.(Lond.), 1965, 879, 4728-35.
26. Schreurs, J., Ph.D. Thesis, University of Technology: Eindhoven, The Netherlands, 1983, 69-72.
27. Siegbahn, K.; Nordling, C.; Fahlman, A.; et. al. "Electron Spectroscopy For Chemical Analysis", NTIS AFML-TR-68-189, 1968, 102-12.
28. Britz, D. "Digital Simulation In Electrochemistry", Springer Verlag: Berlin, 1981.
29. Cenas, N.; Rozgaite, J.; Pocius, A.; Kulyz, A. J. Electroanal. Chem., 1983, 154, 121 and references therein.
30. Kao, W.-H.; Kuwana, T. J. Electroanal. Chem., 1984, 169, 167-79.
31. Ross, Jr., P.N. J. Electrochem. Soc., 1979, 126, 67.

RECEIVED June 21, 1985

## Author Index

- Adkins, Sayra R., 57  
Alnot, P., 317  
Asscher, M., 154  
Beebe, Thomas, 404  
Behm, R. J., 317  
Belton, D. N., 80  
Benziger, J. B., 449  
Biebesheimer, V. A., 280  
Brazdil, J. F., 26  
Brundle, C. R., 317  
Bujor, M., 98  
Burwell, R. L., Jr., 385  
Butt, J. B., 385  
Campbell, Charles T., 210  
Carver, James C., 133  
Castner, D. G., 144  
Christmann, K., 222  
Cieslinski, R. C., 37  
Cohen, J. B., 385  
Cowley, J. M., 329  
Cox, D. M., 111  
Dang, T. A., 305  
Davis, Burtron H., 57  
Davis, S. Mark, 133  
Dwyer, D. J., 124  
Eddy, E. L., 305  
Ertl, G., 222  
Feng, S. S., 294  
Fleisch, T. H., 15  
Fripiat, J. J., 98  
Gardner, Lloyd E., 2  
Gelin, Patrick, 404  
Gellman, A. J., 154  
Georgopoulos, P., 385  
Glaeser, L. C., 26  
Gland, J. L., 199  
Goetsch, Duane A., 133  
Golden, William G., 435  
Gonzalez, R. D., 294  
Goodman, D. W., 185  
Goodwin, J. G., Jr., 67  
Grasselli, R. K., 26  
Greegor, R. B., 280  
Grimblot, J., 317  
Haller, Gary L., 464  
Hasenberg, D., 177  
Hawn, D. D., 37  
Hazle, M. A. S., 26  
Hemminger, J. C., 238  
Hercules, D. M., 305  
Hightower, Joe W., 88  
Himelfarb, P. B., 351  
Hopster, H., 317  
Horsley, J. A., 280  
Houalla, M., 305  
Ibach, H., 392  
Jorgensen, S. W., 165  
Jose-Yacaman, M., 351  
Kaldor, A., 111  
Kibby, C. L., 305  
Kingsley, J. R., 238  
Klassen, H. E., 37  
Klier, K., 351  
Koestner, R. J., 199  
Kollin, E. B., 199  
Kunimori, K., 464  
Lester, J. E., 67  
Lyman, C. E., 361  
Lytle, F. W., 253, 280  
Madix, R. J., 165  
Mantell, D. A., 464  
Marcelin, G., 67  
Marks, L. D., 341  
Marques, E. C., 280  
McGovern, S. J., 449  
McIver, R. T., Jr., 238  
Mehicic, M., 26  
Meitzner, G., 253  
Merryfield, Ruth N., 2  
Mitchell, S. F., 67  
Miura, H., 294  
Muller, J. E., 392  
Odier, P., 98  
Papapolymerou, G. A., 177  
Parks, George D., 2  
Peden, C. H. F., 185  
Peri, J. B., 422  
Petrakis, L., 305  
Polzonetti, G., 317  
Ponec, V., 267  
Price, Geoffrey L., 88  
Royce, B. S. H., 449  
Ryali, S. B., 464  
Sandstrom, D. R., 280  
Saperstein, David D., 435  
Saymeh, R., 294  
Schmidt, L. D., 177  
Schwartz, S., 177  
Sherman, M. G., 238  
Simmons, G. W., 351  
Sinfelt, J. H., 253, 280  
Smith, David J., 341  
Somorjai, G. A., 154  
Stohr, J., 199  
Stuve, E. M., 165  
Sun, Y.-M., 80

Targos, William, 374  
Trevor, D. J., 111  
Vannice, M. A., 98  
Via, G. H., 253,280

Wandelt, K., 317  
Watson, P. R., 144  
Whetten, R. L., 111  
White, J. M., 80  
Yates, John T., Jr., 404

## Subject Index

### A

Absorption  
  correction factors, X-ray emission spectroscopy, 364  
  at a metal surface, 552  
Acid fuel cells, catalysts and electrolytes, 575-80  
Activation, carbon surfaces, mechanisms, 583  
Activation energy  
  ethylene oxide production, 212  
  hydrogen adsorption on the Ni(111) surface, 232  
  methanation, effect of sulfur, 193  
Active pair sites, possible formation on CoMo-alumina catalysts, 433f  
Active site structure on the surface, bismuth molybdates, 35f  
Activity measurements, hydrodesulfurization, 4  
Additives, effect on catalytic reactions, 186  
Adsorbed CO layers, bonding and interactions, 559-61  
Adsorbed molecules, vibrational analysis, 392-403  
Adsorbed species and processes on surfaces, IR spectroscopic characterizations, 404-19  
Adsorption  
  clean and sulfur-modified metal surfaces, 199-208  
  effect of electronic structure changes, 271-74,275f  
  equilibrium constant, definition, 178  
  metal surfaces, SIMS studies, 317-26  
  molecular, EMIRS and SNIFTIRS studies, 562-64  
  reactants, effect of velocity on rate of surface reactions, 232,235  
Aerosols  
  difference spectra, 454f  
  photoacoustic spectra, 453f  
Air cathodes, promoters, 576

### Alloys

  binary, surface and bulk characterization, 307-10  
  diffraction studies, 389  
  effect on hydrogenolytic selectivity of hydrocarbon reactions, 277-78  
  elements, Auger electron spectroscopic signals, 269  
  homogeneous binary, ESCA intensity ratio, 306-7  
  Pt and Cu, catalytic and side effects, 274-76  
  Pt and Ti, surface chemistry, 577-78  
  ternary, surface and bulk characterization, 310-12

### Alumina

  difference spectra, 458f  
  hydroxyl-group stretching and bending modes, 457,459  
  IR photoacoustic spectroscopy, 449-61  
  metal precursor-support interactions, 302-3  
  photoacoustic spectra, 456f  
  thermal diffusion lengths, 450  
Alumina-CoMo hydrodesulfurization catalysts, 422-34

Alumina-supported Cu catalyst, X-ray photoelectron spectra, 43f  
Alumina-supported metals, multitechnique characterization, 374-83  
Aluminosilicates, intercalates of, role in heterogeneous catalysis, 472-83

### Aluminum

  compounds containing  
  Auger chemical state plot, 45f  
  chemical state data, 45t  
  X-ray photoelectron spectra, catalysts at various stages of treatment, 53-54f  
Aluminum-cation-exchanged clays, IR spectra, 477f  
Aluminum-Cu catalyst  
  application of X-ray photoelectron spectroscopy, 46

Targos, William, 374  
Trevor, D. J., 111  
Vannice, M. A., 98  
Via, G. H., 253,280

Wandelt, K., 317  
Watson, P. R., 144  
Whetten, R. L., 111  
White, J. M., 80  
Yates, John T., Jr., 404

## Subject Index

### A

Absorption  
  correction factors, X-ray emission spectroscopy, 364  
  at a metal surface, 552  
Acid fuel cells, catalysts and electrolytes, 575-80  
Activation, carbon surfaces, mechanisms, 583  
Activation energy  
  ethylene oxide production, 212  
  hydrogen adsorption on the Ni(111) surface, 232  
  methanation, effect of sulfur, 193  
Active pair sites, possible formation on CoMo-alumina catalysts, 433f  
Active site structure on the surface, bismuth molybdates, 35f  
Activity measurements, hydrodesulfurization, 4  
Additives, effect on catalytic reactions, 186  
Adsorbed CO layers, bonding and interactions, 559-61  
Adsorbed molecules, vibrational analysis, 392-403  
Adsorbed species and processes on surfaces, IR spectroscopic characterizations, 404-19  
Adsorption  
  clean and sulfur-modified metal surfaces, 199-208  
  effect of electronic structure changes, 271-74,275f  
  equilibrium constant, definition, 178  
  metal surfaces, SIMS studies, 317-26  
  molecular, EMIRS and SNIFTIRS studies, 562-64  
  reactants, effect of velocity on rate of surface reactions, 232,235  
Aerosols  
  difference spectra, 454f  
  photoacoustic spectra, 453f  
Air cathodes, promoters, 576

### Alloys

  binary, surface and bulk characterization, 307-10  
  diffraction studies, 389  
  effect on hydrogenolytic selectivity of hydrocarbon reactions, 277-78  
  elements, Auger electron spectroscopic signals, 269  
  homogeneous binary, ESCA intensity ratio, 306-7  
  Pt and Cu, catalytic and side effects, 274-76  
  Pt and Ti, surface chemistry, 577-78  
  ternary, surface and bulk characterization, 310-12

### Alumina

  difference spectra, 458f  
  hydroxyl-group stretching and bending modes, 457,459  
  IR photoacoustic spectroscopy, 449-61  
  metal precursor-support interactions, 302-3  
  photoacoustic spectra, 456f  
  thermal diffusion lengths, 450  
Alumina-CoMo hydrodesulfurization catalysts, 422-34

Alumina-supported Cu catalyst, X-ray photoelectron spectra, 43f  
Alumina-supported metals, multitechnique characterization, 374-83  
Aluminosilicates, intercalates of, role in heterogeneous catalysis, 472-83

### Aluminum

  compounds containing  
    Auger chemical state plot, 45f  
    chemical state data, 45t  
  X-ray photoelectron spectra, catalysts at various stages of treatment, 53-54f  
Aluminum-cation-exchanged clays, IR spectra, 477f  
Aluminum-Cu catalyst  
  application of X-ray photoelectron spectroscopy, 46

- Aluminum-Cu catalyst--Continued**  
 elemental atomic ratios, 48t  
 X-ray photoelectron spectroscopy wide scans, 47f
- Amines formed from cyclohexylamine and benzylamine, relative molar yields, 477f**
- Ammonia**  
 chemical bonding to  
 Al(100), 397-98, 399f  
 decomposition on metals, 179-82  
 elimination from amines, 476  
 on Fe(110), dipole active modes, 396f  
 reaction on metals, 178  
 reaction with methane on Rh, 183, 184f  
 synthesis on metal single-crystal surfaces, 154-64
- Amoxidation, propylene, 28, 31f**
- Analytical electron microscopy characterization of catalysts, 361-71**  
 signals generated in a thin specimen, 363f  
 specimen preparation, 364-65  
 techniques, 362-64
- Angle of incidence, effect on the sticking probability of molecules, 227**
- Angular distribution of the relative scattered intensity**  
 deuterium molecules, 226, 228f  
 hydrogen molecules, 224-26f
- Anisotropic energy barriers, magnetic systems, 519**
- Aromatics from n-paraffins over Te-NaX zeolite, 88-96**
- Arrhenius plots**  
 ethane hydrogenolysis, 192f  
 hydrodesulfurization of thiophene on the Mo(100) surface, 160f  
 methane synthesis, 189, 191f, 192f
- Arsenic poisoning, hydrodesulfurization catalysts, 2-13**
- Arsenic reference materials, binding energies, 5t**
- Ascorbic acid at glassy carbon electrodes**  
 cyclic voltammograms, 588f, 592-94  
 oxidation, 585-87, 592-94
- Asymmetric carboxylate stretch, cadmium arachidate on silver, 442-43**
- Atom-addition mechanism of cluster growth, 112, 114f**
- Atomic cluster size, effect on the proportion of edge and surface atoms, 345, 346f, 348f**
- Atomic form factor, electron shells, 386**
- Atomic imaging of particle surfaces, 341-48**
- Atomic oxygen coverage on silver, selective epoxidation of ethylene, 214, 216**
- Atomic structure of Pt catalysts, determination by X-ray absorption spectroscopy, 280-92**
- Atomic surface structure, gold, 342-44**
- Auger electron spectroscopy characterization of TiO<sub>2</sub> single crystal covered with Pt, 101**  
 chemical state plot, Al compounds, 45f  
 effect of beam on the composition of the TiO<sub>2</sub>(100) surface, 106  
 electron-beam damage, 104  
 oxidized Ti, 82f  
 Pt following exposure to NO, 180f  
 positions and relative intensities of transitions, 44f  
 rutile(100) single-crystal and TiO<sub>2</sub> powder surfaces, 98-108  
 signals of elements in an alloy, 269  
 study of Pt deposition on Ti, 84-85  
 study of small particles, 334  
 surface of Pt-TiO<sub>2</sub> powder, 105f  
 TiO<sub>2</sub>(100) during cleaning procedures, 100f  
 TiO<sub>2</sub> overlayers on Pt, 577
- Aurichalcite mineral**  
 bright-field images, 358f  
 CuO diffraction spots, 354, 356, 357f  
 electron diffraction pattern, 357-58f  
 electron micrographs, 353f, 357-59f  
 X-ray diffraction spectra, 355f  
 Zn-to-Cu ratios, 354t  
 ZnO diffraction spots, 354-60  
 synthetic, electron micrographs, 353f

## B

- Backbonding, adsorbed CO layers, 559-60**
- Backscattering atoms, contributions to EXAFS of Os-Cu catalyst, 260f**
- Beidellite, sodium- and aluminum-cation-exchanged forms, magic angle spinning NMR spectra, 479f**
- Bend, internal, adsorbed molecules, 401**
- Benzene**  
 conversion of cyclohexane into, 94  
 on gold, 343, 346f  
 motional state, phase diagram, 496f

- Benzene--Continued  
 in Pt cluster reactions, 120,121f  
 in X-type zeolites, dynamics, 485-96
- Bimetallic catalysts**  
 containing Pt, surface chemistry and catalysis, 267-78  
 reduced, valence state of Re, 57-65  
 structure, 253-65
- Bimetallic clusters**  
 effect of support-metal precursor interactions, 294-304  
 EXAFS function, 254-55
- Binary alloys**  
 methanation activity, 312-15  
 preparation, 306  
 surface and bulk  
   characterization, 307-10
- Binding energies**  
 arsenic reference materials, 5t  
 hydrodesulfurization catalysts, 6t  
 Ti in different chemical states, 578t
- Bipolar difference band, origin, 554f**
- Bismuth molybdates**  
 active site structure on the surface, 35f  
 catalytic behavior and phase composition, 29-33  
 characterization by analytical electron microscopy, 366,367f  
 oxide ions in, identification, 33-35  
 Raman data, 31t  
 Raman spectra, 34t  
 redox processes and solid state transformations, 28-29  
 surface restructuring, 29,30f
- Boehmite**  
 difference spectra, 458f  
 photoacoustic spectra, 456f
- Boltzmann distribution, population ratio, 495**
- Bond cleavage with deuterium, 91-92**
- Bonding and interactions in adsorbed CO layers, 559-61**
- Boron-doped carbons**  
 diamagnetic  
   susceptibility, 511,512f  
 Fe on, 507,511-13
- Boundary condition of small surface area, effect on surface reconstructions and chemisorption, 345**
- Bridged-to-linear CO conversion isotopic CO experiments, 412f**  
 one-dimensional model, 413f
- Bright-field STEM images**  
 bismuth molybdate, 367f  
 Cu-ZnO catalyst, 371f  
 mineral aurichalcite, 358f  
 zeolite ZSM-5, 269f
- Broken-bond model, description, 268**
- Bronsted base behavior of adsorbed oxygen, 175**
- C
- Cadmium arachidate**  
 on nickel, 444-46  
 on silver, 437,439-41
- Cadmium sulfide**  
 hydrogen generation, 567,568f  
 systems, induction times, 570  
 X-ray powder diffraction spectra, 568f
- Cadmium sulfide-Nafion, surface spectroscopy, 570-73**
- Cadmium sulfide-Pt-Nafion, surface spectroscopy, 566-73**
- Calcined mineral aurichalcite, electron micrographs, 357-59f**
- Carbon-carbon stretching vibration, 393**
- Carbon clusters, 112,115f,116**
- Carbon dioxide**  
 adsorption on alumina, 461  
 IR spectra for CO oxidation on Pt, 468f  
 production, steady state rate, 212,213f
- Carbon map, untreated catalyst, 50f**
- Carbon monoxide**  
 adsorbed on bimetallic catalysts  
   frequency of stretch vibrations, 272,275f  
   thermal desorption, 271-73  
 adsorbed on CoMo-alumina catalysts, IR spectra, 431f  
 adsorbed layers, bonding and interactions, 559-61  
 adsorption on the sulfur-modified Ni(100) surface, 199-200  
 chemisorption on Pd(111), 414f  
 conversion activity, correlation to surface structure of oxidized alloys, 312-15  
 hydrogenation, effect of Cu, 193,196f  
 hydrogenation catalysts, frequency response chemisorption studies, 67-77  
 hydrogenation of various Fe-carbon catalysts, 511-13  
 IR spectra for oxidation on Pt, 468f  
 oxidation on Pt, 464-69  
 on Pd-silica, chemisorption, 407-15  
 reaction with NO on Pt, 181,183  
 rotor absorbances for increasing surface coverage, 420f  
 thermal desorption spectra, 83t  
 vibrational analysis, 395

- Carbon peak intensities, TiO<sub>2</sub> powder catalysts, 104
- Carbon-14 tracers, reaction intermediate studies, 89-91
- Carbonaceous surfaces, modification, characterization, and uses for electrocatalysis, 582-94
- Carboxylate stretches, cadmium arachidate on silver, 442-43
- Catalysis
- effect of geometry of particle surfaces, 345-48
  - isotopic tracers, 88-96
  - selective epoxidation of ethylene, 210-20
  - and surface chemistry, Pt-bimetallic catalysts, 267-78
  - surface structure and reaction dynamics, 222-36
- Catalysts
- alloy of Pt with Cu, effects, 274,275f
  - bimetallic, structure, 253-65
  - characterization, analytical electron microscopy, 361-71
  - CO hydrogenation, 67-77
    - reduction and sulfidation behavior, 144-51
  - composition
    - silica-supported Ru-Ir bimetallic catalysts, 297
    - silica-supported Ru-Rh bimetallic clusters, 296-97
  - derived from binary and ternary intermetallics, surface characterization and methanation activity, 305-15
  - and electrolytes for acid fuel cells, 575-80
  - hydrodesulfurization
    - arsenic poisoning, 2-13
    - CoMo-alumina, 422-34
    - preparation, 3
  - iron Fischer-Tropsch, surface synthesis at high pressure, 124-32
  - LEISS applications, 133-43
  - materials, levels of analysis, 363f
  - methanol synthesis, 21-23
  - morphology studies, 140-42
  - new, current status, 579-80
  - precursor, methanol synthesis, microanalysis, 351-60
  - reactions, effect of additives, 186
  - reduced bimetallic, preparation, 58-59
- Rh
- hydrogen adsorption and desorption isotherms, 71f
  - preparation, 69
  - properties, 69t
- Catalysts--Continued
- selective oxidation, 26-35
  - sulfiding, 3-4
  - supported metal, diffraction, 385-89
  - surface sensitivity, 137-38
  - systems
    - off-axis reaction cell, 40-42
    - surface analysis techniques, 37-56
- Catalytic behavior
- and phase composition, Bi-Fe molybdates, 29-33
  - and spectroscopic measurements, selective oxidation catalysts, 26-35
- Cell, spectroelectrochemical, IR spectroscopy, 551,554f
- Charge-donating and charge-withdrawing ethylene, 175
- Chemical bonding to Al(100)
- ammonia, 397-98,399f
  - water, 397-98,399f
- Chemical impurities and gas environment, effect on particle morphology, 345,347,348f
- Chemical shifts for some sheet silicates, 478t
- Chemical state data, Al compounds, 45t
- Chemically modified single-crystal surfaces, kinetics, 190,192-97
- Chemisorption
- CO hydrogenation catalysts, 67-77
  - CO on Pd-silica, 407-15
  - frequency response, 70-77
  - static, 69-72
- Cherry model configuration, bimetallic clusters, 295
- Chlorine promoters, selective epoxidation of ethylene, 216-18
- Clays
- intercalates of, role in heterogeneous catalysis, 472-83
  - reactions catalyzed by, 473
- Clusters
- of atoms, 111-22
  - ion characterization during oxygen adsorption and oxidation, SIMS studies, 319-21
  - reactor, 120,121f
  - size distribution, control, 112
  - supported bimetallic, 294-304
- Coadsorption
- and decomposition reactions at metal surfaces, SIMS studies, 325-26
  - oxygen interactions and reactions on Pd(100), 165-76
- Cobalt
- effect of addition to Mo-alumina, 425-28,431f
  - effect of ZSM-5 addition on product compositions, 508t



- Cobalt--Continued  
 nature in CoMo catalysts, 423-25
- Cobalt catalysts  
 activation, 144  
 electron microscopic analysis, 146  
 preparation, 145  
 reduction and sulfidation  
 behavior, 144-51  
 X-ray absorption  
 spectroscopy, 145-47  
 X-ray photoelectron  
 spectroscopy, 145
- Cobalt-Mo-alumina hydrodesulfurization  
 catalysts, 422-34
- Cobalt-Ni(100), coverage and secondary  
 ion yield  
 relationship, 321, 323-24, 326f
- Cobaltous oxide, physisorption,  
 influence on surface SiOH  
 groups, 417f
- Cobaltous oxide catalysts  
 characterization, 146  
 reduction, 146, 148  
 sulfidation, 149, 151
- Coefficient of harmonic number,  
 definition, 385
- Collective magnetic excitation, mag-  
 netic particles, 520
- Composition ratio of two elements,  
 thin specimen, 364
- Computer simulations, Mossbauer spec-  
 tra of magnetite particles, 530f
- Computerized IR studies of  
 CoMo-alumina hydrodesulfurization  
 catalysts, 422-34
- Contamination, surface, dependence of  
 time on pressure, 179
- Controlled reactions, vibrational  
 analysis, 395
- Convergent-beam electron diffraction  
 patterns, small particles, 335
- Copper  
 alloying with Pt, 274-76  
 chemical state changes in a catalyst  
 in feed gas, 21, 22f  
 dark-field imaging of  
 particles, 356, 359f  
 effect on CO hydrogenation, 193, 196f  
 effect on ethane  
 hydrogenolysis, 195, 196f
- Copper-Al catalyst  
 application of X-ray photoelectron  
 spectroscopy, 46, 47f  
 elemental atomic ratios, 48t
- Copper catalysts  
 EXAFS data, 258f  
 EXAFS envelope functions, 259f  
 X-ray photoelectron spectra, 43f, 55f
- Copper-Ni alloy surfaces,  
 reactions, 324-25
- Copper-Os clusters, 255-61
- Copper-Rh clusters, 261-62
- Copper-Ru clusters, 255-61
- Copper-ZnO catalyst, characterization  
 by analytical electron  
 microscopy, 368, 370, 371f
- Copper-ZnO methanol synthesis catalyst  
 precursor, microanalysis, 351-60
- Coverage and secondary ion yield  
 relationship,  
 Ni(100)-CO, 321, 323-24, 326f
- Cupric oxide, diffraction spots,  
 aurichalcite mineral, 354, 356, 357f
- Cyclic voltammograms  
 ascorbic acid at a glassy carbon  
 electrode, 588f  
 Fe compound adsorbed on carbon, 547  
 Fe compound dispersed on carbon, 546  
 oxidation of ascorbic acid, 593f
- Cyclohexane, conversion into  
 benzene, 94
- D
- Dark-field imaging  
 Cu and ZnO particles, 356, 359f  
 Pd on carbon, 369f
- Decomposition  
 and adsorption on clean and sulfur-  
 modified metal surfaces, 199-208  
 and coadsorption reactions at metal  
 surfaces, SIMS studies, 325-26  
 on metals  
 nitrogen dioxide, 181-82  
 nitrous oxide, 181-82  
 vibrational analysis, 395
- Dehydrocyclization, n-paraffins over  
 Te-NaX, 94, 96f
- Dehydrogenation  
 ethylene on Pd(100), 168  
 sequential, of methanethiol on the  
 Pt(111) surface, 202-6  
 use of catalysts, 94-95
- Depth profile, secondary ion mass  
 spectrometry, Pt on oxidized  
 Ti, 83, 85f
- Desorption spectra, CO thermal, 83t
- Deuterium  
 angular distribution of the relative  
 scattered intensity, 226, 228f  
 bond cleavage, 91-92  
 effect on low-frequency vibrational  
 models, 402  
 exchange reaction with  
 hydrogen, 231-32
- Deuterium NMR spectra  
 benzene-d6 in (Cs,Na)X, 488f  
 benzene-d6 in (Na)X, 489-91  
 polycrystalline benzene-d6, 486

- Diamagnetic susceptibility of carbons,  
effect of boron doping, 511,512f
- Diatomic molecules  
direct inelastic scattering, 226  
elastic scattering, 224-26,228f
- Difference spectra  
alumina, 458f  
CO chemisorption on Pd-silica, 410f  
Pt catalyst, 387,388f  
silicas, 454f
- Differential pulse voltammetry, glassy  
carbon electrode, 589f
- Diffraction patterns  
gold, 348f  
Pt catalyst, 387,388f  
single crystal, statistical  
information, 337,339  
small particles, 335-37,338f  
from supported metal  
catalysts, 385-89
- Diffraction spots  
CuO, aurichalcite  
mineral, 354,356,357f  
ZnO, aurichalcite mineral, 354-60
- Diffraction techniques and electron  
microscopy, study of small  
particles, 329-39
- Digital X-ray imaging  
catalytic materials, 365  
Pd on carbon, 369f  
zeolite ZSM-5, 369f
- Dilution, effect on dispersion, sup-  
ported metal catalysts, 298
- Dipole active modes, ammonia on  
Fe(110), 396f
- Dipole-dipole coupling, adsorbed CO  
layers, 560
- Dipole moments  
ammonia adsorbed on  
Al(100), 400f  
water adsorbed on  
Al(100), 399f
- Direct four-electron pathway, oxygen  
reduction, 536
- Direct inelastic scattering of  
diatomic molecules, 226
- Dissociative adsorption of hydrogen  
molecules, 226-29
- Dynamics of benzene in X-type  
zeolites, 485-96
- E
- Edge resonance, Pt catalyst, 286-89
- Elastic scattering of diatomic  
molecules, 224-26,228f
- Electric fields, effect on surface  
bonds of alumina and silica, 460
- Electrocatalysis, modification,  
characterization, and uses of car-  
bonaceous surfaces, 582-94
- Electrocatalysts of oxygen involving  
transition metal macrocycles,  
spectroscopic studies, 535-49
- Electrocatalytic reactions, study of  
molecular structure with IR  
spectroscopy, 550-64
- Electrochemical features, reactions at  
glassy carbon electrodes, 585-87
- Electrochemically activated stark  
effect, 564
- Electrochemically modulated IR spec-  
troscopy (EMIRS)  
absorption bands, 553  
description, 551  
electrocatalytic  
oxidations, 553,556-59,561f  
hydrogen absorption, 553,555f  
molecular adsorption, 562-64
- Electrode potential, effect on elec-  
tronegativity of atoms in an  
electrode surface, 559
- Electrolytes, acid fuel cells, 575-80
- Electron-beam damage, Auger electron  
spectroscopy, 104
- Electron diffraction pattern, mineral  
aurichalcite, 357-58f
- Electron energy loss spectroscopy  
(EELS)  
catalyst characterization, 364  
Cu-ZnO catalyst, 371f  
ethylene on clean and oxygen-covered  
Pd(100), 169f  
study of small particles, 332,334  
vibrational analysis of adsorbed  
molecules, 392-403
- Electron micrographs  
calcined mineral  
aurichalcite, 357-59f  
cubic MgO crystal, 333f  
mineral aurichalcite, 353f,357-59f  
synthetic aurichalcite, 353f
- Electron microscopy  
analytical, characterization of  
catalysts, 361-71  
cobalt catalysts, 146  
small particles, 329-39
- Electron shells, atomic form  
factor, 386
- Electron spectroscopy for chemical  
analysis (ESCA)  
intensity ratio, homogeneous binary  
alloy, 306-7  
pretreatment, reduced bimetallic  
catalysts, 59  
reduced Re catalysts, 64f

- Electron-stimulated desorption  
 effects on surface composition of  
 TiO<sub>2</sub>, 101,104  
 rutile(100) single-crystal and TiO<sub>2</sub>  
 powder surfaces, 98-108
- Electron-transfer rate, Marcus rate  
 theory, 586
- Electronegativity of atoms in an  
 electrode surface, effect of  
 electrode potential, 559
- Electronic dipole transitions, Pt  
 catalysts, 285
- Electronic effects of alloying, 267
- Electronic spectra, Cu, changes  
 upon reduction in hydrogen, 21,23f
- Electronic structure  
 calculations, 397-401  
 clusters of atoms, 116  
 effect of changes on  
 adsorption, 271-74,275f  
 Pt catalysts, determination by X-ray  
 absorption spectroscopy, 280-92  
 Pt-Cu system changes, 269,271
- Elimination of ammonia from  
 amines, 476
- Energy curves  
 ammonia adsorbed on  
 Al(100), 400f  
 water adsorbed on  
 Al(100), 399f
- Energy dispersive X-ray spectroscopy  
 (EDS)  
 analysis of Fe on alumina, 383f  
 analysis of Pt crystallite, 378f  
 study of small particles, 332,334
- Epoxidation of ethylene catalyzed by  
 silver, selective, 210-20
- Ethane hydrogenolysis  
 effect of Cu, 195,196f  
 over Ru catalysts, 190-96  
 effect of sulfur, 193,194f
- Ethylene  
 adsorption and decomposition on  
 Pt(111) surface, 206-8  
 conversion into ethylene oxide, 212  
 dehydrogenation on Pd(100), 168  
 reaction with coadsorbed oxygen on  
 Pd(100), 166-70  
 selective oxidation catalyzed by  
 silver, 210-20
- Ethylene oxide production, steady  
 state rate, 212,213f
- Exchange reaction,  
 deuterium-hydrogen, 231-32
- Extended X-ray absorption fine struc-  
 ture spectroscopy (EXAFS)  
 bimetallic catalysts, 253-65  
 data analysis, 254-55,282-85  
 description, 280-81
- Extended X-ray absorption fine struc-  
 ture spectroscopy (EXAFS)--Continued  
 function  
 bimetallic cluster, 254-55  
 definition, 254  
 uses, 253
- F
- Faulting, small particles, 336
- Fermi energy, Pt catalysts, 289
- Fermi levels, CO hydrogenation  
 of various Fe-carbon  
 catalysts, 511-13
- Ferric chloride intercalates of  
 graphite, 481
- Ferric oxide  
 production of particles, 522-23  
 supported particles,  
 characterization, 518-32  
 in ZSM-5, particle size  
 distribution, 509f
- Ferromagnet, hysteresis curve,  
 schematic, 500f
- Fischer-Tropsch catalysts  
 components, 305  
 containing Fe, surface synthesis  
 at high pressure, 124-32
- Fluorescence correction factors, X-ray  
 emission spectroscopy, 364
- Fourier transform  
 EXAFS data, Pt and Pt  
 catalysts, 283,284f  
 general EXAFS function, 282
- Fourier transform IR (FTIR)  
 spectroscopy  
 CO oxidation on Pt, 466  
 problems, 466-67  
 surface adsorbates and surface-  
 mediated reactions, 435-47
- Frequency-response chemisorption  
 studies of CO hydrogenation  
 catalysts, 67-77
- Frequency shift, Raman band for  
 Fe compound adsorbed on a  
 silver electrode, 541f
- Frequency of stretch vibrations, CO  
 adsorbed on bimetallic  
 catalysts, 272,275f
- Fuel cells, acidic catalysts and  
 electrolytes, 575-80
- G
- Gas environment and chemical  
 impurities, effect on particle  
 morphology, 345,347,348f

- Gas lattice structures, unreconstructed Ni(1x1) surface, 229
- Geometrical effects of alloying, 267
- Geometry of particle surfaces, effect on catalysis, 345-48
- Gibbsite
- difference spectra, 458f
  - photoacoustic spectra, 456f
- Glassy carbon electrodes
- differential pulse voltammetry, 589f
  - preparation, 583, 585
  - reactions
    - electrochemical features, 585-87
    - molecular characterization, 587-94  - redox behavior of
    - 1,4-dihydrobenzene, 584f
- Gold
- atomic surface structure, 342-44
  - benzene on, 343, 346f
  - hill and valley
    - reconstruction, 343, 344f  - image and diffraction pattern, 348f
  - on MgO crystal, STEM image, 333f
  - microfaceted region of crystals, 345, 348f
  - multiply twinned particle, 348f
  - 2x1 reconstruction, 342-43, 344f
  - Shockley partial dislocation, 343, 344f
- Graphite intercalates
- reactions catalyzed by, 473
  - reduced, activities and selectivities, 482t
  - role in heterogeneous catalysis, 472-83
- Grazing angle measurement chamber, optical, schematic, 438f
- H
- Harmonic number, coefficient, definition, 385
- Heterogeneous catalysis, role of intercalates, 472-83
- Hexane, reaction with hydrogen, 89, 90f
- High-resolution EELS
- increasing hydrogen sulfide exposures on the Pt(111) surface, 201f
  - sequential CH<sub>3</sub>SH decomposition on the Pt(111) surface, 203f
- High-resolution electron microscopy, general discussion, 342
- Hindered rotation, adsorbed molecules, 398
- Hindered translation, adsorbed molecules, 398
- Hohenberg-Kohn-Sham calculation, water and ammonia adsorbed on Al(100), 397
- Homogeneous binary alloy, ESCA intensity ratio, 306-7
- Hydrocarbon synthesis
- over iron carbide, steady state rates, 127, 129
  - and rearrangement over clean and chemically modified surfaces, 185-97
- Hydrodesulfurization
- activity measurements, 4
  - on metal single-crystal surfaces, 154-64
  - of thiophene, 158, 160-62
- Hydrodesulfurization catalysts
- arsenic poisoning, 2-13
  - CoMo-alumina, 422-34
- Hydrogen
- adsorption, EMIRS studies, 553, 555f
  - adsorption isotherms, Rh catalysts, 71f
  - adsorption on the Ni(111) surface, activation energy, 232
  - angular distribution of the relative scattered intensity, 224-26f
  - dissociative adsorption, 226-29
  - generation from CdS, 567, 568f
  - generation in a Nafion film, time dependence, 567, 569f
  - interacting with a solid surface, potential energy diagram, 234f
  - lattice gas phase, structure model, 234f
  - stretching vibrations, 393
  - surface phases, 229-31
- Hydrogen cyanide, synthesis on Rh, 183, 184f
- Hydrogen-deuterium exchange reaction, 231-32
- Hydrogen sulfide, adsorption and decomposition on the clean and S-covered Pt(111) surface, 200
- Hydrogen-transfer reactions, water, methanol, and oxygen, 170, 172, 175
- Hydrogenation reactions, 188
- Hydrogenolysis of ethane
- over Ru catalysts, 190-96
  - effect of sulfur, 193, 194f
- Hydrogenolytic selectivity of hydrocarbon reactions, effect of alloys, 277-78
- Hydroxyl group
- reactions with coadsorbed oxygen on Pd(100), 170-71
  - on silica, proton donor function, 300-301
  - stretching and bending modes

Hydroxyl group--Continued

- alumina, 457,459
  - silica, 452,455
- Hysteresis curve for a ferromagnet,  
schematic, 500f

## I

- Image and diffraction pattern,  
gold, 348f
- Imaginary response functions, 73f,75f
- Imaging
- atomic, particle surfaces, 341-48
  - digital, using X-ray signals,  
catalyst materials, 365
- Incidence angle, effect on the sticking  
probability of molecules, 227
- Induction period
- CdS systems, 570
  - promoted and unpromoted Fe  
powder, 131
- Inelastic direct scattering of  
diatomic molecules, 226
- Infrared (IR) spectroscopy
- advantages as a probe of surface  
species character, 404-5
  - aluminum-cation-exchanged  
clays, 477f
  - CO adsorbed on CoMo-alumina  
catalysts, 431f
  - characterization of adsorbed species  
and processes on  
surfaces, 404-19
  - CoMo-alumina hydrodesulfuriza-  
tion catalysts, 422-34
  - developments, 405
  - lineshape comparison, various states  
of CO, 418f
  - NO adsorbed on 2% Co-alumina, 424f
  - NO adsorbed on CoMo-alumina  
catalysts, 426-27f,429f
  - NO isotopes adsorbed on 2% Co-Aero  
1000 alumina, 424f
  - photoacoustic, silica and  
alumina, 449-61
  - physisorbed CO species on silica, 416f
  - sodium-cation-exchanged clays, 477f
  - study of molecular structure in  
electrocatalytic and related  
reactions, 550-64
- Insulating surfaces, LEISS, 135,139f
- Intensities, SIMS clusters for the  
Ni(100)-CO system, 326f
- Interatomic transition, Ti, 106
- Intercalates, role in heterogeneous  
catalysis, 472-83
- Internal bend, adsorbed molecules, 401
- Internal energy, CO oxidation on Pt,  
coverage dependence, 464-69
- Internal stretch, adsorbed  
molecules, 401
- Interstitial Ti formation, 107
- Ion intensity ratios, calcined  
catalyst, 142f
- Ion scattering, low-energy applica-  
tions to catalysts, 133-43
- Ion survival probability  
calcined catalyst, 142f
- definition, 137
- Ionization potential, clusters of  
atoms, 116
- Iridium catalysts, preparation, 295-96
- Iridium-Pt clusters, 262-64
- Iridium-Rh clusters, 264-65
- Iron
- on alumina, EDS analysis, 383f
  - on boron-doped carbons, 507,511-13
  - on carbons, 513-15
  - cluster ionization  
thresholds, 116,117f
  - crystal surfaces
    - kinetics of ammonia synthesis, 156
    - structure sensitivity of ammonia  
synthesis, 156-57  - on doped-carbon catalysts, magnetic  
and Mossbauer  
characterization, 498-516
  - and Fe-Co-zeolite systems, 504-10
  - powder
    - potassium-modified, X-ray  
photoelectron spectra, 129-32
    - preparation, 125
- Iron-bismuth molybdates
- catalytic behavior and phase  
composition, 29-33
  - Raman data, 31f
- Iron carbide, hydrocarbon synthesis  
over, steady state rates, 127,129
- Iron Fischer-Tropsch catalysts, sur-  
face synthesis at high  
pressure, 124-32
- Iron surface concentrations, untreated  
and oxidized alloys, 310-12
- Iron-zeolite, on doped-carbon  
catalysts, magnetic and Mossbauer  
characterization, 498-516
- Isomer shift, Mossbauer  
spectroscopy, 502
- Isotherms, desorption, and hydrogen  
adsorption, Rh catalysts, 71f
- Isotopes, vibrational analysis of  
adsorbed molecules, 394
- Isotopic CO experiments, bridged-to-  
linear CO conversion, 412f
- Isotopic tracers in catalysis, 88-96

## K

- Kinetic description, surface composition, 268
- Kinetic energy of momentum, effect on the sticking probability of molecules, 227
- Kinetics
- ammonia synthesis
    - Fe crystal surfaces, 156
    - Re crystal surfaces, 157-58
  - CO hydrogenation of various
    - Fe-carbon catalysts, 511-13
    - chemically modified single-crystal surfaces, 190,192-97
    - selective oxidation catalysts, 27
    - structure-insensitive reactions over clean single-crystal surfaces, 188-89,191f
    - structure-sensitive reactions over clean single-crystal surfaces, 190-92
    - thiophene hydrodesulfurization, Mo(100) crystal surface, 158,160-6
- Klebsch-Gordon coefficients for randomly oriented magnetic moments, 526
- L
- Landau diamagnetism
- boron-doped carbons, 507
  - graphite and graphitic carbons, 504
- Langevin diamagnetism
- boron-doped carbons, 507
  - closed-shell ions, zeolites, and covalent organic compounds, 502,504
- Langevin function, relative magnetization of superparamagnetic clusters, 501
- Langmuir-Hinshelwood mechanism, oxidation of CO on metals, 464
- Langmuir-Hinshelwood rate expressions, 178
- Laponite, aluminum-cation-exchanged sample, magic angle spinning NMR spectra, 480f
- Lattice gas phase, hydrogen, structure model, 234f
- Lattice gas structures, unreconstructed Ni(1x1) surface, 229
- Lennard-Jones potential energy diagram, 224
- Ligand effects of alloying, 267
- Lone-pair orbital of a molecule, bonding to a metal, 399f
- Low-energy ion-scattering spectroscopy (LEISS)
- applications to catalysts, 133-43
  - description, 133-34
  - fundamental process, 136f
  - metals dispersion from, 138-40
  - molybdenum disulfide, 137-38
  - qualitative aspects, 134-35
  - quantitative aspects, 135,137
  - relative intensities of peaks as a function of ion energy, 135,136f
- Low-field magnetic susceptibility, supported particle growth studies, 528
- M
- Macrocycles, transition metal, oxygen reduction, 537
- Magic angle spinning NMR spectra
- aluminum-cation-exchanged sample of Laponite, 480f
  - sodium- and aluminum-cation-exchanged forms of beidellite, 479f
- Magnesium oxide crystal
- cubic, electron micrograph, 333f
  - gold crystals, STEM image, 333f
- Magnetic characterizations, Fe-zeolite and Fe or Ru on doped-carbon catalysts, 498-516
- Magnetic dipole splitting, Mossbauer spectroscopy, 502
- Magnetic excitation, collective, magnetic particles, 520
- Magnetic moments
- for a group of particles, 521-22
  - superparamagnetic clusters, 499-501
- Magnetic properties, metal clusters, 116,118-19f
- Magnetic relaxation, effect on the shape of Mossbauer spectra, 519
- Magnetic susceptibility
- characterization of supported iron oxide particles, 518-32
  - theory, 521-22
- Magnetite particles, Mossbauer spectra, 524-25f
- Marcus rate theory, electron transfer rate, 586
- Mass spectra, time-of-flight, Pt cluster reactions with benzene, 120,121f
- Matrix elements and vibrational frequencies, water and ammonia adsorbed on metals, 401-3
- Metal(s)
- dispersion from LEISS, 138-40

- Metal(s)--Continued**  
 supported, multitechnique characterization, 374-83
- Metal catalysts, supported,**  
 diffraction, 385-89
- Metal precursor mobilities**  
 catalyst pretreatment, 298  
 determination, 296
- Metal-support precursor interactions,**  
 effect on the surface composition of supported bimetallic clusters, 294-304
- Metal surfaces**  
 absorption and reflection, 552  
 adsorption and reaction, SIMS studies, 317-26  
 ammonia synthesis and hydrodesulfurization, 154-64  
 sulfur-modified, adsorption and decomposition, 199-208
- Metal-titania systems,**  
 spectroscopy, 80-86
- Methanation**  
 rate, promoted and unpromoted iron powder, 131  
 reactions, 186  
 supported bimetallic clusters, 300,301f
- Methanation activity**  
 binary alloys, 312-15  
 catalysts derived from binary and ternary intermetallics, 305-315  
 effect of sulfur, 190,192-94  
 ternary alloys, 315
- Methane**  
 reaction with ammonia on Rh, 183-84  
 synthesis over Ru catalysts, 188-94
- Methanethiol on the Pt(111) surface,**  
 sequential dehydrogenation, 202-6
- Methanol, reaction with coadsorbed oxygen on Pd(100),** 172-75
- Methanol-synthesis catalyst,** 21-23
- Methanol-synthesis catalyst precursor,** 351-60
- Methoxylation of silica, effects,** 460
- Microanalysis**  
 Cu-ZnO methanol-synthesis catalyst precursor, 351-60  
 small particles, 333,335
- Microdiffraction in a STEM instrument,** 335-37,338f
- Microfaceted region of a gold crystal,** 345,348f
- Microreactor, medium pressure, coupled to a vacuum system,** 125,126f
- Mineral aurichalcite**  
 bright-field images, 358f  
 electron diffraction pattern, 357-58f  
 electron micrographs, 353f,357-59f
- Minireactor and reaction interface, reactor and surface analysis system,** 18,20f
- Mobilities, metal precursors**  
 catalyst pretreatment, 298  
 determination, 296
- Model**  
 molecular adsorption, hydrogen on Rh, 74  
 vs. plant catalysts, hydrodesulfurization activity, 8f
- Molecular adsorption**  
 EMIRS and SNIPTIRS studies, 562-64  
 hydrogen on Rh, 74
- Molecular characterization, reactions at glassy carbon electrodes,** 587-94
- Molecular-oxygen coverage on silver, selective epoxidation of ethylene,** 214,216
- Molecular surfaces,** 111-22
- Molecules**  
 having a lone pair orbital, bonding to a metal, 399f  
 sticking probability, 226-29
- Molybdenum, crystal surface, kinetics of thiophene hydrodesulfurization,** 158,160-61
- Molybdenum catalysts, hydrodesulfurization activity,** 8f
- Molybdenum-Co-alumina hydrodesulfurization catalysts,** 422-34
- Molybdenum disulfide, LEISS,** 137-38
- Monocrystal plane, PdCu(111),** 272
- Mordenite, structure,** 510f
- Morphology studies, catalysts,** 140-42
- Mossbauer absorption intensities, as a function of energy,** 519-20
- Mossbauer cell,** 7f
- Mossbauer characterizations, Fe-zeolite and Fe or Ru on doped-carbon catalysts,** 498-516
- Mossbauer effect spectroscopy, oxygen electrocatalysts involving transition metal macrocycles,** 539,543-48
- Mossbauer parameters**  
 nuclear energy states of Fe-57, 503f  
 sulfided catalysts, 11f
- Mossbauer spectroscopy**  
 background on the principles, 499  
 hydrodesulfurization catalysts, 4-5  
 iron catalysts, 506f,515f  
 sulfided catalysts, 12f  
 supported iron oxide particles, 518-32  
 theory, 518-21
- Motional state of benzene, phase diagram,** 496f
- Multiply twinned particle, gold,** 348f

- Multitechnique characterization of supported metals, 374-83
- N
- Nafion-Pt-CdS systems, surface spectroscopy, 566-73
- o-Naphthoquinone, on a glassy carbon surface, 590
- Near-edge X-ray absorption fine structure spectroscopy ethylidyne and ethylene, 207f thiomethoxy and thioformaldehyde, 205f
- Nickel surface concentrations effect on methanation activity, 312-15 untreated and oxidized alloys, 307-12 surface structure, 229-31 use in scattering of hydrogen and deuterium molecules, 224-26, 228f
- Nickel-CO, coverage and secondary ion yield relationship, 321, 323-24, 326f
- Nickel-Cu alloy surfaces, reactions, 324-25
- Nitric oxide adsorbed on 2% Co-alumina, IR spectra, 424f adsorbed on CoMo-alumina catalysts, IR spectra, 426-27f, 429f decomposition on metals, 179-82 isotopes adsorbed on 2% Co-Aero 1000 alumina, IR spectra, 424f reaction with CO on Pt, 181, 183 reactions on metals, 178
- Nitrogen bases, preadsorbed, effects on the exposure of Co and Mo sites, 428, 430
- Nitrogen dioxide, decomposition on metals, 181-82
- Nitrous oxide, decomposition on metals, 181-82
- Nonideality of an alloy, description, 268
- Nuclear magnetic resonance spectra benzene-d<sub>6</sub> in (Cs,Na)X, 488f polycrystalline benzene-d<sub>6</sub>, 486 solid state, for Na, 92, 96f
- O
- Off-axis reaction cell, catalyst system studies, 40-42
- One-dimensional model, bridged-to-linear CO conversion, 413f
- Osmium-Cu clusters, 255-61
- Oxidation of ascorbic acid cyclic voltammetry, 592-94 at glassy carbon electrodes, electrochemical features, 585-87 o-quinones, 587 CO on Pt, 464-69 electrocatalytic, EMIRS studies, 556-59, 561f
- Oxidation catalysts, selective, 26-35
- Oxide ions in bismuth molybdates, identification, 33-35
- Oxidized binary alloys, surface and bulk characterizations, 307-10
- Oxygen adsorption and oxidation, SIMS cluster ion characterization, 319-21 Auger map, catalyst following single reduction, 51f interactions and reactions on Pd(100), 165-76 reduction, 535-36
- Oxygen electrocatalysts involving transition metal macrocycles, spectroscopic studies, 535-49
- Oxygen-Ti Auger signal ratio, TiO<sub>2</sub> single-crystal and powder surfaces, 98-108
- P
- Packing effects, carbon clusters, 112
- Palladium on carbon, characterization by analytical electron microscopy, 366, 368, 369f crystallite size and dispersion data, 380t oxygen interactions and reactions on, 165-76 supported on alumina and silica, STEM and TPD analyses, 377, 380
- Palladium catalysts, diffraction studies, 389
- Palladium-Cu(111) monocrystal plane, 272
- n-Paraffins over Te-NaX aromatics, 88-96 dehydrocyclization, 94, 96f
- Particle, small, electron microscopy and diffraction techniques, 329-39



- Particle morphology, effect of gas environment and chemical impurities, 345,347,348f
- Particle size distribution  
ferric oxide in ZSM-5, 509f  
magnetite particles, 526
- Particle surfaces  
atomic imaging, 341-48  
effect of geometry on catalysis, 345-48
- Peak positions in imaginary response functions for Rh-silica, 75f,76f
- Peak ratios, X-ray photoelectron spectroscopy of CdS in Nafion, 573t
- Peroxide pathway, oxygen reduction, 536
- Phase composition and catalytic behavior, Bi-Fe molybdates, 29-33
- Phase diagram, motional state of benzene, 496f
- o*-Phenylenediamine-derivatized glassy carbon surface, 591f
- Phonon interaction, direct inelastic scattering of diatomic molecules, 226
- Phonon spectra, effect of water adsorbed on aerosil, 459-60
- Phosphoric acid fuel cell, 575-76
- Photoacoustic effect from solids, spectroscopic application, 450
- Photoacoustic signal, definition, 450
- Photoacoustic spectroscopy  
comparison to transmission spectroscopy, 451t  
IR, silica and alumina, 449-61  
transition metals supported on alumina, 381-83
- Photoelectron, wave vector, 254
- Physical adsorption of CO on silica, 415-20
- Physicochemical characterization, catalysts derived from intermetallics, 306-7
- Pilot plant reactor-surface analysis system  
applicability, 24-25  
for catalyst studies, 15-25  
schematic, 17f
- Plant catalysts, poisoned, hydrodesulfurization activity, 7-8f
- Platinum  
agglomeration and dispersion  
  . measured by ion scattering, 139f  
alloying with Cu, 274-76  
bulk and surface atoms, thermal motion, 283,285,287f  
CO oxidation, 464-69  
cluster reactions with benzene, time-of-flight mass spectra, 120,121f  
crystallite size and dispersion data, 376t  
crystallite size and mass distribution, 379f  
effect on rutile(100) single-crystal surfaces, 98-108  
effect on TiO<sub>2</sub> powder surfaces, 98-108  
Fourier transforms of EXAFS data, 283,284f  
supported on alumina and silica, STEM and TPD analyses, 376-77  
surface reactions at low and high pressures, 177-83  
thermal reduction, 576  
Platinum-aluminum oxide catalyst, 63  
Platinum-bimetallic catalysts, surface chemistry and catalysis, 267-78  
Platinum-CdS-Nafion systems, surface spectroscopy, 566-73  
Platinum catalysts  
  determination of the atomic and electronic structure, 280-92  
  difference pattern, 387-88  
  diffraction pattern, 387-89  
  edge resonance, 286-89  
  electronic dipole transitions, 285  
  Fermi energy, 289  
  Fourier transforms of EXAFS data, 283,284f  
  L-edge resonance, 286-89  
  XANES, temperature effects, 286  
Platinum-Cu system, electronic structure changes, 269,271  
Platinum foil, L-absorption edges, 284f  
Platinum-Ir clusters, 262-64  
Platinum-Pd supported on alumina, STEM and TPD analyses, 381  
Platinum-Re catalysts, 57,60,63  
Platinum-Re-alumina catalysts, 60,63  
Platinum-Ru bimetallic clusters, silica-supported, structure, 294-25  
Platinum(111) surface  
  ethylene adsorption and decomposition, 206-8  
  hydrogen sulfide adsorption and decomposition, 200-202  
  sequential dehydrogenation of methanethiol, 202-6  
Platinum-Sn catalyst, description, 59  
Platinum-Sn-alumina catalyst, schematic, 61f  
Platinum-Ti alloys, surface chemistry, 577-80  
Poisoning, arsenic, hydrodesulfurization catalysts, 2-13

- Polycrystalline benzene-d<sub>6</sub>, deuterium NMR spectrum, 486
- Poly(methyl methacrylate), solution deposition on Cr, 444-45
- Potassium-modified iron powder, X-ray photoelectron spectra, 129-32
- Potential energy diagram  
hydrogen molecule interacting with a solid surface, 234f  
Lennard-Jones, 224
- Preadsorbed nitrogen bases, effects on the exposure of Co and Mo sites, 428, 430
- Precursor interactions, support metal, effect on the surface composition of supported bimetallic clusters, 294-304
- Precursor mobilities, metal catalyst pretreatment, 298  
determination, 296
- Pressure  
of ethylene, effect on rate of ethylene epoxidation, 214, 215f  
of oxygen, effect on rate of ethylene epoxidation, 214, 215f  
of reactants  
effect on ammonia synthesis, 156t  
hydrodesulfurization  
dependence, 161t
- Product distribution, thiophene hydrodesulfurization, 161t
- Promoters, air cathodes, 576
- Propylene  
amoxidation over Bi-Fe molybdate, 31f  
selective oxidation and amoxidation, 28
- Proton-donor function, hydroxyl group on silica, 300-301
- Pulsed cluster source, 112, 113f
- Pulsed molecular-beam experiments, CO oxidation on Pt, 465-66
- Q
- Quadrupole splitting, Mossbauer spectroscopy, 502
- Q-Quinones, oxidation of ascorbic acid, 587
- R
- Radiant heat reactor, schematic, 39f
- Raman data, Bi-Fe molybdates, 31t
- Raman experiments, selective oxidation catalysts, 27
- Raman spectra  
bismuth molybdates, 34t  
surface enhanced, oxygen electrocatalysts involving transition metal macrocycles, 539-42
- Rate expressions  
Langmuir-Hinshelwood, 178  
reoxidation of bismuth molybdate catalysts, 28
- Reaction and adsorption at metal surfaces, SIMS studies, 317-26
- Reaction cell, off-axis, catalyst system studies, 40-42
- Reaction dynamics and surface structure in catalysis, 222-36
- Reaction interface and minireactor, reactor and surface analysis system, 18, 20f
- Reaction intermediates, studies using carbon-14 tracers, 89-91
- Reaction kinetics, selective epoxidation of ethylene, 214-16
- Reaction rate coefficient, definition, 178
- Reactor, sample, 7f
- Real response function, 68, 73f
- Rearrangement of hydrocarbons over surfaces, 185-97
- Recoilless fraction, definition, 543
- Redox behavior of 1,4-dihydrobenzene, glassy carbon electrodes, 584f
- Redox processes and solid state transformations, bismuth molybdates, 28-29
- Reduced catalysts, Re ESCA spectra, 64f
- Reduction  
oxygen, 535-36  
TiO<sub>2</sub>, 107
- Reduction and sulfidation  
behavior, Co catalysts, 144-51
- Reflection-absorption at a metal surface, 552
- Reflection electron microscopy, study of small particles, 334
- Relative surface concentrations, hydrodesulfurization catalysts, 6t
- Relaxation time, superparamagnetic clusters, 501
- Reoxidation of bismuth molybdate catalysts  
activation energies, 28t  
rate expression, 28
- Rhenium  
crystal surfaces  
kinetics of ammonia synthesis, 157  
structure sensitivity of ammonia synthesis, 158

Rhenium--Continued

- ESCA spectra for reduced catalysts, 64f
- 4f peak of catalysts, 62f, 64f
- in reduced bimetallic catalysts, valence state, 57-65
- Rhodium, surface reactions at low and high pressures, 177-83
- Rhodium catalysts
  - 3d peaks, 61f
  - hydrogen adsorption and desorption isotherms, 71f
  - preparation, 69, 295-96
  - properties, 69t
- Rhodium-Cu clusters, 261-62
- Rhodium-Ir clusters, 264-65
- Rotation, hindered, adsorbed molecules, 398
- Ruthenium catalysts
  - hydrocarbon synthesis and rearrangement reactions, 185-97
  - preparation, 295-96
  - silica-supported, catalyst and surface composition, 296-99
- Ruthenium-Cu catalysts
  - EXAFS data, 258f
  - EXAFS envelope functions, 259f
  - X-ray absorption spectrum, 256f
- Rutile(100) single-crystal surfaces, effect of Pt, 98-108

## S

- Sample-transfer system, reactor and surface analysis system, 16, 17f
- Saturation magnetization for an entire array of particles, 521-22
- Scanning Auger microprobe analysis, untreated catalyst, 49, 50f
- Scanning electron microscopy, CdS films, 570, 571f
- Scanning reflection electron microscopy, study of small particles, 334-35
- Scanning transmission electron microscope (STEM) analyses
  - catalysts, 362
  - microdiffraction, 335-37, 338f
  - Pd supported on alumina and silica, 377, 380
  - Pt supported on alumina and silica, 376-77
  - small particles, 331-32, 333f
  - supported metals, 374-83
  - transition metals supported on alumina, 381-83
- Scattered intensity of hydrogen and deuterium molecules scattered from Ni, 224-26, 228f
- Scattered ion intensity, definition, 135, 137
- Scavenging of oxygen dependence, 175-76
- description, 166
- Secondary electron micrograph catalyst following single reduction, 51f
- untreated catalyst, 50f
- Secondary ion mass spectroscopy (SIMS) adsorption and reaction at metal surfaces, 317-26
  - cluster ion characterization during oxygen adsorption and oxidation, 319-21
  - clusters for the Ni(100)-CO system, intensities, 326t
  - coadsorption and decomposition reactions at metal surfaces, 325-26
  - depth profile, Pt on oxidized Ti, 83, 85f
  - general discussion, 317-18
- Secondary ion yield and coverage relationship, Ni(100)-CO, 321, 323-24, 326t
- Selective epoxidation of ethylene catalyzed by silver, 210-20
- Selective oxidation and ammoxidation, propylene, 28
- Selective oxidation catalysts preparation, 27
  - spectroscopic measurements and catalytic behavior, 26-35
- Sequential dehydrogenation of methanethiol on the Pt(111) surface, 202-6
- Sheet aluminosilicates
  - idealized compositions, 475t
  - intercalates of, role in heterogeneous catalysis, 472-83
  - structure, 474f
- Shockley partial dislocation, gold(111), 343, 344f
- Silica
  - difference spectra, 454f
  - hydroxyl group
    - proton-donor function, 300-301
    - stretching and bending modes, 452, 455
  - IR photoacoustic spectroscopy, 449-61
  - thermal diffusion lengths, 450
- Silica-supported Cu and Ru-Cu catalysts
  - EXAFS data, 258f
  - EXAFS envelope functions, 259f
  - Silica-supported metals, multitechnique characterization, 374-83

- Silica-supported Os-Cu catalyst, contributions of backscattering atoms to EXAFS, 260f
- Silica-supported Pt-Ir catalyst, X-ray absorption spectrum, 263f
- Silica-supported Ru catalysts catalyst and surface composition, 296-99 structure, 294-95
- Silica-supported Ru-Cu catalysts, X-ray absorption spectrum, 256f
- Silicalite, possible model of pore structure, 505f
- Silicate, sheet, principal building block, 473, 474f
- Silicon anode X-ray source, catalyst system studies, 42-46
- Silicon-29 chemical shifts for some sheet silicates, 478t
- Silver-catalyzed selective epoxidation of ethylene, 210-20
- Single-crystal catalysis studies, ultrahigh vacuum apparatus, 187f
- Single-crystal diffraction patterns, statistical information, 337, 339
- Single-crystal studies of the selective epoxidation of ethylene, 210-20
- Single-crystal surfaces chemically modified, 190, 192-97 metals, ammonia synthesis and hydrodesulfurization, 154-64 structure-insensitive reactions, 188-89, 191f structure-sensitive reactions, 190-92
- Small-angle scattering, study of catalysts, 386
- Sodium, solid state NMR, 92, 96f
- Sodium Auger map, catalyst following single reduction, 51f
- Sodium-cation-exchanged clays, IR spectra, 477f
- Sodium zeolites, X-ray photoelectron spectroscopy, 92
- Solid state transformation and redox processes, bismuth molybdates, 28-29
- Spectroelectrochemical cell, IR spectroscopy, 551, 554f
- Spectroscopic measurements and catalytic behavior, selective oxidation catalysts, 26-35
- Spectroscopic studies of oxygen electrocatalysts involving transition metal macrocycles, 535-49
- Spectroscopy metal-titania systems, 80-86 surface, Pt-CdS-Nafion systems, 566-73
- Stark effect, electrochemically activated, 564
- Static chemisorption, 69-72
- Static SIMS Pt on oxidized Ti, 81-83 Ti substrate without a metal overlayer, oxidized, 84, 85f
- Statistical information from single-crystal diffraction patterns, 337, 339
- Sticking probability of molecules, 226-29
- Stoichiometric interconversion of adsorbed CO species, evidence, 410f
- Streak phase, H-Ni(110) system, 229-31f
- Stretch, internal, adsorbed molecules, 401
- Strong-metal-support interactions background, 80-81 chemisorption on CO hydrogenation catalysts, 67068
- Structure-insensitive reactions over clean single-crystal surfaces, kinetics, 188-89, 191f
- Structure-sensitive reactions over clean single-crystal surfaces, kinetics, 190-92
- Structure sensitivity of ammonia synthesis over Re crystal surfaces, 158
- Subtractively normalized interfacial FTIR spectroscopy (SNIFTIRS), 551 absorption bands, 553 molecular adsorption, 562-64
- Sulfidation and reduction behavior, Co catalysts, 144-51t
- Sulfide, promotional effects in catalysis, 430
- Sulfided catalysts Mossbauer parameters, 11t Mossbauer spectra, 12f
- Sulfur effect on ethane hydrogenolysis, 193, 194f effect on methanation, 190, 192-94 effect on thiophene hydrodesulfurization, 162, 163t
- Sulfur-modified metal surfaces, adsorption and decomposition, 199-208
- Superparamagnetic behavior, magnetic particles, 519-20
- Superparamagnetic clusters magnetic moments, 499-501 relaxation time, 501
- Superparamagnetically relaxing particles, energy in an applied field, 521

- Supported bimetallic clusters, effect of support-metal precursor interactions, 294-304
  - Supported iron oxide particles, characterization using Mossbauer spectroscopy and magnetic susceptibility, 518-32
  - Supported metal catalysts
    - diffraction, 385-89
    - effect of dilution on dispersion, 298
  - Supported metals, multitechnique characterization, 374-83
  - Surface adsorbates and surface-mediated reactions, FTIR studies, 435-47
  - Surface analysis-pilot plant reactor system, for catalyst studies, 15-25
  - Surface analysis techniques, study of catalyst systems, 37-56
  - Surface area, boundary condition, effect on surface reconstructions and chemisorption, 345
  - Surface characterization and methanation activity, catalysts derived from binary and ternary intermetallics, 305-315
  - Surface chemistry
    - alloys of Pt and Ti, 577-78
    - bimetallic catalysts, 267-78
  - Surface composition
    - general discussion, 268-69
    - silica-supported Ru-Ir bimetallic catalysts, 297
    - silica-supported Ru-Rh bimetallic clusters, 296-97
  - Surface contamination, dependence of time on pressure, 179
  - Surface-enhanced Raman spectroscopy, oxygen electrocatalysts involving transition metal macrocycles, 539-42
  - Surface particle, atomic imaging, 341-48
  - Surface phases, hydrogen, 229-31
  - Surface point groups and selection rules, vibrational analysis, 394-95
  - Surface reactions on clean Pt and Rh at low and high pressures, 177-83
  - Surface restructuring, bismuth molybdate catalysts, 29,30f
  - Surface-sensitive techniques, correlations to SIMS, 317-26
  - Surface sensitivity of catalysts, 137-38
  - Surface SiOH groups, influence of CO physisorption, 417f
  - Surface structure
    - atomic, gold, 342-44
    - oxidized alloys, correlation to CO conversion activity, 312-15
    - and reaction dynamics in catalysis, 222-36
  - Surface studies with IR spectroscopy, 404-19
  - Symmetric carboxylate stretch, cadmium arachidate on silver, 442-43
  - Synthesis of hydrocarbons over surfaces, 185-97
  - Synthetic aurichalcite, electron micrographs, 353f
- T
- Teller-Redlich rule, 394
  - Tellurium-NaX zeolite, aromatics from *n*-paraffins over, 88-96
  - Temperature
    - effect on deuterium NMR spectra of benzene-d<sub>6</sub>-(Na)X, 489-91
    - effect on rate of surface reactions, 235
    - effect on the sticking probability of molecules, 227
    - effect on surface composition of TiO<sub>2</sub>, 101,104
    - effect on XANES of a Pt catalyst, 286
  - Temperature-programmed desorption (TPD) analyses, Pd and Pt supported on alumina and silica, 376-77,380-81
  - Temperature-programmed reaction spectra
    - ethylene and hydrogen on clean and oxygen-covered Pd(100), 167f
    - methanol, formaldehyde, and water following methanol coadsorption on Pd(100), 173f
    - water desorption following methanol and oxygen coadsorption on Pd(100), 174f
    - water and oxygen coadsorption system on Pd(100), 171f
  - Temperature-programmed reduction experiments, CoO catalysts, 148,150f
  - Temperature-programmed sulfidation experiments, CoO catalysts, 149,150f
  - Ternary alloys
    - methanation activity, 315
    - preparation, 306
    - surface and bulk characterization, 310-12

- Thermal desorption  
 CO adsorbed on bimetallic catalysts, 271-73  
 spectra, CO, 83t
- Thermal diffusion lengths, silica and alumina, 450
- Thermal motion, relative mean squared, bulk and surface Pt atoms, 283,285,287f
- Thermal reduction, Pt, 576
- Time-of-flight analysis, CO oxidation on Pt foil, 465
- Time-of-flight mass spectra, Pt cluster reactions with benzene, 120,121f
- Time-resolved IR spectroscopy  
 CO oxidation on Pt, 466  
 problems, 466-67
- Tin-Pt catalyst, description, 59
- Titania-based thin-film catalyst models, preparation, 81
- Titania-metal systems, spectroscopy, 80-86
- Titanium  
 chemical state, characterizations as a function of heat-treatment temperature, 579t  
 in different chemical states, binding energies, 578t  
 interatomic transition, 106  
 oxidation, description, 84  
 oxidized, Auger electron spectra, 82f  
 substrate without a metal overlayer, oxidized, 84,85f
- Titanium dioxide  
 during cleaning procedures, Auger spectra, 100f  
 crystals, characteristics, 101  
 overlayers on Pt, surface chemistry, 577  
 single crystals  
   covered with Pt, characterization by Auger electron spectroscopy, 101  
   preparation, 99
- Titanium dioxide powder catalysts, carbon peak intensities, 104  
 preparation, 99  
 surfaces, effect of Pt, 98-108
- Titanium dioxide promoted Pt catalysts, characterization, 578-79
- Tracers, stable and radioactive applications, 88-89
- Transition metal macrocycles, electrocatalysts of oxygen involving, spectroscopic studies, 535-49
- Transition metals supported on alumina photoacoustic spectroscopy, 381-83  
 STEM analysis, 381-83
- Translation, hindered, adsorbed molecules, 398
- Transmission electron microscopy catalyst characterization, 362  
 study of small particles, 330-31,333f
- Transmission spectroscopy  
 advantages over photoacoustic spectroscopy of powders, 450  
 comparison to photoacoustic spectroscopy, 451t
- Tricobalt-ethylidyne-noncarbonyl, vibrational spectrum, 396f
- Trifluoromethane sulfonic acid, use in fuel cells, 580
- Tungsten-oxygen system, SIMS intensities, 319-21
- Turnover number, selective epoxidation of ethylene, 212,216,219
- Twinning, small particles, 336

## U

- Ultrahigh-vacuum apparatus, single-crystal catalysis studies, 187f
- Ultrahigh-vacuum IR cell, 406f
- Ultraviolet cell developments, 405-7
- Ultraviolet-visible reflectance spectroscopy, oxygen electrocatalysts involving transition metal macrocycles, 537-38
- Unpromoted Fe powder, X-ray photoelectron spectra, 127-29
- Untreated binary alloys, surface and bulk characterization, 307,308f
- Untreated ternary alloys, surface and bulk characterization, 310,311f

## V

- Valence state of Re in reduced bimetallic catalysts, 57-65
- Velocity of adsorption of reactants, effect on rate of surface reactions, 232,235
- Vibrational analysis  
 adsorbed molecules, 392-403  
 principles, 393-96
- Vibrational frequencies and matrix elements, water and ammonia adsorbed on metals, 401-3
- Vibrational properties, water and ammonia adsorbed on Al(100), 398-401

Vibrational spectrum, as a fingerprint, 393-94  
 Vibrational temperature, CO oxidation on Pt, 469

## W

## Water

adsorbed on aerosil, effect on phonon spectra, 459-60  
 chemical bonding to Al(100), 397-98, 399f  
 and hydroxyl groups, reactions with coadsorbed oxygen on Pd(100), 170-71  
 Wave vector, photoelectron, 254  
 Wide-angle diffraction pattern, uses, 386

## X

## X-ray absorption near-edge spectroscopy (XANES)

cobalt compounds, 147f  
 data analysis, 285-92  
 description, 280-81  
 supported metal catalysts, 387  
 X-ray absorption spectroscopy  
 characterization of Co catalysts, 144-51  
 determination of the atomic and electronic structure of Pt catalysts, 280-92  
 Pt-Ir catalyst, 263f  
 Ru-Cu catalyst, 256f  
 X-ray diffraction  
 characterization of supported metal catalysts, 385-89  
 spectra, aurichalcite samples, 355f  
 X-ray emission spectroscopy, catalyst characterization, 364

X-ray photoelectron spectroscopy  
 alumina-supported Cu catalyst, 43f  
 arsenic-poisoned hydrodesulfurization catalyst, 10f  
 CdS in Nafion, 570, 572f, 573  
 Co catalysts, 144-51  
 hydrodesulfurization catalysts, 4  
 NaX and Te-NaX zeolites, 92  
 o-phenylenediamine-derivatized glassy carbon surface, 591f  
 positions and relative intensities of transitions, 44f  
 unpromoted Fe powder, 127-29  
 wide scans, Cu-Al extruded catalyst, 47f  
 X-ray powder diffraction spectra of CdS, 568f  
 X-ray signals, digital imaging, catalytic materials, 365

## Z

## Zeolites

characterization by analytical electron microscopy, 368, 369f  
 dynamics of benzene in X-type, 485-96  
 Zinc, chemical state changes in a catalyst in feed gas, 21, 22f  
 Zinc-Cu ratios, aurichalcite samples, 354t  
 Zinc oxide  
 and Cu particles, dark-field imaging, 356, 359f  
 diffraction spots  
 aurichalcite mineral, 354-60  
 schematic, 358f  
 Zinc oxide-Cu methanol-synthesis catalyst precursor, microanalysis, 351-60